Diagenetic, thermal and provenance histories of the Permian lower Ecca Group based on two newly drilled boreholes in the western and eastern main Karoo Basin, South Africa

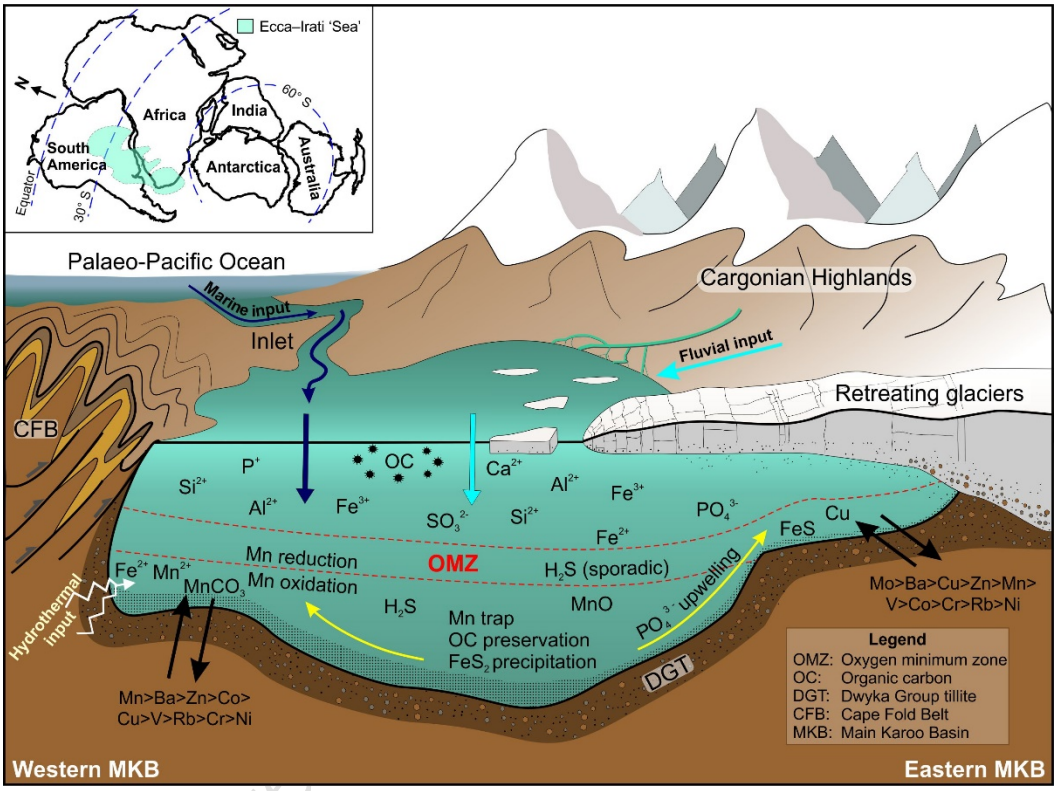

Claire Geel

A thesis submitted to the Faculty of Science, University of Cape Town, in fulfilment of the requirements for the degree of Doctor of Philosophy

July 2020

Supervisor: Associate Professor Emese M. Bordy

DECLARATION

I, *Claire Geel (GLXCLA002)*, hereby declare that the work on which this thesis is based is my original work (except where acknowledgements indicate otherwise) and that neither the whole work nor any part of it has been, is being, or is to be submitted for another degree in this or any other university.

I empower the university to reproduce for the purpose of research either the whole or any portion of the contents in any manner whatsoever.

Signature: Signed by candidate

Date: 29-07-2020.

Acknowledgments

Firstly, I want to thank my PhD supervisor, Associate Professor Emese Bordy, for all her support. She is an outstanding scientist and I am so grateful to have had her as a mentor. She brings a sense of clarity in times of chaos and she taught me to truly believe in myself.

I am grateful for the months I could spend at the drill sites, learning about drill rig operations and all the unexpected and sometimes entertaining events that took place there. I would like to thank Doug Cole for being such a wonderful mentor in the field. Between good laughs and banter, he taught me the fine art of core logging and his advice will stay with me forever. I also want to thank Hermann Lauferts at Shell for being a great mentor and for showing me the high standard that should be expected from all drilling practices.

I would like to thank my international collaborators: Dr Hans-Martin Schulz, Dr Johannes Hermann and Dr Satish Mayanna at the GeoForschungsZentrum (GFZ). Stephan Nolte, Professor Ralf Littke and Dr Alexandra Amann-Hildenbrand at Rheinisch Westfälische Technische Hochschule (RWTH), Aachen, Germany.

I am also thankful to John Compton and Rosalie Tostevin, at the University of Cape Town, for reading through the draft of Chapter 3 and for providing their advice and insight. I also want to thank Professor Peter Booth, a friend and mentor, who is always available for me to ask questions and who also read through some chapters for me.

I want to thank my parents, Gaynor and David, for letting me come home whenever I needed to escape Cape Town to get writing done, and for showering me with endless support and love. My brother Mark, who always inspires me to be the best version of myself and who is always the voice of logic and reason (“If you don’t know, the thing to do is not to get scared, but to learn” -Ayn Rand). I am so grateful to my partner, Wesley Nash, for always supporting my decisions and believing in me. He always reminds me to not take life too seriously and is my soft place to fall when times get tough. I want to thank Claire Browning, my friend and fellow geologist for being my sound board during the hardest times of my PhD (Claire-squared!). I would also like to thank my fellow academics and friends at UCT for always keeping up the morale and who helped me not feel alone on my PhD journey (Miengah Abrahams, Robert Muir, Akhil Rampersadh, Howard Head, Sanda Spelman, Chad Peel and Yambi Dinis).

I would like to thank Professor Nic Beukes and the Karoo Research Initiative (KARIN) at the DST-NRF Centre of Excellence for Integrated Mineral and Energy Resource Analysis (CIMERA), for research funding and for allowing me to be involved with this project from initial borehole siting to the end of the drilling campaign. I would also like to thank Royal Dutch Shell PLC for the PhD sponsorship and for the invaluable internship experience. I would also like to thank the National Research Foundation (NRF) for the Scarce Skills Scholarship and the University of Cape Town for the International Travel Bursary (Sir Robert Kotze Bursary). The funders had no role in study design, data collection and analysis, decision to publish, or preparation of the manuscript. Opinions expressed and conclusions arrived at are those of the author and are not necessarily to be attributed to the DST-NRF Centre for Excellence for Integrated Mineral and Energy Resource Analysis (CIMERA), NRF, Royal Dutch Shell PLC or any other sponsor listed above.

Abstract

Fine-grained sedimentary rocks of the Lower Permian lower Ecca Group in the Main Karoo Basin (MKB) in southern Africa have been identified to form a possible unconventional hydrocarbon reservoir, the gas potential of which is still relatively unknown. The lower Ecca Group is comprised of flysch-like successions of the Prince Albert, Whitehill and Collingham formations, which were impacted by diagenesis as well as contact and regional and metamorphism. Studies of fine-grained sedimentary rocks are notoriously complex as mechanical breakdown and diagenesis result in mineralogical changes and loss of source rock information. Therefore, a variety of analytical techniques are required for their thorough investigation. In this study, we analyse Permian rocks from two boreholes (KZF-1 and KWV-1) that were drilled ~ 830 km apart in the western and eastern MKB, respectively, and compare their composition, thermal maturity and petrophysical characteristics to better assess the hydrocarbon potential of the lower Ecca Group. In addition, whole rock geochemistry is used to reconstruct the palaeo-environment and provenance settings. Lastly, we investigate the influence of shale composition, porosity, well pressure and temperatures on their geomechanical properties such as compressive strength and elastic moduli.

Sedimentary rocks in both boreholes were affected by burial and regional metamorphism (linked to orogenic events), but the sedimentary rocks in BH KWV-1 were also altered by contact metamorphism due to dolerite intrusions in the Early Jurassic. Major mineralogical differences between the boreholes include: 1) Fe-silicate (greenalite); carbonates (rhodochrosite and dolomite) and Mn nodules (birnessite) being found only in BH KZF-1; and 2) metamorphic minerals such as garnet, cordierite, staurolite being found only in BH KWV-1. The results show that these rocks are over mature as evidenced by the low quantity of free hydrocarbons (S1 peak; 0.02–0.06 mg/g) and potential to release hydrocarbons (S2 peak; 0.06–0.14 mg/g) and low hydrogen index (HI) values (2.40–167 mg HC/g TOC) from Rock Eval pyrolysis accompanied with high vitrinite/bitumen reflectance (BH KZF-1 is VR_o= 4 and BH KWV-1 is BR_o= 5). The total organic carbon (TOC) content is the highest in the Whitehill Formation in both boreholes (BH KZF-1: 5.17 wt%; BH KWV-1: 4.87 wt%). Burial diagenesis significantly reduced interparticle porosity and most of the measurable porosity comes from intraparticle nano-pores confined to organic matter

and dolomite. Meso- and macro-porosity are limited to phyllosilicates, pyrite framboids and microfractures.

The Chemical Index of Alteration (CIA) is highest for the Prince Albert Formation (72–78) as the palaeo-environment changed from an ice-house to a green-house, post-glacial period in southern Gondwana. Enrichment of trace elements in BH KZF-1 and BH KWV-1 are in order: Mn > Ba > Zn > Co > Cu > V > Rb > Cr > Ni; and for BH KWV-1: Mo > Ba > Cu > Zn > Mn > V > Co > Cr > Rb > Ni. Geochemical proxies used in determining levels of anoxia were: V/Cr, V(V+Ni), Ni/Co and Fe-S-TOC plots. Salinity was deduced using Rb/K ratios and with identification of potential benthic foraminifera and minerals such as apatite, birnessite and phosphate nodules, which are assumed to be syn-sedimentary in origin. Overall, the geochemical results indicate that the depositional conditions fluctuated with respect to anoxia, salinity levels, and that while the sedimentation rates were low and the bio-productivity level was high, at least episodically.

Provenance was investigated using Discriminant Function Diagrams, Principle Component Analysis Results (PCA), Zr/Ti ratios and the Index of Compositional Variability (ICV). Results indicate that the Prince Albert and Whitehill formations in the western MKB comprises sediment that was mostly sourced from the Cambrian to Late Carboniferous Cape Granite Suite, Cape Supergroup, the Dwyka Group and possibly the Precambrian Kango Group (Saldania Belt) and/or the Namaqua-Natal Belt. The Prince Albert and Whitehill formations in the eastern MKB have a mafic signature, indicating that these sediments may have been derived from the Permo-Carboniferous Dwyka Group, Precambrian Kaapvaal Craton, Natal Belt (Tugela Terrane), Natal Group and the Pan-African Mozambique and Maud Belts. The mudstone and wackes in the Collingham Formation were mostly sourced from the quartz-arenites and granites that were most likely associated with the Cape Fold Belt, the orogen immediately adjacent to and largely coeval with the MKB.

Geomechanical results from BH KZF-1 show that the lower Ecca Group has a high proportion (~ 50–70 vol%) of mechanically strong minerals (e.g., quartz, feldspar, pyrite), ~ 30–50 vol% weak minerals (e.g., clay, organic matter) and up to ~ 0–50 vol%, highly variable, intermediate components (e.g., carbonates). Constant strain rate deformation experiments ($T \leq 100$ °C; $p \leq 50$ MPa) and compressional tests performed perpendicular and parallel to bedding show that the Prince Albert Formation is the strongest and most brittle followed by the Collingham Formation and then the Whitehill Formation. Triaxial compressive strength as well as static Young's

moduli increased with increasing hard minerals and decreased with increasing mechanically weak minerals and porosity. On comparison with European and American shales, the shales in the lower Ecca Group are geomechanically stronger and more brittle, and thus may allow for fracture propagation without rock breakdown under pressure.

The lower Ecca Group varies from the western to the eastern MKB in mineralogy, thermal maturity, palaeo-depositional environment and provenance. These observations directly challenge the previous assumptions that these black shales were deposited under predominantly anoxic conditions. Indeed, during deposition, the levels of anoxia appear to have been inconsistent across the MKB and were likely dependent on the changing primary bio-productivity levels, sedimentation rates and basin morphology. Neither borehole contained significant gas, likely due to degasification by dolerite intrusions in the Early Jurassic and structural deformation during syn- and post-Karoo times. In summary, this study quantitatively confirms that the lower Ecca Group has the potential to be an easily frackable, unconventional shale gas reservoir. However, this study also attests to the compositional and geomechanical complexity of these Karoo rocks, and this inevitably translates to a gas potential that is expected to vary significantly across the basin.

Table of Contents

1 Introduction

1.1 Motivation and aims

Historically, the study of fine-grained sedimentary rocks did not advance as rapidly as the study of coarser grained lithologies, among others due to low economic interest in the former group (Schieber, 2001). However, after the turn of the millennium, shale gas completely transformed the global energy market, which in turn re-directed research interests. With the development of directional drilling and hydraulic fracturing (fracking), natural gas extraction became profitable and spurred on relevant research. Shale gas is either biogenic, thermogenic, or mixed and is stored in nanometer sized pores or adsorbed to mineral surfaces within fine-grained source rocks. Although it is termed “shale gas”, the host rock types are not just ‘shale’ but a variety of lithologies from mudstones to limestones and marls (Fishman et al., 2011). In this study, the term used for all fine-grained sedimentary rocks that are finer than 0.0625 mm is “mudstone”, whereas “shale” is used to describe a mudstone that has fissility (e.g., Macquaker & Adams, 2003; Potter el al., 2005; Lazar et al., 2015).

High prospectivity and production of shale gas is expected from rocks with the following chief characteristics: 1) fine-grained and deposited most commonly in marine settings (Horsfield et al., 2018, p.7); 2) originally rich in organic matter (OM; > 2 wt% TOC); 3) maturity of > 1.2 % vitrinite reflectance; 3) contain significant silica content (> 30 %) with some non-swelling clays and carbonates; 4) contain 4–7 % porosity down to the nanoscale; 5) display less than 1000 nanodarcy permeability; 6) slightly to highly over-pressured; 7) found at depths < 4000 m; 8) have known principle stress fields, which allow for fracking and 9) can be drilled away from structural deformed zones (e.g., faulted/folded successions; Jarvie et al., 2007; Slatt & O’Brien, 2011; Jarvie, 2012; Bernard & Horsfield, 2014; Horsfield et al., 2018). Examples of shale gas plays that exhibit these characteristics are the Barnett, Bakken and Marcellus Shale in the USA. These plays occur in foreland basin settings and were deposited in anoxic marine environments (Curtis, 2002; Jarvie; 2012; Hill et al., 2007).

The main Karoo Basin (MKB; Figure 1.1) covers nearly 600 000 km^2 of southern Africa and is regarded as an intracratonic, retro-arc foreland basin (Tankard et al., 2012) comprising ~ 130 million years of mainly clastic sediment accumulation (from ~ 312 to ~ 183 Ma; e.g., Bangert et al., 1999; Catuneanu et al., 1998, 2005; Johnson et al., 2006; Isbell et al., 2008; Milani & de Wit, 2008; Duncan et al., 1997). The MKB was

formed adjacent the Cape Orogen, known as the Cape Fold Belt (CBF), which once formed part of the greater Pan-Gondwanian Mobile Belt (de Wit & Ransome, 1992).

In the last 10 years, the organic-matter-rich shale of the lower Ecca Group of the Karoo Supergroup has become an attractive target for potential shale gas exploration. Initially, a prospective area of between 155 000 and 183 000 km^2 was calculated to contain ~ 500 trillion cubic feet (Tcf) of potential gas (Kuuskraa et al., 2011). However, a more realistic range of between ~ 79 000 and 92 000 km^2 with only ~ 14 to 172 Tcf has been suggested in more recent studies (Decker & Marot, 2012; Cole, 2014; Geel et al., 2015). The stratigraphic units of particular interest are the Prince Albert, Whitehill and Collingham formations. For the sake of simplicity, these three formations will be referred to as the lower Ecca Group from here on, even though this is not a formal stratigraphic designation. Understanding the evolution of the MKB with respect to changes in its tectonic and palaeo-environmental depositional conditions, as well as the burial history and the petrophysical properties of its contained sedimentary rocks, including the lower Ecca Group, is critical in constraining the reservoir potential in these Permian rocks.

Deposition in the MKB began in the Late Carboniferous, when southern Gondwana was covered by 70 000 km^2 of ice-sheets, and when a polyphase deglaciation resulted in the widespread Permo-Carboniferous diamictite (Dwyka Group; Crowell, 1978; Visser, 1993). The final deglaciation event in the southern MKB occurred ~ 290 Ma (Bangert et al., 1999) when the MKB turned into an extensive inland lake, sometimes referred to as the “Karoo Sea”, the “Ecca Sea”, the “Whitehill Sea” or the “Mesosaurus Inland Sea” (e.g. Oelofsen,1986, 1987; Werner, 2006). For sake of consistency, this study will refer to this inland body of water as the “Ecca Inland Sea” to emphasize the fluctuating salinity levels within it. It will be referred to as the “Whitehill-Irati Sea” when discussing its connection within Gondwana. The lower Ecca Group represents the initial Permian basin filling phase of the MKB and comprises mostly mudstones and subordinate siltstones and fine-grained sandstones. The entire Ecca Group in the southern MKB forms large, upward-coarsening successions where the older fine-grained mudstone-dominated part is succeeded by siltstones and sandstones. This temporal facies change resulted from the gradual filling up of the southern MKB in the Permian and is linked to evolving depositional conditions that changed from being characterized by deeper water, turbiditic (deep-water fans; Figure 1.2 B) to shallower water, deltaic systems plain, delta front and pro-delta environments (e.g., Visser & Loock, 1978; Smith et al., 1990; Catuneanu et al., 2002). The deposition of the Ecca Group was followed by that of the Beaufort, Stormberg

and Drakensberg Groups, which together comprise the Karoo Supergroup (Johnson et al., 2006). Karoo sedimentation came to an end during the Early Jurassic (183 Ma) with the emplacement of the Toarcian Karoo continental flood basalts and associated dolerite intrusions (sills and dykes; Figure 1.1), which heralded the subsequent break-up of Gondwana (Duncan et al., 1997; Catuneanu et al., 1998; Muir et al., 2020).

The lower Ecca Group has high TOC content, especially the Whitehill Formation (up to 17 wt%; e.g., Rowsell & De Swart, 1976; Cole & McLachlan, 1991; Cole, 2014; Chukwuma & Bordy, 2016). It is generally accepted that the mudstones of the lower Ecca Group accumulated under anoxic conditions allowing for the preservation of their OM content (Smith, 1990; Cole, 1992). However, opinions still differ over prevailing environmental and climatic conditions during the time of their deposition (McLachlan & Anderson, 1973; Anderson & McLachlan, 1977; Oelofsen, 1987; Visser, 1992; Faure & Cole, 1999; Scheffler et al., 2006; Geel et., 2015; Chukwuma & Bordy, 2016). Polarizing opinions on the conditions required for the preservation of organic-matter-rich mudstone are not limited to the MKB. Many authors believe that anoxic conditions are required for the preservation of OM, while others suggested that high productivity of OM in the water-column should be sufficient (e.g., Calvert, 1987; Oschmann, 1991; Calvert & Pedersen, 1992; Macquaker & Gawthorpe, 1993; Schieber, 2001).

Other points of controversy regarding the early sedimentation in the MKB are related to: a) salinity levels in the MKB (i.e., fully marine or brackish) and b) the spatial and temporal extent of the connection between the southern MKB and the global Permian Oceans (i.e., Palaeo-Pacific Ocean; e.g., McLachlan & Anderson, 1973; Anderson & McLachlan, 1979; Oelofsen, 1986; Veevers et al., 1994; Faure & Cole, 1992; Scheffler et al., 2006; Geel et al., 2015; Herbert & Compton, 2007; Götz et al., 2017). The latter point would have ramifications for the origin of the well-documented transgressive events in the early MKB, which, to-date, are contested for their eustatic origin (e.g., Catuneanu et al., 2002; Götz et al., 2017; Cole & Barbolini, 2019). Martin & Wilczewski (1970) suggest that marine invasion in the MKB occurred from the final Dwyka to pre-Whitehill depositional period, after which the MKB was no longer connected to the global ocean. Fossils such as palaeoniscoid fish, bivalves, brachiopods, putative cephalopods (McLachlan & Anderson, 1973), foraminifera, sponge spicules, radiolarians, acritarchs (Visser, 1994), possibly sharks (Oelofsen, 1986), free-swimming reptiles (mesosaurids) and benthic crustaceans have been found in the lower Ecca Group (McLachlan & Anderson, 1973; Anderson & McLachlan, 1979; Faure & Cole, 1999; Almond, 2008; Chukwuma & Bordy, 2016).

However, except for those detected near the base of the Prince Albert Formation, these fossils have no definite marine affinity (John Almond, personal comms 2020) and therefore the degree of salinity in the MKB through most of the lower Ecca depositional phase is irresolute on palaeontological grounds as well.

The developing orogenic front of the Cape Orogen (CFB) and the dynamics of flexural tectonics within the MKB controlled the early drainage across southern Gondwana (Visser, 1987; Smith et al., 1993; Catuneanu et al., 1998). It is thought that most of the sediment encompassed in the southern Ecca Group was derived from the CFB situated to the south and west of the MKB (e.g., Ryan, 1967; Ryan & Whitfield, 1979; Hälbich et al., 1983; Cole, 1992; Wickens, 1994; Scott, 1997; Catuneanu et al., 1998). The provenance study of fine-grained sedimentary rocks is complicated as chemical and mechanical break-down can severely alter grains from their original parental assemblages (Weltje & Eynatten, 2004). This can result in environmental and diagenetic biases (Garzanti, 2016). Analysing the major and trace element geochemical composition of sedimentary rocks, especially in conjunction with other sedimentological proxies (e.g., palaeo-current measurements) has become a robust technique in identifying regions of provenance. However, the biases needed to be taken into consideration and an integrated approach to provenance diagnosis is important. Investigating the provenance regions of the lower Ecca Group will assist in the accounting for the nuanced differences in the composition and other, economically important properties (e.g., porosity, permeability, brittleness) of these rocks, which were deposited in the vast sedimentary basin of the MKB.

Post-depositional deep burial increased the thermal maturity of the lower Ecca Group allowing the development of hydrocarbons (e.g., Rowsell & De Swart, 1976). The gas potential of the MKB has been known since the 1960s when the South Africa National Oil and Gas Agency, Southern Oil Exploration Company (SOEKOR, presently PetroSA) conducted country wide exploration. Dry gas (e.g., methane) was detected from boreholes in the southern MKB (Leith, 1970; Rowsell & De Swart, 1976). The intrusion of lower Jurassic dolerite may have contributed to the degassing of the basin and gas escape structures such as hydrothermal vents and breccia pipes have been observed across the southern MKB (Svensen et al., 2007; Harris et al., 2019). The intrusion of the dolerite has thermally destroyed potential for adjacent shale to form gas (Svensen et al., 2007). The dolerite-free region within the MKB falls south of latitude 32° 30’S (Cole et al., 2011), however, especially in the southern part of this region, the impact of the Cape Orogeny and thus the northward propagating deformational front of the CFB caused the overmaturation of the lower Ecca shales

(i.e., vitrinite reflectance values between 3 and 5 %; Rowsell & De Swardt, 1976; Branch et al., 2007; Geel et al., 2015; Smithard et al., 2015; Nolte et al., 2019).

Investigating the lower Ecca Group in two boreholes, drilled about 830 km apart, in the western and eastern MKB (Figure 1.1), this study intends to assess the geological evolution of these two regions, including the syn-depositional (e.g., marine or lacustrine, temperate or cold, anoxic or oxic) and post-depositional (e.g., metamorphic) conditions, and their influence on natural gas exploration. Furthermore, this study also aims to highlight the petrophysical characteristics (i.e., TOC, porosity, permeability, maturity, Young's modulus, brittleness) of these organic-matter-rich rocks and their bearing on the shale-gas potential of the lower Ecca Group in the MKB. With a focus on the hydrocarbon potential of the OM-rich sedimentary rocks of the Lower Permian Prince Albert, Whitehill and Collingham formations, this study covers the following three main themes:

1) the effect of burial diagenesis and metamorphism on the petrophysical characteristics of the OM-bearing rocks based on sedimentology, petrography and geochemistry;
2) the palaeo-environments and sediment provenance based on major and trace element geochemistry; and
3) the geomechanical properties and their influence on the hydraulic fracturing of the OM-bearing rocks based on petrophysics and rock mechanics.

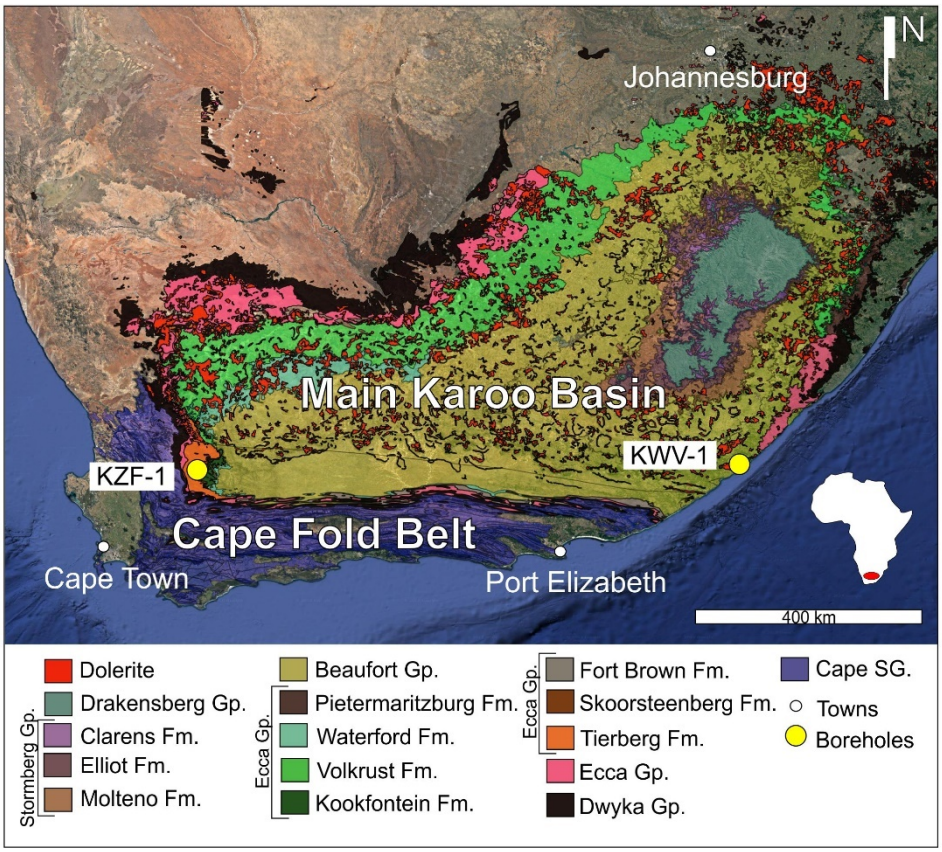

Figure 1.1: Simplified geological map of South Africa showing the surface exposures of Karoo Supergroup of the main Karoo Basin (MKB). The MKB is bounded by the Cape Supergroup of the Cape Fold Belt (CFB) to the southwest and the south. BH KZF-1 is located in the Tankwa Karoo Sub-basin and BH KWV-1 in the eastern MKB. Abbreviations: SG = Supergroup; Gr = Group; Fm = Formation.

1.2 Technical background of the KARIN Project

Founded in 2014, the Karoo Research Initiative (KARIN) is a South African academic project dedicated to reconstructing the depositional history and deep structure of the MKB and to determine physical and petrochemical characteristics of its organic-matter-rich shale deposits via modern scientific methods (Beukes et al., 2015). In addition to collaboration among the project-initiating South African universities (e.g., University of Cape Town, University of Johannesburg, University of Pretoria), KARIN also involves collaboration with international universities (e.g., Keele University in the United Kingdom, Technische Universität Darmstadt in Germany). Currently, KARIN forms part of the NRF-DST Centre of Excellence for Integrated Mineral and Energy Resource Analysis (CIMERA; Beukes et al., 2015).

Under the auspices of KARIN, two deep boreholes were drilled (Figures 1.1; 1.2; 1.3) by Geoserve Exploration Drilling (Pty) Ltd.: BH KZF-1 (32°50’30.43” S, 19°44’33.02” E) and BH KWV-1 (32°14’43.10” S, 28°35’08.10” E), in the western and eastern MKB,

respectively. The main purpose of these deep boreholes was to collect primary research data via modern geoscientific techniques in line with the project aims of KARIN. During drilling blow-out prevention was installed, both boreholes were monitored for possible gas shows, and cores were sampled and tested for desorbed and residual gas (Figure 1.2 D, E; de Kock et al., 2016). No gas was detected during drilling and the desorbed gas content of the samples was very low. Residual gas content was mostly methane in negligible quantity (0.00–0.74 m3/t). Drilled to 671 m depth, BH KZF-1 intersected thrust faults, which led to the structural duplication of strata. Drilled to 2353 m depth, BH KWV-1 intersected 19 dolerite sills (Figure 1.3).

Cores from both boreholes were sedimentologically and geotechnically logged by me, Doug Cole, Alec Birch and Haaijera Mosavel, at centimetre- to decimetre-scale on site in 2015 to 2016 and are now stored in the Donkerhoek Core Library of the Council for Geoscience in Pretoria. The most organic-rich intervals of the cores (i.e., the Whitehill Formation) are preserved in plastic casings (Figure 1.3 B) to delay subaerial weathering of sulfides to sulfate (gypsum) as observed in weathered outcrop (Figure 1.2 C).

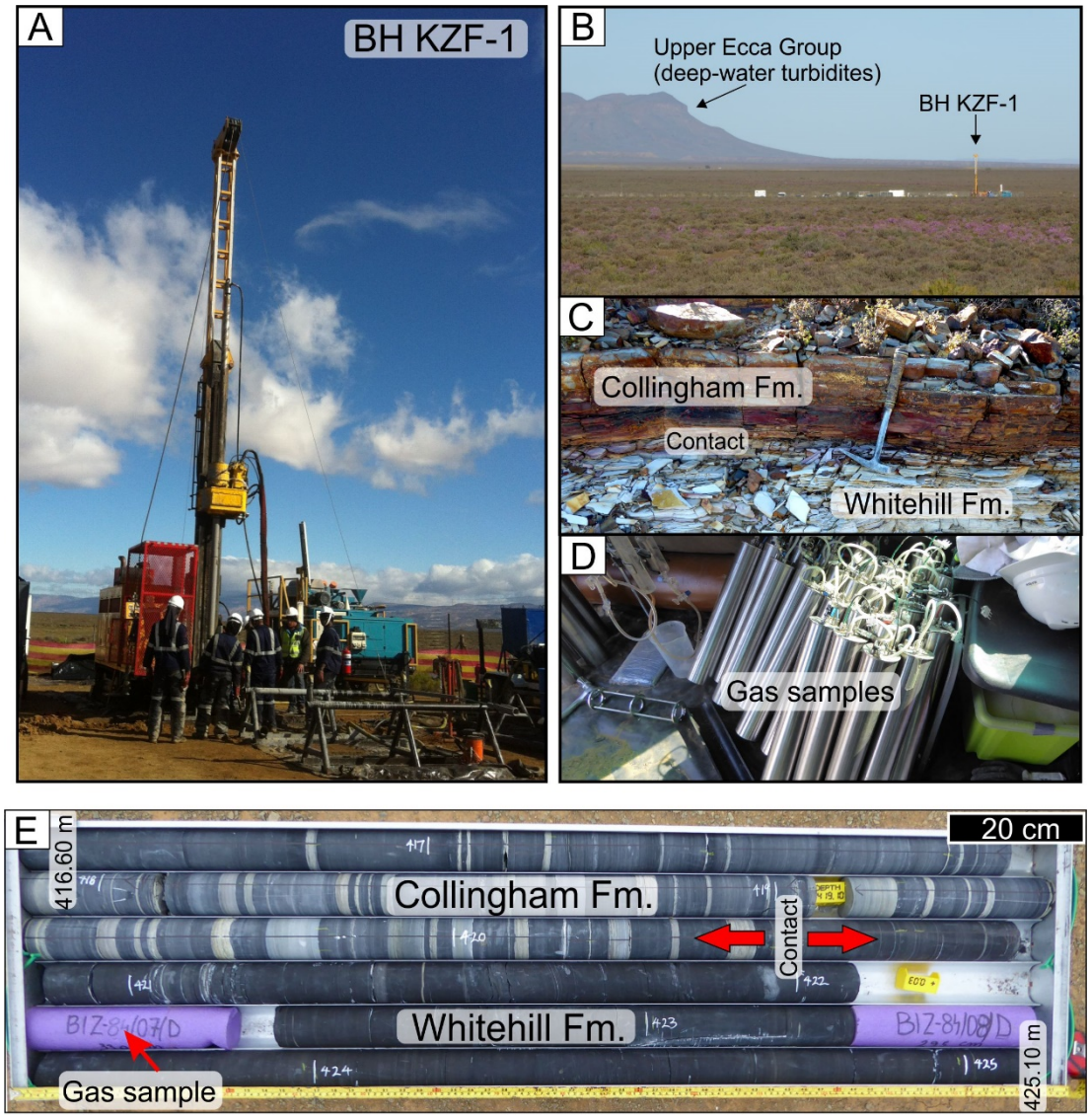

Figure 1.2: BH KZF-1 drilled in the Tankwa Karoo Sub-basin (western MKB). A) Rotary drill rig. B) BH KZF-1 in relation to the Tankwa deep-water fan complex. C) White-weathered Whitehill Formation and its contact with the overlying Collingham Formation outcropping near the drill site. D) Sample cylinders for gas testing. E) Core tray with the Collingham and Whitehill formations, including place markers of gas tested core samples.

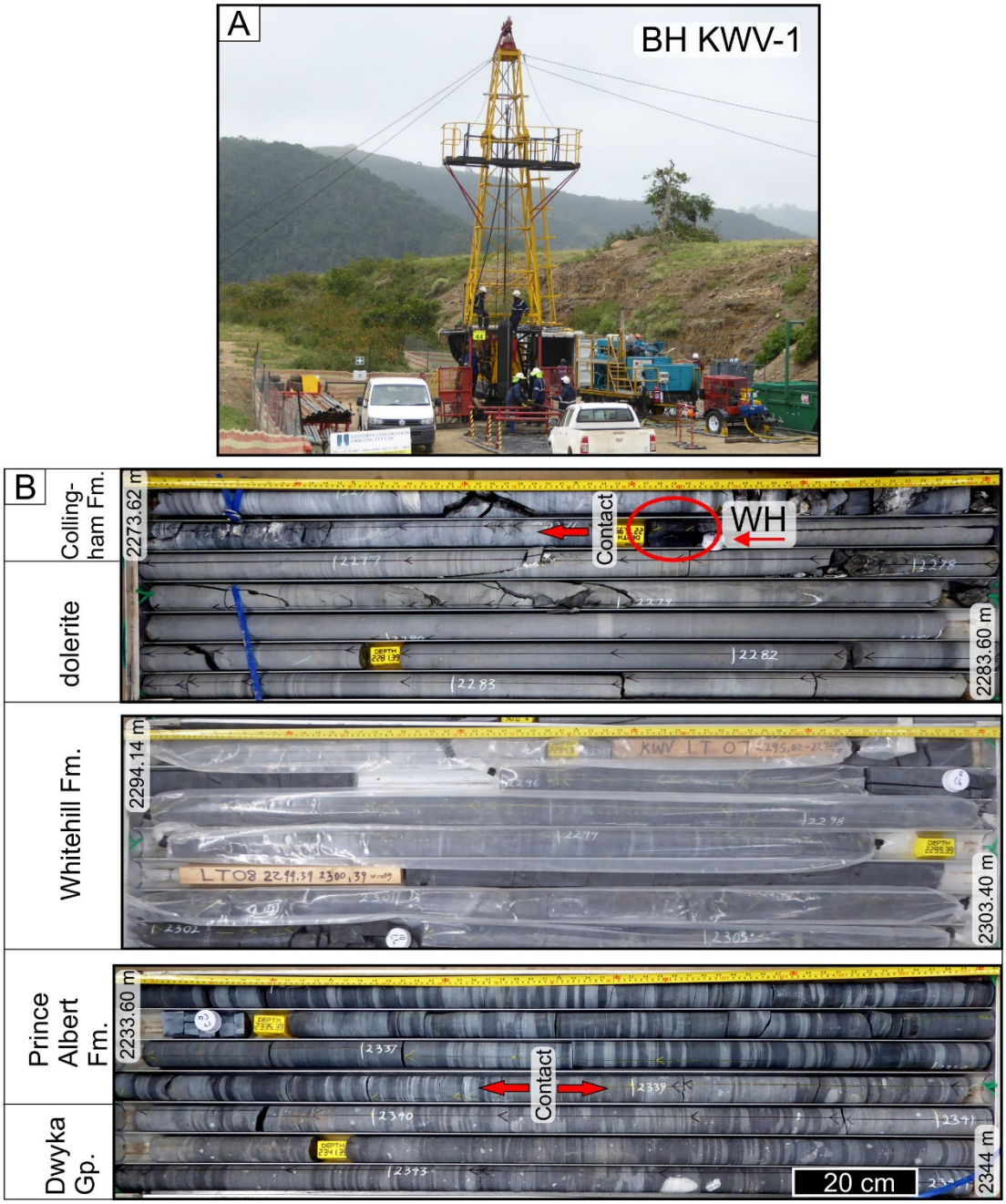

Figure 1.3: A) Borehole KWV-1 drilled in the eastern main Karoo Basin, near Willowvale, Eastern Cape, South Africa. B) Examples of cores from the Prince Albert, Whitehill and Collingham formations, the Dwyka Group and dolerite.

1.3 Layout of the thesis

Following the introduction, this thesis is divided into the following main chapters:

- Chapter 2: Diagenetic and metamorphic effects on the petrophysical properties of the lower Ecca Group black shales in the southern Karoo Basin, South Africa;
- Chapter 3: Palaeo-environmental reconstruction of the lower Ecca Group mudstones from the western and eastern Karoo Basin, South Africa;
- Chapter 4: Provenance of the lower Permian Ecca Group in the southern main Karoo Basin, South Africa;
- Chapter 5: Geomechanical properties of the Permian black shales in the southern main Karoo Basin (South Africa): lessons from compositional and petrophysical studies; and
- Chapter 6: Synthesis and conclusion

Because post-examination, I intend to submit the above chapters as standalone manuscripts to peer-reviewed academic journals, there is some repetition (e.g., geological background) in them that was not easy to avoid.

1.4 References

Almond, J.E. 2008. *Fossil record of the Loeriesfontein sheet area (1: 250 000 geological sheet 3018)*. (Unpublished report for the Council for Geoscience). Pretoria, South Africa. 32p.

Anderson, A.M. & McLachlan, I.R. 1979. The oil shale potential of the Early Permian White Band Formation in southern Africa. *Geological Society of South Africa, Special Publication*. 6: 83–89.

Bangert, B., Stollhofen, H., Lorenz, V. & Armstrong, R. 1999. The geochronology and significance of ash-fall tuffs in the glaciogenic Carboniferous-Permian Dwyka Group of Namibia and South Africa. *Journal and African Earth Sciences*. 29: 33–49.

Bernard, S. & Horsfield, B. 2014. Thermal maturation of gas shale systems. *Annual Review of Earth and Planetary Sciences*. 42: 635–651.

Beukes, N., Götz, A.E., de Kock, M.O. & Campbell, S. 2015. *Karoo Research Initiative (KARIN)*. (Progress Report 1). Johannesburg, South Africa: University of Johannesburg. 17p.

Branch, T., Ritter, O., Weckmann, U., Sachsenhofer, R.F. & Schilling, F. 2007. The Whitehill Formation - a high conductivity marker horizon in the Karoo Basin. *South African Journal of Geology*. 110: 465–476.

Calvert, 1987. Oceanic controls on the accumulation of organic matter in marine sediments. In *Marine petroleum source rocks*. J. Brooks & A.J. Fleet, Eds. Oxford: Blackwell Scientific Publications. 137–157.

Calvert, S.E. & Pedersen, T.F. 1992. Organic carbon accumulation and preservation in marine sediments: how important is the anoxia? In *Organic matter: productivity, accumulation and preservation in recent and ancient sediments*. J.K. Whelan & J.W. Farrington, Eds. Columbia University Press: New York. 231–263.

Catuneanu, O., Hancox, P.J. & Rubidge, B.S. 1998. Reciprocal flexural behaviour and contrasting stratigraphies: a new basin development model for the Karoo retroarc foreland system, South Africa. *Basin Research*. 10: 417–439.

Catuneanu, O., Hancox, P.J., Cairncross, B. & Rubidge, B.S. 2002. Foredeep submarine fans and forebulge deltas: orogenic off-loading in the underfilled Karoo Basin. *Journal of African Earth Sciences*. 35: 489–502.

Catuneanu, O., Wopfner, H., Eriksson, P.G., Cairncross, B., Rubidge, B.S., Smith R.M.H. & Hancox P.J. 2005. The Karoo basins of south-central Africa. *Journal of African Earth Sciences*. 43: 21–253.

Chukwuma, K. & Bordy, E.M. 2016. Spatiotemporal sedimentary facies variations in the Lower Permian Whitehill Formation, Ecca Group, Karoo Basin. In *Origin and evolution of the Cape Mountains and Karoo Basin*. B. Linol & M.J. de Wit, Eds. Regional Geology Reviews, Springer.101–110.

Cole, D.I. & McLachlan, I.R. 1991. Oil potential of the Permian Whitehill Shale Formation in the main Karoo Basin, South Africa. In *Gondwana Seven Proceedings.* H. Ulbrich Rocha & A.C. Campos, Eds. 379–390.

Cole, D.I. 1992. Evolution and development of the Karoo Basin. In *Inversion tectonics of the Cape Fold Belt, Karoo and Karoo and Cretaceous basins of Southern Africa*. M.J. de Wit & I.D.G. Ransome, Eds. Rotterdam: Balkema. 23–26.

Cole, D. I., Robey, K., Chevallier, L. & Viljoen, J. 2011. *The geology of shales with a gas potential in the Main Karoo Basin of South Africa and impact of hydraulic fracturing on groundwater.* (Council for Geoscience Report 2011-0142). Bellville, South Africa: Council for Geoscience Western Cape Regional Office. 43p

Cole, D.I. 2014. Geology of Karoo Shale Gas and how this can Influence Economic Gas Recovery. Gas – The Game Changer for Southern Africa? *Fossil Fuel Foundation*. 21 May 2014. Glen Hove: Johannesburg. 11–12.

Cole, D. & Barbolini, N. 2019. Marine flooding surfaces recorded in Permian black shales and coal deposits of the Main Karoo Basin (South Africa): Implication for basin dynamics and cross-basin correlations: Discussion. *International Journal of Coal Geology.* 209: 130–131.

Crowell, J.C. 1978. Gondwana glaciation, cyclothems, continental positioning and climate change. *American Journal of Science*. 278: 1345–1372.

Curtis, J.B. 2002. Fractured shale-gas systems. *AAPG Bulletin*. 86 (11): 1921–1938.

de Kock, M.O., Beukes, N.J., Adeniyi, E.O., Cole, D., Götz, A.E., Geel, C. et al. 2017. Deflating the shale gas potential of South Africa's Main Karoo basin. *South African Journal of Science*.113: 9-10.

de Wit, M.J. & Ransome, I.G.D. 1992. Regional inversion tectonics along the southern margin of Gondwana. In *Inversion tectonics of the Cape Fold Belt, Karoo and Cretaceous Basins of Southern Africa*. M.J. de Wit & I.G.D. Ransome, Eds. Netherlands, Rotterdam: Balkema. 15–20.

Decker, J. & Marot, J. 2012. *Investigation of hydraulic fracturing in the Karoo of South Africa*. Annexure A, Resource Assessment. Cape Town: Petroleum Agency of SA. Available: http://www.dmr.gov.za/publications/viewdownload/ 182/854.html [01-11-13].

Duncan, R.A., Hooper, P.R., Rehacek, J., Marsh, J.S. & Duncan, A.R. 1997. The timing and duration of the Karoo igneous event, southern Gondwana. *Journal Geophysical Research*. 102 (18): 127–138.

Faure, K. & Cole, D. 1999. Geochemical evidence for lacustrine microbial blooms in the vast Permian Main Karoo, Paraná, Falkland Islands and Huab basins of southwestern Gondwana*. Palaeogeography, Palaeoclimatology, Palaeoecology.* 152: 189–213.

Fishman, N.S., Bereskin, S.R., Bowker, K.A., Cardott, B.J., Chidsey, T.C., Dubiel, R.F., Enomoto, C.B., Harrison, W.B. et al., 2011. Gas shale/shale oil. In: *Unconventional energy resources, 2011 review.* P.D. Warwick, Eds. Natural Resources Research. 20: 288–301.

Garzanti, E. 2016. From static to dynamic provenance analysis- sedimentary petrology upgraded. *Sedimentary Geology*. 336: 3–13.

Geel C., de Wit, M., Booth, P., Schulz, H-M. & Horsfield, B. 2015. Palaeo-environment, diagenesis and characteristics of Permian black shales in the lower Karoo Supergroup flanking the Cape Fold Belt near Jansenville, Eastern Cape, South Africa: Implications for the shale gas potential of the Karoo Basin. *South African Journal of Geology*.118(3): 249–274.

Götz, A.E., Ruckweid, K. & Wheeler, A. 2017. Marine flooding surfaces recorded in Permian black shales and coal deposits of the Main Karoo Basin (South Africa): Implications for basin dynamics and cross-basin correlation*. Coal Geology*. 190: 178–190.

Hälbich, H. 1983. A tectogenesis of the Cape Fold Belt (CFB). *Special publication - Geological Society of South Africa*. 12: 165–175.

Harris, C., Buthelezi, N., Kahle, B., Kahle, R., Ramahala, K. & Smith, G. 2019. Stable isotope constraints on the fluid source of hydrothermal breccia pipes in the Tankwa Karoo depocentre, South Africa: Breakdown of authigenic minerals during sill intrusion*. Basin Research*. 31(1): 114–135.

Herbert, C.T. & Compton, J.S. 2007. Depositional environments of the lower Permian Dwyka diamictite and Prince Albert shale inferred from the geochemistry of early diagenetic concretions, southwest Karoo Basin, South Africa. *Sedimentary Geology.* 194: 263–277.

Hill, R. J., Jarvie, D. M., Zumberge, J., Henry M. & Pollastro, R. M. 2007. Oil and gas geochemistry and petroleum systems of the Fort Worth Basin. *AAPG Bulletin*. 91 (4): 445–473.

Horsfield, B., Schulz, H-M., Bernard, S., Mahlstedt, N., Yuanjia, H. & Kuske, S. 2018. Oil and Gas Shales. In *Hydrocarbons, Oils and Lipids: Diversity, Origin, Chemistry and Fate*.*Handbook of Hydrocarbon and Lipid Microbiology*. H. Wilkes, Eds. Springer, Cham. 1–34.

Isbell, J.L., Cole, D.I. & Catuneanu, I. 2008. Carboniferous-Permian glaciation in the main Karoo Basin, South Africa: Stratigraphy, depositional controls, and glacial dynamics. In *Resolving the Late Paleozoic ice age in time and space fielding*. C.R. Fielding, T.D. Frank. & J.L. Isbell, Eds. Geological Society of America Special Paper. 441:71–82.

Jarvie, D.M., Hill, R.J., Ruble, T.E. & Pollastro, R.M. 2007. Unconventional shale-gas systems: the Mississippian Barnett Shale of north-central Texas as one model for thermogenic shale-gas assessment. *AAPG Bulletin*. 91:475–499.

Jarvie, D.M. 2012. Shale resource systems for oil and gas: part 1 – shale-gas resource systems. In *Shale reservoirs – Giant resources for the 21st century*. J.A. Breyer, Ed. AAPG Memoir. 97: 69–87.

Johnson, M.R., Van Vuuren, C.J., Visser, J.N.J., Cole, D.I., Wickens, H. deV., Christie, A.D.M., Roberts, D.L. & Brandl, G. 2006. Sedimentary rocks of the Karoo Supergroup. In *The Geology of South Africa*. M.R. Johnson, C.R., Anhaeusser & R.J. Thomas, Eds. Johannesburg: Geological Society of South Africa/ Council for Geoscience. 461–499.

Kuuskraa, V., Stevens, S., Van Leeuwen, T. & Moodhe, K. 2011. *World shale gas resources: An initial assessment of 14 regions outside the united states*. (Washington, DC: US DOE EIA, open access file). Available: eia.gov/analysis/studies/worldshalegas/archive/2011/pdf/fullreport.pdf. [27-07-20].

Lazar, R.O., Bohacs, K.M., Macquaker, J.H.S., Schieber, J. & Demko, T.M. 2015. Capturing key attributes of fine-grained sedimentary rocks in outcrop, cores and thin sections: nomenclature and description guidelines. *Journal of Sedimentary Research*. 85: 230–246.

Leith MJ (1970) *Well completion report of SP1/69*. Internal Soekor Report vol PSV684a.

Macquaker, J.H.S. & Gawthorpe, R.L. 1993. Mudstone lithofacies in the Kimmeridge Clay Formation, Wessex Basin, southern England: implications for the origin and controls of the distribution of mudstones. *Journal of Sedimentary Petrology*. 63: 1129–1143.

Macquaker, J.H.S. & Adams, A.E. 2003. Maximizing information from fine-grained sedimentary rocks: an inclusive nomenclature for mudstones. *Journal of Sedimentary Research*. 73: 735–744.

Martin, H. & Wilczewski, N. 1970. Palaeoecology, conditions of deposition and palaeogeography of the marine Dwyka beds of South West Africa. *Second Gondwana Symposium Proceedings and Papers*. 225–232.

McLachlan, I.R. & Anderson, A.M. 1973. A review of the evidence for marine conditions in southern Africa during Dwyka times. *Palaeontologia Africana*. 15: 37–64.

Milani, E.J. & de Wit, M.J. 2008. Correlations between the classic Paraná and Cape-Karoo sequences of South America and southern Africa and their basin infills flanking the Gondwanides: Du Toit revisited. In *West Gondwana: Pre-Cenozoic correlations across the South Atlantic –the ties that bind*. R.J. Pankhurst, R.A.J. Trouw, B. Brito Neves & M.J. de Wit, Eds. London: The Geological Society, Special Publication. 319–342.

Muir, R.A., Bordy E.M., Mundil, R. & Frei, D. 2020. Recalibrating the breakup history of SW Gondwana: U-Pb radioisotopic age constraints from the southern Cape of South Africa. *Gondwana Research*. 177–193.

Oelofsen, B.W. 1986. A fossil shark neurocranium from the Permo-Carboniferous (lowermost Ecca Formation) of South Africa. In *Proceedings of the 2nd International Conference of Indo-Pacific Fishes*. T. Uyeno, R. Arai, T. Tanuichi, K. Matsuura, Eds. Tokyo: Icthyological Society of Japan. 107–124.

Oelofsen, B.W. 1987. The biostratigraphy and fossils of the Whitehill and Irati Shale Formations of the Karoo and Paraná Basins. Department of Zoology, University of Stellenbosch, RSA. In *Gondwana six: stratigraphy, sedimentology, and paleontology, USA*. G.D McKenzie, Eds. AGU geophysical Monograph Board. 131–138.

Oschmann, W. 1991. Distribution, dynamics and paleoecology of Kimmeridgian (Upper Jurassic) shelf anoxia in western Europe. In *Modern and ancient continental shelf anoxia*. R.V. Tyson & T.H. Pearson, Eds. Geological Society of London Special Publication. 58: 381–395.

Potter, P.E., Maynard, J.B. & Depetris, P.J. 2005. *Mud and Mudstones: Introduction and Overview*. Berlin: Springer. 297p.

Rowsell, D.M. & De Swart, A.M.J.1976. Diagenesis in Cape and Karroo sediments, South Africa, and its bearing on their hydrocarbon potential. *Transactions of the Geology Society of South Africa*. 79: 81–145.

Ryan, P.J. 1967. *Stratigraphic and paleocurrent analysis of the Ecca Series and lowermost Beaufort beds in the Karroo Basin of South Africa*. Unpublished Ph.D. thesis. Johannesburg: University of the Witwatersrand. 210p.

Ryan, P.J. & Whitfield, G.G. 1979. Basinal analysis of the Ecca and lowermost Beaufort Beds and associated coal, uranium and heavy mineral beach sand occurrences. *Geological Society South Africa Publication*. 6: 91–101.

Scheffler et al., 2006. Analyses of late Palaeozoic glacial to postglacial sedimentary successions in South Africa by geochemical proxies- response to climate evolution and sedimentary environment. *Palaeogeography, Palaeoclimatology, Palaeoecology*. 240: 184–203.

Schieber, J. 2001. A role for organic petrology in integrated studies of mudrocks: Examples from Devonian black shales of the Eastern US. *International Journal of Coal Geology*. 47(3–4): 171–187.

Scott, E.D. 1997. *Tectonics and sedimentation: the evolution, tectonic influences and correlation of the Tanqua and Laingsburg subbasins, southwest Karoo basin, South Africa*. Unpublished Ph.D. thesis. Louisiana State University. 234p.

Slatt, R.M. & O' Brien, N.R. 2011. Pore types in the Barnett and Woodford gas shales: contribution to understanding gas storage and migration pathways in fine-grained rocks. *APPG Bulletin*. 95: 2017–2030.

Smith, R.M.H. 1990. A review of the stratigraphy and sedimentary environments of the Karoo Basin. South Africa. *Journal of African Earth Sciences*. 10: 117–137.

Smith, R.M.H, Eriksson, P.G. & Botha, W.J. 1993. A review of the stratigraphy and sedimentary environments of the Karoo-aged basins of Southern Africa. *Journal of African Earth Sciences*. 16: 143–169.

Smithard, T., Bordy, E.M. & Reid, D.L. 2015. The effect of dolerite intrusions on the hydrocarbon potential of the lower Permian Whitehill Formation (Karoo Supergroup) in South Africa and southern Namibia: A preliminary study. *South African Journal of Geology*. 118(4): 489–510.

Svensen, H., Planke, S., Chevallier, L., Malthe-Sorenssen, A., Corfu, F. & Jamtveit, B. 2007. Hydrothermal venting of greenhouse gases triggering Early Jurassic global warming. *Earth Planet. Science. Letters*. 256: 554–566.

Tankard, A., Welsink, H., Aukes, P., Newton, R. & Stattker, E. 2012. Geodynamic interpretation of the Cape and Karoo basins, South Africa. In *Phanerozoic passive margins, cratonic basins and global tectonics maps*. D.G. Roberts, Ed. USA & UK: Elsevier. 869–932.

Veevers, J.J., Cole, D.I. & Cowan, E.J. 1994. Southern Africa: Karoo basin and Cape Fold Belt. In *Permian-Triassic Pangean basins and Foldbelts along the Panthalassan margin of Gondwanaland*. J.J. Veevers & C. M. Powell, Eds. Boulder, Colorado: G.S.A. Memoir. 184: 223–279

Visser, J.N.J. & Loock, J.C. 1978. Water depth in the main Karoo Basin in South Africa during Permian sedimentation. *Transactions of The Geological Society of South Africa.* 81: 185–191.

Visser, J.N.J. 1987. The influence of topography on the Permo-Carboniferous glaciation in the Karoo basin and adjoining areas, Southern Africa. In *Gondwana six: stratigraphy, sedimentology and paleontology, vol 41*. D.H. Elliot, J.W. Collison, G.D. McKenzie & S.M. Haban, Eds. American Geophysical Union. 123–129.

Visser, J.N.J. 1992. Deposition of the Early to Late Permian Whitehill Formation during a sea-level highstand in a juvenile foreland basin*. South African Journal of Geology*. 181–193.

Visser, J.N.J. 1993. Sea-level changes in a back-arc–foreland transition: The Late Carboniferous–Permian Karoo Basin of South Africa. *Sedimentary Geology*. 83: 115–131.

Visser, J.N.J. 1994. A Permian argillaceous syn- to post-glacial foreland sequence in the Karoo Basin, South Africa. In *Earth's Gacial Record: International Geological Correlation Project 260.* M. Deynoux, J.M.G. Miller, E.W. Domack, N. Eyles, I.J. Fairchild & G.M. Young, Eds. Cambridge: Cambridge University Press. 193–203.

Weltje, G. J. & von Eynatten, H. 2004. Quantitative provenance analysis of sediments: review and outlook. *Sedimentary Geology*. 171: 1–11.

Werner, M. 2006. *The stratigraphy, sedimentology and age of the Late Palaeozoic Mesosaurus Inland Sea, SW-Gondwana: new implications from studies on sediments and altered pyroclastic layers of the Dwyka and Ecca Group (lower Karoo Supergroup) in southern Namibia*. Unpublished Ph.D. thesis. University of Würzburg, Germany. 428p.

Wickens, H. DeV. 1994. *Basin floor fan building turbidites of southwestern Karoo Basin, Permian Ecca Group, South Africa*. Unpublished Ph.D. thesis. University of Port Elizabeth. 223p.

2 Diagenetic and metamorphic effects on petrophysical properties of the lower Ecca Group black shales in the southern Karoo Basin, South Africa

Abstract

Fine-grained sedimentary rocks of the lower Ecca Group in the Main Karoo Basin (MKB) have been identified as a possible unconventional hydrocarbon reservoir, the gas potential of which is still essentially unknown. The lower Ecca Group is comprised of flysch-like successions of the Prince Albert, Whitehill and Collingham formations, which are impacted in various ways by diagenesis and metamorphism. In this study, we analyse two boreholes (BH) KZF-1 (Tankwa Karoo Sub-basin, western MKB) and KWV-1 (eastern MKB), drilled ~ 830 km apart, to compare composition, thermal maturity and petrophysical characteristics for the assessment of the hydrocarbon potential of the lower Ecca Group.

Sedimentary rocks in both boreholes were affected by burial and regional metamorphism (linked to orogenic events), but sedimentary rocks in BH KWV-1 were also altered by contact metamorphism due to dolerite intrusions in the Early Jurassic. Major differences in the mineralogy of the lower Ecca rocks in these boreholes include: 1) Fe-silicate (greenalite); carbonates (rhodochrosite and dolomite) and Mn nodules (birnessite) only occur in BH KZF-1; and 2) metamorphic minerals such as garnet, cordierite, staurolite only occur in BH KWV-1. Phosphorites, birnessite nodules and putative agglutinated benthic foraminifera indicate that marine conditions likely existed, at least intermittently, during the deposition of the Prince Albert and Whitehill formations in both regions of the basin.

The total organic carbon (TOC) content is highest in the Whitehill Formation in both boreholes (BH KZF-1: 5.17 wt%; BH KWV-1: 4.87 wt%). Low quantity of free hydrocarbons (S1 peak; 0.02–0.06 mg/g) and potential to release hydrocarbons (S2 peak; 0.06–0.14 mg/g) and low hydrogen index (HI) values (2.41–167 mg HC/g TOC) from Rock Eval pyrolysis accompanied with high vitrinite and bitumen reflectance (i.e., VR_o= 4 in BH KZF-1; BR_o= 5 in BH KWV-1) collectively indicate that these rocks are over mature at these locations. Burial diagenesis significantly reduces interparticle porosity and most of the measurable porosity comes from intraparticle nano-pores confined to organic matter and dolomite. Both meso- and macro-porosity is limited to phyllosilicates, pyrite framboids and microfractures. Due to mineral-boundary

recrystallization, the permeability of the lower Ecca Group is limited to the connectivity of the organic matter, micro-fractures and tuffaceous laminae.

Neither borehole contained significant gas, likely due to degasification by post-depositional structural deformation and Jurassic dolerite intrusions. Whether gas is trapped elsewhere in the basin is still to be determined.

2.1 Introduction

In recent years, the Main Karoo Basin (MKB) has become a target for unconventional hydrocarbon investigations in South Africa, reigniting research into the fine-grained, organic-matter-rich mudstones and shales of the lower Ecca Group in the Karoo Supergroup. The MKB formed from the Late Carboniferous to the Early Jurassic within the interior of Gondwana (Rowsell & De Swart, 1976; Cole, 1992; Catuneanu et al., 2005; Johnson et al., 2006; Tankard et al., 2012). The MKB was initially formed by subsidence created by lithostratigraphic glacial load followed by multiphase, basin margin orogenic uplift, which ultimately formed the “Ecca Inland Sea” allowing for sediment deposition and preservation (e.g., Catuneanu et al., 1998; Isbell et al., 2008; Tankard et al., 2012). During the Permian, the MKB was situated between the Cape Fold Belt (CFB) in the south and west, and the Kalahari Craton in the north (Cargonian Highlands; Figure 2.1; Visser, 1987; Hälbich, 1983; Isbell et al., 2008).

In order to predict reservoir quality of the lower Ecca Group, the understanding of the entire “life cycle” of the reservoir is essential. Burial history of sedimentary basins, as a function of syn- and post-depositional tectonic and diagenesis processes, is fundamental in considering the controls on the hydrocarbon generation and evolution of reservoir quality (Bjørlykke, 2010). Diagenesis is a collective term describing those post-depositional processes that modify sediments through compaction, cementation, dissolution recrystallization and authigenesis (Tucker, 2001; Boggs, 2009). Some of the factors that control these reactions in fine-grained sediments are: water chemistry, type and concentration of organic matter (OM), quantity of reactive solid phases in the primary mineral assemblages and burial/sedimentation rate (Arning et al., 2011). Dissolution and precipitation of minerals in a geochemically open system are facilitated by flow rate (fluid flux) of pore water. During diagenesis, the compaction-driven pore water flux may be too low to transport solids in solution resulting in a closed system where minerals would require different pressure and temperatures to become stable (Bjørlykke & Jahren, 2012). Diagenesis is considered to stop before the onset of low-grade metamorphism, which occurs at temperatures of about 150–

200 °C and therefore can be used to constrain temperature history in a basin (Tucker, 2001; Boggs, 2009).

Early diagenesis influences the petrophysical properties of a sedimentary rock. Diagenesis impacts the quality of the source rock with respect to organic-carbon richness, organic-sulfur contents, pore-spaces, relative proportions of cements present and their varying mechanical properties, specifically their brittleness and ductility (Macquaker et al., 2014). Therefore, when diagenetic alterations are assessed with respect to hydrocarbon geology, two major factors must be considered: 1) the degree of diagenesis; 2) whether the resulting porosity is suitable for a reservoir? (Von Engelhardt, 1960; De Segonzac, 1968).

This study investigates the diagenetic and metamorphic effects on the petrophysical characteristics of the Lower Permian Prince Albert, Whitehill and Collingham formations of the lower Ecca Group of the Karoo Supergroup. Boreholes from the western and eastern MKB are investigated for their shale gas potential and the depositional settings under which the lower Ecca Group accumulated.

2.2 Geological setting

2.2.1 Main Karoo Basin

The MKB covers an area of nearly 600 000 km^2 in southern Africa, and its sedimentary fill, the Karoo Supergroup, reaches a cumulative thickness of ~ 6 km in the south of the basin (e.g., Lindeque et al., 2007, 2011; Tankard et al., 2012; Scheiber-Enslin et al., 2015). The depositional period of the Karoo Supergroup spans ~ 130 million years, from the Late Carboniferous to Early Jurassic. It is stratigraphically subdivided into the Dwyka, Ecca, Beaufort, Stormberg and Drakensberg groups (e.g., Bangert et al., 1999; Catuneanu et al., 2005; Johnson et al., 2006; Isbell et al., 2008; Milani & de Wit, 2008; Rubidge et al., 2013). Following the final Dwyka deglaciation event around the Permo-Carboniferous boundary, the transgressing meltwater formed a regionally extensive inland “sea” in the region, which trapped the mainly fine-grained OM-rich sediments that comprise the Permian lower Ecca Group, namely the Prince Albert, Whitehill and Collingham formations (Figure 2.1; Smith, 1990; Milani & de Wit, 2008). It is generally accepted that these sediments accumulated under anoxic conditions allowing for the preservation of their OM contents, specifically kerogen types II and III (e.g., Smith, 1990; Cole, 1992; Geel et al., 2015; Chukwuma & Bordy, 2016; Chukwuma et al., 2018). During the Permo-Triassic, the MKB gradually filled up with sediments (upper Ecca Group), and the

depositional environments changed to alluvial plains with rivers and lakes (Beaufort Group; lower Stormberg Group), and subsequently into a large desert (upper Stormberg Group; Catuneanu et al., 2005; Bordy et al., 2020). The lower Jurassic continental rocks are conformably overlain by the Toarcian (183 ± 1 Ma) continental flood basalts of the Drakensberg Group, which are associated with dolerite sills and dykes (e.g., Duncan et al., 1997; Catuneanu et al., 1998; Jourdan et al., 2005; Rubidge et al., 2013). This extensive network of sills and dykes was emplaced in most regions of southern Africa, but not adjacent to the CFB in the southern and south-western extremities of the MKB. Locally, sills form up to 70% of the MKB stratigraphy (Rowsell & De Swart, 1976), and are most extensive and thickest in the Ecca Group (Chevallier & Woodford, 1999). The high total organic carbon (TOC) contents of the lower Ecca Group potentially may have converted into large amounts of methane during the Early Jurassic intrusive event upon intrusion resulting in the degasification by the cracking of OM by metamorphism (Aarnes et al., 2011; Smithard et al., 2015).

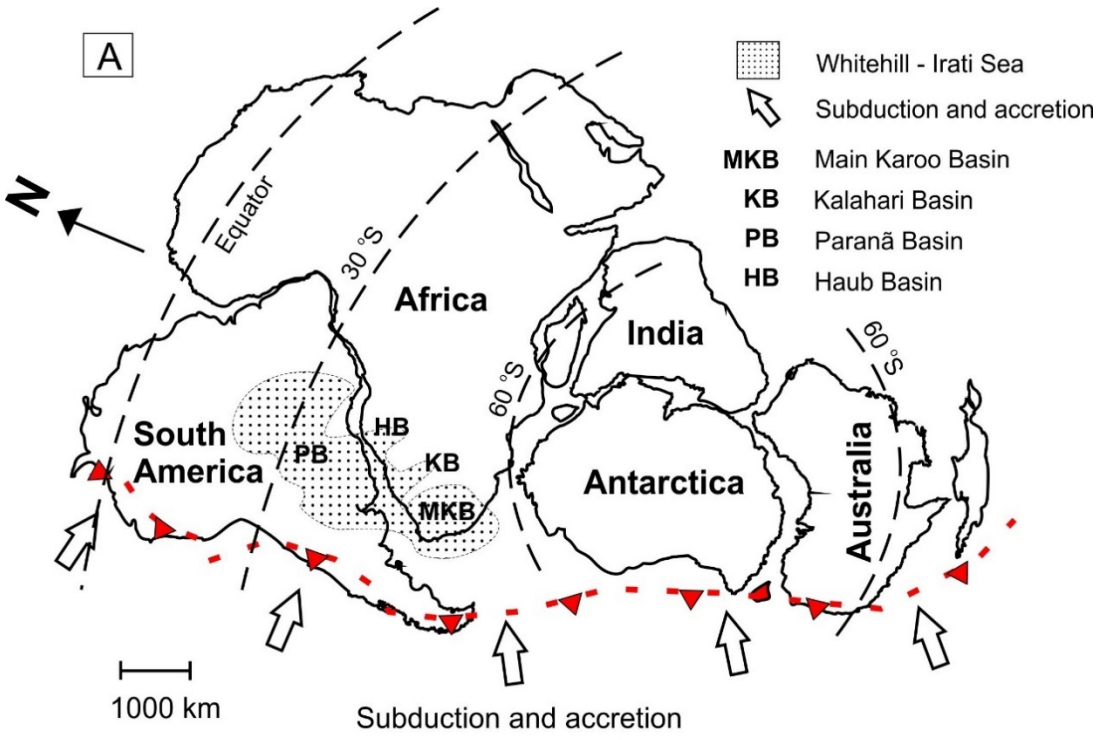

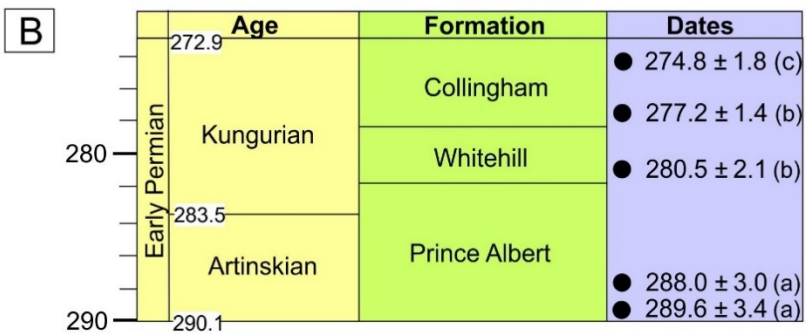

Figure 2.1: (previous page) A) Early Permian map of Gondwana showing the extent of the "Whitehill-Irati Sea" across southern Africa and South America. Adapted from Faure and Cole, 1999. B) The chronostratigraphy of the Lower Permian Ecca Group (Karoo Supergroup) in the southern main Karoo Basin and Namibia (modified after Rubidge, 2005 and Smithard et al., 2015). Radiometric dates are marked with black circles, shown in million years and taken from a: Bangert et al., 1999; b: Werner, 2006; c: Fildani et al., 2007. Geological time scale based on 2013 ICS Time Chart.

2.2.2 Lithostratigraphy and regional variation of the lower Ecca Group

The Prince Albert, Whitehill and Collingham formations are referred to in this study as the lower Ecca Group, an informal stratigraphic name. The Prince Albert Formation comprises mudstone, thinly-bedded shale, breccia, fine-grained wacke and silty rhythmites (Visser, 1992). Distal turbidites suggest the Prince Albert Formation was deposited by sediment gravity flows (Smith et al., 1993) in a basin to shelf setting (Visser, 1994). Marine fossils such as palaeoniscoid fish, bivalves, brachiopods, cephalopods (McLachlan & Anderson, 1973), foraminifera, sponge spicules, radiolarians, acritarchs (Visser, 1994) and a possibly marine fossil shark (Oelofsen, 1986), have been detected near the base. Phosphate nodules and lenses occur in the southern part of the basin (Visser, 1992). Overall, the Prince Albert Formation is between 50 and 320 m thick (Cole, 2005).

The Whitehill Formation forms a gradational contact with the underlying Prince Albert Formation. It comprises OM-rich thinly laminated shale formed by suspension settling of fine-grained material. The presence of pyrite and lack of bioturbation structures indicate anoxic conditions (Visser, 1992). Coarser-grained units are present in upper Whitehill Formation in the north-west of the basin and are linked to sediment-laden hyperpycnal currents (Chukwuma & Bordy, 2016). Carbonate nodules in the Whitehill Formation have been described as dolomitic limestones (Oelofsen, 1987) with carbon-rich microlaminations (McLachlan & Anderson, 1977). The dolomite concretions occur in the lower Whitehill Formation and have stromatolite-like features (McLachlan & Anderson, 1977; Geel et al., 2015). The carbonate horizon is correlated to a temporary lowstand allowing influx of brines creating evaporative conditions (Oelofsen, 1987; Visser, 1992). Fossils such as mesosaurid reptiles, crustaceans, palaeoniscoid fish, insect wings, sponge spicules and *Glossopteris* leaves have no marine affinities (McLachlan & Anderson, 1977; Oelofsen,1978; Visser, 1992; Chukwuma & Bordy, 2016). The Whitehill Formation is between 10 and 80 m thick (Johnson et al., 2006; Chukwuma & Bordy, 2016).

The Collingham Formation conformably overlies the Whitehill Formation. It comprises of silica-rich mudstone, siltstone and very-fine-grained sandstone. The Collingham

Formation is frequently intercalated with tuffaceous laminae and beds (Smith et al., 1993; Viljoen, 1994). The alteration of mudstone with siltstone and fine-grained sandstone layers is interpreted as distal turbidites that accumulated under oxygenated conditions. Fossils are rare, but invertebrate trace fossils are common (Viljoen, 1994; Almond, 2002; Johnson et al., 2006). The formation is 30 to 70 m thick (Johnson et al., 2006).

Dating of interbedded tuffaceous layers (Figure 2.1) indicate that deposition of the Prince Albert Formation started in the Early Artinskian (~ 289.6 Ma) and ended in the Early Kungurian ~ 283.5 Ma. The Whitehill Formation is Kungurian (~ 283.5 Ma to ~ 275 Ma) and the Collingham is Late Kungurian to Early Guadalupian (~ 275 Ma to ~ 269 Ma; Bangert et al., 1999; Werner, 2006; Fildani et al., 2007; Barbolini et al., 2018). The acidic tuffaceous beds, which are most dominant in the Collingham Formation, suggest that the driving force responsible for the CFB orogeny had started south of the present-day coastline, by the convergence of the western margin of South America, together with pre-Andean magmatic rocks in northern Patagonia (Hälbich, 1983; Viljoen, 1990, 1992, 1994; Faure & Cole, 1999; Tankard et al., 2012; Navarrete et al., 2019).

During the Permian Cape Orogeny, mountain ranges which developed in the far south and north-west, supplied sediments into the MKB (e.g., Smith, 1990; Catuneanu et al., 1998). The first paroxysm for the CFB Orogeny occurred ~ 278 Ma and there was simultaneous folding in the western and southern branches of the CFB (Hälbich et al., 1983; De Beer, 1990). Following the deposition of the lower Ecca Group, tectonic uplift led to the formation of a major anticlinorium with a basin-floor high where the two branches of the CFB converge. Subsidence and increased clastic sedimentation formed prograding deep-water fans (upper Ecca Group), leading to the formation of the Tankwa Sub-basin in the south-west and the Laingsburg Sub-basin in the south (Figure 2.2; De Beer, 1990; Wickens, 1994; Adelmann & Fiedler, 1996). It is likely that folding of the western and southern branches of the CFB did not have much surface expression during deposition of the Dwyka Group (Tankard et al., 2012) or during the lower Ecca Group, because these units can be laterally correlated across the Tankwa and Laingsburg Sub-basins of the MKB (Figure 2.2).

In the Tankwa Karoo Sub-basin, the mudstones of the Collingham Formation grade upwards into fine-grained turbiditic sandstones that dominate the Tierberg and Skoorsteenberg formations (e.g., Wickens, 1994; Viljoen, 1994; Turner, 1999; Andersson & Worden, 2004; Wickens & Cole, 2017a). The Skoosteenberg submarine

deep-water fan is deposited north of the Baviaanshoek mega-anticline (Figure 2.2) and displays ripple marks and slump features indicating unstable slope conditions. The Skoorsteenberg Formation contains sandstone-rich turbidites interbedded with mudstones. The overlying Kookfontein Formation comprises of pro-delta and delta-front mudstones and sandstones. The rising Hex Anticlinorium resulted in eastward and northward dipping palaeo-current directions that are recorded in the delta plain and delta front mudstones and sandstones of the Koedoesberg and the Waterford formations (Wickens & Cole, 2017a). The depositional period of the entire Ecca Group (lower and upper parts) in the Tankwa Karoo Sub-basin is confined to the Early Permian and was determined from tuffaceous beds in the Prince Albert Formation (~ 290 Ma), as well as the basal fossiliferous Beaufort Group (~ 262–268 Ma; e.g., Bangert et al., 1999; Rubidge et al. 2013; Day et al., 2015; Lanci et al., 2013; Belica et al., 2017; Barbolini et al., 2018). Although there is some controversy with these dates as U-Pb ages of 275–250 Ma have been presented for the Laingsburg and Skoorsteenberg Formation (Fildani et al., 2007, 2009).

In the Laingsburg Sub-basin, the Collingham Formation is overlain by hemipelagic mudstones and fine-grained turbidites of the Vischkuil Formation, which is conformably overlain by the Laingsburg Formation, a stratigraphic equivalent of the Skoorsteenberg Formation in the Tankwa Karoo Sub-basin. The Laingsburg deep-water fans are wedged out along the north-eastward extension of the south limb of the Hex River mega-anticline. The Fort Brown Formation constitutes of dark pelites and rhythmic alternating sandstones and mudstones typical of a pro-delta. Similar to the Tankwa Karoo Sub-basin, the Waterford Formation is the youngest unit of the Ecca Group and reflects transition from the fluvially-dominated upper delta front to the lower delta plain (e.g., Adelmann & Fiedler, 1996; Johnson, 2009; Rubidge et al. 2013; Day et al., 2015; Lanci et al., 2013; Belica et al., 2017).

The Ecca Group thins from the west to the east in the southern central part of the MKB (Kingsley,1977; Cole, 2005). Therefore, in the eastern MKB, the Ecca Group comprises fewer formations, which are the Prince Albert, Whitehill, Collingham, Ripon, Fort Brown and Waterford formations (Cole & Basson, 1991; Viljoen, 1992; Catuneanu et al., 2005; Cole, 2005; Johnson et al., 2006; Johnson, 2009). The Vischkuil and Laingsburg formations grade into the Ripon Formation at ~ 22° E (Johnson, 2009). The Ripon Formation consists of shale, siltstone and greywackes arranged into Bouma sequences representative of deep-water fan facies (Visser & Loock, 1978; Johnson et al., 2006).

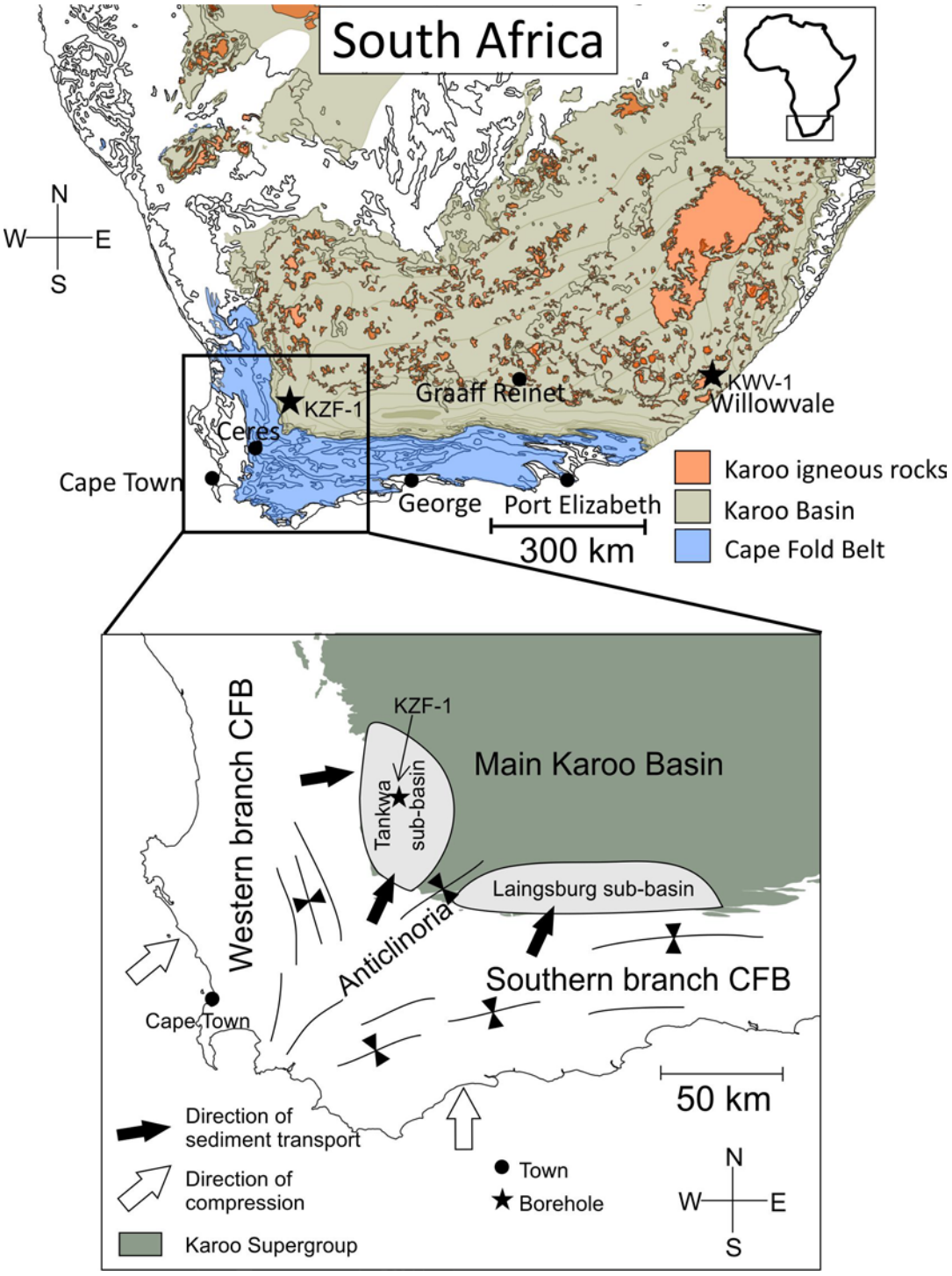

Figure 2.2: Map of the Main Karoo Basin (MKB), Cape Fold Belt (CFB) and Karoo igneous rocks in South Africa, with inset map of the SW MKB showing the Tankwa Karoo and Laingsburg Sub-basins (adapted from Anderson & Worden, 2004). Borehole locations (BH KZF-1 and BH KWV-1) are marked by stars.

2.2.3 Petrophysics of the lower Ecca Group

The TOC is relatively high in the lower Ecca Group of the southern MKB and up to 17 wt% TOC is recorded in the black shales of the Whitehill Formation (Cole & McLachlan, 1991). Only two historic boreholes (BH 1/KLN and BH CR 1/68), drilled in the 1960's, recorded gas shows with methane briefly emerging from fractures of Ecca Group. In a preliminary study of BH KZF-1 and BH KWV-1, de Kock et al. (2017) reported very low desorbed gas (max 0.20 m^3/t) and residual gas concentrates of 0.01 m^3/t – 0.74 m^3/t. Residual gas was mostly methane (61 – 99%) with small amounts of nitrogen and carbon dioxide. Moreover, it has been shown that during the evolution of the MKB, the thermal maturity of these OM-rich rocks increased not only because of deep burial and subsurface palaeo-temperatures that ranged from 150 °C to 300 °C under lower greenschist facies metamorphic conditions near the CFB, but also due to a complex syn-Karoo unroofing history during which 3500–5000 m of rock record was eroded (e.g., Rowsell & De Swardt, 1976; Frimmel et al., 2001; Tinker et al., 2008). This complex basin-evolution history resulted in a regional trend of vitrinite-reflectance values that range from 1% in the north to 4.3% VR_o in the south (e.g., Rowsell & De Swardt, 1976; Geel et al., 2015; de Kock et al., 2017; Nolte et al., 2019), and illite crystallinity (KI) values that range from > 5 in the north to > 3 in the south and drop to as low as 1 near dolerite intrusions (Rowsell & De Swardt, 1976; Smithard et al., 2015). Initial porosity measurements were done by Geel et al. (2015) in an Eastern Cape borehole BH SFT2, using the Mercury Intrusion Porosimetry (MIP) technique, which measures meso- and macroporosity (0.29–2.91 %). In collaboration with this current study, Nolte et al. (2019) used the He pycnometry technique on samples KZF01P–KZF10P from BH KZF-1, which includes the nano-, meso- and macroporosity of the shales (3.64–6.07 %; Table 2.1). The Whitehill Formation has the highest porosity of the lower Ecca Group, and in the case of BH SFT2, it appears that dolomite occurring in the Whitehill Formation can contribute to increasing porosity values (Geel et al., 2015; Nolte et al., 2019).

Table 2.1: Average porosity (%) and permeability (m^2) for the lower Ecca Group summarized from Geel et al. (2015) and Nolte et al. (2019).

Formations	***Hg intrusion tests (Geel et al., 2015).***		***He pycnometry tests (Nolte et al., 2019)***		
	Average porosity (%)		**Average porosity (%)**		**Average (m^2)**
Collingham	0.29		3.64		10^{-19}–10^{-20}
Whitehill	**Shale**	**Dolomite**	**Shale**	**Dolomite**	10^{-20}–10^{-22}
	1.35	2.91	6.07	4.25	
Prince Albert	0.53		4.13		10^{-22}

2.3 Materials and methods

2.3.1 Borehole KZF-1

BH KZF-1 is 671 m deep and is located in the Tankwa Karoo Sub-basin in the Western Cape (32° 50’ 30.43” S, 19° 44 ’33.02” E; Figure 2.3). It was drilled south of the dolerite line, which is a regional zone in the MKB north of which dolerite dykes and sills are common. The borehole intersected Prince Albert, Whitehill, Collingham and Tierberg formations, and stopped after penetrating ~ 15 m into the uppermost Dwyka Group.

Desorbed and residual gas contents and composition were analysed by Geokrak (Poland). Desorbed gas was very low as were residual gas volumes (0.01 m^3/t and 0–0.74 m^3/t, respectively). Residual gas was mostly methane (61–99%) with small amounts of nitrogen and carbon dioxide (de Kock et al., 2017).

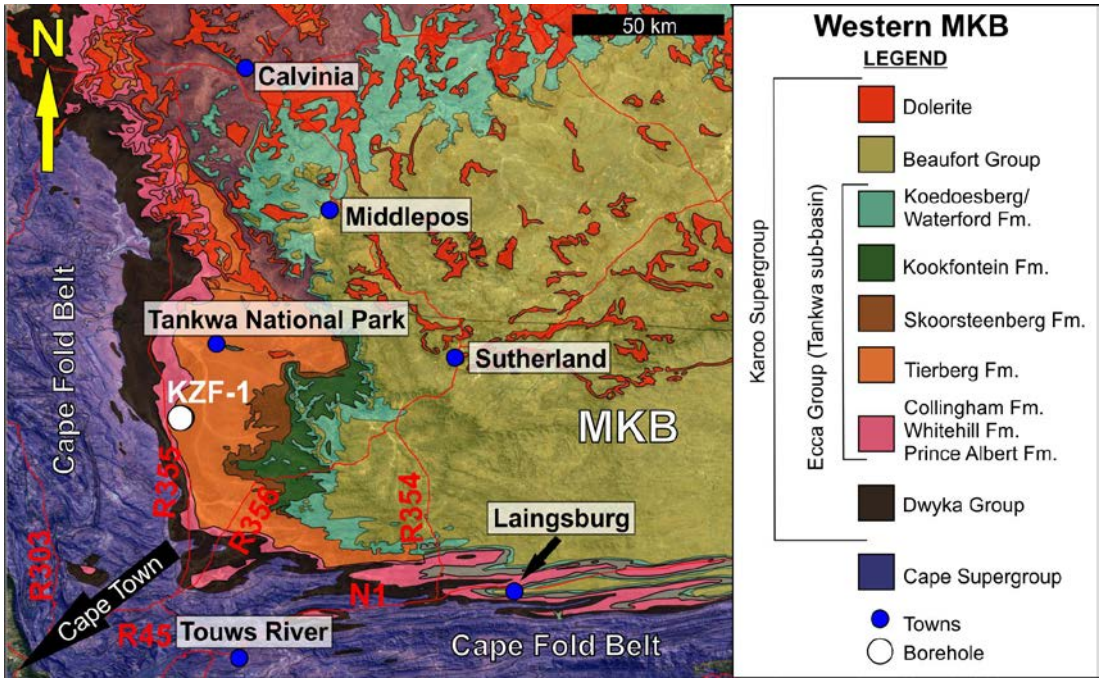

Figure 2.3: Simplified geological map of borehole KZF-1 in the Tankwa Karoo Sub-basin in the MKB (32° 50' 30.43" S, 19° 44' 33.02" E).

2.3.2 Borehole KWV-1

BH KZW-1 is 2353 m deep and is located in the far eastern MKB (32° S 14' 41'', 28° E 35' 08'') near a town called Willowvale in the Eastern Cape Province (Figure 2.4). Stratigraphic information is limited for this region of the country, due to thick vegetation cover and few outcrops. It is, however, a region of high density of dolerite intrusions (Figure 2.4). The borehole intersected part of the lower Beaufort Group (Koonap Formation), the Ecca Group (from oldest to youngest: Prince Albert, Whitehill, Collingham, Ripon, Fort Brown, Waterford formations), and after intersecting the first ~15 m of the Dwyka Group, drilling was stopped.

Desorbed and residual gas content and composition was analysed by Latona Consulting (South Africa). No residual gas was measured, and 0.20 m^3/t desorbed methane was detected only in the Wonderfontein Member of the Ripon Formation, which is the upper Ecca Group (de Kock et al., 2017).

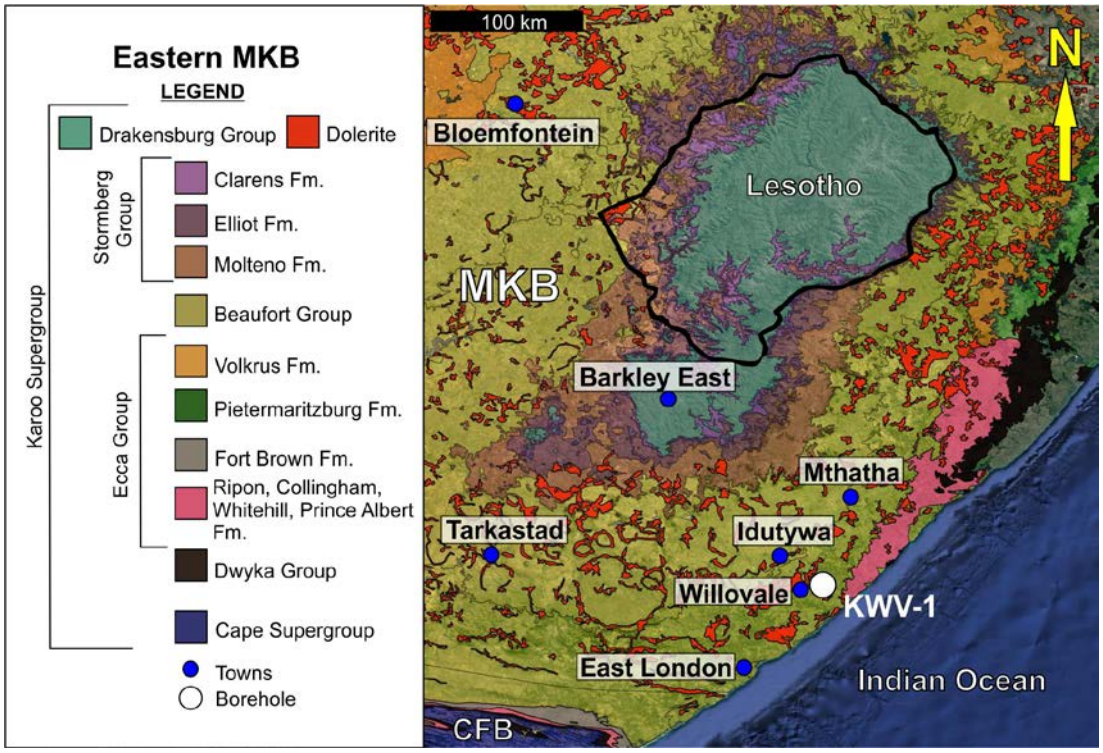

Figure 2.4: Simplified geological map of borehole KWV-1 in the Transkei, eastern MKB (32° S 14' 41'', 28° E 35' 08''.

2.3.3 Composition and petrophysics

Sedimentological logging of the lower Ecca Group in BH KZF-1 and BH KWV-1 included the macroscopic assessment of composition, grain size, sedimentary structures and textural characteristics (e.g., sorting, roundness, clast shape where applicable) of the strata in dry cores and was aided by standard sedimentological comparator charts (Pettijohn et al., 1987; Tucker, 1988) as well as a Munsell Rock Colour Chart (Appendix D, E). Geophysical data were logged by Weatherford Slimline Services and included *in situ* measurements of the physical rock properties and fracture orientations. A total of 43 core samples were selected from BH KZF-1 and 17 samples from BH KWV-1. Sample taken for analyses from both boreholes are summarized in Figure 2.5.

Samples were prepared as standard petrographic thin-sections and analysed using a Zeiss Axiocam A1 microscope in the Department of Geological Sciences at the University of Cape Town. Eight samples from each borehole were polished and Au-coated for analysis with a Zeiss MERLIN FEG scanning electron microscope (SEM) at the Central Analytical Facilities in the University of Stellenbosch. Two samples from each borehole were analysed using a the JEOL Hyperprobe JXA-8230 at the GFZ in Potsdam, Germany.

Porosity was investigated using three different techniques:

1) Micro CT Scanning using the XT H 225 ST, Large Cabinet Computed Tomography (CT) system at X-sight X-Ray Services in Cape Town, South Africa. Software used to control the acquisition of the dataset is Inspect-X. X-ray parameters are: kV = 140; mA = 200; 0.5 mm Cu filtration source; 4000 projection images. The CT data set was then reconstructed into 3D voxel data using the Nikon CTPro 3D. The 3D voxel data is viewed and manipulated using Volume Graphics voxel manipulation software. The focal-spot size of the x-ray source was 3–5 µm; the voxel size was 20–30 µm.
2) Broad Ion Beam (BIB) polishing and scanning electron microscope (SEM) analyses were carried out at two institutes: 1) GeoForschungsZentrum (GFZ) in Potsdam, Germany, using the Jeol IB-19520CCP BIB polisher with argon beam, followed by SEM analysis using the Ultra 55 Plus (Carl Zeiss) SEM, and 2) Rheinisch Westfälische Technische Hochschule (RWTH) Aachen, Germany, using the JEOL SM-09010 cross section polisher, followed by SEM analysis using the Zeiss Supra 55 SEM. BIB polishing in combination with SEM allows for the serial sectioning of larger areas (2 mm^2) at the resolution of an SEM (< 5nm). BIB milling allows for microstructure analysis and the imaging of nano-pores. A back-scatter detector (BSE) was used for phase contrast imaging, whereas a secondary electron detector (SE2) was used for surface topography investigation.
3) Focused Ion Beam (FIB)-SEM and 3D reconstruction tomography was performed at the GFZ in Potsdam, Germany. Samples were coated with the BAL-TEC MED 020 coating system, and an area of ~ 25 μm^3 was selected for tomography using the "Slice and View" software from Thermo Fischer Scientific. Using a Ga^+ ion source at 30 KV, ~ 100 nm thick slices were cut, taking backscattered images (BSE) images at 20 KV using the FEI Quanta 3D FEG. The slices were processed in Avizo 7.0 software to obtain 3D reconstruction of porosity/organic carbon in black shale.

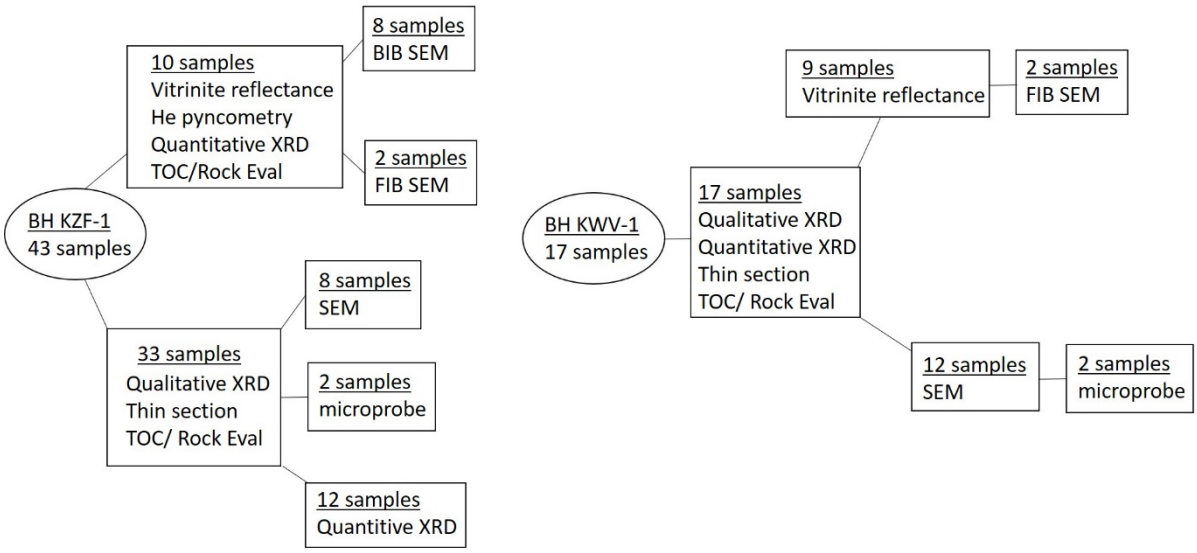

Figure 2.5: Flow charts summarizing the sample analyses from BH KZF-1 and BH KWV-1.

Qualitative XRD was carried out with a Phillips PW 3830/40 Generator with PW 37010 mpd control using the X'pert data collector/identifier in the Department of Geological Sciences at the University of Cape Town. Quantitative XRD was measured in wt% with a Malvern Panalytical AERIS diffractor meter with PIXcel detector and fixed slits with Fe filtered Co-Kα radiation by XRD Analytical and Consulting Laboratory in Pretoria, South Africa. The phases were determined using X'pert Highscore Plus software.

Vitrinite reflectance (VR_o) is the parameter used to measure thermal maturity in rocks and is in linear correlation with bitumen reflectance (BR_o; Jacob, 1985; Landis & Castaño, 1995). Vitrinite forms part of the macerals, which are organic materials or a mixture of organic compounds that occur in sedimentary rocks and coal. Bitumen, on the other hand, is a secondary product of mature organic matter (Curiale, 1986). Because vitrinite is not always present in the lower Ecca Group of the MKB, but solid bitumen is a common component (Geel et al., 2015), both methods were used in the reflectance measurements. Bitumen reflectance measurements was carried out by the author at the Institute of Geology and Geochemistry of Petroleum and Coal at RWTH in Aachen, Germany on 9 samples from BH KWV-1. Samples, cut in 2 x 2 cm squares were analysed using a Zeiss microphotometric system, which was calibrated with Zeiss yttrium-aluminium-garnet standard (R = 0.906), using 50x objective lens under immersion oil (ne = 1.518). Vitrinite reflectance, helium pycnometry/expansion and fluid-flow experiments were performed on 10 samples (KZF01P to KZF10P) from BH KZF-1. These analyses were also carried out at RWTH in Aachen, Germany. Details of this measurements were documented by Nolte et al. (2019) as part of a collaboration during this study.

2.3.4 Geochemistry

Organic geochemistry measurements (i.e., TOC/Rock Eval analyses) were completed by the Indian Institute of Technology in Bombay, India on all samples from both boreholes. The samples were cut and milled and 5 g of rock powder per sample was selected for analysis. Rock-Eval pyrolysis is a technique used to identify the hydrocarbon release of organic-rich sedimentary rocks, which helps to analyse the maturity, weight percentage and type of the contained organic matter (Nunez-Betelu & Baceta, 1994). Additional TOC/Rock Eval data obtained from the KARIN project (de Kock et al., 2017) for BH KZF-1 are added to this study to provide a more robust dataset.

The Rock Eval technique establishes the quantity of kerogen converted into hydrocarbons in a shale sample. Slow increase in temperature under laboratory conditions will release hydrocarbons from the remaining organic matter in the rock. The Rock Eval process records the free hydrocarbons outputs information as graphs. The S1 peak of the graph represents the content of hydrocarbons between C1 and C25 (i.e., already produced hydrocarbons). The S2 peak represents the hydrocarbons that can still be produced after heating the sample to 550–600 °C. During Rock Eval pyrolysis the TOC, carbon (C), oxygen index (OI), hydrogen index (HI), total hydrocarbons (PY) and the temperature (Tmax) corresponding to hydrocarbon production is measured. The more mature the rock, the higher the amount of energy is required to release the remaining hydrocarbons. The H/C and O/C ratios are illustrated in Van Krevelen diagrams and predict kerogen type and thermal maturation (Nuñez-Betelu & Baceta, 1994). The production index (PI) is an additional maturity indicator and is used to quantify the hydrocarbons that have already been generated relative to the total amount capable of being generated (Sihra, 2010).

2.4 Petrological results from BH KZF-1

BH KZF-1 intersected 671 m of sedimentary rocks in the lower Karoo Supergroup of which 13.63 m belong to the Dwyka Group, 158.55 m to the Prince Albert Formation, 65.50 m to the Whitehill Formation, 80.13 m to the Collingham Formation and 338.62 m to the Tierberg Formation. The core was logged at the drill site and the lithostratigraphic core log is available in Appendix D. A lithostratigraphic column in Figure 2.6 illustrates 340 m of drilled succession, of which the lower 8 m is the uppermost part of the Dwyka Group, and the upper 20 m is the lowermost Tierberg Formation. In addition to the main lithostratigraphic units, Figure 2.6 also shows their

sedimentological properties, and the gamma-ray and TOC (wt%) data recorded in BH KZF-1 for these lower Karoo Supergroup rocks. Quantitative XRD data (Appendix A) is visually represented in Figure 2.7. For each of the formations, data pertaining to their qualitative composition, mineralogical composition, TOC content, structures and texture are shown in Figures 2.8–2.21 and summarized in Table 2.2. For the purpose of this study we will only focus on the Prince Albert, Whitehill and Collingham formations (the lower Ecca Group).

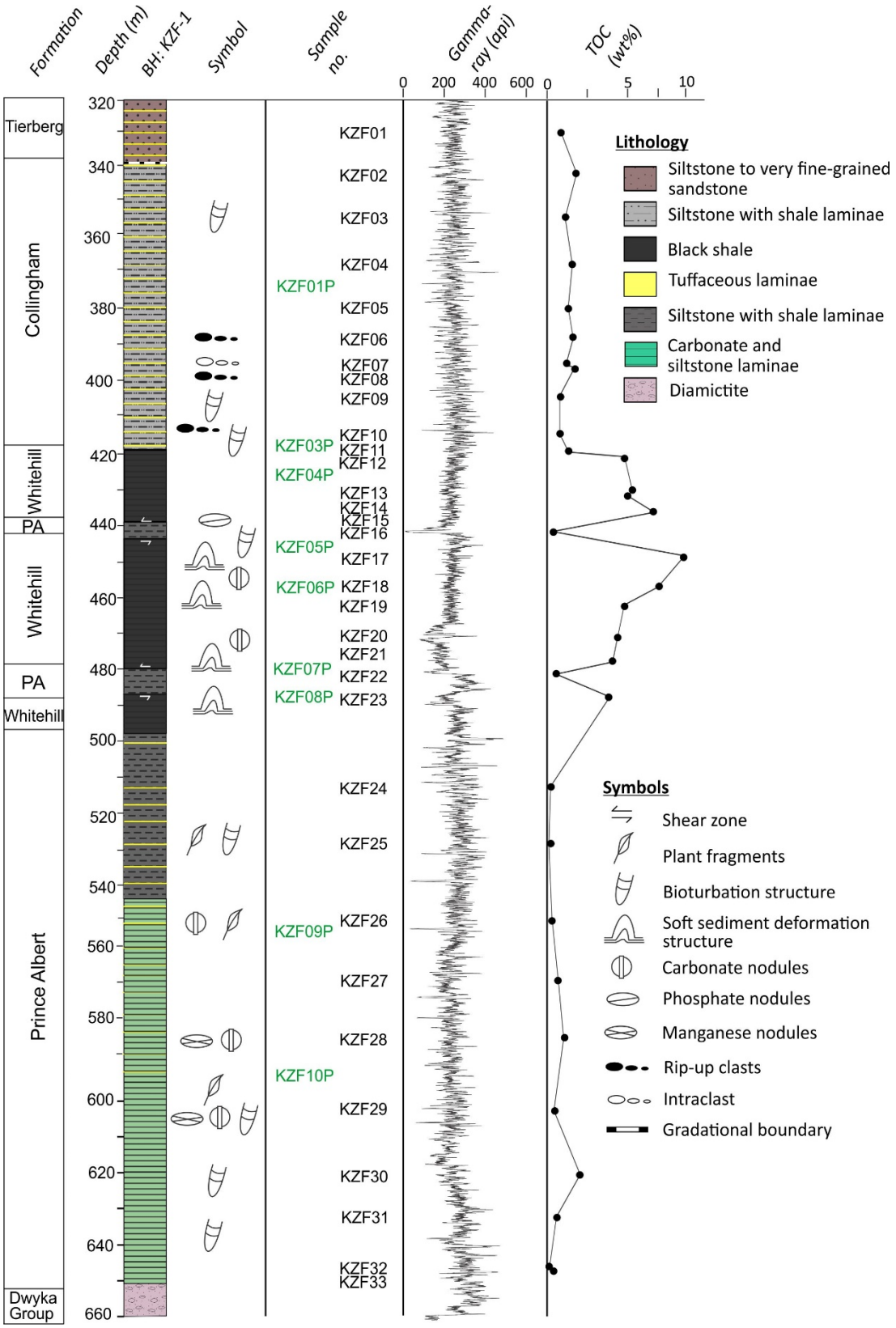

Figure 2.6: Depth profile of BH KZF-1 showing lithostratigraphic units, the main rock types with associated sedimentary features, sampling intervals, gamma-ray (API) and TOC (total organic carbon in wt%) data.

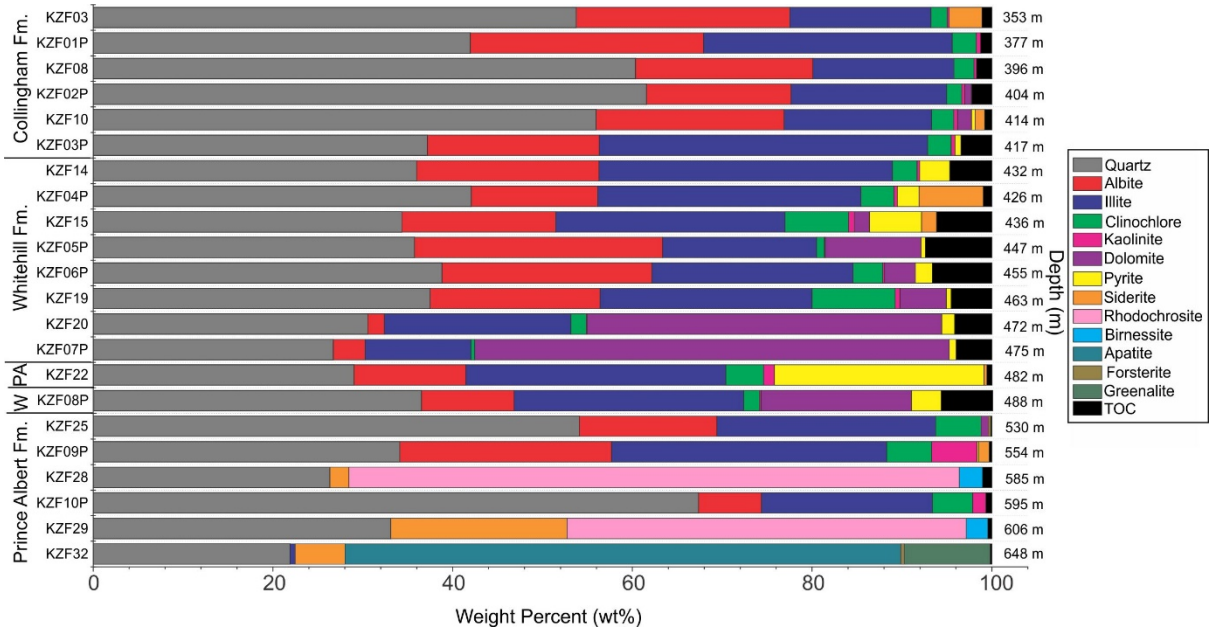

Figure 2.7: Quantitative XRD analyses of the mineralogical composition and TOC content from BH KZF-1 in wt%. PA: Prince Albert Formation; W: Whitehill Formation.

2.4.1 Prince Albert Formation

The Prince Albert Formation consists of dark grey carbonaceous mudstone, medium grey calcareous mudstone, dark grey shale, light grey to very light grey siltstones and subordinate light olive-grey to greenish-grey tuffaceous laminae. Pyrite lenses and calcite veining are common. The Prince Albert Formation is 158.55 m thick and appears to be structurally duplicated and repeatedly thrusted between fissile layers of the Whitehill Formation (Figure 2.6). The thrusted layers of Prince Albert Formation are 3.35 m and 8.6 m thick and are bounded by fracture zones.

The Prince Albert Formation forms a sharp bottom contact with the dropstone-rich mudstone and diamictites of the underlying Dwyka Group. Exotic lonestones are identified in sample KZF33 (~ 650 m; Figure 2.8 A–B) and is associated with partial melt-out of ice-rafted debris (e.g., Isbell et al., 2008; Blignaut & Theron, 2015). Sample KZF32 is ~ 2 cm above the Dwyka Group contact, and contains greenalite (10 wt%), stilpnomelane, fluorapatite (62 wt%) and minor lonestone associated forsterite (0.4 wt%; Figures 2.7; 2.8 C, D).

The lower Prince Albert Formation (~ 649 to 550 m) is comprised of calcareous mudstone consisting primarily of quartz (37.18 wt%), rhodochrosite (28.08 wt%) and siderite (6.12 wt%) intercalated with clay (Illite = 4.91 wt%; clinochlore = 1.12 wt%) and siltstone laminae. Samples contain bioturbation structures (Figure 2.9 K–L) and organic-matter aggregates (Figure 2.10 U–V). Additionally, in samples KZF29, KZF28

and KZF26, Mn-oxide, identified as birnessite (1.25 wt%), is identified occurring as nodules and cement between rhodochrosite crystals (Figures 2.9 I–N; 2.10 O–T, W–X). At ~ 624 m quartz grains are corroded and coated with chlorite with evidence for quartz reprecipitation. These authigenic mineral growths reduce the interparticle porosity (Figure 2.12 G–H).

In the upper Prince Albert Formation (~ 550 to 500 m), there is an increase in the frequency of siltstone and mudstone beds, and tuffaceous laminae. The clay mineral content is higher in the upper Prince Albert Formation (illite = 27.96 wt%, clinochlore = 4.75 wt%, kaolinite = 2.09 wt%; Table 2.2). Structures include soft-sediment deformation structures, bioturbation structures, organo-mineralic aggregates, phosphate nodules and carbonate nodules are recorded. Carbonate minerals include siderite (0.54 wt%) and ankerite. Rhythmite units of ~ 1 cm laminated siltstone beds fine upward to claystone (Figure 2.11 D'). Tuffaceous laminae have altered to siderite and chlorite and are intercalated with the mudstone (Figures 2.11 A'–B'; 2.12 C–E). Sample KZF16 is thrust into the Whitehill Formation but likely comes from the upper Prince Albert Formation as it contains layers of mudstone and tuff with some lag deposits with silt-sized particles including glass shards (Figure 2.11 G'–H'). High pyrite content (8.14 wt%) is associated with the thrust zone and hydrothermal veining. The upper Prince Albert Formation forms a post-depositional brecciated contact with the overlying Whitehill Formation (Figure 2.11 E').

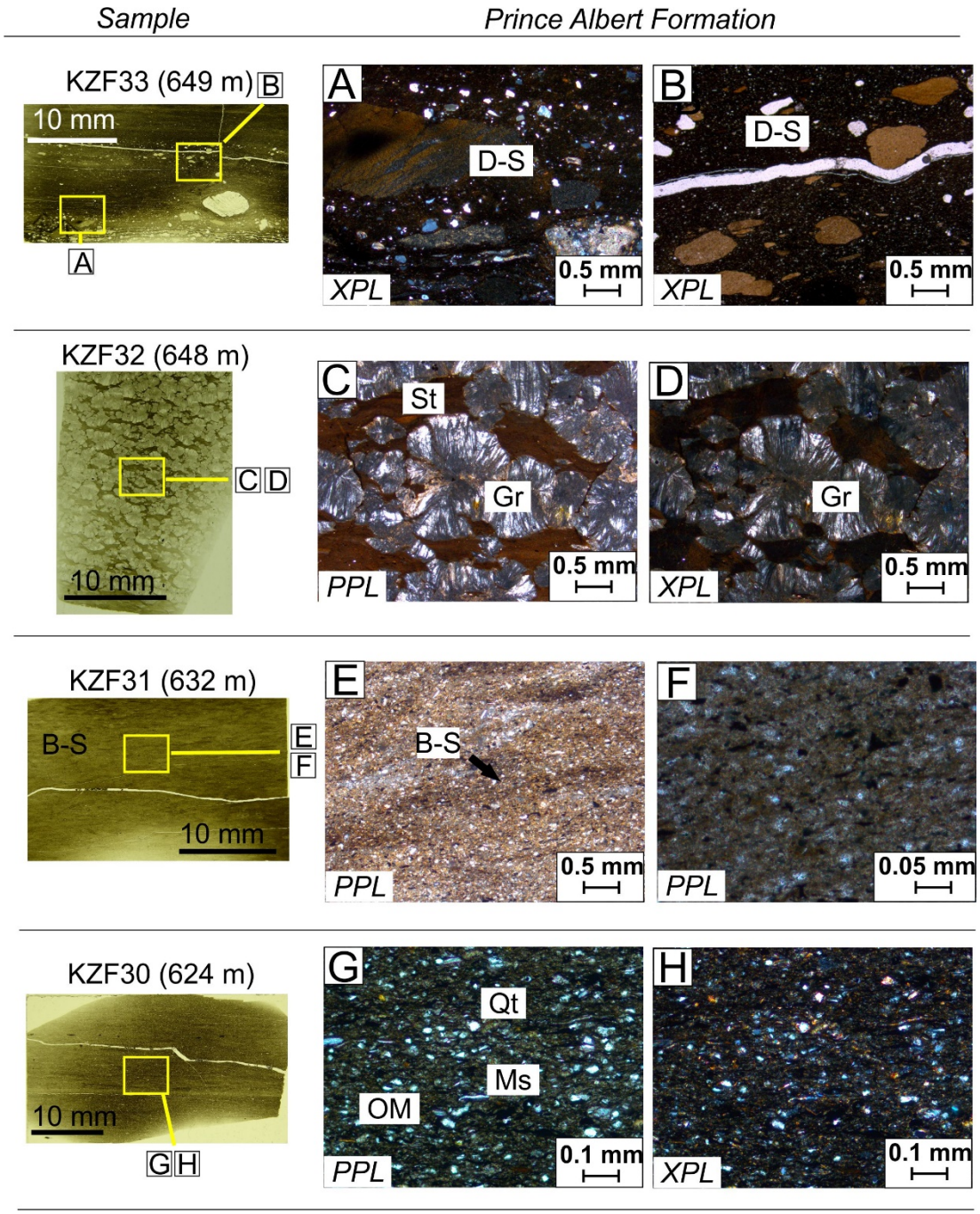

Figure 2.8: Thin section micrograph of samples KZF30, KZF31, KZF32 and KZF33 from the Prince Albert Formation in BH KZF-1. A, B) Dropstones in clay-rich matrix at the contact between the Dwyka Group and Prince Albert Formation. C, D) Microcrystalline, radial greenalite growths enveloped by stilpnomelane. E, F) Clay- and silt- sized grains and possible bioturbation structures. G, H) Clay-and silt-sized grains and bioturbation structures. Abbreviations: D-S: dropstones; St: stilpnomelane; Gr: greenalite; B-S: bioturbation; Qt: quartz; OM: organic matter; Ms: muscovite.

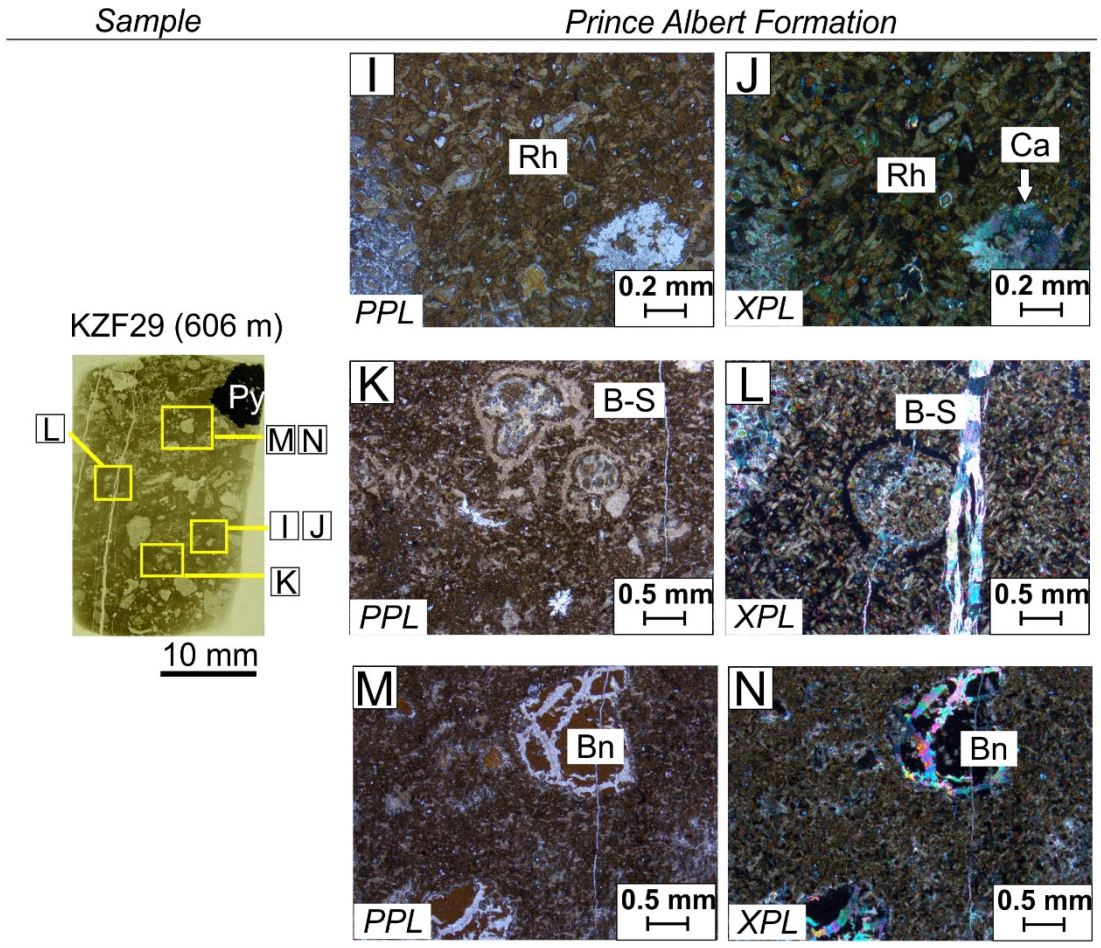

Figure 2.9: Thin section micrographs of sample KZF29 from the Prince Albert Formation in BH KZF-1. I, J) Rhombohedral and scalenohedral rhodochrosite crystals. K, L) Possible feeding traces in rhodochrosite. M, N) Birnessite nodules and rhodochrosite. Abbreviations: Rh: rhodochrosite; Ca: calcite; B-S: bioturbation structure; Bn: birnessite; Py: pyrite.

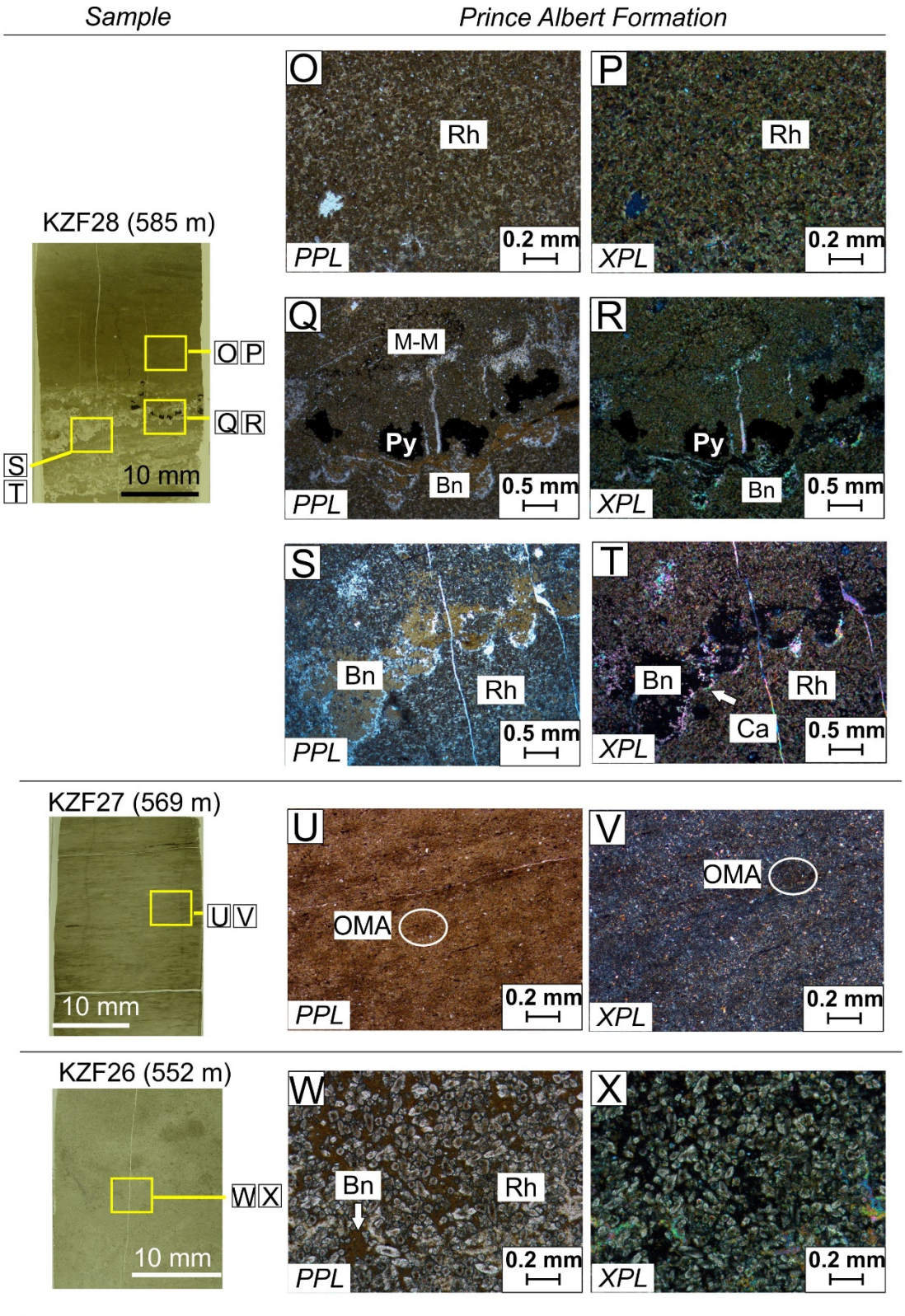

Figure 2.10: Thin section micrograph of samples KZF26, KZF27 and KZF28 from the Prince Albert Formation from BH KZF-1. O, P) Rhodochrosite-rich matrix. Q, R) Soft-sediment deformation formed by birnessite in rhodochrosite matrix. U, V) Organo-mineralic aggregates in mudstone. W, X) Birnessite and rhodochrosite matrix. Abbreviations: Py: pyrite; Ca: calcite; Bn: birnessite; Rh: rhodochrosite; OMA: organo-matter aggregate.

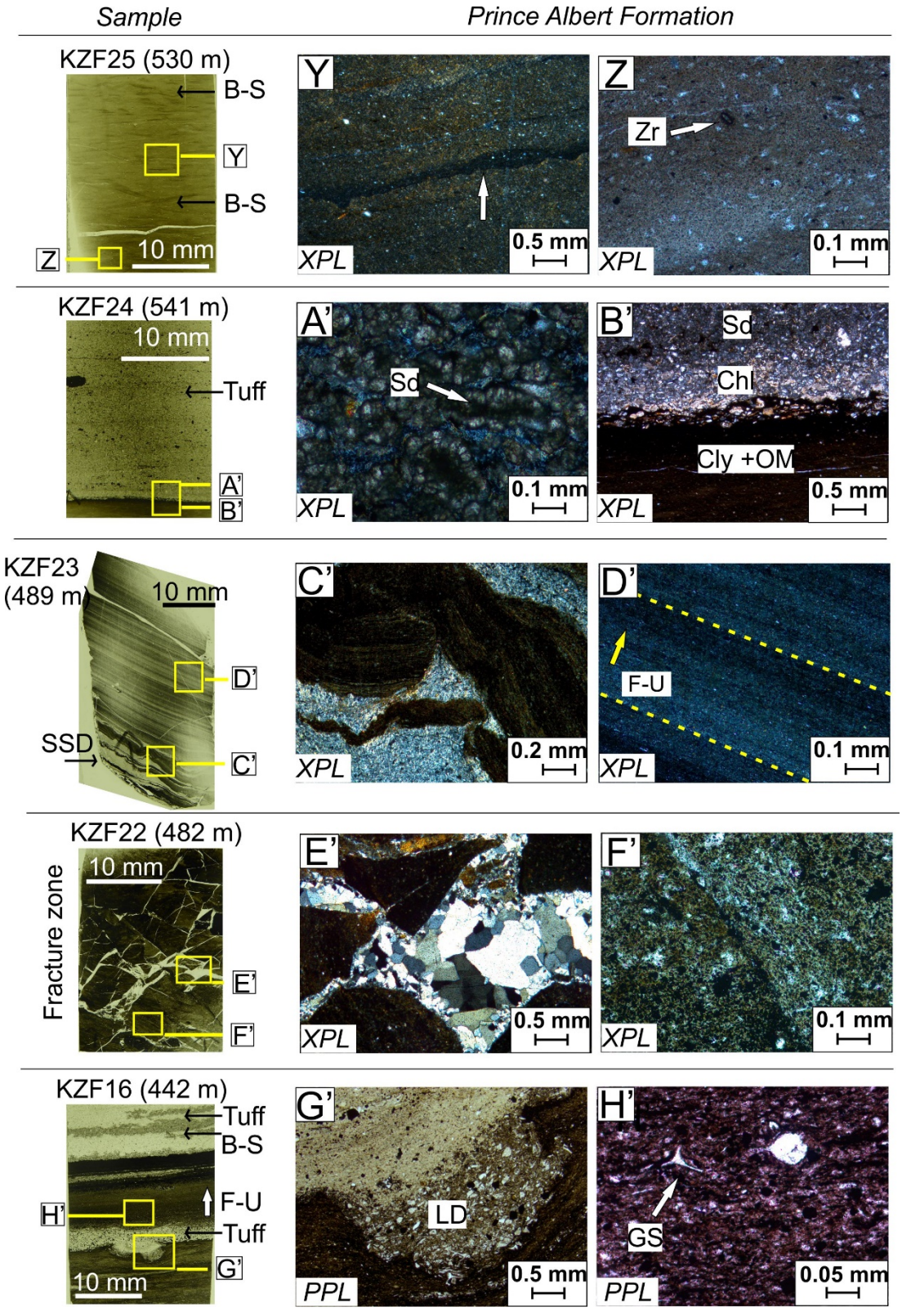
Sample
Prince Albert Formation
KZF25 (530 m)
B-S
Y
B-S
Z
10 mm
Y
0.5 mm
XPL
Z
Zr
0.1 mm
XPL
KZF24 (541 m)
10 mm
Tuff
A'
B'
A'
Sd
0.1 mm
XPL
B'
Sd
Chl
Cly +OM
0.5 mm
XPL
KZF23
(489 m)
10 mm
D'
SSD
C'
C'
0.2 mm
XPL
D'
F-U
0.1 mm
XPL
KZF22 (482 m)
Fracture zone
10 mm
E'
F'
E'
0.5 mm
XPL
F'
0.1 mm
XPL
KZF16 (442 m)
Tuff
B-S
H'
F-U
Tuff
G'
10 mm
G'
LD
0.5 mm
PPL
H'
GS
0.05 mm
PPL

Figure 2.11: (previous page) Thin section micrographs of samples KZF16, KZF22, KZF23, KZF24, and KZF25 from the Prince Albert Formation from BH KZF-1. Y) Wavy lamina (up to ~ 25 µm thick). Z) Zircon grain. A') Siderite. B') Organic matter-rich and clay-rich laminae overlain by chlorite-rich and siderite-rich horizons. C') Soft-sediment deformation of organic-matter-rich and quartz-rich laminated mudstone. D') Fining-upward sequences of laminated mudstone. E') Brecciated mudstone with quartz veining. F') Predominately clay-rich matrix. G') Lag deposit of silt-sized mineral grains and tuff. H') Glass shard within silt- and clay-sized minerals. Abbreviations: LD: lag deposit; GS: glass shard; Sd: siderite; Ch: chlorite; Zr: zircon; Cly: clay minerals; OM: organic matter; SSD: soft-sediment deformation structures; F-U: fining-upward; B-S: bioturbation structure.

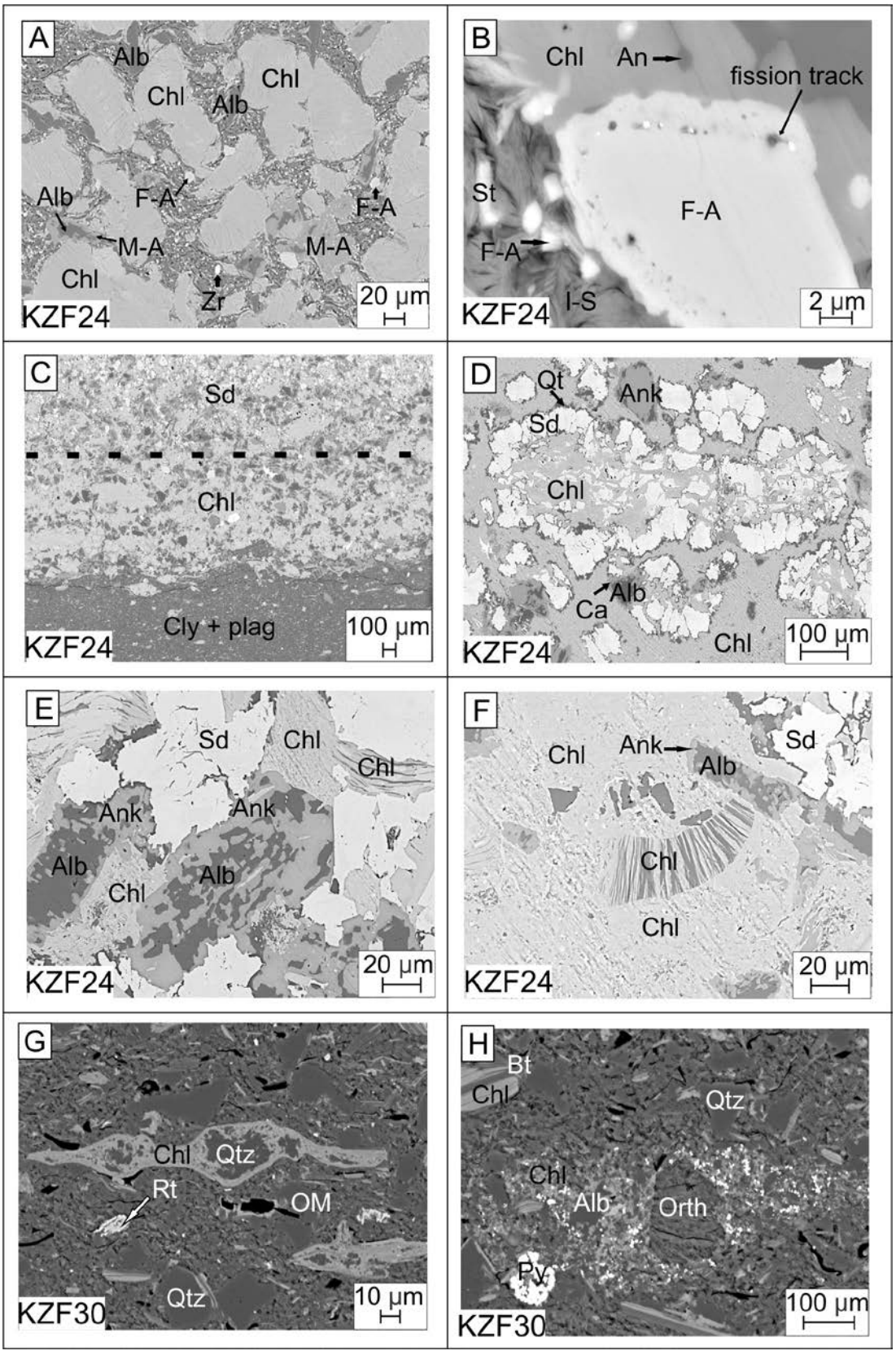
A
Alb
Chl
Chl
Alb
Alb
F-A
F-A
M-A
M-A
Chl
Zr
20 µm
KZF24
B
Chl
An
fission track
St
F-A
F-A
I-S
2 µm
KZF24
C
Sd
Chl
Cly + plag
100 µm
KZF24
D
Qt
Ank
Sd
Chl
Ca
Alb
Chl
100 µm
KZF24
E
Sd
Chl
Chl
Ank
Ank
Alb
Alb
Chl
20 µm
KZF24
F
Chl
Ank
Alb
Sd
Chl
Chl
20 µm
KZF24
G
Chl
Qtz
Rt
OM
Qtz
10 µm
KZF30
H
Bt
Chl
Qtz
Chl
Alb
Orth
Py
100 µm
KZF30

Figure 2.12: (previous page) SEM micrographs of samples KZF24 and KZF30 from the Prince Albert Formation from BH KZF-1: A) Chlorite grains. B) Fluorapatite with grain boundary dissolution. C) Clay- and plagioclase-rich lamina overlain by chlorite- and siderite-rich laminae. D) Chlorite with siderite rim. E) Alteration of Albite to ankerite. G, H) Minerals with chlorite coating. Abbreviations: Alb: albite; Chl: chlorite; F-A: fluorapatite; M-A: manganoan ankerite; Zr: zircon; An: anorthite; St: stilpnomelane; I-S: illite-smectite; Sd: siderite; Cly: clay-rich laminae; plag: plagioclase; Qt: quartz; Ank: ankerite; Ca: calcite; OM: organic matter; Rt: rutile; Py: pyrite; F-A: fluorapatite; Bt: biotite; Orth: orthoclase.

2.4.2 Whitehill Formation

In BH KZF-1, the Whitehill Formation is repeatedly intersected by low-angle thrust faults and fracturing at 439.95 m, 443.3 m, 479.55 m and 489.15 m depths below the surface (Figure 2.6). This suggests that segments of the Whitehill and Prince Albert formations were structurally duplicated (an observation made in the southern MKB earlier by Kingsley (1981) and Lindeque et al. (2007), for example. Consequently, the true thickness of the Whitehill Formation in this area is not 65.5 m but more likely only 19.5 m.

The Whitehill Formation consists of organic-matter-rich black shale with siltstone laminae and lenses that are grey- to light grey, light olive-grey and greenish-grey. In thin section, shales are distinctly laminated and contain some soft-sediment deformation structures (Figure 13 A, B, E). The Whitehill Formation is rich in quartz (35.36 wt%) and albite (15.23 wt%; Figure 2.7). Quartz grains are heavily corroded (Figure 2.15 A–D) and there is quartz re-precipitation reducing pore spaces. Clay minerals are predominately illite (23.19 wt%), chlorite (3.42 wt%) and minor kaolinite (0.26 wt %; Table 2.2). Total pyrite content is 2.22 wt% and framboidal aggregates, euhedral pyrite grains and pyrite stringers are present (Figure 2.15 A–D). Phosphate nodules are detected at ~ 436 m (Figure 2.14 K–L) and calcite nodules at ~ 432 m (Figure 2.14 M–N). Fluorapatite grains are detected by SEM (Figure 2.15 B).

Ferroan dolomite is the most abundant carbonate mineral. The highest quantity of dolomite (up to 52 wt% in sample KZF07P; Figure 2.7) is detected near the base of the Whitehill Formation (472 to 475 m). SEM micrographs of dolomite at 472 m show “ooid-like” cement grains (Figure 2.15 E). Oxy-phlogopite is detected between the dolomite precipitates (Figure 2.15 F). In the middle to upper part of the formation (~ 457 m), dolomite occurs as isolated concretions precipitated around clay flocculants (Figure 2.16 A–C).

Other diagenetic carbonate minerals detected are siderite (0.98 wt%) and ankerite. Quartz and calcite veins are detected throughout the Whitehill Formation, often

associated with micro-folds and faults (Figure 2.13 E, I, J). Cone-in-cone (CiC) structures are observed both macroscopically and in thin section (Figure 2.14 O–P).

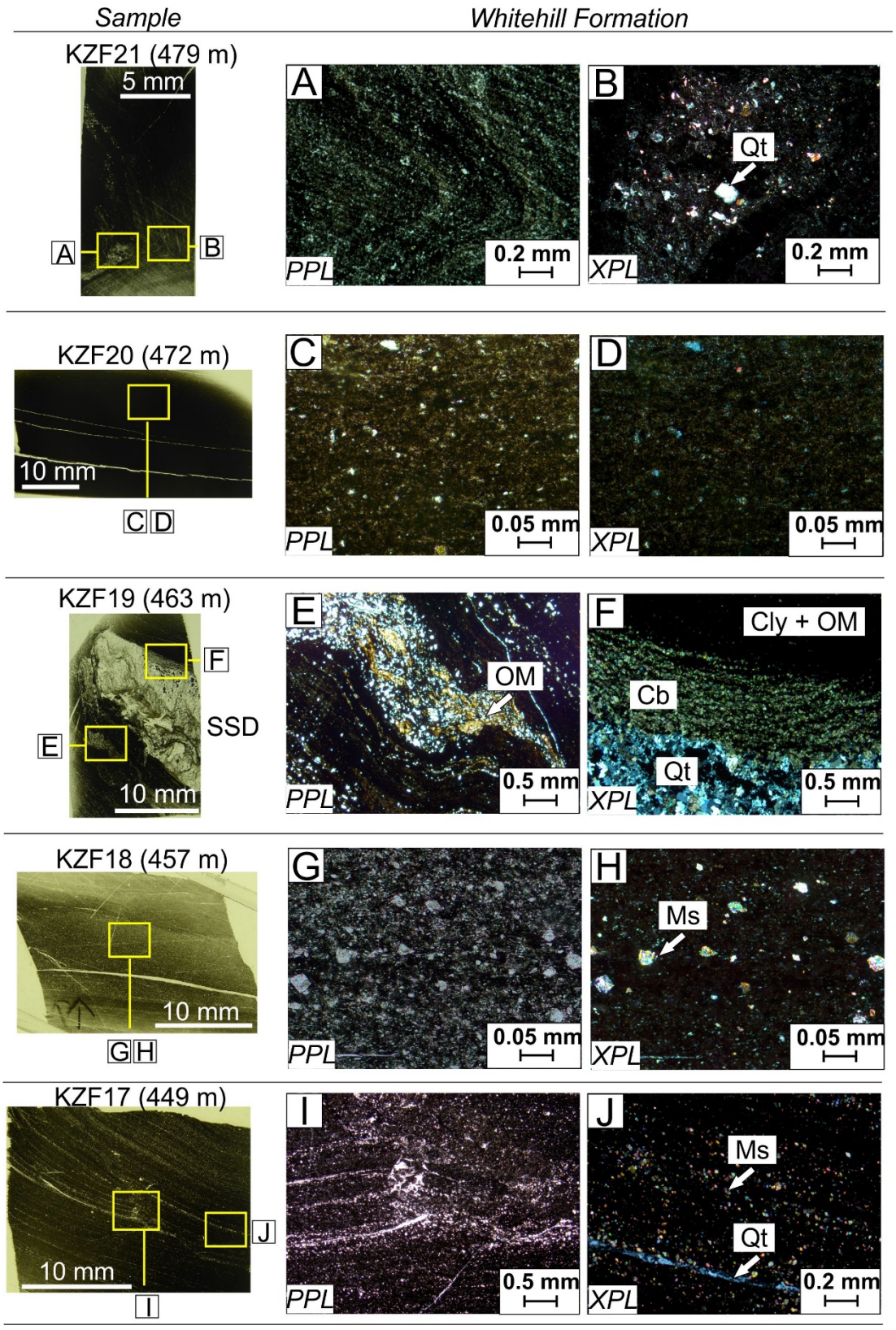

Figure 2.13: (previous page) Thin section micrographs of samples KZF17, KZF18, KZF19, KZF20 and KZF21 from the Whitehill Formation from BH KZF-1. A) Microfolding. B) Quartz grains within silty lamina. C, D) Organic matter-rich black shale. E) Soft-sediment deformation structure. F) Quartz-rich and carbonate-rich laminae. G, H) Muscovite grains and quartz vein parallel to lamination. I) Fracture in the black shale. J) Muscovite grains and quartz vein. Abbreviations: Qt: quartz; SSD: soft-sediment deformation structure; Cly: clay; Cb: carbonate; Ms: muscovite; OM: organic matter.

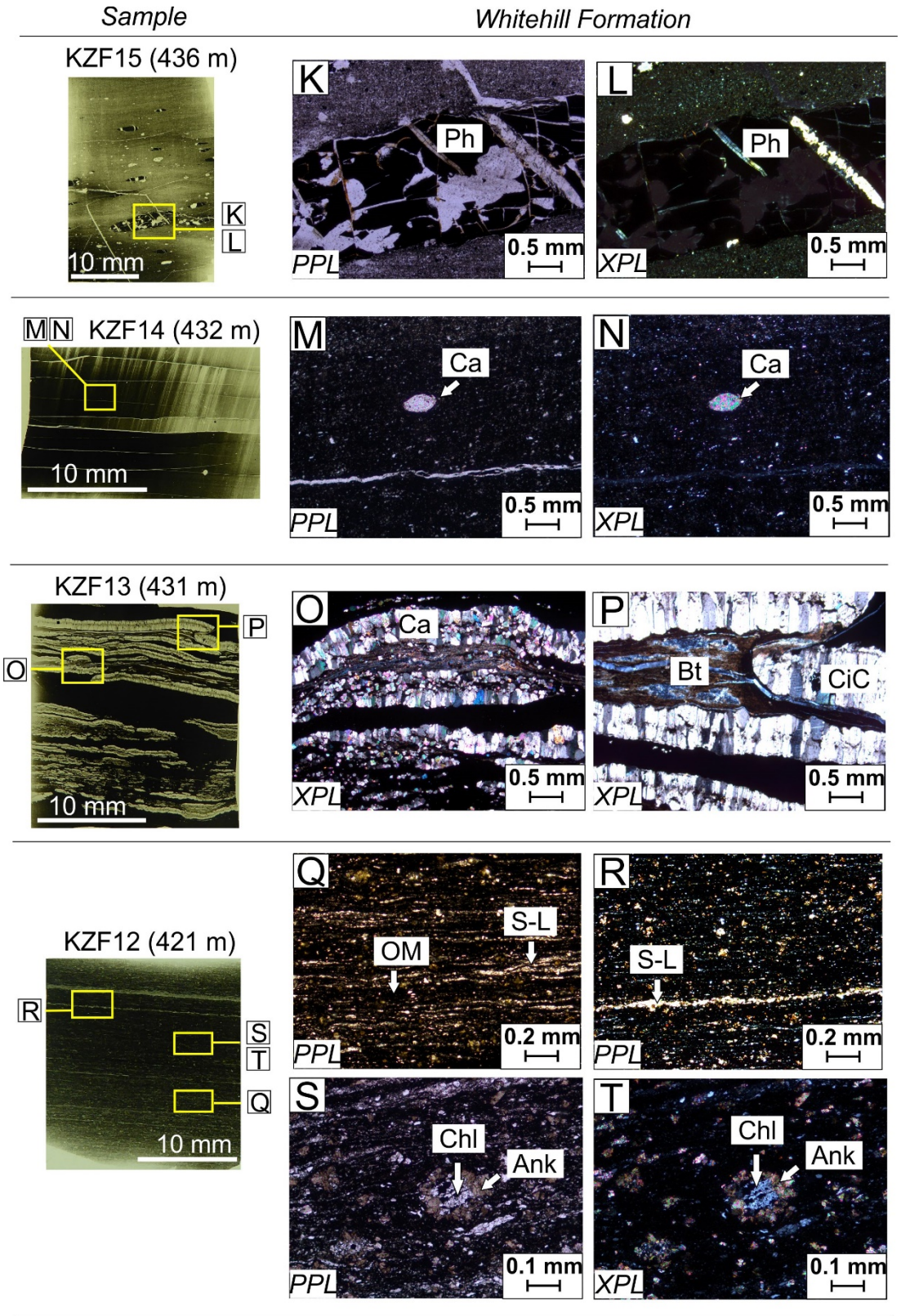

Figure 2.14: Thin section micrographs from samples KZF12, KZF13, KZF14 and KZF15 from the Whitehill Formation. K, L) Phosphate nodule. M, N) Calcite nodule. O, P) Cone-in-cone calcite structures. Q, R) Parallel lamination. S, T) Chlorite with ankerite growth rings. Abbreviations: OM: Organic matter; Chl: chlorite; Ank: ankerite; Ca: calcite; Bt: biotite; CiC: cone-in-cone; Ph: phosphorite; S-L: silty lamina.

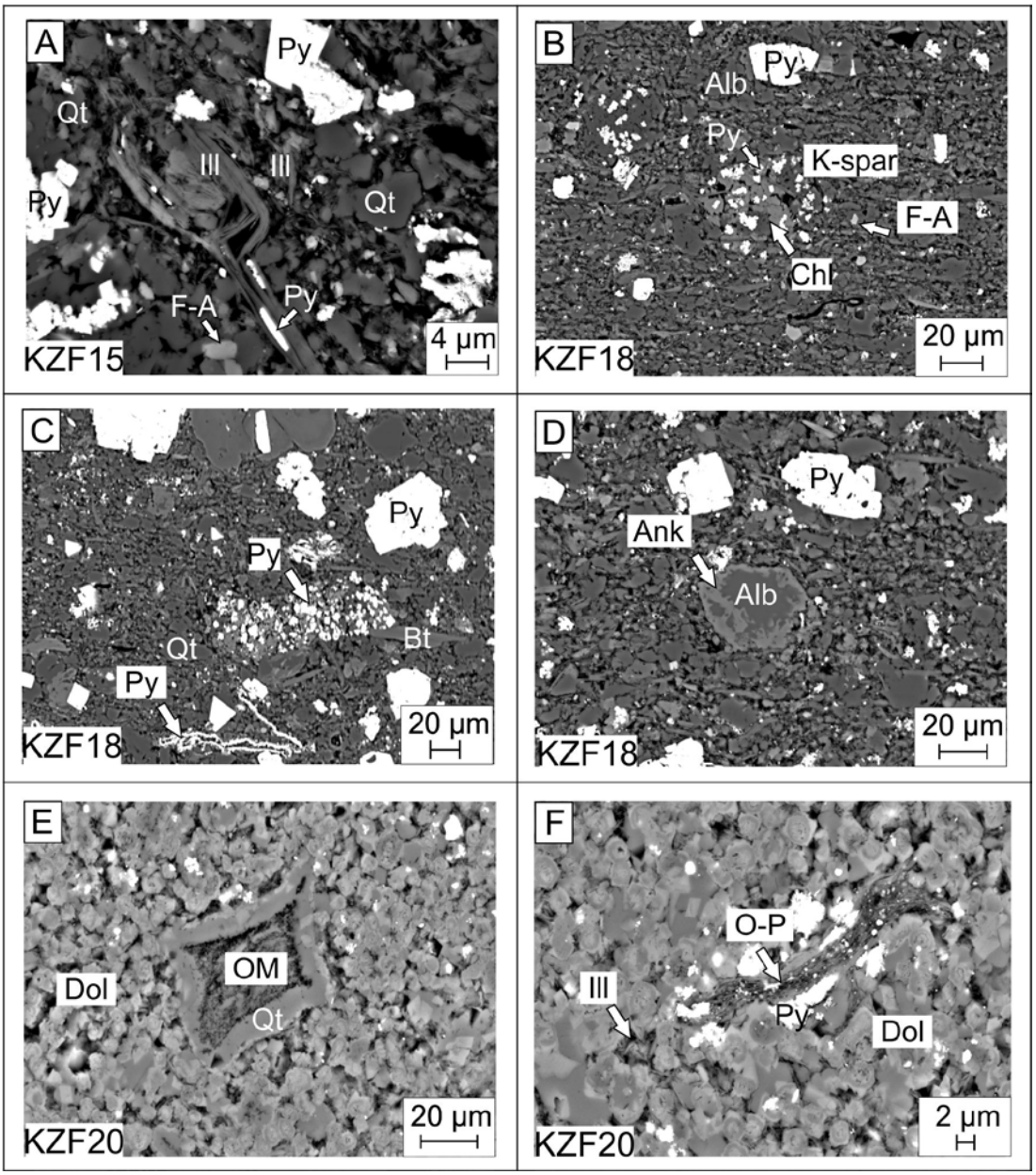

Figure 2.15: SEM micrographs of samples KZF15, KZF18 and KZF20 from the Whitehill Formation from BH KZF-1. A–D) Most common minerals present in the Whitehill Formation black shale. E, F) "Ooid-like" cement grains of dolomite. Abbreviations: Py: pyrite; Ill: illlite; Qt: quartz; F-A: fluorapatite; Alb: albite; K-spar: K-feldspar; Chl: chlorite; Ank: ankerite; OM: organic matter; Dol: dolomite; O-P: oxy-phlogopite.

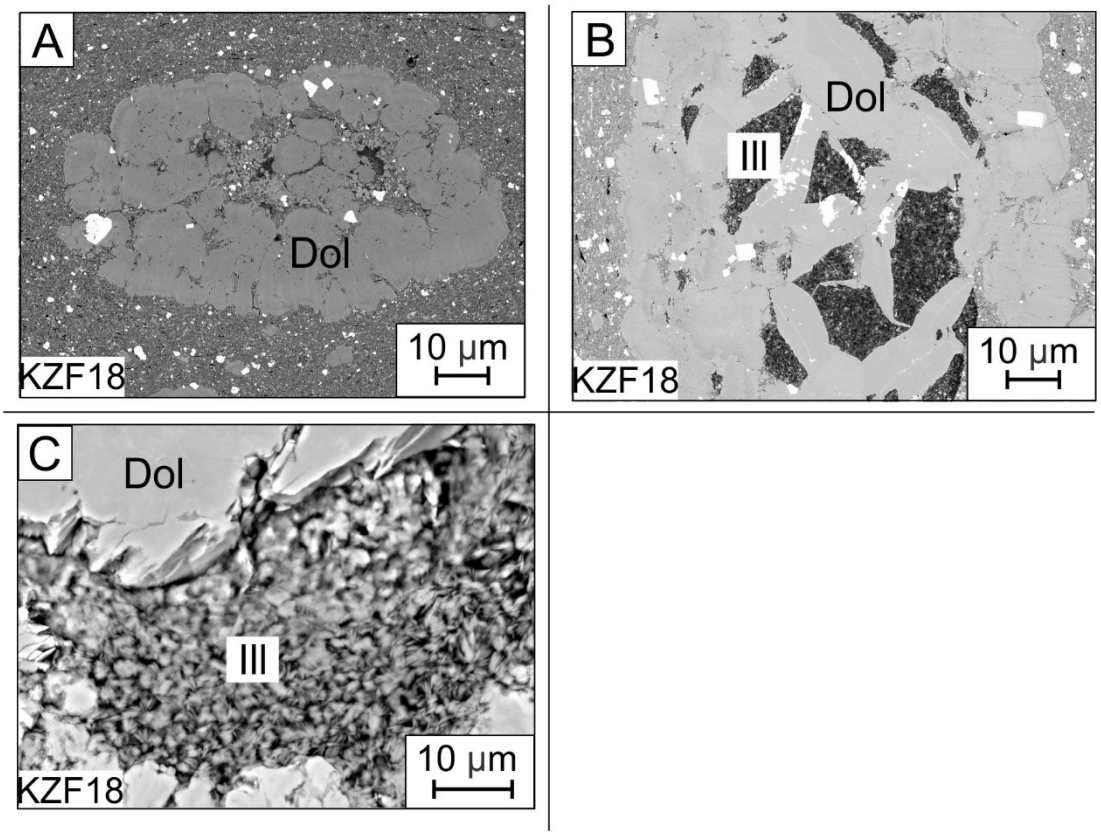

Figure 2.16: Microprobe micrographs of sample KZF18 from the Whitehill Formation from BH KZF-1. A–C: Dolomite nodule. Abbreviations: Ill: Illite; Dol: dolomite.

2.4.3 Collingham Formation

The Collingham Formation is 80.13 m thick, and comprises medium grey, medium dark-grey to dark-grey mudstone with very light-grey to light-grey siltstone laminae and light olive-grey and olive-grey to greenish-grey tuffaceous layers. The Collingham Formation forms a sharp contact with the underlying Whitehill Formation and grades upwards into the Tierberg Formation.

The Collingham Formation consists of rip-up clasts and intraclasts of tuff and mudstone. Intraclast-rich beds usually grade upwards into fine-grained laminated beds with occasional lithoclasts that are 50–100 µm in diameter, well rounded and ellipsoidal in shape. They are relatively rare and only detected at depths 419 m, 403 m, 395 m, 366 m and 340 m. Bioturbation structures, organic matter particulates (Figures 2.17 I–J; 2.19 W, Y–B') and framboidal pyrite aggregates (Figures 2.17 C–E) are prevalent throughout the Collingham Formation. The average pyrite content is low (0.19 wt%; Table 2.2).

The Collingham Formation has the highest quantity of quartz (52 wt%) and albite (20.93 wt%; Figure 2.7). Well-defined rhombohedral (40 µm) ankerite crystals are

unique to the Collingham Formation (Figures 2.18 R; 20 E). Tuffaceous laminae have undergone diagenetic alteration to calcite, albite, ankerite and ferroan dolomite (0.38 wt%; Figure 2.20). Albitization of Ca-feldspar is shown in Figure 2.21 A. Additional diagenetic transformations include chlorite (2.25 wt%) to ankerite (Figure 2.20 F) and growth of syn-depositional (Figure 2.18 O, P) and post-depositional (Figure 2.21 B, C) calcite nodules. K-feldspar (microcline) has been detected by SEM but not in large enough quantities to be recorded by quantitative XRD analyses. Calcite veining, exhibiting cone-in-cone texture, is often detected at the boundaries between shale and tuffaceous layers (Figure 2.18 T).

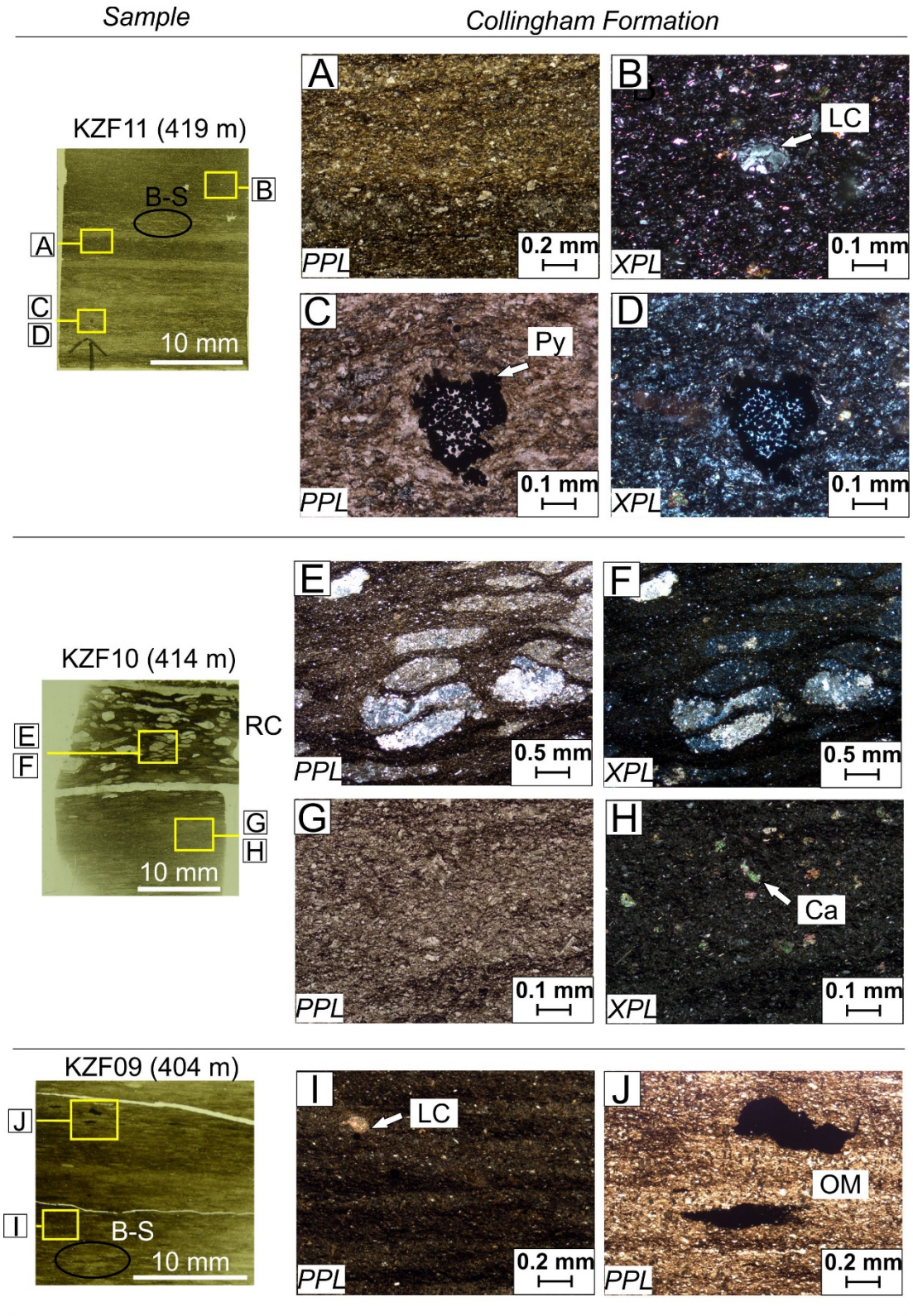

Figure 2.17: Thin section micrographs from samples KZF09, KZF10 and KZF11 from the Collingham Formation from BH KZF-1. A) Silt-rich and clay-rich lamina. B) Lithoclast. C, D) Framboidal pyrite aggregate. E, F) Rip-up clasts of tuff. G, H) Reworked tuff. I) Lithoclast in clay-and organic matter-rich matrix. J) Organic matter particulates. Abbreviations: B-S: bioturbation structure; RC: rip-up clasts; OM: organic matter; Ca: calcite; LC: lithoclast; Py: pyrite.

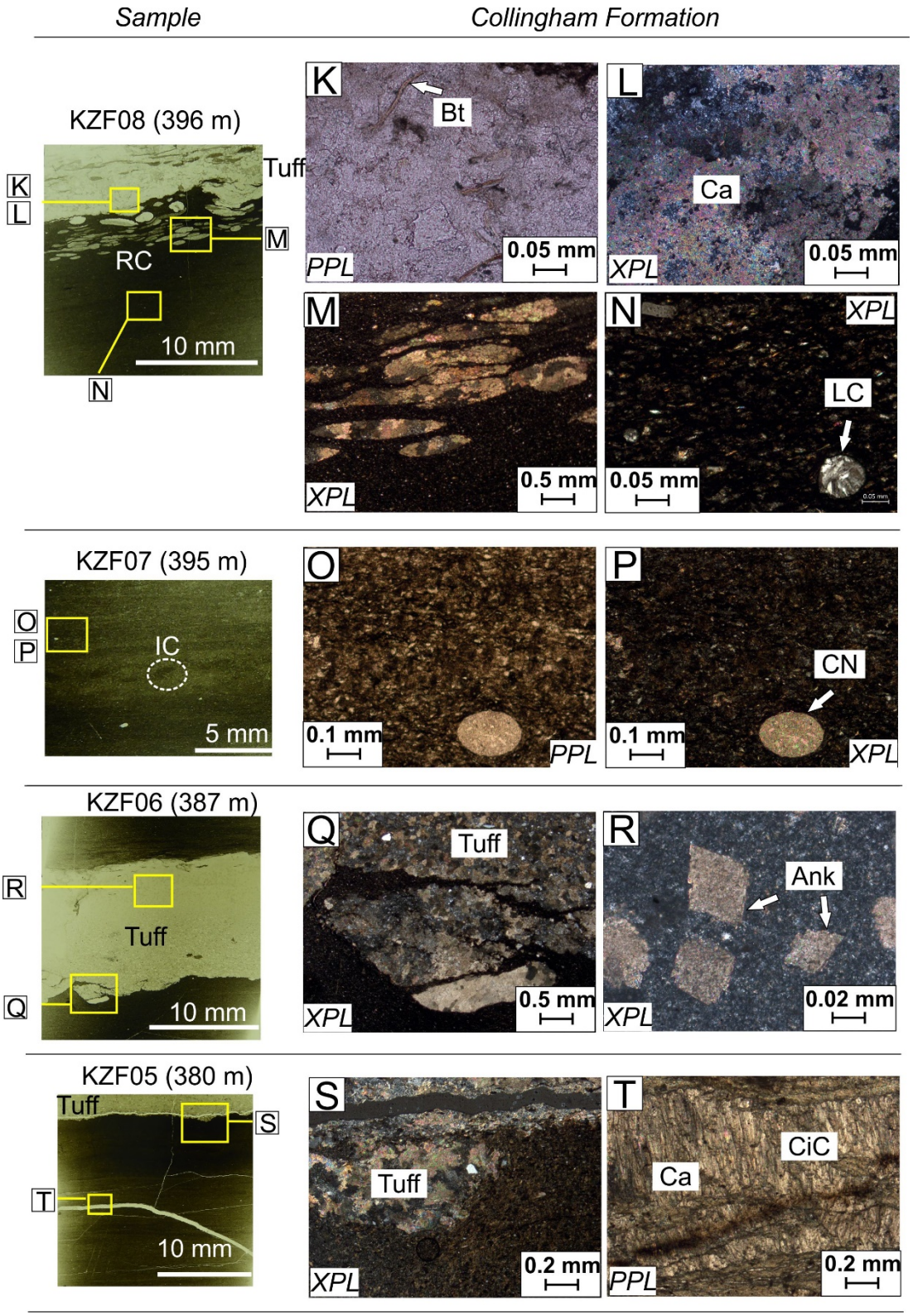

Figure 2.18: Thin section micrographs from samples KZF05, KZF06, KZF07 and KZF08 from the Collingham Formation from BH KZF-1. K, L) Volcanic tuff. M) Rip-up clasts of tuff. N) Lithoclast in clay- and organic matter-rich matrix. O, P) Carbonate nodule. Q) Tuff bed and soft sediment deformation structure. R) Rhombohedral ankerite crystals. S) Load cast with tuff infill. T) Calcite cone-in-cone structures. Abbreviations: Ca: calcite; CiC: cone-in-cone; Ank: ankerite; IC: intraclast; CN: carbonate nodule; Bt: biotite; LC: lithoclast; RC: rip-up clasts.

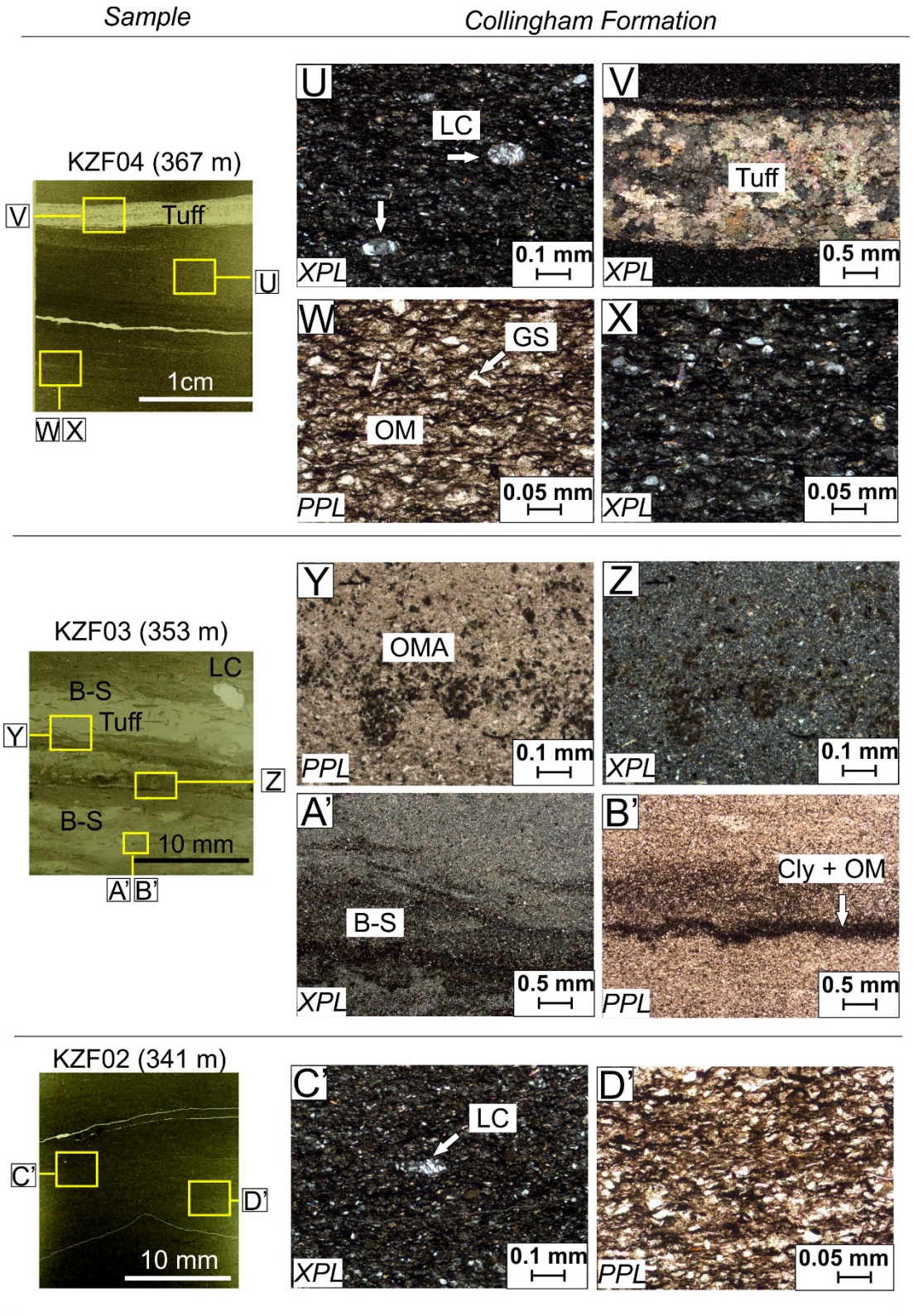
Sample
Collingham Formation
KZF04 (367 m)
V
Tuff
U
1cm
W X
U
LC
0.1 mm
XPL
V
Tuff
0.5 mm
XPL
W
GS
OM
0.05 mm
PPL
X
0.05 mm
XPL
KZF03 (353 m)
LC
B-S
Y
Tuff
Z
B-S
10 mm
A' B'
Y
OMA
0.1 mm
PPL
Z
0.1 mm
XPL
A'
B-S
0.5 mm
XPL
B'
Cly + OM
0.5 mm
PPL
KZF02 (341 m)
C'
D'
10 mm
C'
LC
0.1 mm
XPL
D'
0.05 mm
PPL

Figure 2.19: (previous page) Thin section micrographs of samples KZF02, KZF03 and KZF04 from the Collingham Formation from BH KZF-1. U) Lithoclasts in fine-grained siltstone. V) Tuff lamina. W, X) Silt-sized grains and possible glass shards bounded in organic matter. Y, Z) Organic matter in bioturbated fine-grained siltstone and tuff. A') Bioturbation structures in fine-grained siltstone and tuff. B') Clay- and organic matter-rich wavy lamina. C') Lithoclast in predominantly clay- and silt-rich matrix. D') Organic matter and silt-sized grains. Abbreviations: LC: lithoclast; OMA: organo-mineralic aggregate; B-S: bioturbation; GS: glass shard; Cly: clay; OM: organic matter.

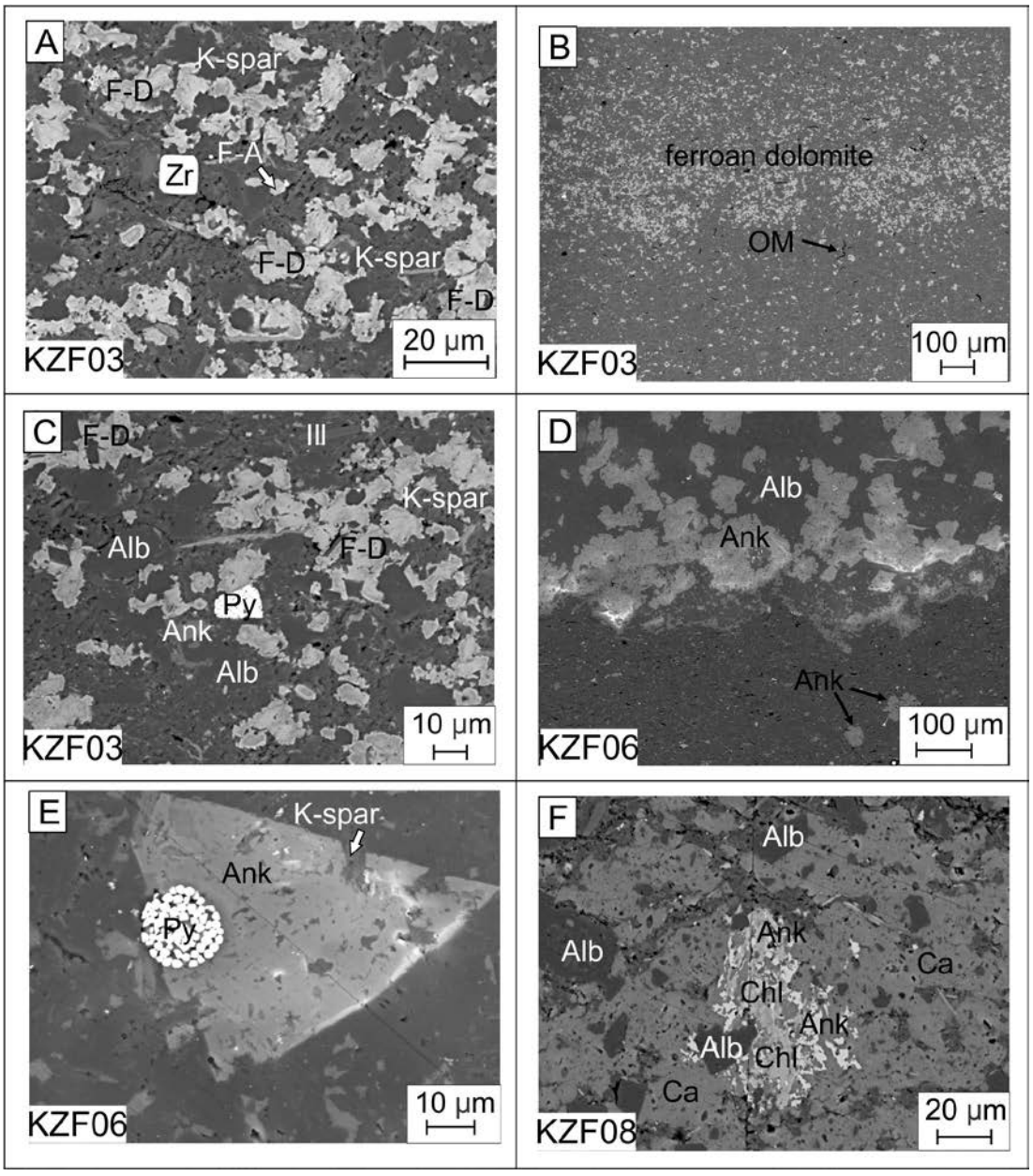

Figure 2.20: SEM micrographs of samples KZF03, KZF06 and KZF08 from the Collingham Formation from BH KZF-1. A–C) Ferroan dolomite grains concentrated into lamina. D) Ankerite- and albite-rich lamina. E) Ankerite grain and framboidal pyrite. F) Chlorite grain with ankerite rim. Abbreviations: K-spar: K-feldspar; F-A: fluorapatite; Zr: zircon; F-D: ferroan dolomite; OM: organic matter; Alb: albite; Py: pyrite; Ill: illite; Ca: calcite; chl: chlorite.

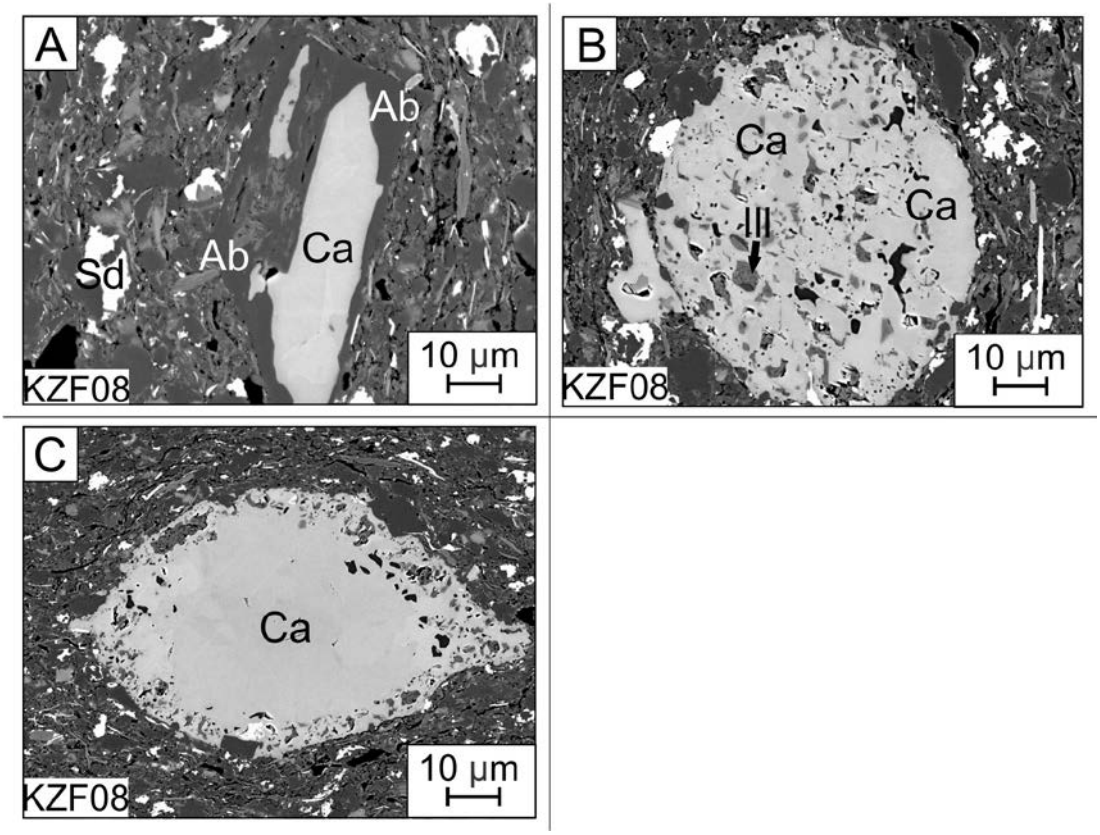

Figure 2.21: Microprobe micrographs of sample KZF08 from the Collingham Formation from BH KZF-1. A) Calcite-albite alteration. B, C) Calcite nodules. Ca = calcite; Ab = albite; Ill- Illite; Sd = siderite.

Table 2.2: Summary of the average quantitative composition (wt%), trace minerals and structure and texture for the lower Ecca Group from BH KZF-1. Sample numbers are given when a mineral only occurs in that sample.

Average quantitative composition (wt%)			
Prince Albert Fm.		***Whitehill Fm. (480 m – 420 m)***	***Collingham Fm. (420 m – 339 m)***
lower part (649 m – 550 m)	***upper part (550 m – 480 m)***		
Quartz = 37.18 Albite = 1.75 Illite = 4.91 Clinochlore = 1.12 Kaolinite = 0.36 Rhodochrosite = 28.08 Siderite = 6.12 Birnessite = 1.25 Apatite (KZF32) = 61.84 Greenalite (KZF32) = 9.57 Forsterite (KZF32) = 0.37 TOC = 0.58	Quartz = 39.07 Albite = 17.11 Illite = 27.96 Clinochlore = 4.75 Kaolinite = 2.09 Dolomite = 0.29 Siderite = 0.48 Pyrite = 0.18 TOC = 0.34	Quartz = 35.36 Albite = 15.23 Illite = 23.19 Siderite = 0.98 Clinochlore = 3.42 Kaolinite = 0.26 Dolomite = 14.44 Pyrite = 2.22 TOC = 4.91	Quartz = 51.80 Albite = 20.93 Illite = 19.86 Siderite = 0.67 Clinochlore = 2.25 Dolomite = 0.38 Pyrite = 0.19 TOC = 1.75
Trace minerals/accessory minerals			
K-feldspar (orthoclase, sanidine, microperthite) Pyrite Ferroan-dolomite Zircon Ankerite Rutile Sphalerite Stilpnomelane		Saponite orthoclase	Microcline Kaolinite Biotite Calcite Ankerite
Structure and texture			
Bioturbation structures Framboidal pyrite Phosphate nodules Manganese nodules		Thinly laminated (fabric anisotropy) Soft-sediment deformation structure Phosphate nodules Brecciation	Rhythmite Soft-sediment deformation structure Bioturbation structure Carbonate nodules Framboidal pyrite

2.5 Petrological results from BH KWV-1

BH KWV-1 was drilled to a depth of 2353 m. The borehole started in the Koonap Formation of the Beaufort Group and ended 14.73 m into the uppermost the Dwyka Group. The Ecca Group in the area consists of the Prince Albert Formation (30 m), Whitehill Formation (13 m), Collingham Formation (91 m), Ripon Formation (1286 m), Fort Brown Formation (481 m) and the Waterford Formation (53 m). The Koonap Formation section is 212 m thick. Moreover, there are 18 dolerite intrusions within the borehole with thicknesses that range between 0.03 m and 149 m. The accumulative

thickness of the intrusions is 408.09 m. Figure 2.22 shows the main lithostratigraphic units and their key sedimentological features, as well as TOC (wt%) and gamma-ray data recorded from BH KWV-1. Quantitative XRD data are visually represented in Figure 2.23 and available in Appendix A. Mineralogical composition, sedimentary structures and texture are shown in Figures 2.24–2.36, and they are summarized in Table 2.3. The lower Ecca Group (Prince Albert, Whitehill and Collingham formations) in BH KWV-1 is the focus of this study. The lithostratigraphic log is available in Appendix E.

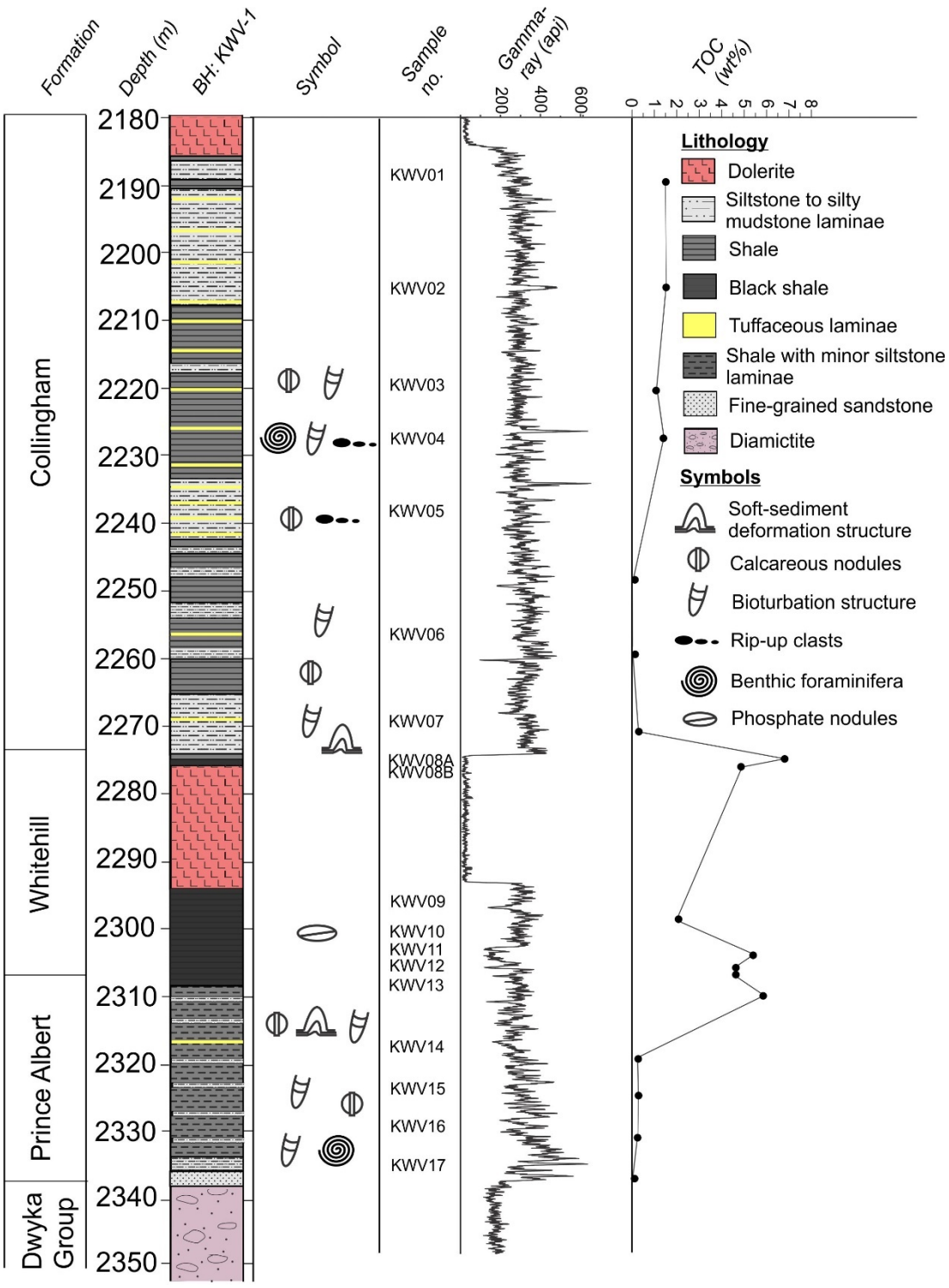

Figure 2.22: Depth profile of BH KWV-1 showing lithostratigraphic units, the main rock types with associated sedimentary features, sampling intervals, gamma- ray (API) and TOC (total organic carbon in wt%) data.

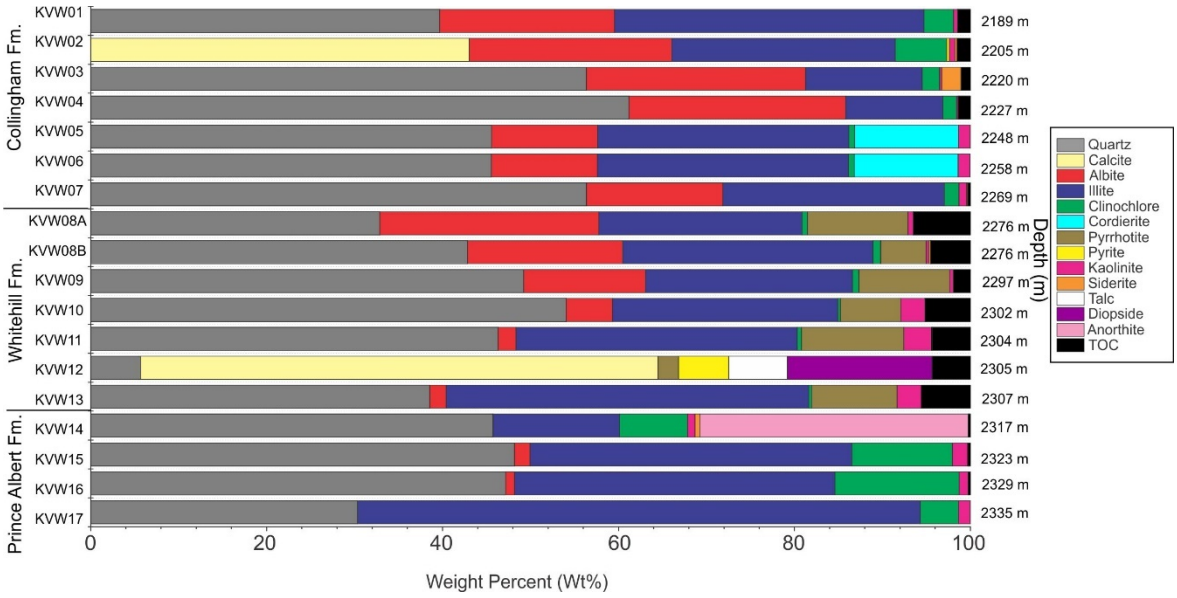

Figure 2.23: Quantitative XRD analyses of the mineralogical composition and TOC content from BH KWV-1 in wt%.

2.5.1 Prince Albert Formation

The basal 36 cm (2338 m) of the Prince Albert Formation is a silty mudstone with very fine-grained lonestones (~ 2 mm wide) of sandstone, which grades upwards into very light-grey to dark-grey silty-mudstone rhythmites, which dominates the lower 14 m of the Prince Albert Formation. The upper Prince Albert Formation (2308 to 2324 m) is a medium light-grey to dark-grey massive silty shale. Calcareous concretions (very light-grey to medium light-grey and brownish-grey) occur throughout the formation. The top of the Prince Albert Formation is a brecciated zone with disseminated pyrite, calcite veins and a gradational base with the overlying Whitehill Formation.

Samples KWV17, KWV16 and KWV15 are bioturbated siltstones with fragmented microbial filaments (Figures 2.24 C–D; 2.25 G–H) and agglutinated benthic foraminifera (Figure 2.24 A–B). Sample KWV14, from near the top of the Prince Albert Formation, has layers of reworked tuff, soft-sediment deformation structures, possible ripple-like structures, organo-mineralic aggregates and siderite-rich layers (Figure 2.25 I–N).

Common clay minerals are: illite (37.83 wt%), kaolinite (1.24 wt%), clinochlore (9.41 wt%; Figure 2.7; Table 2.3) detrital grains of chlorite (chamosite) and biotite. The most abundant feldspar is anorthite (up to 30.5 wt%; Figures 2.23; 2.26 B) with lesser amounts of sanidine (Figure 2.26 C–D) and albite (0.70 wt%). Carbonate minerals include siderite (0.13 wt%), ankerite and calcite (Figure 26 A–C). Accessory minerals

include euhedral fluorapatite grains with reaction rims (Figure 2.26 E), titanite (sphene), rutile (Figure 2.26F) and cordierite (Figure 2.24 E).

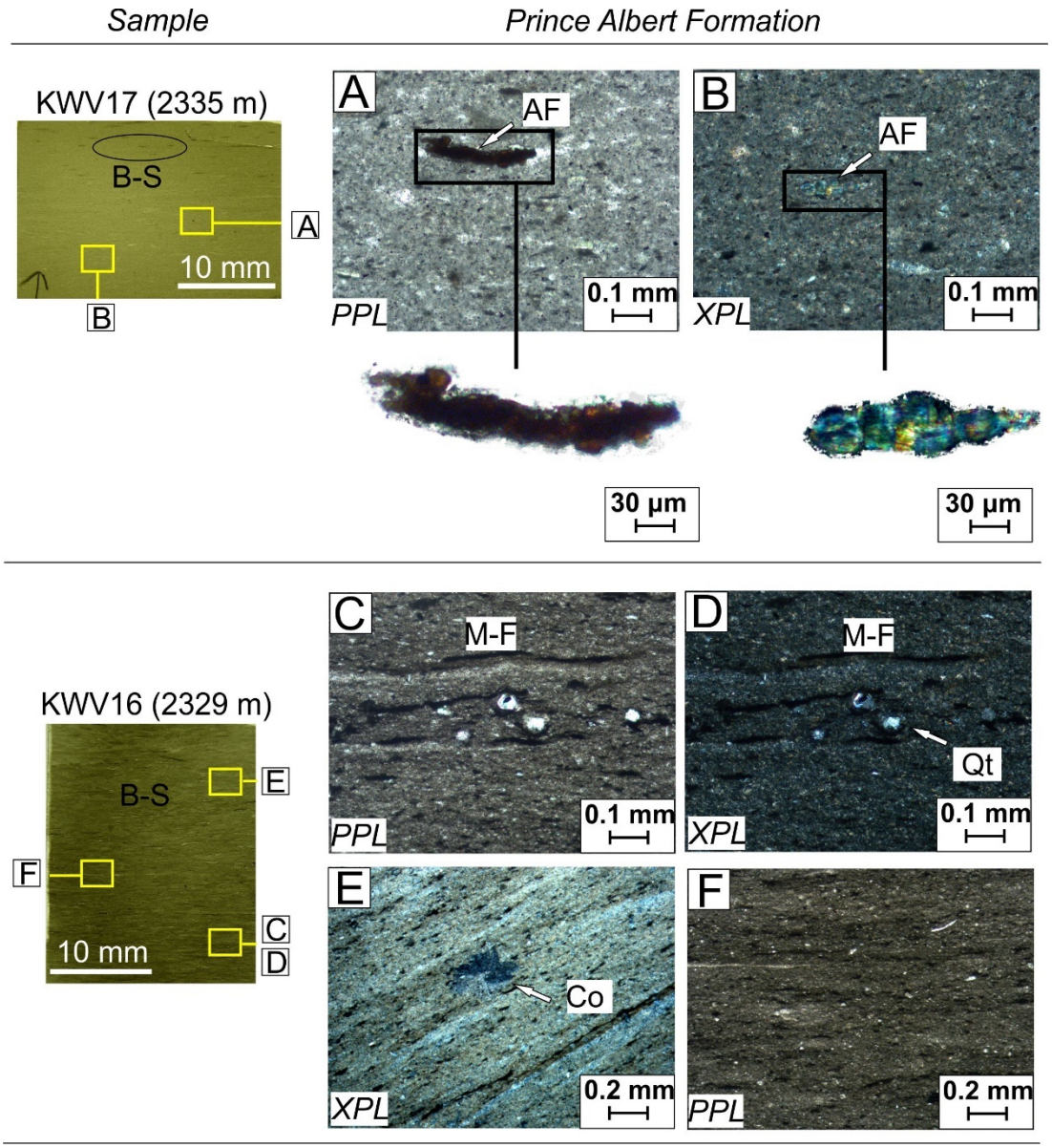

Figure 2.24: Thin section micrograph of samples KWV16 and KZF17 from the Prince Albert Formation in BH KWV-1. A, B) Agglutinated benthic foraminifera. C, D) Microbial filaments draped over quartz grains. E) Cordierite poikiloblast. F) Bioturbated structures in very fine-grained siltstone. Abbreviations: Co: cordierite; AF: agglutinated benthic foraminifera; B-S: bioturbation structure; M-F: microbial filaments.

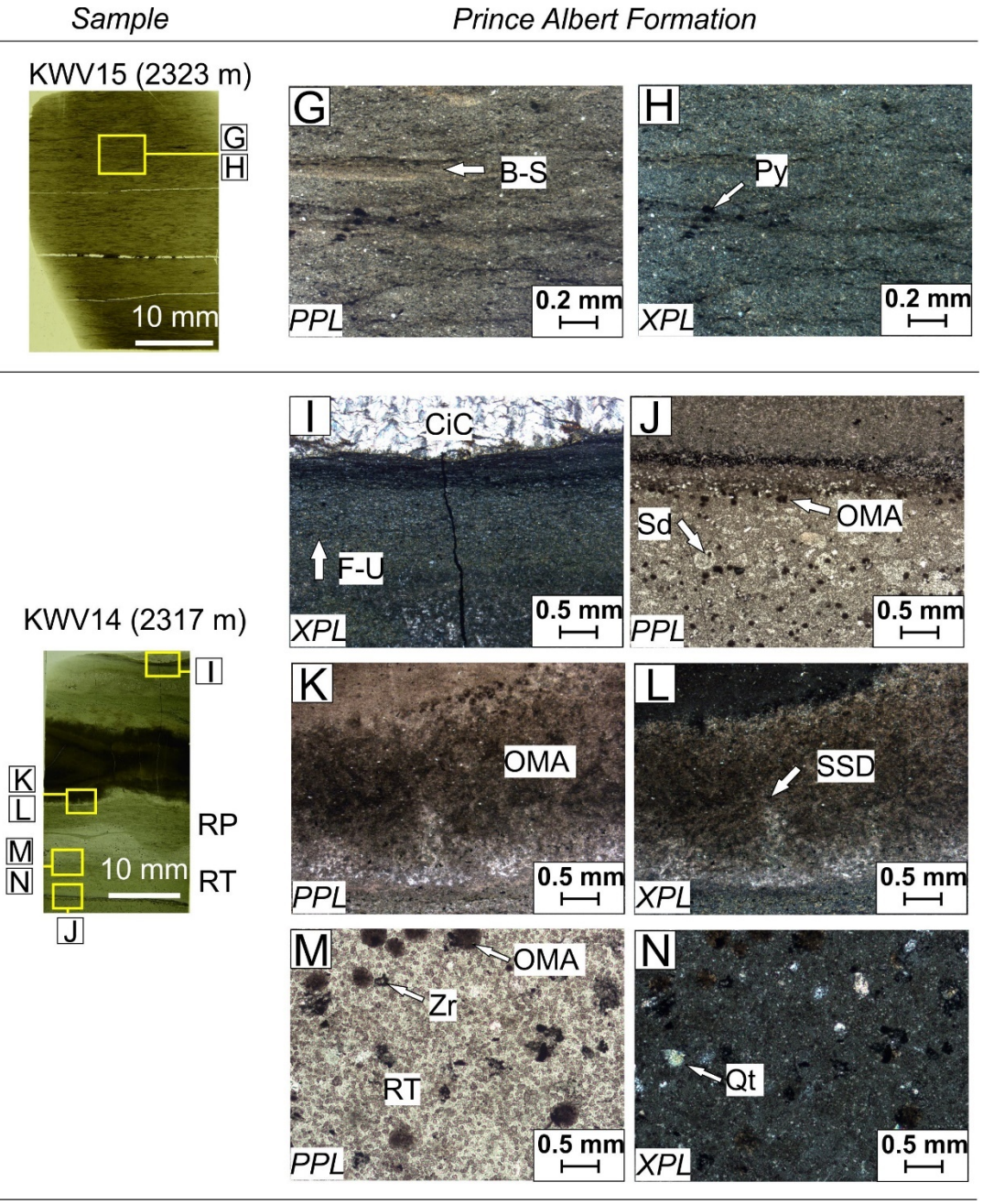

Figure 2.25: Thin section micrograph of samples KWV14 and KZF15 from the Prince Albert Formation from BH KWV-1. G, H) Bioturbation structures and pyrite grains. I) Fining-upward grains and cone-in-cone structures. J) Siderite-rich lamina and organo-mineralic aggregates. K, L) Organo-mineralic aggregates and soft-sediment deformation (flame structure). M, N) Reworked tuff with zircon grains, organo-mineralic aggregates and silt-sized quartz grains in clay-rich matrix. Abbreviations: SSD: soft-sediment deformation structure; OMA: organo-mineralic aggregates; CiC: cone-in-cone; RT: reworked tuff; RP: ripple; Zr: zircon; Qt: quartz; Sd: siderite; B-S: bioturbation structure; Py: pyrite.

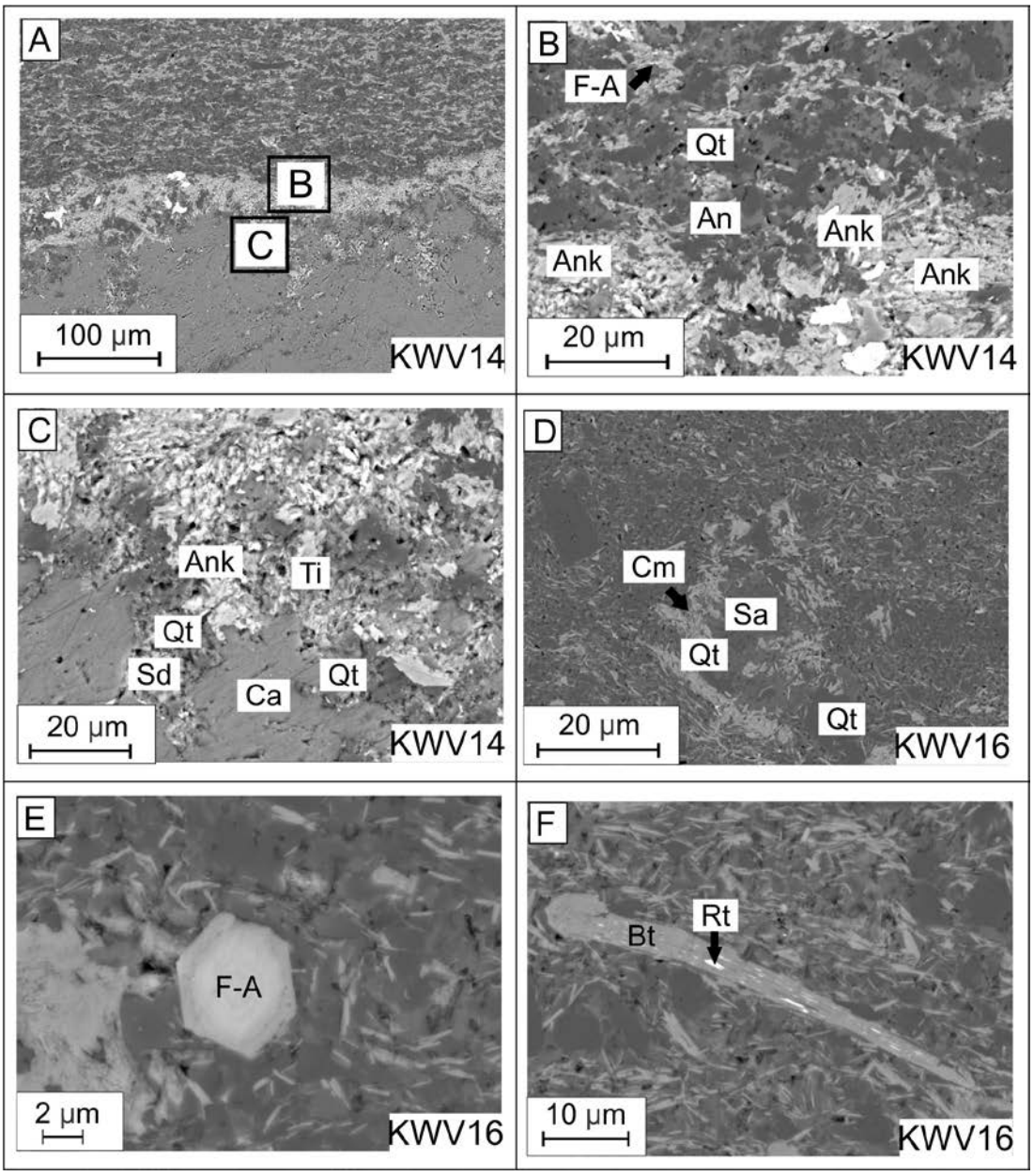

Figure 2.26: SEM micrographs of samples KWV14 and KWV16 from the Prince Albert Formation from BH KWV-1. A–C) Horizons enriched with calcite, ankerite and quartz and feldspar. D) Sanadine and quartz grains with chamosite coating. E) Euhedral fluorapatite. F) Biotite grain. Abbreviations: F-A: fluorapatite; Qt: quartz; An: anorthite; ank: ankerite; Ti: titanite; Sd: siderite; Ca: calcite; Cm: chamosite; Sa: sanidine; Bt: biotite; Rt: rutile.

2.5.2 Whitehill Formation

The Whitehill Formation consists of massive black shale with very light-grey, light-grey to medium light-grey siltstone laminae with disseminated pyrite and pyrite-rich lenses. A 19 cm thick dolerite layer is intruded in the top 13 cm of the Whitehill Formation.

The Prince Albert Formation grades upwards into the Whitehill Formation with a series of upward-fining parallel-laminated and thin-bedded mudstone (Figure 2.27 A,

D, C) with occasional overfolding (Figure 2.27 B). Samples KWV12 and KWV13 are near the contact with the Prince Albert Formation. There is no visual evidence of dolerite in the core at this depth (2307 m). However, dolerite minerals such as diopside (2.35 wt%), enstatite and talc (0.95 wt%) are detected using XRD and SEM techniques (Figures 2.23; 2.30 I; Table 2.3).

The majority of the Whitehill Formation is a massive black shale interspersed with possible benthic microbial filaments that incorporate silt-sized particles and wavy laminated pyritic beds (Figures 2.27 I–J; 2.28 O–R). Clay minerals include: illite (24.83 wt%), kaolinite (1.42 wt%) and clinochlore (0.48 wt%; Table 2.3). The Whitehill Formation is quartz-rich (38.51 wt%). Quartz grain boundaries are recrystalized, eliminating interparticle porosity (Figure 2.30 G). Disseminated pyrite (0.81 wt%) and pyrrhotite occur as amorphous and euhedral grains (Figures 2.27 H, I–J; 2.26 O–R) and clusters of framboids (Figure 2.30 B). Pyrrhotite (8.20 wt%) occurs only in the Whitehill Formation. Phosphate nodules are detected at 2302 m (Figure 2.28 K–L) and carbonate minerals detected are calcite (8.40 wt%) and siderite (0.04 wt%).

Samples KWV08A and KWV08B are taken from the direct contact with the dolerite intrusion (Figure 2.29), where calcite and quartz veins penetrate the Whitehill Formation. These veins are highly concentrated within 1 cm of the contact. Thereafter the thin parallel-laminated beds of the black shale are easily identified. Near the contact (also sample KWV09), the Whitehill Formation exhibits quartz-rich and clay-rich patches and resembles spotted hornfels (Figures 2.30 A, C, D; 2.31 B). Metamorphic minerals identified in the Whitehill Formation are chalcedony nodules, cordierite, almandine, staurolite, and titanite (Figures 2.27, 2.28, 2.30, 2.31), however these metamorphic minerals occur in too low quantities to be detected by XRD.

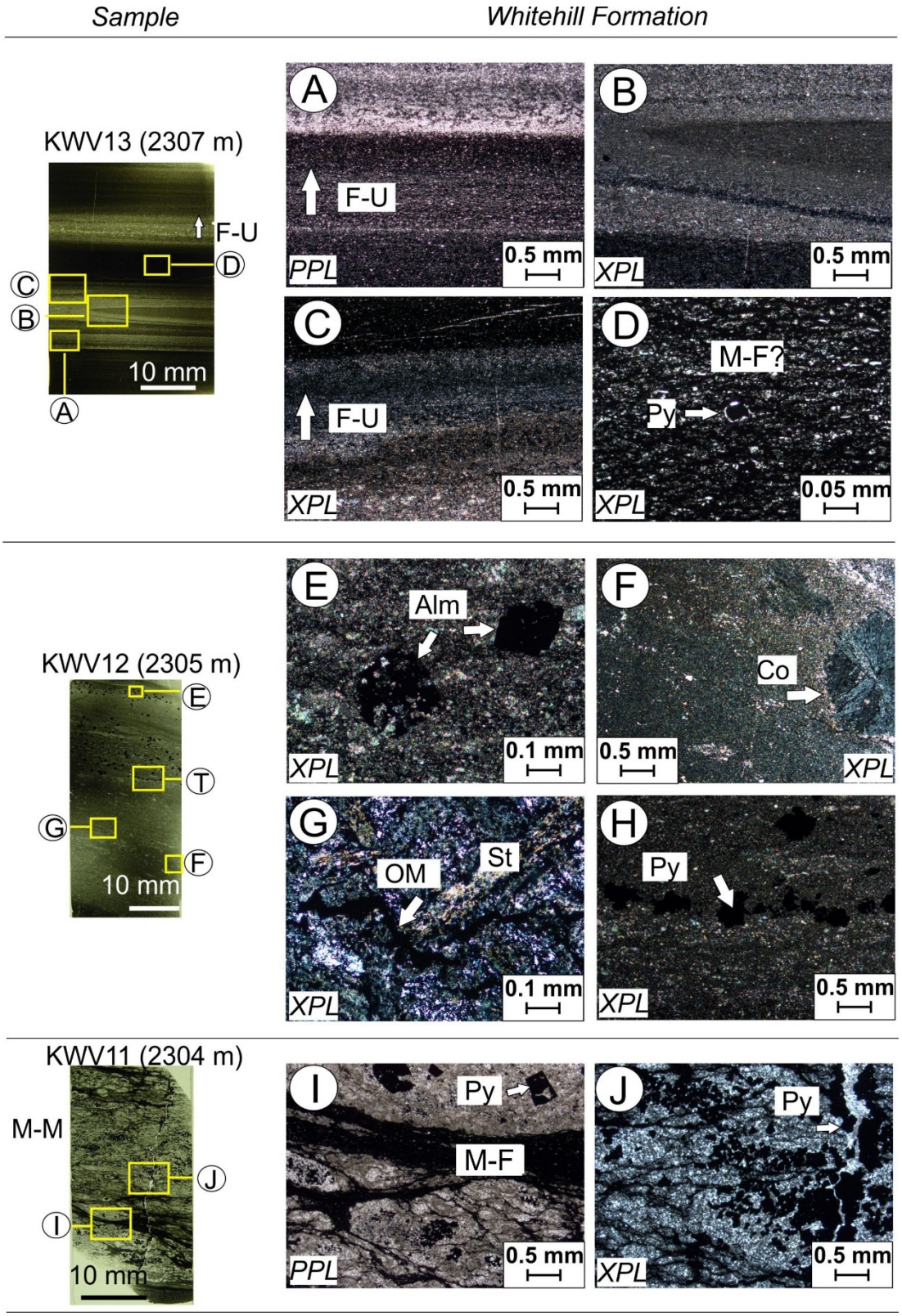

Figure 2.27: Thin section micrograph of samples KWV11, KWV12 and KWV13 from the Whitehill Formation from BH KWV-1. A, B) Fining-upward laminae. D) Carbonaceous laminae (possible microbial filaments) draping over medium silt-sized grains and pyrite. E) Almandine crystals. F) Cordierite poikiloblast. G) Staurolite and discontinuous, wavy microbial filaments. H) Pyrite-rich lamina. I) Microbial filaments draped over silt-sized quartz grains. J) Pyrite grains along quartz veins. Abbreviations: F-U: fining-upward; M-F: microbial filaments; Py: pyrite; Alm: almandine; Co: cordierite; OM: organic matter; St: staurolite.

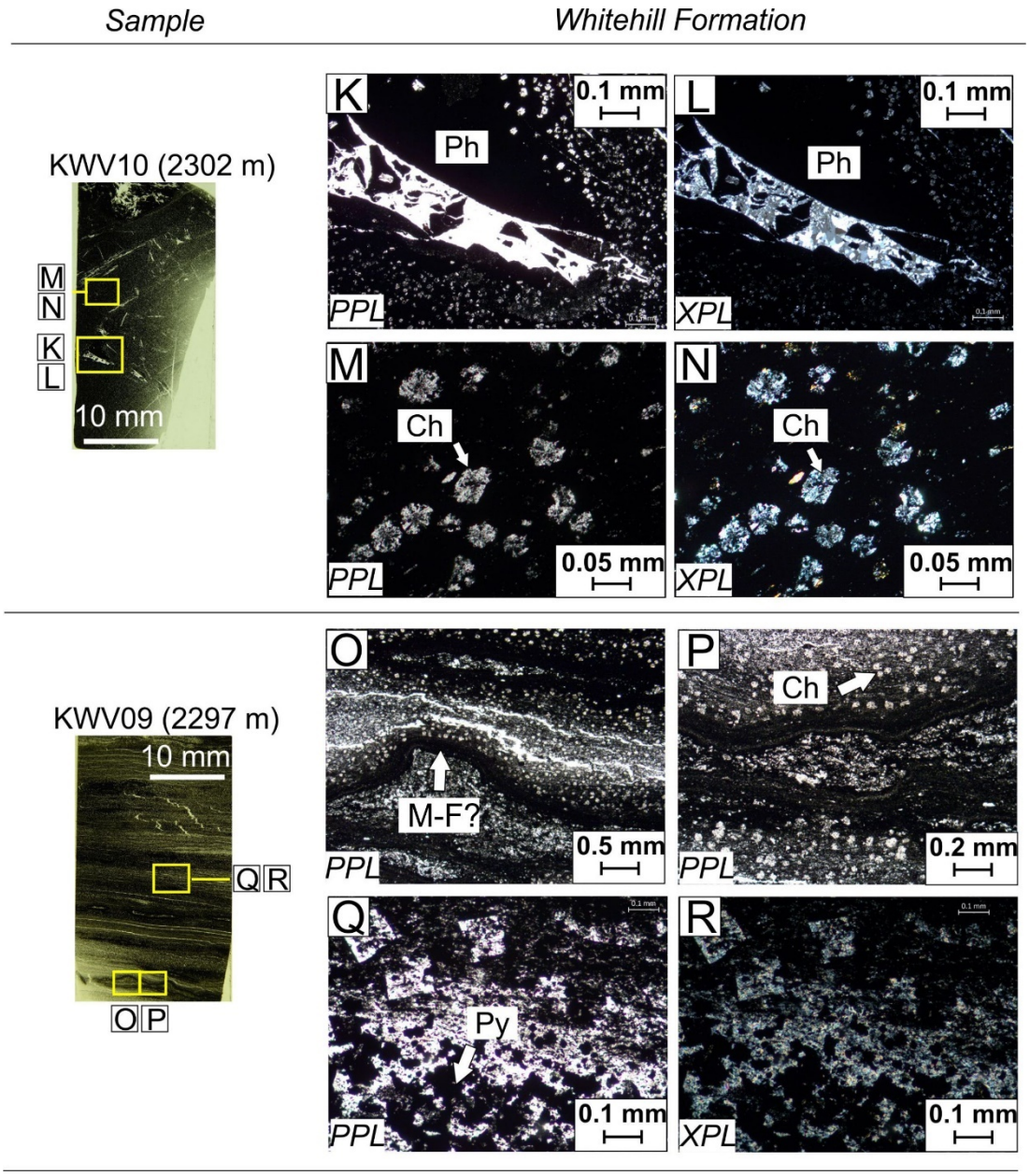

Figure 2.28: Thin section micrograph of samples KWV09 and KWV10 from the Whitehill Formation from BH KWV-1. K, L) Phosphate nodule. M, N) Chalcedony. O, P) Possible wavy, continuous microbial filaments and chalcedony crystals. Q, R) pyrite/pyrrhotite crystals. Abbreviations: Ph: phosphate; M-F: microbial filaments; Ch: chalcedony; Py: pyrite/pyrrhotite.

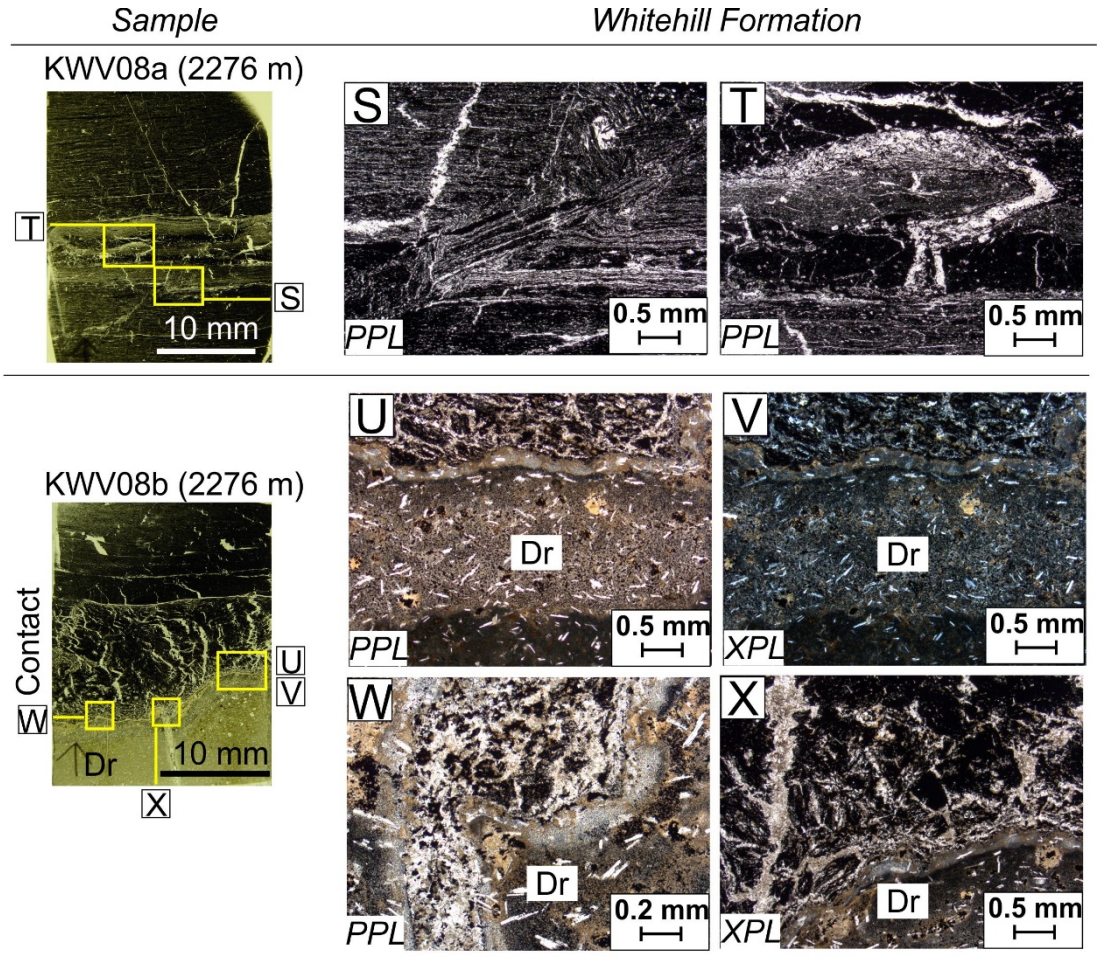

Figure 2.29: Thin section micrograph of samples KWV08a and KWV08b from the Whitehill Formation from BH KWV-1. S, T) Fractured black shale with quartz veining. U–X) Contact between black shale and dolerite intrusion. Abbreviation: Dr: dolerite.

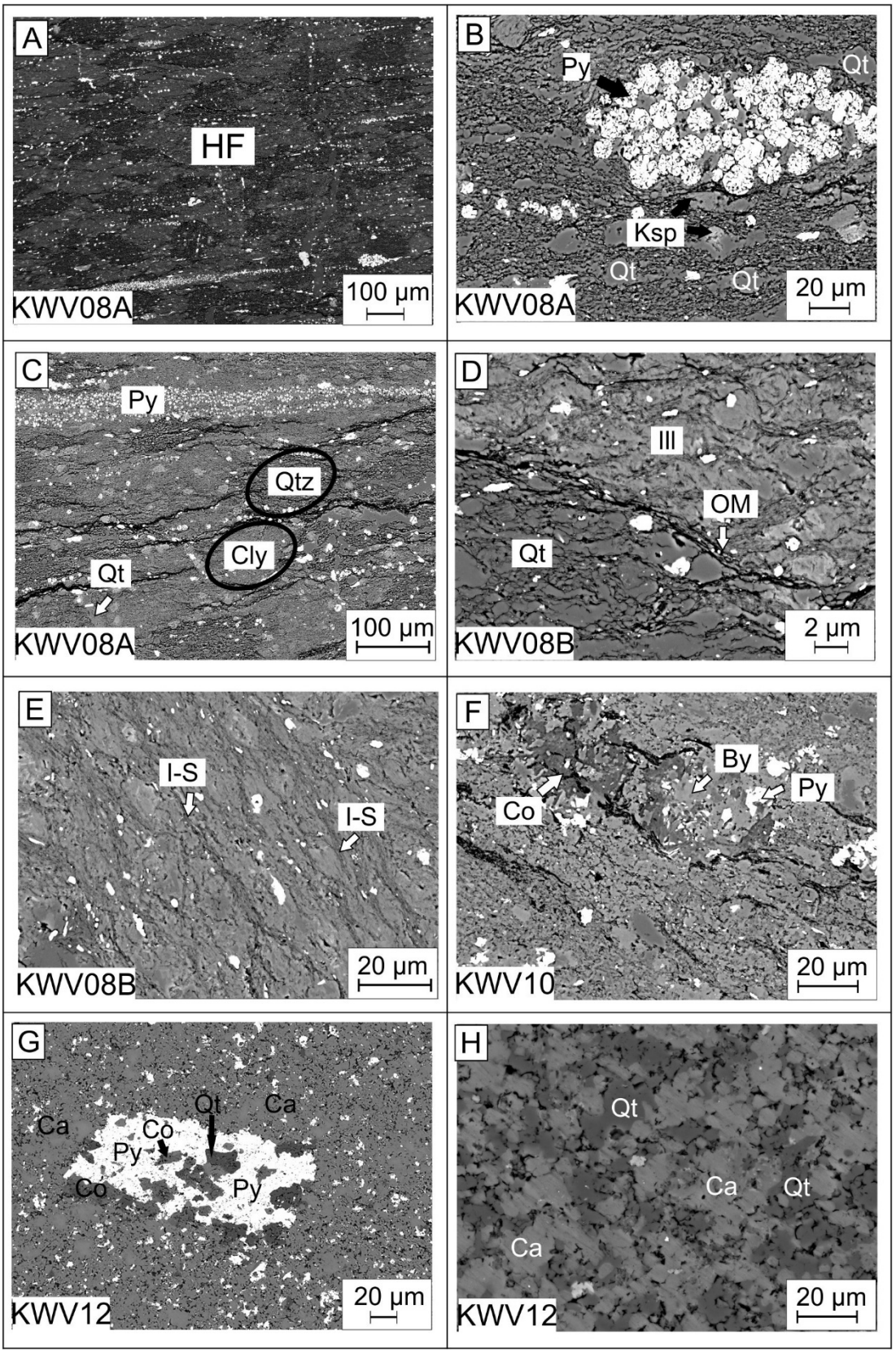
A
HF
100 µm
KWV08A
B
Py
Qt
Ksp
Qt
Qt
20 µm
KWV08A
C
Py
Qtz
Cly
Qt
100 µm
KWV08A
D
Ill
OM
Qt
2 µm
KWV08B
E
I-S
I-S
20 µm
KWV08B
F
By
Py
Co
20 µm
KWV10
G
Ca
Qt
Ca
Co
Py
Co
Py
20 µm
KWV12
H
Qt
Ca
Qt
Ca
20 µm
KWV12

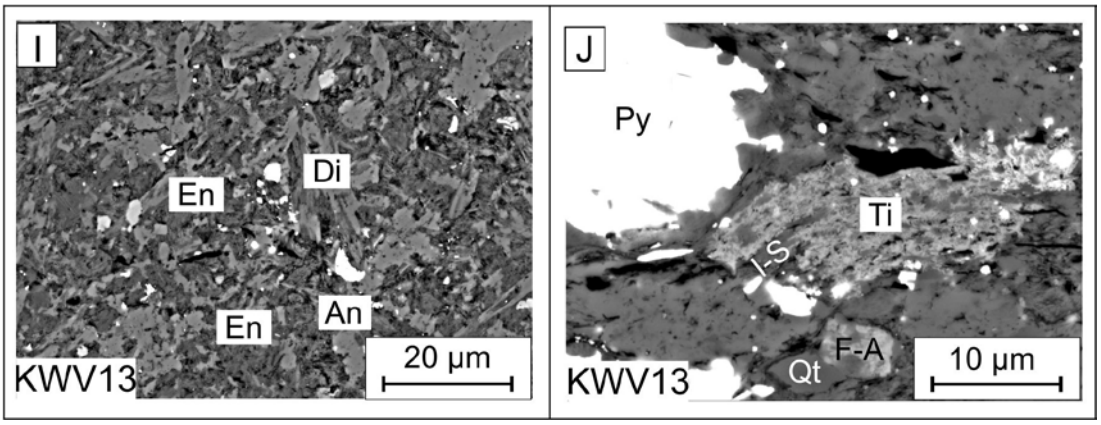

Figure 2.30: (previous page) SEM micrographs of samples KWV08, KWV12 and KWV13 from the Whitehill Formation from BH KWV-1. A) Overview of spotted hornfels. B, C) Framboidal pyrite concentrated within lamina. C, D) Quartz- and clay-rich patches resembling 'spotted hornfels'. E) Illite-smectite-rich laminae. F, G) Cordierite. H) Recrystalized grain boundaries between quartz and calcite. (this page) I) Dolerite minerals enstatite, diopside and anorthite. J) Pyrite and titanite. Abbreviations: Py: pyrite/pyrrhotite; Ksp: K-feldspar; Qt: quartz; Cly: clay; Ill: illite; I-S: illite-smectite; Co: cordierite; By: bytownite; Ca: calcite.; Di: diopside; En: enstatite; An: anorthite.

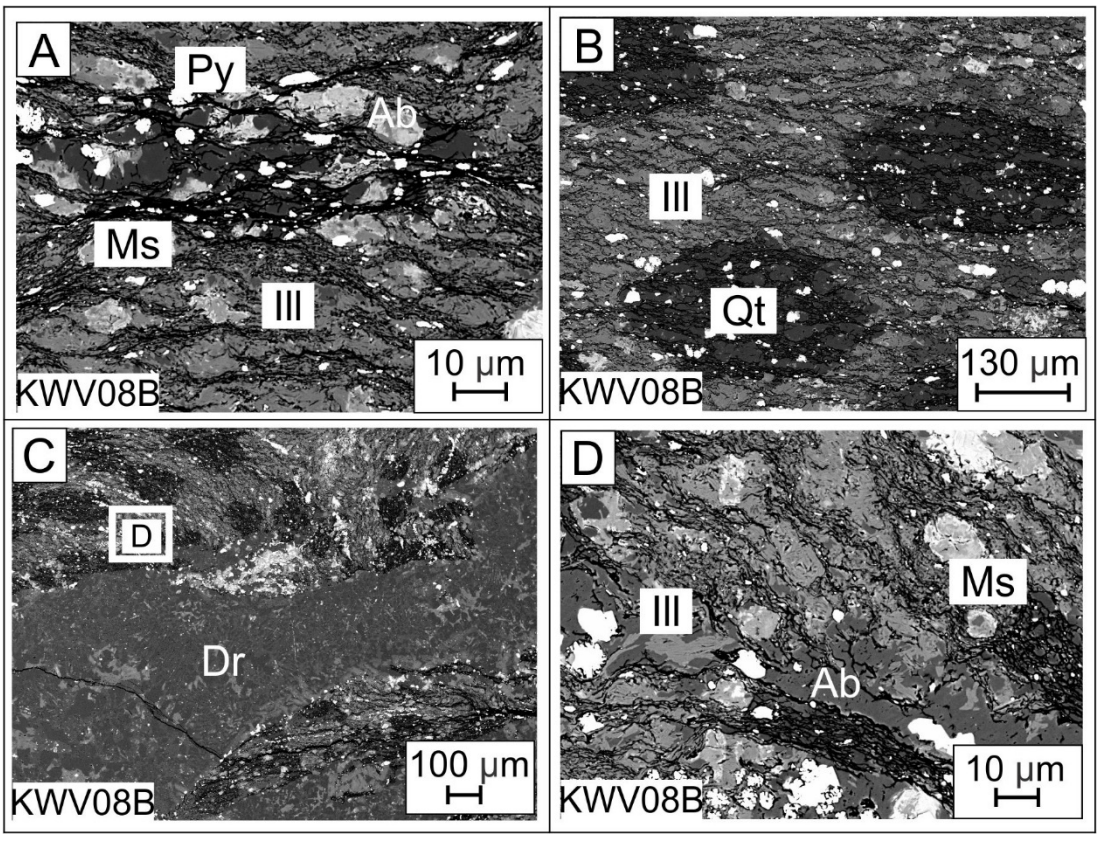

Figure 2.31: Microprobe micrographs of sample KWV08B from the Whitehill Formation from BH KWV-1. A, B) Spotted hornfels. C) Dolerite intruding into the Whitehill Formation. D) Contact between black shale and dolerite. Abbreviations: Ms: muscovite; Ab: albite; Ill: illite, Dr: dolerite; Qt: quartz; Py: pyrite.

2.5.3 Collingham Formation

The Collingham Formation consists of light grey to dark-grey and pinkish-grey massive silty shale, intercalated with medium grey and very light to light grey siltstone laminae and greyish-black to very light-grey rhythmite layers. Greenish-grey, olive-grey, light olive-brown and light olive-grey tuffaceous laminae are less frequent than in BH KWV-1 compared to BH KZF-1. Very light grey, pale red, pale-yellowish brown, dark yellowish-brown, pale brown, dusky-yellow, dark greenish-grey and light olive-grey calcareous concretions are distributed throughout the sequence. In the core there is a 19 m thick dolerite at the base of the formation and a 149 m thick dolerite at the top of the Collingham Formation.

Tuff laminae consists of montmorillonite and glass shards, which have mostly altered to calcite and plagioclase feldspars (e.g., bytownite, andesite, albite, labradorite; Figures 2.32 C; 2.35 C, D, H). The tuff layer in KWV07 (Figure 2.32 C; 2269 m) shows some degree of foliation. The accessory oxide minerals are reoriented, presumably at right angles to pressure from the intrusion below. Sample KWV07 also displays boudinage texture, where silty laminae are resistant to stresses, forming lenticular boudins (Figure 2.32 D, E). Almandine garnets (pyrope–spessartite range) occur in layers, which are sometimes cut by anorthite veins lined with pyrite (Figure 2.32 A, B; Figure 2.35 K, L). Possible bioturbation structures are detected in sample KZF04 (Figure 2.33 Q–R).

Cordierite (2.24 wt%; Figure 2.23; Table 2.3) occurs as poikiloblasts as well as hexagonal to rounded crystals with cyclic twinning (Figures 2.32 I–J; 2.33 M–O; 2.35 G, I). Patches of quartz, illite and poikiloblastic cordierite resembles spotted hornfels (Figures 2.32 I–J; 2.34 U–V, Y; 2.35 L).

Of all the phases of plagioclase (i.e., albite, andesine, labradorite, bytownite and anorthite) only albite occur in significant quantities (18.86 wt%). Clay minerals identified are: illite (23.88 wt%), montmorillonite (Figure 2.35 D), smectite, kaolinite (0.72 wt%; Figure 2.35 I, J) and clinochlore (2.24 wt%). Carbonate minerals are mostly calcite, ankerite and siderite (0.37 wt%; Table 2.3). Ankerite is only seen as replacing microfossils (possibly benthic foraminifera) or faecal pellets in Figure 2.36 E. Common oxides are rutile (Figure 2.35 E) and ilmenite (Figure 2.35 C, I). Other accessory minerals are sphene (titanite) (Figure 2.35 D, F), fluorapatite (Figure 2.35 B, I, J) and euhedral zircon grains (Figure 2.36 A, F).

Other common features in the Collingham Formation are bioturbation structures (Figure 2.33 Q, R), lag deposits (Figure 2.33 K, L), organo-mineralic aggregates (Figures 2.33 N; 2.34 Z) and rip-up clasts and intraclasts (Figure 2.33 K, L, O, P). The mineral grains are mostly recrystallized with irregular or sutured boundaries, leaving little to no intergranular porosity. The top of the Collingham Formation (2189 m) is a coarse-grained siltstone to a very fine-grain sandstone (Figure 2.34 A', B').

KWV07 (2269 m)

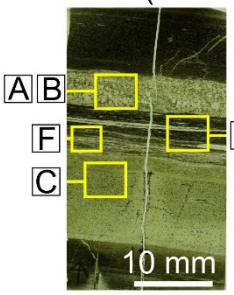

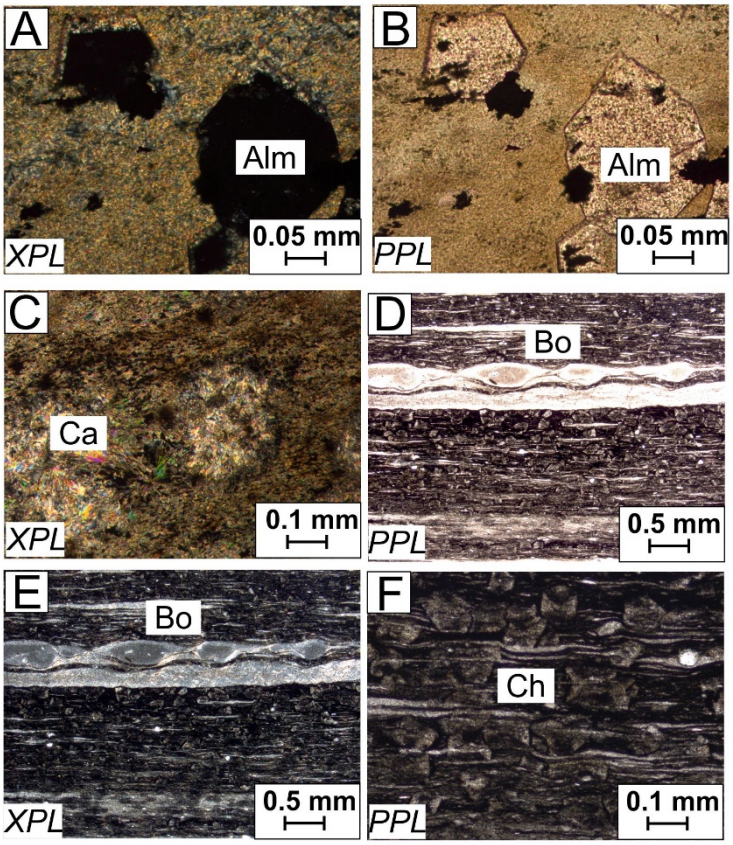

KWV06 (2258 m)

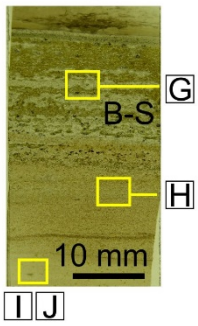

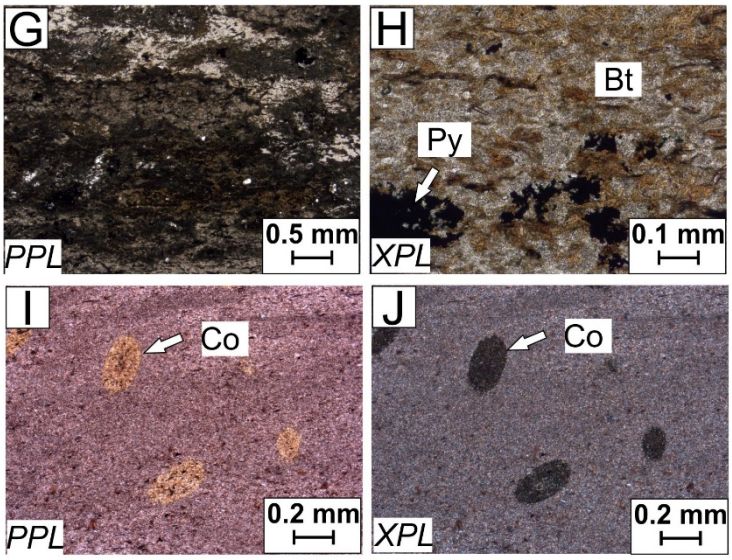

Figure 2.32: (previous page)Thin section micrograph of samples KWV06 and KWV07 from the Collingham Formation from BH KWV-1. A, B) Almandine crystals. C) Altered tuff. D, E) Lenticular boudins of quartz. F) Chalcedony crystals. G) Organic matter and clay-rich laminae and possible bioturbation structures. H) Pyrite and biotite grains. I, J) Cordierite poikiloblast. Abbreviations: Py: pyrite/pyrrhotite; Bt: biotite; Co: cordierite; Alm: almandine; Ca: calcite; Bo: boudinage; Ch: chalcedony.

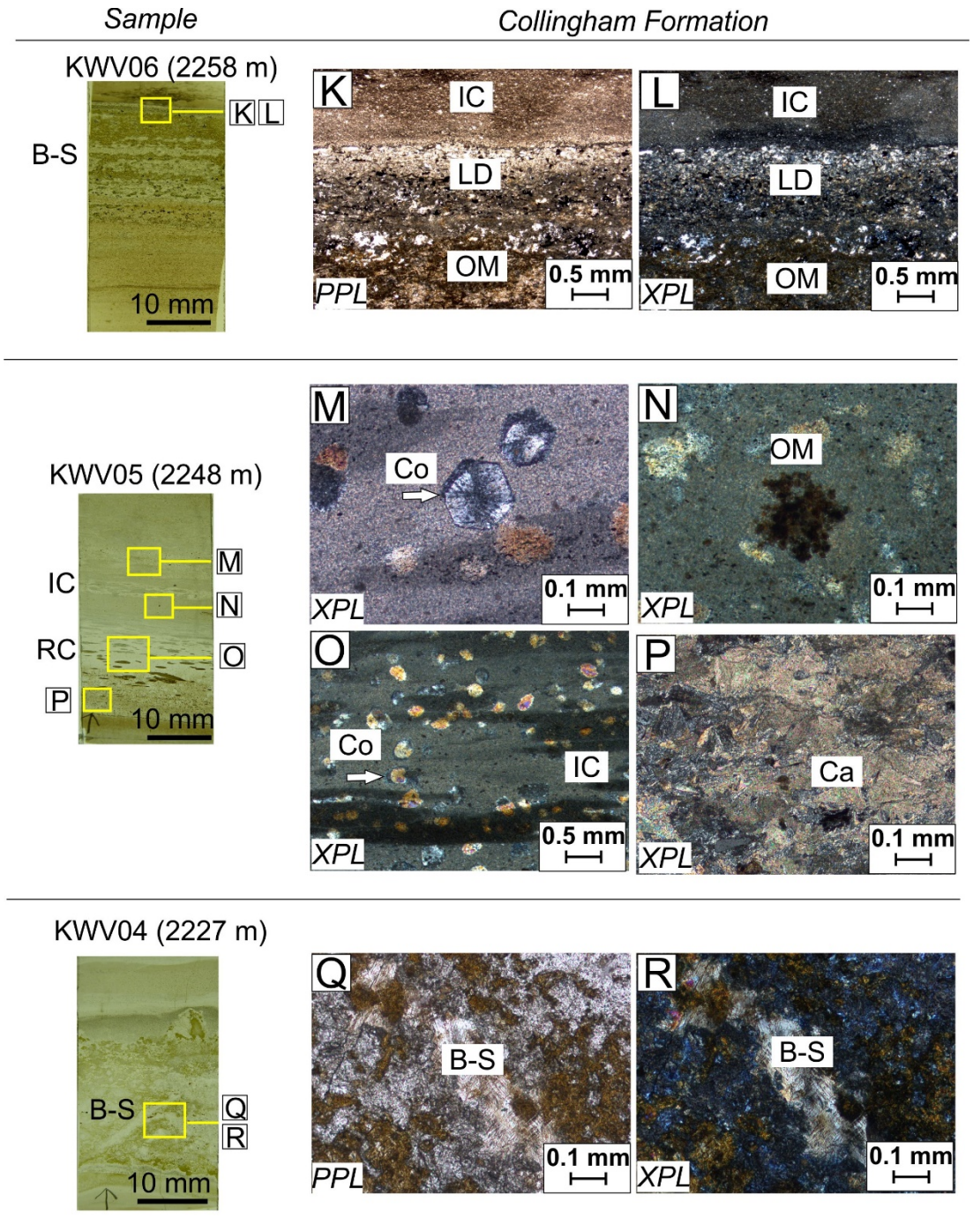

Figure 2.33: Thin section micrograph of samples KWV04, KWV05 and KWV06 from the Collingham Formation from BH KWV-1. K, L) Organic matter-rich lamina, possible lag deposits and intraclast rich lamina. M) Cordierite. N) Organic matter aggregate. O) Cordierite poikiloblasts and intraclasts. P) Calcite. Q, R) Bioturbation structure. Abbreviations: B-S: bioturbation structure; Co: cordierite; IC: intraclast; RC: rip-up clast; LD: lag deposit; OM: organic matter; Ca: calcite.

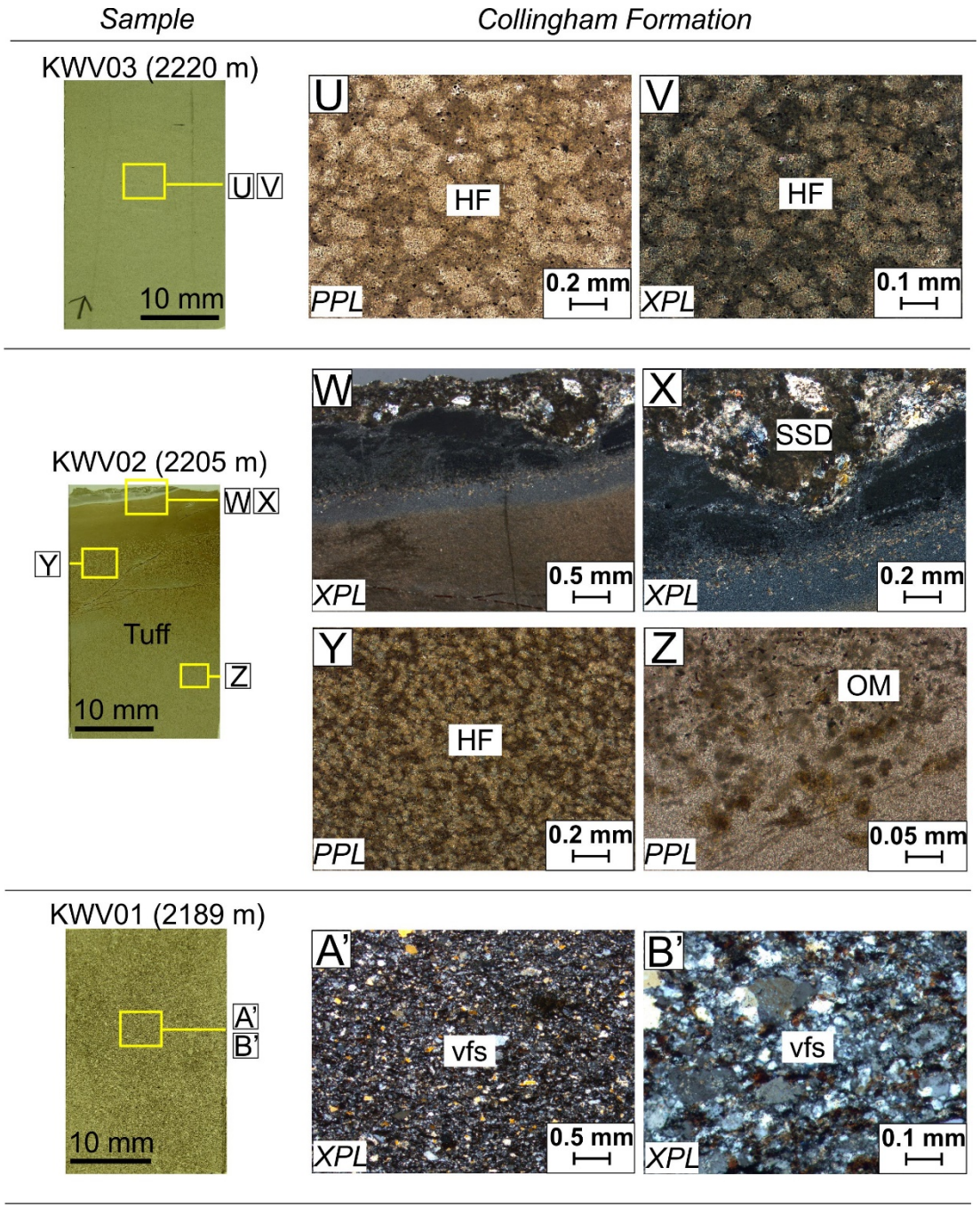

Figure 2.34: Thin section micrograph of samples KWV01, KWV02 and KWV03 from the Collingham Formation from BH KWV-1. U, V) Spotted hornfels. W, X) Soft sediment deformation structure. Y) Spotted hornfels. Z) Organic matter. A', B') Very fine-grained sandstone. Abbreviations: Vfs: very fine-grained sandstone; SSD: soft sediment deformation structure; HF: hornfels; OM: organic matter.

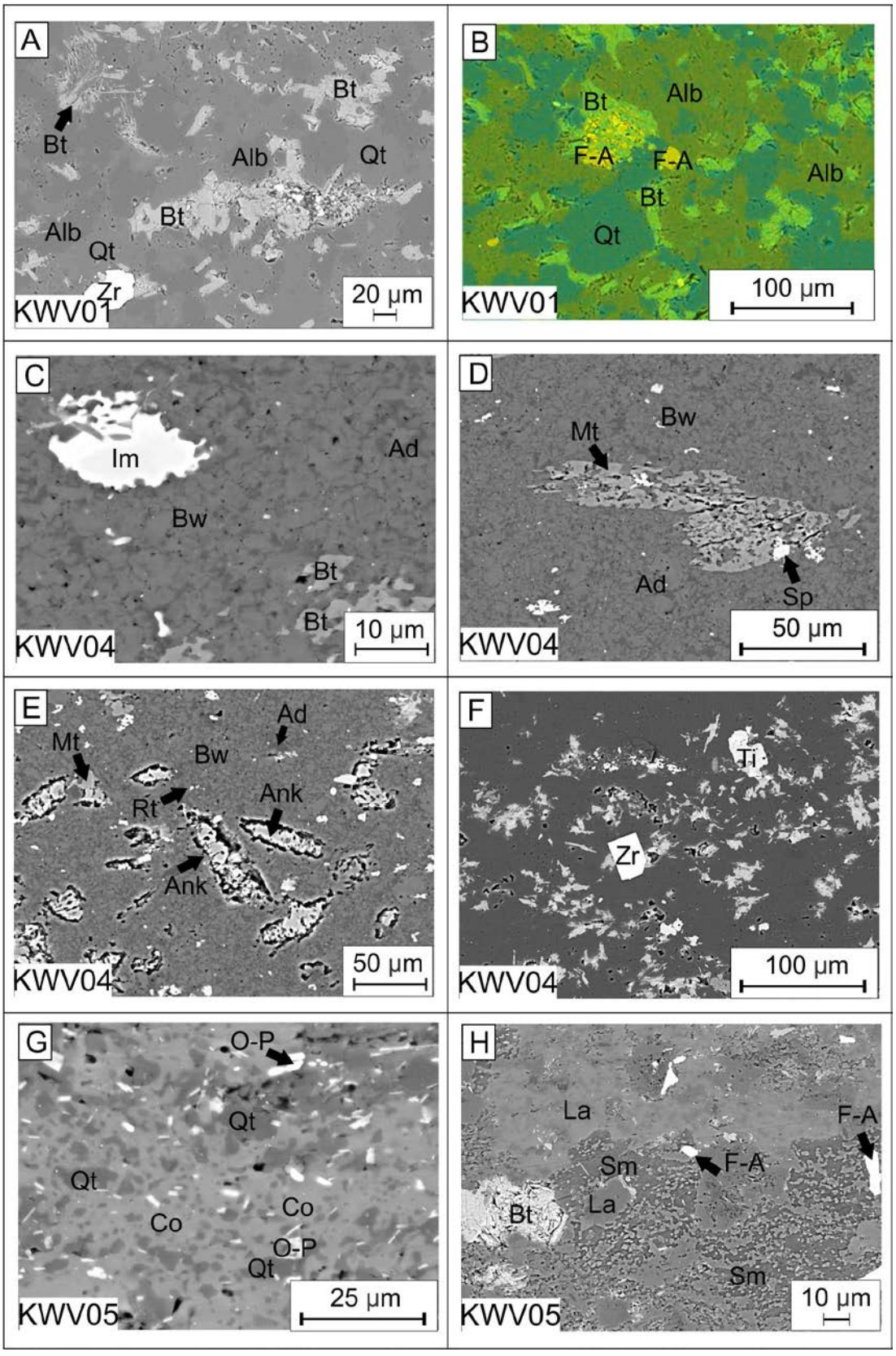
A
Bt
Bt
Alb
Qt
Bt
Alb
Qt
Zr
KWV01
20 µm
B
Bt
Alb
F-A
F-A
Alb
Bt
Qt
KWV01
100 µm
C
Im
Ad
Bw
Bt
Bt
KWV04
10 µm
D
Mt
Bw
Ad
Sp
KWV04
50 µm
E
Mt
Ad
Bw
Rt
Ank
Ank
KWV04
50 µm
F
Ti
Zr
KWV04
100 µm
G
O-P
Qt
Qt
Co
Co
O-P
Qt
KWV05
25 µm
H
La
F-A
Sm
F-A
Bt
La
Sm
KWV05
10 µm

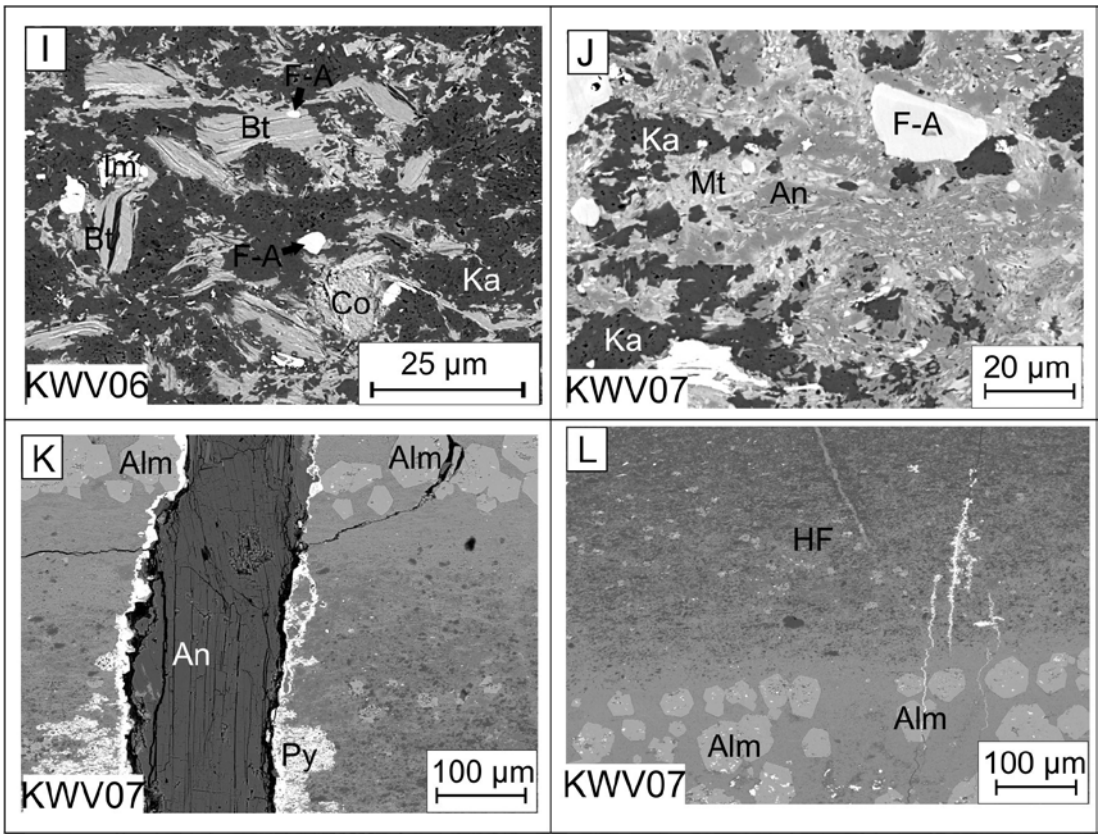

Figure 2.35: Micrographs of sample KWV01, KWV04, KWV05, KWV06 and KWV07 from the Collingham Formation from BH KWV-1. A–L) Nearly all minerals from the plagioclase feldspar series. B) Elemental mapping. D) Porous montmorillonite. E) Microfossils replaced by ankerite. F) Euhedral zircon and anhedral titanite. G) Cordierite and quartz grains with recrystalized grain boundaries. H–J) Kaolinite, smectite and montmorillonite clay minerals. K) Anorthite vein. K–L) Almandine crystals. Abbreviations: Bt: biotite; Alb: albite; Qt: quartz; Zr: zircon; Ad: andesine; Ti: titanite; La: labradorite; Bw: bytownite; Sm: smectite; Co: cordierite; ank: ankerite; Rt: rutile; Im: ilmenite; Sp: sphene; F-A: fluorapatite. Mt: montmorillonite; Ka: kaolinite; An: anorthite; Alm: almandine; Py: pyrite; HF: hornfels.

Table 2.3: Summary of the average quantitative composition (wt%), trace minerals and structure and texture for the lower Ecca Group from BH KWV-1. Sample numbers are given when a mineral only occurs in that sample.

Average quantitative composition (wt%)		
Prince Albert Fm. (2238 m – 2308 m)	***Whitehill Fm. (2308 m – 2295 m)***	***Collingham Fm. (2276 m – 2186 m)***
Quartz = 42.86 Albite = 0.70 Illite = 37.83 Clinochlore = 9.41 Kaolinite = 1.24 Siderite = 0.13 Anorthite = 7.63 TOC = 0.81	Quartz = 38.51 Calcite (KWV12) = 58.82 Albite = 9.36 Illite = 24.83 Clinochlore = 0.48 Pyrrhotite = 8.20 Pyrite = 0.81 Kaolinite = 1.42 Siderite = 0.04 Talc = 0.95 Diopside = 2.35 TOC = 5.17	Quartz = 43.53 Calcite (KWV02) = 43.05 Albite = 18.86 Illite = 23.88 Clinochlore = 2.24 Cordierite = 3.38 Pyrite = 0.04 Kaolinite = 0.72 Siderite = 0.37 TOC = 1.44
Trace minerals/accessory minerals		
Pyrrhotite Calcite Fluorapatite Ankerite Sanidine Cordierite Biotite Titanite Rutile pyrite	Orthoclase Anorthoclase Titanite Cordierite Staurolite Fluorapatite	Labradorite Bytownite Andesine Anorthite Actinolite Ilmenite Titanite Rutile
Structure and texture		
Soft-sediment deformation Bioturbation structures Cone-in-cone Ripples?	Thinly laminated (fabric anisotropy) Soft-sediment deformation Phosphate nodules Brecciation	Boudinage laminae Bioturbation structures Foliation Rip-up clasts Intraclasts

2.6 Porosity

In BH KZF-1, macro- and meso-scale porosity is insignificant in thin-section and SEM micrographs. The only exceptions are: 1) interparticle porosity resulting from partially dissolved and corroded quartz grain boundaries (Figures 2.12, 2.15, 2.20); and 2) the intraparticle porosity in the phyllosilicates and dolomite cement (Figure 2.36 A–B). Most of the pore spaces are filled with organic matter (black in SEM), reprecipitated quartz and other diagenetic minerals (e.g., calcite, ankerite, siderite, dolomite, chlorite and albite). The insignificant meso- and macro-porosity is further confirmed with a CT-scan of sample KZF12 from the Whitehill Formation (Figure 2.37). The voxel size for the CT scanner is 20–30 µm, which is too large to identify accurately the nanopores that dominate tight black shales. The scan, however, was able to detect silty laminae within the shale, which have a maximum void space of 0.25 mm^2.

A study of the Whitehill Formation, south of Graaff-Reinet in the Eastern Cape by Geel et al. (2015) identified increased porosity (Table 2.1) in dolomite. The dolomite contained rounded pores which resemble moulds in dolomite crystals. Figure 2.36 C, D compares the dolomite from south of Graaf-Reinet to the dolomite from BH KZF-1 in the Tankwa Karoo Sub-basin (Figure 2.36 A, B).

In BH KWV-1, interparticle porosity is virtually non-existent. Grain boundaries have been recrystallized, most likely by compaction and pressure solution and, in some cases, are barely visible (Figures 2.26, 2.30, 2.31 and 2.35). Intraparticle porosity was identified in montmorillonite (Figure 2.35 D) and kaolinite (Figure 2.35 I, J).

The BIB polished back scatter electron (BSE) and secondary electron (SE2) SEM micrographs allow for the characterization of both the interparticle and intraparticle porosity (Figure 2.38 A–F). Intraparticle porosity is rare in minerals of these samples, except for dolomite, which contains rounded intra-particle pores (Figure 2.38 D). The intraparticle porosity concentrated in the organic matter consisted of round to ellipsoid nanopores that range from 5–500 nm in diameter (Figure 2.38 E, F). Some of the pores have internal structures, and others are elongated and align to the interfaces between the organic matter and mineral grains. Some OM pores are larger, curved and have a higher aspect-ratio aligned with the lamination in the samples.

While BIB-SEM imaging confirmed that nano-porosity is confined to the organic matter, FIB-SEM was useful in determining connectivity and permeability by creating a 3D network of the porous organic matter in the black shale. Samples from both BH KZF-1 and BH KWV-1 were analysed using the FIB-SEM technique (Figure 2.39, 2.40).

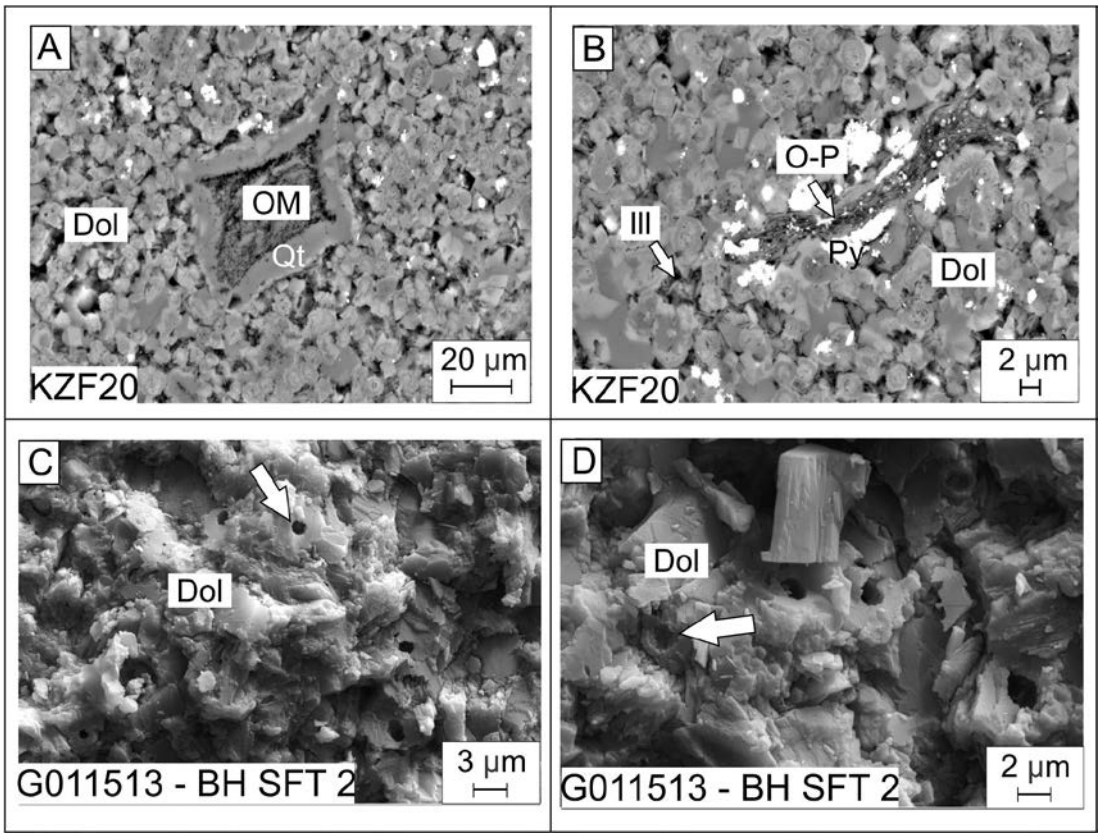

Figure 2.36: SEM micrographs of dolomite occurring in the Whitehill Formation from BH KZF-1 (this study) and BH SFT2 (Geel, 2014). A–B) Dolomite in BH KZF-1 showing rounded grains. C–D) Dolomite from BH SFT2 showing rounded mould-like pores. The arrow in micrograph C indicates a deep pore and the arrow from micrograph D indicates pore indent. Abbreviations: Dol: dolomite; OM: organic matter; O-P: oxyphlogopite; Py: pyrite; Ill: illite; Qt: quartz.

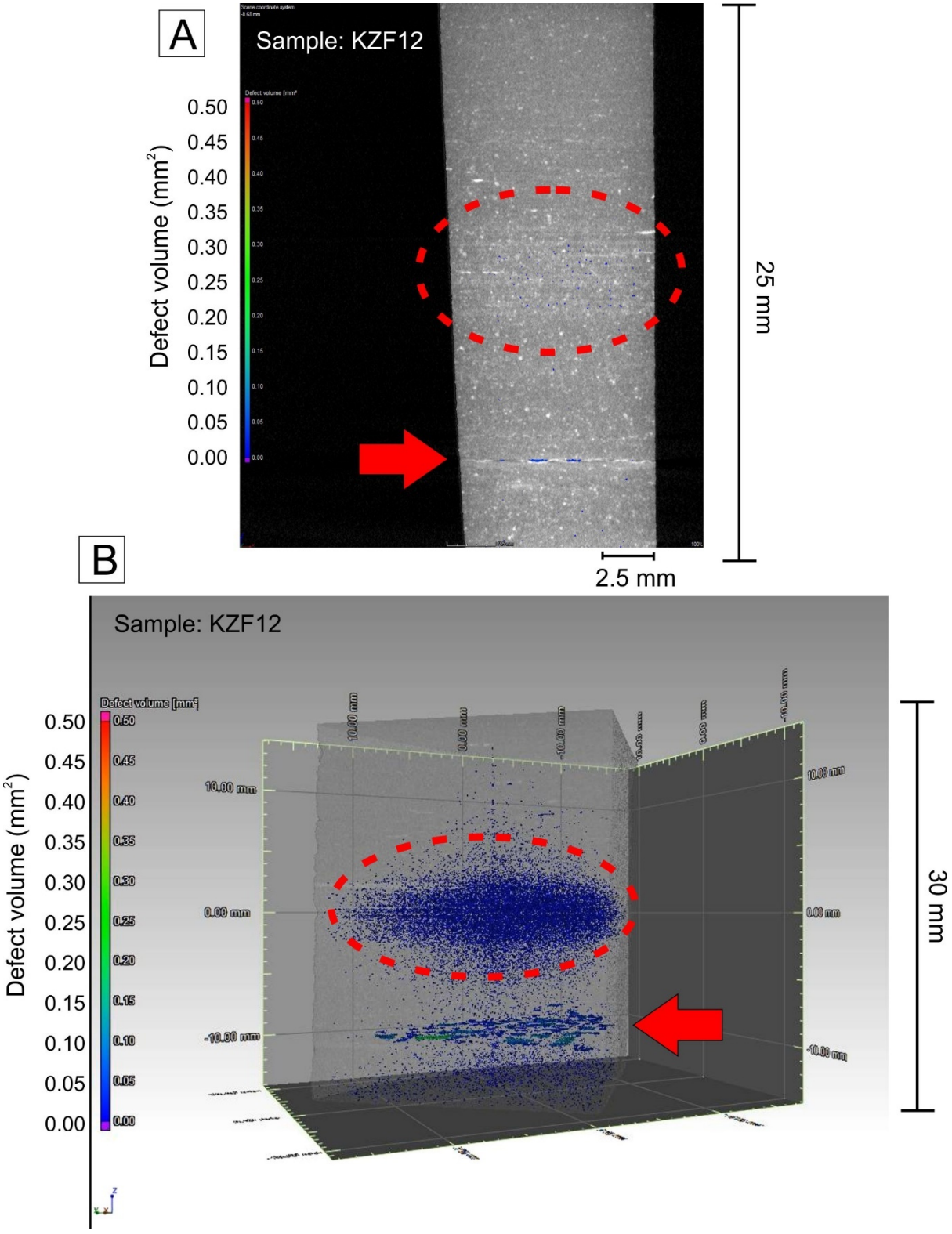

Figure 2.37: CT scan of sample KZF12 from the Whitehill Formation from BH KZF-1. Defect volume represents void space in sample. Porosity measured by CT scanning is confined to siltstone laminae indicated by the red arrow. The "porosity" in the dashed ellipsis is an artefact and is to be disregarded.

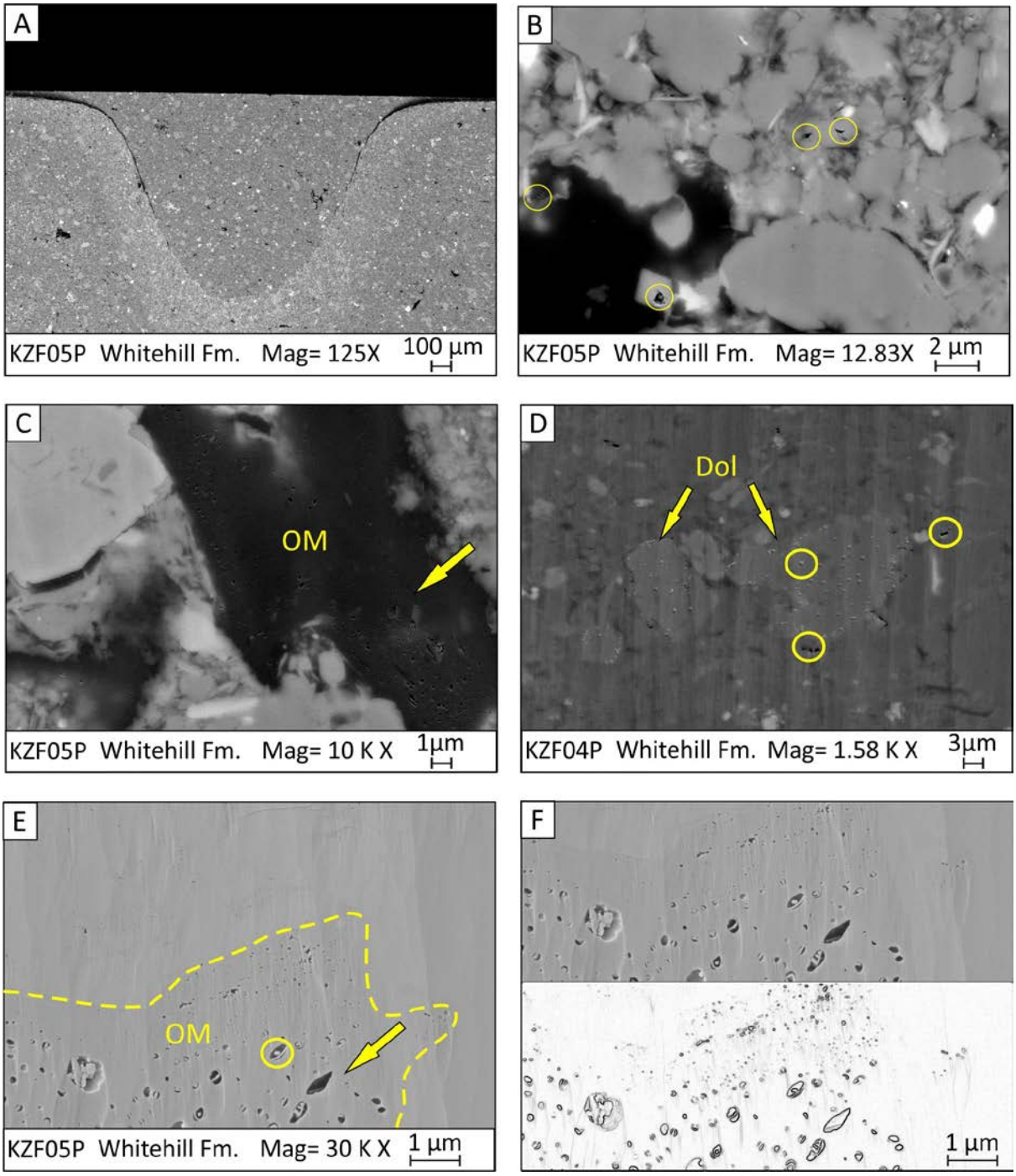

Figure 2.38: Sample KZF05P of the Whitehill Formation prepared by BIB-polishing and imaged by BSE. B) Intra-particle porosity in quartz grains. C) Intra-particle porosity in organic matter. D) Intra-particle and inter-particle porosity associated with dolomite grains. E–F) SE2 images of intra-particle porosity confined to organic matter. Abbreviations: OM: organic matter; Dol: dolomite.

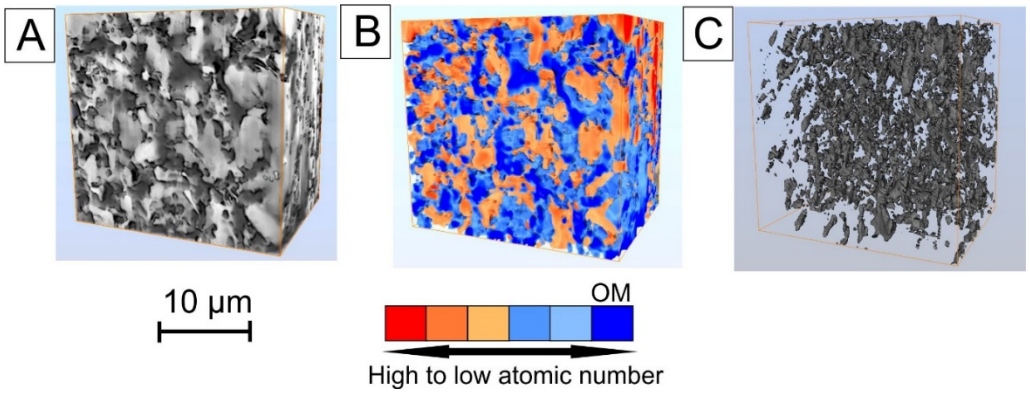

Figure 2.39: FIB-SEM 3D model of sample KZF05P from the Whitehill Formation in BH KZF-1. A) 3D reconstructed model using SEM micrographs after slicing. B) Colour corrected 3D model showing minerals with heavy to light atomic weights. Dark blue represents the disseminated organic matter within the sample. C) Isolated organic matter.

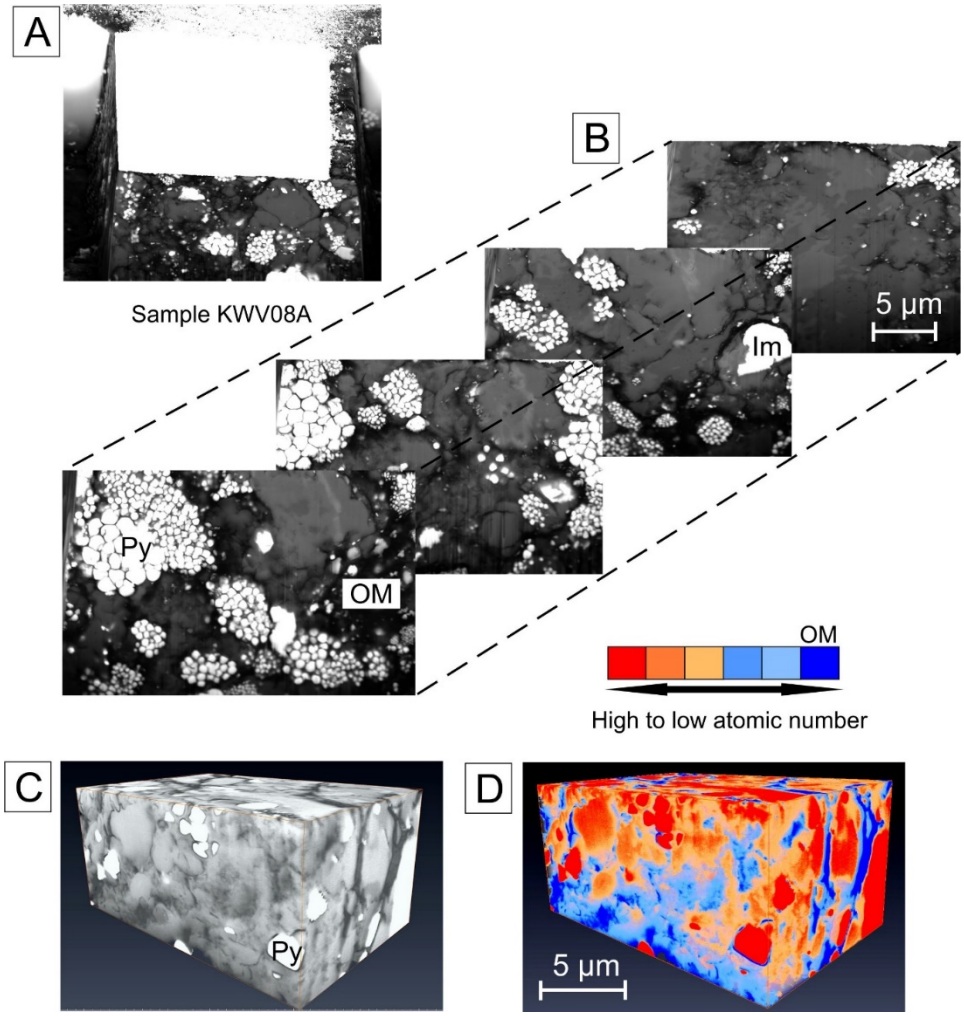

Figure 2.40: FIB-SEM analyses of sample KWV08A from the Whitehill Formation in BH KWV-1. A) Sample being sliced into a 25 µm^3 cube. B) Four representative slices out of 95 total slices. C) 3D reconstructed model using all 95 slices of sample KWV08A. D) 3D reconstruction showing minerals with heavy to light atomic weights. Dark blue represents the disseminated organic matter. Abbreviations: OM: organic matter; Py: pyrite; Im: ilmenite.

2.7 Thermal history

2.7.1 Vitrinite/bitumen reflectance

In BH KWV-1 reflectance measurements (Table 2.4) were obtained from solid bitumen (BR_o; Figure 2.41 A). Solid bitumen has similar reflectance to vitrinite (VR_o) but is stringy and without internal structure (Figure 2.41 B). The mean BR_o values for the Prince Albert Formation are 5.4 %, for the Whitehill Formation are 4.7 % and for the Collingham Formation are 5.6 %.

VR_o was measured in BH KZF-1 by Nolte et al. (2019). Their mean VR_o value is 4% for the lower Ecca Group (i.e., Prince Albert, Whitehill and Collingham formations). Table 2.4 compares the above reflectance values in BH KZF-1 (Nolte et al., 2019) to those in BH KWV-1 (this study).

Table 2.4: Vitrinite (VR_o) and bitumen (BR_o) reflectance for BH KWV-1 and BH KZF-1. Data from BH KZF-1 provided by Nolte et al. (2019).

***BH KWV-1* (this study)**			
Formation	***Sample no.***	***VR_o/BR_o***	***Mean***
Collingham	KWV03	5.4	5.6
Collingham	KWV04	5.7	
Collingham	KWV05	5.7	
Whitehill	KWV10	5.7	4.7
Whitehill	KWV11	4.2	
Whitehill	KWV12	4.2	
Prince Albert	KWV15	6	5.4
Prince Albert	KWV16	4.8	
Prince Albert	KWV17	5.4	
***BH KZF-1* (Nolte et al., 2019)**			
Collingham	KZF01P	4.2	4
Collingham	KZF02P	4	
Collingham	KZF03P	4	
Whitehill	KZF04P	4	4
Whitehill	KZF05P	4.2	
Whitehill	KZF06P	4	
Whitehill	KZF07P	4.2	
Whitehill	KZF08P	4	
Prince Albert	KZF09P	4	4
Prince Albert	KZF10P	4.1	

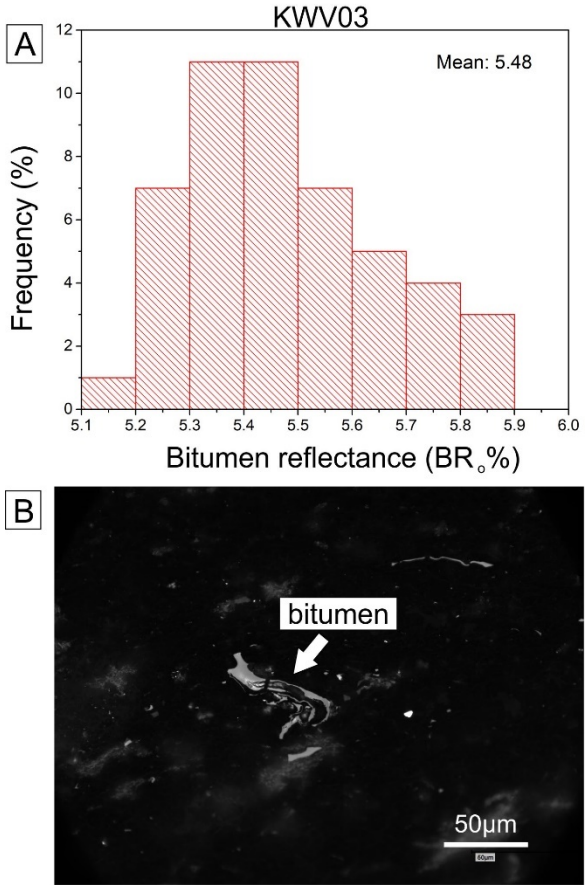

Figure 2.41: Thermal maturity determined by bitumen reflectance measurements. A) Histogram from sample KZW03 presenting bitumen reflectance values (BR_o) for the Collingham Formation. B) Photomicrograph of solid bitumen from sample KWV03 from the Collingham Formation.

2.7.2 TOC/Rock Eval analyses

Average values from TOC/Rock Eval analyses in both boreholes are recorded in Table 2.5. Individual sample data is available in Appendix A. The Whitehill and Collingham formations in the Tankwa Karoo Sub-basin have the highest TOC content at 5.17 wt% and 1.44 wt%, respectively. The Prince Albert Formation in both boreholes has the same TOC of 0.81 wt%. Low S1, S2, PY and PI values reflect poor hydrocarbon yield from all formations, additionally the low S1 and S2 values may lead to dubious Tmax ratios. Van Krevelan diagrams depicting HI, OI and Tmax values are shown in Figure 2.42 A–D. Average Tmax values for the Prince Albert Formation in BH KZF-1 and the Whitehill and Prince Albert formations in BH KWV-1 are < 430 °C, therefore in Figures 2.42 B, D some samples plot within the “immature zone” of the diagram. Low HI values make kerogen classification for some samples difficult. However, the HI values for the Prince Albert and Collingham formations in BH KWV-1 are much higher and their plot in the Kerogen II and Kerogen III zones are likely to be more accurate.

Table 2.5: Average TOC/Rock Eval data from BH KZF-1 and BH KWV-1. S1: free hydrocarbons; S2: hydrocarbons released from kerogen; Tmax: maximum temperature at the peak of S2; S3: organic carbon dioxide; TOC: total organic carbon (wt% and vol%); HI: hydrogen index (S2/TOC) x 100; OI: oxygen index (S3/TOC) x 100; PY: total hydrocarbons; PI: production index S1/(S1+S2).

BH KZF-1 / **Formation**	***S1 (mg/g)***	***S2 (mg/g)***	***Tmax (°C)***	***S3 (mg/g)***	***TOC (wt%)***	***HI (mg HC/g TOC)***	***OI (mg CO_2/g TOC)***	***PY (mg/g)***	***PI***
Collingham	0.03	0.14	571.80	0.33	1.44	9.87	24.60	0.17	0.18
Whitehill	0.05	0.12	449.88	0.21	5.17	2.41	4.12	0.17	0.28
Prince Albert	0.03	0.07	418.44	0.63	0.81	15.56	112.56	0.10	0.26
BH KWV-1 / **Formation**	***S1 (mg/g)***	***S2 (mg/g)***	***Tmax (°C)***	***S3(mg/g)***	***TOC (wt%)***	***HI (mg HC/g TOC)***	***OI (mg CO_2/g TOC)***	***PY (mg/g)***	***PI***
Collingham	0.02	0.08	430.71	0.14	0.83	86.71	117.71	0.10	0.19
Whitehill	0.06	0.12	334.14	0.18	4.87	2.57	4.14	0.18	0.34
Prince Albert	0.02	0.06	409.75	0.09	0.81	167	225.25	0.08	0.25

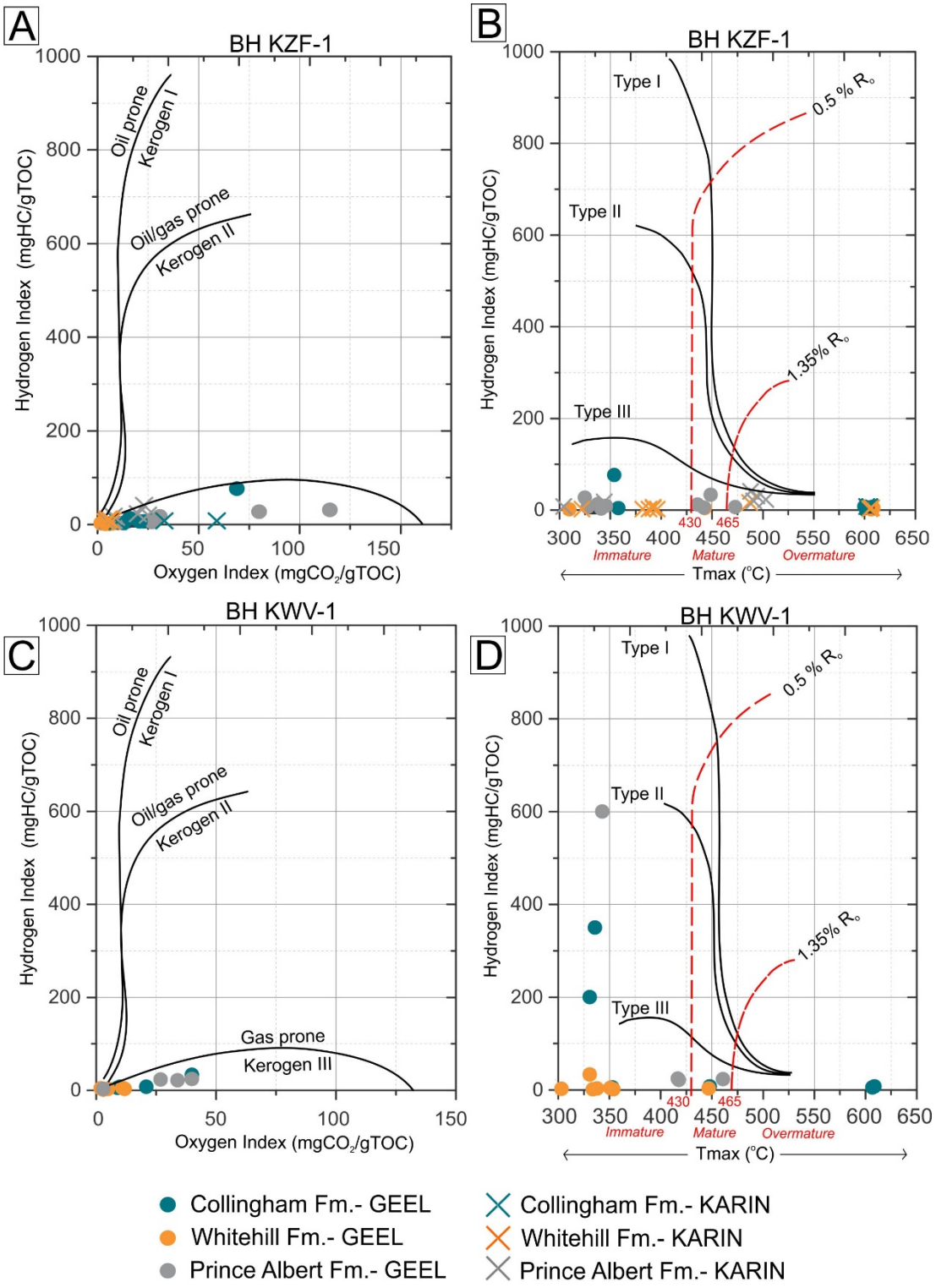

Figure 2.42: Modified Van Krevelen diagrams for BH KZF-1 and BH KWV-1. A, C) Hydrogen index versus oxygen index. B, D) Hydrogen index versus Tmax. Hydrogen index values become unreliable due to such high thermal maturity. Additional data available from BH KZF-1 is included (KARIN = de Kock et al., 2016).

2.8 Discussion

2.8.1 Mineralogical composition and diagenesis of lower Ecca Group

The lower Ecca Group in BH KZF-1 and BH KWV-1 was deposited ~ 830 km apart in the western Tankwa Karoo Sub-basin and eastern MKB (Figures 2.2, 2.3, 2.4). Here we discuss the syn- and post-depositional conditions (including diagenesis and metamorphism) that led to the mineralogical composition of these Karoo sedimentary rocks. The types of diagenetic processes and their products are subdivided into three phases: eogenetic (early diagenesis), mesogenetic (burial diagenesis/late stage diagenesis) and telogenetic (uplifted/exhumed diagenesis; De Segonzac, 1968; Choquette & Pray, 1970). Eogenesis occurs at temperatures of < 20–70 °C. Mesogenesis begins between temperatures of 30–70 °C and continues up to 200–250 °C (De Segonzac, 1968; Worden & Burley, 2003; Boggs, 2009).

2.8.1.1 Prince Albert Formation – Tankwa Karoo Sub-basin

The Prince Albert Formation in the Tankwa Karoo Sub-basin can be subdivided into the lower post-glacial Prince Albert Formation (~ 650–550 m) and upper Prince Albert Formation (550–500 m; Figure 2.6). The post-glacial sedimentation of the Prince Albert Formation begins at a sharp contact with the underlying Dwyka Group diamictites. About 2 cm above the contact with the Prince Albert Formation (648 m) is a layer of greenalite ($(Fe, Mg)_6Si_4O_{10}(OH)_8$; Figures 2.7; 2.8 C, D). Greenalite is an iron silicate derived from the rapid nucleation of a hydrous Fe (II)-silicate gel at 25 °C from Fe^{2+} and SiO_2 (aq) solutions in anoxic seawater. Greenalite is typically nucleated from waters with a pH of 7.7–8.3, implying high-alkalinity conditions (Tosca et al., 2015). It is likely that upwelling of silica-rich alkaline waters occurred as a result of melting glacial ice-sheets. Stilpnomelane occurs between greenalite crystals and forms due to the reaction between Al-containing greenalite + quartz + siderite + K^+ (aqueous). The stilpnomelane would have formed during late-stage burial diagenesis (Klein, 1983). In the same sample with greenalite, XRD analyses detected 61.84 wt% of apatite (Figure 2.7). Similarly, to greenalite, apatite will precipitate when there is an increase in temperature, pH and salinity (Gulbrandsen, 1964). Although it must also be considered that the high apatite content may be detected from Dwyka Group dropstones.

In the lowermost 81 m of the Prince Albert Formation, there are Mn-oxide nodules identified as birnessite (depths 632–551 m). In thin section micrographs the birnessite nodules and cement appears to be syn-depositional (Figures 2.9 I–N; 2.10 W, X).

However, post-depositional soft sedimentation deformation structures with birnessite and rhodochrosite is also observed (Figure 2.10 Q–T). Birnessite typically forms from another manganese oxide called todorokite. Todokorite is formed diagenetically through precipitation from pore waters that are modified by chemical reactions between sea water and sediments (Baker & Beaudoin, 2013). Mn is usually supplied to deposits by overlying waters and upward diagenetic migration from underlying sediments via physicochemical gradients. Marine birnessite is found to occur under low sedimentation rates between 4000 and 6500 m depths. Marine bacteria may also act as a dominant catalyst for Mn oxide (Ehrlich, 1963; Crerar & Barnes, 1974; Baker & Beaudoin, 2013). Birnessite in the Prince Albert Formation is found occurring in bioturbated zones with trace fossils indicating that high levels of biological activity were present in these horizons. The bottom waters in the "Ecca Inland Sea" during the Prince Albert depositional phase may have become oxygenated as cold water, near glacial peripheries sank and migrated towards equatorial regions in an oceanic conveyer-belt system (e.g., the Atlantic Gulf Stream and the Antarctic circumpolar current; Rintoul, 2009; Rintoul & Garabato, 2013).

Occurring alongside birnessite is rhodochrosite ($MnCO_3$; 44–69 wt%; Figures 2.7; 2.9 I–N; 2.10 O–T, W–X) and siderite (2–20 wt%; Figure 2.7). Therefore, the lower Prince Albert Formation may be described as a calcareous mudstone. Siderite is consistent with early diagenetic and/or metamorphic origin and may be precipitated during early diagenesis. In the case of early diagenetic siderite precipitation, goethite would have to be present in the water column (Schulz et al., 2018). Rhodochrosite precipitation requires the addition of carbonate species to the system, low Eh and pH ~ 8. The addition of Mn in the system may be fluvially introduced as manganite and Fe from goethite (Schulz et al., 2018). In reducing marine sediments iron becomes fixed as sulfide and manganese remains mobile. Fresh water pH is typically too low for rhodochrosite precipitation (Maynard, 2003; Schulz et al., 2018). $MnCO_3$ mineralization requires consumption of organic matter and probably occurs during early diagenesis (Maynard, 2003).

In the lower Prince Albert Formation, the clay minerals detected are illite (4.91 wt%), clinochlore (1.12 wt%) and kaolinite (0.63 wt%; Table 2.3). The average quartz content is comparably higher (37.18 wt%). In the upper Prince Albert Formation, the frequency of illite-rich laminae and quartz-rich siltstone increase. Detrital and authigenic quartz (39.07 wt%), albite (17.11 wt%), illite (27.96 wt%), clinochlore (4.75 wt%) and kaolinite (2.09 wt%; Table 2.3) dominate the mineral composition in the upper Prince Albert Formation. Apatite is also detected in trace amounts throughout

the rest of the Prince Albert Formation. Detrital and authigenic fluorapatite crystals were identified with SEM. Micrographs of detrital apatite crystals show them to be anhedral with pressure dissolution of the grain boundaries (e.g., Figure 2.12 B). Authigenic phosphate nodules were identified in both the Prince Albert and Whitehill formations. Fluorapatite ($Ca_5[PO_4]_3[OH, F, Cl]$) is commonly found in marine sediments. It occurs as early diagenetic precipitate near the sediment surface in uncompacted, organic-carbon-rich muds (Tucker, 1981; Hesse & Schacht, 2003). Phosphate is formed from strong upwelling and high productivity and apatite formation is a function of the residence time of the sediment close to the seafloor, while clastic (terrigenous) sedimentation needs to be extremely low. There is usually a significant quantity of PO_4^{3-} within the sediment near the sediment-water-interface, when apatite is precipitated in modern day analogues (e.g., offshore Peru and Chile; Hesse & Sacht, 2003; Bjørlykke, 2010). Phosphate precipitation also may be directly related to suboxic bacterial degradation of organic matter, dissolution of fish debris or an Fe-reducing mechanism called “iron-pumping”.

Both Fe-rich chlorite (chamosite) and Mg-rich chlorite (clinochlore) is identified in the Prince Albert Formation. Authigenic chlorite is formed during both eogenesis and mesogenesis. Typically, detrital K-feldspar reacts with smectite releasing Mg^{2+} and Fe^{2+} into the system and chlorite, illite and quartz are precipitated (Selley, 2000; Weaver, 1990). In micrographs, iron-rich chlorite has siderite rims, which demonstrate the reaction between Fe^{2+}, provided from siderite, with kaolinite to form late-stage chlorite (e.g., Figures 2.11 A’, 2.12 D; Surdam et al., 1989; Weaver, 1990; Compton, 1991). The precipitation of siderite indicates that sulfate had been depleted by reduction from the water column (Schulz et al., 2018). The alteration of smectite and the increase of available Mg^{2+} and Fe^{2+} will also lead to the precipitation of ankerite (Weaver, 1990; Selley, 2000).

The average TOC content of the Prince Albert Formation is 0.81 wt% and over all the pyrite content is low (0–0.2 wt%), with the exception of sample KZF22 at 482 m. Sample KZF22 is rich in pyrite (23 wt%, Figure 2.7), which is associated with hydrothermal veining due and brecciation due to thrust faulting.

2.8.1.2 Prince Albert Formation – Eastern Main Karoo Basin

The contact between the Dwyka Group and the Prince Albert Formation is gradational. The postglacial sediment is bioturbated, silty mudstone with organo-mineralic aggregates, fragmented microbial beds and agglutinated benthic foraminifera.

Agglutinated benthic foraminifera was identified in sample KWV17 (~ 3.75 m above the contact; Figure 2.24 A, B). The agglutinated benthic foraminifera has a high trochospiral test with decreased spirals in each whorl as it tapers near the one end. It is possibly part of the subclass Textulariana (Mikhalevich & Kaminski, 2008; Kaminski, 2014). Agglutinated foraminifera are marine protozoans and many species are found in modern oceans (Kaminiski, 2014).

The Prince Albert Formation has the highest quantity of illite (37.83 wt%) and clinochlore (9.41 wt%) in the lower Ecca Group in both BH KWV-1 and BH KZF-1. Conversely, there are less carbonates in BH KWV-1 compared to BH KZF-1. Carbonates that are identified are siderite (0.13 wt%), calcite and ankerite (Table 2.4). The carbonates, likely formed from the alteration of tuffaceous layers, occur at the top of the Prince Albert Formation (2371 m). The tuff layers show evidence for soft-sedimentation deformation structures and micro-ripples and have possibly been reworked.

Chamosite (Fe-chlorite) is identified coating detrital sanidine grains (Figure 2.26 D). Grain coating by chlorite occurs at temperatures between 90–100 °C, at burial depths > 3 km (Worden & Burly, 2003). During mesogenesis K-feldspar reacts with smectite to form chlorite, illite and quartz. The stability of kaolinite decreases at 70–100 °C and 2–3 km depths (Bjørlykke & Jahren, 2012). If kaolinite is present with K-feldspar, it will be replaced by illite at temperatures >130 °C (Bjørlykke et al., 1986; Ehrenberg & Nadeau, 1989). The kaolinite content (1.24 wt%) of the Prince Albert Formation is low and K-feldspar is nearly negligible, having mostly converted to illite.

Up to 30 wt% of anorthite occurs in the lower Prince Albert Formation. During mesogenesis, Ca-rich feldspars are often altered to albite in a process called albitization (Boggs, 2009). The Prince Albert Formation in BH KWV-1 is exposed to deep burial diagenesis, however, the continuing presence of anorthite suggests that albitization did not occur. As burial diagenesis increases, fluid flux of pore water under compaction may become limited and will reduce mass transport of solids in solution, thereby preventing some reactions from taking place (Shaw & Primmer, 1989; Bjørlykke & Jahren, 2012).

No pyrite was detected by XRD analyses, and only minor pyrite was detected with SEM and in thin section. This indicates that little sulfate reduction was taking place and that the water was probably oxygenated, which is further substantiated by the presence of bioturbation structures and fossil shells of agglutinated benthic foraminifera. However, some OM was still preserved, and the average TOC content

of BH KWV-1 is the same as in BH KZF-1 (0.81 wt%). Other accessory minerals that are very common are biotite laths and euhedral fluorapatite grains with growth rims (Figure 2.26 E, F). The absence of birnessite nodules is an indication that the “Ecca Inland Sea” was probably shallower in the eastern MKB compared to the Tankwa Karoo Sub-basin during the Prince Albert depositional phase.

2.8.1.3 Whitehill Formation – Tankwa Karoo Sub-basin

Structural duplication of the Whitehill Formation in the Tankwa Karoo Sub-basin has resulted in a total thickness of 65.5 m. However, the true thickness is closer to 19.5 m (Figure 2.6). The Whitehill Formation consists mostly of thinly laminated, TOC-rich clay beds intercalated with very thin siltstone laminae (e.g., Figures 2.13 I, J; 2.14 Q, R). The Whitehill Formation in BH KZF-1 has the highest TOC content (5.14 wt%). OM is typically preserved under conditions of low sedimentation rates, density stratification, low oxygen levels or reduced oxygenation by high OM accumulation (Tourtelot, 1979). OM preserved under these conditions is converted to water-soluble methane, carbon dioxide, molecular hydrogen and acetic acid (Schulz et al., 2018). The Whitehill Formation has the highest pyrite content in the lower Ecca Group, which is an indicator of sulfate-bearing water and later sulfate reduction by organic matter (Figure 2.7; Table 2.3). However, 2.2 wt% of pyrite is still low, which can indicate that periods of anoxia may have fluctuated, or that that it was the high productivity that allowed for OM preservation. Phosphate nodules, similar, but less frequent, than those of the Prince Albert Formation, were detected in sample KZF15 at 436 m (Figure 2.14 K). Phosphate nodules suggest that the marine conditions from the Prince Albert Formation prevailed well into the deposition of the Whitehill Formation sediments.

The Whitehill Formation is described across the basin as a décollement zone (Kingsley, 1981; Lindeque et al., 2007) and the black shale is frequently disrupted by micro-faults and folds and soft sediment deformation structures (e.g., Figure 2.13 I). The micro-faulting and folding are often associated with hydrothermal veining linking the deformation with tectonic activity, which probably, occurred during later stages of the CFB orogeny. However, the soft-sediment deformation structures represent small-scale deformation prior to lithification (Figure 2.13 E).

The Whitehill Formation has high quartz (35.36 wt%) and illite content (23.19 wt%; Table 2.3) of both detrital and authigenic origin. Authigenic quartz can be formed as a by-product of smectite to illite (S-I) transformation (Hower et al., 1976; Hoffman & Hower, 1979; Boles & Franks, 1979). The quartz grains are corroded and recrystallized and it is difficult to determine which grains are detrital (e.g., Figure 2.15

C). Quartz cementation typically forms at ~ 70–80 °C (Bjørlykke et al., 1986; Ehrenberg, 1990; Walderhaug, 1994).

Dolomite occurring at 475 m and 472 m depths presents as ~ 2 µm diameter spheres that resemble ooids, dispersed with rare laths of oxy-phlogopite (Figure 2.15 E, F). Oxy-phlogopite is a product of regional metamorphism and is formed by the reaction between dolomite and K-feldspar or muscovite (Deer et al., 1966). The ooid-like texture of the dolomite would be better described as micro-oncoids, due to their smaller size (Flügel, 2004). In the top half of the Whitehill Formation, at 436 m and 463 m, dolomite occurs as concretions precipitated around clay flocculants (Figure 2.16 A–C). The concretions do not exhibit the same ooid-like texture as the dolomite occurring near the base of formation. If smectite reacts with K-feldspar to form quartz, illite, chlorite and kaolinite, then additional Mg and Fe may be available to form late ankerite, ferroan-dolomite or siderite (Boles & Franks, 1979). These concretions may be formed late-stage diagenetic growths, when burial temperatures increase to 60 °C or more, in pore waters with relatively low Mg/Ca values (Boggs, 2009).

Dolomite, composed of similar micro-oncoids was also detected in the Whitehill Formation in BH SFT2, at ~ 225 m depth by Geel et al (2015). However, the centres of the grains in the BH SFT2 sample were hollow, thereby increasing the porosity of the sample (Figure 2.36 C–D). In comparison, the dolomite-rich sample in BH KZF-1 (KZF07P; ~ 52 wt% dolomite) did not have significantly greater porosity than the clay-rich samples from the Whitehill Formation. The increased porosity detected in BH SFT2 may be a consequence of telogenetic reactions that dissolved the centres of the coated grains. The sample from BH SFT2 is 247 m closer to the surface than dolomite samples from BH KZF-1. Dolomite from BH SFT2 is isotopically light with $\delta^{13}C$ values of -24.7 ‰ (Geel et al., 2015). One way that the dolomite from the lower Whitehill Formation could have formed like this was during eogenesis via methanogenesis. Methanogenesis in a shallow sea will increase the ρCO_2 in the water column, which can contribute to the precipitation of carbonates (Tourtelot, 1979; Curtis, 1978; Surdam et al., 1989). However, in the case of the MKB, ρCO_2 of the water column would be significantly increased after the transition from an ice-house to a green-house climate (Visser, 1993). Alternatively, on steep margins, fronting oceanic basins, there may be dissolution of aragonite followed by the precipitation of radial calcite, the dissolution of calcite and lastly the precipitation of dolomite below the “calcite lysocline” (Saller, 1984; 1986). It may also be the case that the lower Whitehill Formation dolomite was formed in deeper water environments (>100 m) by ramp-or slope-mud-mounds, which may exhibit stromatolitic fabrics as a result of

microbial processes. Carbonate mounds located near seafloor hydrothermal vents and petroleum or methane cold seeps can drive chemoautotrophic bacteria oxidization (Kaufman et al., 1996; Moore & Wade, 2013b). In the case of the MKB, the dolomite of the Whitehill Formation may have formed in the subsurface (mesogenetic zone) by a mixture of marine-meteoric waters and basinal-derived brines (Moore & Wade, 2013a). With many possibilities for genesis of the Whitehill dolomite, further in-depth investigation is required.

2.8.1.4 Whitehill Formation – Eastern Karoo Basin

The Whitehill Formation is 13 m thick in BH KWV-1, 6.5 m thinner than the unduplicated Whitehill Formation in the Tankwa Karoo Sub-basin. Similarly, to its western counterpart, it consists mostly of thinly laminated organic-rich clay beds intercalated with very thin siltstone laminae. The preservation of organic matter is due to density stratification and anoxic-bottom water conditions. Most common clay minerals are illite (24.83 wt%) and kaolinite (1.42 wt%) with lesser clinochlore (0.48 wt%).

Pyrite (0.81 wt%) has been converted to pyrrhotite (8.20 wt%; Figure 2.23; Table 2.4) in BH KWV-1 due to contact metamorphism (Ferry, 1981) caused by the dolerite sill intruded at the top of the Whitehill Formation (Figures 2.29 U–X; 2.31 C) . Textures associated with contact metamorphism include foliation of illite-smectite layers (Figure 2.30 E) and pressure solution along quartz and calcite grain boundaries (Figure 2.30 H). This has resulted in near-complete recrystallization that eliminates almost all porosity. Other metamorphic minerals identified are chalcedony nodules (Figure 2.29 P), staurolite (Figure 2.27 G), almandine (Figure 2.27 E), cordierite (Figures 2.27 F; 2.30 F, G), biotite, enstatite (Figure 2.30 I), diopside (Figure 2.30 I), talc and titanite (Figure 2.30 J). The garnet falls in the pyrope-almandine-spessartine garnet series called pyralspite (Deer et al., 1966). The paragenesis of garnet occurs with ferromagnesian minerals, for example, cordierite, biotite, pyroxene, which occur in a hornfels rock (Chinner, 1962, Deer et al., 1966). The occurrence of biotite suggests that there was dehydration, due to the breakdown of chlorite. For this to occur, the temperature would have had to reach at least 350 °C (Aarnes et al., 2011). Patches of quartz and clay minerals, as well as poikiloblasts of cordierites give some samples a “spotted” appearance (e.g., Figures 2.29 U–X; 2.31 C). Metapelites are often described as spotted hornfels (Pownall et al., 2012). Although metamorphic minerals are identified, they are not abundant enough for the rock to have transformed entirely into a metapelite.

Phosphate nodules were detected at ~ 2302 m in sample KWV10 and are similar to those identified in BH KZF-1 (Figure 2.28 K, L). Nearly all sedimentary phosphates (phosphorites) have marine origin (Boggs, 2009; Dar et al., 2017) and often occur in areas of upwelling as seen off the coast of Namibia (Bremner & Rogers, 1990; Dar, 2013) and Peru-Chile (Veeh et al., 1973). Therefore, the phosphate nodules detected in the Prince Albert and Whitehill formations may indicate high levels of primary production in marine conditions. No dolomite in any form was detected in the Whitehill Formation in BH KWV-1. The only significant carbonate identified is calcite (59 wt%; Figure 2.23) in sample KZF12, which is directly related to calcite veining linked to dolerite intrusion.

XRD analyses detected diopside (2.35 wt%) and talc (0.95 wt%) in the sample KWV12 and SEM analyses detected diopside and enstatite in sample KWV13 (Figure 2.23). These suggest that dolerite is likely to be in proximity of this samples, although dolerite was not directly observed in the core or in thin sections of these samples. This implies that it can be difficult to predict the exact position of dolerite intrusions by only viewing hand specimens and thin sections of borehole core.

2.8.1.5 Collingham Formation – Tankwa Karoo Sub-basin

The Collingham Formation is intercalated with organic-matter-rich mudstone, siltstones and tuffaceous laminae (Figure 2.6). The Collingham Formation has the highest quartz (51.80 wt%) and albite (20.93 wt%) content of all three formations in both boreholes (Table 2.3). Clay minerals identified are illite (19.86 wt%) and clinochlore (2.25 wt%; Table 2.3), and the average TOC content of 1.44 wt%. Framboidal pyrite aggregates (Figures 2.17 C, D; 2.20 E) indicated that sulfate reduction occurred in microbe-rich, anaerobic conditions (Boggs, 2009). The conversion of organic matter is also responsible for early diagenetic siderite formation (0.67 wt%).

Volcanic ash, consisting of glass and unstable volcanic mineral assemblages, often alters to smectite on the seafloor during eogenesis (Compton, 2001; Bjørlykke, 2010). The tuffs of the Collingham Formation have been described as K-bentonites, because of their high illite content (Viljoen, 1994). In BH KZF-1 the tuff layers (Figures 2.18 L, Q, S; 2.19 V) are converted from bentonite to illite, calcite, albite, ankerite (Figures 2.18 L; 2.20 C–F) and ferroan dolomite (0.38 wt%; Table 2.3). Ferroan dolomite (Figure 2.20 A–C) is an end-member and indicator of late-stage, deep-burial diagenesis (Surdam et al., 1989). Most of the authigenic albite is a result of alteration from calcite and albitization of Ca-feldspars (Figure 2.21 A). Albite is generally

precipitated at burial depths greater than 3 km and at temperatures up to 100 °C (Mu et al., 2016). The occurrence of both syn- and post-depositional calcite nodules (Figure 2.21 B, C) further indicates that calcium carbonate was readily available in the system.

Common features of the Collingham Formation are bioturbation structures (Figure 2.19 A') and intraclasts. The shape of the rip-up intraclasts suggests they were deposited as partially consolidated particles that were able to resist mechanical disruption (Figures 2.17 E, F; 2.18 M). Mudstone lithoclasts have been interpreted as transported by high-density flows referred to as hyperpycnal flows. Hyperpyncal flows usually develop due to frequent supply of high-density currents transported by rivers into standing waterbody (lake or sea) and occur near deltas (e.g., Bates, 1953; Schieber et al., 2010; Zavala & Pan, 2018; Boulesteix, 2019). The sediment density flows likely oxygenated the basin floor, however, high organic supply rates still preserved some OM.

2.8.1.6 Collingham Formation – Eastern Main Karoo Basin

The Collingham Formation is intercalated with organic-matter-rich mudstone, siltstones and tuffaceous laminae. Similar to the Collingham Formation in BH KZF-1, common features are bioturbation structures, rip-up clasts, intraclasts and lag deposits. It is evident that low-density flows existed in the east of the basin. The Collingham Formation is ~ 90 m thick, 9 m thicker than the Collingham Formation in BH KZF-1. The average TOC content is 0.82 wt%. The Collingham Formation is bounded by two dolerite intrusions (Figure 2.22); therefore, it is subject to significant contact metamorphism. Similar to the underlying Whitehill Formation, the Collingham Formation shows evidence for incipient alteration into spotted hornfels (Figures 2.34 U, V, Y; 2.35 L) and some silty laminae are deformed into boudins (Figure 2.32 D, E). Minerals associated with hornfels facies in BH KWV-1 are cordierite (Figures 2.32 I, J, 2.33 M–O), almandine (pyralspite; Figures 2.32 A, B; 2.35 K, L), biotite (Figure 2.35 I), sphene (titanite) and chalcedony nodules (Figures 2.32 F). High calcite in sample KWV02 (43 wt%; Table 2.23) is associated to dolerite intrusion.

Smectite (montmorillonite), kaolinite (0.72 wt%) and illite (24 wt%) were identified in the Collingham Formation (Table 2.4). Smectite is typically formed from early stage diagenesis of tuff and smectite to illite conversion usually takes place between 55 °C to 200 °C (Weaver, 1990). However, in geothermal regions of New Zealand, it has even been reported that smectite to illite conversion occurs up to 240 °C (Eslinger & Savin, 1973). Kaolinite is destroyed between 170° and 210 °C (Weaver, 1990;

Compton, 1991, Worden and Burley, 2003). Therefore, the presence of some kaolinite and montmorillonite implies that although these rocks went beyond the phase of mesogenesis, some clays were still preserved. This is further confirmed by the occurrence of Ca-feldspars such as labradorite, bytownite and anorthite (Figure 3.32 C, H), which, unlike the Ca-feldspars in BH KZF-1, did not undergo albitization. This further affirms that burial depth (2185–2349 m), resulting in compaction and destruction of porosity, inhibits fluid flux, a driving mechanism for epigenesis. Carbonates minerals include minor siderite (0.37 wt%) and ankerite. Ankerite was identified as a replacement mineral in microfossils (Figure 2.32 E). Tuff laminae have not undergone diagenetic alteration to ankerite and siderite to the same extent as the tuff in BH KZF-1, due to the limitations on epigenesis by compaction.

2.8.2 Porosity

Compaction, late stage diagenesis and contact metamorphism of the lower Ecca Group sedimentary rocks resulted in recrystallized grain boundaries and precipitation of syn- and post-depositional carbonate nodules and cement, thereby reducing overall interparticle porosity. In BH KZF-1, the average porosity is 4.13 % in the Prince Albert Formation, 6.07 % in the Whitehill Formation and 6.64% in the Collingham Formation (Table 2.1; Nolte et al., 2019). Micro CT scanning (Figure 2.37), SEM (Figures 2.12; 2.15; 2.20; 2.26; 2.30; 2.35) and BIB-SEM (Figure 2.38) imaging of the lower Ecca Group confirm that macro- and meso-porosity of the Whitehill Formation is low, and that nano-porosity is mostly confined to intraparticle organic matter. The pores are diagenetic, although some may be primary in origin. Other forms of intraparticle porosity is seen between framboidal pyrite crystals, within kaolinite and montmorillonite (mostly in BH KWV-1) and between cleavage planes of clay-mineral aggregates. Organic material occupies most of the interparticle space and is likely to facilitate any permeability (10^{-22} to 10^{-19} m^2, Table 2.1; Nolte et al., 2019) in the lower Ecca Group. The Collingham Formation is intercalated with tuff layers, which are fissile and possibly the reason it has the highest permeability of all three formations (10^{-19} to 10^{-20} m^2; Nolte et al., 2019).

There are two types of OM occurring in these rocks: 1) detrital organic matter (DOM); 2) secondary organic matter (SOM), which fills up pore spaces generated during burial diagenesis. These types of organic matter develop pores by gas generation. If a rock contains both DOM and SOM, it can be considered both a source rock and a reservoir (Milliken et al., 2013). 3D reconstruction of organic material explores the density and connectivity of OM within samples from the Whitehill Formation (KZF05P and

KWV08A; Figures 2.39; 2.40). Sample KZF05P from BH KZF-1 appears to mostly consist of disseminated DOM, which is not well connected. Sample KWV08A from BH KWV-1 contains SOM that is better connected, which may facilitate permeability.

BIB-SEM micrographs (Figures 2.38) show rounded bubble-like pores on some dolomite grains. This could be interpreted as fluid inclusions (Goldstein, 2003; Klaver et al., 2015). In some samples, dolomite cementation occurs in concentric rings, which contributes to increased porosity previously recorded from dolomite in the Whitehill Formation (Geel et al., 2015), although in BH KZF-1 the porosity in the dolomite-rich sample (KZF07P) is not significantly increased (Table 2.1). Even if there is increased porosity in some dolomite, it does not necessarily mean that there is high permeability in these samples. Negative impressions of dolomite pores could mean that the pores are limited in size and may not be connected (Figure 2.36).

2.8.3 Thermal maturity

The lower Karoo Supergroup throughout the southern MKB was affected by deformation and low-grade metamorphism that caused by the Cape Orogeny (Hälbich et al., 1983; Craddock et al., 2007; Milani & de Wit; 2008; Tinker et al., 2008; Hansma et al., 2015; Blewett & Phillips et al., 2016; Blewett et al., 2019). In the southwestern part of the basin, geothermometry data suggests temperatures reaching ~ 300 °C in the tectonic domains of the CFB and lower-greenschist-facies metamorphic conditions (Frimmel et al., 2001).

In BH KZF-1, structural duplication by low angle thrust faults resulted in the tectonic displacement of the Prince Albert and Whitehill formations and their brecciated contacts. This structural damage implies variability of the strength of the Whitehill Formation, depending on proximity to CFB. Cone-in-cone (CIC) structures in calcite veining was detected in both the Whitehill and Collingham formations and consists of stacks of nested calcite forming the appearance of cones (Figures 2.14 P; 2.18 T; 2.25 I). The post-depositional features are further evidence for tectonic stress (Le Breton et al., 2013). The elevated thermal maturity has resulted in over-mature organic matter. The average VR_o is 4 % (Nolte et al., 2019; Table 2.5) for the lower Ecca Group in the Tankwa Karoo Sub-basin.

The lower Ecca Group in BH KWV-1 does not show structural deformation, as in BH KZF-1. CIC structures were identified in the Prince Albert Formation, which suggests that tectonic stress from the CFB also impacted the sedimentary rocks in BH KWV-1. However, the greatest thermal alteration is from the dolerite emplacement. In total,

the borehole is intersected by 18 dolerite intrusions. The intrusions vary in thickness from 0.03 m to 149 m in thickness. The Collingham Formation is bounded by two dolerite intrusions. The first, being the thickest dolerite intrusion of the borehole (149 m), intruded near the top of the Collingham Formation. The second, 13 cm below the contact with the Whitehill Formation, is 18.76 m thick. The intrusion temperature was probably between 1150 °C and 1300 °C (Toplis & Carrol, 1995; Neumann et al., 2011). The elevated heat flow leads to maturation of organic matter that can occur hundreds of metres away from the intrusions (Aarnes et al., 2011). Metamorphic minerals such as almandine, cordierite, staurolite, biotite, sphene, diopside and enstatite are mineral assemblages correlated with intermediate to high metamorphism, which can occur at temperatures between 500 °C and 600°C and 2 to 8 kPa (Winkler, 1980). The average bitumen reflectance (BR_o) for the lower Ecca Group in BH KWV-1 is 5% with the Whitehill Formation having the lowest reflectance value of 4.7 %. The Prince Albert Formation (5.4 %) and the Collingham Formation (5.6 %) from BH KWV-1 has higher reflectance values then their corresponding formations in BH KZF-1 (4 %; Table 2.5). Previous studies have indicated that TOC loss may occur close to dolerite intrusions (Aarnes et al., 2011). However, the TOC values of the Whitehill Formation in BH KWV-1 are only 0.54 % less than the values in the Whitehill Formation in the Tankwa Karoo Sub-basin, where dolerite intrusions appear to be less abundant in the vicinity of BH KZF-1. The dolerite intrusions may have accelerated gas formation and subsequent degassing in the MKB.

Rock-Eval is the technique used to establish how much kerogen has been converted into hydrocarbons (Table 2.6). In BH KZF-1 the TOC values are the highest for the Whitehill Formation (5.17 wt%), followed by the Collingham Formation (1.44 wt%) and then the Prince Albert Formation (0.81 wt%). The HI (2.41–15.56 mg HC/g TOC) and S2 (0.07–0.14 mg/g) values from TOC/Rock Eval data are low and this can be a result of the mineral-matrix effect. HI values become unreliable due to the high thermal maturity. To create the mineral-matrix effect, oil which is released from kerogen, becomes absorbed onto the surface of clay minerals, which reduces the S2 peak and consequently the HI values (e.g., Dembicki et al., 1983; Espitalié, 1984; Hunt, 1996). This effect is seen to be greatest in illite- and montmorillonite-rich shale (Hartwig, 2009). Previous research shows the Whitehill Formation to have the lowest HI values, which are probably due to a combination of low S2 values, high clay-mineral content, high sulfur content and the presence of solid bitumen (Geel et al., 2015, Schulz et al., 2018). In BH KWV-1, the TOC values also the highest for the Whitehill Formation (4.87 wt%), followed by the Collingham Formation (0.83 wt%) and the Prince Albert

Formation (0.81 wt%). The HI values are also low for the Whitehill Formation (2.57 mg HC/g TOC). However, the HI and OI values of the Prince Albert Formation (167 mg HC/g TOC; 225.25 mg CO_2/ g TOC) are high and more reliable for determining kerogen type from Van Krevelen Diagrams (Figure 2.42). Therefore, the organic matter in the Prince Albert Formation is mostly kerogen III and of terrestrial origin in BH KWV-1. In BH KZF-1, the average Tmax values for the lower Ecca Group range from 418.44 °C to 571.80 °C. In BH KWV-1, they range from 408.75 °C to 430.71 °C. Samples with low HI and high Tmax values are classified as over-mature. Although BH KWV-1 is intruded by dolerite and contains high-temperature minerals such as garnet, staurolite and cordierite, the Tmax values are lower than those estimated in BH KZF-1. High Tmax values typically should result in high PI values (i.e., > 1.0). However, these values are very low for both boreholes (PI KZF-1: 0.18–0.28; PI KWV-1: 0.19–0.34). This is due to the low hydrocarbon release seen from the low S1 and S2 peaks. Low S1 and S2 values are a result of expulsion and migration of hydrocarbons (Bordenave, 1993). The highest PI value (0.34) comes from the Whitehill Formation in BH KWV-1. Considering the high vitrinite/bitumen-reflectance values (>4 %) measured in the lower Ecca Group from both boreholes, Tmax values should be greater than 430 °C. However, the average Tmax values for the Prince Albert Formation in BH KZF-1 and the Whitehill and Prince Albert formations in BH KWV-1 are < 430 °C.

Mineralogy of the BH KZF-1 indicate that the strata matured into greenschist facies, whereas in BH KWV-1, P-T conditions are that of hornfels facies. In both boreholes, the post- Ecca temperatures significantly exceeded the temperatures required for the formation of thermogenic natural gas (>150 °C) (Hunt, 1996; Seewald, 2003). Although BH KWV-1 has the highest BR_o values and would have reached the highest temperatures, due to dolerite intrusion, the TOC/Rock Eval results are not that different from BH KZF-1 and even exhibits lower Tmax values and higher OI, HI and PI results.

2.9 Conclusion

2.9.1 Palaeo-environment

After the Early Permian deglaciation, the Tankwa Karoo Sub-basin was initially anoxic, with increasing temperature, pH and salinity allowing for the precipitation of greenalite and apatite. The bottom sediments of the Prince Albert Formation become increasingly oxygenated as cold water, near glacial peripheries sank. These oxygenated traction currents allowed for the persistence of biological activity indicated

by possible bioturbation structures. The water in the basin was highly alkaline with low sedimentation rates, which allowed for the extensive precipitation of rhodochrosite and manganese nodules (birnessite). If the birnessite nodules were formed syn-depositionally, it would indicate that the water depth of the lower Prince Albert Formation was up to 6500 m deep. However, post-depositional features are also observed, and water depth estimates must be made with caution. The upper Prince Albert Formation is dominated by clay- and silt-rich laminae and lesser tuffaceous laminae. Changes from the lower Prince Albert to upper Prince Albert Formation include increasing illite, albite, clinochlore and kaolinite content. In the eastern MKB the Prince Albert Formation is 30 m thick and thus ~130 m thinner than in the Tankwa Karoo Sub-basin. The deposition of the Prince Albert Formation in the eastern MKB, became oxygenated soon after deglaciation and was possibly subjected to marine incursion evident by phosphorites. Less carbonate minerals and the absence of Mn nodules may cautiously suggest that the eastern MKB was shallower and less alkaline with lower pCO_2. BH KWV-1 has high anorthite content and low albite content, which suggests that albitization implying over-pressurizing and compaction will hinder fluid flux and therefore diagenetic reactions. Further SEM analyses on unusual minerals such as greenalite, rhodochrosite and the high percentages of fluorapatite detected at the base of the Prince Albert Formation in BH KZF-1, are required for more robust palaeo-environmental interpretation.

The Whitehill Formation is 19.5 m thick in the Tankwa Karoo Sub-basin and 13 m thick in the eastern MKB. The Whitehill Formation in both boreholes has similar quartz (BH KZF-1 = 35.36 wt%; BH KWV-1 = 42.86) and illite (BH KZF-1 = 23.19 wt%; KWV-1 = 24.83 wt%) content. Both boreholes have phosphate nodules which suggests that marine conditions may have occurred during the deposition of the Whitehill Formation. Pyrrhotite (altered pyrite) content (8.20 wt%) in BH KWV-1 is higher than pyrite content in BH KZF-1 (2.22 wt%). This implies that sulfate reduction and anoxic settings were more prevalent in the eastern MKB than in the Tankwa Karoo Sub-basin, however organic matter perseveration was still high in both regions (average TOC ~ 5 wt%). The major difference between the two boreholes is the lack of carbonate minerals detected in BH KWV-1. In BH KZF-1 dolomite is usually concentrated in the lower half of the Whitehill Formation. The formation of dolomite is contentious. It is possible that it was formed by methanogenesis in a shallow sea with increased levels of pCO_2 by organic organisms in the water column, which can contribute to the precipitation of carbonates (Tourtelot, 1979; Curtis, 1978; Surdam et al., 1989). Another possibility is that it is formed on steep-slopes of continental

margins as mud-mounds that were originally calcite and altered to dolomite during mesogenesis (Saller, 1984; 1986). Last but not least, the dolomite in the lower half of the Whitehill Formation may have formed due to post-depositional diagenetic processes.

The depositional history of the Collingham Formation in both boreholes fluctuated between dysoxic, suboxic and oxic conditions as hyperpycnal density flows wax and waned. Major differences between the Collingham Formation in west and the east of the MKB is the diagenetic alteration of tuffaceous laminae. In the Tankwa Karoo Sub-basin the tuffs are diagenetically altered to ankerite, ferroan-dolomite, albite and calcite. Similar alteration is not detected in BH KWV-1. Kaolinite, montmorillonite and Ca-feldspars were identified in BH KWV-1, which implies that epigenetic reactions were limited possibly due to over-pressurization (Shaw & Primmer, 1989; Bjørlykke & Jahren, 2012). In BH KZF-1, the Collingham strata were not as over-pressured, allowing for fluid migration for diagenetic reactions to proceed.

2.9.2 The effect of diagenesis and metamorphism on reservoir properties

The source rock potential of the lower Ecca Group depends on the OM content, thermal maturity and porosity and permeability. The TOC content is high in the Whitehill Formation (4.87–5.17 wt%) and moderate for the Prince Albert (0.81 wt%) and Collingham formations (0.83–1.44 wt%) and the total porosity is highest in the Whitehill Formation (4.25–6.33 %; Nolte et al., 2019). In comparison, successful unconventional shales such as the Barnett and Marcellus shales have porosity of ~ 6% (Bruner & Smosna, 2011). Diagenetic mineral precipitation effects the overall porosity. Illite is the dominant clay mineral detected within the lower Ecca Group. Some illite may be detrital but considering the presence of mesogenetic minerals in the lower Ecca Group, it is likely that it mostly precipitated due to smectite-illite conversion. Common diagenetic minerals occurring in the lower Ecca Group are chlorite, calcite, siderite, ankerite and ferroan-dolomite. During early diagenesis the precipitation of illite between mineral grains was accompanied by syntaxial quartz overgrowths. Later increased compaction from burial diagenesis resulted in dissolution of minerals, mineral replacement and precipitation of quartz and carbonate cements. This greatly reduced interparticle porosity of the lower Ecca Group.

Intraparticle porosity in OM is the most common type of porosity preserved in the lower Ecca Group. As a result, the permeability is limited to the connectivity of the OM. In BH KZF-1 some interparticle porosity may be preserved in very-fine siltstone

laminae, whereas as no intergranular porosity is detected in BH KWV-1 due to dissolution and recrystallization of grain boundaries. Natural fractures, which occur most commonly in the Whitehill Formation, may act as a mechanism to trap free gas.

The Tankwa Karoo Sub-basin, as with the entire southern MKB, was highly influenced by the Cape Orogeny and burial diagenesis. This is evident by thrust faulting, diagenetic mineral formation, high vitrinite reflectance (~ 4 %; Nolte et al., 2017), high Tmax values (418.44 °C– 571.80 °C) and low HI (2.41-15.56 mg HC/g TOC) values. In addition to the tectonic impact from the Cape Orogeny, the eastern MKB is greatly influenced by the contact metamorphism due to the lower Jurassic dolerite intrusions. In BH KWV-1, there are 18 intruded dolerite intrusions, one of which intrudes into the top 13 cm of the Whitehill Formation. The lower Ecca Group in some sections can be described as a spotted hornfels and has metamorphic minerals such as cordierite, garnet (pyralspite), staurolite, biotite and chalcedony nodules. These minerals form under intermediate to high metamorphic conditions at temperatures between 500 and 600 °C (Winkler, 1980). The bitumen reflectance values were high for BH KWV-1 (4.7–5.6 %), but surprisingly, the Tmax values were lower (409 °C–334.14 °C) and HI values were higher (2.57–167 HC/g TOC) than those for BH KZF-1. Anorthite and clay minerals such as montmorillonite and kaolinite were detected in BH KWV-1. This suggests that sediments in BH KWV-1 was over-pressured enough to stop the diagenetic conversion.

Most of the OM in the lower Ecca Group has been identified as solid bitumen. The presence of solid bitumen indicates that thermal cracking of kerogen has taken place and the remaining preserved OM was converted to thermogenic gas (Tissot & Welte, 1984; Ungerer, 1990; Hunt, 1996). Hydrothermal events can either enhance the gas potential or destroy it. For kerogen to produce oil or gas (catagenesis) the temperature must reach a range from 50–150 °C, under pressure of 300 to 1500 bars (Tissot & Welte, 1984) over a period of 1–100 million years. Methane is thermodynamically stable even at 500–600 °C or more and can exist at great depths (6–8 km) beneath the Earth's crust (Bjørlykke, 2010). Trace amounts of methane was detected from the Whitehill Formation in the boreholes (de Kock et al., 2017). The low quantities of gas detected during drilling implies that gas has escaped from the formation, a likely consequence of tectonic thrust-faulting across the southern margin of the MKB and thermal degassing in dolerite-rich regions, like the area around BH KWV-1. For this study, the TOC content of the Whitehill Formation remains high in samples near dolerite sills, even where the rock has been altered to hornfels.

The Whitehill Formation is the most likely formation to produce exploitable gas, based on its high TOC content, porosity, thickness and depth. The thermal impact of variable dolerite intrusions make reservoir estimates difficult to predict. Gas was surely formed in the MKB, but the question of preservation is to be determined. The intrusion of dolerites in the Early Jurassic would have facilitated the early conversion of kerogen to oil and gas. However, dolerite intrusions may also be responsible for the degassing in regions with high dolerite densities. It has been repeatedly shown in this study and others that the hydrocarbon potential for the MKB will only truly be determined once regional “sweet spots” are identified, most probably in areas of low dolerite concentrations and vitrinite reflectance values below 3.5 % (e.g., Cole, 2014; Geel et al., 2015; Smithard et al., 2015; de Kock et al., 2017).

2.9.3 Future Studies

Comprehensive investigation of dolomite formation in the lower Whitehill Formation is required to better understand the palaeo-environmental conditions during deposition, especially via trace element and ^{18}O and ^{13}C isotopes studies of these rocks. The dolomite of the Whitehill Formation has the potential to be porous if fluid flow is possible for dissolution to occur. Porous dolomite could greatly improve physical properties of the lower Whitehill Formation as a hydrocarbon reservoir. Furthermore, research should be conducted on the illite-smectite conversion and TOC/Rock Eval measurements near the dolerite intrusions to determine the extent at which dolerite intrusions affected the progression eogenesis and the hydrocarbon potential of proximal mudstones.

2.10 References

Aarnes, I., Svensen, H., Polteau, S. & Planke, S. 2011. Contact metamorphism of shales in the Karoo Basin, South Africa, and the effect of multiple sill intrusions. *Chemical Geology*. 281: 181–194.

Adelmann, D. & Fiedler, K. 1996. Sedimentary development of the Upper Ecca and Lower Beaufort Groups (Karoo Supergroup) in the Laingsburg subbasin (SW Karoo Basin, Cape Province/South Africa). S*chriftenreihe der Deutschen Geologischen Gesellschaft*. 1: 88–89.

Almond, J.E. 2002. Giant arthropod trackway, Ecca Group. *Geobulletin*. 45: 28.

Andersson, P.O.D. & Worden, R.H. 2004. Mudstone of the Tanqua Basin, South Africa: an analysis of lateral and stratigraphic variations within mudstones, and

comparison of mudstones within and between turbidite fans. *Sedimentology*. 51 (3): 479–502.

Arning, E.T., Fu, Y., van Berk, W. & Schulz, H.-M. 2011. Organic carbon remineralization and solid-aqueous solution-gas interactions: Case study ODP Leg 204, Site 1246 (Hydrate Ridge). *Marine Chemistry*. 126: 120–131.

Baker, E. & Beaudoin, Y. 2013. *Deep Sea Minerals: Manganese Nodules. A physical, biological, environmental, and technical review. Vol. 1B*. Secretariat of the Pacific Community (SPC). 51p.

Bangert, B., Stollhofen, H., Lorenz, V. & Armstrong, R. 1999. The geochronology and significance of ash-fall tuffs in the glaciogenic Carboniferous-Permian Dwyka Group of Namibia and South Africa. *Journal of African Earth Sciences*. 29: 33–49.

Barbolini, N., Rubidge, B. & Bamford, M.K. 2018. A new approach to biostratigraphy in the Karoo retroarc foreland system: Utilising restricted-range palynomorphs and their first appearance datum for correlation. *Journal of African Earth Sciences*. 140: 114–133.

Bates, C. 1953. Rational theory of delta formation. *AAPG Bulletin*. 37：2119–2162.

Belica, M.E., Tohver, E., Poyatos-Moré, M., Flint, S., Parra-Avila, L.A., Lanci, L., Denyszyn, S. & Pisarevsky, S.A. 2017. Refining the chronostratigraphy of the Karoo Basin, South Africa: magnetostratigraphic constraints support an Early Permian age for the Ecca Group. *Geophysical Journal International*. 211(3): 1354–1374.

Bjørlykke, K., Aagaard, P., Dypvik, H., Hastings, D.S. & Harper, A.S. 1986. Diagenesis and reservoir properties of Jurassic sandstones from the Haltenbanken area, offshore mid-Norway: In *Habitat of hydrocarbons on the Norwegian continental shelf*. A.M. Spencer, E. Holter, C.J. Campell, S.H. Hanslien, P.H.H. Nelson, E. Nysæther & E.G. Ormaasen, Eds. London: Graham & Trotman. 275–386.

Bjørlykke, K. 2010. *Petroleum geoscience: from sedimentary environments to rock physics*. Berlin: Springer. 508p.

Bjørlykke, J. & Jahren, J. 2012. Open or closed geochemical systems during diagenesis in sedimentary basins: Constraints on mass transfer during diagenesis and the prediction of porosity in sandstone and carbonate reservoirs. *AAPG Bulletin*. 96 (12): 2193–2214.

Blewett, S.C.J. & Phillips, D. 2016. An overview of Cape Fold Belt geochronology: Implications for sediment provenance and the timing of orogenesis. In *Origin and*

evolution of the Cape Mountains and Karoo Basin: Geo-biohistory in a terrain with shale gas resources and need for conservation. B. Linol & M. de Wit, Eds. Regional Geology Reviews. 8643: 45–55.

Blewett, S.C.J., Phillips, D. & Matchan. E.L. 2019. Provenance of Cape Supergroup sediments and timing of Cape Fold Belt orogenesis: Constraints from high-precision $^{40}Ar/^{39}Ar$ dating of muscovite. *Gondwana Research*. 70: 201–221.

Blignaut, H.J. & Theron, J.N. 2015. The facies association tillite, boulder beds, boulder pavements, liquefaction structures and deformed drainage channels in the Permo-Carboniferous Dwyka Group, Elandsvlei area, South Africa. *South African Journal of Geology*. 118.2: 15–172.

Boggs, S. 2009. *Petrology of sedimentary rocks, 2nd edition*. USA: Cambridge University Press. 600p.

Boles, J. R. & Franks, S. G. 1979. Clay diagenesis in Wilcox sandstones of southwest Texas: Implications of smectite diagenesis on sandstone cementation. *Journal of Sedimentary Petrology*. 49: 55–70.

Bordenave, M. L. 1993. *Applied petroleum geochemistry*. Paris: Technip. 524p.

Bordy E. M., Abrahams M., Sharman G. R., Viglietti P. A., Benson R. B. J., McPhee B. W., Barrett P. M., Sciscio L., Condon D., Mundil R., Rademan Z., Jinnah Z., Clark J. M., Suarez C. A., Chapelle K. E. J. & Choiniere J. N. 2020. A chronostratigraphic framework for the upper Stormberg Group: implications for the Triassic-Jurassic boundary in southern Africa. *Earth-Science Reviews*. 203: 103120.

Boulesteix, K., Pyatos-Moré, M., Flint, S.S., Taylor, K.G., Hodgson, D.M. & Hasiotis, S.T. 2019. Transport and deposition of mud in deep-water environments: Processes and stratigraphic implications. *Sedimentology* (in press).

Bremner, J.M. & Rogers, J. 1990. Phosphorite deposits on the Namibian continental shelf. In *Phosphate Deposits of the World, vol. 3*. W.C. Burnett & S.R. Riggs, Eds. Cambridge, U. K: Cambridge University Press. 143–158.

Catuneanu, O., Hancox, P.J. & Rubidge, B.S. 1998. Reciprocal flexural behaviour and contrasting stratigraphies: a new basin development model for the Karoo retroarc foreland system, South Africa. *Basin Research*. 10: 417–439.

Catuneanu, O., Wopfner, H., Eriksson, P.G., Cairncross, B., Rubidge, B.S., Smith R.M.H. & Hancox P.J. 2005. The Karoo basins of south-central Africa. *Journal of African Earth Sciences*. 43: 211–253.

Chevallier, L. & Woodford, A. 1999. Morpho-tectonics and mechanism of emplacement of the dolerite rings and sills of the western Karoo, South Africa. *South African Journal of Geology*. 102: 43–54.

Chinner, G.A. 1962. Almandine in thermal aureoles. *Journal of petrology*. 3: 16–40.

Choquette, P.W. & Pray, L.C. 1970. Geologic nomenclature and classification of porosity in sedimentary carbonates. *American Association of Petroleum Geologists Bulletin*. 54(2): 207–250.

Chukwuma, K. & Bordy, E.M. 2016. Spatiotemporal sedimentary facies variations in the Lower Permian Whitehill Formation, Ecca Group, Karoo Basin. In *Origin and Evolution of the Cape Mountains and Karoo Basin*. B. Linol & M.J. de Wit, Eds. Regional Geology Reviews, Springer.101–110.

Chukwuma, K., Bordy, E.M. & Coetzer, A. 2018. Evolution of porosity and pore geometry on the Permian Whitehill Formation of South Africa- A FE-SEM image analysis study. *Marine and Petroleum Geology*. 91: 262–278.

Cole, D.I. & McLachlan, I.R. 1991. Oil potential of the Permian Whitehill Shale Formation in the main Karoo Basin, South Africa. In *Gondwana Seven Proceedings*. H. Ulbrich Rocha & A.C. Campos, Eds. Instituto de Geosciências, Universidad de Sau Paulo, Brazil. 379–390.

Cole, D.I. & Basson, W.A. 1991. Whitehill Formation. In *Catalogue of South African Lithostratigraphic Units*. M.R. Johnson, Ed. South African Committee for Stratigraphy, Pretoria. 3: 51–52.

Cole, D.I. 1992. Evolution and development of the Karoo Basin. In *Inversion Tectonics of the Cape Fold Belt, Karoo and Karoo and Cretaceous basins of Southern Africa*. M.J. de Wit & I.D.G. Ransome, Eds. Rotterdam: A.A. Balkema. 87–99.

Cole, D.I. 2005. Prince Albert Formation. *Geological Survey of South Africa: Catalogue of South Africa Lithostratigraphic Units*. 8: 33–36.

Cole, D.I. 2014. Geology of Karoo shale gas and how this can influence economic gas recovery. *Presentation, Gas – The Game Changer for Southern Africa?* Glen Hove, Johannesburg: Fossil Fuel Foundation, Abstracts, 11–12.

Compton, J. S. 1991. Origin and diagenesis of clay minerals in the Monterey Formation, Santa Maria Basin Area, California. *Clay and Clay minerals*. 39(5): 449–466.

Craddock, J.P., McKiernan, A.W., & de Wit, M.J. 2007. Calcite twin analysis in syntectonic calcite, Cape Fold Belt, South Africa: Implications for fold and cleavage formation within a shallow thrust front. *Journal of Structural Geology*. 29: 1100–1113.

Crerar, D. A. & Barnes, H. L. 1974. Deposition of deep-sea manganese nodules. *Geochim Cosmochim Acta.* 38: 279–300.

Curiale, J.A. 1986. Origin of solid bitumens, with emphasis on biological marker results. *Organic Geochemistry*. 10: 559–580.

Curtis, C. D. 1978. Possible links between sandstone diagenesis and depth-related geochemical reactions occurring in enclosing mudstones. *Journal of the Geological Society.* 135: 107–117.

Dar, S. A. 2013. *Geochemical and Mineralogical studies of Phosphorites and Associated rocks in parts of Lalitpur district, Uttar Pradesh, India*. Unpublished Ph.D. thesis. Aligarh Muslim University, Aligarh. 35–54

Dar, S.A., Khan, K.F. & Birch, W.D. 2017. Sedimentary: Phosphates. *Reference Model in Earth Systems and Environmental Sciences.* 1–18.

Day, M.O., Ramezani, J., Bowring, S.A., Sadler, P.M., Erwin, D.H., Abdala F., & Rubdige, B.S. 2015. When and how did the terrestrial mid-Permian mass extinction occur? Evidence from the tetrapod record of the Karoo Basin, South Africa. *Proceedings of the Royal Society B, Biological Sciences*. 282: 2015.0834.

De Beer, C.H. 1990. Simultaneous folding in the western and southern branches of the Cape Fold Belt*. South African Journal of Geology*. 93: 583–591.

de Kock, M.O., Beukes, N.J., Adeniyi, E.O., Cole, D., Götz, A.E., Geel., C. & Ossa, F-G. 2017. Deflating the shale gas potential of South Africa's Main Karoo basin. *South African Journal of Science*. 113(9/10).

De Segonzac, G.D. 1968. The birth and development of the concept of diagenesis (1866–1966). *Earth-Science Reviews*. 4: 153–201.

de Wit, M.J. & I.G.D. Ransome, 1992. Regional inversion tectonics along the southern margin of Gondwana. In *Inversion Tectonics of the Cape Fold Belt, Karoo and Cretaceous Basins of Southern Africa*. M.J. de Wit & I.G.D. Ransome, Eds. Netherlands: Balkema. 15–20.

Deer, W.A., Howie, R.A. & Zussman, J. 1966. *An Introduction to the Rock Forming Minerals*. London: Longmans, Green and Co. LTD. 528p.

Dembicki, H., Horsfield, D., Ho, T.T.Y. 1983. Source rock evaluation pyrolysis-gas chromatography. *AAPG Bulletin*. 67 (7): 1094 – 1103.

Duncan, R.A., Hooper, P.R., Rehacek, J., Marsh, J.S. & Duncan, A.R. 1997. The timing and duration of the Karoo igneous event, southern Gondwana. *Journal Geophysical Research*. 102: 18,127–18,138.

Ehrenberg, S.N. & Nadeau, P.H. 1989. Formation of diagenetic illite in sandstones of the Garn Formation, Haltenbanken Area, mid-Norwegian Continental Shelf. *Clay Minerals*. 24: 233–253.

Ehrenberg, S.N. 1990. Relationship between diagenesis and reservoir quality in sandstones of the Garn Formation, Haltenbanken, mid-Norwegian continental shelf. *AAPG Bulletin*. 74: 1538–1558.

Ehrlich, H. L. 1963. Bacteriology of manganese nodules: I. Bacterial action on manganese in nodule enrichments. *Applied Microbiology and Biotechnology.* 11: 15–19.

Eslinger, E.V. & Savin, S.M. 1973. Oxygen isotope geothermometry of the burial metamorphic rocks of the Precambrian Belt Supergroup, Glacier National Park, Montana. *Geological Society of America Bulletin*. 84: 2549–2560.

Espitalié, J. 1987. Use of Tmax as a maturation index for different types of organic matter. Comparison with vitrinite reflectance. In *Thermal Modelling in Sedimentary Basins.* J. Burrus, Ed. Houston, Texas: Gulf Publishing Company. 475–496.

Faure, K. & Cole, D. 1999. Geochemical evidence for lacustrine microbial blooms in the vast Permian Main Karoo, Paraná, Falkland Islands and Huab basins of southwestern Gondwana. *Palaeogeography, Palaeoclimatology, Palaeoecology*. 152: 189–213.

Ferry, J.M. 1981. Petrology of graphite sulfide-rich schists from south-central Maine: an example of desulfidation during prograde regional metamorphism. *American Mineralogist*. 66 (9–10): 908–930.

Fildani, A., Drinkwater, N.J., Weislogel, A., McHargue, T., Hodgson, D.M. & Flint, S.S. 2007. Age controls on the Tanqua and Laingsburg deep-water systems: new insights on the evolution and sedimentary fill of the Karoo basin, South Africa. *Journal of Sedimentary Research*. 77: 901–908.

Fildani, A., Weislogel, A., Drinkwater, N.J., McHargue, T., Tankard, A., Wooden, J., Hodgson, D. & Flint, S. 2009. U-Pb zircon ages from the southwestern Karoo Basin, South Africa-implications for the Permian-Triassic boundary. *Geology*. 37: 719–722.

Flügel, E. 2004. Microfacies of Carbonate Rocks. Analysis, Interpretation and Application. Berlin, Heidelberg, New York: Springer-Verlag. 976p.

Frimmel, H.E., Fölling, P.G. & Diamond, R. 2001. Metamorphism of the Permo-Triassic Cape Fold Belt and its basement, South Africa. *Mineralogy and Petrology*. 73 (4): 325–346.

Geel, C. 2014. *Shale gas characteristics of Permian black shales in the Ecca Group, near Jansenville, Eastern Cape, South Africa*. Unpublished M.Sc dissertation. Nelson Mandela Metropolitan University.164p.

Geel C., de Wit, M., Booth, P., Schulz, H-M. & Horsfield, B. 2015. Palaeo-environment, diagenesis and characteristics of Permian black shales in the lower Karoo Supergroup flanking the Cape Fold Belt near Jansenville, Eastern Cape, South Africa: Implications for the shale gas potential of the Karoo Basin. *South African Journal of Geology*.118(3): 249–274.

Goldstein, R.H. 2003. Petrographic analysis of fluid inclusions. In *Mineralogical Association of Canada. Short course series*, *vol. 32*. I. Samson, A. Anderson & D. Marshall, Eds. Mineralogical Association of Canada, Short Course Series.1–43.

Gulbrandsen, R. A. 1964. Physical and chemical factors in the formation of marine apatite. *Economic Geology*. 64: 365–382.

Hälbich, H. 1983. A tectogenesis of the Cape Fold Belt (CFB). *Special publication - Geological Society of South Africa.* 12: 165–175.

Hansma, J., Tohver, E., Jourdan F., Schrank, C. & Adams, D. 2015. The timing of the Cape Orogeny: New 40Ar/39Ar age constraints on deformation and cooling of the Cape Fold Belt, South Africa. *Gondwana Research*. 32: 122–137.

Hartwig, A. 2009. *Upper Carboniferous and Upper Permian black shales in northeast Germany: Investigations of sedimentary and organic material regarding their shale gas characteristics*. Diplomarbeit, Technische Universität Berlin. Institut für angewandte geowiseenschaften fachberiech explorations geologie. 135p.

Hesse, R. & Sacht, U. 2003. Early diagenesis of deep-sea sediments. In *Treatise on Geochemistry.* H.D. Holland & K.K. Turekian, Eds. 7–9: 289–308.

Hoffman, L. & Hower, J. 1979. Clay mineral assemblages as low grade metamorphic geothermometers: Application to the thrust faulted disturbed belt of Montana, U.S.A. In *Aspects of diagenesis*. P. A. Scholle & P. R. Schluger, Eds. SEPM Special Publication 1. 26: 55–79.

Hower, J., Eslinger, E. V., Hower, M. & Perry, E.A. 1976. The mechanism of burial metamorphism of argillaceous sediments: 1. Mineralogical and chemical evidence. *Geological Society of America Bulletin*. 87: 725–737.

Hunt, J. M. 1996. *Petroleum Geochemistry and Geology (2nd Edition)*. New York: W.H. Freeman. 743p.

Isbell, J.L., Cole, D.I. & Catuneanu, I. 2008. Carboniferous-Permian glaciation in the main Karoo Basin, South Africa: Stratigraphy, depositional controls, and glacial dynamics. In *Resolving the Late Paleozoic ice age in time and space*. C.R. Fielding, T.D. Frank. & J.L. Isbell, Eds. Geological Society of America Special Paper. 441:71–82.

Jacob, H. 1985. Classification, structure, genesis and practical importance of natural solid oil bitumen (migrabitumen). *International Journal of Coal Geology*. 11: 65–79.

Johnson, M.R., Van Vuuren, C.J., Visser, J.N.J., Cole, D.I., Wickens, H. deV., Christie, A.D.M., Roberts, D.L. & Brandl, G. 2006. Sedimentary rocks of the Karoo Supergroup. In *The Geology of South Africa.* M.R. Johnson, C.R., Anhaeusser & R.J. Thomas, Eds. Johannesburg: Geological Society of South Africa/Council for Geoscience. 461–499.

Johnson, M.R. 2009. Ecca Group. *SA Committee for Stratigraphy*. Pretoria: Council for Geoscience.10: 5–7.

Jourdan, F., Fe´raud, G., Bertrand, H., Kampunza, A.B., Tshoso, G., Watkeys, M.K. & Le Gall, B. 2005. Karoo large igneous province: brevity, origin, and relation to mass extinction questioned by new $^{40}Ar/^{39}Ar$ age data. *Geology*. 33: 745–748.

Kaminiski., M.A. 2014. The year 2010 classification of the agglutinated foraminifera. *Micropaleontology*. 60: 89–108.

Kaufman, E.G., Arthur, M.A., Howe, B. & Scholle P.A. 1996. Widespread venting of methane-rich fluids in Late Cretaceous (Campanian) submarine springs (Teepee Buttes), western interior seaway, U.S.A. *Geology*. 24: 799–802.

Kingsley, C.S. 1977. *Stratigraphy and sedimentology of the Ecca Group in the Eastern Cape Province, South Africa*. Unpublished Ph.D. thesis. University of Port Elizabeth. 286p.

Kingsley, C.S. 1981. A composite submarine fan-delta-fluvial model for the Ecca and Lower Beaufort Groups of Permian Age in the Eastern Cape Province. *South Africa. Transactions of the Geological Society of South Africa*. 84: 27–40.

Klaver, J., Desbois, G., Littke, R. & Urai, J.L. 2015. BIB-SEM characterization of pore space morphology and distribution in postmature to overmature samples from the Haynesville and Bossier Shales. *Marine and Petroleum Geology*. 59: 451–466.

Klein, C. 1983. Diagenesis and Metamorphism of Precambrian Banded Iron-Formations. *Developments in Precambrian Geology.* 6: 417–469.

Lanci, L., Tohver, E., Wilson, A. & Flint, S. 2013. Upper Permian magnetic stratigraphy of the lower Beaufort group, Karoo Basin. *Earth Planet Science Letters*. 375: 123–134.

Landis, C.R. & Castanõ, J.R. 1995. Maturation and bulk chemical properties of a suite of solid hydrocarbons. *Organic Geochemistry*. 22: 137–149.

Le Breton, E., Cobbold, P.R. & Zanella, A. 2013. Cenozoic reactivation of the Great Glen Fault, Scotland: additional evidence and possible causes. *Journal of the Geological Society*. 170 (3): 403–415.

Lindeque, A., Ryberg, T., Stankiewicz, J., Weber, M. & de Wit, M. 2007. Deep crustal reflection experiment across the southern Karoo Basin, South Africa. *South African Journal of Geology*. 110: 419–438.

Lindeque, A.S., de Wit, M.J., Ryberg, T., Weber, M. & Chevallier, L. 2011. Deep crustal profile across the southern Karoo Basin and Beattie Magnetic Anomaly, South Africa: An integrated interpretation with tectonic implications. *South African Journal of Geology*. 114: 265–292.

Macquaker, J.H.S., Taylor, K. G., Keller, M. & Polya, D. 2014. Compositional controls on early diagenetic pathways in fine-grained sedimentary rocks: Implications for predicting unconventional reservoir attributes of mudstones. *AAPG Bulletin*. 98(3): 587–603.

Maynard, J.B. 2003. Manganiferous sediments, rocks, ores. In *Treatise on Geochemistry*. F.T. Mackenzie, Ed. Elsevier. 289–308.

McLachlan, I.R. & Anderson, A. 1973. A review for the evidence of marine conditions in Southern Africa during Dwyka times. *Palaeontologia africanan*. 15: 37–64.

McLachlan, I.R. & Anderson, A. 1977. Carbonates, 'stromatolites' and tuffs in the lower Permian White Band Formation. *South African Journal of Science.* 73: 2–94.

Mikhalevich, V. I. & Kaminski, M. A. 2008. Revised systematics of the Schlumbergerinida (Phylum Foraminifera). In *Proceedings of the Seventh International Work-shop on Agglutinated Foraminifera. Grzybowski Foundation Special Publication, 13*. M. A. Kaminski & R. Coccioni, Eds. 157–166.

Milani, E.J. & de Wit, M.J. 2008. Correlations between the classic Paraná and Cape-Karoo sequences of South America and southern Africa and their basin infills flanking the Gondwanides: Du Toit revisited. In *West Gondwana: Pre-Cenozoic correlations across the South Atlantic –the ties that bind*. R.J. Pankhurst, R.A.J. Trouw, B. Brito Neves & M.J. de Wit, Eds. London: The Geological Society, Special Publication. 319–342.

Milliken, K. L., Rudnicki, M., Awwiller, D.N. & Zhang, T. 2013. Organic matter-hosted pore system, Marcellus Formation (Devonian), Pennsylvania. *AAPG Bulletin*. 97(2): 177–200.

Moore, C.H. 1989. *Carbonate diagenesis and porosity. Developments in sedimentology, vol 46*. Amsterdam: Elsevier. 337p.

Moore, C.H. & Wade, W.J. 2013a. Chapter 5- Carbonate diagenesis: Introduction and tools. In *Developments in Sedimentology*. C.H. Moore & W.J. Wade, Eds. 67: 67–89.

Moore, C.H. & Wade, W.J. 2013b. Chapter 6- Marine diagenetic environment. In *Developments in Sedimentology*. C.H. Moore & W.J. Wade, Eds. Elsevier. 67: 93–131.

Mu, N., Fu, Y., Schulz, H-M. & van Berk, W. 2016. Authigenic albite formation due to water-rock interactions- Case study: Magnus Oilfield (UK, Northern North Sea). *Sedimentary Geology*. 33: 30–41.

Navarrete, C., Gianna, G., Encinas, A., Márquez, M., Kamerbeek., Y., Valle, M. & Folguera, A. 2019. Triassic to Middle Jurassic geodynamic evolution of southwestern Gondwana: From a large flat-slab to mantle plume suction in a rollback subduction setting. *Earth-Science Reviews.* 194: 12–159.

Neumann, E-R., Svensen, H., Galerne, C.Y. & Planke, S. 2011. Multistage evolution of dolerites in the Karoo Large Igneous Province, Central South Africa. *Journal of Petrology*. 52: 959–984.

Nolte, S., Geel, C., Amann-Hildenbrand, A., Krooss, M.B., Littke. & R., 2019. Petrophysical and geochemical characterization of potential unconventional gas shale reservoirs in the southern Karoo Basin, South Africa. *International Journal of Coal Geology*. 212: 103249.

Nuñez-Betelu, L. & Baceta, J.L. 1994. Basics and application of Rock-Eval/TOC pyrolysis: an example from the uppermost Paleocene/lowermost Eocene in the Basque Basin, western Pyrenees. *Munibe (Ciencias Naturales - Natur Zientziak)*.46: 43–62.

Oelofsen, B.W. 1986. A fossil shark neurocranium from the Permo-Carboniferous (lowermost Ecca Formation) of South Africa. In *Proceedings of the 2nd International Conference of Indo-Pacific Fishes*. T. Uyeno, R. Arai, T. Tanuichi, K. Matsuura, Eds. Tokyo: Icthyological Society of Japan. 107–124.

Oelofsen, B.W. 1987. The biostratigraphy and fossils of the Whitehill and Irati Shale Formations of the Karoo and Paraná Basins. Department of Zoology, University of Stellenbosch, RSA. In *Gondwana six: stratigraphy, sedimentology, and paleontology, USA*. G.D McKenzie, Eds. AGU geophysical Monograph Board. 131–138.

Pettijohn, F.J., Potter, P.E. & Siever, R., 1987. *Sand and sandstone- Second Edition.* New York: Springer-Verlag. 553p.

Pownall, J.M., Waters, D.J., Searle, M.P., Shail, R.K. & Robb, L.J. 2012. Shallow laccolithic emplacement of the Land's End and Tregonning granites, Cornwall, UK: Evidence from aureole field relations and P-T modelling of cordierite-anthophyllite hornfels. *Geosphere*. 8(6): 1467–1504.

Rintoul, S.R. 2009. Antarctic circumpolar current. In *Encyclopedia of Ocean Sciences, 2nd edition.* J.H. Steele, Ed. Academic Press. 178–190.

Rintoul, S.R. & Garabato, A.C.G. 2013. Dynamics of the Southern Ocean Circulation. *International Geophysics.* 103: 471–492.

Rowsell, D.M. & De Swart, A.M.J.1976. Diagenesis in Cape and Karroo sediments, South Africa, and its bearing on their hydrocarbon potential. *Transactions of the Geology Society of South Africa*. 79: 81–145.

Rubidge, B.S. 2005. Re-uniting lost continents -Fossil reptiles from the ancient Karoo and their wanderlust. *South African Journal Geology*. 108: 135–172.

Rubidge, B.S., Erwin, D.H., Ramezani, J., Bowring, S.A. & de Klerk, W.J. 2013. High-precision temporal calibration of late Permian vertebrate biostratigraphy: U-Pb constraints from the Karoo Supergroup, South Africa*. Geology*. 41: 363–366.

Saller, A.H. 1984. *Diagenesis of Cenozoic Limestones on Enewetak Atoll.* Unpublished Ph.D. thesis. Louisiana State University, Baton Rouge, Louisiana. 363 pp.

Saller, A.H. 1986. Radiaxial calcite in lower Miocene strata, subsurface Enewetak atoll. *Journal of Sedimentary Petrology*. 56: 743–762.

Scheiber-Enslin, S.E., Ebbing, J. & Webb, S.J. 2015. New depth maps of the main Karoo Basin, used to explore the Cape isostatic anomaly. *South African Journal of Geology*. 118 (3): 225–248.

Schieber, J., Southard, J.B. & Schimmelmann, A. 2010. Lenticular shale fabrics resulting from intermittent erosion of water-rich muds - interpreting the rock record in the light of recent flume experiments. *Journal of Sedimentary Research*. 80: 119–128.

Schulz., H-M., Linol, B., de Wit, M., Schuck, B., Schaepan, I. & Wirth, R. 2018. Early diagenetic signals archived in black shales of the Dwyka and Lower Ecca Groups of the southern Karoo Basin (South Africa): Keys to the deglaciation history of Gondwana during the Early Permian, and its effect on potential shale gas storage. *South African Journal of Geology*. 121 (1): 69–94.

Seewald, J.S. 2003. Organic-inorganic interactions in petroleum producing basins. *Nature*. 426: 327–333.

Selley, R.C. 2000. *Applied sedimentology, 2nd ed.* USA: Academic Press. 523p.

Shaw, H.F. & Primmer, T.J. 1989. Diagenesis in shales from partly overpressured sequence in the Gulf Coast, Texas, USA. *Marine and Petroleum Geology*. 6: 121–128.

Sihra, K. 2010. *Integrating vitrinite reflectance, Rock-Eval pyrolysis, fluorescence microscopy, and palynology of the Athabasca oil sands, Kearl Lake area, northeastern Alberta*. MSc Dissertation. Faculty of Mathematics and Science, Brock University St. Catharines, Ontario. 159p.

Smith, R.M.H. 1990. A review of the stratigraphy and sedimentary environments of the Karoo Basin. *South Africa. Journal of African Earth Sciences*. 10: 117–137.

Smith, R.M.H, Eriksson, P.G. & Botha, W.J. 1993. A review of the stratigraphy and sedimentary environments of the Karoo-aged basins of Southern Africa. *Journal of African Earth Sciences*. 16: 143–169.

Smithard, T., Bordy, E.M. & Reid, D.L. 2015. The effect of dolerite intrusions on the hydrocarbon potential of the lower Permian Whitehill Formation (Karoo Supergroup) in South Africa and southern Namibia: A preliminary study. *South African Journal of Geology*. 118(4): 489–510.

Surdam, R.C., Crossey, L.J., Hagen, E.S. & Heasler, H.P. 1989. Organic-inorganic interactions and sandstone diagenesis. *American Association of Petroleum Geologists Bulletin*. 73:1–23.

Tankard, A., Welsink, H., Aukes, P., Newton, R. & Stattker, E. 2012. Geodynamic interpretation of the Cape and Karoo basins, South Africa. In *Phanerozoic Passive Margins, Cratonic Basins and Global Tectonics Maps*. D.G. Roberts, Ed. USA & UK: Elsevier. 869–932.

Tinker, J., de Wit, M. & Brown, R. 2008. Mesosoic exhumation of the southern Cape, South Africa, quantified using apatite fission track thermochronology. *Tectonophyiscs*. 455: 77–93.

Tissot, B. P. & Welte, D. H. 1984. *Petroleum Formation and Occurrence*. New York: Springer. 540p.

Toplis, M.J. & Carroll, M.R. 1995. An experimental study of the influence of oxygen fugacity on Fe–Ti oxide stability, phase relations, and mineral–melt equilibria in ferro-basaltic systems. *Journal of Petroleum Science and Engineering*. 36 (5): 1137–1170.

Tosca, N.J., Guggenheim, S. & Pufahl, P.K. 2015. An authigenic origin for the Precambrian greenalite: Implications for the iron formation and the chemistry of ancient seawater. *Geological Society of America Bulletin*. 128 (3–4): 511–530.

Tourtelot, H.A. 1979. Black Shale- Its Deposition and Diagenesis 1. *Clays and Clay Minerals*. 27(5): 313–321.

Tucker, M.E. 1981. *Sedimentary Petrology: An Introduction*. UK: Blackwell Scientific Publications. 252p.

Tucker, M.E. 1988. *Techniques in Sedimentology*. UK: Blackwell Scientific Publications. 394p.

Tucker, M.E. 2001. *Sedimentary Petrology: An Introduction to the Origin of Sedimentary Rocks*. UK: Blackwell, Scientific Publication. 272p.

Turner, B.R. 1999. Tectonostratigraphical development of the Upper Karoo foreland basin: orogenic unloading versus thermally-induced uplift. *Journal of African Earth Sciences*. 28: 215–238.

Ungerer, P. 1990. State of the art research in kinetic modeling of oil formation and expulsion. *Organic Geochemistry*. 16:1–25.

Veeh, H.H., Burnett, W.C & Soutar, A. 1973. Contemporary phosphorite on the continental margin of Peru. *Science*. 181: 844–845.

Viljoen, J.H.A. 1990. K-bentonites in the Ecca Group of the southern and central Karoo Basin. Abstracts Geocongress '90. *Geological Society of South Africa*. 576–579.

Viljoen, J.H.A. 1992. Lithostratigraphy of the Collingham Formation (Ecca Group), including the Zoute Kloof, Buffels River and Wilgehout River Members and the Matjiesfontein Chert bed. *Lithostratigraphic Series, South African Committee for Stratigraphy, Council for Geoscience*. 22: 1–10.

Viljoen, J.H.A. 1994. Sedimentology of the Collingham Formation, Karoo Supergroup. *South African Journal of Geology*. 97: 167–183.

Visser, J.N.J. & Loock, J.C. 1978. Water depth in the main Karoo Basin in South Africa during Permian sedimentation. *Transactions of The Geological Society of South Africa.* 81: 185–191.

Visser, J.N.J. 1987. The influence of topography on the Permo-Carboniferous glaciation in the Karoo basin and adjoining areas, Southern Africa. In *Gondwana six: stratigraphy, sedimentology and paleontology, vol 41.* D.H. Elliot, J.W. Collison, G.D. McKenzie & S.M. Haban, Eds. American Geophysical Union. 123–129.

Visser, J.N.J. 1992. Deposition of the Early to Late Permian Whitehill Formation during a sea-level highstand in a juvenile foreland basin. *South African Journal of Geology.* 181–193.

Visser, J.N.J. 1993. Sea-level changes in a back-arc–foreland transition: The Late Carboniferous–Permian Karoo Basin of South Africa. *Sedimentary Geology*. 83: 115–131.

Visser, J.N.J. 1994. A Permian argillaceous syn- to post-glacial foreland sequence in the Karoo Basin, South Africa. In *Earth's Gacial Record: International Geological Correlation Project 260.* M. Deynoux, J.M.G. Miller, E.W. Domack, N. Eyles, I.J. Fairchild & G.M. Young, Eds. Cambridge: Cambridge University Press. 193–203.

Visser, J. N. J. 1997. Deglaciation sequences in the Permo-Carboniferous Karoo and Kalahari basins of southern Africa: a tool in the analysis of cyclic glaciomarine basin fills. *Sedimentology.* 44 (3): 507–521.

Von Engelhardt, W. 1960. *Der Porenraum der Sedimente*. Berlin: Springer. 207p.

Walderhaug, O. 1994. Temperatures of quartz cementation in Jurassic sandstones from the Norwegian shelf: evidence from fluid inclusions. *Journal of Sedimentary Research*. 64: 311–323.

Weaver, C.E. 1990. Diagenesis- metamorphism in clays, muds, shales. *Developments in Sedimentology*. 44: 417–524.

Werner, M. 2006. *The stratigraphy, sedimentology and age of the Late Palaeozoic Mesosaurus Inland Sea, SW-Gondwana: new implications from studies on sediments and altered pyroclastic layers of the Dwyka and Ecca Group (lower Karoo Supergroup) in southern Namibia*. Unpublished Ph.D. thesis, University of Würzburg, Germany. 428p.

Wickens, H. de V. 1994. *Basin floor fan building turbidites of southwestern Karoo Basin, Permian Ecca Group, South Africa*. Ph.D Thesis. University of Port Elizabeth. 223p.

Wickens, H. de V. & Cole, D.I. 2017a. Lithostratigraphy of the Skoorsteenberg Formation (Ecca Group, Karoo Supergroup), South Africa. *South African Journal of Geology*. 120 (3): 433–446.

Wickens, H. de V. & Cole, D.I. 2017b. Lithostratigraphy of the Kookfontein Formation (Ecca Group, Karoo Supergroup), South Africa. *South African Journal of Geology*. 120 (3): 447–458.

Winkler, H.C.R., Zhang, Qi, Zhou, Yunsheng, Translated by, 1980. *Origin of metamorphic rock*. Science Press, Beijing.

Worden, R.H & Burley, S.D. 2003. Sandstone diagenesis: The evolution of sand to stone. In *Sandstone diagenesis: Recent and ancient.* S.D. Burley & R.H. Worden, Eds. Blackwell Publishing. 3–44.

Zavala, C. & Shuxin, P. 2018. Hyperpycnal flows and hyperpycnites: Origin and distinctive characteristics. *Lithologic Reservoirs*. 30 (1): 1–27.

3 Palaeo-environmental reconstruction of the lower Ecca Group mudstones from the western and eastern Karoo Basin, South Africa

Abstract

The palaeo-environmental reconstruction of the lower Ecca Group of the main Karoo Basin (MKB) has been long debated due to conflicting results with respect to levels of basin anoxia and salinity. This study uses major oxide and trace element geochemistry, mineral compositions and sedimentary structures, to further refine the palaeo-environmental conditions under which the argillaceous sedimentary rocks of Prince Albert, Whitehill and Collingham formations were deposited. Two boreholes, BH KZF-1 in the western MKB (Tankwa Karoo Sub-basin) and BH KWV-1 in the eastern MKB, are compared. The results show that the Chemical Index of Alteration (CIA) is highest for the Prince Albert Formation (72–78), as the environment changed from an ice-house to green-house setting, and decreases into the Collingham Formation (64–66) as conditions became more arid. Trace element enrichment in BH KZF-1 are in the order of Mn > Ba > Zn > Co > Cu > V > Rb > Cr > Ni and BH KWV-1 in the order of Mo > Ba > Cu > Zn > Mn > V > Co > Cr > Rb > Ni. Geochemical comparison between V/Cr, V(V+Ni) and Ni/Co values and Fe-S-TOC ternary plots were used to determine the redox conditions. The results show fluctuations between anoxic and oxic conditions during deposition. Furthermore, there is evidence, albeit somewhat equivocal, for changing salinity levels, low sedimentation-rates and high bio-productivity. The Tankwa Karoo Sub-basin (western MKB; BH KZF-1), was probably proximal to an inlet to the Early Permian oceans and as a result the Prince Albert and Whitehill formations in this part of the basin have the greatest compositional variability hosting greenalite (a common mineral in banded-iron formations), Mn-nodules (birnessite), and carbonate nodules rich in rhodochrosite and dolomite. Higher concentrations of S, Mo and pyrrhotite in the Whitehill Formation in the eastern MKB (BH KWV-1) suggest dysoxic to anoxic depositional conditions. It is probable that repeated marine incursions were still occurring during the deposition of the Collingham Formation in the Tankwa Karoo Sub-basin, whereas marine influence only prevailed until the end of the Whitehill depositional phase in the eastern MKB. The extent of anoxia was variable across the MKB and would have fluctuated depending on levels of primary-productivity, sedimentation rates, distance from the connection to the Early Permian oceans and basin floor morphology (bottom water ventilation). Therefore, it is inaccurate to assume that the mudstone of the lower Ecca

Group, especially the Whitehill Formation, were deposited under predominantly anoxic conditions uniformly across the MKB.

3.1 Introduction

The geochemical composition of sedimentary rocks can archive important clues to the palaeo-environmental conditions that prevailed during the time of deposition. Sedimentary detritus delivered into a basin will undergo biogeochemical cycling, which can fractionate elements between solid and solution phases. This fractionation process can continue during the post-depositional processes, e.g., during diagenesis or metamorphism (Calvert & Pedersen, 1992). Major and trace element compositions can be used as proxies for the syn- and post-depositional processes of black shales and the optimal conditions for OM preservation. The latter is typically a combination of reducing conditions, sediment starvation, high primary bio-productivity and protection from OM decay by clay mineral coating (e.g., Pedersen & Calvert, 1990; Tyson & Pearson, 1991; Calvert & Pedersen, 1992; Arthur & Sageman, 1994; Macquaker & Gawthorpe, 1993; Schieber, 1999; Murphy et al., 2000; Sageman et al., 2003). Black shale formation is best understood in a holistic approach that combines evidence from compositional, sedimentological, palaeo-ecological and geochemical datasets (Schieber, 2001).

The main Karoo Basin (MKB; Figure 3.1) hosts Early Permian OM-rich mudstones and shales. Once an extensive inland “sea”, the MKB was formed after the transition from an ice-house to a green-house climate during the Permo-Carboniferous. During the Carboniferous until the Earliest Permian, over a period of ~ 90 Myr, southern Gondwana was covered by giant (up to 70 million km^2) ice sheets, the intermittent melting of which resulted in the deposition of the Dwyka Group tillites and other glacigenic rocks (e.g., Crowell, 1978; Visser, 1993; Isbell et al., 2008).

During the initial depositional period in the MKB, there were repeated deglaciation periods that provided an influx of fine-grained sediments into the MKB (e.g. Crowel, 1978; Veevers & Powell, 1987; Scheffler, 2004). Compressional tectonics and ensuing deformation along the southern margin of Gondwana resulted in flexural subsidence and the development of an extensive inland “sea”, fed by large volumes of meltwater from all directions (except from SW-SSW) into the basin, but mostly from the north (e.g., Smith et al., 1993; Visser et al., 1997; Catuneanu et al., 1998, 2005; Isbell et al., 2008; Chukwuma & Bordy, 2016).

The transition from glacial to non-glacial conditions in the MKB during the Early Permian is captured by the post-glacial sedimentary rocks in the lower Ecca Group,

which is the focus of this study. The lower Ecca Group is the collective term referring to the Prince Albert, Whitehill and Collingham formations, which are dominated to variable degrees by organic matter-rich mudstones. The Whitehill Formation has the highest total organic carbon (TOC) content, as it contains up to 17 wt% organic carbon (Rowsell & De Swart, 1976; Cole & McLachlan, 1991; Cole, 2014; Chukwuma & Bordy, 2016) and has recently become a target for potential shale gas exploration. The Karoo inland "sea" is variously referred to as the "Whitehill- Irati Sea" or "Ecca Inland Sea" and is thought to have been connected to the Paraná Basin in South America (Oelofsen, 1981, 1986, 1987; Oelofsen & Araujo, 1983; Werner, 2006). Research results from the lower Ecca Group are contentious regarding the water depths (e.g., Oelofsen 1981; Cole & McLachlan, 1991) and salinity levels in this Early Permian basin (e.g., Faure & Cole, 1999 vs Scheffler et al., 2006). Moreover, it is not yet clear whether the sediments were deposited under fully or partially marine (brackish) conditions, and the degree to which the MKB was connected to global oceans at the time (e.g., McLachlan & Anderson, 1973; Anderson & McLachlan, 1979; Oelofsen, 1986; Veevers et al., 1994; Pickford, 1995; Faure & Cole, 1999; Werner, 2006, Scheffler et al., 2006; Herbert & Compton, 2007; Flint et al., 2011; Geel et al., 2015; Chukwuma & Bordy, 2016; Chukwuma, 2017; Götz et al., 2017; Chukwuma et al., 2018; Cole & Barbolini, 2019).

There are two theories concerning the deposition of the Whitehill Formation: 1) the ocean link theory (Oelofsen, 1987), and 2) the highland barrier theory (Araujo, 1976; Anderson & McLachlan, 1979). Both *Mesosaurus temuidens* and *Stereosermum tumidum* (swimming reptile species) and various crustacean species are recorded in South Africa and South America (McLachlan & Anderson, 1973; Anderson & McLachlan, 1979; Almond, 2008). Martin & Wilczewski (1970) suggest that marine inundation in the MKB occurred during late stages of Dwyka Group deposition and by the time the Whitehill Formation was deposited, the basin was no longer connected to the ocean. It is further suggested that the Cape Orogeny probably eliminated the ocean connection, cutting off inflow of saline water and restricting circulation, creating stratified anoxic conditions, which allowed for the preservation of the TOC-rich shale of the Whitehill Formation (e.g., Visser, 1992; Veevers et al., 1994; Faure & Cole, 1999). Fossils found in the Whitehill Formation do not account for fully marine conditions, and this includes the notocarid crustaceans, which are bottom-living, shrimp-like arthropods (McLachlan & Anderson, 1973, Anderson & McLachlan, 1979; Faure & Cole 1999; Almond et al., 2008; Chukwuma & Bordy, 2016; Almond personal

com. 2020). Therefore, determining the cut off time and extent of the final marine incursion into the “Ecca Inland Sea” is difficult.

In an attempt to further elucidate on these contested environmental conditions, this study expands on the timing and regional extent of the marine incursions, fluctuating salinity levels and degrees of anoxia of the lower Ecca Group. Using geochemical and other proxies, extracted from two Karoo boreholes drilled in 2015 (Figures 3.1 & 3.2), this study aims to decipher the palaeo-environments and climate during post-glacial sedimentation of the lower Ecca Group. Specifically, the following questions are addressed herein:

1) does the mudstone geochemistry change significantly from west to east within the basin?

2) were these sediments deposited under marine or brackish conditions?

3) what was the level of oxygenation during the Whitehill depositional period? and

4) what environmental conditions allowed for OM preservation in the lower Ecca Group?

3.2 Geological history

The MKB is one of the major depocentres that formed in the Late Palaeozoic in southern Gondwana. The MKB (Figure 3.1 A) contains a sedimentary record (i.e., the Karoo Supergroup) that began with the formation of the glacial Dwyka Group in the Late Carboniferous (~ 350 to 340 Ma) and terminated with the outpouring of the Drakensberg Group basalts in the Early Jurassic (~ 183 ± 1 Ma; Duncan et al., 1997; Isbell et al., 2008; Milani & de Wit; 2008). The Karoo Supergroup is deposited on Early Palaeozoic basement rocks of the Cape Supergroup and consists of the Dwyka, Ecca, Beaufort, Stormberg and Drakensburg groups (Visser, 1989; Visser, 1994; Smith et al., 1993; Johnson et al., 2006). Here, we focus on the post-glacial sedimentary rocks in the lower Ecca Group, which include the Prince Albert, Whitehill and Collingham formations (Figure 3.1 B). The argillaceous rocks of the lower Ecca Group have a basin-wide distribution in the southern MKB, along E-W trending zones, just north of the Cape Fold Belt, with their surface distribution confined to the margins of the MKB (Figure 3.1; Cole & Basson, 1991; Viljoen, 1992; Smith et al., 1993; Cole, 2005; Johnson et al., 2009).

During the Late Proterozoic glaciation of Gondwana, the supercontinent rotated clockwise through the polar regions resulting in different phases of glaciation and deglaciation (Crowell, 1978; Veevers & Powell, 1987; Isbell et al., 2008). The final

phase of deglaciation occurred in South Africa between 297 Ma to 290 Ma (Bangert et al., 1999) resulting in sea level rise within the early foreland basin system in southern Gondwana (e.g., Isbell et al., 2008). The oldest orogenic event, recorded at 292 ± 5 Ma (Hälbich et al.,1983), corresponds with the last stage of deglaciation, and therefore may have triggered shelf subsidence and final collapse of the ice-sheets (Visser, 1991). The MKB, at the time, was located between palaeolatitudes 50° and 70 °S; therefore, it was postulated that the climate was cold to temperate when the lower Ecca Group was deposited (Visser, 1982; Visser & Young, 1990; Smith et al., 1993). The Chemical Index of Alteration (CIA) has been recorded to increase rapidly from the Dwyka Group into the lower Ecca Group further corroborating a rather rapid amelioration during this interval (e.g., Visser & Young, 1990; Scheffler et al., 2006).

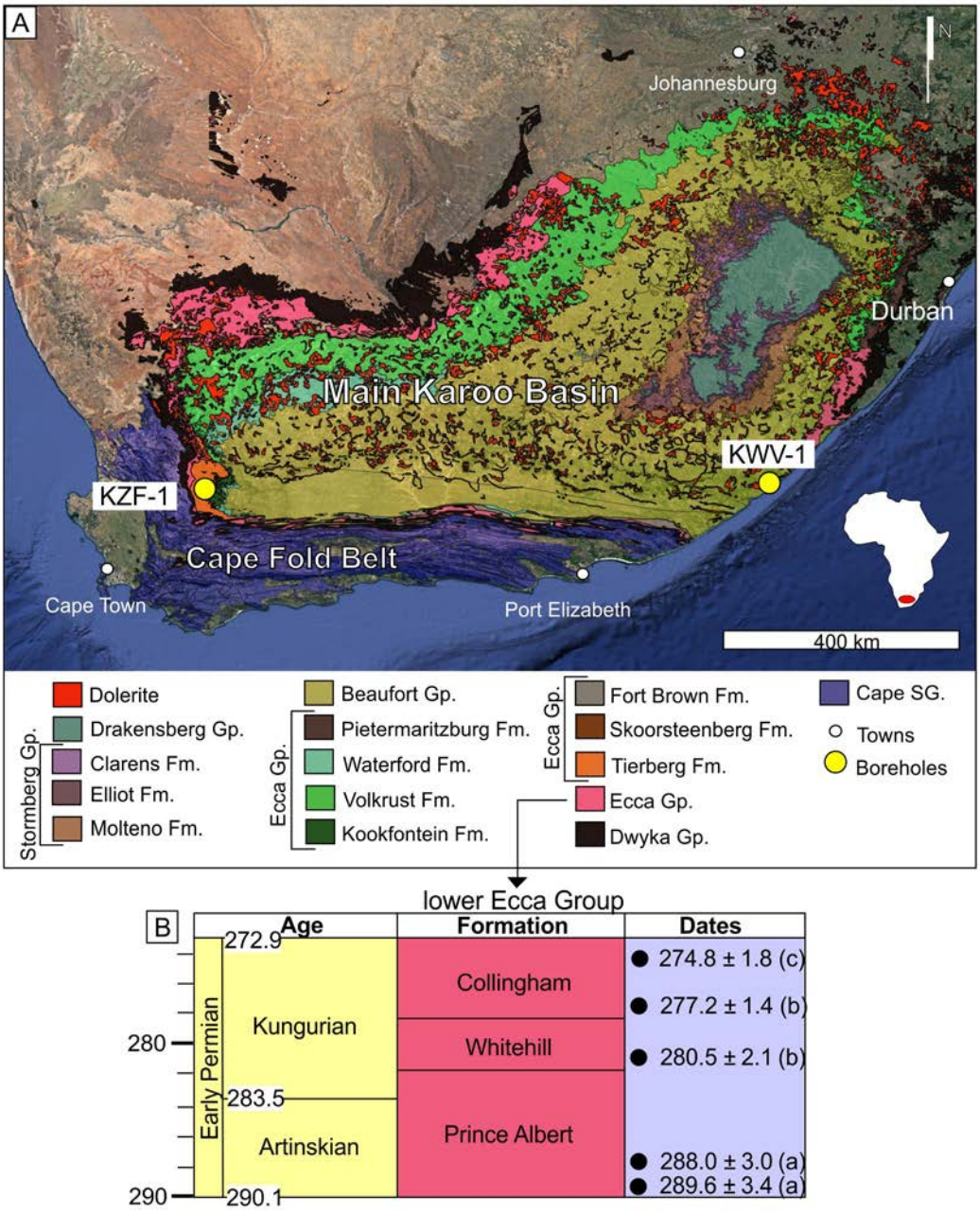

Figure 3.1: A) Simplified geological map of South Africa showing the surface exposures of Karoo Supergroup of the main Karoo Basin (MKB). The MKB is bounded by the Cape Supergroup of the Cape Fold Belt to the southwest and the south. BH KZF-1 is located in the Tankwa Karoo Sub-basin and BH KWV-1 in the eastern MKB. B) The chronostratigraphy of the Early Permian Ecca Group (Karoo Supergroup) in the southern main Karoo Basin and Namibia (modified after Rubidge, 2005 and Smithard et al., 2015). Radiometric dates are marked with black circles, shown in million years and taken from a: Bangert et al. (1999); b: Werner (2006); c: Fildani et al. (2007). Geological time scale based on 2013 ICS Time Chart.

3.2.1 Lithostratigraphy and palaeo-environment of the lower Ecca Group

3.2.1.1 Prince Albert Formation

The Prince Albert Formation is comprised of the oldest post-glacial sedimentary rocks, which depending on location, forms a sharp or gradational contact with the underlying Dwyka Group diamictites (Visser & Young, 1990; Visser, 2003). Dropstones can be detected in the Prince Albert Formation indicating that deglaciation was not protracted (Visser, 1994; Wickens, 1994; Visser, 2003; Cole, 2005; Geel et al., 2015). The Prince Albert Formation comprises mostly mudstone and silty rhythmite with carbonate and phosphatic lenses (Smith et al., 1990; Visser, 1994; Cole, 2005). The early MKB was interpreted by some authors to be marine (e.g., Oelofsen, 1986; Visser, 1993, 1994; Scheffler et al., 2006; Geel et al., 2015; Götz et al., 2017) and others as fresh-water to brackish (e.g., Cole & McLachlan, 1991; Veevers et al., 1994; Faure & Cole, 1999; Herbert & Compton, 2007). Fossils such as shark remains, sponge spicules, foraminifera, acritarch's, radiolaria, cephalopods, lamellibranch (bivalves), brachiopods, paleoniscoid fish, coprolites and fossil wood have been identified in the Prince Albert Formation (e.g., Strydom, 1950; McLachlan & Anderson, 1973; Oelofsen, 1986).

Elemental ratios of Rb/K are used as a proxy for palaeo-salinity as Rb^+ concentrations tend to be higher in marine water (0.12 ppm) than in fresh water (0.0013 ppm; Taylor & McLennan, 1985). Rb/K values from the Prince Albert Formation are high (≤ $6 * 10^{-3}$), and thus suggest dominantly marine conditions (Visser & Young, 1990; Scheffler et al., 2006; Geel et al., 2015). Furthermore, stable isotope data ($\delta^{13}C$ = –22.6‰ to –23.8‰ VPDB, and $\delta^{15}N$ = 5.6 to 6.2‰ AIR) and C/N values are also indicative of marine algae (Geel et al., 2015).

However, the suggestion of marine conditions is contested with geochemical evidence from the carbonate and phosphate nodules collected in the western MKB (near Laingsburg). According to Herbert and Compton (2007), the oxygen and carbon isotopes of these carbonate nodules ($\delta^{18}O$ = 7.8 to 8.9‰ SMOW; $\delta^{13}C$ = −15 to −3‰ VPDB) and strontium isotopes of phosphate nodules ($^{87}Sr/^{86}Sr$= 0.716–0.737) in the Dwyka Group and the Prince Albert Formation, indicate that deposition occurred in a meteoric-glacial melt-water lake. Isotope studies by Faure and Cole (1999), on samples both from the northern and southern MKB also suggest deposition in meteoric water ($\delta^{13}C$ = -8 ‰ VPDB; $\delta^{18}O$ = 7 ‰ SMOW) during the Prince Albert depositional episode.

3.2.1.2 Whitehill Formation

The carbonaceous Whitehill Formation has a sharp contact with the underlying Prince Albert Formation (Cole & Basson, 1991), and is dominated by black shales that, under surface conditions, chemically weather to a conspicuous white colour as its pyrite content is altered to gypsum. The shale is thinly laminated, contains lesser grey, silty laminae and contains up to 17% TOC (e.g., Rowsell & De Swart, 1976; Cole & McLachlan, 1991; Visser, 1994; Geel et al., 2015; Chukwuma et al., 2018). Other notable characteristics are up to one-meter thick dolomite concretions, as well as gypsum and chert nodules (McLachlan & Anderson, 1977a; Geel et al., 2015; Chukwuma, 2017). Fossils identified in the Whitehill Formation include a swimming reptile (*Mesosaurus tenuidens*), plant remains (*Glossopteris*), sponge spicules, arthropods (e.g., notocarid crustaceans) and palaeoniscoid fish and insect wings (McLachlan & Anderson, 1973, Anderson & McLachlan, 1979; Faure & Cole, 1999; Almond, 2008; Chukwuma & Bordy, 2016).

Lateral facies variations indicate that the Whitehill Formation accumulated in shallower waters in the northern relative to the southern parts of the MKB (Chukwuma & Bordy, 2016). The lack of coarse clastic sediment in the Whitehill Formation implies that the basin was sediment starved, and a low-lying, almost flat, marshland acted as a sediment trap in the northern region. The even distribution of fine-grained sediments in the Whitehill Formation may be due to windblown sediment transport (Visser, 1992). It may be postulated that during the Whitehill depositional episode, the basin received some sediment from volcanic sources (Mclachlan & Anderson, 1977a). These might have been in the same Patagonian volcanic area that was identified as source for tuffs in the Collingham Formation (Visser, 1992; Johnson et al., 2006; Navarrete et al., 2019). The basin water was likely stratified and is believed have been anoxic in some regions, preventing the establishment of a diverse benthic fauna in the overall low energy environments (Oelofsen, 1981; Mclachlan & Anderson, 1977b).

The relatively high pyrite content in the Whitehill Formation may be an indicator of marine conditions as diagenetic pyrite is rare in sediments that accumulate in freshwater (Berner & Raiswell, 1984). However, the total organic carbon (TOC; 0–17 wt%) and total sulfur contents (0.2–9 wt%) are highly variable in the Whitehill Formation (Rowsell & De Swart, 1976; Faure & Cole, 1999; Geel et al., 2015; Chukwuma et al., 2018).

Stable isotope data, including organic carbon ($\delta^{13}C$ = –23 to –19 ‰ VPDB), sulfur ($\delta^{34}S$= 3.7 to –0.3 ‰ CDT) and calcite ($\delta^{13}C$ = –2 to –11 ‰ VPDB; $\delta^{18}O$= 6 to 17 ‰

SMOW), indicate that brackish to fresh water conditions prevailed with terrestrial plant material (type III kerogen; Faure & Cole, 1999). However, it must be considered that diagenetic alteration can affect these isotopic values (Veizer, 1999). Other authors suggest mixing of marine algae and terrestrial plant material responsible for the isotope values ($\delta^{13}C$ = –18.9 to –24.7 ‰ VPDB; $\delta^{15}N$ =7.7 to 10.1 ‰ AIR; C/N= 16.7 ‰; Geel et al., 2015; $\delta^{13}C$ = –18 to –22.4 ‰ VPDB; $\delta^{15}N$ =4.9 to 10.9 ‰ AIR; C/N = 2.04–17.62 ‰; Chukwuma, 2017) and rather suggest a transition from marine to brackish conditions in the Whitehill Formation. Rb/K elemental ratios are suggestive of marine conditions becoming increasingly brackish with values between $4*10^{-3}$ and $6*10^{-3}$ (Scheffler et al., 2006; Chere, 2015; Geel et al., 2015; Chukwuma et al., 2018).

A palynostratigraphic study by Götz et al. (2017) correlated acritarchs (*Micrhystridium*) from the Whitehill Formation with coal seams No.2 and No.5 of the Vryheid Formation. These acritarchs were also postulated to be an indicator for marine conditions. However, this claim is contested by Cole & Barbolini (2019), who point out that acritarchs are polyphyletic, common in both marine and non-marine environments. Alternatively, glauconite detected in the Vryheid Formation may be suggestive of marine conditions (Van Vuuren, 1983; Götz et al., 2017), but the glauconite-bearing part of the Vryheid Formation cannot be accurately correlated with the entire Whitehill Formation due to lack of reliable age indicators (Cole & Barbolini, 2019). Although there are several transgressive events that were identified during the deposition in the upper Ecca Group (Catuneanu et al., 2002), these bear no relevance for the current stratigraphic interval that concerns the lower Ecca Group.

In a recent geochemical study, Costin et al. (2019), used trace element, modal mineral and palynofacies analysis in samples from BH KZF-1 and BH KWV-1, and interpreted the depositional environment of the Whitehill Formation as a marine outer shelf dominated by low-energy sediment fallout processes.

3.2.1.3 Collingham Formation

The Whitehill Formation is sharply overlain by the Collingham Formation and comprises mudstone and siltstones that are intercalated with volcanic ash (tuffs), derived from volcanism that is suspected to have occurred in northern Patagonia (Viljoen, 1992; 1994). The Collingham Formation was probably deposited on a shelf to basin plain setting from under- and overflow suspension. Moreover, the distal turbidites that are common in the upper part of the formation and are dominated by siltstones and fine-grained sandstones, formed in turbidity currents that developed on deep water fans (Viljoen, 1992). Tuffaceous laminae and beds become less frequent

towards the east of the basin (Viljoen, 1992;1994). The Collingham Formation is rich in trace fossils and burrows (e.g., *Planolites, Umfolozia longula;* tracks of giant water scorpions; Almond, 2002*)*, but none of these have clear marine affinity.

Rb/K values in the Collingham Formation are typically below ~ 4 $*10^{-3}$ and thus suggest dominantly non-marine conditions (Campbell & Williams, 1965; Scheffler et al., 2006; Geel, et al., 2015). Evidence for an oxygenated setting is provided by V/(V+Ni) and V/Cr elemental ratios, increased bioturbation and lower overall TOC and pyrite content (Viljoen, 1992; Scheffler et al., 2006; Geel, et al., 2015; Chere, 2015). Collectively, these geochemical proxies imply increasingly oxygenated and fresher water conditions during the Collingham depositional phase. The chemical index of alterations (CIA) decreases from the Prince Albert Formation to the Collingham Formation indicating that conditions became increasingly more arid, with low to moderate weathering rates near the top of the Whitehill Formation and into the Collingham Formation (Andersson & Worden, 2004; Scheffler et al., 2006; Geel, et al., 2015; Chere, 2015).

Flysch-like sedimentary deposits increase up-sequence from the Collingham Formation in the southern MKB, and these upper Ecca units, together with the fluvio-deltaic units in the northern MKB have been linked to depositional regime strongly induced by foreland basin tectonics (Catuneanu et al., 1998; 2002; 2005).

3.3 Materials and methods

This study focuses on major and trace element compositions of the mudstones (i.e., shales and siltstones) of the lower Ecca Group. The relevant geochemical data is extracted from two boreholes, namely BH KZF-1 and BH KWV-1, that were drilled as part of the Karoo Research Initiative (KARIN Project), in the western (Tankwa Karoo Sub-basin) and eastern MKB, respectively.

A total of 43 samples from BH KZF-1 and 17 samples from BH KWV-1 were obtained from the Prince Albert, Whitehill and Collingham formations (Figure 3.2). Samples were crushed using a custom-built hydraulic splitter, Sturtevant laboratory jaw-crusher and powdered using Siebtechnik swing mill with carbon-steel cassettes. XRF analyses were performed at the University of Cape Town using a Panalytical Axios wavelength-dispersive XRF spectrometer with a rhodium end-window X-ray tube. A Claisse Fluxer is used to prepare fusion discs and a hydraulic cold press and die are used for the preparation of powder briquettes. Concentrations of major (Si, Ti, Al, Fe, Mn, Ca, Na, K, P, S, Cr, Ni) and trace (Zn, Cu, Ni, Mo, Nb, Zr, Y, Sr, Rb, U, Th, Pb, Co, Mn, Cr, V, F, S, Cl, Sc, Ba) elements are provided in the Appendix A. Cr_2O_3 is

below detection-limits and U and Mo are mostly below 5 ppm. In BH KZF-1, the samples which contain high Mo concentrations are near a fracture zone that is rich with hydrothermal veining. All calculations using XRF data were carried out with Origin Pro 9 software. Samples KZF01P to KZF10P were analysed for vitrinite reflectance and porosity (Chapter 2) as well as total sulfur content using the LECO S-200 Sulfur Determinator at RWTH Aachen University (Nolte et al., 2019).

TOC/Rock Eval analyses were completed by the Indian Institute of Technology in Mumbai (Bombay) in India on all samples from both boreholes. The samples were cut and milled and 5 g of rock powder per sample were selected for analysis. TOC/Rock Eval analyses is reported on in Chapter 2 and are not repeated here. The average TOC content in BH KZF-1: Prince Albert Formation = 0.81 wt%; Whitehill Formation = 5.14 wt%; Collingham Formation = 1.44 wt%. Average TOC content in BH KWV-1: Prince Albert Formation = 0.81 wt%; Whitehill Formation = 4.87 wt%; Collingham Formation = 0.82 wt%.

Quantitative XRD was carried out on 22 and 17 samples from BH KZF-1 and BH KWV-1, respectively. XRD was measured in wt% with a Malvern Panalytical AERIS diffractor meter with PIXcel detector and fixed slits with Fe filtered Co- Kα radiation by XRD Analytical and Consulting laboratory in Pretoria, South Africa. The phases were determined using X'pert Highscore plus software. XRD analyses and Harker diagrams are used to identify sample outliers. In BH KZF-1, samples KZF20, KZF26, KZF28, KZF29 and KZF32 contain very high concentration of carbonate and phosphate minerals (> 60%) and were omitted from certain calculations and plots. Sample KZF-16 was also omitted from certain plots as it contains enrichment from hydrothermal veins observed near this sample in the core. In BH KWV-1, sample KWV12 was omitted from calculations as XRD detected permeation of dolerite into the sample, likely from an adjacent intrusion. When samples are omitted, it is clearly stated and justified within the results subsections of this chapter.

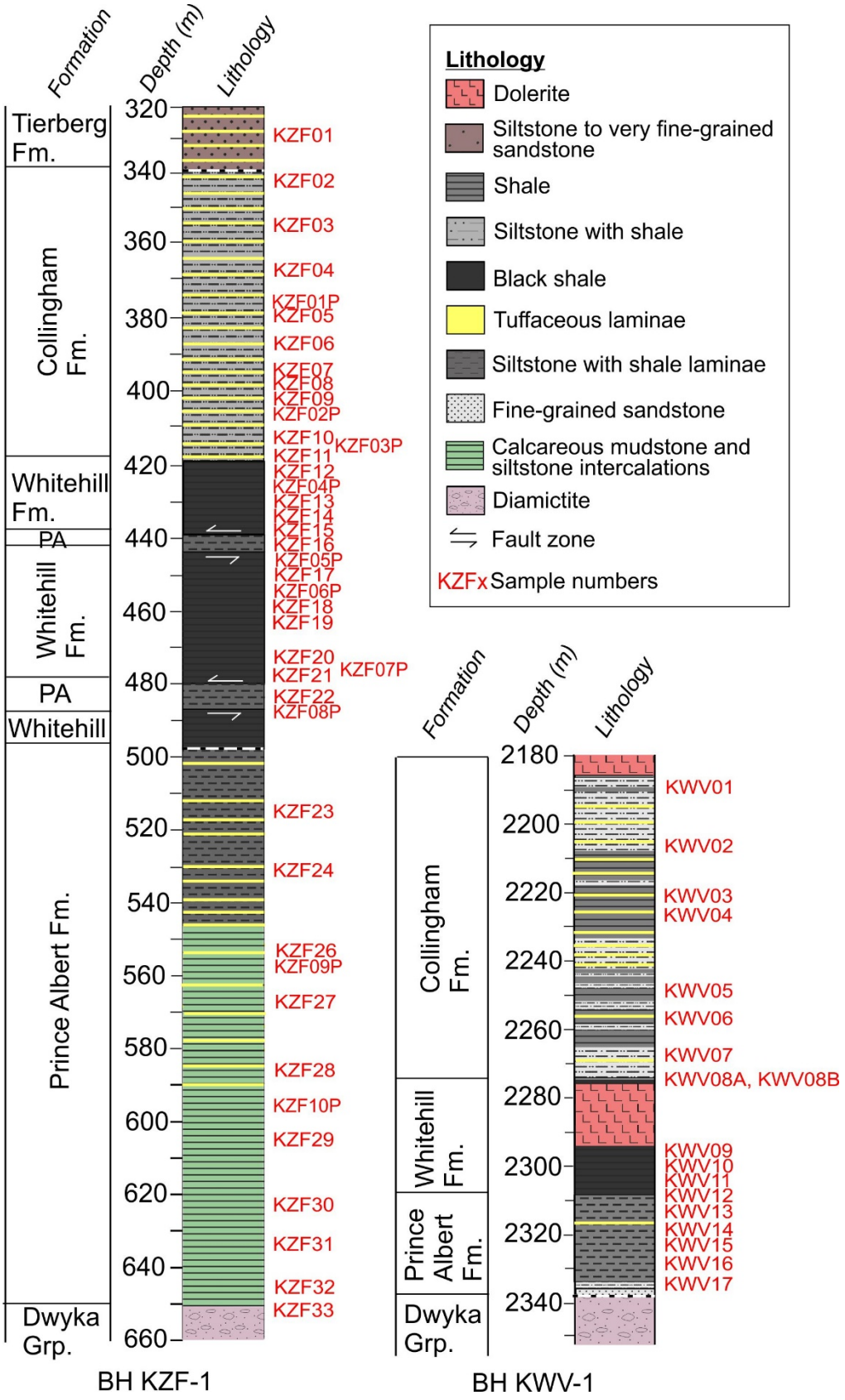

Figure 3.2: Lithostratigraphic profiles for BH KZF-1 and BH KWV-1, showing sample intervals.

3.3.1 Geochemical analysis of sedimentary rocks

An important aspect of interpreting geochemical data is correlating the association between oxides, trace elements and sedimentology. Bulk geochemistry analysis represents a suitable complementary approach to petrography and XRD analysis (Chapter 2). Bivariant graphs or Harker Diagrams are used to examine the correlation (either positive or negative) between major elements and SiO_2 (Rollinson, 1993). For example, an increase in SiO_2 will reflect increased mineralogical maturity (Bhatia, 1983).

Correlation coefficients are used to test the linearity between different elements. The Pearson (*r*) and Spearman (ρ) correlation coefficients and Shapiro-Wilk tests (W) are calculated for major oxides in this study. Pearson's correlation coefficient is used when samples are normally distributed. The Spearman's rank order coefficient is not restricted to a population with normal distribution and is better at identifying outliers in the data set. Some element correlations have low W values, indicating that they deviate from normal distribution. Therefore, both Pearson's and Spearman methods of correlation are used. When the W values are ≤ 0.8, then the Spearman's correlation is used instead of the Pearson's correlation coefficient.

3.3.2 Palaeo-climate – Chemical Index of Alteration

Bulk chemistry is useful in determining past conditions of physical and chemical weathering. Chemical weathering increases proportionally under humid conditions. Progressive chemical weathering of labile minerals like feldspar leads to the loss of Ca^{2+}, K^+ and Na^+. Ultimately chemical weathering of silicate rocks results in the formation of shales rich in clay minerals like illite and kaolinite, and Fe-oxyhydrates like goethite. Chemical weathering leads, through hydrolysis, to an exchange of the cations: Na^+, K^+, Ca^{2+} and Mg^{2+} for H^+, and maybe a loss of Si^{4+} (Nesbitt & Young, 1982; Goldberg & Humayun 2010). The calculation of the Chemical Index of Alteration (CIA) can be instrumental in documenting changes between icehouse and greenhouse climates and in recognizing shorter-term climate oscillations between glacial and warm-humid conditions (Nesbitt & Young, 1982; Rollinson, 1993; Potter et al., 2005; Bahlburg & Dobrzinski, 2011).

The CIA is represented by a ratio of Al_2O_3 to the mobile cations Na^+, K^+ and Ca^{2+} given as oxides (Nesbitt & Young, 1982):

$$CIA = [Al_2O_3 / (Al_2O_3 + CaO^* + K_2O + Na_2O] \times 100 \quad (3.1)$$

CaO^* is represented by the silicate-fraction of the sample. Raw abundances are converted into moles by dividing the weight percent by molecular weight. Values in molar proportions emphasize mineralogical relationships. The CIA reflects the degree of weathering to clay minerals. Ternary plots using (CaO + Na_2O) – Al_2O_3 – K_2O endmembers, show loss of K_2O and removal of Ca and alkalis with increased weathering (Nesbitt & Young, 1984). Index values that are higher than 90%, indicate extensive chemical weathering and conversion of feldspar to clay minerals. A up-sequence vertical change of CIA weathering values may reflect mixing of first-cycle and recycled sources.

To avoid being constrained by summing to 100 % as in Equation 3.1, Goldberg & Huayan (2010) use Equation 3.2, which is calculated so that the results are a proportion between alumina and alkalis plus calcium.

$$CIA = [Al_2O_3 / (CaO^* + K_2O + Na_2O] \quad (3.2)$$

CIA index is calibrated against a database of chemical data from modern and ancient sediments in order to obtain humidity field comparisons (Retallack, 2009; Goldberg & Humayan, 2010).

The calculation of CaO* is complicated in sedimentary basins that may contain abundant extrabasinal and/or intrabasinal carbonate grains and in sedimentary rocks that have undergone diagenesis and precipitation of carbonates. When correcting CaO*, there is a risk that samples can be overcorrected resulting in negative values (Bahlburg & Dobrzinski, 2011; Garzanti & Resentini, 2016). For this study the method proposed by McLennan et al. (1993) is used to correct CaO* by assuming reasonable Ca/Na values in silicate material. CaO is first corrected to CaO* using P_2O_5, which is assumed to be associated with apatite and all inorganic carbon. If the remaining number of CaO* moles is greater than Na_2O, CaO* is assumed to be equivalent to Na_2O. If the number of moles of CaO* is less after the correction, then this CaO* value was used (McLennan et al., 1993).

3.3.3 Palaeo-environmental analysis

The major and trace element content of sedimentary rocks can be used to investigate palaeo-climate and palaeo-environments, especially in conjunction with other sedimentological and palaeontological observations. Elements and oxides are normalized to aluminium content to eliminate a dilution effect caused by carbonates and quartz. The best way to consider compositional variation is in the form of logarithms of ratios of components (Aitchison, 1982; 1986). Log ratios are free of the

“dilution effect” and have no linear equality constraints. It must also be considered that the biogeochemical cycling of elements in the ocean, the way at which they are delivered to the sea floor and post depositional conditions can lead to diagenetic sediment recycling or precipitation (Calvert & Pedersen, 1992).

Sediments rich in organic carbon (OC) are usually also rich in Fe and S, which is almost always present as diagenetic FeS_2. Where OC supply is sufficient to consume available oxygen, bacteria will begin to respire ferric iron minerals, producing Fe (II). Once Fe (III)-minerals are consumed, sulfate-reducing bacteria will utilize pore-water sulfate for the oxidation of sedimentary organic matter. Reduced sulfur (H_2S and/or HS^-) will then diffuse upwards to the sediment-water interface, where it may encounter Fe^{2+} and precipitate as sulfide minerals such as pyrite, marcasite, chalcopyrite, pyrrhotite, etc. (Berner, 1974; Berner & Westrich, 1985; Dean & Arthur, 1989; Arthur & Sageman, 1994). The degree of pyritization (DOP) is the ratio of pyritic iron to total reactive iron (Berner & Raiswell, 1984). The distribution of data along C/S plots has long been used as a method to determine whether samples have been deposited in anoxic or anoxic settings (Berner, 1970; Leventhal, 1987). However, contradictory results have been noted. For example, the Chatanooga Shale in the USA plots as anoxic Fe-S-TOC ternary diagrams, but clearly has evidence for bioturbation. Moreover, Schieber (2003), showed pyritic trails formed due to bioturbation in black shales suggesting oxic conditions. Some sediments could undergo rapid changes in oxygenation or even periods of seasonal anoxia (Tyson & Pearson, 1991; Oschmann, 1991). Elements associated with high bio-productivity are P, Cd and Ba. Enrichment of Mn can be associated with both anoxic and oxygenated conditions and can suggest low pelagic sedimentation rates (Brumsack, 2006).

OC-rich sediments are often rich in trace metals like Mo, V, Zn, Ni, Cr, Cu, Zn or U and their enrichment occur in low concentrations of sea water. Elements such as Al, Ti, Ga, Zr, Sc are often associated with detrital elements and Ca, Mg, Mn and Sr with carbonates (Vine & Tourtelot, 1970). Bacterial sulfate reduction and associated H_2S near the sediment-water interface may result in trace metal fixation. Available H_2S in the water column depends on organic matter available for degradation, the sulfate-reduction rate, amount of detrital material containing elements like Fe and mixing of the water column or ventilation (Brüchert et al., 2003). In anoxic basins, such as Norwegian fjords and the narrow Gulf of California, oxygen levels can decrease dramatically to zero and H_2S will reach high values, especially in saline water. Elements like Cu, Zn and Cd can become highly soluble and become trapped as sulfides (Wedepohl, 1971; Jacobs et al., 1985; Brumsack, 2006).

Sediments that contain organic compounds are effective at fixing V, especially if Ni is being removed from pore waters as sulfide complexes in anoxic settings (Lewan & Maynard, 1982). Slow sedimentation rates and reduction by sulfides allow the diffusion of V into sediment-pore water, which will bind with organic compounds (Breit & Wanty, 1991). If V is increasing in enrichment over Ni, it may indicate euxinic conditions. If the sedimentation rate is high, then V diffusion can be limited (Arthur & Sageman, 1994). Therefore, V(V+Ni) values can indicate changes in oxygenation of the water column and values between 0.46–0.60 can indicate dysoxic conditions, 0.54 –0.82 anoxic conditions and > 0.82 euxinic conditions (Hatch & Leventhal, 1992). Ni/Co and Vr/Cr values are also used to determine palaeo-redox conditions. High Ni/Co values indicate reducing conditions as both Ni and Co are fixed in pyrite (Jones & Manning, 1994). Ni/Co values of < 5 indicate oxic conditions, 5–7 indicate dysoxic conditions and > 7 suboxic conditions. V/Cr values < 2 infers oxic conditions, 2–4.25 dysoxic and > 4.25 suboxic to anoxic conditions (Hatch & Leventhal, 1992; Jones & Manning, 1994).

Rb/K values can be used as a salinity proxy. It is assumed that marine shales have higher Rb concentrations than freshwater environments. K in illite can be substituted by Rb and Rb/K values are highest in marine shales. A Rb/K value of $6*10^{-3}$ is indicative of seawater and a Rb/K values of $4*10^{-3}$ of fresh-brackish water (Campbell & Williams, 1965; Taylor & McLennan, 1985).

Element/Al ratios help to show any excess or depletion of elements when compared to the average shale. The enrichment factor (EF) of elements in a shale can be calculated as follows: $EF= (element/Al)_{sample}/(element/Al)_{average\ shale}$. The average shale should be analogous with terrigenous detrital background (Table 3.1). In this case, the composition of the average shale is obtained from Wedepohl (1971). If there are any enrichments, then EF > 1 and if there is depletion, then EF < 1.

Table 3.1: Average geochemical data (µg/g) for shale (Wedepohl, 1971; Heinrichs et al., 1980).

Elements	***Average shale***	***Elements***	***Average shale***
Mn	850	**Ni**	68
Ba	650	**U**	3
Cd	0.3	**V**	130
Co	19	**Zn**	95
Cr	90	**Rb**	280
Cu	45	**Al**	88 900
Mo	1.3		

3.4 Results

3.4.1 Average composition

BH KZF-1 and BH KWV-1 were drilled ~ 830 km apart in the Tankwa Karoo Sub-basin and in the eastern MKB (Figure 3.1). In BH KZF-1, the Prince Albert Formation is 158.55 m thick, the Whitehill Formation (without duplication) is 19.5 m thick and the Collingham Formation is 80.13 m thick. In BH KWV-1, the Prince Albert Formation is 30 m thick, the Whitehill Formation is 13 m thick and the Collingham Formation is 91 m thick. While the thickness of the latter two are comparable despite the large distance between the two boreholes, the Prince Albert Formation is more than 5 times thicker in the west than in the east. In BH KZF-1, the contact between the Dwyka Group and the Prince Albert Formation is sharp, whereas in BH KWV-1 it is gradational.

The Whitehill Formation has the highest TOC content in both boreholes (~ 5 wt%). The Collingham Formation has higher TOC content in BH KZF-1 (1.44 wt%) than BH KWV-1 (0.83 wt%), and the Prince Albert Formation has the same TOC content in both boreholes (0.81 wt%; Figure 3.3). Differences between the Prince Albert Formation in BH KZF-1 and BH KWV-1 are that there is notable rhodochrosite, birnessite, greenalite, apatite, siderite and albite in BH KZF-1 and anorthite in BH KZF-1 (Figure 3.3). Major differences in the Whitehill Formation is the presence of dolomite in BH KZF-1 and pyrhottite in BH KWV-1 (Figure 3.3). The Collingham Formation has similar mineral composition except for calcite and metamorphic minerals such as cordierite, garnet, diopside occurring in BH KWV-1. Mudstone in BH KWV-1 was altered to spotted hornfels in response to contact metamorphism with the above and below lying dolerite intrusions as indicated on the lithostratigraphic column in Figure 3.2.

Average TOC contents per formation are summarized in Table 3.2 and the average mineral percentages are summarized in Figure 3.3. The data are provided in Appendix A and they have been elaborated on in Chapter 2.

Table 3.2: The average TOC content (wt%) for the lower Ecca Group from BH KZF-1 and BH KWV-1.

Formation	**Western MKB**	**Eastern MKB**
	KZF-1	**KWV-1**
Collingham Fm.	1.44	0.83
Whitehill Fm.	5.17	4.87
Prince Albert Fm.	0.81	0.81

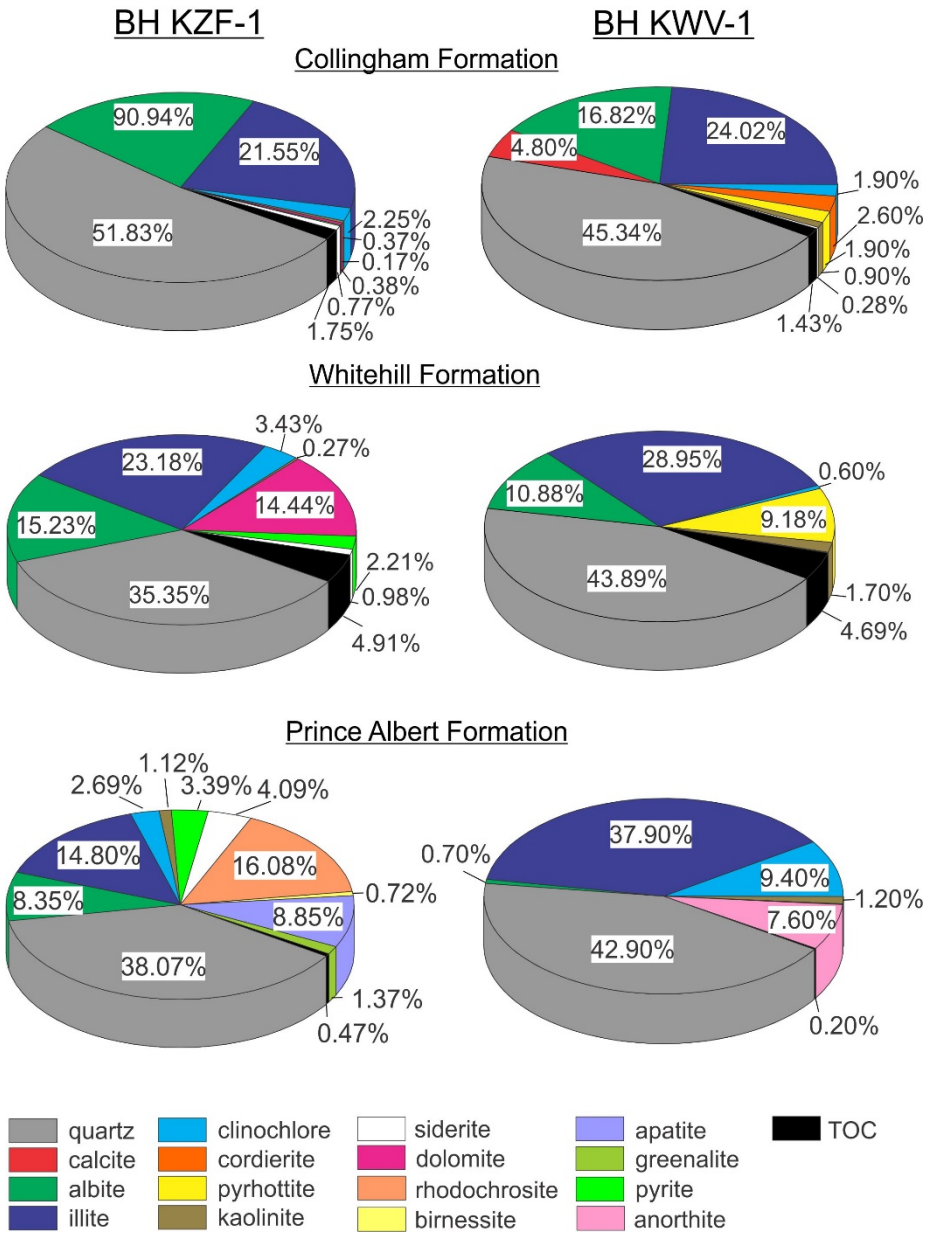

Figure 3.3: XRD data represented as pie-charts for the Prince Albert, Whitehill and Collingham formations for BH KZF-1 and BH KWV-1.

3.4.2 Elemental correlations

3.4.2.1 Harker diagrams

Harker variation diagrams are plotted (Figures 3.4–3.6) for the Prince Albert, Whitehill and Collingham formations for BH KZF-1 and BH KZW-1 to detect trends and sample anomalies. TiO_2, Al_2O_3, Fe_2O_3, MgO, Na_2O and K_2O are plotted against SiO_2. Large variations are detected in samples with high carbonate content and high proportions of tuffaceous material. Samples KZF20, 26, 28, 29, 32 and KWV12 are omitted entirely from the Harker discrimination diagrams due to high carbonate detected in those from BH KZF-1 and dolerite in the sample from BH KWV-1.

The Whitehill and Prince Albert formations show more compositional variability then the Collingham Formation. Few linear correlations are evident in the Prince Albert Formation (Figure 3.4), apart from the clear decrease in Fe and Mg oxides with increasing SiO_2 content. However; clear clustering of samples from BH KZF-1 and BH KWV-1 for the Prince Albert Formation indicates compositional variation between the boreholes. In the Whitehill Formation, Al_2O_3, Fe_2O_3 and K_2O decrease with increasing silica content and an increase in Na_2O with increasing SiO_2 content (Figure 3.5).

The most distinct linear trends are observed in the Collingham Formation (Figure 3.6). There are two outlier samples (KZF05 and KZF07), which contain more tuffaceous material compared to the other samples, which are mostly mudstones and siltstones. Ignoring the outliers, it is evident that TiO, Al_2O_3, Fe_2O_3, MgO and K_2O decrease with increasing SiO_2. Na_2O increases with increasing SiO_2 content.

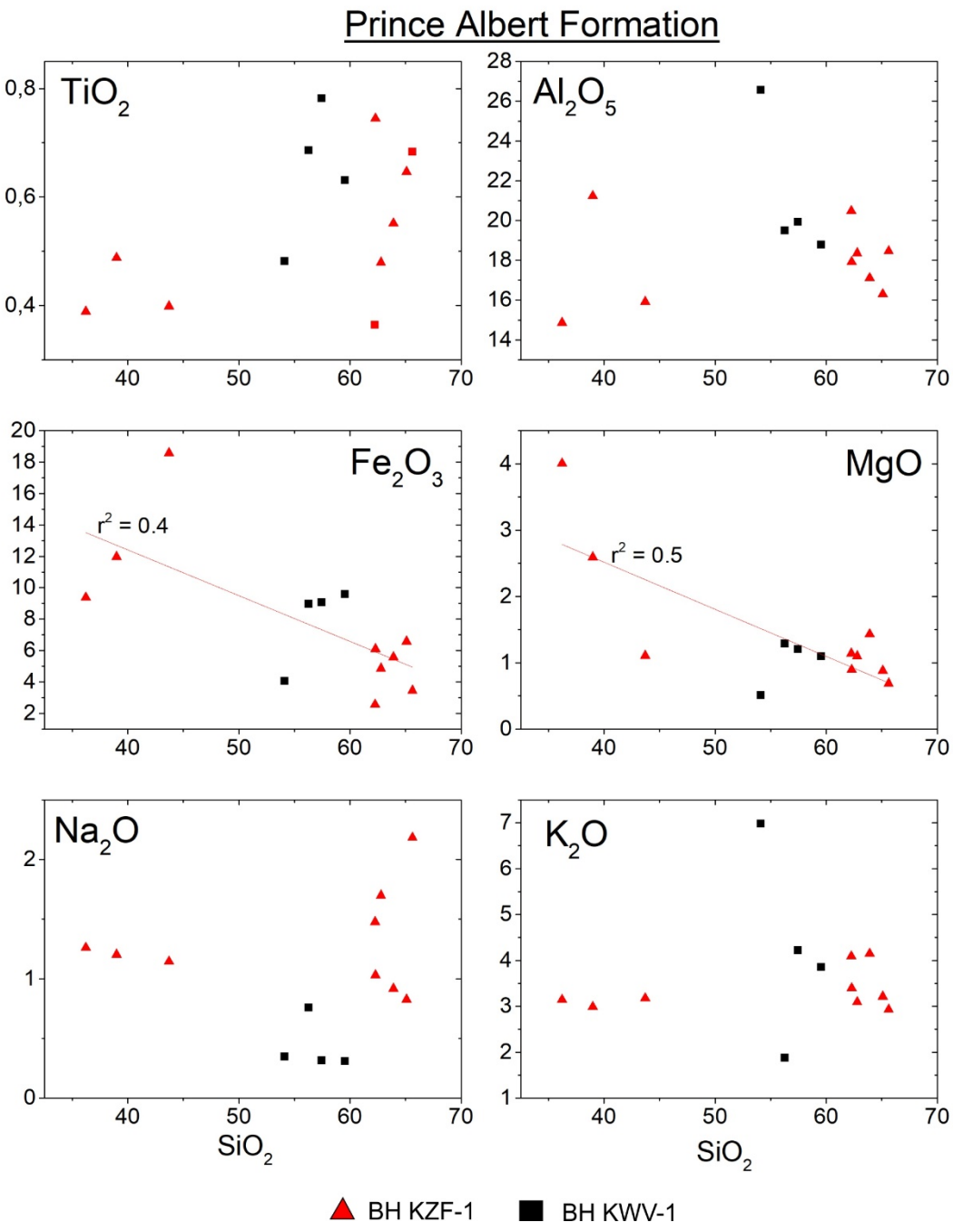

Figure 3.4: Harker diagrams of TiO_2, Al_2O_5, Fe_2O_3, MgO, Na_2O and K_2O versus SiO_2 from the Prince Albert Formation. r^2= linear regression.

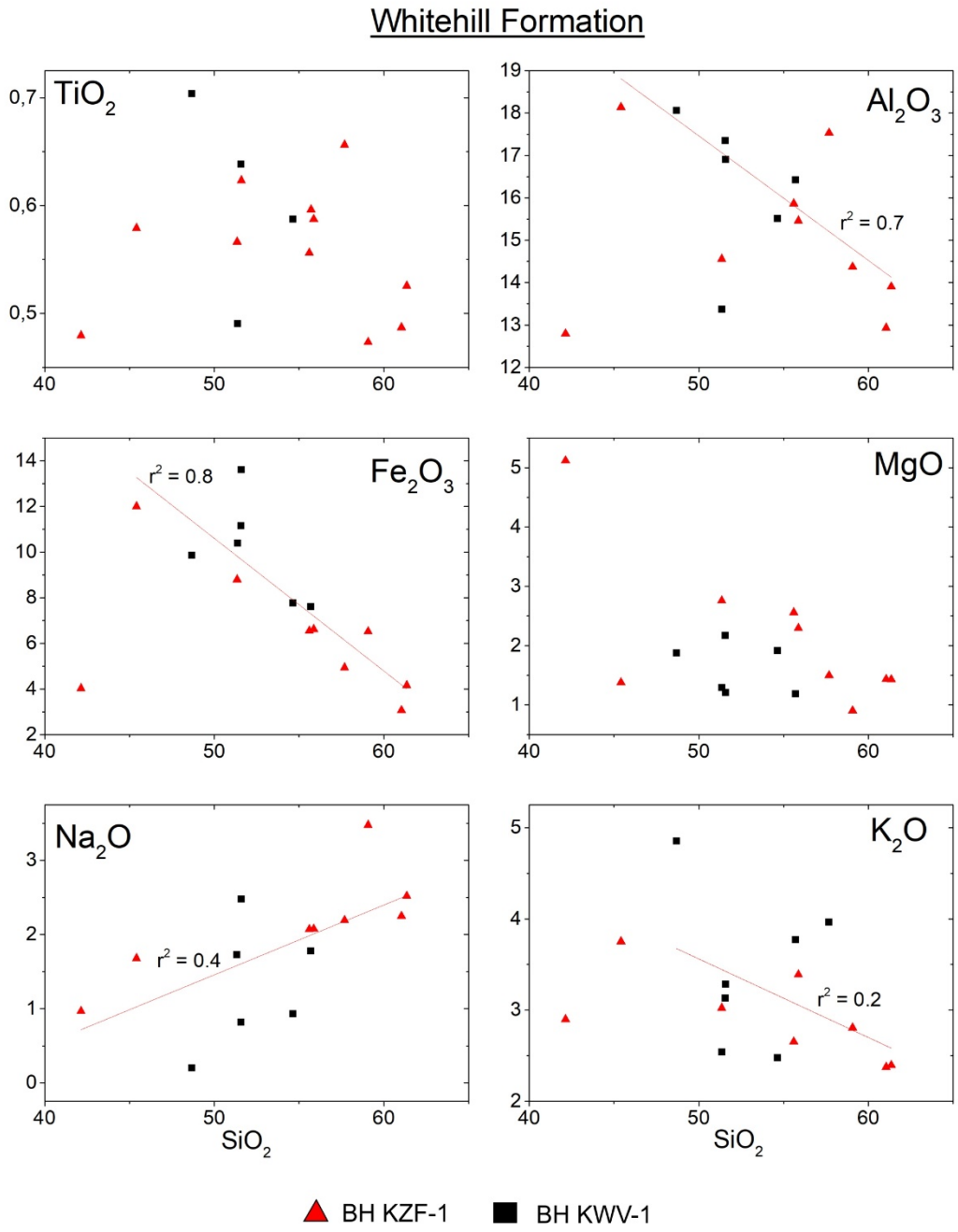

Figure 3.5: Harker diagrams of TiO_2, Al_2O_5, Fe_2O_3, MgO, Na_2O and K_2O versus SiO_2 from the Whitehill Formation. Abbreviation: r^2= linear regression.

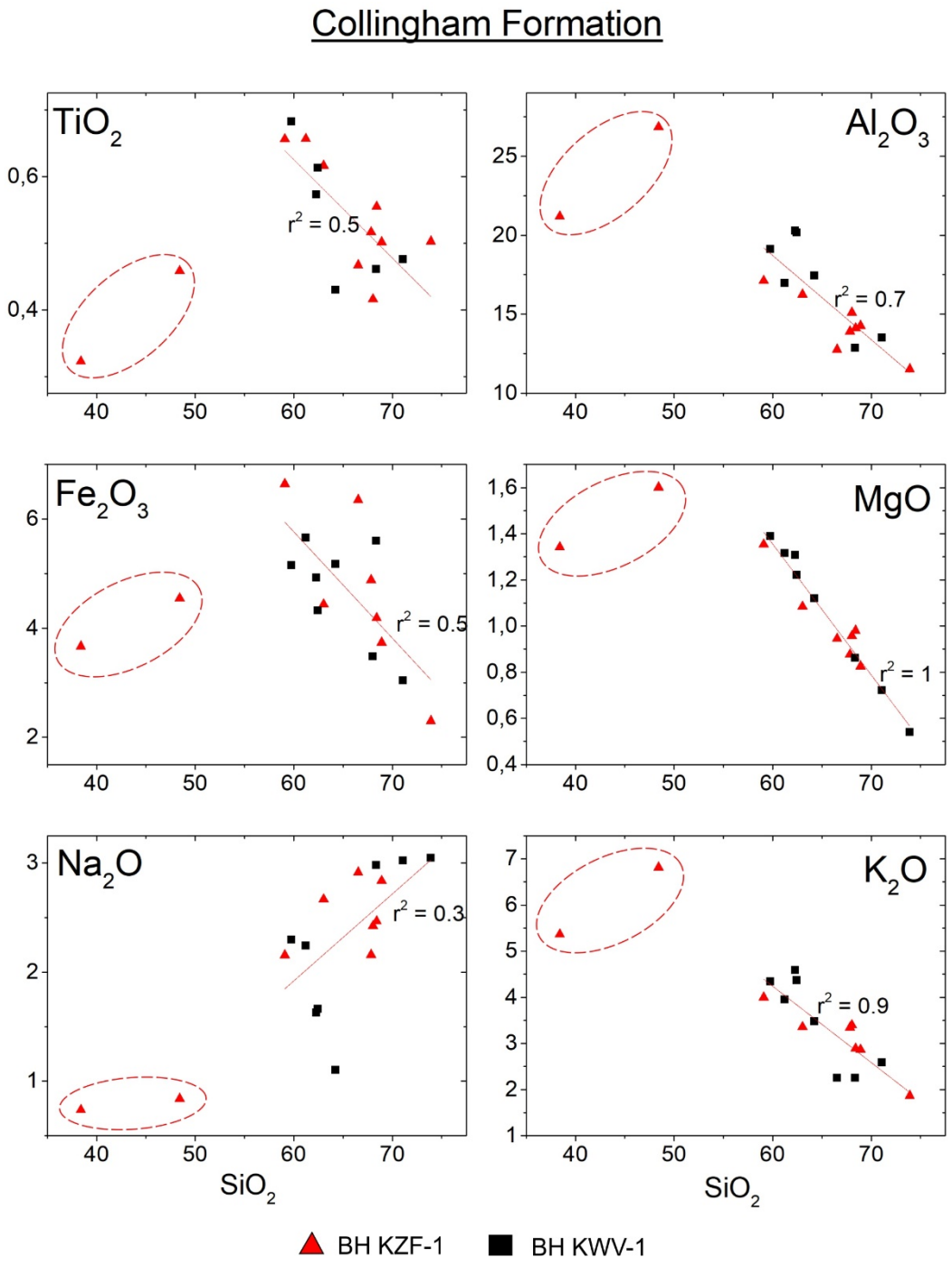

Figure 3.6: Harker diagrams of TiO_2, Al_2O_5, Fe_2O_3, MgO, Na_2O and K_2O versus SiO_2 from the Collingham Formation. Trend lines calculated by omitting two tuff-rich outlier samples from BH KZF-1 (indicated by dashed red-ellipse). Abbreviation: r^2= linear regression.

3.4.2.2 Correlation coefficients

Prince Albert Formation

In BH KZF-1 (Table 3.3), SiO_2, Fe_2O_3, P_2O_5, SO_3 and TOC deviate most from normal distributions. There is weak positive correlation between Al_2O_3 and SiO_2 (ρ = 0.6), as opposed to in BH KWV-1, where there is a strong negative correlation between Al_2O_3 and SiO_2 (*r* = -0.9). P_2O_5 is positively correlated with CaO (ρ = 0.9), indicating that phosphates are mostly associated with apatite.

In BH KWV-1 (Table 3.4), Al_2O_3, Fe_2O_3, MgO, K_2O, P_2O_5 and TOC deviate the most from normal distributions. MgO is negatively correlated with P_2O_5 (ρ = -0.9) and SiO_2 (ρ = -0.8). K_2O is positively correlated with Al_2O_3 (ρ = 0.8). MnO is positively correlated with CaO (*r* = 1), Na_2O (*r* = 1) and SO_3 (*r* = 0.9). SO_3 is positively correlated with Fe_2O_3 and MgO (*r* = 1) and negatively correlated with Al_2O_3 (*r* = -1) and P_2O_5 (*r* = -0.9).

Whitehill Formation

In BH KZF-1 (Table 3.5), SiO_2, Na_2O, SO_3 and TOC deviate the most from normal distribution. In BH KWV-1, only SiO_2 deviates from normal distribution. In both boreholes SiO_2 is positively correlated with Na_2O (BH KZF-1 ρ = 0.9; BH KWV-1 ρ = 0.6). In BH KZF-1, SO_3 is positively correlated with CaO (*r* = 0.9) and TiO is positively correlated with Al_2O_3 (*r* = 0.8). In BH KWV-1 (Table 3.6), TiO is also positively correlated with Al_2O_3 (*r* = 1) and MgO is positively correlated with P_2O_5 (*r* = 0.9) and SO_3 (*r* = 1).

Collingham Formation

Oxides from the Collingham Formation in both boreholes shows the least deviation from normal distribution of the three formations, except for TOC in BH KZF-1 (W = 0.7). In BH KZF-1 (Table 3.7), SiO_2 is positively correlated with Na_2O_3 (*r* = 0.9). MgO is negatively correlated to SiO_2 (*r* = -0.8) and positively correlated to K_2O (*r* = 0.9). In BH KWV-1 (Table 3.8), SiO_2 is weakly correlated with Na_2O (*r* = 0.6) and negatively correlated with MgO (*r* = -1). Al_2O_3 is positively correlated with MgO (*r* = 0.9) and K_2O (*r* = 1) and negatively correlated with Na_2O (*r* = -0.8). TOC has weak but notable positive correlations with P_2O_5 (*r* = 0.5), SO_3 (*r* = 0.5) and Na_2O (*r* =0.7).

Table 3.3: Major element correlation for the Prince Albert Formation BH KZF-1 using the Pearson's (r) correlation coefficient in the top right triangle and the Spearman's (ρ) correlation in the bottom left triangle. The Shapiro-Wilk test is highlighted and displayed in the diagonal array. Correlation is significant at the 0.05 level.

W	SiO_2	TiO_2	Al_2O_3	Fe_2O_3	MnO	MgO	CaO	Na_2O	K_2O	P_2O_5	SO_3	TOC
SiO_2	0.8	0.8	0.8	-0.7	-0.7	-0.3	-0.7	0.7	0.8	-0.5	-0.3	-0.1
TiO_2	0.8	0.9	0.8	-0.8	-0.8	-0.1	-0.3	0.6	0.7	-0.2	-0.1	0.1
Al_2O_3	0.6	0.7	0.9	-0.8	-0.9	0.1	-0.5	0.8	0.9	-0.3	0.0	0.1
Fe_2O_3	-0.7	-0.6	-0.7	0.8	0.9	0.0	0.0	-0.7	-0.8	-0.1	-0.1	-0.1
MnO	-0.6	-0.6	-0.8	0.7	0.9	-0.2	0.2	-0.7	-0.9	0.0	-0.1	0.0
MgO	-0.4	-0.3	0.0	0.2	0.1	0.9	0.2	0.1	0.1	0.1	0.8	0.6
CaO	-0.8	-0.6	-0.5	0.4	0.6	0.5	0.9	-0.5	-0.5	0.9	0.2	0.0
Na_2O	0.6	0.5	0.8	-0.7	-0.8	0.0	-0.4	0.9	0.7	-0.4	0.1	0.1
K_2O	0.6	0.6	0.6	-0.7	-0.6	0.1	-0.6	0.5	0.9	-0.4	0.1	0.2
P_2O_5	-0.7	-0.6	-0.3	0.4	0.4	0.5	0.9	-0.3	-0.6	0.8	0.0	-0.2
SO_3	-0.8	-0.6	-0.5	0.6	0.4	0.6	0.6	-0.3	-0.3	0.6	0.8	0.9
TOC	0.1	0.2	-0.2	0.1	0.2	-0.4	-0.3	0.1	0.1	-0.6	0.0	0.8

Table 3.4: Major element correlation for Prince Albert Formation BH KWV-1 using the Pearson's (r) correlation coefficient in the top right triangle and the Spearman's (ρ) correlation in the bottom left triangle. The Shapiro-Wilk test is highlighted and displayed in the diagonal array. Correlation is significant at the 0.05 level.

W	SiO_2	TiO_2	Al_2O_3	Fe_2O_3	MnO	MgO	CaO	Na_2O	K_2O	P_2O_5	SO_3	TOC
SiO_2	0.9	0.5	-0.9	0.9	0	0.7	-0.1	-0.2	-0.5	-0.9	-0.3	0.8
TiO_2	0.4	0.9	-0.8	0.8	0.4	0.9	0.3	0.2	-0.7	-0.7	0	0.9
Al_2O_3	-0.8	-0.2	0.8	-1	-0.5	-0.9	-0.3	-0.2	0.9	1	-0.1	-1
Fe_2O_3	1	0.4	-0.8	0.8	0.5	0.9	0.3	0.2	-0.8	-1	0.1	1
MnO	0.2	0.8	-0.4	0.2	0.9	0.7	1	1	-0.9	-0.5	0.9	0.5
MgO	0.2	0.8	-0.4	0.2	1	0.8	0.5	0.4	-0.9	-0.9	0.3	1
CaO	0.2	0.8	-0.4	0.2	1	0.5	0.9	1	-0.8	-0.4	1	0.3
Na_2O	-0.8	0	0.4	-0.8	0.4	0.4	0.4	0.9	-0.7	-0.3	1	0.2
K_2O	-0.4	-0.4	0.8	-0.4	-0.8	-0.9	-0.8	-0.2	0.7	0.9	-0.6	-0.8
P_2O_5	-0.8	-0.2	1	-0.8	-0.4	-0.9	-0.4	0.4	0.8	0.8	-0.2	-0.9
SO_3	-0.6	-0.4	0	-0.6	0.2	0.3	0.2	0.8	-0.4	0	0.9	0
TOC	0.8	0.8	-0.4	0.8	0.4	1	0.4	-0.6	-0.2	-0.4	-0.8	0.8

Table 3.5: Major element correlation for Whitehill Formation BH KZF-1 using the Pearson's (r) correlation coefficient in the top right triangle and the Spearman's (ρ) correlation in the bottom left triangle. The Shapiro-Wilk test is highlighted and displayed in the diagonal array. Correlation is significant at the 0.05 level.

W	SiO_2	TiO_2	Al_2O_3	Fe_2O_3	MnO	MgO	CaO	Na_2O	K_2O	P_2O_5	SO_3	TOC
SiO_2	0.7	-0.2	-0.5	-0.6	-0.5	-0.7	-0.6	0.8	-0.6	-0.4	-0.4	-0.2
TiO_2	-0.2	0.9	0.8	0.4	-0.5	-0.1	-0.4	-0.2	0.8	0.6	-0.5	0.0
Al_2O_3	-0.4	0.8	0.9	0.7	0.0	-0.1	-0.3	-0.2	0.9	0.5	-0.4	0.0
Fe_2O_3	-0.6	0.6	0.8	1.0	0.3	0.0	-0.2	-0.3	0.6	0.7	-0.4	0.0
MnO	-0.6	-0.4	0.0	0.4	1.0	0.3	0.5	-0.1	0.1	-0.2	0.4	-0.3
MgO	-0.7	0.2	0.1	0.2	0.1	0.9	0.8	-0.8	0.2	0.1	0.8	0.1
CaO	-0.3	-0.5	-0.3	-0.2	0.2	0.3	0.9	-0.6	-0.1	-0.3	0.9	-0.1
Na_2O	0.9	-0.3	-0.4	-0.5	-0.3	-0.7	-0.4	0.8	-0.4	-0.5	-0.5	-0.2
K_2O	-0.6	0.7	0.8	0.7	0.2	0.3	-0.4	-0.5	0.9	0.6	-0.3	0.0
P_2O_5	-0.6	0.7	0.6	0.6	-0.1	0.4	-0.2	-0.6	0.6	0.9	-0.4	0.2
SO_3	-0.2	-0.7	-0.5	-0.3	0.3	0.5	0.7	-0.2	-0.5	-0.4	0.8	0.2
TOC	0.3	0.1	0.0	0.0	-0.5	0.2	-0.2	0.2	-0.1	0.1	0.2	0.8

Table 3.6: Major element correlation for Whitehill Formation BH KWV-1 using the Pearson's (r) correlation coefficient in the top right triangle and the Spearman's (ρ) correlation in the bottom left triangle. The Shapiro-Wilk test is highlighted and displayed in the diagonal array. Correlation is significant at the 0.05 level.

W	SiO_2	TiO_2	Al_2O_3	Fe_2O_3	MnO	MgO	CaO	Na_2O	K_2O	P_2O_5	SO_3	TOC
SiO_2	0.8	-0.4	-0.3	-0.6	-0.7	-0.3	0.2	0.4	-0.5	-0.6	-0.5	-0.1
TiO_2	-0.4	0.9	1	0.1	0.7	0.5	-0.2	-0.5	0.8	0.8	0.5	-0.3
Al_2O_3	-0.4	1	0.9	0.2	0.5	0.4	-0.3	-0.4	0.7	0.7	0.4	-0.4
Fe_2O_3	-0.4	0.3	0.3	0.9	0	-0.1	-0.1	0.4	0	0.1	-0.1	-0.6
MnO	-0.3	0.4	0.4	0	0.9	0.2	-0.3	-0.6	0.9	0.5	0.4	0.2
MgO	-0.4	0.3	0.3	0.2	-0.6	1	0.5	-0.8	0.1	0.9	1	0.1
CaO	0	-0.3	-0.3	0.3	-0.8	0.8	0.9	-0.2	-0.6	0.1	0.4	-0.1
Na_2O	0.6	-0.5	-0.5	0.1	0.1	-0.8	-0.3	0.9	-0.4	-0.8	-0.9	-0.5
K_2O	-0.2	0.7	0.7	-0.1	0.8	-0.4	-0.9	-0.1	0.9	0.5	0.2	0.1
P_2O_5	-0.4	0.8	0.8	0.1	0.1	0.7	0.1	-0.8	0.3	0.9	0.9	0
SO_3	-0.5	0.4	0.4	0	-0.4	0.9	0.4	-0.9	-0.1	0.7	0.9	0.3
TOC	-0.4	-0.3	-0.3	-0.5	0.2	-0.1	-0.3	-0.3	0.1	-0.3	0.1	0.9

Table 3.7: Major element correlation for the Collingham Formation in BH KZF-1 using the Pearson's (r) correlation coefficient in the top right triangle and the Spearman's (ρ) correlation in the bottom left triangle. The Shapiro-Wilk test is highlighted and displayed in the diagonal array. Correlation is significant at the 0.05 level.

W	SiO_2	TiO_2	Al_2O_3	Fe_2O_3	MnO	MgO	CaO	Na_2O	K_2O	P_2O_5	SO_3	TOC
SiO_2	0.9	0.4	-0.9	-0.1	-0.4	-0.8	-0.8	0.9	-0.9	-0.2	-0.6	-0.1
TiO_2	0.2	1.0	-0.3	0.4	-0.3	-0.1	-0.7	0.5	-0.3	0.1	-0.5	0.6
Al_2O_3	-0.8	-0.2	0.9	0.0	0.0	0.9	0.4	-0.9	1.0	0.6	0.6	0.1
Fe_2O_3	-0.3	0.3	0.0	0.9	0.5	0.4	-0.2	0.0	0.1	0.2	-0.3	0.1
MnO	-0.5	-0.1	0.0	0.6	0.9	0.2	0.5	-0.2	0.0	0.0	0.2	-0.2
MgO	-0.8	-0.1	0.8	0.4	0.4	0.9	0.3	-0.8	0.9	0.5	0.3	0.1
CaO	-0.4	-0.4	0.1	-0.2	0.4	0.3	0.9	-0.6	0.4	-0.4	0.5	0.0
Na_2O	0.7	0.2	-0.7	-0.2	-0.3	-0.8	0.0	0.9	-0.9	-0.3	-0.6	0.1
K_2O	-0.8	-0.2	1.0	0.0	0.0	0.9	0.1	-0.8	0.9	0.5	0.5	0.0
P_2O_5	-0.1	0.3	-0.2	0.5	0.2	0.5	0.1	0.2	-0.1	1.0	0.4	0.0
SO_3	-0.4	-0.3	0.2	-0.1	0.3	0.3	0.4	-0.3	0.2	0.4	0.9	0.0
TOC	-0.1	0.6	0.3	0.0	-0.2	0.1	0.0	0.1	0.1	0.1	0.1	0.7

Table 3.8: Major element correlation for the Collingham Formation in BH KWV-1 using the Pearson's correlation (r) coefficient in the top right triangle and the Spearman's (ρ) correlation in the bottom left triangle. The Shapiro-Wilk test is highlighted and displayed in the diagonal array. Correlation is significant at the 0.05 level.

W	SiO_2	TiO_2	Al_2O_3	Fe_2O_3	MnO	MgO	CaO	Na_2O	K_2O	P_2O_5	SO_3	TOC
SiO_2	0.9	-0.8	-0.8	-0.6	0.1	-1	-0.2	0.6	-0.9	-0.2	0.2	0.2
TiO_2	-0.8	1	0.6	0.2	-0.3	0.8	-0.4	-0.1	0.7	0.6	-0.2	0.2
Al_2O_3	-0.6	0.4	0.9	0.2	-0.1	0.9	0.4	-0.8	1	-0.1	-0.6	-0.6
Fe_2O_3	-0.3	0	-0.4	1	0.6	0.5	0.4	-0.2	0.2	0.4	0.6	0
MnO	0.1	-0.5	0.1	0.4	0.9	0	0.6	-0.1	-0.2	0.1	0.6	-0.4
MgO	-1	0.8	0.6	0.3	-0.1	0.9	0.2	-0.6	0.9	0.2	-0.3	-0.2
CaO	0	-0.4	0.5	0.1	0.7	0	1	-0.8	0.2	-0.6	-0.1	-0.8
Na_2O	0.3	0.1	-0.7	-0.1	-0.4	-0.3	-0.9	0.9	-0.7	0.6	0.6	0.7
K_2O	-0.7	0.6	1	-0.3	0	0.7	0.4	-0.6	0.9	0	-0.6	-0.4
P_2O_5	-0.4	0.5	-0.3	0.5	0.2	0.4	-0.3	0.5	-0.1	1	0.6	0.5
SO_3	-0.1	0	-0.7	0.8	0.1	0.1	-0.3	0.4	-0.6	0.6	0.9	0.5
TOC	-0.3	0.4	-0.6	0.4	-0.6	0.3	-0.8	0.6	-0.4	0.4	0.7	1

3.4.2.3 Enrichment factors

Trace element enrichment was calculated by normalizing the element concentrations to Al and dividing by the normalized “average shale” composition, as determined Wedepohl (1971). The trace element enrichment factors are tabulated in Appendix A and presented in Figure 3.7. Mo was not included from BH KZF-1, because it is clearly correlated with thrust-zones and hydrothermal veining and otherwise is not detected in the shale. There is, however, high Mo enrichment in the Whitehill Formation in BH KWV-1.

The order of enrichment of trace elements in BH KZF-1 are: Mn > Ba > Zn > Co > Cu > V > Rb > Cr > Ni. In BH KWV-1 Mo has the highest enrichment values, but only occurs in the Whitehill Formation. The order of enrichments are: Mo> Ba > Cu > Zn > Mn > V > Co > Cr > Rb > Ni.

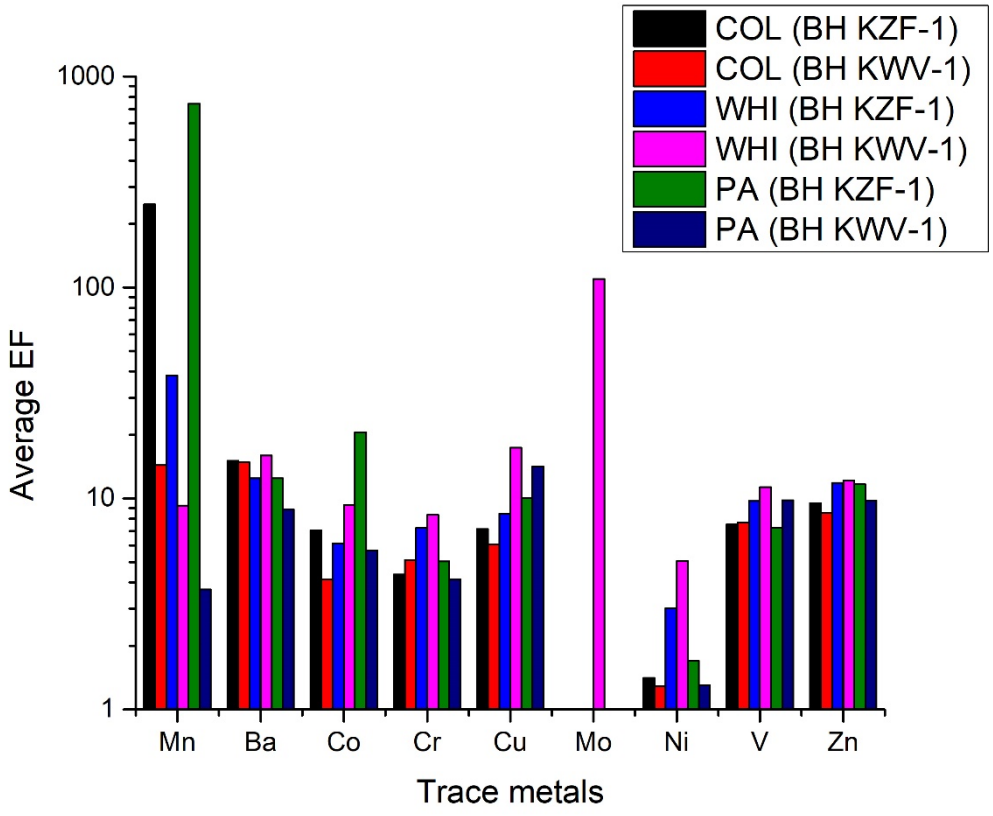

Figure 3.7: Enrichment factors of trace elements in BH KZF-1 and BH KWV-1. Abbreviations: EF: enrichment factor; COL= Collingham Formation; WHI= Whitehill Formation; PA = Prince Albert Formation.

3.4.3 Chemical Index of Alteration

The CIA (molar) method is applied to samples which have less than 30% carbonate content and CaO values have been corrected for carbonate minerals and phosphate minerals. Samples with more than 30 % carbonate content were excluded entirely. In total, 29 samples from BH KZF-1 and 16 samples from BH KWV-1 were analysed to calculate their CIA (Table 3.9 and 3.10).

Using Equation 3.1, CIA values range between 56.48 and 76.09 in BH KZF-1 and between 59.33 and 81.20 in BH KWV-1. On average, the CIA index in BH KZF-1 and KWV-1 is between 72 and 78 for the Prince Albert Formation, 64 and 67 for the Whitehill Formation and 64 and 66 for the Collingham Formation. The CIA index is the highest for the Prince Albert Formation and lowest for the Collingham Formation. In Figure 3.8 A, data from both boreholes indicate an albite to illite weathering trend. Illite, chlorite, kaolinite and smectite are clay minerals that increase the Al_2O_3, which indicates the degree of chemical weathering. These values suggest intermediate weathering and fall between typical granite and gabbro weathering trends marked on the diagram. Using CIA values obtained with Equation 3.2, Al_2O_3 vs CIA and K_2O/Na_2O vs CIA plots indicate that the lower Ecca Group plot similar to comparative samples obtained from areas with weathering conditions typical in arid and subtropical climates (Figure 3.8 B, C). CIA values plotted in depth profiles (Figure 3.9) show the changes between CIA trends for each formation. There is an overall decrease in the CIA index from Prince Albert Formation to the Collingham Formation in both boreholes.

Table 3.9: Chemical analysis and Chemical Index of Alteration from BH KZF-1. Abbreviations: CIA[a,b] = Chemical Index of Alteration calculated by: a) Nesbitt & Young (1982); b) Golden & Humayan (2010); CaO[*]= silicate-fraction of the sample. SD for CIA[a]= 5.8; CIA [b] = 0.7.

Formation	Sample	Na_2O	CaO*	K_2O	Al_2O_3	CIA[a]	CIA[b]
Collingham	KZF-1	3.49	1.11	2.90	12.60	63.00	1.70
Collingham	KZF-2	3.48	0.81	4.24	16.78	66.59	1.99
Collingham	KZF-3	4.70	1.68	2.39	12.51	59.10	1.45
Collingham	KZF-4	4.57	0.57	3.04	13.98	63.30	1.73
Collingham	KZF-5	1.19	1.19	5.69	20.78	72.04	2.58
Collingham	KZF-6	4.30	1.70	3.56	15.93	62.73	1.68
Collingham	KZF-7	1.35	1.35	7.23	26.32	72.60	2.65
Collingham	KZF-8	3.98	1.03	3.07	13.84	63.39	1.73
Collingham	KZF-9	3.48	0.78	3.55	13.63	63.85	1.77
Collingham	KZF-10	3.91	1.34	3.60	14.80	62.80	1.69
Collingham	KZF-11	4.91	1.66	1.98	11.30	57.22	1.34
Whitehill	KZF-12	5.61	1.56	2.98	14.09	58.35	1.40
Whitehill	KZF-13	3.35	1.24	3.60	15.16	65.37	1.89
Whitehill	KZF-14	3.54	0.74	4.20	17.19	67.31	2.06
Whitehill	KZF-15	2.78	1.61	3.21	14.27	65.83	1.93
Prince Albert	KZF-16	2.38	0.39	4.34	20.08	74.11	2.86
Whitehill	KZF-17	3.63	3.63	2.52	12.68	56.48	1.30
Whitehill	KZF-18	4.06	2.22	2.54	13.63	60.96	1.56
Whitehill	KZF-19	3.34	3.34	2.82	15.56	62.09	1.64
Whitehill	KZF-20	1.56	1.56	3.08	12.55	66.97	2.03
Whitehill	KZF-21	2.71	2.27	3.98	17.79	66.91	2.02
Whitehill	KZF-22	1.85	0.34	3.37	15.60	74.08	2.86
Prince Albert	KZF-23	2.03	2.03	3.34	14.57	66.31	1.97
Prince Albert	KZF-24	1.94	1.94	3.17	20.82	74.71	2.95
Prince Albert	KZF-25	2.74	1.33	3.28	18.00	71.93	2.56
Prince Albert	KZF-27	3.52	0.42	3.11	18.10	72.20	2.60
Prince Albert	KZF-30	1.66	0.36	3.60	17.57	75.94	3.16
Prince Albert	KZF-31	1.33	0.34	3.41	15.98	76.09	3.18
Prince Albert	KZF-33	1.48	1.34	4.40	12.60	70.39	2.38

Table 3.10: Chemical analysis and Chemical Index of Alteration from BH KWV-1. Abbreviations: CIA[a,b] = Chemical Index of Alteration calculated by: a) Nesbitt & Young (1982); b) Golden & Humayan (2010); CaO[*]= silicate-fraction of the sample. SD for CIA[a]= 6.6; CIA [b] = 0.8.

Formation	Sample no.	Na_2O	CaO*	K_2O	Al_2O_3	CIA[a]	CIA[b]
Collingham	KWV-1	3.71	1.17	4.61	18.74	66.69	2
Collingham	KWV-2	3.62	0.90	4.19	16.64	65.98	1.9
Collingham	KWV-3	4.81	1.58	2.39	12.62	59.33	1.5
Collingham	KWV-4	4.87	0.71	2.75	13.24	61.62	1.6
Collingham	KWV-05	2.62	1.91	4.86	19.88	68.11	2.1
Collingham	KWV-06	2.68	1.61	4.63	19.78	69.16	2.2
Collingham	KWV-07	1.78	1.78	3.69	17.09	70.23	2.4
Whitehill	KWV-08A	2.77	2.75	2.70	13.11	61.81	1.6
Whitehill	KWV-08B	1.50	1.50	2.63	15.21	72.98	2.7
Whitehill	KWV-09	3.99	2.64	3.48	16.58	62.43	1.7
Whitehill	KWV-10	2.86	1.48	4.00	16.10	66.20	2
Whitehill	KWV-11	1.31	1.31	3.32	17.01	74.08	2.9
Prince Albert	KWV-13	0.32	0.32	5.15	17.71	75.33	3.1
Prince Albert	KWV-14	1.22	1.22	1.99	19.12	81.20	4.3
Prince Albert	KWV-15	0.51	0.51	4.48	19.54	78.04	3.6
Prince Albert	KWV-16	0.50	0.50	4.09	18.42	78.38	3.6
Prince Albert	KWV-17	0.56	0.56	7.40	26.04	75.35	3.1

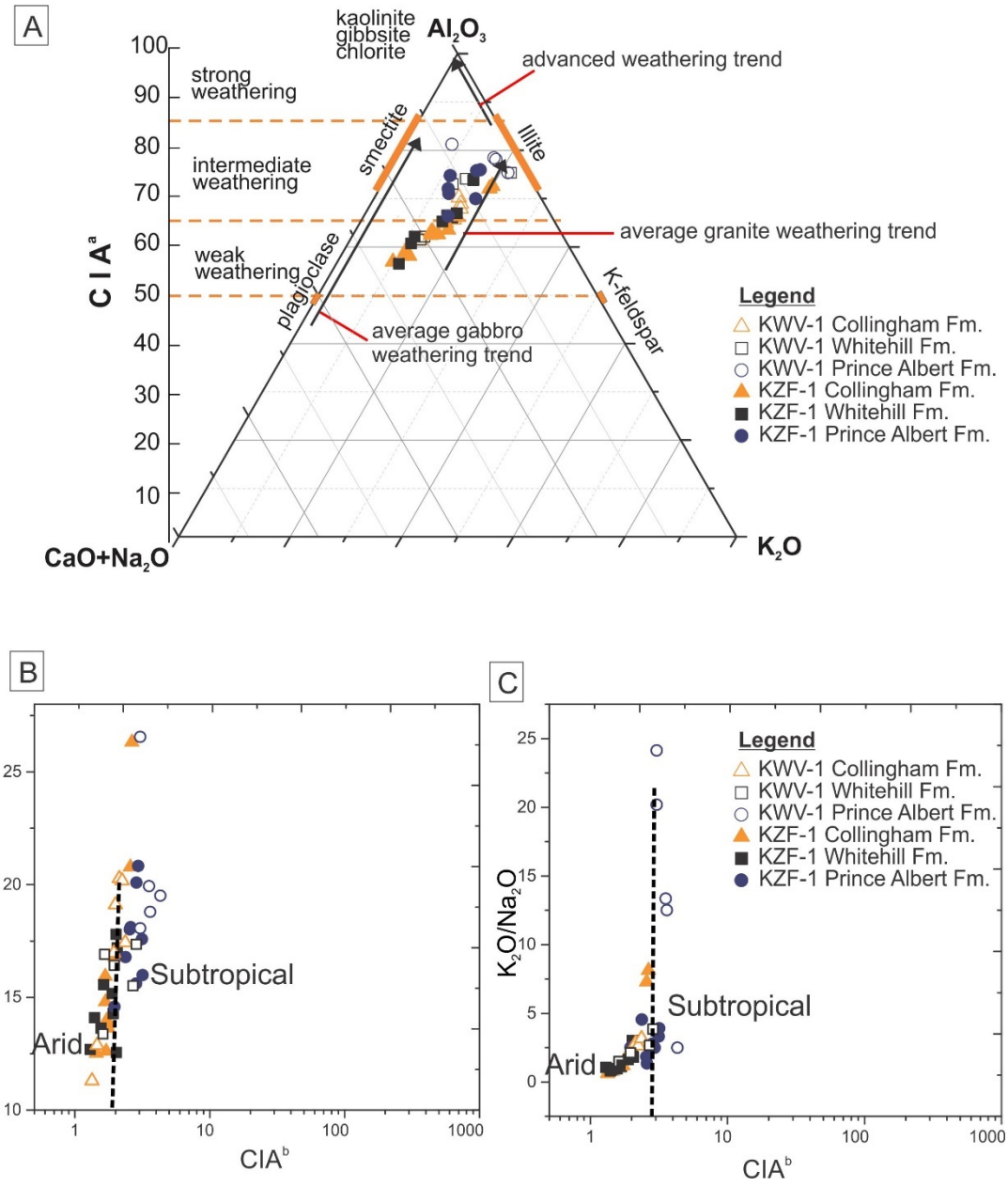

Figure 3.8: The Chemical Index of Alteration of the lower Ecca Group from BH KZF-1 and BH KWV-1. A) Ternary diagram indicating strength of weathering and weathering trend (adapted from Nesbitt and Young (1984)). B and C) Scatter plots of CIA versus Al_2O_3 and K_2O/Na_2O (adapted from Goldberg & Humayan (2010)). Abbreviations: Chemical Index of Alteration = CIA; $CIA^{a,b}$ = a) Nesbitt & Young (1982); b) Goldenberg & Humayan (2010).

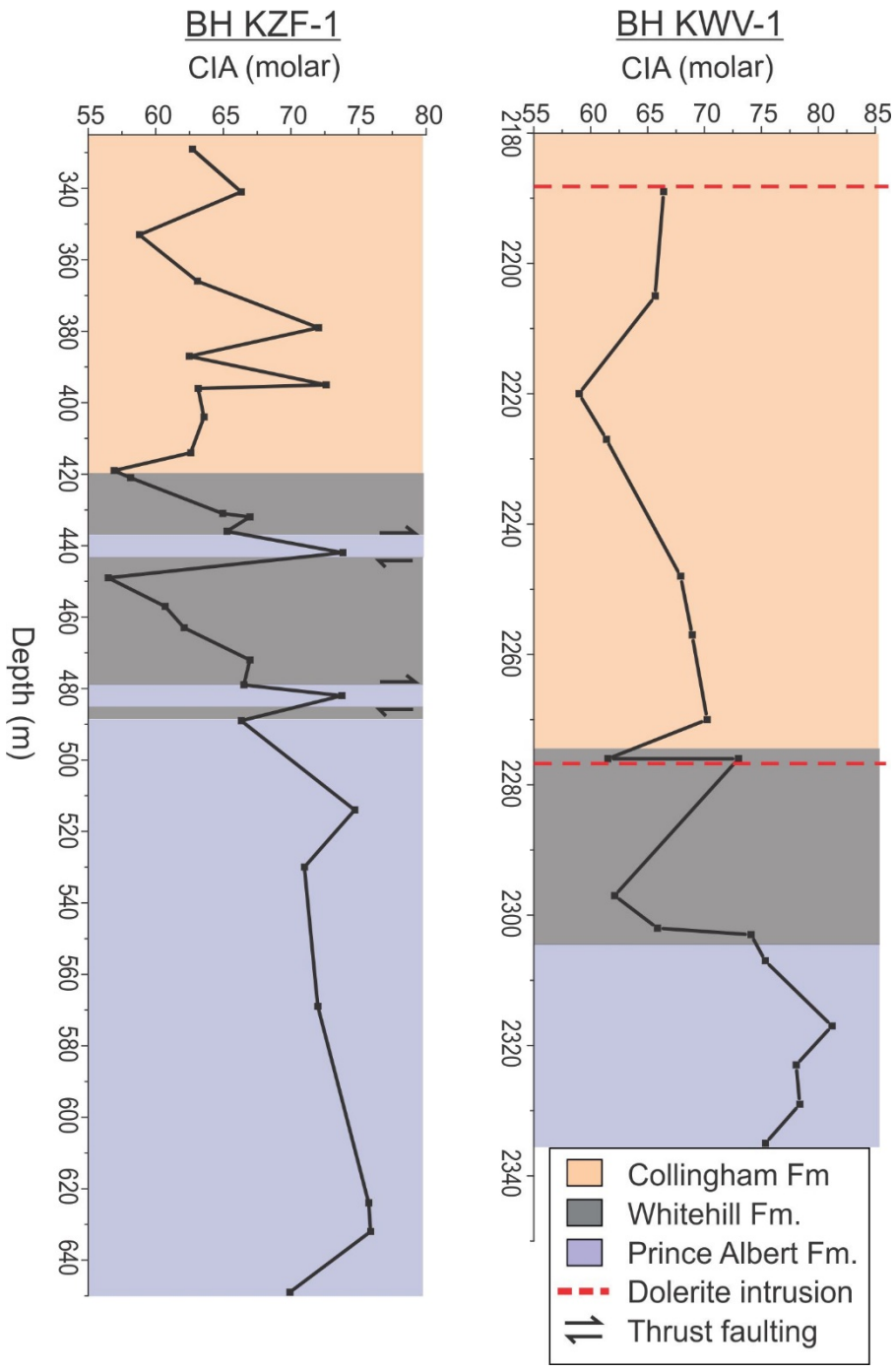

Figure 3.9: Depth profiles showing the Chemical Index of Alteration (CIA) signatures for BH KZF-1 and BH KWV-1.

3.4.4 Palaeo-environmental indicators

3.4.4.1 Petrographic micrograph observations

The Prince Albert Formation in BH KZF-1 shows evidence for bioturbation (Figures 3.10 A, B). Notable authigenic minerals are: rhodochrosite, birnessite and greenalite (Figures 3.10 B, C). In BH KWV-1, the Prince Albert Formation contains bioturbation structures (Figure 3.11 A) and fossilized agglutinated foraminifera, which is very tentatively identified as *Textularia* (Figure 3.11 B; Mikhalevich & Kaminski, 2008; Kaminski, 2014).

In the Whitehill Formation, bioturbation structures were not observed in hand specimen or thin section. Sample KZF11 from BH KZF-1 displays crinkly carbonaceous parallel laminae which may be cautiously interpreted as benthic microbial filaments (Figure 3.12 A). Sample KZF19 from BH KZF-1 displays soft-sediment deformation structure with possible microbial filaments within a silty layer (Figure 3.12 B). More convincing filamentous microbial layers in a silt-rich horizon were also identified in BH KWV-1 (Figure 3.12 F). Phosphate and dolomite nodules were detected in BH KZF-1 (Figures 3.12 C–E), whereas only phosphate nodules were detected in BH KWV-1 (Figure 3.12 G).

Bioturbation and soft sediment deformation structures are common in the Collingham Formation in both boreholes (Figure 3.13). Organic matter aggregates were observed in both boreholes as well as euhedral and anhedral apatite grains (Figures 3.13 H, I).

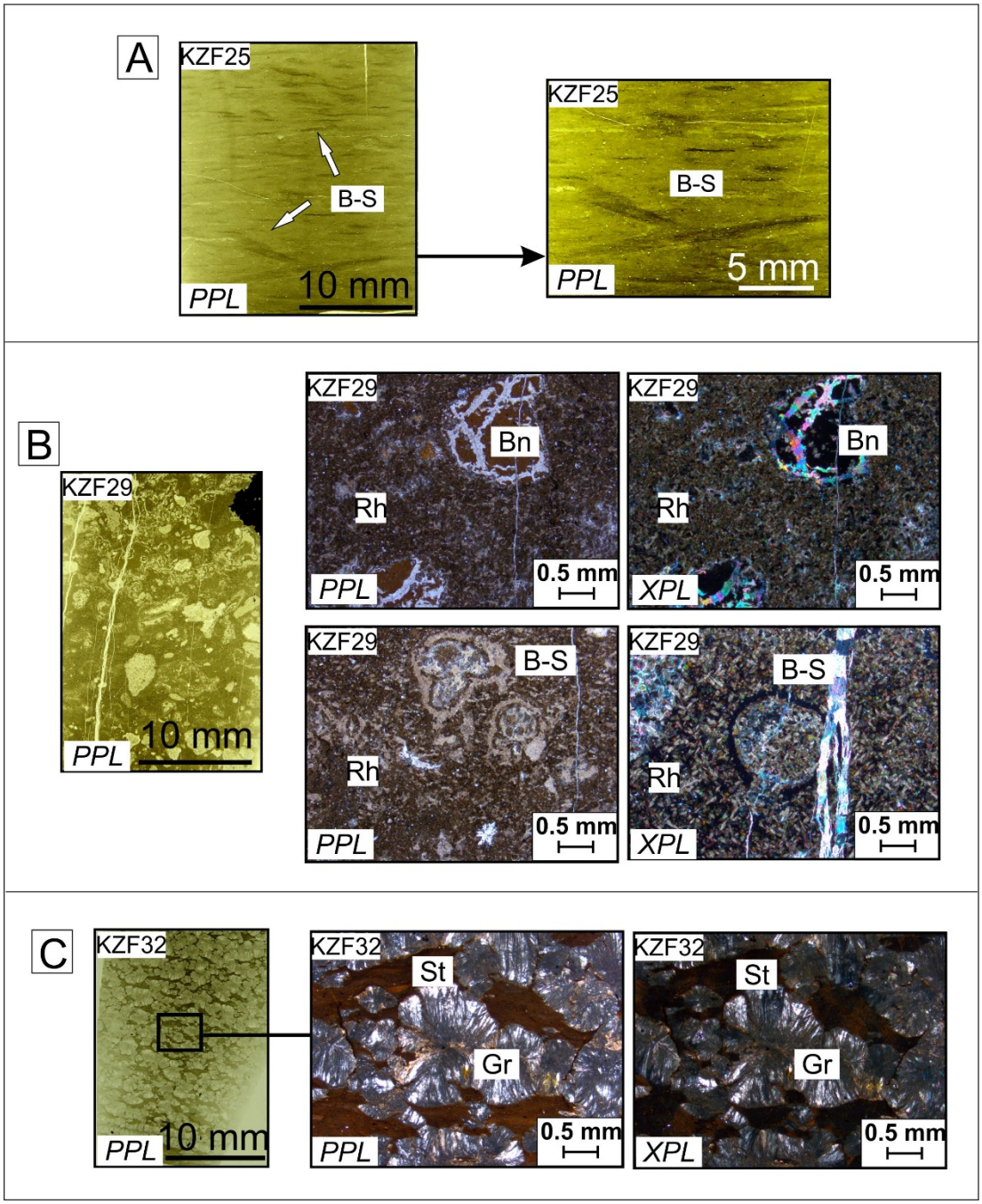

Figure 3.10: Thin section micrographs from the Prince Albert Formation from BH KZF-1. A) Bioturbation structures. B) Birnessite nodules, rhodochrosite and bioturbation structures. C) Greenalite. Abbreviations: B-S: bioturbation structure; Rh: rhodochrosite; Gr: greenalite; St: stilpnomelane.

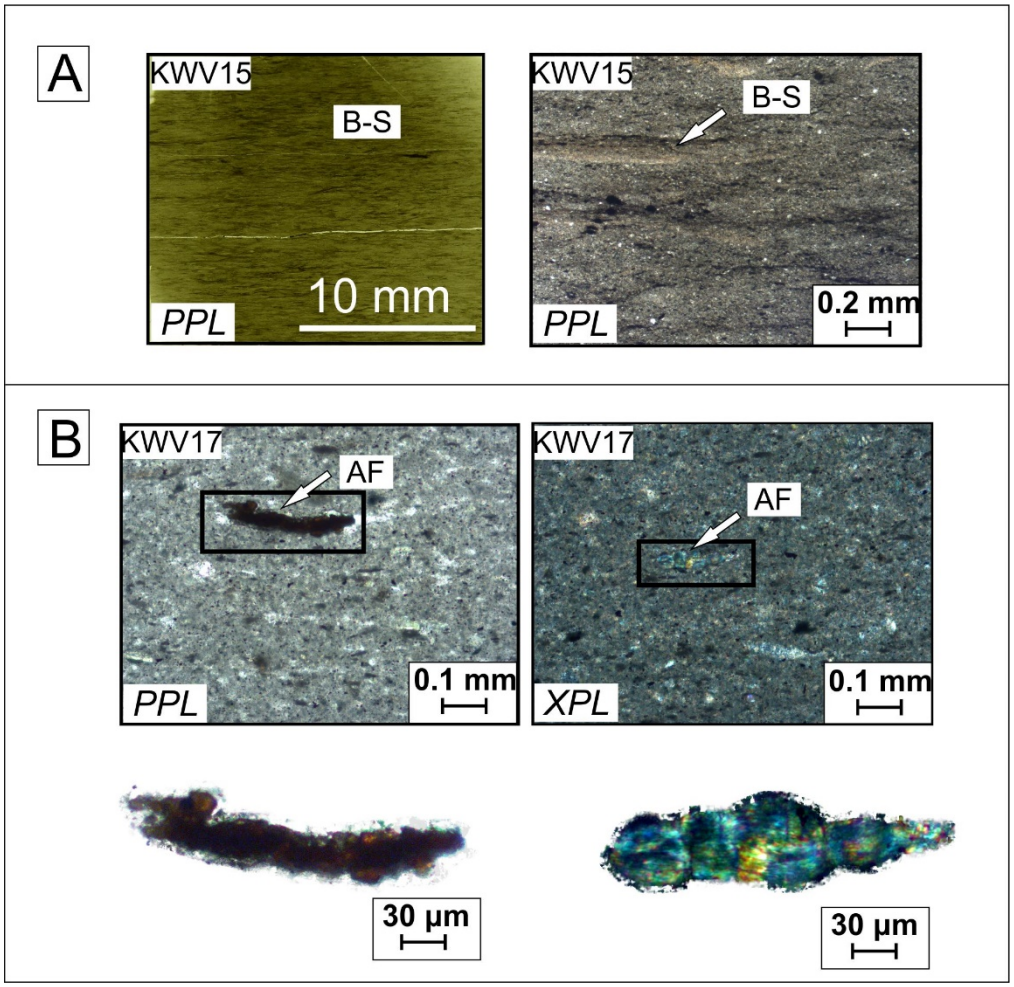

Figure 3.11: Thin section micrographs from the Prince Albert Formation from BH KWV-1. A) Bioturbation structures. B) Agglutinated foraminifera. Abbreviations: B-S: bioturbation structure; AF: agglutinated foraminifera.

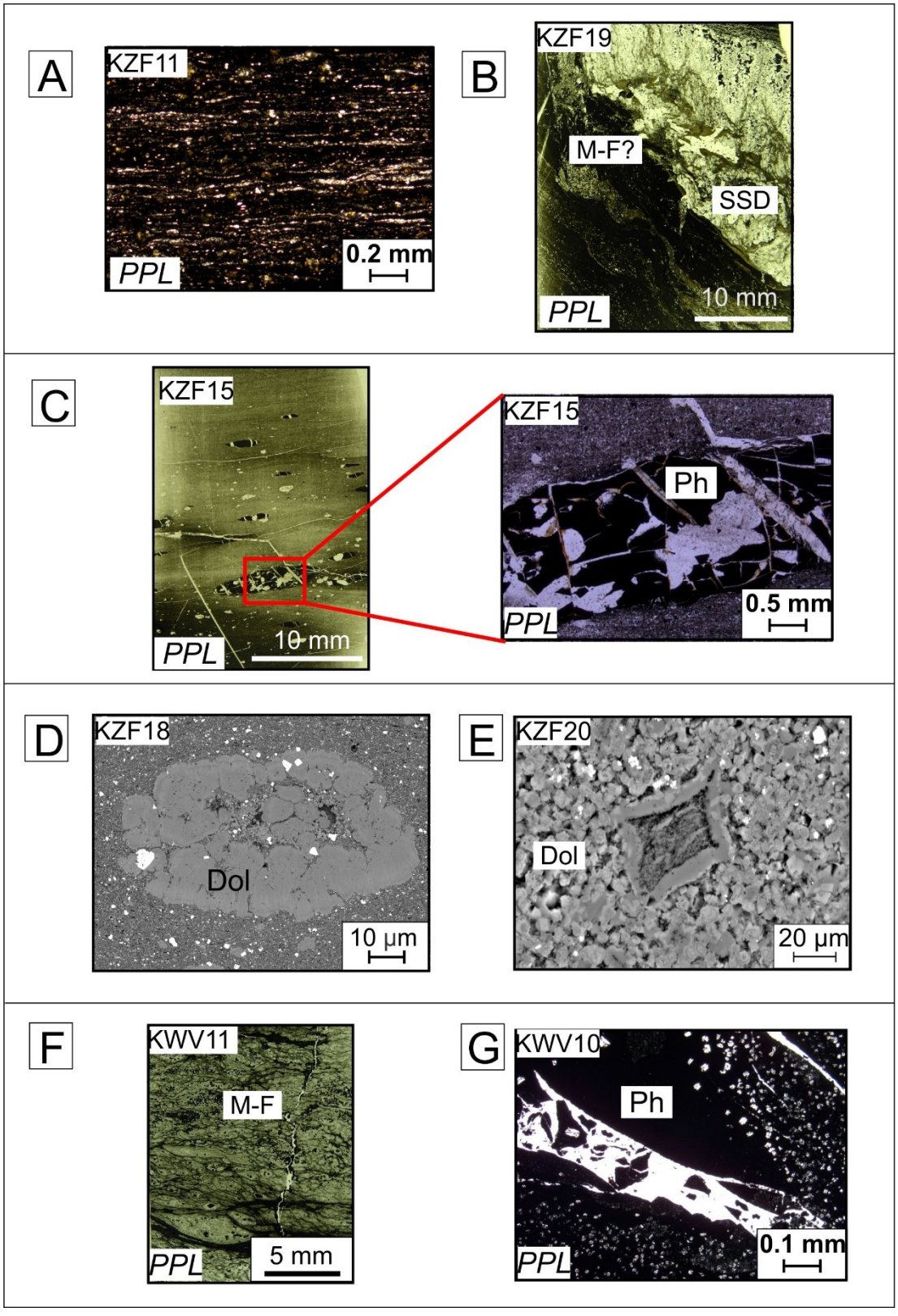

Figure 3.12: Thin section (A–C), microprobe (D) and SEM (E) images from the Whitehill Formation in BH KZF-1 and thin section images (F–G) from BH KWV-1. A) Organic matter rich laminae. B) Possible microbial filaments and soft-sediment deformation structures. D, E) Dolomite nodule. F) Microbial filaments. Abbreviations: SSD: soft-sediment deformation structure; M-MF: microbial filaments; Dol: dolomite; Ph: phosphate.

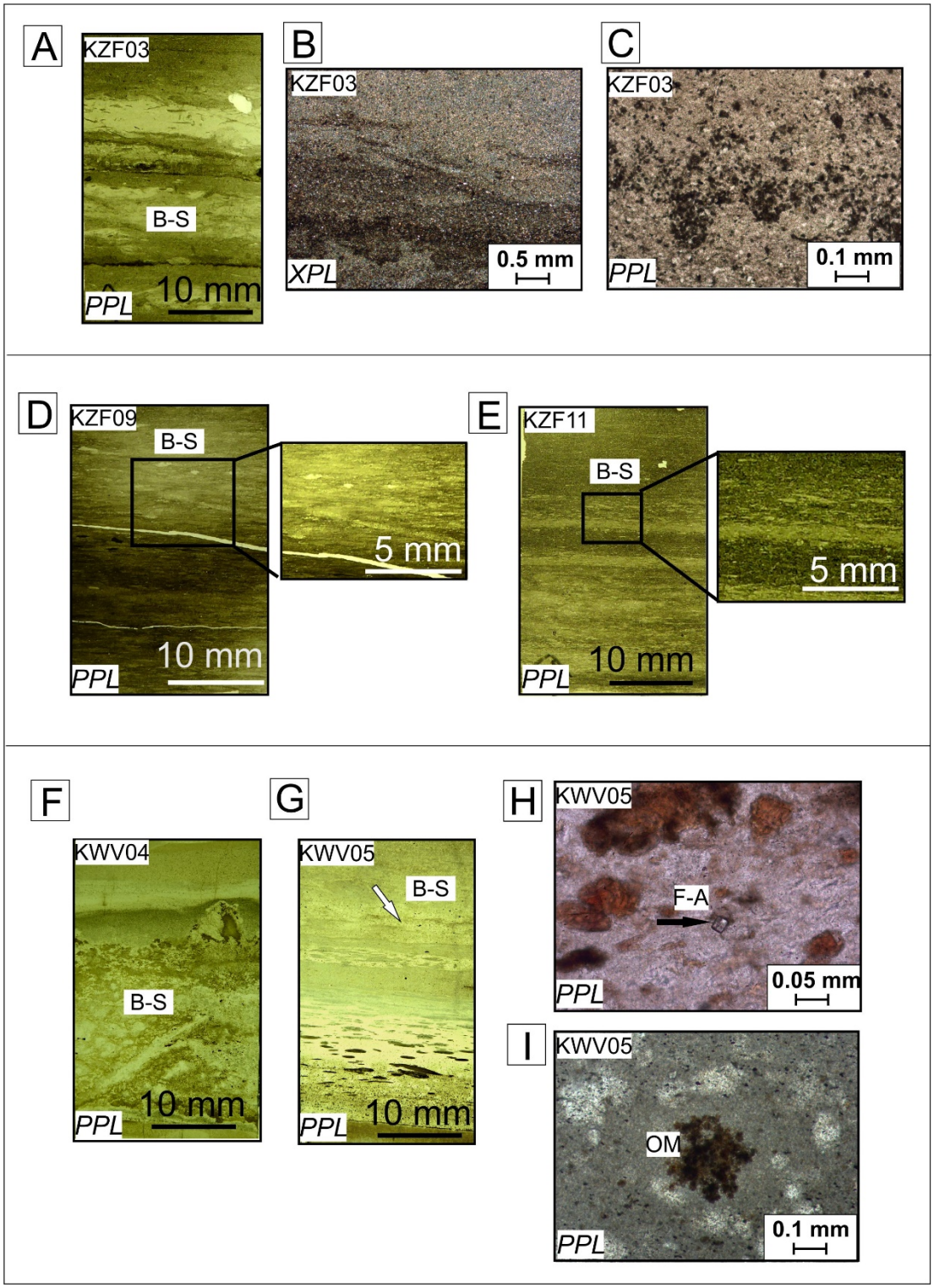

Figure 3.13: Thin section micrographs from the Collingham Formation from BH KZF-1 (A–E) and BH KWV-1 (F–I). A–G) Bioturbation structures. H) Euhedral apatite grain. I) Organic matter aggregate. Abbreviations: B-S: bioturbation structure; F-A: fluorapatite; OM: organic matter.

3.4.4.2 Palaeo-environmental proxies

In the Prince Albert Formation (BH KZF-1), Fe_2O_3/Al_2O_3, CaO/Al_2O_3, MgO/Al_2O_3, MnO/Al_2O_3 and P_2O_5/Al_2O_3 values are very high relative to other elements in other formations (Figures 3.14; 3.16). Therefore, the log ratios must be used in order to observe trends. These oxides trends correlate with one another as a response to mudstone layers rich in carbonate, manganese and phosphate. Si_2O/Al_2O_3 values are the highest in the lower Prince Albert Formation but decrease near the contact with the Whitehill Formation. Si_2O/Al_2O_3 values are the lowest in the Whitehill Formation, increasing in content near the base of the Collingham Formation (Figure 3.15). Fluctuations with SiO_2/Al_2O_3 and K_2O/Al_2O_3 in the Collingham Formation indicate alternating clay-rich and quartz- and albite-rich beds. Na_2O/Al_2O_3 values are lowest in the Prince Albert Formation but increase in the Whitehill and Collingham formations. TOC follows similar trends with Ni/Co, especially in the Whitehill Formation. TOC also follows similar trends to Cu in the Prince Albert and Collingham formations (Figure 3.17). The highest peak of S is associated with the thrust zone and is probably hydrothermal in origin. Zn/Al_2O_3 values are the highest for the Prince Albert Formation and correlate with Ni/Co values in the Collingham Formation only (Figure 3.17).

In BH KWV-1, log-ratios were not used, because the trends and correlations could be observed by plotting the ratios in wt% (Figures 3.18–3.21). SiO_2/Al_2O_3 values are the highest in the Collingham Formation. In all three formations, SiO_2/Al_2O_3 trends correlate with Na_2O/Al_2O values and with increases in quartz and albite. K_2O/Al_2O correlate with illite and kaolinite trends. A significant difference between BH KWV-1 and BH KZF-1 is that in BH KWV-1 the Fe_2O/Al_2O_3 ratio trends correlate with S/Al_2O_3, pyrite, pyrrhotite, TOC and Cu. It is only at the base of the Prince Albert Formation where Cu does not correlate with Fe_2O/Al_2O_3. Ba/Al_2O_3 and P_2O_5/Al_2O_3 values follow similar trends in the Whitehill Formation. CaO/Al_2O_3 and MnO/Al_2O_3 values have correlating trends with the highest peaks in the Prince Albert Formation. Siderite and MnO/Al_2O_3 and P_2O_5/Al_2O_3 peak correlate with one another in sample KWV03, in the Collingham Formation.

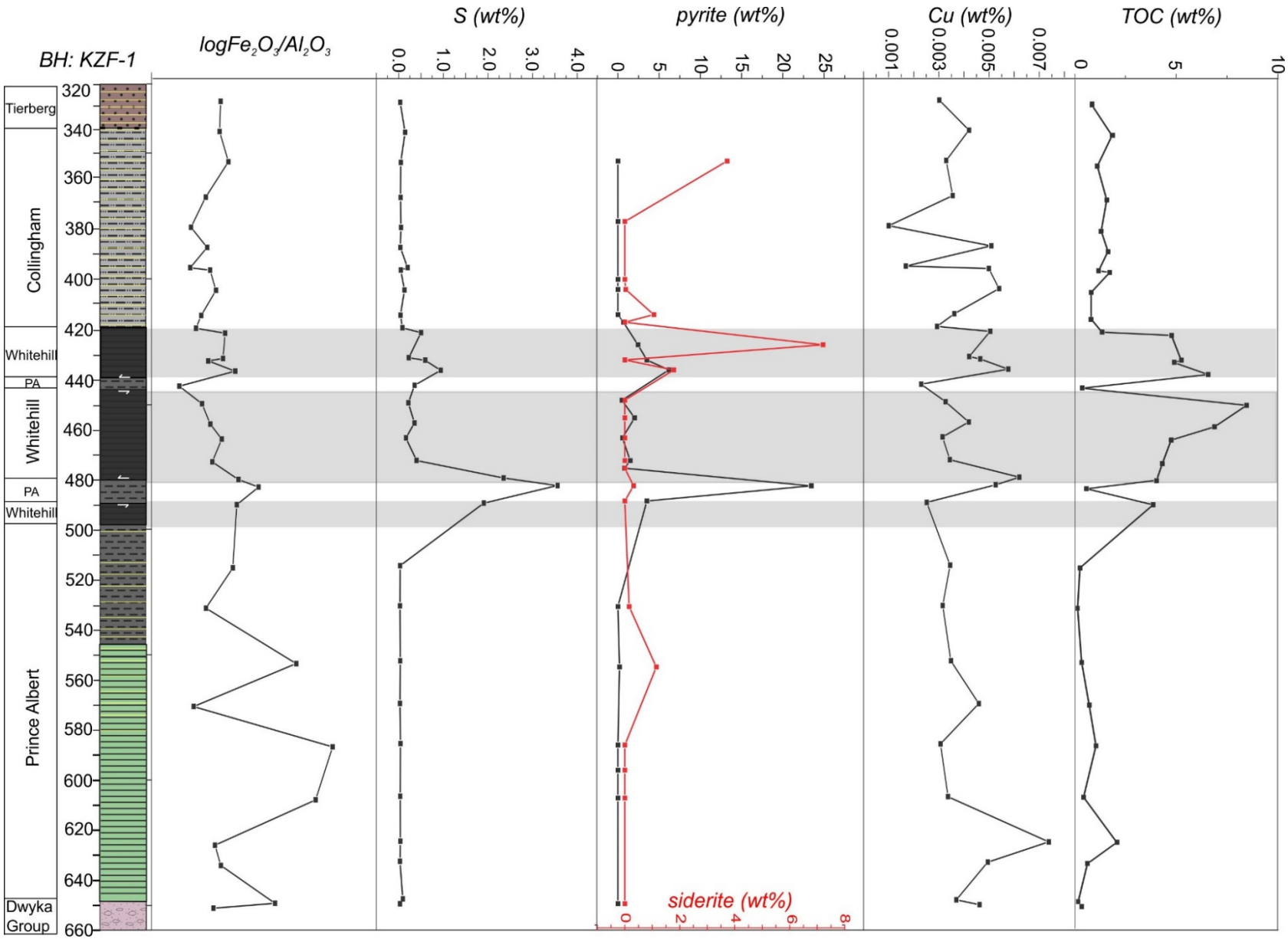

Figure 3.14: Depth profile for BH KZF-1 comparing Fe_2O_3/Al_2O_3; S; pyrite; Cu and TOC. See Figure 3.2 for stratigraphic legend.

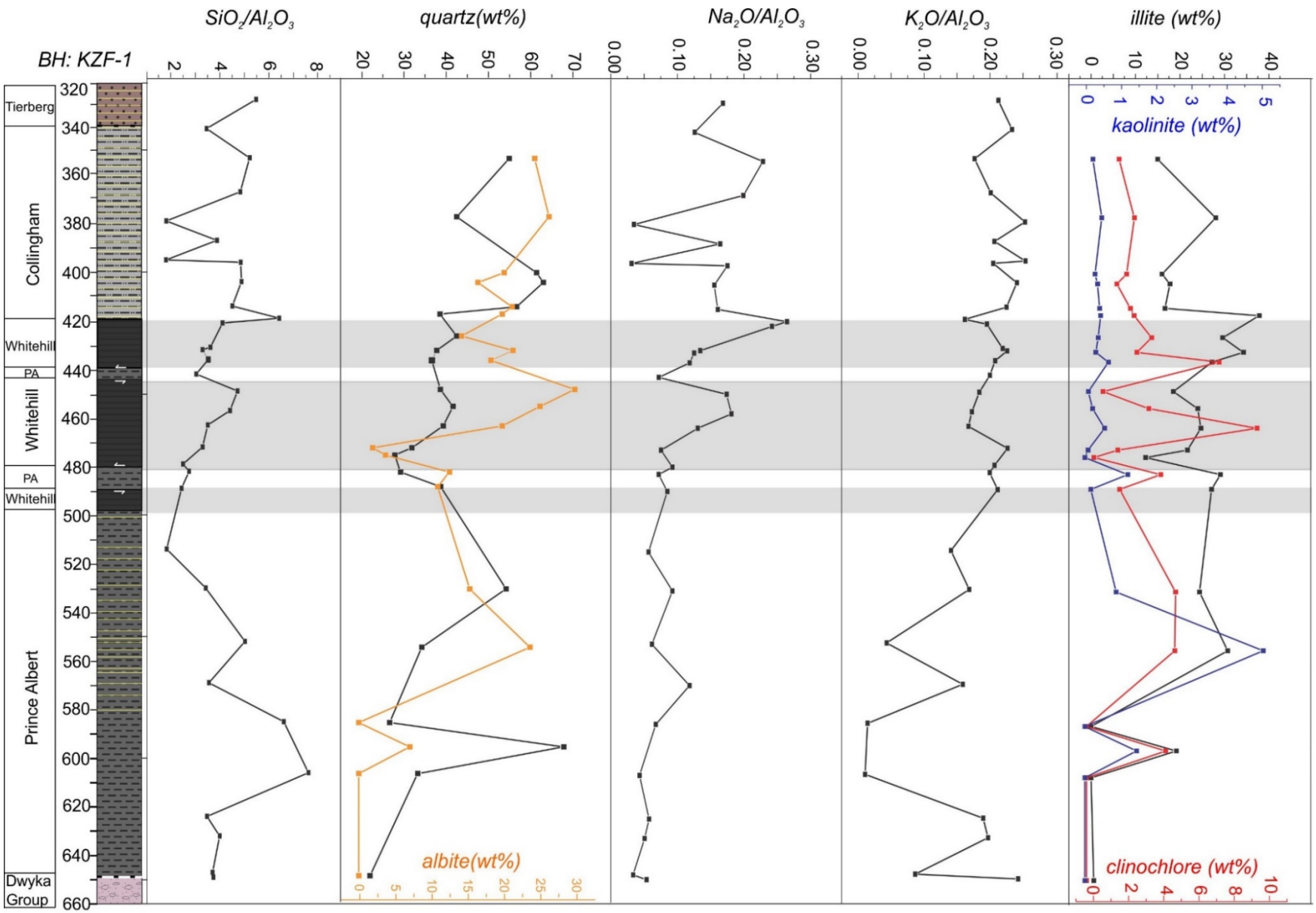

Figure 3.15: Depth profile for BH KZF-1 comparing SiO/Al_2O_3; quartz; albite; Na_2O/Al_2O_3; K_2O/Al_2O_3; illite; kaolinite and clinochlore. See Figure 3.2 for stratigraphic legend.

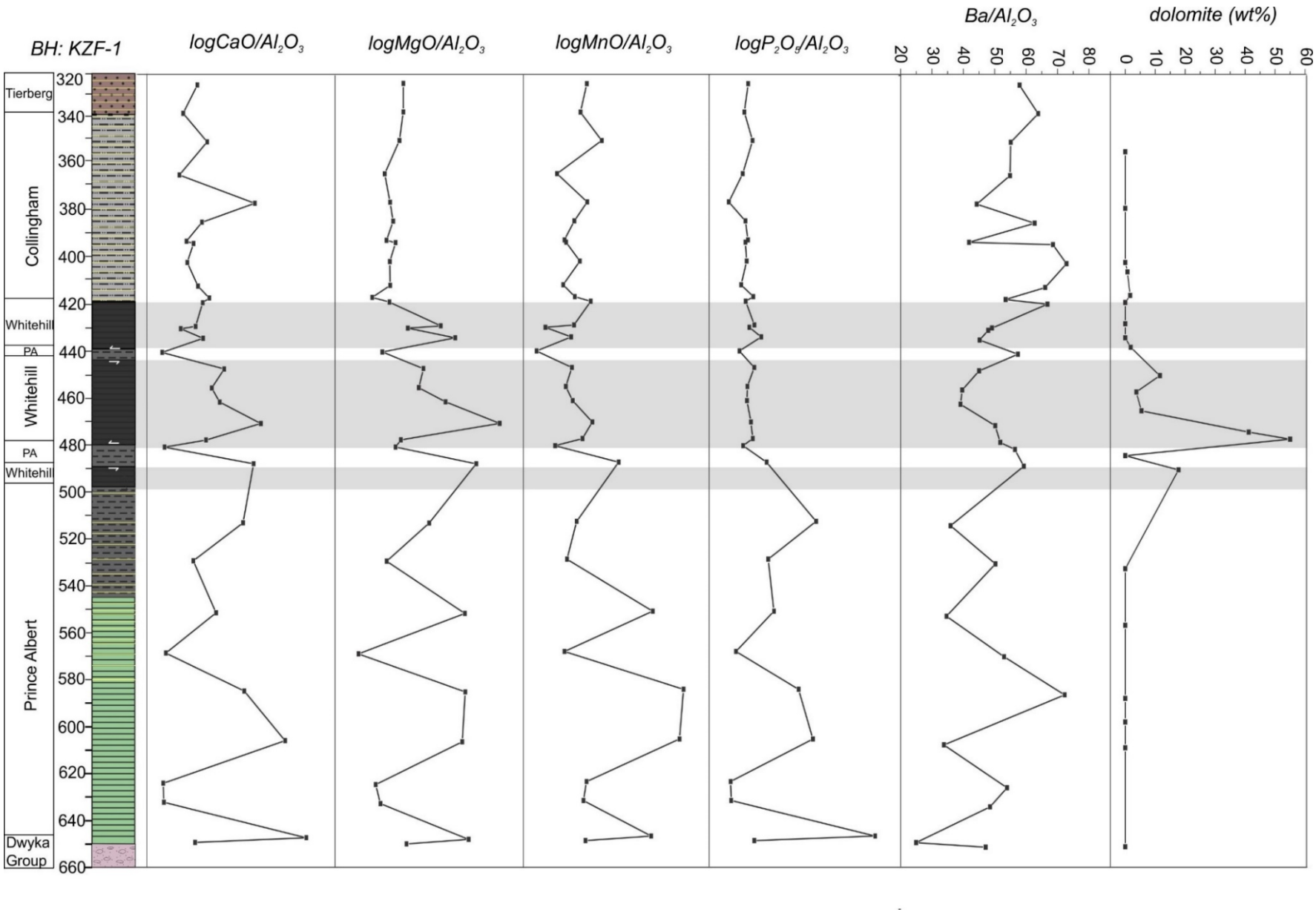

Figure 3.16: Depth profiles for BH KZF-1 comparing CaO/Al_2O_3; MgO/Al_2O_3; P_2O_5/Al_2O_3; Ba/Al_2O_3 and dolomite. See to Figure 3.2 for stratigraphic legend.

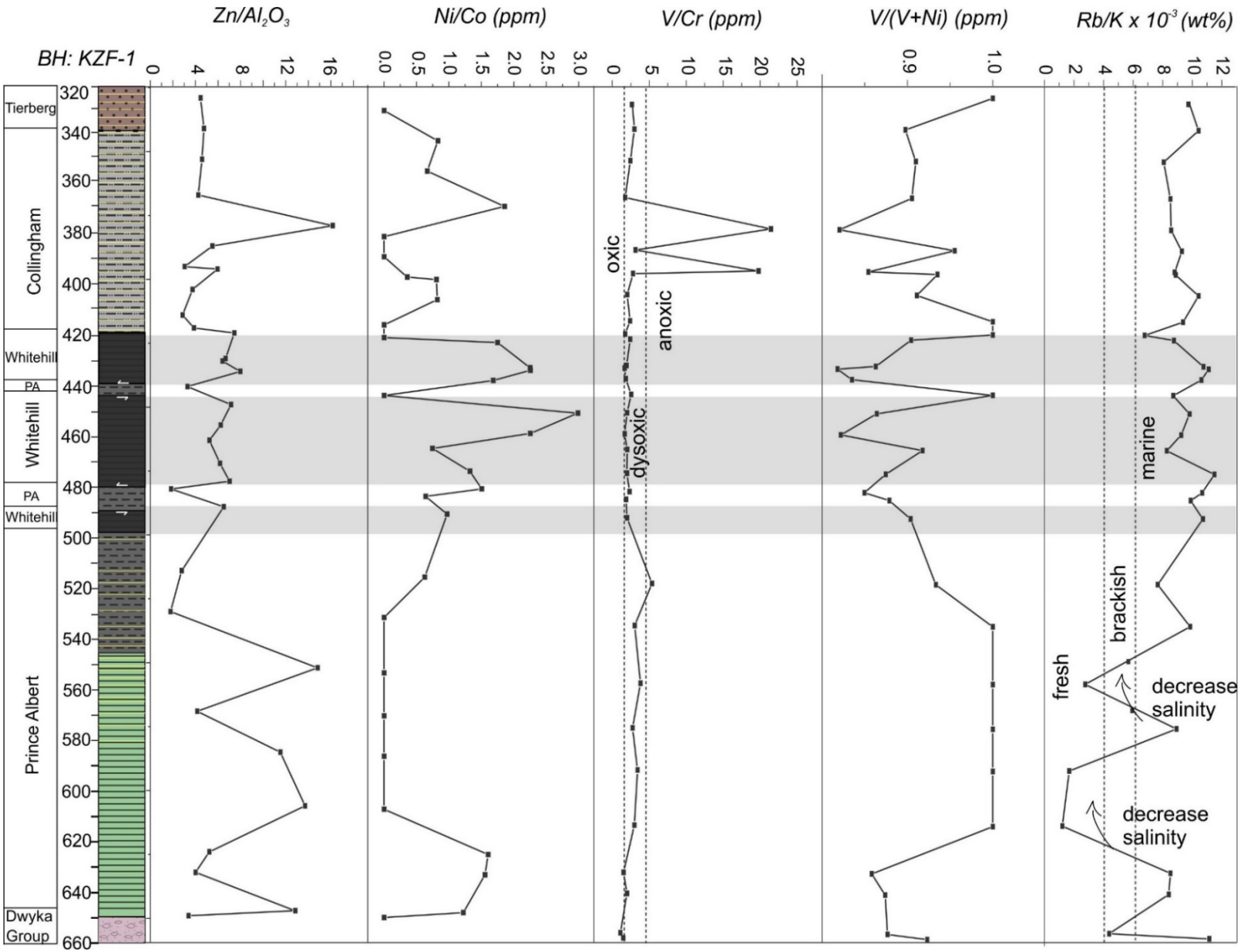

Figure 3.17:Depth profile for BH KZF-1 comparing Zn/Al_2O_3; Ni/Co; V/Cr; V/(V+Ni) and Rb/K. See to Figure 3.2 for stratigraphic legend.

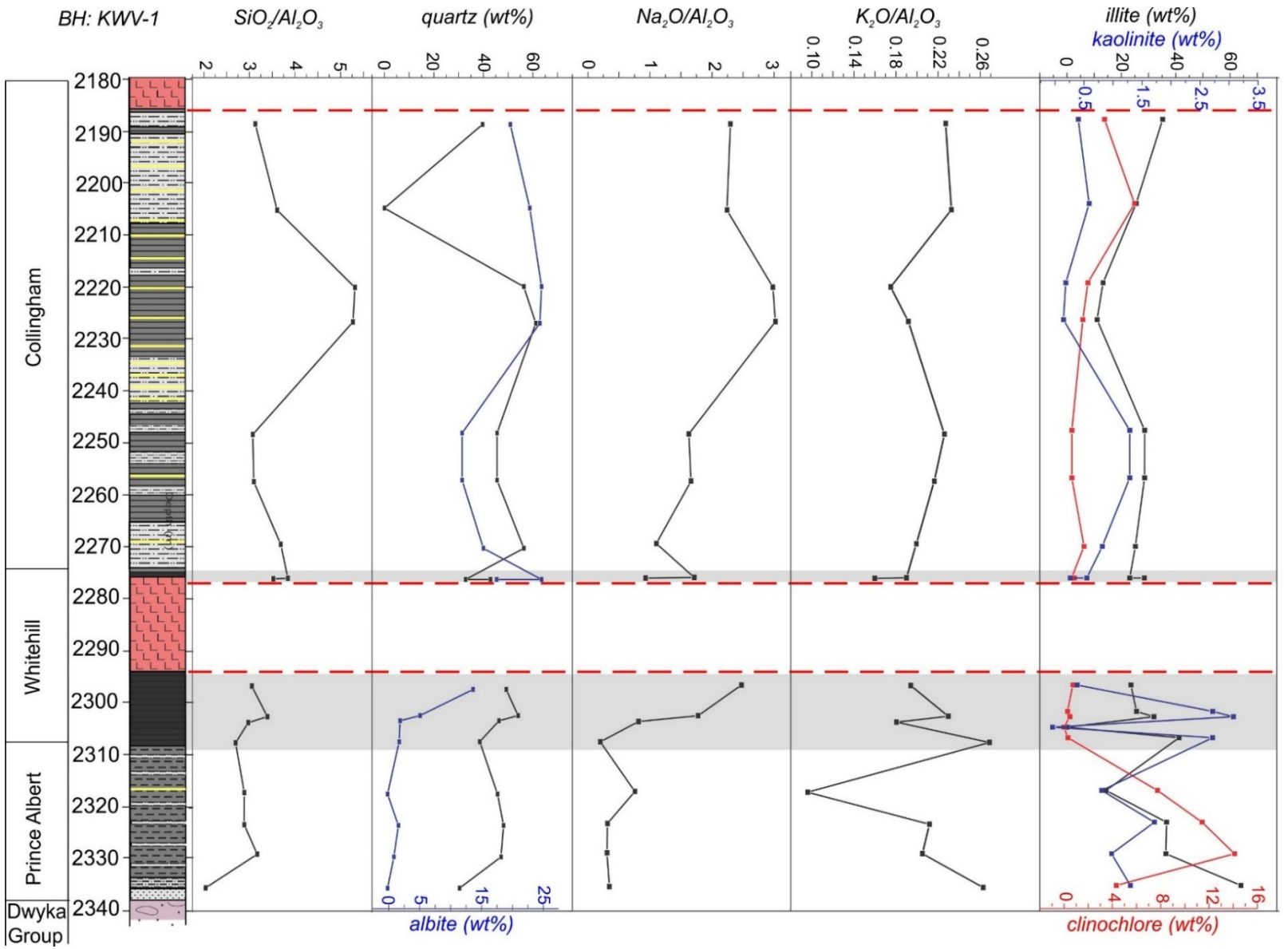

Figure 3.18: Depth profiles for BH KWV-1 comparing Si_2O/Al_2O_3; quartz; albite; Na_2O/Al_2O_3; K_2O/Al_2O_3; illite; kaolinite and clinochlore. Red dashed line = dolerite. See to Figure 3.2 for stratigraphic legend.

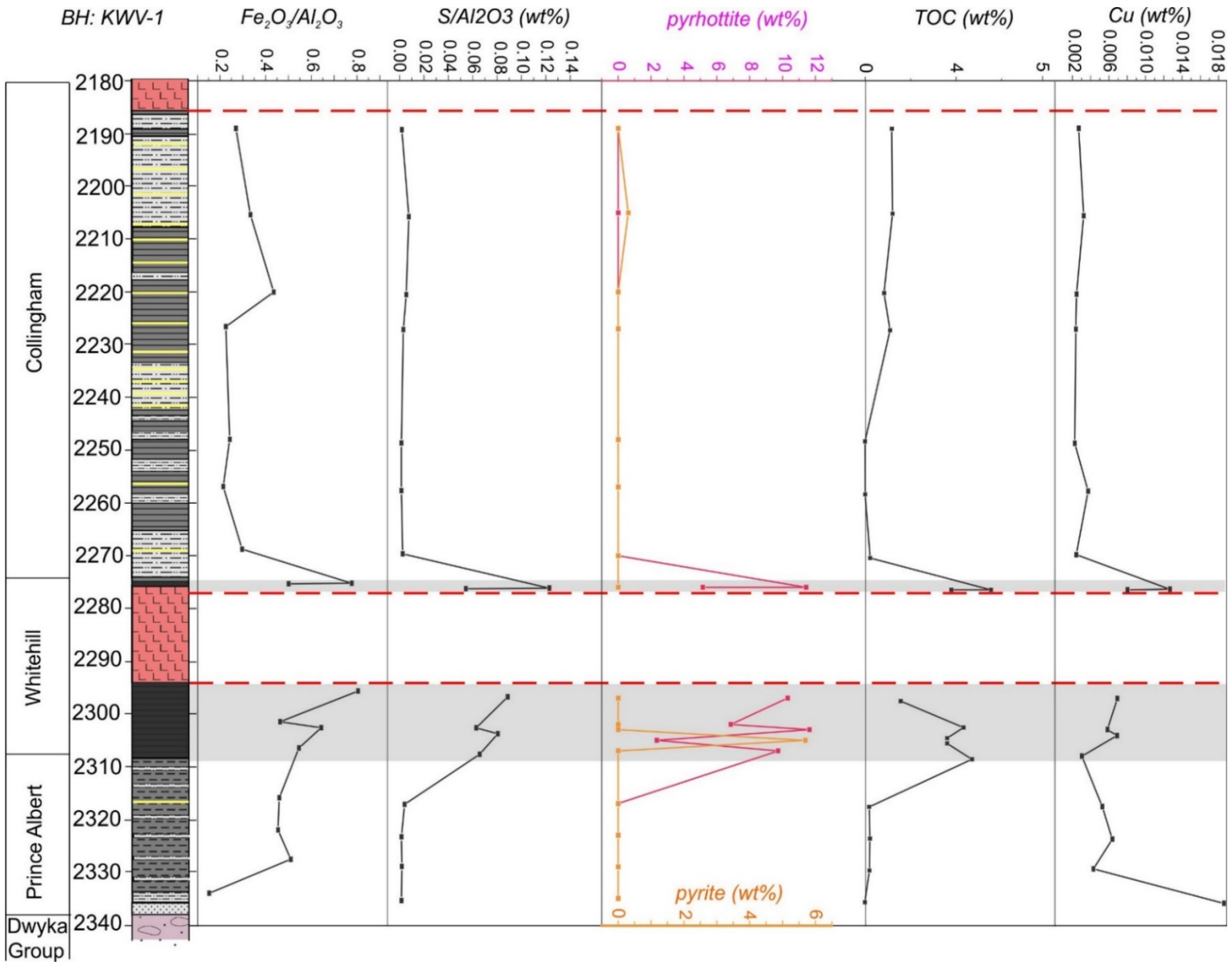

Figure 3.19: Depth profiles for BH KWV-1 comparing Fe_2O/Al_2O_3; S/Al_2O_3; pyrrhotite; pyrite; TOC and Cu. Red dashed line = dolerite. See to Figure 3.2 for stratigraphic legend.

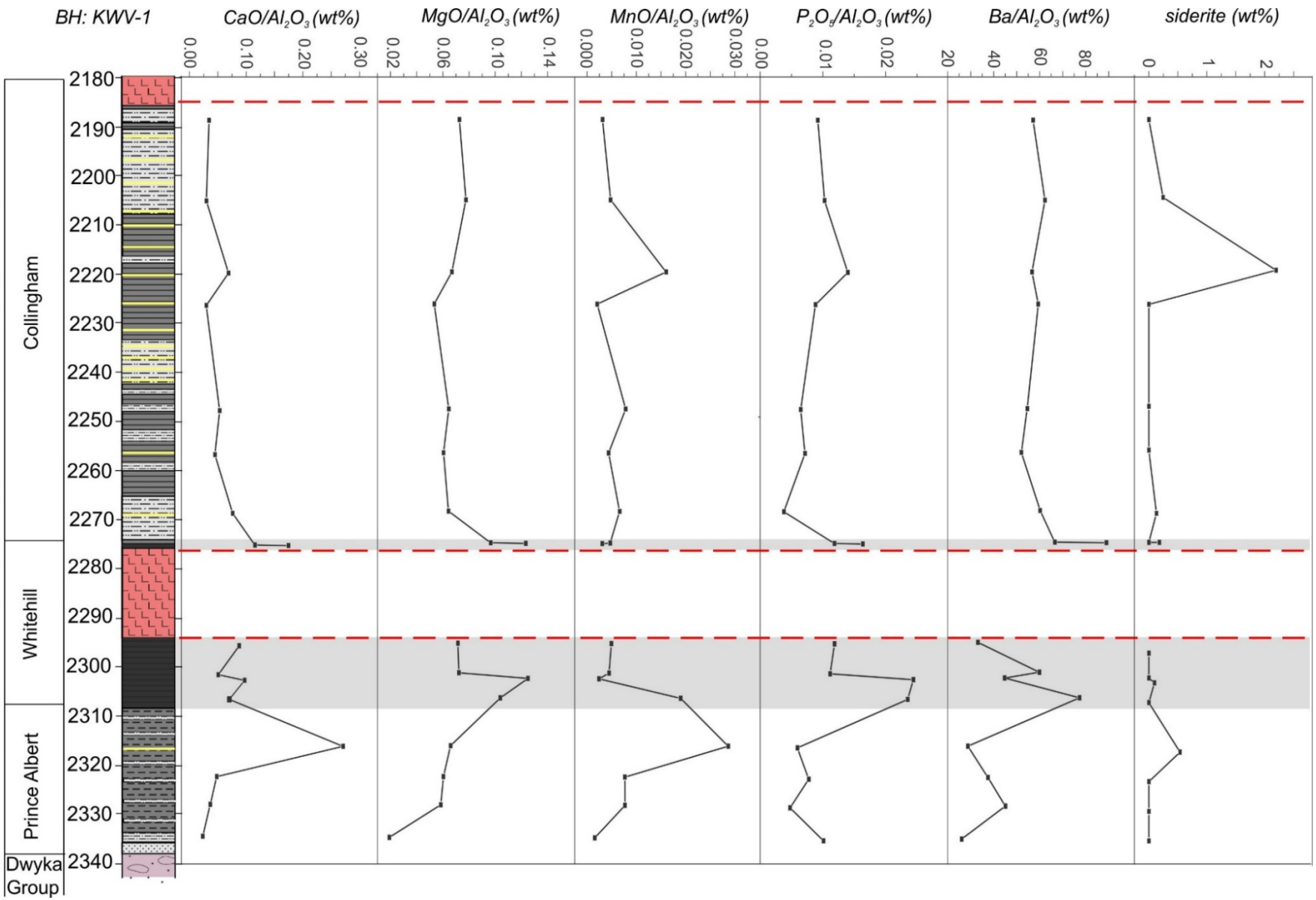

Figure 3.20: Depth profiles for BH KWV-1 comparing CaO/Al_2O_3; MgO/Al_2O_3; MnO/Al_2O_3; P_2O_5/Al_2O_3; Ba/Al_2O_3 and siderite. Red dashed line = dolerite. See Figure 3.2 for stratigraphic legend.

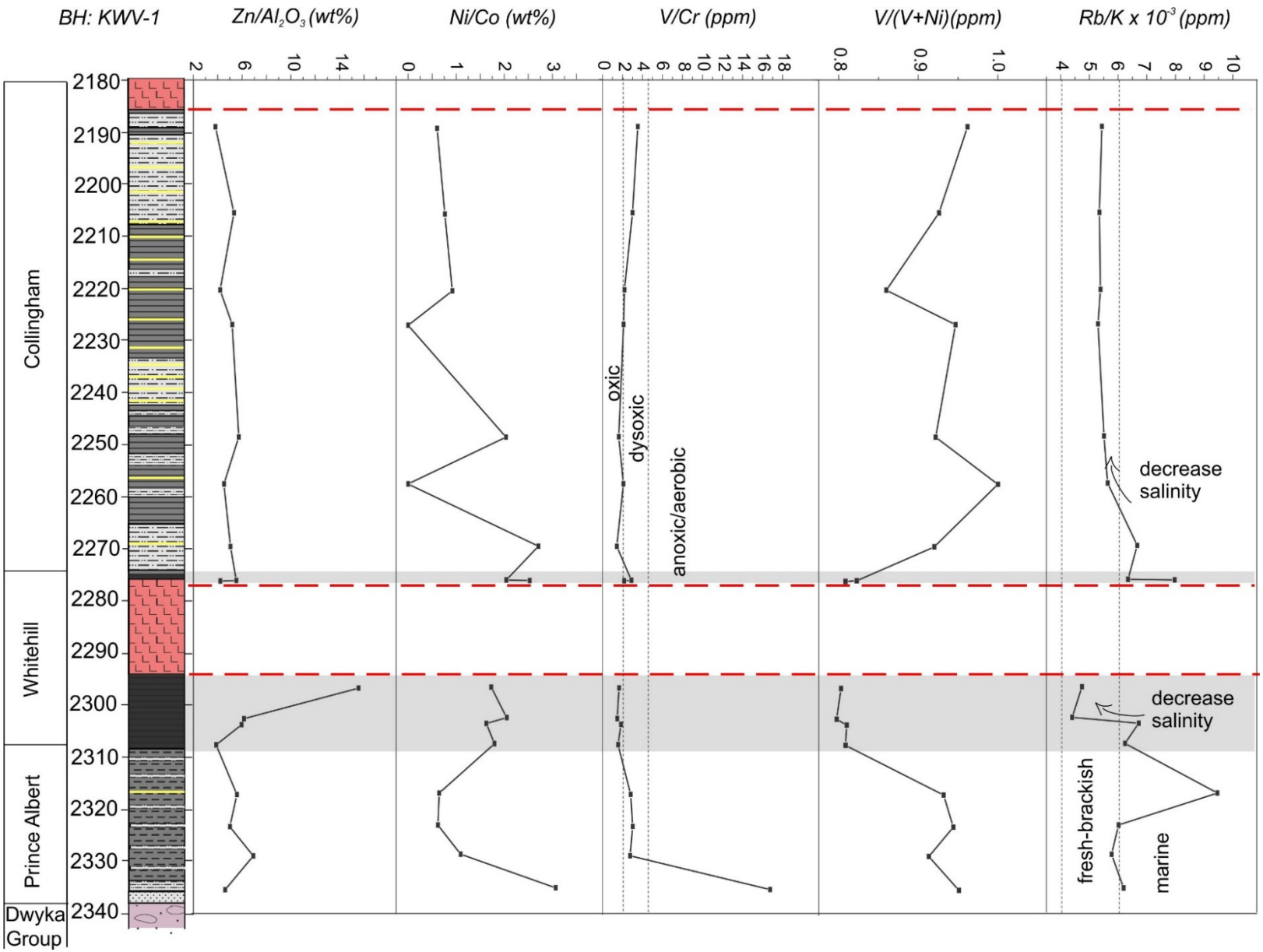

Figure 3.21: Depth profile for BH KWV-1 comparing Zn/Al_2O_3; Ni/Co; V/Cr; V/(V+Ni) and Rb/K. Red dashed line = dolerite. See Figure 3.2 for stratigraphic legend.

3.4.4.2.1 V/(V+Ni) and V/Cr

In both boreholes, V/(V+Ni) values range between 0.8 and 1. High V/(V+Ni) values indicates relatively low sedimentation rate overall for both the western and eastern MKB. Relative to TOC content, the Prince Albert and Collingham formations have higher sedimentation rates than the Whitehill Formation (Figure 3.22).

V/Cr values < 2 indicates oxic conditions, 2–4.25 dysoxic and > 4.25 suboxic to anoxic conditions (Hatch & Leventhal, 1992; Jones & Manning, 1994). In both boreholes, V/Cr values indicate mostly anoxic to dysoxic conditions for the Prince Albert Formation and dysoxic to oxic conditions for the Whitehill and Collingham formations (Figure 3.17; 3.21).

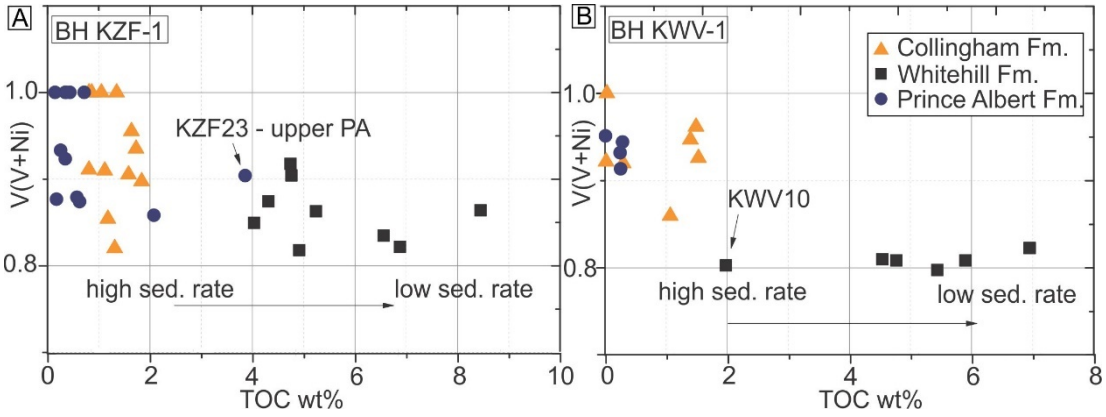

Figure 3.22: Plot of V/V+Ni against TOC (wt%) for a) BH KZF-1, and b) BH KWV-1. Adapted from Arthur & Sageman (1994). Abbreviations: PA = Prince Albert Formation; TOC = total organic carbon; sed. = sedimentation.

3.4.4.2.2 Fe-S-TOC

In depth profile, the log for Fe_2O/Al_2O_3 within the Prince Albert Formation (BH KZF-1) displays high peaks, which correlate with Fe-rich carbonate minerals (Figures 3.14; 3.16). These samples are excluded when plotting Fe versus S in scatter graphs for BH KZF-1 (Figures 3.24 A; 3.25 A). In the BH KWV-1 depth profiles, Fe_2O/Al_2O_3 trends correlate with S/Al_2O_3, pyrite, pyrrhotite, TOC (Figure 3.19).

In both boreholes, Fe and S content is moderately correlated (Figures 3.24 A, B; 3.25 A). In BH KZF-1, low carbonate samples show a moderate positive regression trend (r^2 = 0.5) and BH KWV-1, only samples from the Whitehill Formation similarly display a moderate positive regression trend (r^2 = 0.5). Samples KZF01P to KZF10P, in BH KZF-1 are plotted using total S values versus Fe (Figure 3.25). A weak to moderate positive regression trend line (r^2 = 0.4) is plotted for samples from the Whitehill and Collingham formations. There is a very weak positive trend (r^2 = 0.2) for S and TOC

in BH KZF-1 (Figure 3.24 B, C; 3.25 B) and a moderate to strong correlation between S and TOC is detected in BH KWV-1 ($r^2 = 0.7$).

In Fe-S-TOC ternary diagrams, limitation lines are drawn in with their respective ratios (OC/S = 2.5 or S/OC= 0.4; S/Fe = 0.57; S/Fe= 1.15; Figures 3.24 E–F; 3.25 C). In both boreholes, samples fall close, or left of, the OC/S limitation line. This is the approximation of a regression slope using “normal” marine sediments from the Holocene that were deposited in oxic conditions (Dean & Arthur, 1989). The regression slopes for S/OC for BH KZF-1 is 0.2 and BH KWV-1 is 0.7 (Figure 3.24 A, B). The S/Fe= 1.15 stoichiometric-pyrite line indicates when nearly all the S and Fe are deposited as pyrite and suggests an euxinic setting. Some samples from the Whitehill Formation in BH KZF-1 plot near the FeS line. In the ternary plot (Figure 3.25 C) that uses total S values, one sample from the Whitehill Formation plots below the euxinic line and two samples near FeS line, which indicates dysoxic conditions.

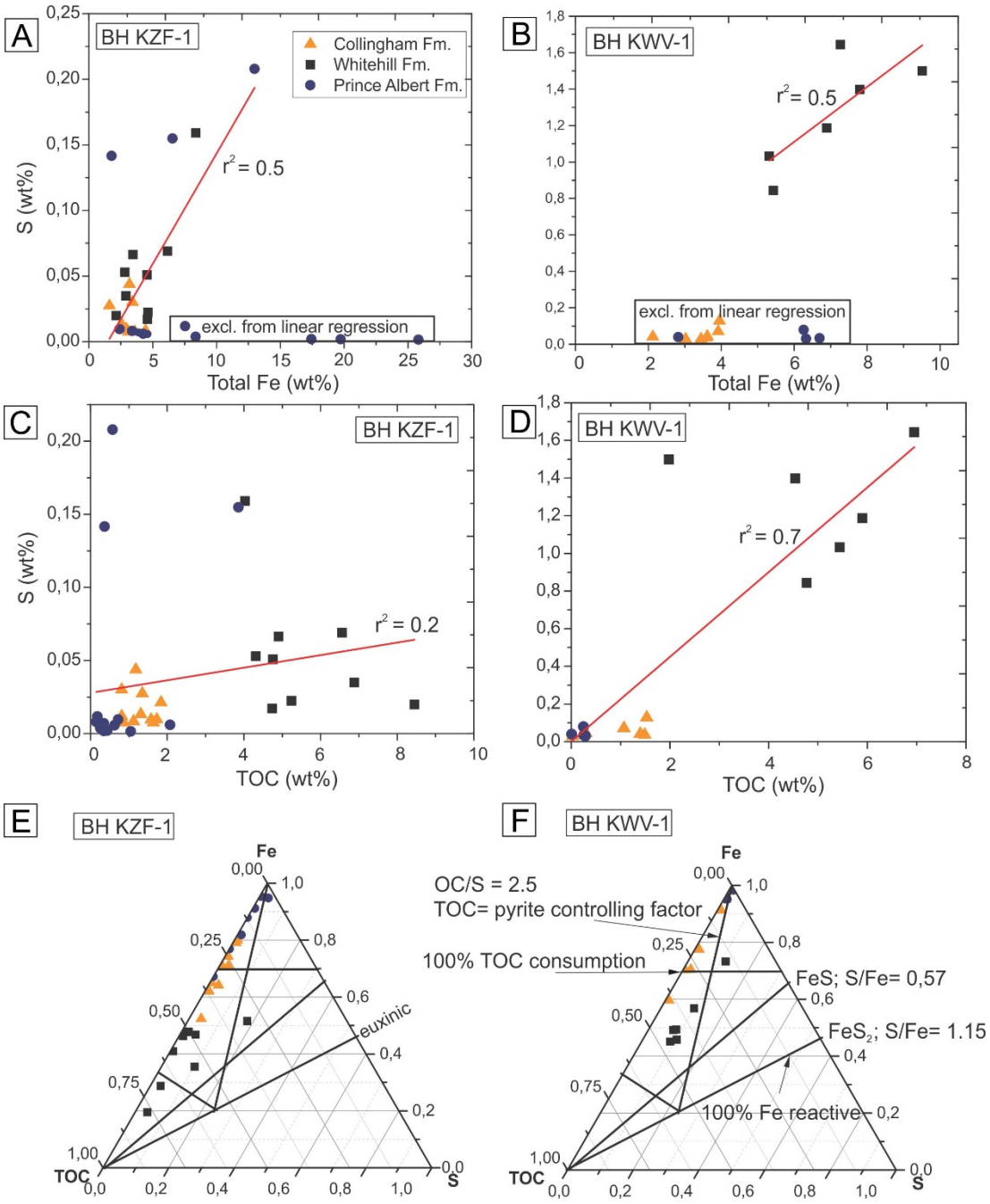

Figure 3.23: The relationship between iron, sulfur and TOC. Data from BH KZF-1 and BH KWV-1. A–B) S (wt%) versus Fe(wt%). C–D) S (wt%) versus TOC (wt%). E–F) Fe-S-TOC ternary diagrams. Abbreviations: TOC: total organic carbon; r^2: linear regression.

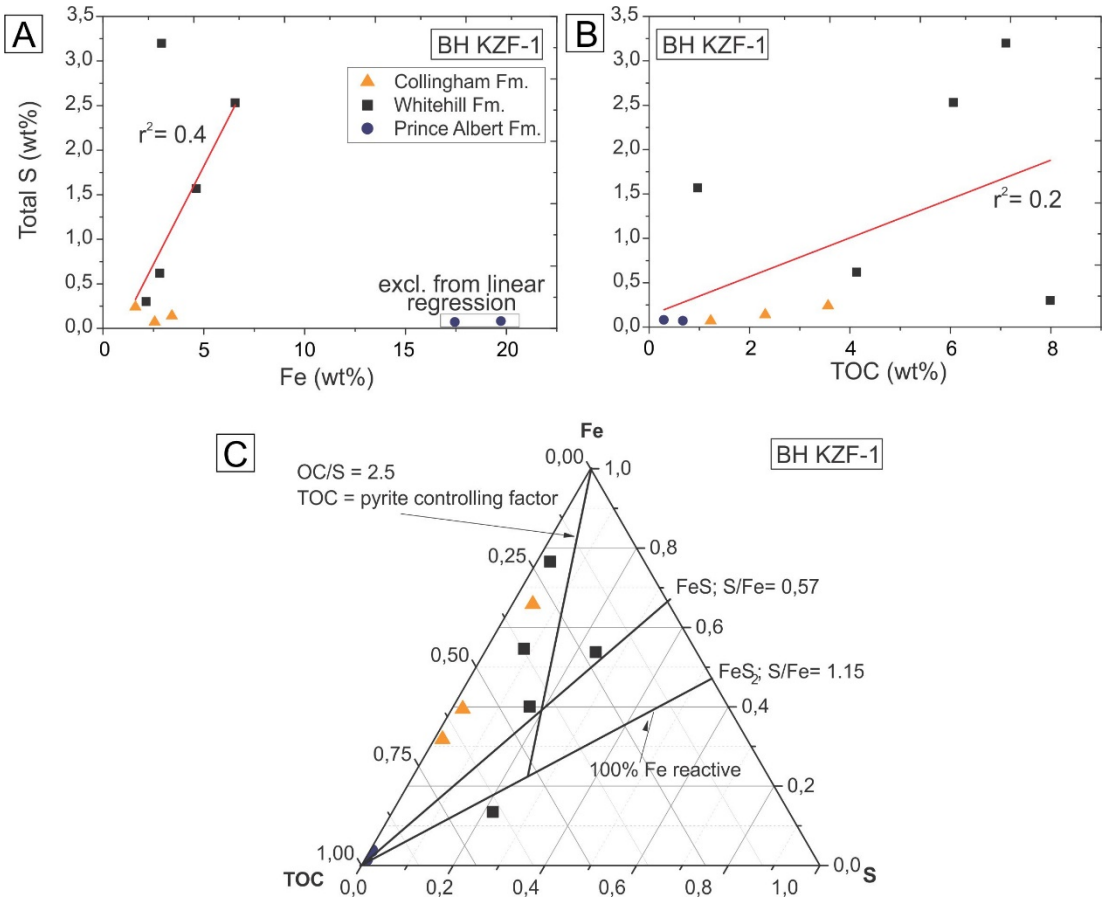

Figure 3.24: The relationship between iron, sulfur and TOC. Data from samples KZF01P to KZF10P from BH KZF-1. A) Total S (wt%) versus Fe (wt%). B) Total S versus TOC (wt%). C) Fe-TOC-S ternary diagram. Abbreviations: TOC: total organic carbon; r^2: linear regression.

3.4.4.2.3 Ba/Al_2O_3 and P_2O_5/Al_2O_3

In BH KZF-1, Ba/Al_2O_3 trends vary in the Prince Albert and Collingham formations but appear to be more consistent in the Whitehill Formation (Figure 3.16). Ba/Al_2O_3 and P_2O_5/Al_2O_3 trends are negatively correlated in the Prince Albert Formation and the high P_2O_5/Al_2O_3 peaks detected in the Prince Albert Formation are accounted for by high apatite content. Ba/Al_2O_3 values are lowest in the bottom of the Whitehill Formation and increase near the contact with the Collingham Formation. The Ba/Al_2O_3 trends in the Whitehill Formation correlate with P_2O_5/Al_2O_3. The overall Ba/Al_2O_3 values are the highest in the Collingham Formation.

In BH KWV-1 (Figure 3.20), Ba/Al_2O_3 and P_2O_5/Al_2O_3 trends are strongly correlated in the Whitehill Formation. The highest Ba/Al_2O_3 peak is at the base of the Whitehill Formation. Ba/Al_2O_3 and P_2O_5/Al_2O_3 trends are negatively correlated in the Prince Albert and Collingham formations.

3.4.4.2.4 Ni/Co

In BH KZF-1, Ni/Co values are the highest in the Whitehill Formation and range from 0.7 to 2.3 (Figure 3.17). These range between 0 and 1.6 in the Prince Albert Formation and between 0 and 1.9 in the Collingham Formation. In BH KWV-1, Ni/Co values are also the highest for Whitehill Formation, ranging between 1.6–2.5 (Figure 21). These range between 0 and 1.6 in the Prince Albert Formation 0.6–3 and between 0 and 2.7 in the Collingham Formation. The increase in Ni/Co values correlate with the TOC trends in both boreholes. Because Ni/Co is an indicator of palaeo-redox conditions (Jones & Manning, 1994), the very low Ni/Co values (< 5) indicate oxic conditions.

3.4.4.2.5 Rb/K

In BH KZF-1, Rb/K values for the Prince Albert Formation fluctuates between marine, brackish and freshwater conditions (Figure 3.17; < Rb/K $4*10^{-3}$ to > Rb/K $6*10^{-3}$). The Whitehill and Collingham formations have Rb/K values that constantly remain above $6*10^{-3}$, suggesting marine conditions during the deposition of these units.

In BH KWV-1, Rb/K values for the lower Prince Albert Formation indicate fluctuating fresh, brackish and marine conditions during deposition, which appear to have turned progressively more marine during the depositional phase of the upper Prince Albert and lower Whitehill formations. The lower Collingham Formation has Rb/K values above $6*10^{-3}$ but reduce to a range between $4*10^{-3}$ to $6*10^{-3}$, indicating that remaining period of deposition occurred in fresh and brackish water (Figure 3.21).

3.5 Discussion

The Permian sedimentary rocks in this Karoo study have all undergone some degree of metamorphism. In addition to the burial metamorphism, the rocks in both boreholes were subjected to regional metamorphism due to Cape Orogeny (e.g., thrust faulting and duplication evident in BH KZF-1; regional folding mapped on both areas near the boreholes). Moreover, the rocks in BH KWV-1 (eastern MKB) also suffered contact metamorphism from the lower Jurassic dolerite intrusions which are common in this region (Figures 3.1, 3.2). Sedimentary rocks in both boreholes have vitrinite reflectance values of VR_o > 4, further indicating that they are over-mature. Trace element enrichment may be linked to syn- and post- depositional sulfide mineralization, as well as primary redox conditions, OM type, sediment accumulation-rates, diagenesis and metamorphism (Pratt & Davis, 1992). Therefore, it is important to combine all available evidence when interpreting the data to decipher the syn-sedimentary conditions in palaeo-environmental reconstructions.

3.5.1 Palaeo-climate

The geochemical composition of the Permian lower Ecca Group changes from the oldest to the youngest unit and this suggests changing syn- and post-dispositional conditions. The well-documented post-glacial melting in the Early Permian (e.g., Visser, 2003; Isbell et al., 2008) led to the expansion of the vegetation and an increase in atmospheric pCO_2, which increased weathering of silicates and carbonates, ultimately increasing the nutrient budget available in the early "Ecca Inland Sea" (Figure 3.25; Berner, 1994; Scheffler, 2004). Considering the two boreholes, the lower Ecca Group is the thickest in the Tankwa Karoo Sub-basin implying greater accommodation space in the western part of the MKB during the early Permian. Present day differences between northern and southern Dwyka facies suggest that towards the end of Dwyka glaciation, the regional depositional profile dipped towards the south. Diachronous ages between the top of the Dwyka facies in the north and the south indicate that continental glaciation could have lasted longer in the north due to the higher altitude (e.g., Tankard et al., 1982; Cole, 1992; Catuneanu et al., 1998; Isbell et al., 2008). During the Early Permian, the position of the BH KZF-1 in western and BH KWV-1 in the eastern MKB, would have been at palaeo-latitudes ~ 60° S and ~ 70° S, respectively (UTIG PLATES model, ~ 290.1 Ma). BH KWV-1 would have been at higher altitude than BH KZF-1. Additionally, the contact between the Dwyka Group and the Prince Albert Formation is dropstone poor in BH KWV-1 (Appendix E), indicating an absence of a floating ice-sheet. Therefore, it is possible that the melting of the ice-sheets probably first occurred in the western MKB allowing for longer periods of time where water may have warmed up accompanied by an increased period of sedimentation. The ice-sheets probably only retreated later from the eastern MKB, during which time that part of the basin had already undergone some degree of isostatic rebound (Catuneanu et al., 1998).

The CIA values suggests intermediate to high weathering from samples in both boreholes (Figures 3.8, 3.9). High CIA values (80–100) are usually associated with rocks that originate from source areas that have undergone intensive weathering under tropical conditions, while CIA values that range from 50 to 70 indicate glaciated source regions (Nesbitt & Young, 1982). High CIA values in the Prince Albert Formation (73–78) indicate intermediate to high weathering conditions, which would be expected in the early post-glacial period when temperatures and ρCO_2 began to increase. Intermediate weathering trends as observed for Whitehill and Collingham formations (64–67), which would be expected of colder climates as predicted by Permian (Sakmarian and Wordian) temperature models developed by Gibbs et al.

(2002). These models have a strong bias towards cold, high-latitude southern oceans with temperatures that are only 5 °C in the summer months and fall as low as -35 °C in the winter months.

CIA values plotted against Al_2O_3 and K_2O/Na_2O (Figure 3.8 B, C) indicate that overall the lower Ecca Group sediments were supplied from areas that underwent weathering conditions typical in arid to subtropical climates. More specifically, the data from the Prince Albert Formation plots closer to the boundary with the subtropical field, which reflects the intensive chemical weathering in the source areas during this initial depositional phase. Intermediate weathering intensity observed in the Whitehill and Collingham formations may be taken as evidence for slowing chemical weathering more common under arid to subtropical conditions. While the dataset in this study is not exhaustive, similar CIA trends in the lower Ecca Group were observed elsewhere in the MKB too (e.g., Scheffler et al., 2004; Chere, 2015).

3.5.2 Early diagenesis and palaeo-environmental analysis

The Prince Albert and Whitehill formations have a high percentage of fluorapatite and phosphate nodules (see Chapter 2) that can be tentatively described as being both authigenic and allogenic. Apatite precipitation is favoured at higher temperature, pH and Ca^{2+} concentration (Gulbrandsen, 1969). Phosphorite formation in the lower Ecca Group may be formed by “ice margin upwelling” (Figure 3.25; Hay, 1995; Gibbs et al., 2002). Phosphate nodules and fluorapatite precipitation are typical in marine settings and common in modern-day oceans (e.g., offshore Namibia, Peru, Chile; Calvert & Price, 1983; Hesse & Sacht, 2003, Bjørlykke, 2010).

The Prince Albert Formation in BH KZF-1 is also highly enriched with Mn, which occurs in the form of Mn-nodules and cement (birnessite) as well as carbonate such as rhodochrosite. The high carbonate content in BH KZF-1 extends into the Whitehill Formation with the presence of ferrous dolomite. In contrast, BH KWV-1 has very little carbonate (mostly siderite and ankerite), is lacking dolomite and has overall lower Mn enrichment. Neither birnessite nor rhodochrosite were detected in BH KWV-1. Mn deposits, in many cases, are synonymous with marine depositional environments and common in all modern-day marine sediments (Crerar & Barnes,1974). Hydrothermal fluids discharged to the sea floor is responsible for 90% of Mn introduced to the ocean (Figure 3.25; Glasby, 2006).

Rhodochrosite in the modern-day brackish Baltic Sea precipitates during sporadic inflow of oxygenated saline water from the North Sea. This results in the precipitation of MnO_2 and the formation of Mn-rich layers at the water-sediment interface. Mn^{2+} will

be released into porewater once conditions become anoxic again and MnO_2 is reduced (Figure 3.25; Hesier et al., 2001; Huckriede & Meischner, 1996; Neumann et al., 1997). In BH KZF-1, rhodochrosite in the lower Prince Albert Formation occurs in samples with mudstone lamina, birnessite nodules and bioturbation structures, which may suggest similar settings. However, it must also be considered that remobilization of Mn into the water column can be achieved by bioturbation (Glasby, 2006; Thamdrup & Canfield, 1996). There is a correlation between Mn and Fe in birnessite-rich samples in BH KZF-1. It can be that there was autocatalytic precipitation of oxyhydroxides, such as birnessite, onto pre-existing ferric-precipitates or detrital Fe-rich material (Burns & Brown, 1972; Calvert & Pedersen, 1992). A well-developed halocline prevents mixing of water and can lead to the extensive diffusion of Mn^{2+} and Fe^{2+} into the water column from underlying sediments (Glasby, 2006). The formation of rhodochrosite together with birnessite nodules suggest fluctuations in salinity and oxygen levels in the western part of the MKB.

Mn-carbonates can act as a sink for Mn, which is often introduced into a basin in either dissolved or particulate form or sedimentary phases of suboxic shelf sediments. For example, O_2/H_2S can act as a barrier for Mn loss and if Mn is not dissolved by the reducing water column, it can form Mn-carbonates (Figure 3.25). $MnCO_3$ precipitation can occur in anoxic waters granted that $MnCO_3$ has been supplied (Brumsack, 2006). In this case the supply may be from hydrothermal sources. Mn-enrichment can indicate a slow pelagic sedimentation rate and scavenging of trace metals, such as Cu, Co, Mo and V. Cu and Zn become enriched in sediments that experience production from H_2S from bacterial sulfate reduction allowing for the precipitation of heavy metals whose sulfides are less soluble in seawater (Wedepohl, 1971). Cu, Co, V and Zn are enriched in all three formations in both boreholes (Figure 3.25). Costin et al., 2019, correlated Mo with TOC in the Whitehill Formation in this borehole.

In BH KZF-1, greenalite is identified 2 cm above the basal contact between Dwyka Group and the Prince Albert Formation. Greenalite is an iron silicate derived from rapid nucleation of a hydrous Fe (II)-silicate gel at 25 °C from Fe^{2+} and SiO_2 (aq) solutions in anoxic seawater. Greenalite is typically nucleated from water with a pH of 7.7–8.3, implying high alkalinity conditions and is common in Archean BIF (Gole, 1980; Tosca et al., 2015). Some Archean BIF formed as a response to post-glacial deposition as sea water became increasingly oxygenated (e.g., Young, 2010). Similar conditions may have existed in the early “Ecca Inland Sea”. An alternative mode of greenalite precipitation is when iron-bearing hydrothermal solutions become discharged along fractures caused by tectonic activity. The contribution of

hydrothermal fluids to the ocean floor to form greenalite may also be the reason for the high Mn content observed in the lower Prince Albert Formation as discussed previously. The source for hydrothermal fluid would most likely be from early stages of CFB deformation (Figure 3.25). However, geochemical analyses of the greenalite itself would be necessary to further test the theories for its precipitation.

In BH KWV-17, the oldest sample analysed from the Prince Albert Formation, ~ 3.75 m above the contact with the Dwyka Group, is enriched with respect to Cu, which can be indicative of anoxia. However, there is little pyrite, low FeO_2 content and agglutinated benthic foraminifera in this sample. In studies of modern-day benthic foraminifera, *Textularia* is observed occurring in both oxic and dysoxic conditions (Kaminski et al., 1995).

3.5.3 Geochemical proxy correlation

Rb/K is a well-established proxy for palaeo-salinity. In BH KZF-1, the lower Prince Albert Formation has Rb/K values that correlate with increases and decreases of MnO/Al_2O_3 (Figures 3.16; 3.17). This would suggest that in the Tankwa Karoo Sub-basin, the deposition of the lower Prince Albert Formation, fluctuated between marine and fresh-water conditions as a possible consequence of repeated episodes of melt water influx to the western MKB. The Whitehill and Collingham formations have Rb/K values ($> 6*10^{-3}$) that suggest that the depositional conditions were predominantly marine. In BH KWV-1, Rb/K values point to fluctuating marine and brackish water conditions during the Prince Albert and Whitehill depositional episodes (Figure 3.21). Rb/K values level out between ratios of $4*10^{-3}$ and $6*10^{-3}$ indicating fresh to brackish conditions prevailed during the deposition of the Collingham Formation. Similarly, Rb/K values in BH KWV-1 correlate with MnO/Al_2O_3 values apart from one sample in the Collingham Formation (Figure 3.20). A further indicator for marine conditions, at least episodically, is high V content in bituminous mudstone where the V-enrichment factor is up to 12 in both boreholes (Figure 3.7).

Fe-S-TOC relationships are investigated using elemental data in wt% obtained from XRF in this study and compared with total S data, calculated from a sulfur determinator instrument by Nolte (2017). The total S values obtained by the sulfur determinator were slightly higher than S obtained by XRF, but not significantly so, which confirms that the S content is low in both boreholes (Figures 3.23; 3.24). High TOC content in the Whitehill Formation is indicative of OM preservation, which is thought to occur under anoxic conditions. However, Fe-S-TOC ternary diagrams plot samples from both boreholes mostly above the S/Fe = 0.57 delineation, which

indicates precipitation of FeS in the “oxic zone” (Figures 3.24; 3.25). Only one sample from the Whitehill Formation in BH KZF-1, plots below the euxinic line. The ternary diagrams emphasize relative concentrations and ratios, so that the relationships are not affected by the dilution effects caused by biogenic silica or $CaCO_3$ (Dean & Arthur, 1989). Fe occurs in diagenetic Fe-carbonate minerals in both boreholes, especially in the Prince Albert Formation. These results suggest the Prince Albert and Collingham formations in both boreholes were deposited under oxic conditions, whereas the Whitehill Formation was mostly deposited in an oxic to dysoxic setting. The results from high Fe-carbonate samples in the Prince Albert Formation may plot as more oxic due to Fe- signature overprint. In BH KWV-1, the Whitehill Formation has 9.18 wt% pyrrhotite and has the highest enrichment of Mo (Figure 3.7). This suggests that the Whitehill Formation in the eastern MKB was deposited under dysoxic to anoxic settings.

Minerals that formed during later stages of diagenesis do not reflect redox conditions at the surface-water interface during time of deposition. Trace fossils are often a more convincing indicator for oxygenation. Bioturbation structures are detected in the Collingham and Prince Albert formations in both boreholes. The fine-grained nature and high TOC content of the Whitehill Formation makes it difficult to detect trace fossils in this unit. However, possible microbial filaments are detected in the Whitehill Formation in both boreholes, and these indicate that oxygen levels and sedimentation rates were possibly low. The plot of V+Ni values against TOC further confirms that sedimentation rates were low overall, but more so during the deposition of the Whitehill Formation (Figure 3.22).

Ni/Co can also be used as a palaeo-redox indicator as these trace elements are often trapped by sulfides. Overall, these ratios are < 5 for both boreholes, which is indicator of oxic conditions (Jones & Manning, 1994). The Whitehill Formation in both boreholes have overall the highest Ni/Co values, although the values are still much lower than expected in oxic settings (Figures 3.17; 3.21).

Contrasting with the Ni/Co values, V/(V+Ni) values are high, ranging from 0.8–1, which is supposed to be indicative of euxinic conditions for both boreholes (Figures 3.17; 3.21). However, according to Fe-S-TOC relationships and total pyrite content, it is more likely that euxinic conditions were not predominant. V/Cr values (Figures 3.17; 3.21) further indicate that conditions fluctuated between oxic and dysoxic in both parts of the MKB, with spikes in anoxia only detected in the Prince Albert and Collingham formations in the western MKB (BH KZF-1).

Denitrifying redox conditions of bottom water conditions are maintained when there is a sufficient influx of biogenic matter with average residence time in the water column. Denitrifying conditions allow for the accumulation of V and Cr, but preclude the precipitation of Zn, Mo, Cu, Cd in sulfides (Piper & Perkins, 2004). This may explain the low Mo contents in the boreholes with the exception of the Whitehill Formation in eastern MKB (BH KWV-1).

Barium can be interpreted as a proxy for bio-productivity (Dymond et al., 1992; Prakash Babu et al., 2002; von Breymann et al., 1992). Ba is only stable and mobile under sulfate concentrations typical under marine conditions (Brumsack & Gieskes, 1983; McManus et al., 1998; Brumsack, 2006). In marine sediments, Ba can occur in carbonates, biogenic silica and organic matter (Robin et al., 2003). Ba can, however, be a component of both wind-blown silicates and Fe-Mn oxyhydroxides, in which case it cannot be linked to palaeo-productivity (Paytan et al., 1996). Ba is the second most enriched trace element in both boreholes.

In BH KZF-1, Ba/Al_2O_3 values are the highest in the lower Prince Albert and Collingham formations. The highest content of apatite (~ 9 wt%) is also detected in the lower Prince Albert in BH KZF-1, which is associated with high P_2O_5/Al_2O_3 values (Figure 3.16). Upwelling can be an important factor for phosphorous supply along continental margins (Baturin, 1982; Glenn et al., 1994). Low sedimentation rates, strong bottom currents and an abundance of organic matter are required for the formation of phosphorite (Baturin, 1999). Along with evidence for bioturbation from the lower Prince Albert Formation in BH KZF-1, it may be inferred that there was high palaeo-productivity in the western MKB after deglaciation in the earliest Permian.

In BH KWV-1, Ba/Al_2O_3, P_2O_5/Al_2O_3 and TOC proxies are well correlated and reach the highest values in the Whitehill Formation, which is also the only formation enriched in Mo. In turn, Mo is well correlated with organic matter and bottom water sulphate reduction (Piper & Dean, 2002; Brumsack, 1986; Coveney et al., 1987). Pyrrhotite (FeS) instead of pyrite (FeS_2) occurs in the Whitehill Formation of BH KWV-1. It is likely that Mo was removed once H_2S levels were increased in the water column and incorporated in the mineralization of pyrrhotite (Piper & Perkins, 2004). Elevated levels of Cu may also indicate increased bio-productivity and can be a response to nutrient upwelling (Piper & Perkins, 2004).

In summary, the oldest parts of the Prince Albert Formation, found near the contact with the underlying Dwyka Group, may have been deposited in an initially anoxic setting that quickly turned more oxic and then progressively dysoxic by the start of the

Whitehill depositional episode. Later, during the deposition of the Whitehill and Collingham formations, the oxygen levels in the basin fluctuated between dysoxic and oxic conditions. These may be taken as indicator for episodic late melting periods in the mountain glaciers (e.g., Cargonian Highlands, rising CFB) during the early part of the lower Ecca depositional period (Figure 3.25).

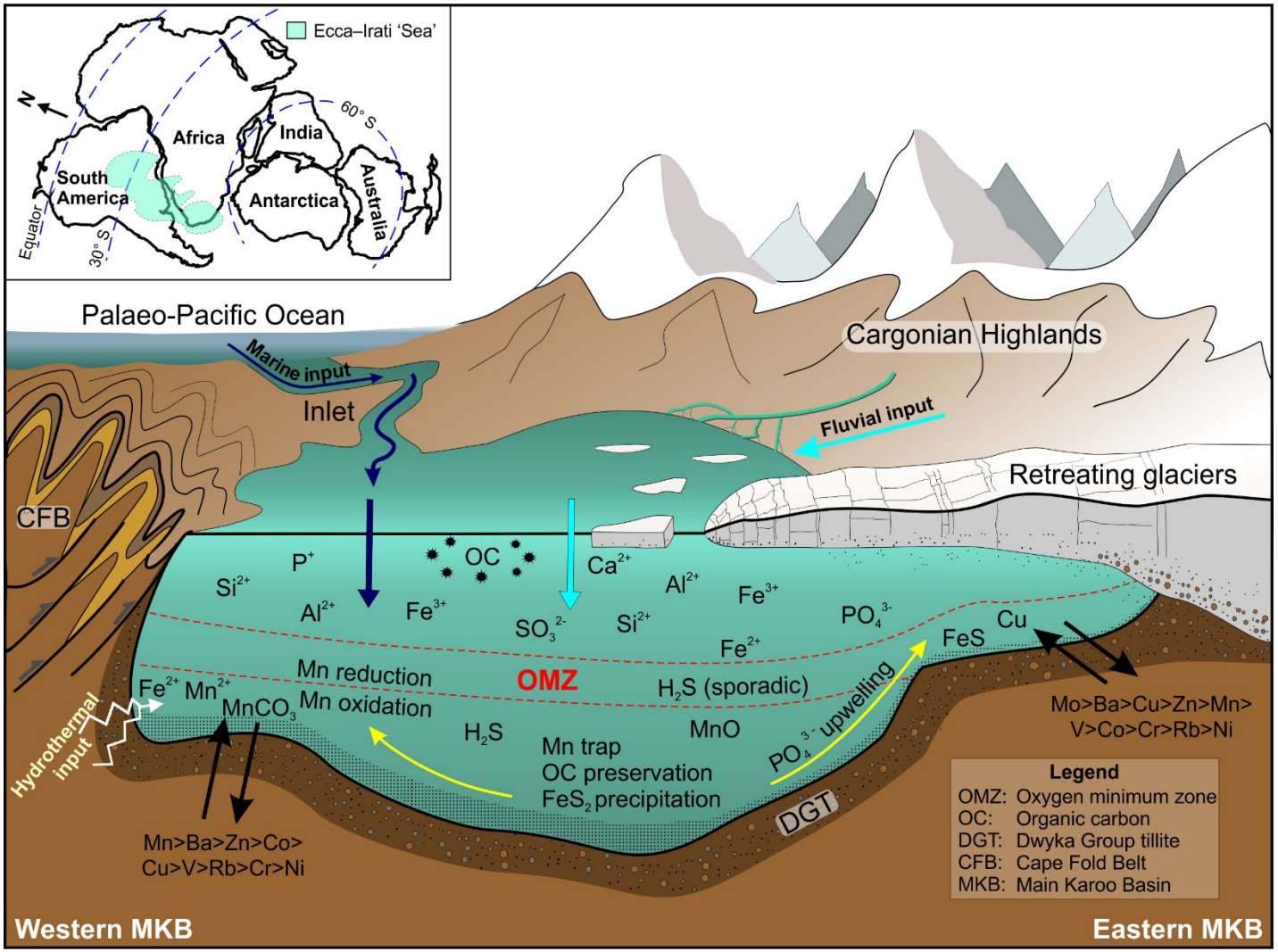

Figure 3.25: Reconstruction of the depositional conditions in the MKB during the Early Permian. View from the south

3.6 Conclusion

Sedimentation rates, OM preservation and levels of bottom water oxygenation fluctuated during the deposition of the lower Ecca Group, which in BH KZF-1 and BH KWV-1 is dominated by thermally over-mature mudstones. Burial and contact metamorphism that impacted these rocks, altering and overprinting their original composition in diagenetic mineralization processes. Therefore, the reconstruction of the palaeo-environmental conditions during the lower Ecca depositional episode in the MKB remains a challenging task.

The northward shift of Gondwana in the latest Carboniferous caused not only the melting of ice-sheets in the southern hemisphere supercontinent (e.g. Isbell et al., 2008) but also facilitated an increase in chemical weathering demonstrated by high CIA and carbonate content detected in the Prince Albert and Whitehill formations in the Tankwa Karoo Sub-basin (western MKB).

The Prince Albert Formation shows the greatest mineralogical and thickness variation between the western and eastern MKB. Assuming that minerals such as greenalite, rhodochrosite (in Mn-carbonate nodules), apatite and birnessite (in Mn-nodules) are primary precipitates in the studied rocks, their occurrence in BH KZF-1 suggest the presence of hydrothermal processes and occasional influx of saline water into the western MKB. To put it differently, the Tankwa Karoo Sub-basin was probably located proximal to a marine inlet towards the west (Figure 3.25). This link to the Palaeo-Pacific Ocean may be the reason for the increased amount of apatite, manganese nodules and rhodochrosite detected in the lower Prince Albert Formation in BH KZF-1. Changes in the geochemical composition of these lower Ecca rocks may also be linked to fluctuation between marine and brackish water conditions, as well as and anoxic and dysoxic conditions, allowing for preservation of organic material and thus accounting for the elevated TOCs.

In both boreholes, the transition from the Prince Albert Formation to the Whitehill Formation shows fluctuations between dysoxic and oxic conditions during deposition. The TOC in the Whitehill Formation, is ~ 5 wt% (on average) suggesting that the sedimentation rates were low during deposition. Therefore, periods of anoxia may have been seasonal to allow for the preservation of OM and enrichment of V, but not frequently enough to preserve significant quantities of S, Ni, Co, Cu and Mo typical of fully anoxic black shales. Based on Rb/K values, the Whitehill Formation in the Tankwa Karoo Sub-basin may have been deposited in fully marine conditions, at least

for some part of the overall Whitehill depositional episode. Whereas in the eastern MKB, over the same interval, the salinity conditions fluctuated, and were not fully marine. However, additional indicators, such a palaeontological evidence, are required to further elaborate on the salinity levels in the basin during the Whitehill depositional episode. Similarly, Rb/K values in the Collingham Formation in BH KZF-1 suggest that deposition occurred under fully marine conditions in the western MKB. In contrast to this, in the eastern MKB, the lower Collingham Formation was initially deposited under marine conditions, which became increasingly brackish with time. The abundance of bioturbation structures and TOC (average: ~1.14 wt%) in the Collingham Formation in both regions of the MKB are similar. However, based on the above lines of evidence, it is likely that periods of anoxia were more frequent in the western than in the eastern MKB.

Overall, the redox conditions for both boreholes are oxic to dysoxic, punctuated with periods of anoxia. Sedimentation rates were low for birnessite nodules to form in the western MKB. Here, the sedimentation rates were at their lowest during the deposition of the Whitehill Formation. Depending on where the lower Ecca Group is sampled, one may detect evidence for anoxic to oxic conditions and for saline or brackish waters, and this must be considered when discussing the palaeo-environmental settings of the lower Ecca Group.

It is recommended that future studies should incorporate REE analyses and geochemical investigation of birnessite and dolomite nodules. A data base of geochemical composition of the lower Ecca Group should be compiled over many study areas in the MKB to facilitate an integrated, and more robust basin-wide palaeo-environmental reconstruction given the vast distances across the MKB.

3.7 References

Aitchison, J. 1982. The statistical analysis of compositional data (with discussion). *Journal of the Royal Statistical Society*. *Series B*. 44: 139–177.

Aitchison, J. 1986. *The Statistical Analysis of Compositional Data*. London: Chapman and Hall. 416p.

Almond, J.E. 2002. Giant arthropod trackway, Ecca Group. *Geobulletin*. 45: 28.

Almond, J.E. 2008. *Fossil record of the Loeriesfontein sheet area (1: 250 000 geological sheet 3018)*. (Unpublished report for the Council for Geoscience). Pretoria, South Africa. 32p.

Anderson, A.M. & McLachlan, I.R. 1979. The oil shale potential of the early Permian White Band Formation in Southern Africa. *Geological Society of South Africa, Special Publication*. 6: 83–89.

Andersson, P.O.D. & Worden, R.H. 2004. Mudstone of the Tanqua Basin, South Africa: an analysis of lateral and stratigraphic variations within mudstones, and comparison of mudstones within and between turbidite fans. *Sedimentology*. 51 (3): 479–502.

Araujo, D.C. 1976. Taxonomia e Relações dos Proganosauria de Bacia do Paraná. *Anais Academia Brasileirade Ciências*. 48 (1): 91–116.

Arthur, M.A. & Sageman, B.B. 1994. Marine black shales: a review of depositional mechanisms and significance of ancient deposits. *Annual Review of Earth and Planetary Sciences.* 22: 499–551.

Bahlburg, H. & Dobrzinski, N. 2011. A review of the Chemical Index of Alterations (CIA) and its application to the study of Neoproterozoic glacial deposits and climate transitions. In *The Geological record of Neoproterozoic glaciations*, *Memoir*. E. Arnaud, G.P. Halverson & G.A. Shields, Eds. London: Geological Society. 723p.

Bangert, B., Stollhofen, H., Lorenz, V. & Armstrong, R. 1999. The geochronology and significance of ash-fall tuffs in the glaciogenic Carboniferous-Permian Dwyka Group of Namibia and South Africa. *Journal of African Earth Sciences*. 29: 33–49.

Baturin, G.N. 1982. *Phosphorites on the Sea Floor*. Elsevier. 342p.

Baturin, G. 1999. Hypotheses of phosphogenesis and oceanic environment. *Lithology and mineral resources C (C of litologiia I poleznye iskopaemye)*. 34: 411–430.

Berner, R. 1970. Sedimentary pyrite formation. *American Journal of Science*. 268: 1–23.

Berner, R.A. 1974. Kinetic models for the early diagenesis of nitrogen, sulfur, phosphorus, and silicon in anoxic marine sediments. In *The Sea, v 5, Marine Chemistry*. E.D. Goldberg, Ed. New York: John Wiley & Sons. 427–449.

Berner, R.A. & Raiswell, R. 1984. C/S method for distinguishing freshwater from marine sedimentary rocks. *Geology*. 12: 365–368.

Berner, R.A. & Westrich, J.T. 1985. Bioturbation and the early diagenesis of carbon and sulfur. *American Journal of Science*. 285: 15–92.

Bhatia, M.R. 1983. Plate tectonics and geochemical composition of sandstones. *Journal of Geology*. 91: 611–627.

Bjørlykke, K. 2010. *Petroleum Geoscience: from Sedimentary Environments to Rock Physics.* Berlin: Springer. 508p.

Breit, G.N. & Wanty, R.B. 1991. Vanadium accumulation in carbonaceous rocks: a review of geochemical controls during deposition and diagenesis. *Chemical Geology*. 91: 83–97.

Brüchert, V., Jørgensen, B.B., Neumann, K., Riechmann, D., Schlösser, M. & Schulz, H. 2003. Regulation of bacterial sulfate reduction and hydrogen sulfide fluxes in the central Namibian coastal upwelling zone. *Geochimica et Cosmochimica Acta*. 67: 4505–4518.

Brumsack, H.J. & Gieskes, J.M. 1983. Interstitial water trace-element chemistry of laminated sediments of the Gulf of California (Mexico). *Marine Chemistry*. 14: 89–106.

Brumsack, H.J. 1986. The inorganic geochemistry of Cretaceous black shales (DSDP leg 41) in comparison to modern upwelling sediments from the Gulf of California. In *North Atlantic Palaeoceanography*. C.P. Summerhayes & N.J. Shackleton, Eds. Geological Society Special Publication. 21: 447–462.

Brumsack, H.J. 2006. The trace metal content of recent organic carbon-rich sediments: Implication for Cretaceous black shale formation. *Palaeogeography, Palaeoclimatology, Palaeoecology*. 232: 344–361.

Burns, R.G. & Brown, B.A. 1972. Nucleation and mineralogical controls on the composition of manganese nodules. In *Ferromanganese deposits on the ocean floor*. D.R. Horn, Ed. Lamont-Doherty Observatory, Columbia University. 51–62.

Calvert, S.E. & Price N.B. 1983. Geochemistry of Namibian Shelf Sediments. In *Coastal Upwelling Its Sediment Record. NATO Conference Series (IV Marine Sciences, vol 10B*. E. Suess & J. Thiede, Eds. Boston, MA: Springer. 337–375.

Calvert, S.E. & Pedersen, T.F. 1992. Organic carbon accumulation and preservation in marine sediments: how important is the anoxia? In *Organic matter: productivity, accumulation and preservation in recent and ancient sediments*. J.K. Whelan & J.W. Farrington, Eds. Columbia University Press: New York. 231– 263.

Campbell, F.A. & Williams, G.D. 1965. Chemical composition of shales of Mannville Group (Lower Cretaceous) of Central Alberta, Canada. *AAPG Bulletin*. 49(1): 81–87.

Catuneanu, O., Hancox, P.J. & Rubidge, B.S. 1998. Reciprocal flexural behaviour and contrasting stratigraphies: a new basin development model for the Karoo retroarc foreland system, South Africa. *Basin Research*. 10: 417–439.

Catuneanu, O., Hancox, P.J., Cairncross, B. & Rubidge, B.S. 2002. Foredeep submarine fans and forebulge deltas: orogenic off-loading in the underfilled Karoo Basin. *Journal of African Earth Sciences*. 35: 489–502.

Catuneanu, O., Wopfner, H., Eriksson, P.G., Cairncross, B., Rubidge, B.S., Smith R.M.H. & Hancox P.J. 2005. The Karoo basins of south-central Africa. *Journal of African Earth Sciences*. 43: 211–253.

Chere, N. 2015. *Sedimentological and geochemical investigations on borehole cores of the lower Ecca Group black shales, for their gas potential - Karoo Basin, South Africa*. Unpublished M.Sc. dissertation. Nelson Mandela University. 268p.

Chukwuma, K. & Bordy, E.M. 2016. Spatiotemporal sedimentary facies variations in the Lower Permian Whitehill Formation, Ecca Group, Karoo Basin. In *Origin and Evolution of the Cape Mountains and Karoo Basin. Regional Geology Reviews*. B. Linol & de Wit, M.J., Eds. Springer. 101–110.

Chukwuma, K. 2017. *Spatial and temporal variations in the geometry and composition of the Permian Whitehill Formation South Africa*. Unpublished Ph.D. thesis. University of Cape Town. 216p.

Chukwuma, K., Bordy, E.M. & Coetzer, A. 2018. Evolution of porosity and pore geometry in the Permian Whitehill Formation of South Africa – A FE-SEM image analysis study. *Marine and Petroleum Geology*. 91: 262–278.

Cole, D.I. & McLachlan, I.R. 1991. Oil potential of the Permian Whitehill Shale Formation in the main Karoo Basin, South Africa. In *Gondwana Seven Proceedings*. H. Ulbrich Rocha & A.C. Campos, Eds. 379–390.

Cole, D.I. & Basson, W.A. 1991. Whitehill Formation. In *Catalogue of South African Lithostratigraphic Units*. M.R. Johnson, Ed. South African Committee for Stratigraphy, Pretoria. 3: 51–52.

Cole, D.I. 1992. Evolution and development of the Karoo Basin. In *Inversion tectonics of the Cape Fold Belt, Karoo and Cretaceous basins of Southern Africa*: M.J. de Wit & I.G.D., Ransome, Eds. Rotterdam: A.A. Balkema. 87–99.

Cole, D.I. 2005. Prince Albert Formation. In *Catalogue of South African Lithostratigraphic Units*. M.R. Johnson, Ed. South African Committee for Stratigraphy, Pretoria. 8: 33–36.

Cole, D. & Barbolini, N. 2019. Marine flooding surfaces recorded in Permian black shales and coal deposits of the Main Karoo Basin (South Africa): Implication for basin dynamics and cross-basin correlations: Discussion. *International Journal of Coal Geology.* 209: 130–131.

Costin, G., Götz, A.E. & Ruckwied, K. 2019. Sedimentary organic matter characterization of the Whitehill shales (Karoo, Basin, South Africa): An integrated quantitative approach using FE-EPMA and LA-ICP-MS*. Review of Palaeobotany and Palynology*. 268: 29–42.

Coveney, R.M., Jr., Leventhal, J.S., Glascock, M.D. & Hatch, J.R. 1987. Origins of metals and organic matter in the Mecca quarry shale member and stratigraphically equivalent beds across the Midwest. *Economic Geology*. 82: 915–933.

Crerar, D.A. & Barnes, H.L. 1974. Deposition of deep-sea manganese nodules. *Geomichica et Cosmochimica Acts*. 38: 279–300.

Crowell, J.C. 1978. Gondwana glaciation, cyclothems, continental positioning and climate change. *American Journal of Science*. 278: 1345–1372.

Dean, W.E. & Arthur, M.A. 1989. Iron-sulfur-carbon relationships in the organic-carbon-rich sequences I: Cretaceous western interior seaway. *American Journal of Science*. 289: 708–743.

Duncan, R.A., Hooper, P.R., Rehacek, J., Marsh, J.S. & Duncan, A.R. 1997. The timing and duration of the Karoo igneous event, southern Gondwana. *Journal of Geophysical Research*. 102 (18): 127–138.

Dymond, J., Suess, E. & Lyle, M. 1992. Barium in deep-sea sediment: A geochemical proxy for palaeoproductivity. *Paleoceanography*. 7(2): 163–181.

Faure K. & Cole D.I. 1999. Geochemical evidence for lacustrine microbial blooms in the vast Permian Main Karoo, Paranã, Falkland Islands, and Huab basins of southwestern Gondwana. *Palaeogeography, Palaeoclimatology, Palaeoecology*. 152: 189–213.

Flint, S.S., Hodgson, D., Sprague, A.R., Brunt, R.L., Van der Marwe, W.C., Figueiredo J., Prélat, A., Box, D. et al. 2011. Depositional architecture and sequence stratigraphy

of the Karoo basin floor to shelf succession, Laingsburg depocentre, South Africa. *Marine and Petroleum Geology*. 28: 658–674.

Garzanti, E. & Resentini, A. 2016. Provenance control on chemical indices of weathering (Taiwan river sands). *Sedimentary Geology*. 336: 81–95.

Geel C., de Wit, M., Booth, P., Schulz, H-M. & Horsfield, B. 2015. Palaeo-environment, diagenesis and characteristics of Permian black shales in the lower Karoo Supergroup flanking the Cape Fold Belt near Jansenville, Eastern Cape, South Africa: Implications for the shale gas potential of the Karoo Basin. *South African Journal of Geology*. 118(3): 249–274.

Gibbs, M.T., McAllister Rees, P., Kutzbach, J.E., Ziegler, A.M., Behling, P.J. & Rowely, D.B. 2002. Simulations of Permian climate and comparisons with climate-sensitive sediments. *The Journal of Geology*. 110:33–55.

Glasby, G.P. 2006. Manganese: Predominant Role of Nodules and Crusts. In *Marine Geochemistry*. H.D. Schulz & M. Zabel, Eds. Springer, Berlin, Heidelberg. 371–427.

Glenn, C.R. Fölmi, K.B. Riggs, S.R. & Baturin, G.N. 1994. Phosphorus and phosphorites: sedimentology and environments of formation. *Eclogae Geologicae Helvetiae*. 87 (3): 747–788.

Goldberg, K. & Humayun, M. 2010. The applicability of the chemical index of alteration as a paleoclimatic indicator: an example from the Permian of the Parana Basin, Brazil. *Palaeogeography, Palaeoclimatology, Palaeoecology*. 293: 175–183.

Gole, M.J. 1980. Mineralogy and petrology of very-low-metamorphic grade Archean banded iron-formation, Weld Range, Western Australia. *American Mineralogist*. 65: 8–25.

Götz, A.E., Ruckweid, K. & Wheeler, A. 2017. Marine flooding surfaces recorded in Permian black shales and coal deposits of the Main Karoo Basin (South Africa): Implications for basin dynamics and cross-basin correlation. *Coal Geology*. 190: 178–190.

Gulbrandsen, R.A. 1969. Physical and chemical factors in the formation of marine apatite. *Economic Geology*. 64: 365–382.

Hatch, J.R. & Leventhal, J.S. 1992. Relationship between inferred redox potential of the depositional environment and geochemistry of the Upper Pennsylvanian (Missourian) stark shale member of the Dennis Limestone, Wabaunsee County, Kansas, USA. *Chemical Geology*. 99: 65– 82.

Hay, W. H. 1995. Paleoceanography of marine organic-rich sediments. In *Paleogeography, paleoclimate, and source rocks.* A.Y. Huc, Ed. American Association of Petroleum Geologists. 40:21–59.

Hälbich, H. 1983. A tectogenesis of the Cape Fold Belt (CFB). Special publication - Geological Society of South Africa. 12: 165–175.

Heinrichs, H., Schulz-Dobrick, B. & Wedepohl, K.H. 1980. Terrestrial geochemistry of Cd, Bi, Ti, Pb, Zn and Pb. *Geochimica et cosmochimica Acta*. 4 (10): 1519–1533.

Heiser, U., Neumann, T., Scholten, J. & Stüben, D. 2001. Recycling of manganese from anoxic sediments in stagnant basins by seawater inflow: a study of surface sediments from the Gotland Basin, Baltic Sea. *Marine Geology*. 177:151–166.

Herbert, C.T. & Compton, J.S. 2007. Depositional environments of the lower Permian Dwyka diamictite and Prince Albert shale inferred from the geochemistry of early diagenetic concretions, southwest Karoo Basin, South Africa. *Sedimentary Geology*. 194: 263–277.

Hesse, R. & Sacht, U. 2003. Early diagenesis of deep-sea sediments. In *Treatise on Geochemistry.* H.D. Holland & K.K. Turekian, Eds. 7–9: 289–308.

Huckriede, H. & Meischner, D. 1996. Origin and environment of manganese-rich sediments within black-shale basins. *Geochimica et Cosmochimica Acta.* 60(8): 1399–1413.

Isbell, J.L., Cole, D.I. & Catuneanu, O. 2008. Carboniferous- Permian glaciation in the main Karoo Basin, South Africa: Stratigraphic, depositional controls and glacial dynamics. In *Resolving the Late Palaeozoic Age in Time and Space.* C.R. Fielding, T.D. Frank & J. L Isabell, Eds. Geological Society of America, Special Paper. 441: 71–82.

Jacobs, L., Emerson, S. & Skei, J. 1985. Partitioning and transport of metals across the O_2/H_2S interface in a permanently anoxic basin: Framvaren Fjord, Norway. *Geochimica et Cosmochimica Acta*. 49: 1433–1444.

Johnson, M.R., Van Vuuren, C.J., Visser, J.N.J., Cole, D.I., Wickens, H. de V., Christie, A.D.M., Roberts, D.L. & Brandl, G. 2006. Sedimentary rocks of the Karoo Supergroup. In *The Geology of South Africa.* M.R. Johnson, C.R., Anhaeusser & R.J. Thomas, Eds. Geological Society of South Africa/Council for Geoscience. 461–499.

Johnson, M.R. 2009. Ecca Group. Karoo Supergroup. *Catalogue of South African Lithostratigraphic Units. SACS*. 10: 5–7.

Jones, B. & Manning, D.A.C. 1994. Comparison of geochemical indices used for the interpretation of palaeoredox conditions in ancient mudstones. *Chemical Geology*. 111: 111–129.

Kaminski, M.A., Boersma, A, Tyszka, J. & Holbourn, A.E.L. 1995. Response of deep-water agglutinated foraminifera to dysoxic conditions in the California Borderland basins. In *Proceedings of the Fourth International Workshop on Agglutinated Foraminifera*. M.A. Kaminski, S. Geroch & M.A., Gasinski, Eds. Grzybowski Foundation: London, UK. 131–140

Kaminski, M.A. 2014. The year 2010 classification of the agglutinated foraminifera. *Micropaleontology*. 60: 89–108.

Leventhal, J.S. 1987. Carbon and sulfur relationships in Appalachian Devonian shales as an indicator of environment of deposition. *American Journal of Science*. 287: 23–40.

Lewan, M.D. & Maynard, J.B. 1982. Factors controlling enrichment of vanadium and nickel in the bitumen of organic sedimentary rocks. *Geochimica et Cosmochimica Acta*. 46: 2547–2560.

Macquaker, J.H.S. & Gawthorpe, R.L. 1993. Mudstone lithofacies in the Kimmeridge Clay Formation, Wessex Basin, southern England: implications for the origin and controls of the distribution of mudstones. *Journal of Sedimentary Petrology.* 63: 1129–1143.

Martin, H. & Wilczewski, N. 1970. Palaeoecology, conditions of deposition and palaeogeography of the marine Dwyka beds of South West Africa. *Second Gondwana Symposium Proceedings and Papers*. 225–232.

McLachlan, I.R. & Anderson, A.M. 1973. A review of the evidence for marine conditions in southern Africa during Dwyka times. *Palaeontologia Africana*. 15: 37–64.

McLachlan, I.R. & Anderson, A.M. 1977a. Carbonates, 'stromatolites' and tuffs in the lower Permian White Band Formation. *South African Journal of Science*. 73: 92–4.

McLachlan, I.R. & Anderson, A.M. 1977b. Fossil insect wings from the early Permian White Band Formation, South Africa. *Palaeontologia Africana*. 20: 83–86.

McLennan, S.M., Hemming, S., McDaniel, D.K. & Hanson, G.N. 1993. Geochemical approaches to sedimentation, provenance and tectonics. *Geological Society of America Special Paper*. 284: 21–40.

McManus, J., Berelson, W.M., Klinkhammer, G.P., Johnson, K.S., Coale, K.H., Anderson, R. F., Kumar, N., Burdige, D.J. et al. 1998. Geochemistry of barium in marine sediments: implications for its use as a paleoproxy. *Geochimica et Cosmochimica Acta.* 62 (21–22): 3453–3473.

Mikhalevich, V. I. & Kaminski, M. A. 2008. Revised systematics of the Schlumbergerinida (Phylum Foraminifera). In *Proceedings of the Seventh International Work-shop on Agglutinated Foraminifera*. M. A. Kaminski & R. Coccioni, Eds. Grzybowski Foundation, Special Publication. 13: 157–166.

Milani, E.J. & de Wit, M.J. 2008. Correlations between the classic Paraná and Cape Karoo sequences of South America and southern Africa and their basin infills flanking the Gondwanides: du Toit revisited. In *West Gondwana: Pre-Cenozoic correlations across the South Atlantic region.* R.J. Pankurst, R.A.J. Trouw, B.B. Brito Neves & M.J. de Wit, Eds. London: The Geological Society, Special Publications. 294: 319–342.

Murphy, A.E., Sageman, B.B., Hollander, D.J., Lyons, T.W. & Brett, C.E. 2000. Black shale deposition and faunal overturn in the Devonian Appalachian Basin: clastic starvation, seasonal water column mixing, and efficient biolimiting nutrient recycling. *Paleoceanography.* 15: 280–291.

Navarrete, C., Gianna, G., Encinas, A., Márquez, M., Kamerbeek, Y., Valle, M. & Folguera, A. 2019. Triassic to Middle Jurassic geodynamic evolution of southwestern Gondwana: From large flat-slab to mantle plume suction in a rollback subduction setting. *Earth Science Reviews*. 194: 125–159.

Nesbitt, H.W. & Young, G.M. 1982. Early Proterozoic climates and plate motions inferred from major element chemistry of lutites. *Nature*. 299: 715–717.

Nesbitt, H.W. Young, G.M. 1984. Prediction of some weathering trends of plutonic and volcanic rocks based on thermodynamics and kinetic considerations. *Geochemica et Comsochimica Acta.* 48: 1523–1534.

Neumann, T., Christiansen, C., Clasen, S., Emeis, K.C. & Kunzendorf, H. 1997. Geochemical records of seawater inflows into the deep basins of the Baltic Sea. *Continental Shelf Research.* 17: 98–115.

Nolte, S. 2017. *Petrophysical characterization of potential unconventional gas shale reservoirs in the southern Karoo Basin, South Africa*. Unpublished M.Sc. dissertation. RWTH Aachen University. 91p.

Oelofsen, B.W. 1981. *An anatomical and systematic study of the family Mesosauridae (Reptilia: Proganosauria) with special reference to its associated fauna and*

palaeoecological environment in the Whitehill Sea. Unpublished Ph.D. thesis. University of Stellenbosch. 163p.

Oelofsen, B. & Aranjo, D.A. 1983. Palaeoecological implications of the distribution of Mesosaurid reptiles in the Permian Irati sea (Parana Basin), South America. *Revista Brasileira de Geociencias*. 13(1): I–6.

Oelofsen, B.W. 1986. A fossil shark Neurocranium from the Permo-Carboniferous (lowermost Ecca Formation) of South Africa. In *Indo-Pacific fish biology: proceedings of the Second International Conference on Indo-Pacific Fishes*. T. Uyeno, R. Arai, T. Taniuchi & K. Matsuura, Eds. Tokyo: Ichthyological Society of Japan. 107–24.

Oelofsen, B.W. 1987. The biostratigraphy and fossils of the Whitehill and Irati Shale Formations of the Karoo and Parana Basins. In *Gondwana Six: Sratigraphy, Sedimentology, and Paleontology*. G.D. McKenzie, Ed. Geophysical Monograph of the American Geophysical Union. 41:131–8.

Oschmann, W. 1991. Distribution, dynamics and paleoecology of Kimmeridgian (Upper Jurassic) shelf anoxia in western Europe. In *Modern and Ancient Continental Shelf Anoxia*. R.V. Tyson & T.H. Pearson, Eds. Geological Society of London Special Publication. 58: 381–395.

Paytan, A., Kastner, M. & Chavez, F.P. 1996. Glacial to interglacial fluctuations in productivity in the equatorial Pacific as indicated by marine barite. *Science*. 274: 1355–1357.

Pedersen, T.F. & Calvert, S.E. 1990. Anoxia vs productivity: what controls the formation of organic carbon-rich sediments and sedimentary rocks? *AAPG Bulletin*. 74: 454–466.

Pickford, M. 1995. Karoo Supergroup palaeontology of Namibia and brief description of a conodont from Omingonde. *Palaeontolology Africana*. 32: 51–66.

Piper, D. Z. & Dean, W.E. 2002. Trace-element deposition in the Cariaco Basin, Venezuela shelf, under sulfate-reducing conditions—a history of the local hydrography and global climate, 20 Ka to the present: U.S. *Geological Survey Professional Paper 1670*. 41p.

Piper, D.Z. & Perkins, R.B. 2004. A modern vs. Permian shale — the hydrography, primary productivity, and water-column chemistry of deposition. *Chemical Geology*. 206: 177–197.

Potter, P.E., Maynard, J.B. & Deptris P.J. 2005. Provenance of Mudstones. In *Mud and Mudstones*. Berlin, Heildeberg: Springer.157–174.

Prakash Babu, C., Brumsack, H.-J., Schnetger, B. & Böttcher, M.E. 2002. Barium as a productivity proxy in continental margin sediments: a study from the eastern Arabian Sea. *Marine Geology*. 184: 189–206.

Pratt, L.M. & Davis, C.L. 1992. Intertwined fates of metals, sulfur and organic carbon in black shales. In *Geochemistry of Organic Matter in Sediments and Sedimentary Rocks*. L.M. Pratt, J.B. Comer & S.C. Brassell, Eds. Society of Sedimentary Geology (S.E.P.M.). 27: 1–27.

Raiswell, R. & Berner, R.A. 1986. Pyrite and organic matter in Phanerozoic normal marine shales. *Geochim. Cosmochim. Acta*. 50: 1967–1976.

Retallack, G.J. 2009. Greenhouse crises of the past 300 million years. *Geological Society of America Bulletin*. 121: 1441–1455.

Robin, E., Rabouille C., Martinez G., Lefevre I., Reyss J., Van Beek, P. & Jeandel, C. 2003. Direct barite determination using SEM/EDS-ACC system: implication for constraining barium carriers and barite preservation in marine sediments. *Marine Chemical*. 82: 289–306.

Rollinson, H. 1993. *Using Geochemical Data. Evaluation, Presentation, Interpretation*. New York: Longman Scientific & Technical. 352p.

Rowsell, D.M. & De Swart, A.M.J. 1976. Diagenesis in Cape and Karroo sediments, South Africa, and its bearing on their hydrocarbon potential. *Transactions of the Geology Society of South Africa*. 79: 81–145.

Rubidge, B.S. 2005. Re-uniting lost continents -Fossil reptiles from the ancient Karoo and their wanderlust. *South African Journal Geology*. 108: 135–172.

Sageman, B.B., Murphy, A.E., Werne, J.P., Ver Straeten, C.A., Hollander, D.J. & Lyons, T.W. 2003. A tale of shales: the relative roles of production, decomposition, and dilution in the accumulation of organic-rich strata, Middle-Upper Devonian, Appalachian basin. *Chemical Geology*. 195: 229–273.

Scheffler, K. 2004. *Reconstruction of sedimentary environment and climate conditions by multi-geochemical investigations of Late Palaeozoic glacial to postglacial sedimentary sequences from SW-Gondwana*. Unpublished Ph.D. thesis. Rheinischen Friedrich-Wilhelms-Universität Bonn. 243p.

Scheffler, K., Buehmann, D & Schwark, L. 2006. Analyses of late Palaeozoic glacial to postglacial sedimentary successions in South Africa by geochemical proxies-response to climate evolution and sedimentary environment. *Palaeogeography, Palaeoclimatology, Palaeoecology*. 240: 184-203.

Schieber, J. 1999. Distribution and deposition of mudstone facies in the Upper Devonian Sonyea Group of New York. *Journal of Sedimentary Research*. 69: 909–925.

Schieber, J. 2001. A role for organic petrology in integrated studies of mudrocks: Examples from Devonian black shales of the Eastern US. *International Journal of Coal Geology*. 47(3–4): 171–187.

Schieber, J. 2003. Simple gifts and buried treasures- Implications of finding bioturbation and erosion surfaces in black shales. *The Sedimentary Record*. 1: 4–8.

Smith, R.M.H. 1990. A review of the stratigraphy and sedimentary environments of the Karoo Basin, South Africa. *Journal of African Earth Sciences*. 10: 117–137.

Smith, R.M.H, Eriksson, P.G. & Botha, W.J. 1993. A review of the stratigraphy and sedimentary environments of the Karoo-aged basins of Southern Africa. *Journal of African Earth Sciences*. 16: 143–169.

Smithard, T., Bordy, E.M. & Reid, D.L. 2015. The effect of dolerite intrusions on the hydrocarbon potential of the lower Permian Whitehill Formation (Karoo Supergroup) in South Africa and southern Namibia: A preliminary study. *South African Journal of Geology*. 118(4): 489–510.

Strydom, H.C. 1950. The geology and chemistry of the Laingsburg Phosphorites. *Annals of the University of Stellenbosch*. 26A: 267–85.

Tankard, A.J., Jackson, M.P.A., Erikson, K.A., Hobday, D.K., Hunter, D.R. & Minter, W.E.L. 1982. *Crustal evolution of Southern Africa. 3.8 billion Years of Earth History*. New York: Springer-Verlag. 532p.

Taylor, S.R. & McLennan, S.M. 1985. *The continental crust. Its composition and evolution*. USA: Blackwell Science. 312p.

Thamdrup, B. & Canfield, D.E. 1996. Pathways of carbon oxidation in continental margin sediments off central Chile. *Limnology and Oceanography*. 41:1629–1650.

Tosca, N.J., Guggenheim, S. & Pufahl, P.K. 2015. An authigenic origin for the Precambrian greenalite: Implications for the iron formation and the chemistry of ancient seawater. *Geological Society of America Bulletin*. 128 (3–4): 511–530.

Tyson, R.V. & Pearson, T.H. 1991. Modern and ancient continental shelf anoxia: an overview. In *Modern and Ancient Continental Shelf Anoxia*. R.V. Tyson & T.H. Pearson, Eds. Special Publication Geological Society. 58: 1–24.

Van Vuuren, C.J. 1983. *A basin analysis of the northern facies of the Ecca Group*. Unpublished Ph.D. thesis, University of the Orange Free State, Bloemfontein. 249p.

Veevers, J.J. & Powel, C. McA. 1987. Late Paleozoic glacial episodes in Gondwanaland reflected in transgressive-regressive depositional sequences in Euramerica. *Geological Society of America Bulletin.* 98: 475–487.

Veevers, J.J., Cole, D.I. & Cowan, E.J. 1994. Southern Africa: Karoo Basin and Cape Fold Belt. In *Permian–Triassic Pangean Basins and Foldbelts along the Panthalassan Margin of Gondwanaland*. J.J. Veevers & C. McA. Powell, Eds. Memoirs- Geological Society of America. 184: 223–278.

Veizer, J., Ala, D., Azmy, K., Bruckschen, P., Buhl, D., Bruhn, F., Carden, G.A.F. & Diener, A. 1999. $^{87}Sr/^{86}Sr$, $\delta^{13}C$ and $\delta^{18}O$ evolution of Phanerozoic seawater. *Chemical Geology*. 161: 59–88.

Viljoen, J.H.A. 1992. Lithostratigraphy of the Collingham Formation (Ecca Group), including the Zoute Kloof, Buffels River and Wilgehout River Members and the Matjiesfontein Chert bed. *Lithostratigraphic Series, South African Committee for Stratigraphy, Council for Geoscience*. 22: 1–10.

Viljoen, J.H.A. 1994. Sedimentology of the Collingham Formation, Karoo Supergroup. *South African Journal of Geology*. 97: 167–183.

Vine, J. D. & Tourtelot, E. B. 1970. Geochemistry of black shale deposits; a summary report. *Economic Geology*. 65(3): 253–272.

Visser. J.N.J. 1989. The Permo-Carboniferous Dwyka Formation of southern Africa: deposition by a predominantly subpolar marine ice sheet. *Palaeogeography, Palaeoclimatology, Palaeoecolology*. 70: 377–391.

Visser, J.N.J. & Young, G.M. 1990. Major element geochemistry and paleoclimatology of the Permo-Carboniferous glacigene Dwyka Formation and post-glacial mudrocks in southern Africa. *Palaeogeography, Palaeoclimatology, Palaeoecology.* 81:49–57.

Visser, J.N.J. 1991. The palaeoclimatic setting of the late Paleozoic marine ice sheet in the Karoo Basin of southern Africa. *Geological Society of America, Special Paper.* 261: 181–190.

Visser, J.N.J. 1992. Deposition of the early to Late Permian Whitehill Formation during a sea-level highstand in a juvenile foreland basin. *South Africa Journal of Geology*. 95 (5/6): 181–193.

Visser, J.N.J. 1993. Sea-level changes in a back-arc-foreland transition: the late Carboniferous-Permian Karoo Basin of South Africa. *Sedimentary Geology*. 83: 115–131.

Visser, J.N.J. 1994. A Permian argillaceous syn- to post-glacial foreland sequence in the Karoo Basin, South Africa. In *Earth's Glacial Record: International Geological Correlation Project 260.* M. Deynoux, J.M.G. Miller, E.W. Domack, N. Eyles, I.J. Fairchild & G.M. Young, Eds. Cambridge: Cambridge University Press. 193–203.

Visser, J.N.J., van Niekerk, B.N. & van der Merwe, S.W., 1997. Sediment transport of the late Palaeozoic glacial Dwyka Group in the southwestern Karoo Basin: South African Journal of Geology. 100: 223–236.

Visser, J.N.J. 2003. Lithostratigraphy of the Elandsvlei Formation (Dwyka Group). *Council for Geoscience (South Africa)*. 39: 1–11.

Von Breymann, M.T., Emeis, K-C. & Suess, E. 1992. Water depth and diagenetic constraints on the use of the barium as a palaeoproductivity indicator. In *Upwelling Systems: Evolution since the Early Miocene*. C.P. Summerhayes, W.L Prell & K.C. Emeis, Eds. Geological Society Special Publication. 64: 273–284.

Wedepohl, K.H. 1971. Environmental influences on the chemical composition of shales and clays. In *Physics and Chemistry of the Earth, vol. 8*. L.H. Ahrens, F. Press, S.K. Runcorn & H.C. Urey, Eds. Oxford: Pergamon. 305–333.

Werner, M. 2006. *The stratigraphy, sedimentology and age of the Late Palaeozoic Mesosaurus Inland Sea, SW-Gondwana: new implications from studies on sediments and altered pyroclastic layers of the Dwyka and Ecca Group (lower Karoo Supergroup) in southern Namibia*. Unpublished Ph.D. thesis. University of Würzburg, Germany. 428p.

Wickens, H. de V. 1994. *Basin Floor Fan building Turbidites of the South Western Karoo Basin. Permian Ecca Group, South Africa*. Unpublished Ph.D. thesis. University of Port Elizabeth, South Africa. 223p.

Young, G.M. 2010. Precambrian and Phanerozoic postglacial processes. *Geological Society of America*. 38 (12): 1147–1148.

4 Provenance of the lower Permian Ecca Group in the southern main Karoo Basin, South Africa

Abstract

Provenance studies of fine-grained sedimentary rocks are notoriously complex as mechanical breakdown and diagenesis results in mineralogical changes and loss of source rock information. This study provides an investigation into transfer paths from source to sink for the lower Ecca Group during the early evolution of the main Karoo Basin (MKB) using bulk geochemistry. More specifically, the study shows used geochemical ratios to: 1) categorize the lithologies of the lower Ecca Group, and 2) determine their potential source origins.

Geochemical data was obtained and compared from three boreholes in the MKB: BH KZF-1 in the western MKB (Tankwa Karoo Sub-basin), BH SFT2 in the south-central MKB and BH KWV-1 in the eastern MKB. Data was analysed using Discriminant Function Diagrams, Principle Component Analysis Results (PCA), Zr/Ti values, the Index of Compositional Variability (ICV) and the Chemical Index of Alteration (CIA). Trace element PCA and the ICV imply different provenance regions for each borehole with stronger felsic and intermediate signatures in the western MKB and stronger mafic signatures in the eastern MKB. Mudstones of the Prince Albert and Whitehill formations in the western MKB comprises sediment that was mostly sourced from the Cape Granite Suite, Cape Supergroup, Dwyka Group and possibly the Kango Group (Saldania Belt) and/or the Namaqua-Natal Belt. The mafic signature in the Prince Albert and Whitehill formations in the eastern MKB indicate sediment source areas dominated by the Dwyka Group, Natal Group, and various metaphoric and igneous stratigraphic units that make up the Archean Kaapvaal Craton as well as Precambrian mobile belts in southern Africa (e.g., Natal, Pan-African Mozambique and Maud Belts). The Collingham Formation is composed of mudstones and wackes in BH KZF-1 and BH KWV-1 and arkoses in BH SFT2. In all three boreholes, the Collingham Formation were mostly sourced from the quartz-arenites and granites most likely associated with the Cape Fold Belt. This study indicates that the potential source regions for the lower Ecca Group is similar to what has been suggested based on existing palaeo-current data for the underlying upper Dwyka Group and overlying upper Ecca Group.

4.1 Introduction

The study of mudstone has been a challenge in the past, due to their fine-grained nature, deceptive homogenous texture and geochemical complexity. During mechanical break-down of sedimentary rocks, there is both physical and chemical alteration and sorting of particles during transport and deposition. The chemical alteration can lead to enrichments of certain minerals in certain grain-size fractions. For example, it has been noted that SiO_2/Al_2O_3 values will often decrease with decreasing textural maturity and grain size (Pettijohn et al., 1972; Weltje & von Eynatten, 2004). Provenance studies of fine-grained sedimentary rocks become increasingly complex when the detrital minerals loose paragenetic information as they are broken down or undergo chemical and/or mineralogical changes through diagenesis and weathering (Weltje & von Eynatten, 2004). Overall, the provenance of the mudstones is not as well constrained as the coarse-grained sedimentary rocks (van Lente, 2004; Johnson, 1991; Vorster, 2013).

Provenance analysis is the reconstruction of the sedimentary record and palaeo-geographic landscapes by tracking the sediment pathways 'backwards' from sink to source. To determine the early Karoo provenance, understanding the potential source areas surrounding the main Karoo Basin (MKB) during early Karoo times is essential (Figure 4.1). The MKB is a foreland basin, bounded to the south and west by the Cape Fold Belt (CFB). The CFB formed part of the Pan Gondwanian Mobile Belt, resulting in terrane accretion through collision and compression along southern Gondwana. During the Late Palaeozoic multiple episodes of orogenic deformation occurred in the southernmost South America (Sierra de la Ventana), South Africa, the Antarctic Peninsula and eastern Australia (Tankard et al., 1982; Catuneanu et al., 1998; Pankhurst et al., 2006). The timing and development of the CFB is still controversial, but multiple lines of evidence suggest that: 1) orogenic cycles of loading and unloading in the CFB and 2) tectonically controlled flextural subsidence probably existed until at least the Latest Triassic (Catuneanu et al., 1998; Bordy et al., 2004a; Hansma et al., 2015; Blewett & Phillips, 2016; Blewett et al., 2019).

Within the MKB, the sedimentary rocks of Karoo Supergroup were deposited on the Archaean Kaapvaal Craton, the Proterozoic Namaqua-Natal Belt, the Pan-African Saldania-Gariep Belts and partly over the Early Palaeozoic Cape Supergroup and Natal Group of the Cape Basin and Natal Basin, respectively (Figure 4.2; Cole, 1992; Johnson et al., 2006).

From the Late Carboniferous until the Early Jurassic, the depositional environments in the MKB changed from glacial (Dwyka Group) to continental-slope deltaic-lacustrine (Ecca Group) to alluvial fans and fluvial plains (Beaufort Group) to ephemeral streams and dune complexes (upper Stormberg Group; e.g., Smith, 1990; Catuneanu et al., 1998; Johnson et al., 2006). The deglaciation events that dominated the Dwyka depositional episode ended ~ 290 Ma ago, and resulted in a southward thickening succession of tillites, diamictites, and varvites (e.g., Bangert et al., 1999; Visser, 2003; Isbell et al., 2008; Craddock & Thomas et al. 2011). The post-glacial mudstones and sandstones of the lower Ecca Group were deposited in a large inland basin from ~ 290 to ~ 272 Ma ago in the Early Permian. In the southern half of the MKB, the lowermost Ecca unit is the Prince Albert Formation (~ 289.6 ±3.4 Ma; Bangert et al., 1999) and comprises basin-plain pelagic mudstones and rhythmites (Johnson et al., 2006). The conformably overlying black shales of the Whitehill Formation (280.5 ±2.1 Ma; Werner, 2006) give way up-sequence to distal turbidites and tuffaceous laminated mudstones in the Collingham Formation (Viljoen, 1992). The silicic air-fall tuffs in the latter unit were dated at 277 ±1.4 Ma to 274 ±1.8 Ma (Werner, 2006; Fildani et al., 2007; Belica et al., 2017).

Although the tuffs are most concentrated in the Collingham Formation, they are also identified in the Upper Dwyka, the rest of the Ecca and Beaufort groups (Ellis & Watts, 1974; Lock & Wilson, 1975; Viljoen, 1990). Overall, the tuff beds in the MKB are found to be decreasing from south to north and from west to east, indicating a general source emanating from the south and southwest (Viljoen, 1998). Correlation between tuff zones detected in the Upper Dwyka Group indicated that the Dwyka/Prince Albert contact is younging southwards in the basin (Visser, 1982; Viljoen, 1998). Additionally, the tuffs were detected in stratigraphically equivalent Permian rocks in other Gondwanan basins, for example in the Parana Basin, central Argentine basins, Sauce Grande Basin, Ellisworth Mountains and the Transantarctic Mountains (Barrett, 1969; Lopez-Gamundi et al., 1990; Coutinho et al., 1991; Miller & Collinson, 1994), which suggests that the Permian basins were close to the volcanic source.

The Prince Albert and Whitehill formations partially correlate with the Pietermaritzburg and Vryheid formations (Bordy et al., 2017) and the Collingham Formation to the Volkrust Formation in the northeast of the basin (Viljoen, 1998). Here, in the northern half of the MKB, continental glaciation may have lasted longer (Cole, 1992), and gave way to coal-bearing fluviodeltaic successions (Smith et al., 1993; Catuneanu et al., 1998).

It has been assumed that most of the sedimentary material that constitute the Ecca and Beaufort groups was sourced from the CFB (Hälbich et al., 1983; Cole, 1992; Wickens, 1994; Scott, 1997). However, this may not hold true for all the early Karoo sedimentation when the CFB was still in early stages of development.

This study aims to use bulk geochemistry of three boreholes from the western Tankwa Karoo Sub-basin, the south-central main Karoo Basin and the eastern Karoo Basin, to identify chemostratigraphic correlations and identify provenance of the sediments during the early Karoo times.

4.2 Evolution and provenance in the early main Karoo Basin evolution

4.2.1 The Cape Fold Belt

Overall, the most accepted explanation for the evolution of the MKB is that of a foreland basin that was strongly influenced by thrusting in the CFB in the Permo-Triassic (Figures 4.1; 4.2 B; e.g., de Wit & Ransome, 1992; Cole, 1992; Catuneanu et al., 1998; Bordy et al., 2004a, b; Hansma et al., 2015; Blewett & Phillips et al., 2019; Blewett et al., 2019). The MKB developed as part of a series of basins across Gondwana (e.g., Paranã Basin, Bowen and Beacon Basins) as a response to flexural tectonics due to orogenic loading.

The Cape Orogeny resulted in the simultaneous folding of the Cape Supergroup (and formation of the CFB) south and the west of the MKB (Figure 4.2 B,). The two branches of the CFB are separated by a major anticlinorium, which divides the southwestern part of MKB into two sub-basins (Figure 4.2 C; Hälbich et al., 1983; De Beer, 1982). The Tankwa Karoo Sub-basin and the Laingsburg Sub-basin contained prograding submarine fans that received sediment from the emerging CFB during the upper Ecca depositional phase (De Beer, 1982; Wickens, 1994; Adelmann & Fiedler, 1996). However, prior to this phase, i.e., during lower Ecca and Dwyka depositional phases, there is no facies change across these two sub-basins, suggesting that their physical separation had not yet occurred (e.g., Johnson et al., 2006). This is corroborated by the earliest record of orogenic activities that seem to have occurred ~ 278 Ma (Hälbich et al., 1983) in the western part of the CFB. According to Adelmann & Fielder (1996), the eastern CFB only began to develop during deposition of upper Beaufort Group in the latest Permian.

The formation of the MKB along the south-western margin of Gondwana as a retro-arc foreland basin due to northward subduction of the Palaeo-Pacific Plate beneath

the continent, is somewhat contested (e.g., Lindeque et al., 2007, 2011; Tankard et al., 2012) For example, Lindeque et al. (2007; 2011) used seismic-reflection data to tentatively postulate that the Cape and MKB developed into a wide, thin-skinned Jura-type fold-belt. Moreover, Tankard et al. (2012) suggested the oblique reactivation of a southern Namaqua suture, resulting in a sinistral strike-slip orogen forming the Karoo foreland basin.

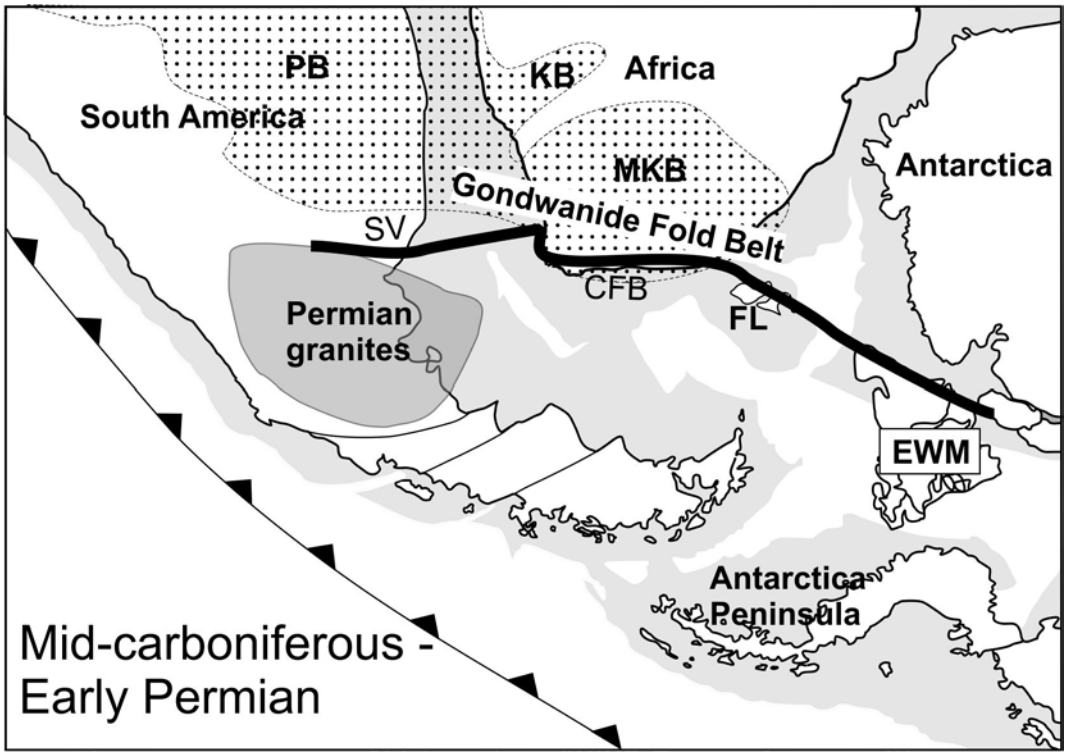

Figure 4.1: Schematic reconstruction of SW Gondwana from the Middle-Carboniferous to the Early Permian. EWM = Ellsworth-Whitmore mountains crustal block; FL= Falkland Islands; CFB = Cape Fold Belt; SV = Sierre le de Ventana; MKB = Main Karoo Basin; KB = Kalahari Basin; PB = Paranã Basin. Adapted from Pankhurst et al. (2006).

4.2.2 Provenance regions for the Dwyka and lower Ecca groups

The MKB is an east–west striking basin and is at its deepest in the south and is situated between the Cargonian Highlands (on the northern Kaapvaal Craton) to the north and the CFB to the south (Figure 4.2 A; Johnson et al., 1997). Although this study focuses on the provenance investigation of the lower Ecca Group, this aim cannot be accomplished without brief review of the provenance history of the conformably underlying Dwyka Group, which consists of glacial sediments, most fully developed in the southern MKB. The Dwyka Group lies unconformably over the Ordovician to Middle Carboniferous Cape Supergroup in the southernmost MKB. Further to the north (Figure 4.2 A), over the pre-Dwyka basement dominated by rocks of the Palaeoproterozoic to Mesoproterozoic Namaqua-Natal Belt and in the

northernmost parts by the Archean stratigraphic units contained in the Kaapvaal Craton (Visser et al., 1990; Cole; 1992). The Dwyka Group is represented in the East Falkland Island by the Fitzroy Tillite Formation, which overlies the Bluff Cove Formation, an equivalent of the Witteberg Formation in the upper Cape Supergroup (Trewin et al., 2002; Craddock & Thomas, 2011).

Glacial striations on pre-Dwyka bedrock indicate changing directions of ice-flow across southern Africa, thereby providing clues of early sediment transport directions during the Permo-Carboniferous. Overall, prominent flow directions were from the north-northeast to south-southeast (Figure 4.2 B; Theron & Blignaut, 1975; Visser, 1997; Isbell et al., 2008; Dietrich & Hoffman, 2019). Detrital zircons analysed from the Dwyka Group show a major Neoproterozoic, a secondary Mesoproterozoic and a minor Cambrian to Ordovician age populations (Craddock & Thomas, 2011; Vorster, 2013). Therefore, source regions for the Dwyka Group are related to the Namaqua-Natal Belt, the Pan-African Orogeny (including the Saldania, Gariep and Maud Belts), southern Cape Supergroup and the Natal Group in the north north-east (Figure 4.2 A; e.g., Cole, 1992; Vorster, 2013; Craddock & Thomas, 2011). This is corroborated by representative boulder lithologies e.g., quartzites and sandstones, granites and gneisses, lava, intermediate to mafic intrusive, carbonates, mudstone and shale and chert-carbonate-banded ironstone (Visser et al., 1986, 1987; Visser, 1997; Blignaut & Theron, 2012).

Similarly, to the Dwyka Group, palaeo-current data from the entire Ecca Group suggests that sediment was entering the basin from north, northeast, east, south, southwest and west (Figure 4.2 B; e.g., Ryan, 1967; Ryan & Whitfield, 1979; Wickens, 1984; Veevers et al., 1994; Hastie et al., 2019). The palaeo-current directions during early Karoo times also indicate that there were prominent palaeo-highs in the north, the east and the south (e.g., Ryan, 1967; Ryan & Whitfield, 1979; Visser, 1990, 1992, 1997; Bordy et al., 2017; Hastie et al., 2019).

Provenance domains specifically for the lower Ecca Group are very poorly constrained, because the fine-grained facies associations that dominate this part of the Karoo succession lack reliable palaeo-current indicators (e.g., large-scale cross-beds, flute casts, clast imbrications). However, inferences on the source areas can be made indirectly, because primary palaeo-current indicators tend to be common in the conformably underlying glacial Dwyka Group and overlying upper Ecca Group, which is dominated by turbidites and shallower water to deltaic successions (Johnson et al., 2006). However, even in the upper Ecca Group, the overall palaeo-current pattern in the eastern MKB is less well defined than in the western MKB, partly due to the

eastern facies being finer-grained (e.g., upper Pietermaritzburg Formation) and the sediment-source areas having been lost in post-Karoo times during Gondwana break-up (Marshall, 1994; Ryan 1967; Ryan & Whitfield, 1979; von Brunn, 1996; Haldorsen et al., 2001; Bangert & von Brunn, 2001). Based on lateral facies relationships, it has been suggested that, the regional palaeo-slope during Whitehill times may have dipped in a south-southwest direction (e.g., Chukwuma & Bordy, 2016). This is further corroborated by the fact that all pre-Triassic Karoo units in the northeast MKB, including but not limited to the fluvio-deltaic Vryheid Formation, had been supplied from sources in the north, northeast and east (e.g., Ryan, 1967; Ryan & Whitfield, 1979; Johnson et al., 2006; Bordy & Prevec, 2008 ; Hastie et al., 2019).

Presently, the MKB (Figure 4.2 A) covers the southern half of the Kaapvaal Craton and the southern central part of Namaqua-Natal Mobile Belt that wraps around the Kaapvaal Craton (Figure 4.2 A; Thomas et al., 1994; McCarthy et al., 2018). The eastern part of the Namaqua-Natal Mobile Belt is overlain by the siliciclastic Natal Group deposited in a south-southwest sloping graben in the Ordovician (Figure 4.2 A; Hobday & Von Brunn,1979; Thomas et al., 1994).

The most likely source regions around the MKB during Early Permian Karoo depositional episode were the Mesoproterozoic Namaqua–Natal Belt in the east and west, and the Ordovician–Carboniferous Cape Supergroup in the south (Figure 4.2. A, B). Furthermore, the Pan-African Mozambique Belt, which extends from East Africa to the Dronning Maud Land in East Antarctica, as well as the Natal Group were also likely provenance regions in the east. The Archean Kaapvaal Craton must have also acted as a key sediment source area in the lower Ecca, because this region has been repeatedly demonstrated as a key detritus supply area for the conformably underlying Dwyka as well upper Ecca Groups (Table 4.1; Ryan & Whitfield, 1979; Craddock and Thomas, 2011; Vorster, 2013; Ryan, 1967; Ryan & Whitfield, 1979; Johnson et al., 2006; Hastie et al., 2019).

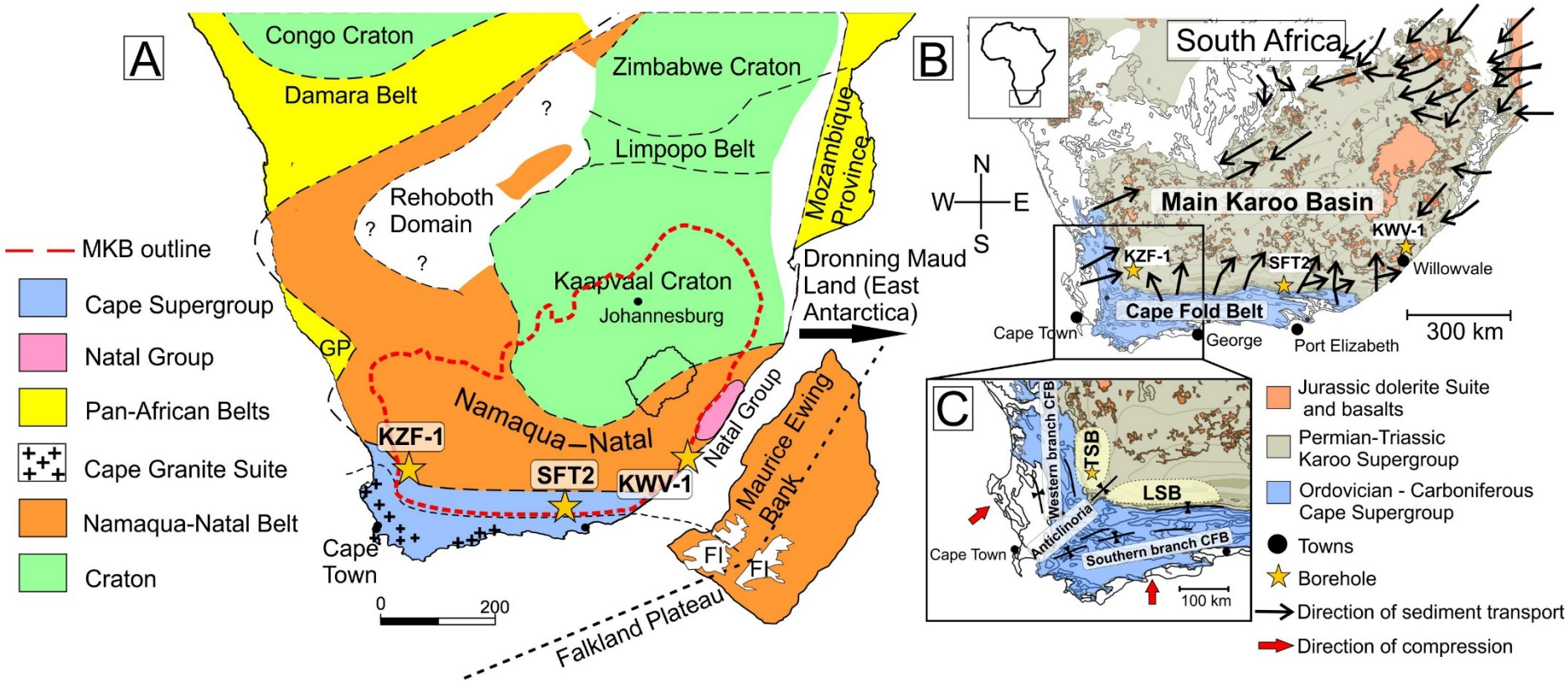

Figure 4.2: A) Summary of the regional extent of basement rocks in southern Africa. Adapted from Thomas et al., 1994; Marshall, 1994; Eglington, 2006. B) Geological map of the main Karoo Basin, Cape Fold Belt and Karoo igneous rocks showing upper Ecca Group palaeo-current directions (adapted from Ryan & Whitfield, 1979; Hastie et al., 2019). C) Inset map of the Tankwa and Laingsburg Sub-basins (adapted from Wickens, 1994; Andersson & Worden, 2004). Locations of boreholes (BH KZF-1, BH KWV-1 and BH SFT2) are marked by stars. Abbreviations: MKB = Main Karoo Basin; CFB = Cape Fold Belt; Fl = Falkland Islands; TSB = Tankwa Sub-basin; LSB = Laingsburg Sub-basin; GP = Gariep Province.

Table 4.1: A summary of potential provenance source regions to the lower Ecca Group, Karoo Supergroup in South Africa.

Province Domain	***Stratigraphic units***		***Rock types***		***Ages***	***References***
Choiyoi Magmatic Province (South America)			Granite-rhyolite magmatic arc; volcaniclastic ash.		Late Carboniferous-Early Jurassic	Llambias (1999); Elliot (2013); Sato et al. (2015); Bordy & Ambrahams (2016); Navarrete et al. (2019).
Dwyka Group	Elandsvlei and Mbizane formations		Diamictite, mudstone, lesser sandstone and dropstones of quartzites/sandstones, granites/gneiss, intermediate and mafic intrusives, lava, carbonates, mudstone/shales, chert/BIF.		Middle- Late Carboniferous	Bangert et al. (1999); Visser (1987; 1997; 2003); Blignaut & Theron (2012).
Cape Supergroup	Table Mountain, Bokkeveld and Witteberg groups		Orthoquartzite, quartz arenite, lesser volumes of siltstone and diamictite.		Early Ordovician to Early Carboniferous	Booth & Shone (2002); Thamm & Johnson (2006); De Beer et al. (1982); Tankard et al. (2012).
Natal Group	Msikaba, Marianhill and Durban formations.		Siliciclastic sedimentary rocks (quartz arenites).		Late Cambrian to Early Ordovician	Marshall (2003a, b, 2006); Thamm & Johnson (2006); Vorster et al. (2015)
Cape Granite Suite			S-I type granitoids and lesser mafic and intermediate plutonism.		Late Neoproterozoic to Middle Cambrian	Scheepers & Armstrong (2002); Gresse et al. (2006); Chemale et al. (2011).
Pan African Orogeny	Damara, Gariep, Saldania Belts, Mozambique and Maud (East Antarctica) Belts		Quartzites, gneisses, schists, metamorphosed carbonates.		Mesoproterozoic, Neoproterozoic, Middle Cambrian.	Rozendaal et al. (1999); Frimmel et al. (2001); Jacobs et al. (2003).
Namaqua-Natal Belt	***Namaqua-Belt***	***Natal-Belt***	***Namaqua-Belt***	***Natal-Belt***	Late Paleoproterozoic to Mesoproterozoic	Eglington & Armstrong (2003); Eglington (2006); Hartnady et al. (1985); Thomas et al. (1994); Hörstmann et al. (1990); Matthews (1972, 1981); Allen & Tucholke (1981); Groenewald et al. (1991); Grantham et al. (1997).
	Richterveld Bushmanland	Margate, Mzumbe Tugela	Para-orthogneisses, Granites, charkonites, granitoids, calc-alkaline lavas, quartzites, phyllites, metabalsalts.	Granitoid gneisses mafics and ultra- mafics, amphibolite-facies, mafic and felsic orthogneisses, metasedimentary rocks.		
Kaapvaal and Zimbabwe Cratons			Variety of granitic plutons.		Archean	Brandl & de Wit (1997); Windley (1995); de Wit et al. (2002).

4.3 Materials and methods

4.3.1 Sample analyses

Two boreholes were drilled by the Karoo Research Initiative (KARIN Project) in the western MKB (KZF-1) (32°50'30.43" S, 19°44'33.02" E) and in the eastern MKB (KWV-1) (32°14'43.10" S, 28°35'08.10" E) (Figure 4.2). A total of 33 samples from BH KZF-1 (KZF01– KZF33) and 17 samples from BH KWV-1 (KWV01– KWV17), were collected from the Prince Albert, Whitehill and Collingham formations (Figure 4.3). One sample from the bottom of the Tierberg Formation (KZF01) was sampled in BH KZF-1. Samples from BH KZF-1 and BH KWV-1 were crushed using a custom-built hydraulic splitter, Sturtevant laboratory jaw-crusher and powdered using Seribtechnik swing mill with carbon steel cassettes. XRF analyses were performed at the University of Cape Town using a Panalytical Axios wavelength-dispersive XRF spectrometer with rhodium end-window X-ray tube. A Claisse Fluxer is used to prepare fusion discs and hydraulic cold press and dye is used for preparation of powder briquettes. Concentrations of major elements (Si, Ti, Al, Fe, Mn, Ca, Na, K, P, S, Cr, Ni) and trace elements (Zn, Cu, Ni, Mo, Nb, Zr, Y, Sr, Rb, U, Th, Pb, Co, Mn, Cr, V, F, S, Cl, Sc, Ba) were obtained. In BH KZF-1, the samples taken from near a fracture-zone containing hydrothermal veining and have high Mo content, are therefore omitted from provenance analyses.

Quantitative XRD was carried out on 22 samples from BH KZF-1 and 17 samples from BH KWV-1. XRD was measured in wt% with a Malvern Panalytical AERIS diffractor meter with PIXcel detector and fixed slits with Fe filtered Co- Kα radiation by XRD Analytical and Consulting Laboratory in Pretoria. The phases were determined using X'pert Highscore plus software.

For a more comprehensive understanding of provenance of the lower Ecca Group, data from BH SFT2, from the south-central MKB, are included in this study (Figures 4.2 and 4.3). BH SFT2 was drilled in 2012 by the African Earth Observatory Network (AEON), based at Nelson Mandela University, Port Elizabeth. Geochemical data (XRF and XRD) from 16 samples are found in Geel (2014; Appendix A).

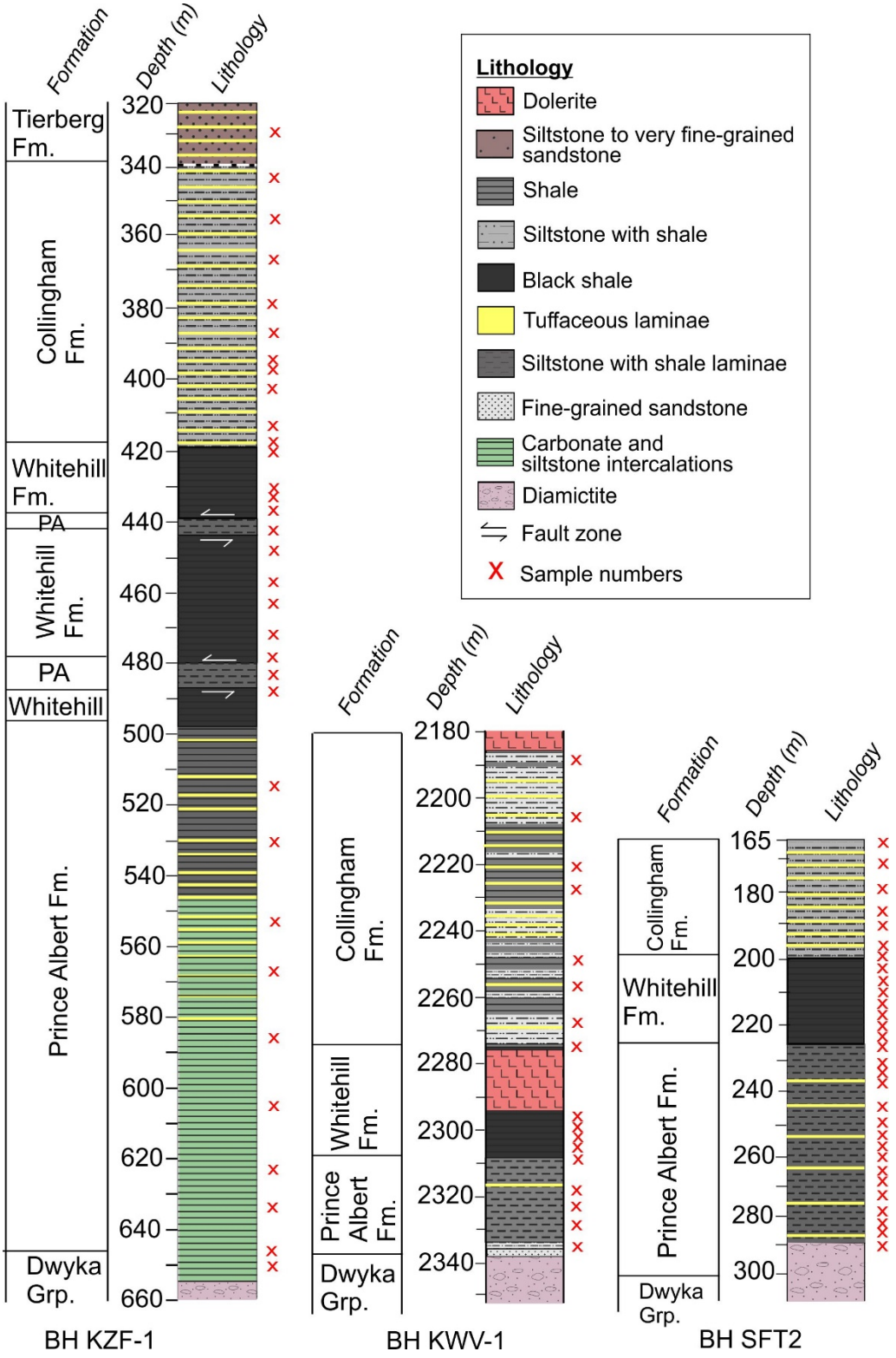

Figure 4.3: Lithostratigraphy of lower Ecca Group in BH KZF-1, BH SFT2 (Geel, 2014) and BH KWV-1. Sample intervals are indicated by the x.

4.3.2 Geochemical techniques

The provenance analysis of mudstones requires an integrated sedimentary petrographical and geochemical approach (von Enyatten et al., 2012). The geochemical techniques used in this study are discussed below.

General discrimination of sedimentary rocks can be determined by plotting their bulk geochemistry on sediment-geochemical classification charts. Fe_2O_3/K_2O vs SiO_2/Al_2O_3 values distinguishes between quartz-rich and clay-rich sediments (Pettijohn et al., 1972; Herron, 1988). General discrimination diagrams, using these ratios, distinguish between Fe-rich mudstone, mudstone, wacke, Fe-rich sandstone, arkose, subarkose, litharenite, sublitharenite and quartz-arenite.

Because most elements occur in a variety of minerals and rock-types, tracing (fingerprinting) source rocks based on the elemental composition of the derived sediments is challenging. Source rock material will undergo physical and chemical modification during transportation and burial, resulting in an “environmental bias” and/or a “diagenetic bias” (Garzanti, 2016). Burial diagenesis can make heavy minerals unstable, and at 3–4 km depth, only zircon, apatite, rutile and Cr spinel can survive (Morton & Hallswork, 2007). Elements such as Mg, Ni and Cr, hosted mainly in mafic and ultramafic rocks, remain relatively unaltered and can provide clues to their sources (von Eynatten et al., 2003; Garzanti & Resentini, 2016).

Principal Component Analysis (PCA) is a useful tool to reduce the dimensionality of a data set representing multivariant data in a two-dimensional space. PCA’s are used to transform raw data to principal components (PCs), which are a set of variables ordered so that the components retain the variation of the original variables in decreasing order. PCA can be used to identify element-assemblages associated with geological processes. A PCA plot correlates the variable elemental data into smaller “uncorrelated variables” referred to as a PCs, whose covariance matrix is diagonal. PC1 accounts for as much data variance as possible and each succeeding PC will account for the remaining variables. Data are plotted on a PC1 vs. PC2 plot, which will account for most of the variance (Daunis-I-Estadella et al., 2011; Lever et al., 2017). Correlation between geochemical data and framework minerals with PCA’s or geochemical proxies can be useful when interpreting data. Table 4.2 summarizes some of the common mineral phases and their element associations and can be used identify sedimentary rocks types.

Table 4.2: Element- mineral associations. Adapted from Scheffler, 2004.

Rock forming minerals	***Element association***	***Mineral phases***
Silicates	Si, Al, Ti, Fe, Mg, Ca, Na, K, Rb, Sr, Ba, transition metals.	Quartz, feldspar, mica, clay minerals
Carbonates	Ca, Mg, Fe, Mn, Sr, Ba	Calcite, dolomite, siderite, rhodochrosite etc.
Phosphates	P, Ca, Ce	apatite
Metal-oxides/hydroxides/sulf	Fe, Mn transition metals, Zr, Ba	Goethite, haematite, pyrite etc.
Total Organic Carbon (TOC)	Transition metals, Ba	

A method for the discrimination of parent rock using geochemistry is the Index of Compositional Variability (ICV):

$$ICV = (CaO + K_2O + Na_2O + Fe_2O_3\,(t) + MgO + MnO + TiO) / Al_2O_3) \quad (4.1)$$

Where Fe_2O_3 (t) = total iron and CaO includes all sources of Ca. However, for this study samples that contained more than 60% carbonates were excluded from the ICV calculations. In this index weight oxides are used, and the values decrease with increasing degree of weathering (Potter et al., 2005).

A common geochemical technique used to determine the extent of weathering is the Chemical Index of Alteration (CIA; Nesbitt & Young, 1982):

$$CIA = [Al_2O_3 / (Al_2O_3 + CaO^* + K_2O + Na_2O] \times 100 \quad (4.2)$$

CIA is only applied to samples with carbonate abundances < 30%. XRF data is converted from wt% to molar weight, which emphasises differences in mineralogical relationships. CaO^* is represented by the silicate-fraction of the sample and is corrected for using the method by McLennan et al. (1993).

Zr/Ti is also useful in provenance discrimination, as they are among the most inert components, that are least likely to undergo alteration. Different provenance types can be distinguished by their Zr/Ti values. High ratios indicate a granite source, e.g., G1 granite = 0.14 and quartz arenite = 0.13 (Boryta & Condie, 1990). Lower Zr/Ti values of 0.067 indicate upper crust (Taylor & McLennan, 1985). Basic igneous rocks will also have low Zr/Ti values. Andean volcanic rocks are between 0.034 for andesites and 0.024 for basalts. The lowest Zr/Ti values (0.01) are found in primitive magmas of oceanic island basalts and mid-oceanic ridge basalts. The North American Shale Composite (NASC) yields a Zr/Ti values of 0.043 (Ewart, 1982).

Discriminant Function Analysis is another way to define provenance groups. Diagrams using 2 discriminant functions based on TiO_2, Al_2O_3, Fe_2O_3, MgO, CaO, Na_2O and K_2O plots into four different provenance types: felsic igneous, mafic igneous, intermediate and quartzose sedimentary provenances. To circumvent the issue with biogenic CaO and SiO_2 the afore mentioned values are normalized to Al_2O_3 (Roser & Korsch, 1988):

1) Discriminant Function 1 = 30.638 TiO_2/Al_2O_3 – 12.541 Fe_2O_3/Al_2O_3 + 7.329 MgO/Al_2O_3 + 12.031 Na_2O/Al_2O_3 + 35.401 K_2O/Al_2O_3 -6.382
2) Discriminant Function 2 = 56.500 TiO_2/Al_2O_3 – 10.879 Fe_2O_3/Al_2O_3 + 30.875 MgO/Al_2O_3 - 5.404 Na_2O/Al_2O_3 + 11.112 K_2O/Al_2O_3 – 3.89

4.4 Results

4.4.1 Lithological discrimination

The Prince Albert Formation in BH KZF-1 is ~ 158 m thick, ~ 60 m thick in BH SFT2 and ~ 30 m thick in BH KWV-1. The Whitehill Formation is ~ 20 m thick in BH KZF-1, ~ 27 m thick in BH SFT2 and ~ 13 m thick in BH KWV-1. The Collingham Formation is ~ 80 m thick in BH KZF-1, 35 m thick in BH SFT2 and ~ 90 m thick in BH KWV-1.

In all three boreholes the Prince Albert Formation has the highest clay-mineral content, which increases from west to east (Figure 4.4; BH KZF-1= 18 wt%; BH SFT2= 46 wt%; BH KWV-1= 49 wt%). Diagenetic iron- and magnesium- rich carbonate minerals, such as dolomite, ankerite and siderite occur in all three formations, but most significantly in the Prince Albert and the Whitehill formations in BH KZF-1 and BH SFT2. Rhodochrosite (20 wt%) only occurs in the Prince Albert Formation in BH KZF-1 (Figure 4.4). Anorthite was detected in the Prince Albert Formation, but only in BH SFT2 (2 wt%) and BH KWV-1 (8 wt%). Albite is the predominant feldspar that occurs in the Prince Albert Formation in the western MKB (Figure 4.4; BH KZF-1; 8 wt%). The Whitehill Formation has the highest TOC content (Figure 4.4; BH KZF-1= 5 wt%; BH KWV-1= 4 wt%; BH KWV-1: 5 wt%). Subsequently, the Whitehill Formation contains the highest pyrite or pyrrhotite of all three formations (Figure 4.4; BH KWV-1: 2.21 wt%; BH SFT2: 7.24 wt%; BH KZF-1: 9.18 wt%). This is an indication for basin anoxia, allowing for the preservation of organic matter. Ferrous-dolomite occurs prominently in the Whitehill Formation in BH KZF-1 and BH SFT2. Other diagenetic iron-rich carbonates, such as ankerite, siderite and calcite are identified in all three boreholes. The Collingham Formation has the highest quartz content of all three formations (Figure 4.4; KZF-1: 52 wt%; BH SFT2: 63 wt%; BH

KWV-1: 45 wt%), with the highest measure of quartz detected in BH SFT2. The most commonly occurring feldspar is albite, which is predominantly detected in the Collingham Formation (Figure 4.4; BH KZF-1: 21 wt%; BH SFT2: 10 wt%; BH KWV-1: 17 wt%). Accessory minerals rutile and fluorapatite are detected in all three formations. Zircon was detected in all formations except in the Whitehill Formation in BH KZF-1 and BH KWV-1. Biotite is mostly detected in BH SFT2.

To accompany mineralogical data, sedimentary-geochemical classification diagrams are used to differentiate between terrigenous sandstones and shale using $\log(Fe_2O_3/K_2O)$ vs $\log(SiO_2/Al_2O_3)$ ratios (Figure 4.5). The Prince Albert Formation in all three boreholes is classified as mudstone. In BH KZF-1 the Whitehill Formation is classified as a mudstone or wacke. In BH SFT2 the Whitehill Formation is mostly classified as a mudstone, with only one sample plotting as a wacke and in BH KWV-1, the Whitehill Formation plots only as mudstone. In BH KZF-1 and BH KWV-1 samples from the Collingham Formation are classified as either a mudstone or wacke, but in BH SFT2 all the samples from the Collingham Formation are classified as arkosic.

All three boreholes have undergone burial diagenesis. The effect of diagenesis on BH KZF-1 and BH KWV-1 is discussed in Chapter 2. Table 4.3 summarizes the different detrital and diagenetic minerals found in each borehole.

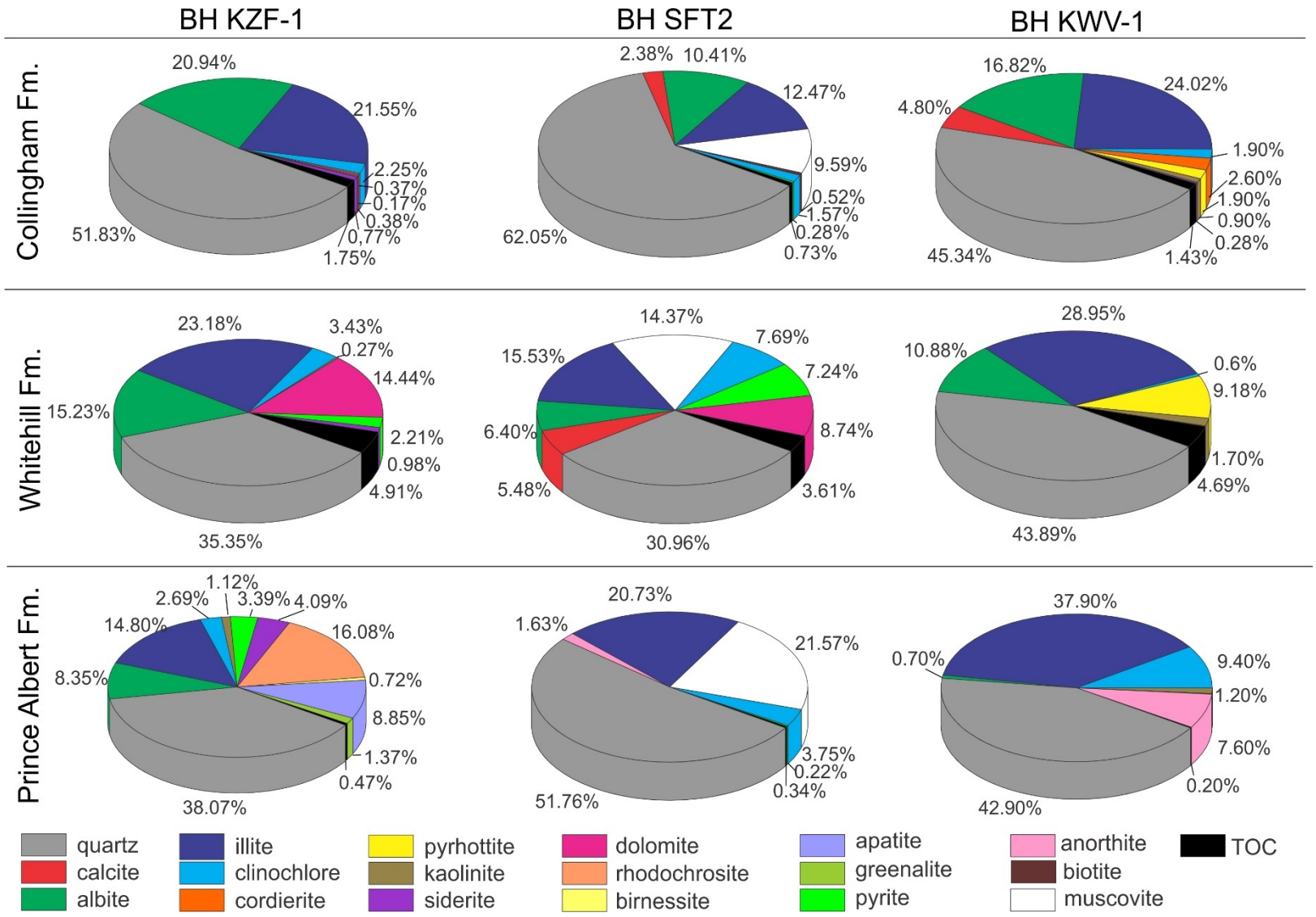

Figure 4.4: Average mineralogical composition for the Prince Albert, Whitehill and Collingham formations for BH KZF-1, BH SFT2 and BH KWV-1.

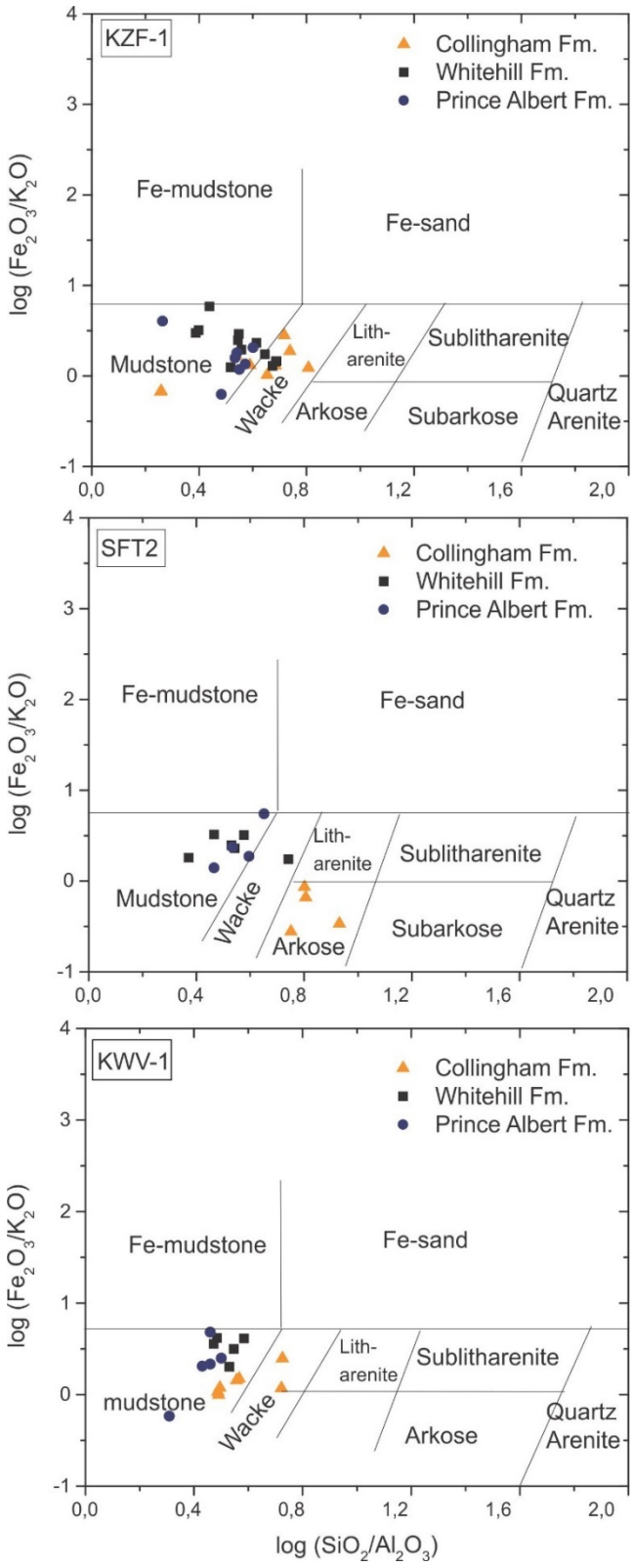

Figure 4.5: Sample discrimination using sediment-geochemical classification chart. Adapted from Herron (1988).

Table 4.3: Summary of mineral occurrences in BH KZF-1, BH SFT2, BH KWV-1. Minerals that are underlined are likely diagenetic. Average quantities (wt%) are given for each category.

Formation	***Minerals***	***Boreholes***		
		BH KZF-1	***BH SFT2***	***BH KWV-1***
Prince Albert Formation	**quartz**	38 wt%	52 wt%	43 wt%
	feldspar	albite (8 wt %)	anorthite (2 wt%)	anorthite (8 wt%)
	clay minerals	illite/muscovite kaolinite clinochlore (18 wt%)	illite muscovite kaolinite clinochlore (46 wt%)	illite/muscovite kaolinite clinochlore (49 wt%)
	carbonates	rhodochrosite siderite (20 wt%)		
	other	birnessite greenalite apatite pyrite (14 wt%)		
	trace/accessory	K-feldspar (orthoclase, sanadine, microperthite) ferroan-dolomite zircon ankerite rutile sphalerite stilpnomelane	pyrite biotite zircon rutile apatite	siderite pyrite biotite pyrrhotite fluorapatite sanidine titanite rutile ankerite
Whitehill Formation	***quartz***	35 wt%	32 wt%	44 wt%
	feldspar	albite (15 wt%)	albite (7 wt%)	albite (11 wt%)
	clay minerals	illite/muscovite kaolinite clinochlore (27 wt%)	illite muscovite kaolinite clinochlore (39 wt%)	illite/muscovite kaolinite clinochlore (31 wt%)
	carbonates	dolomite siderite (15%)	calcite dolomite (15 wt%)	
	other	pyrite (2 wt%)	pyrite (7 wt%)	pyrhottite (9 wt%)
	trace/accessory	saponite orthoclase ankerite	biotite fluorapatite zircon	orthoclase anorthoclase titanite fluorapatite siderite

Table 4.3: (Continue)

Collingham Formation	***quartz***	52 wt%	63 wt%	45 wt%
	feldspar	albite (21 wt%)	albite (11 wt%)	albite (17 wt%)
	clay minerals	illite/muscovite clinochlore (24 wt%)	illite muscovite clinochlore (24 wt%)	illite/muscovite clinochlore kaolinite (27 wt%)
	carbonates	siderite dolomite (1 wt%)	calcite (2 wt%)	calcite (5 wt%)
	other		biotite pyrite (1 wt%)	pyrrhotite (2 wt%)
	trace/accessory	microcline zircon kaolinite biotite calcite ankerite	smectite fluorapatite zircon chalcopyrite	zircon siderite cordierite labradorite bytownite andesine anorthite actinolite ilmenite titanite rutile

4.4.2 Compositional variation

4.4.2.1 Principal Component Analyses (PCA)

The multiple directions on a PCA plot, represented by vectors, indicates the directions in which data varies. The directions with the greatest variance are the most important, that is the most principle (e.g., PC1 and PC2). The closer the vectors on the PCA plots, the more positively correlated they are. Samples plotted on the same side of a given variable have a high value of that variable, whereas a sample on the opposite side of a given variable has a low value for that variable. A lower number of variables and data points on a PCA-biplot provides more accurate representation of the data. Therefore, data from each borehole are plotted independently and then combined for multiple perspectives (Figures 4.6; 4.7).

Both major and trace element geochemical compositions for BH KZF-1 and BH KWV-1 show distinctive outliers for the carbonate-rich samples from the Prince Albert Formation from BH KZF-1 (Figure 4.6 A–C). The remaining samples from the Prince Albert Formation in BH KZF-1 are more closely correlated with SiO_2 eigenvectors falling within the siliciclastic sub-quadrant, along with most samples from the Collingham Formation from both boreholes. The Whitehill Formation from both

boreholes plots mostly within the clay-mineral sub-quadrant with greater trace element enrichment.

The PCA of major oxides from BH KWV-1 and BH SFT2, show the Prince Albert and Whitehill formations to plot with near eigenvalues that represent clay and carbonate minerals (Figure 4.7 A–D). When all the boreholes are plotted together it is clear that the major elements show the Collingham Formation to plot near SiO_2 and Na_2O eigenvectors, indicating a preference for siliciclastic and arkosic mineral compositions, whereas the Whitehill and Prince Albert formations show preference for elements occurring in clay and carbonate minerals (Figures 4.7 E). The Prince Albert Formation shows the greatest compositional variability between the formations. When all the trace elements are plotted in a PCA diagram (Figure 7 F), there is a clear distinction between each borehole. Although with this many data points, the details of the geochemistry itself becomes indistinct. Figure 4.7 F merely shows the variation between the boreholes.

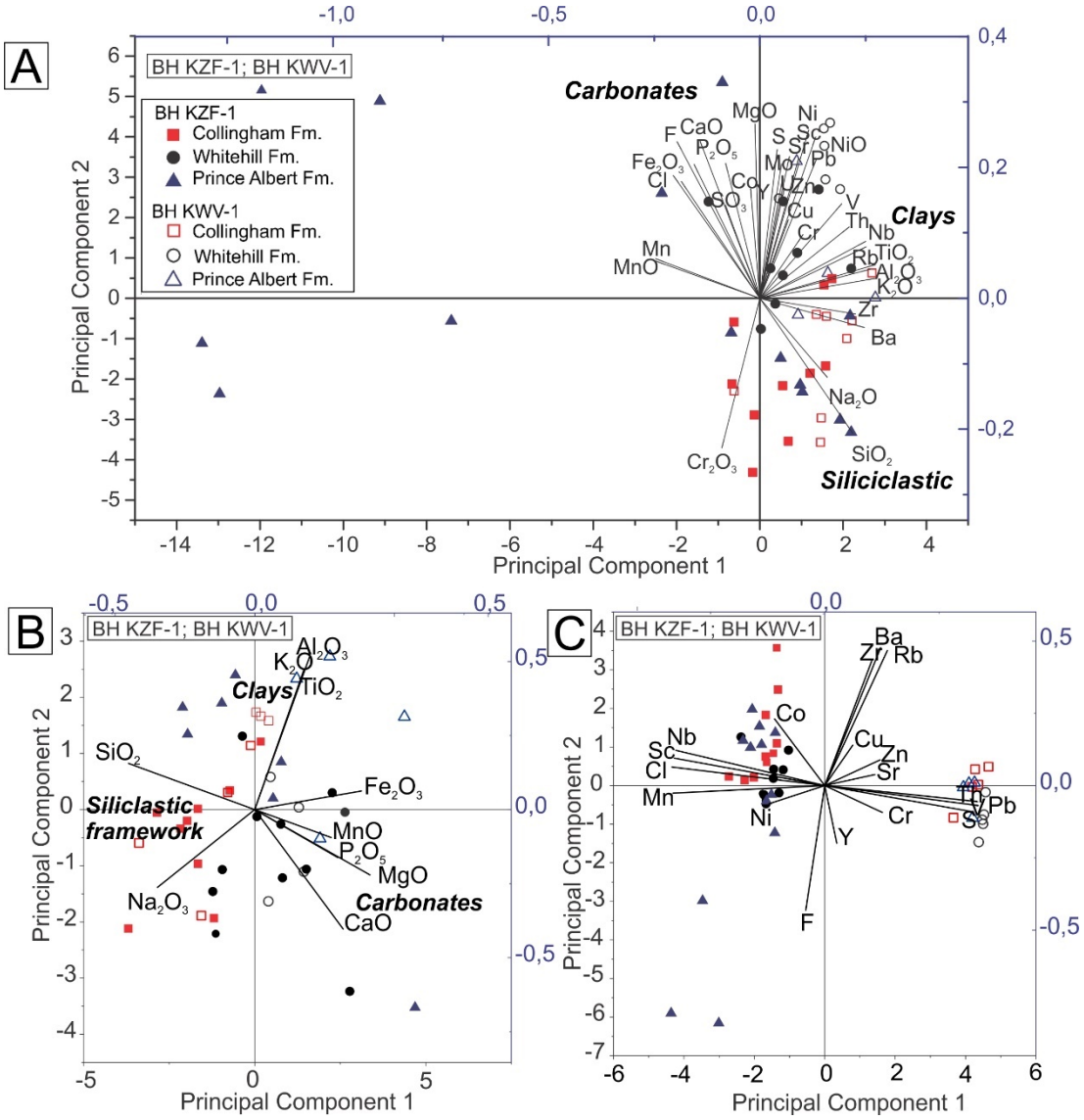

Figure 4.6: Principle Component Analysis (PCA). A) All major and trace element geochemistry from BH KZF-1 and BH KWV-1. B) Major element geochemistry from BH KZF-1 and BH KWV-1. C) Trace element geochemistry from BH KZF-1 and BH KWV-1.

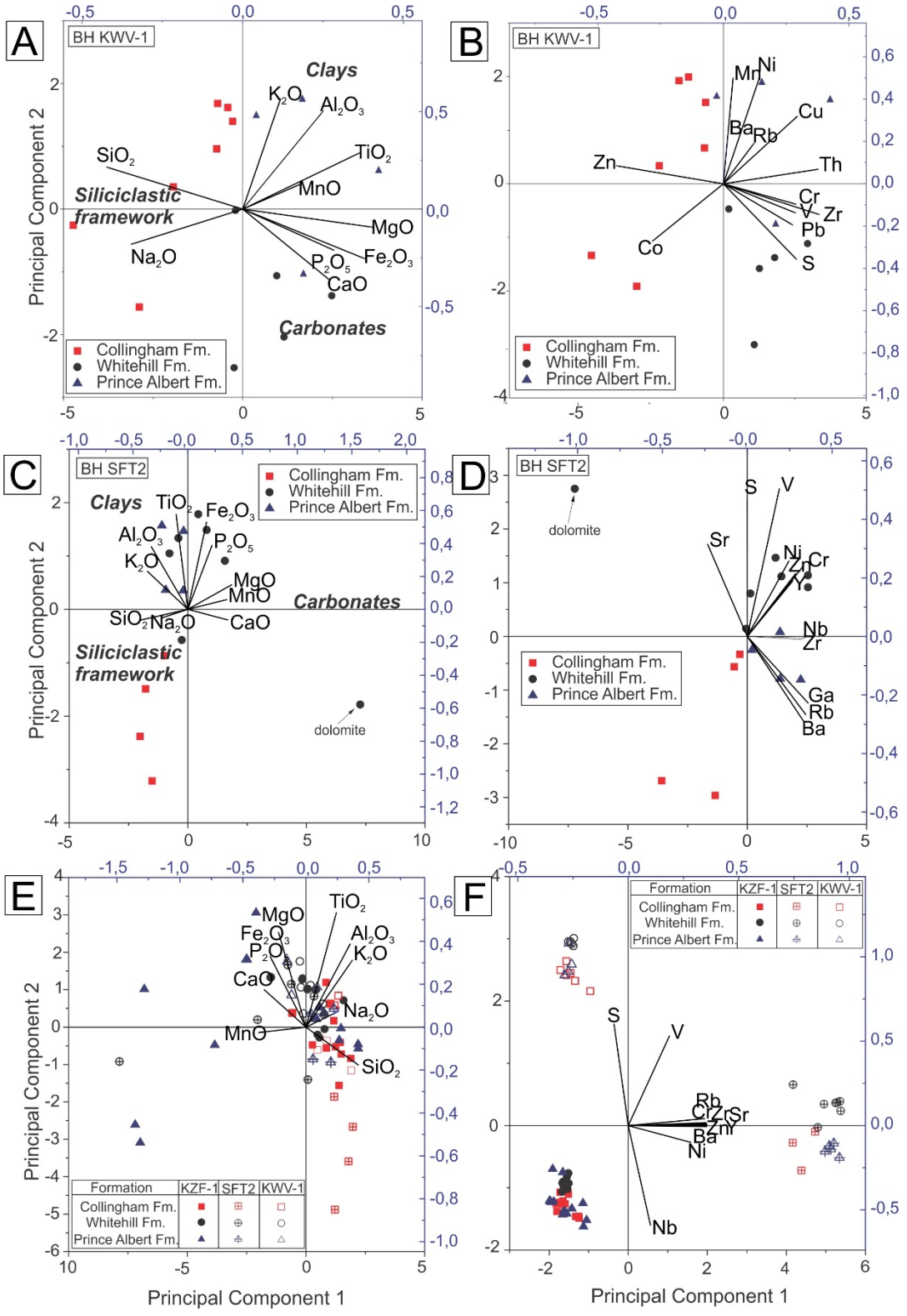

Figure 4.7: Principle Component Analysis (PCA). A) Major element geochemistry from BH KWV-1. B) Trace element geochemistry from BH KWV-1. C) Major element and trace element geochemistry from BH SFT2. D) Trace element geochemistry from BH SFT2. E) Major element geochemistry from BH KZF-1, BH SFT2 and BH KWV-1. F) Trace element geochemistry from BH KZF-1, BH SFT2 and BH KWV-1.

4.4.2.2 Geochemical signatures

The ICV and Zr/Ti values typically indicate differences between bulk composition and possible differences in source material. These ratios are best visualized when plotted as depth profiles. The CIA is plotted to compare with the ICV and Zr/Ti values (Tables 4.4–4.7; Figure 4.8–4.10). An increase in ICV values indicate that there was a decrease in weathering. The highest average ICV values were detected in the Whitehill Formation (0.96–1.15) followed by the Prince Albert Formation (0.72–0.95). The lowest ICV values were detected in the Collingham Formation (0.70–0.078).

Conversely, an increase in the CIA indicates an increase in weathering. CIA values are the highest for the Prince Albert Formation (79.2–73.0), followed by the Whitehill Formation (63.4–68.8) and decreases into the Collingham Formation (64.4–65.9). In BH KZF-1, CIA peaks correlate with two spikes in Zr/Ti values for two samples that are rich in tuffaceous material. The CIA is plotted against the ICV in Figure 4.11. Samples from the Prince Albert Formation and Whitehill Formation from all three boreholes, tend towards the basalt trend line, whereas the Collingam Formation from all three boreholes tend towards the granite trend line.

BH SFT2 had the highest overall Zr/Ti values of all three formations (Table 4.5). In BH SFT2 the average Zr/Ti values for the Prince Albert Formation is 0.078, the Whitehill Formation is 0.080 and the Collingham Formation had the highest average value of 0.134. Overall Zr/Ti values were slightly higher in BH KZF-1 (Table 4.4) compared to BH KWV-1 (Table 4.6). In BH KZF-1 the average Zr/Ti value for the Prince Albert Formation was 0.061 and 0.045 for the Whitehill Formation. In BH KZF-1 the Zr/Ti value for the Collingham Formation was 0.060 but can be reduced to 0.051 once samples with notable tuffaceous material were excluded. In BH KWV-1 the average Zr/Ti values for the Prince Albert Formation was 0.059, the Whitehill Formation was 0.043 and the Collingham Formation was 0.062.

Table 4.4: ICV (SD= 0.3), CIA (SD= 5.8) and Zr/Ti values for BH KZF-1.

Sample	Formation	ICV	CIA	Zr/Ti	Formation	Average ICV	Average CIA	Average Zr/Ti
KZF-1	Tierberg	0.78	63.0	0.052	Collingham	0.70	64.4	0.067 and 0.051 excluding high tuff samples (KZF05 and KZF07)
KZF-2	Collingham	0.77	66.6	0.051				
KZF-3	Collingham	0.86	59.1	0.052				
KZF-4	Collingham	0.58	63.3	0.056				
KZF-5	Collingham	1.07	72.0	0.117				
KZF-6	Collingham	0.64	62.7	0.051				
KZF-7	Collingham	0.53	72.6	0.164				
KZF-8	Collingham	0.65	63.4	0.042				
KZF-9	Collingham	0.72	63.9	0.042				
KZF-10	Collingham	0.60	62.8	0.060				
KZF-11	Collingham	0.53	57.2	0.049				
KZF-12	Whitehill	0.81	58.4	0.053	Whitehill	0.96	63.4	0.046
KZF-13	Whitehill	0.88	65.4	0.041				
KZF-14	Whitehill	0.65	67.3	0.036				
KZF-15	Whitehill	1.10	65.8	0.038				
KZF-16	Prince Albert	0.41	74.1	0.110				
KZF-17	Whitehill	0.72	56.5	0.045				
KZF-18	Whitehill	0.70	61.0	0.042				
KZF-19	Whitehill	0.90	62.1	0.045				
KZF-20	Whitehill	1.71	67.0	0.035	Prince Albert	0.95	73.0	0.061
KZF-21	Whitehill	1.05	66.9	0.075				
KZF-22	Prince Albert	1.47	74.1	0.048				
KZF-23	Prince Albert	1.67	66.3	0.052				
KZF-24	Prince Albert	1.19	74.7	0.063				
KZF-25	Prince Albert	0.56	71.9	0.081				
KZF-27	Prince Albert	0.43	72.2	0.051				
KZF-30	Prince Albert	0.63	75.9	0.053				
KZF-31	Prince Albert	0.71	76.1	0.057				
KZF-33	Prince Albert	0.73	63.0	0.035				

Table 4.5: ICV (SD= 0.3), CIA (SD= 5.8) and Zr/Ti values for BH SFT2.

Sample	Formation	ICV	CIA	Zr/Ti	Formation	Average ICV	Average CIA	Average Zr/Ti
G011483	Collingham	1.18	57.6	0.050	Collingham	0.70	65.2	0.138
G011485	Collingham	0.47	72	0.215				
G011486	Collingham	0.50	73.8	0.179				
G011487	Collingham	0.73	60.5	0.070				
G011489	Collingham	0.62	62.2	0.082	Whitehill	1.06	74.1	0.080
G011491	Whitehill	0.92	67.1	0.112				
G011497	Whitehill	1.03	66.4	0.043				
G011499	Whitehill	0.98	66.2	0.071				
G011505	Whitehill	1.68	79.9	0.121				
G011509	Whitehill	0.80	83.9	0.094				
G011510	Whitehill	0.96	81	0.040	Prince Albert	0.72	79.7	0.078
G011518	Prince Albert	0.67	79.8	0.076				
G011522	Prince Albert	0.97	85.3	0.062				
G011528	Prince Albert	0.63	79.8	0.058				
G011531	Prince Albert	0.53	81.3	0.111				
G011534	Dwyka/PA contact	0.79	72.3	0.071				

Table 4.6: ICV (SD=0.2), CIA (SD= 6.6) and Zr/Ti values for BH KWV-1.

Sample	Formation	ICV	CIA	Zr/Ti	Formation	Average ICV	Average CIA	Average Zr/Ti
KWV-1	Collingham	0.76	66.7	0.066	Collingham	0.78	65.9	0.062
KWV-2	Collingham	0.85	66.0	0.050				
KWV-3	Collingham	1.03	59.3	0.051				
KWV-4	Collingham	0.76	61.6	0.061				
KWV-05	Collingham	0.70	68.1	0.080				
KWV-06	Collingham	0.65	69.2	0.054				
KWV-07	Collingham	0.73	70.2	0.072				
KWV-08A	Whitehill	1.35	61.8	0.059	Whitehill	1.15	68.8	0.043
KWV-08B	Whitehill	1.06	73.0	0.041				
KWV-09	Whitehill	1.35	62.4	0.045				
KWV-10	Whitehill	0.96	66.2	0.044				
KWV-11	Whitehill	1.13	74.1	0.039				
KWV-13	Whitehill	1.06	75.3	0.031				
KWV-14	Prince Albert	0.99	81.2	0.043	Prince Albert	0.80	78.2	0.059
KWV-15	Prince Albert	0.84	78.0	0.045				
KWV-16	Prince Albert	0.87	78.4	0.053				
KWV-17	Prince Albert	0.49	75.4	0.093				

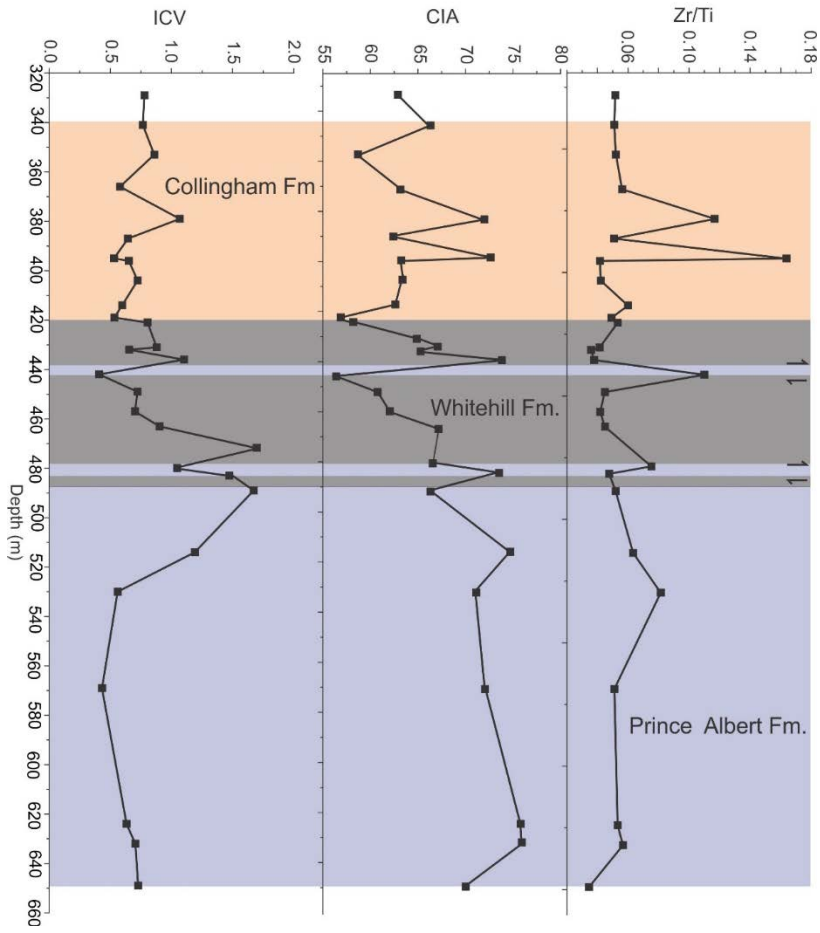

Figure 4.8: Change in provenance and weathering indicated by ICV, the CIA and Zr/Ti values for BH KZF-1. Arrows indicate zones of thrust faulting and duplication.

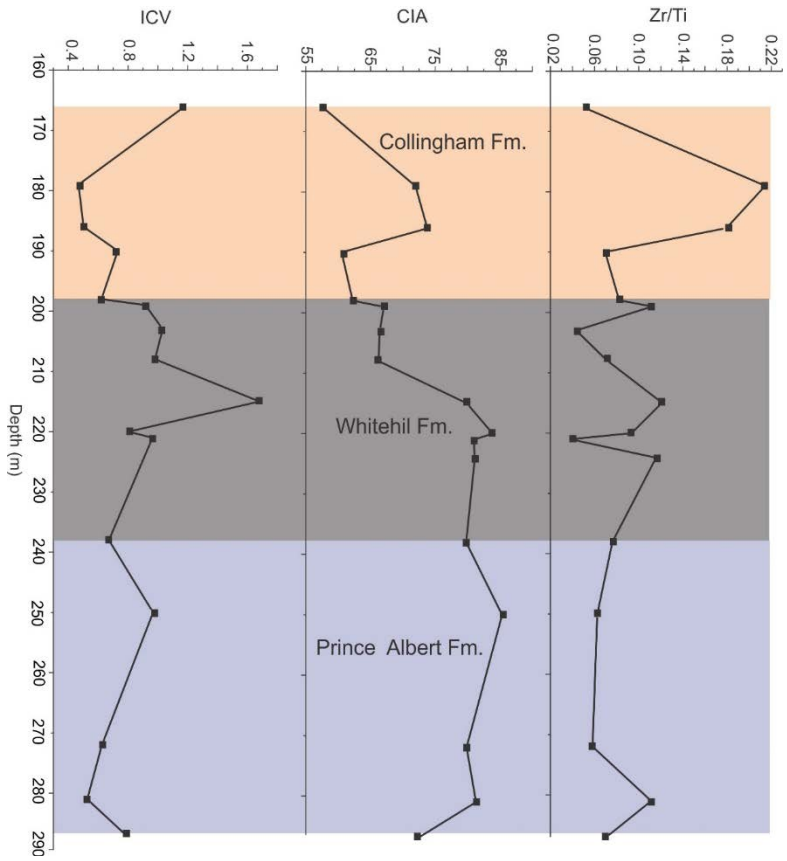

Figure 4.9: Change in provenance and weathering indicated by ICV, the CIA and Zr/Ti values for BH SFT2.

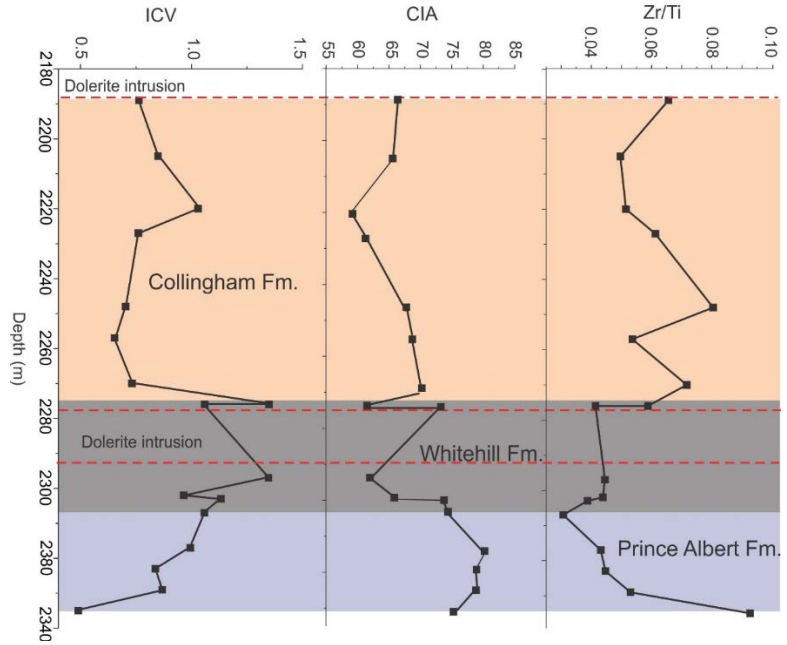

Figure 4.10: Change in provenance and weathering indicated by ICV, the CIA and Zr/Ti values for BH KWV-1.

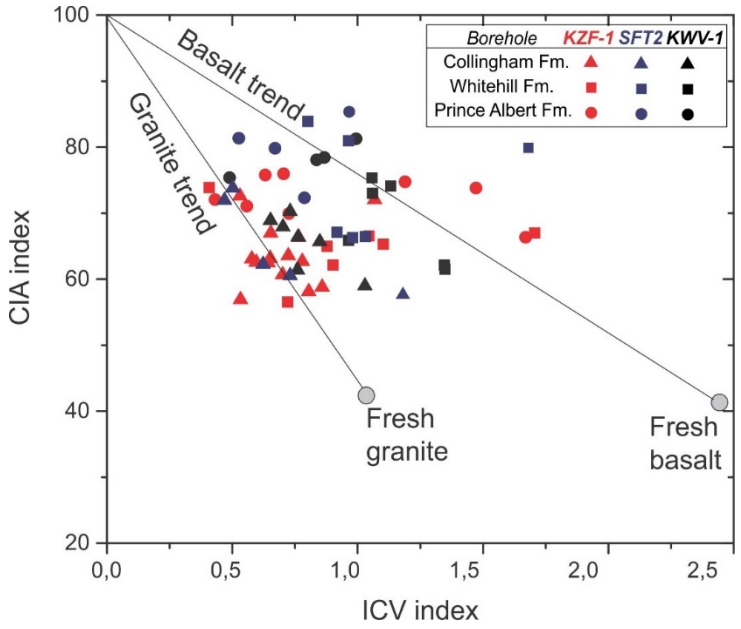

Figure 4.11: The CIA vs the ICV for all samples from the BH KZF-1, BH SFT2 and BH KWV-1. Figure adapted from Potter et al., 2005.

4.4.3 Provenance discrimination

Discriminant Function Diagrams (Figure 4.12) use oxide data that are normalized to Al_2O_3, to counter the influence of biogenic carbonate or silica. Samples from all three formations across the basin plot in either mafic, intermediate, felsic igneous or quartzose sedimentary provenance categories. The Prince Albert Formation in BH KZF-1 plots in the mafic, intermediate and felsic igneous provenances and in BH SFT2 and BH KWV-1, in the mafic and felsic igneous provenances. The Whitehill Formation in BH KZF-1 plots mostly in intermediate to felsic igneous provenances and in BH SFT2 and BH KWV-1, in mafic and intermediate igneous provenances. The Collingham Formation in BH KZF-1 plots mostly in the felsic igneous provenance with one sample in the intermediate igneous provenance. In BH SFT2, the Collingham Formation plots in the felsic igneous provenance and in BH KWV-1, in felsic and intermediate igneous provenances.

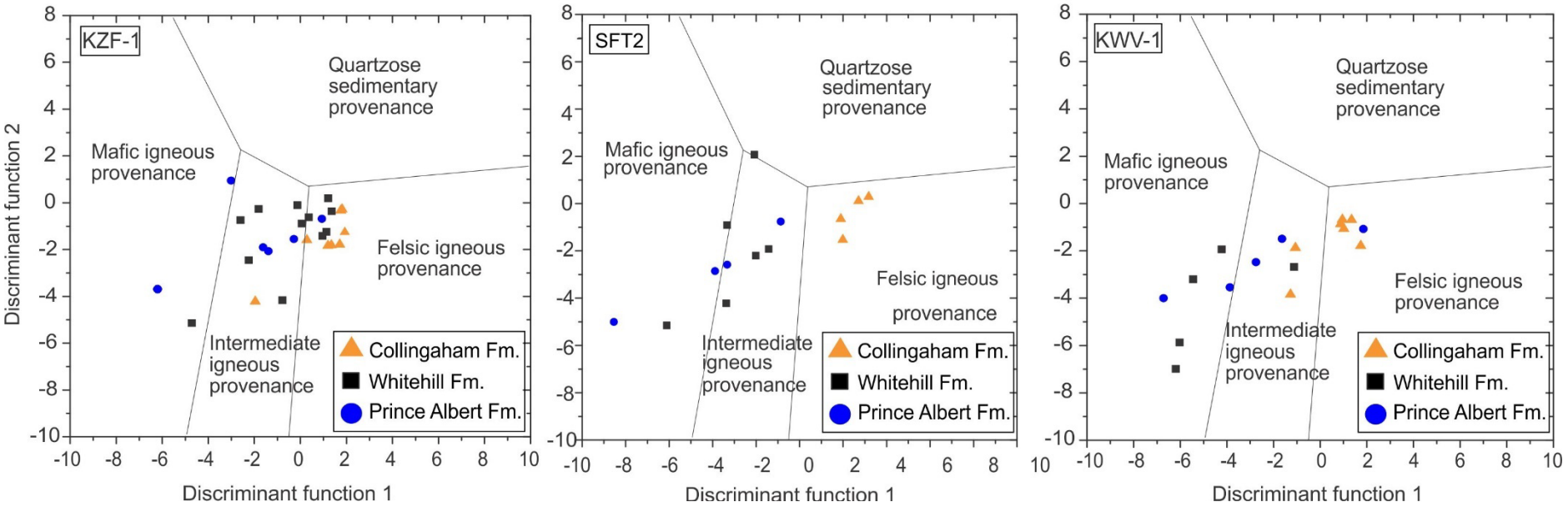

Figure 4.12: Discriminant Function plots for BH KZF-1, BH SFT2 and BH KWV-1. Discriminant Function 1 = 30.638 TiO_2/Al_2O_3 – 12.541 Fe_2O_3/Al_2O_3 + 7.329 MgO/Al_2O_3 + 12.031 Na_2O/Al_2O_3 + 35.401 K_2O/Al_2O_3 -6.382. Discriminant Function 2 = 56.500 TiO_2/Al_2O_3 – 10.879 Fe_2O_3/Al_2O_3 + 30.875 MgO/Al_2O_3 - 5.404 Na_2O/Al_2O_3 + 11.112 K_2O/Al_2O_3 – 3.89

4.5 Discussion

Analysing bulk-sediment geochemistry is a suitable method of provenance analyses for mudstones, that cannot be analysed using conventional methods such as point counting of petrographic thin sections. However, many detrital minerals have diverse elemental composition that can blur the fingerprint of source areas, therefore integrated analyses are used in this study.

Major element oxides plotted using PCA (Figures 4.6–4.7) support the ICV results and indicate that both the Prince Albert and Whitehill formations have high compositional variability, whereas the Collingham Formation has the highest compositional homogeneity. This is due to the high quartz (63–45 wt%) and albite content (10–21 wt%) in the Collingham Formation. However, in outcrop, the siliceous mudstone is interbedded with volcanic tuff, siltstone and chert, which varies in proportion in different parts of the basin. For example, the number of tuff beds and their thicknesses are greater in the western portion of the basin (Viljoen, 1992; 1998). PCA diagrams of major element oxides show that the samples from the Whitehill Formation regularly overlap with those from the Prince Albert Formation due to their high clay and carbonate content. In all three boreholes the Prince Albert Formation has the highest clay-mineral content, which increases from west to east (BH KZF-1= 18 wt%; BH SFT2= 46 wt%; BH KWV-1= 49 wt%), whereas the Whitehill Formation has consistent clay content throughout. The Prince Albert and Whitehill formations are the thinnest in BH KWV-1, which supports the idea that the north-eastern portion of the basin was possibly distal, with glacial melting occurring last in this region (Catuneanu et al., 1998).

Trace element plotted in PCA diagrams (Figures 4.6 C; 4.7 F), presents a distinction between all three boreholes. Trace elements are the least likely to alter with diagenesis and will remain immobile. According to palaeo-current and palaeo-ice-flow indicators, in the final stage of Dwyka deglaciation, sediment was mostly delivered into the western MKB from highlands to the south and the southeast (Visser et al., 1997; Isbell et al., 2008). Later, palaeo-current directions detected in the upper Ecca Group includes sediment supply from the west (Ryan & Whitfield, 1979). Sedimentation of the Prince Albert Formation in the western MKB is likely sourced from the east with increasing input from the west beginning to occur during the deposition of the Collingham Formation, thereby distinguishing the overall western MKB trace element signature from the eastern MKB.

The CIA for samples from the Prince Albert Formation are the highest, indicating that they have undergone the highest degree of weathering, whereas the Collingham Formation had the lowest and thus experienced the least amount of weathering. The high CIA values in the Prince Albert Formation indicate that there was a rise in temperature and humidity correlated with tropical to temperate climates in the source regions (Nesbitt & Young, 1982). Whereas, increasingly arid conditions recurred during the deposition of the Collingham Formation. Similar CIA trends are observed by other authors (e.g., Scheffler et al., 2006; Chere, 2015) and is discussed in depth in Chapter 3.

The ICV is also used to determine the extent of weathering at the source areas, however CIA and ICV values will vary depending on the source terrane as ICV values for basalt and granite are vastly different. Therefore, a cross plot between ICV and CIA (Figure 4.11) is useful in comparing differences of composition of source areas (Li, 2000; Lee, 2002). CIA plotted against ICV for the lower Ecca Group, from all three boreholes, suggests that the rocks from the Prince Albert and Whitehill formations follow more closely a basalt weathering trend, whereas the Collingham Formation rocks follows closer to the granite weathering trend.

Tuffaceous laminae occur predominantly in both the Prince Albert and Collingham formations. This increases the overall Zr content, even in samples comprising mostly mudstone. This must be considered when interpreting Zr/Ti values. The ash-fall tuffs of the lower Ecca Group are thought to have been produced by magmatism in the southwest of Gondwana, where the present day Patagonia is located (Veevers et al., 1994; Bangert et al., 1999; Lopez-Gamundi, 2006; Rocha-Campos et al., 2011; Sato et al., 2015; McKay et al., 2015; Muir et al., 2020). The ash-fall tuffs have a basaltic-andesite to rhyolite-dacite source (Viljoen, 1992; 1998; McKay et al., 2016), which will likely influence the intermediate and felsic geochemical signatures detected in the Prince Albert and Collingham formations. The average values for Zr/Ti for the Prince Albert Formation in all three boreholes (0.059–0.078) and the Collingham Formation in BH KZF-1 (0.067) and BH KWV-1 (0.062), indicates that the source material originates from the upper crust (Taylor & McLennan, 1985). The average Zr/Ti values for the Whitehill Formation are 0.046 in BH KZF-1, and 0.043 in BH KWV-1. These values are close to the NASC average yields for shale (Ewart, 1982). However, the Whitehill Formation in BH SFT2 has Zr/Ti values of 0.080, nearly double that of the other two boreholes. The average Zr/Ti values from the western Cape Supergroup is 0.105 and in the eastern Cape Supergroup is 0.96 (Fourie et al., 2011). Therefore, increased sediment input from the Cape Supergroup, combined with reworked

volcanic tuffs, may result in higher Zr/Ti values for the Whitehill Formation in BH SFT2. Furthermore, in BH SFT2 the Collingham Formation has the highest average Zr/Ti of 0.138, which suggest quartz arenite and granite source rocks (Boryta & Condie, 1990).

When considering known palaeo-current directions from the Dwyka and upper Ecca groups (e.g., Ryan, 1967; Ryan & Whitfield, 1979; Theron & Blignaut, 1975; Visser, 1997; Isbell et al., 2008; Blignaut & Theron, 2012; Dietrich & Hoffman et al., 2019), Discriminant Function Diagrams can be used to tentatively make inferences about source regions. Overall, there appears to be stronger felsic and intermediate signatures in the western MKB and a stronger mafic signature in the eastern MKB.

In the Tankwa Karoo Sub-basin, palaeo-current directions from the upper Ecca Group originated from the south and southwest (Wickens, 1994), which suggests that the strong felsic and intermediate signatures probably originate from the Cape Granite Suite and the Cape Supergroup. To precipitate the carbonate assemblages, as seen in the Prince Albert and Whitehill formations, there would have been high ρCO_2 in the basin at the time of deposition. The Prince Albert Formation in BH KZF-1 has elevated Fe_2O_3, MgO, CaO and MnO percentages in comparison to the other boreholes. Therefore, possible source regions would be the north-western sub-provinces of the Namaqua-Natal Belt, which consists of orthogneisses, granites, calc-alkaline lavas, charnockites, metabasalts and quartzites (Bushmanland and Gordonia sub-provinces; Table 4.1; Hartnady et al., 1985; Thomas et al., 1994; Eglington, 2006). It is even more likely that the carbonate-rich sediments were partly derived from the carbonate-rich Kango Group of the Pan-African Saldania Belt, situated to the south-southeast of the Tankwa Karoo Sub-basin (Figure 4.2; le Roux, 1997).

It is likely that much of the lower Prince Albert Formation in both the western and the eastern MKB would have been partly sourced from the Dwyka Group, which could account for the increase in compositional variability. An increasing amount of intermediate and mafic intrusive clasts detected in the Dwyka Group in the eastern MKB (Visser, 1997) are contributing factors to the intermediate to mafic signatures detected in the Prince Albert Formation in the eastern MKB. The sedimentary material that comprise the Prince Albert Formation in the eastern MKB was probably sourced from the Archean Kaapvaal Craton, the north-eastern subprovinces of the Namqua-Natal Belt (Tugela Terrane), Natal Group and the Pan-African Mozambique and Maud Belts.

The felsic and intermediate source for the Collingham Formation in BH KZF-1 originates from the Cape Granite Suite, Cape Supergroup and tuffs from Patagonian volcanism. Another possible granite source is the Sierras Pampeanas and North Patagonian Massif in South America (van Lente, 2004), although a more localized granitic source (i.e., Cape Granites) is more likely. In BH SFT2 and BH KWV-1, the felsic and intermediate source regions are probably derived from the Cape Supergroup, which is rich in quartz-arenites and the eastern Cape Granite Suites (Figure 4.2).

4.6 Conclusion

The argillaceous sedimentary rocks of the lower Ecca Group were investigated from boreholes located in the western (BH KZF-1), the south-central (BH SFT2) and the eastern MKB (BH KWV-1). PCA infers that the Prince Albert, Whitehill and Collingham formations, from the respective boreholes, share similar geochemical characteristics such as major oxide geochemistry, but differing trace element geochemistry.

Discriminant Function Diagrams and the ICV vs CIA plot suggests that the sedimentary rocks of the lower Ecca Group in BH KZF-1 have a stronger felsic and intermediate signature, compared to the samples from BH SFT2 and BH KWV-1, which have a stronger mafic signature. The ICV, Zr/Ti values and PCA diagrams show that higher compositional variability occurs in the Prince Albert and Whitehill formations. A higher percentage of carbonate minerals in the Prince Albert and Whitehill formations in BH KZF-1 and BH SFT2 implies that carbonates may have been introduced from the southern Kango Group (Saldania Belt), Cape Supergroup, Cape Granite Suite and the Dwyka Group. The same proxies suggest that in the eastern MKB the source regions were predominantly the Dwyka Group, Namaqua-Natal Belt, Natal Group, Mozambique and Maud Belts. This is corroborated by existing literature on palaeo-ice-flow directions in the Dwyka Group and palaeo-current directions from the upper Ecca Group, which strongly indicate source regions in the east (e.g., Ryan 1967; Ryan & Whitfield, 1979; Visser et al., 1986, 1987; Visser, 1990, 1992, 1997; Blignaut & Theron, 2012; Bordy et al., 2017).

The Collingham Formation had the lowest CIA of the three stratigraphic units in all three regions, indicating decreased weathering with time, possibly due to more arid climatic conditions and reduced transportation distances from the source areas. In all boreholes, sediments during the Collingham Formation depositional phase likely originated from nearby regions of the Cape Supergroup and the Cape Granite Suite.

4.7 References

Adelmann, D. & Fiedler, K. 1996. Sedimentary development of the Upper Ecca and Lower Beaufort Groups (Karoo Supergroup) in the Laingsburg subbasin (SW Karoo Basin, Cape Province/South Africa). *Schriftenreihe der Deutschen Geologischen Gesellschaft*. 1: 88–89.

Allen, R.B. & Tucholke, B.E. 1981. Petrography and implications of continental rocks from the Agulhas Plateau, southwest Indian Ocean. *Geology*. 9: 463–468.

Andersson, P.O.D. & Worden, R.H. 2004. Mudstone of the Tanqua Basin, South Africa: an analysis of lateral and stratigraphic variations within mudstones, and comparison of mudstones within and between turbidite fans. *Sedimentology*. 51 (3): 479–502.

Bangert, B., Stollhofen, H., Lorenz, V. & Armstrong, R. 1999. The geochronology and significance of ash-fall tuffs in the glaciogenic Carboniferous–Permian Dwyka Group of Namibia and South Africa. *Journal of African Earth Sciences*. 29: 33–49.

Bangert, B. & von Brunn, V. 2001. Tuffaceous beds in glaciogenic argillites of the Late Palæozoic Dwyka Group of KwaZulu-Natal, South Africa. *Journal of African Earth Sciences*. 32: 133–140.

Barrett, P J. 1969. *Photomicrographs of some sedimentary and volcaniclastic Permian and Triassic Beacon rocks from the Beardmore Glacier Area, Antarctica*. Ohio State University, Columbus: Institute of Polar studies. 30 p.

Belica, M.E., Tohver, E., Poyatos-Moré, M., Flint, S., Parra-Avila, L.A., Lanci, L., Denyszyn, S. & Pisarevsky, S.A. 2017. Refining the chronostratigraphy of the Karoo Basin, South Africa: magnetostratigraphic constraints support an Early Permian age for the Ecca Group. *Geophysical Journal International*. 211(3): 1354–1374.

Blewett, S.C.J. & Phillips, D. 2016. An overview of Cape Fold Belt geochronology: Implications for sediment provenance and the timing of orogenesis. In *Origin and evolution of the Cape Mountains and Karoo Basin: Geo-biohistory in a terrain with shale gas resources and need for conservation*. B. Linol & M. de Wit, Eds. Part of the series Regional Geology Reviews. 8643: 45–55.

Blewett, S.C.J., Phillips, D. & Matchan. E.L. 2019. Provenance of Cape Supergroup sediments and timing of Cape Fold Belt orogenesis: Constraints from high-precision $^{40}Ar/^{39}Ar$ dating of muscovite. *Gondwana Research*. 70: 201–221.

Blignault, H.J. & Theron, J.N. 2012. Modes of Sedimentation and Glaciological Aspects of The Permo-Carboniferous Dwyka Group in the Elandsvlei–Elandsdrif Area, South Africa. *South African Journal of Geology*. 115(2): 211–224.

Booth, P.W.K. & Shone, R.W. 2002. A review of thrust faulting in the Eastern Cape Fold Belt, South Africa, and the implications for current lithostratigraphic interpretation of the Cape Supergroup. *Journal of Africa Earth Sciences*. 34: 179–190.

Bordy, E. M., Hancox, P.J & Rubidge, B. S. 2004a. Basin development during the deposition of the Elliot Formation (Late Triassic - Early Jurassic), Karoo Supergroup, South Africa. *South African Journal of Geology*. 107: 395–410.

Bordy, E. M., Hancox, P. J. & Rubidge, B. S. 2004b. Fluvial style variations in the Late Triassic - Early Jurassic Elliot Formation, main Karoo Basin, South Africa. *Journal of African Earth Sciences*. 38: 383–400.

Bordy, E.M. & Prevec, R. 2008. Sedimentology, palaeontology and palaeo-environments of the Middle (?) to Upper Permian Emakwezini Formation (Lebombo Basin, South Africa). *South African Journal of Geology*. 111 (4): 429–458.

Bordy, E.M. & Abrahams, M. 2016. Geochemistry of the Pronksberg Bentonite of the Upper Elliot Formation (Early Jurassic), Eastern Cape, South Africa. In *Origin and Evolution of the Cape Mountains and Karoo Basin.* B Linol & M.J. de Wit, Eds. Springer. 119–193.

Bordy, E.M., Spelman, S., Cole, D.I., Mthembi, P. 2017. Lithostratigraphy of the Pietermaritzburg Formation (Ecca group, Karoo Supergroup), South Africa. *South African Journal of Geology*. 120: 293–302.

Boryta, M. & Condie, K.C. 1990. Geochemistry and origin of the Archaean Beit Bridge Complex, Limpopo Belt, South Africa. *Journal of the Geological Society (London).* 147: 229–239.

Brandl, G. & de Wit, M.J., 1997. The Kaapvaal Craton, South Africa. In G*reenstone Belts*. M.J. de Wit & L.D. Ashwal, Eds. Oxford Monograph on Geology and Geophysics. 35. 581.p

Catuneanu, O., Hancox, P.J. & Rubidge, B.S. 1998. Reciprocal flexural behaviour and contrasting stratigraphies: a new basin development model for the Karoo retroarc foreland system, South Africa. *Basin Research*. 10: 417–439.

Chemale. Jr. F., Scheepers, R., Gresse, P.G. & Van Schmus, W.R. 2011. Geochronology and sources of late Neoproterozoic to Cambrian granites of the Saldania Belt. *International Journal of Earth Science*. 100: 431–444.

Chere, N. 2015.*Sedimentological and geochemical investigations on borehole cores of the lower Ecca Group black shales, for their gas potential - Karoo Basin, South Africa*. Unpublished M.Sc. dissertation. Nelson Mandela University. 268p.

Chukwuma, K. & Bordy, E.M. 2016. Spatiotemporal sedimentary facies variations in the Lower Permian Whitehill Formation, Ecca Group, Karoo Basin. In *Origin and Evolution of the Cape Mountains and Karoo Basin*. B. Linol & de Wit, M.J., Eds. Regional Geology Reviews, Springer. 101–110

Cole, D.I. 1992. Evolution and development of the Karoo Basin. In *Inversion tectonics of the Cape Fold Belt, Karoo and Karoo and Cretaceous basins of Southern Africa*. M.J. de Wit & I.D.G. Ransome, Eds. Rotterdam: Balkema. 23–26.

Coutinho, J.M.V., Hachiro, J., Colmbra, A.M. & Santos, P.R 1991. *Ash-fall derived tuffaceous sediments in the Permian of the Paranã Basin and their provenance*. São Paulo, Brazil: Abstracts, 7th International Gondwana Symposium. 147–160.

Craddock, J.P & Thomas, R.J. 2011. Detrital Zircon provenance ages of the “Dwyka Tillite” in South Africa and the Falkland Islands [Abstract]. *Geosynthesis, Cape Town*. 33–34.

Daunis-I-Estadella, J., Thió-Henestrosa, S. & Mateu-Figueras, G. 2011. Two more things about compositional biplots: Quality of projection and inclusion of supplementary elements. *Proceedings of the 4th International Workshop on Compositional Data Analysis*. 9-11 May 2011. Universitat de Girona, Spain: CODAWORK11.

De Beer, J.H., Van Zijl, J.S.V. & Gough, D.I. 1982. The Southern Cape Conductive Belt (South Africa): Its composition, origin and tectonic significance. *Tectonophysics.* 83: 205–225.

de Wit, M.J. & Ransome, I.G.D. 1992. Regional inversion tectonics along the southern margin of Gondwana. In *Inversion Tectonics of the Cape Fold Belt, Karoo and Cretaceous Basins of Southern Africa*. M.J. de Wit & I.G.D. Ransome, Eds. Netherlands: Balkema, Rotterdam. 15–20.

de Wit, M.J., Roering, C., Hart, R.J., Armstrong, R.A., de Ronde, C.E.J., Green, R.W.E., Tredoux, M., Peberdy E. & Hart R.A. 2002. Formation of an Archaean continent. *Nature*. 357 (6379). 553–562.

Dietrich, P. & Hofmann, A. 2019. Ice-margin fluctuation sequences and grounding zone wedges: The record of the Late Palaeozoic Ice Age in the eastern Karoo Basin (Dwyka Group, South Africa). *The Depositional Record*. 5: 247–271.

Eglington, B.M. & Armstrong, R.A. 2003. Geochronological and isotropic constrains on the Mesoproterozoic Namaqua-Natal Belt: evidence from deep borehole intersection in South Africa. *Precambian research*. 125: 17–189.

Eglington, B.M. 2006. Evolution of the Namaqua-Natal Belt, Southern Africa – A geochronological and isotope geochemical review. *Journal of African Earth Sciences*. 46: 93–111.

Elliot, D. M. & Watts, D. R. 1974. The nature and origin of volcaniclastic material in some Karoo and Beacon rocks. *Transactions Geological Society South Africa*. 77: 109–11.

Elliot, D.H. 2013. The geological and tectonic evolution of the Transantarctic Mountains: A review. In *Antarctic Paleoenvironments and Earth-Surface Processes* M.J. Hambrey, P.F. Barker., V. Bowman, B. Davies, J.L. Smellie & M. Tranter, Eds. Geological Society, London: Special Publications. 381: 7–35.

Ewart, A. 1982. Petrogenesis of the Tertiary anorogenic volcanic series of Southern Queensland, Australia, in the light of trace element geochemistry and O, Sr, and Pb isotopes. *Journal of Petrology*. 23: 344–382.

Fildani, A., Drinkwater, N.J., Weislogel, A., McHargue, T., Hodgson, D.M. & Flint, S.S. 2007. Age controls on the Tanqua and Laingsburg deep-water systems: New insights on the evolution and sedimentary fill of the Karoo Basin, South Africa. *Journal of Sedimentary Research*. 77: 901–908.

Frimmel, H.E., Zartman, R.E. & Späth, A. 2001. The Richtersveld Igneous Complex, South Africa: U-Pb Zircon and Geochemical Evidence for the Beginning of Neoproterozoic Continental Breakup. *Journal of Geology*. 109: 493–508.

Fourie, P.H., Zimmermann, U., Beukes, N.J., Naidoo, T., Kobayashi, K., Kosler, J., Nakamura, E., Tait, J. & Theron, J.N. 2011. Provenance and reconnaissance study of detrital zircons of the Palaeozoic Cape Supergroup in South Africa: revealing the interaction of the Kalahari and Rio de la Plata cratons. *International Journal of Earth Sciences*. 100: 527–541.

Garzanti, E. 2016. From static to dynamic provenance analysis- sedimentary petrology upgraded. *Sedimentary Geology*. 336: 3–13.

Garzanti, E. & Resentini, A. 2016. Provenance control on chemical indices of weathering (Taiwan river sands). *Sedimentary Geology*. 336: 81–95.

Geel, C. 2014. *Shale gas characteristics of Permian black shales in the Ecca Group, Near Jansenville, Eastern Cape, South Africa*. Unpublished M.Sc. dissertation. Nelson Mandela Metropolitan University. 163p.

Grantham, G.H., Storey, B.C., Thomas, R.J. & Jacobs, J. 1997. The pre- breakup position of Haag nunataks within Gondwana: Possible correlatives of Natal and Dronning Maud Land. In *The Antarctic Region: Geological Evolution and Processes. Proceedings of the VII International Symposium on Antarctic Sciences (ISAES).* C.A. Ricci, Ed. Siena: Terra Antarctica Publication. 13–20.

Gresse, P.G., Von Veh, M.W. & Frimmel, H.E. 2006. Namibian (Neoproterozoic) to Early Cambrian Successions. In *The Geology of South Africa*. M.R. Johnson, C.R. Anhaeusser & R.J. Thomas, Eds. Pretoria: Geological Society of South Africa, Johannesburg/Council for Geoscience. 395–420.

Groenewald, P., Grantham, G. & Watkeys, M. 1991. Geological evidence for a Proterozoic to Mesozoic link between southeastern Africa and Dronning Maud Land, Antarctica. *Journal of the Geological Society of London*. 148: 1115–1123.

Hälbich, H. 1983. A tectogenesis of the Cape Fold Belt CFB. *Special publication - Geological Society of South Africa.* 12: 165–175.

Haldorsen, S., Von Brunn, V., Maud, R. and Truter, E.D. 2001. A Weichselian deglaciation model applied to the Early Permian glaciation in the northeast Karoo Basin, South Africa. *Journal of Quaternary Science*. 16: 583–593.

Hansma, J., Tohver, E., Jourdan F., Schrank, C. & Adams, D. 2015. The timing of the Cape Orogeny: New 40Ar/39Ar age constraints on deformation and cooling of the Cape Fold Belt, South Africa. *Gondwana Research.* 32: 122–137.

Hartnady, C.J.H., Joubert, P. & Stowe, C.W. 1985. Proterozoic Crustal evolution in Southwestern Africa. *Episodes*. 8: 236–244.

Hastie, W. W., Watkeys, M.K. & Smith, A.M. 2019. Tectonic significance of the sedimentary and palaeocurrent record at the eastern edge of the Karoo Basin. *Journal of African Earth Sciences.* 158: 1–11.

Herron, M. M. 1988. Geochemical classification of terrigenous sands and shales from core or log data. *Journal of Sedimentary Research*. 58: 820–829.

Hobday, D.K. & von Brunn, V. 1979. Fluvial sedimentation and palaeogeography of an early Palaeozoic failed rift, southeastern margin of Africa. *Palaeogeography, Palaeoclimatology, Palaeoecology*. 28: 169–184.

Hörstmann, U.E., Ahrendt, H., Clauer, N. & Porada, H. 1990. The metamorphic history of the Damara Orogen based on K/Ar data of detrital white micas from the Nama Group, Namibia. *Precambrian Research*. 48: 41–46.

Isbell, J.L., Cole, D.I. & Catuneanu, I. 2008. Carboniferous-Permian glaciation in the main Karoo Basin, South Africa: Stratigraphy, depositional controls, and glacial dynamics. In *Resolving the Late Paleozoic ice age in time and space*. C.R. Fielding, T.D. Frank. & J.L. Isbell, Eds. Geological Society of America Special Paper. 441:71–82.

Jacobs, J., Bauer, W. & Fanning, C.M. 2003. Late Neoproterozoic/Early Palaeozoic events in central Dronning Maud Land and significance for the southern extension of the East African Orogen into East Antarctica. *Precambrian Research*. 126: 27–53.

Johnson, M.R. 1991. Sandstone petrography, provenance and plate tectonic setting in Gondwana context of the southeastern Cape-Karoo Basin. *South African Journal of Geology*. 91(2/3): 137–154.

Johnson, M.R., van Vuuren, C.J., Visser, J.N.J., Cole, D.J., Wickens, H. de V., Christie, A.D.M. & Roberts, D.L. 1997. The foreland Karoo Basin, South Africa. In *African Basins—Sedimentary Basins of the World*. R.C. Selley, ed. Amsterdam: Elsevier. 269–317.

Johnson, M.R., Van Vuuren, C.J., Visser, J.N.J., Cole, D.I., Wickens, H. de V., Christie, A.D.M., Roberts, D.L. & Brandl, G. 2006. Sedimentary rocks of the Karoo Supergroup. In *The Geology of South Africa.* M.R. Johnson, C.R. Anhaeusser, R.J. Thomas, Eds. Johannesburg/Council for Geoscience: Geological Society of South Africa. 461–499.

le Roux, J.P. 1997. Cycle hierarchy of a Neoproterozoic carbonate-siliciclastic shelf: Matjies River Formation of the Kango Group, South Africa. *South African Journal of Geology.* 100 (1): 1–10.

Lee, Y.I. 2002. Provenance derived from the geochemistry of late Paleozoic-early Mesozoic mudrocks of the Pyeongan Supergroup, Korea. *Sedimentary Geology.* 149: 219–235.

Lever, J., Krzywinski, M. & Altman, N. 2017. Principal component analysis. *Nature Methods.* 14**:** 641–642.

Li, Y-H. 2000. *A Compendium of Geochemistry*. Princeton, NJ: Princeton University Press. 475p.

Lindeque, A., Ryberg, T., Stankiewicz, J., Weber, M. & de Wit, M. 2007. Deep crustal reflection experiment across the southern Karoo Basin, South Africa. *South African Journal of Geology*. 110: 419–438.

Lindeque, A.S., de Wit, M.J., Ryberg, T., Weber, M. & Chevallier, L. 2011. Deep crustal profile across the southern Karoo Basin and Beattie Magnetic Anomaly, South Africa: An integrated interpretation with tectonic implications. *South African Journal of Geology*. 114: 265–292.

Llambias, E.J. 1999. Las rocas igneas gondwanicas. In *Geologia Argentina. vol. 29(12)*. R. Caminos, Ed. Instituto de Geologia y Recursos Minerales: Buenos Aires. 349–376.

Lock, B.E. & Wilson, J.D. 1975. Discussion on "The nature and origin of volcaniclastic material in some Karoo and Beacon rocks" by D.H Elliot and D.R. Watts. *Transactions Geological Society of South Africa.* 78: 171.

Lopez-Gamundi, O R., Espejo, I. S. & Alonso, M. S. 1990. Sandstone composition changes and paleocurrent reversal in the Upper Paleozoic and Triassic deposits of the Huaco area, western Paganzo Basin, West-central Argentina. *Sedimentary Geology*. 66: 99–111.

Lopez-Gamundi, O. 2006. Permian plate margin volcanism and tuffs in adjacent basins of west Gondwana: Age constraints and common characteristics. *Journal of South American Earth Sciences*. 22: 227–238.

Marshall, J.E.A. 1994. The Falkland Islands: A key element in Gondwana palaeogeography. *Tectonics*. 13: 499–514.

Marshall, C. G. A. 2003a. Lithostratigraphy of the Durban Formation (Natal Group), Including the Ulundi, Eshowe, Melmoth, Kranskloof, Situndu and Dassenhoek Members. *Council for Geoscience, SACS Lithostratigraphic Series No. 36*. 1–28.

Marshall, C. G. A. 2003b. Lithostratigraphy of the Mariannhill Formation (Natal Group), Including the Tulini, Newspaper and Westville Members. *Council for Geoscience, SACS Lithostratigraphic Series No. 37*. 1–17.

Marshall, C. G. A. 2006. The Natal Group. In *The Geology of South Africa.* M. R. Johnson, C. R. Anhaeusser & R. J. Thomas, Eds. Johannesburg: Geological Society of South Africa, Council for Geoscience. 433–41.

Matthews, P.E. 1972. Possible Precambrian obduction and plate tectonics in southeastern Africa. Nature. 240: 37–39.

Matthews, P.E. 1981. Eastern or Natal sector of the Namaqua-Natal Mobile belt in southern Africa. In *Precambrian of the southern hemisphere.* D.R. Hunter, Ed*.* Netherlands: Elsevier. 705–725.

McCarthy, T.S., Corner, B., Lombard, H., N.J., Beukes, Armstrong, R.A. & Cawthorn, R.G. 2018. The pre-Karoo geology of the southern portion of the Kaapvaal Craton, South Africa. *South African Journal of Geology*. 121: 1–22.

McKay, M.P., Weislogel, A.L., Fildani A., Brunt, R.L., Hodgson, D.M. & Flint, S.S. 2015. U-PB zircon tuff geochronology from the Karoo Basin, South Africa: implications of zircon recycling on stratigraphic age controls. *International Geology Review*. 57(4): 393–410.

McLennan, S.M., Hemming, S., McDaniel, D.K. & Hanson, G.N. 1993. Geochemical approaches to sedimentation, provenance and tectonics. *Geological Society of America Special Paper*. 284: 21–40.

Miller, M. F. & Collinson, J. W. 1994. Late Paleozoic post-glacial inland sea filled by fine-grained turbidites. Mackellar Formation, Central Transantarctic Mountains. In *Earth's Glacial Record*. M. Deynoux, J. M. G. Miller, E. W. Domack, N. Eyles, I. J. Fairchild & G. M. Young, Eds. Cambridge: Cambridge University Press. 215–233.

Morton, A.C. & Hallsworth, C. 2007. Stability of detrital heavy minerals during burial diagenesis. In: *Heavy Minerals in Use*. M.A. Mange, D.T. Wright, Eds. Amsterdam: Elsevier, Developments in Sedimentology Series 58. 215–245p.

Muir, R.A., Bordy E.M., Mundil, R. & Frei, D. 2020. Recalibrating the breakup history of SW Gondwana: U-Pb radioisotopic age constraints from the southern Cape of South Africa. *Gondwana Research*. 177–193.

Navarrete, C., Gianna, G., Encinas, A., Márquez, M., Kamerbeek, Y., Valle, M. & Folguera, A. 2019. Triassic to Middle Jurassic geodynamic evolution of southwestern Gondwana: From large flat-slab to mantle plume suction in a rollback subduction setting. *Earth Science Reviews*. 194: 125–159.

Nesbitt, H.W. & Young, G.M. 1982. Early Proterozoic climates and plate motions inferred from major element chemistry of lutites. Nature. 299: 715–717.

Pankhurst, R., Rapela, C., Fanning, M. & Márquez, M. 2006. Gondwanide continental collision and the origin of Patagonia. *Earth Science Reviews*. 76: 235–257.

Pettijohn, F.J., Potter, P.E. & Siever, R. 1972. *Sand and sandstone*. New York: Springer. 618p.

Potter, P.E., Maynard, J.B & Deptris P.J. 2005. *Mud and Mudstones*. Berlin, Heildeberg: Springer. 157–174.

Rocha-Campos, A.C., Basei. M.A., Nutman, A.P, Kleiman, L.E., Varela, R., Llambias, E., Canile, F.M. & da Rosa, O.C.R. 2011. 30 million years of Permian volcanism recorded in the Choiyoi igneous province (W Argentina) and their source for younger ash fall deposits in the Paraná Basin: SHRIMP U–Pb zircon geochronology evidence. *Gondwana Research*. 19: 509–523.

Roser, B.P. & Korsch, R.J. 1988. Provenance signatures of sandstone-mudstone suites determined using discriminant function analysis of major-element data. *Chemical Geology*. 67: 119–139.

Rozendaal, A., Gresse, P.G., Scheepers, R. & Le Roux, J.P. 1999. Neoproterozoic to early Cambrian crustal evolution of the Pan-African Saldania Belt, South Africa. *Precambrian Research*. 97: 303– 323.

Ryan, P.J. 1967. *Stratigraphic and paleocurrent analysis of the Ecca Series and lowermost Beaufort beds in the Karroo Basin of South Africa*. Unpublished Ph.D. thesis. Johannesburg: University of the Witwatersrand. 210pp.

Ryan, P.J. & Whitfield, G.G. 1979. Basinal analysis of the Ecca and lowermost Beaufort Beds and associated coal, uranium and heavy mineral beach sand occurrences. *Geological Society South Africa Publication*. 6: 91–101.

Sato, A. M., Llambias, E.J., Basei, M.A.S. & Castro, C.E. 2015. Three stages in the Late Paleozoic to Triassic magmatism of southwestern Gondwana, the relationships with the volcanogenic events in coeval basins. *Journal of South American Earth Science*. 63: 48–69.

Scheepers, R. & Armstrong, R. 2002. New U-Pb SHRIMP zircon ages for the Cape Granite Suite: implications for the magmatic evolution of the Saldania Belt. *South African Journal of Geology*. 105: 241–256.

Scheffler, K. 2004. *Reconstruction of sedimentary environment and climate conditions by multi-geochemical investigations of Late Palaeozoic glacial to postglacial sedimentary sequences from SW-Gondwana*. Unpublished Ph.D. thesis. Rheinischen Friedrich-Wilhelms-Universität Bonn. 243p.

Scheffler, K., Buehmann, D & Schwark, L. 2006. Analyses of late Palaeozoic glacial to postglacial sedimentary successions in South Africa by geochemical proxies-response to climate evolution and sedimentary environment. *Palaeogeography, Palaeoclimatology, Palaeoecology*. 240: 184-203.

Scott, E.D. 1997. *Tectonics and sedimentation: the evolution, tectonic influences and correlation of the Tanqua and Laingsburg subbasins, southwest Karoo basin, South Africa.* Unpublished Ph.D. thesis. Louisiana State University. 234p.

Smith, R.M.H. 1990. A review of stratigraphy and sedimentary environments of the Karoo Basin of South Africa. *Journal of African Earth Sciences*. 10 (1/2): 117–137.

Smith, R.M.H, Eriksson, P.G. & Botha, W.J. 1993. A review of the stratigraphy and sedimentary environments of the Karoo-aged basins of Southern Africa. *Journal of African Earth Sciences*. 16: 143–169.

Tankard, A.J., Jackson, M.P.A., Eriksson, K.A., Hobday, D.K., Hunter, D.R. & Minter, W.E.L. 1982. *3.5 Billion Years of Crustal Evolution of Southern Africa.* New York: Springer-Verlag. 523p.

Tankard, A., Welsink, H., Aukes, P., Newton, R. & Stattker, E. 2012. Geodynamic interpretation of the Cape and Karoo basins, South Africa. In *Phanerozoic Passive Margins, Cratonic Basins and Global Tectonics Maps*. D.G. Roberts, Ed. USA & UK: Elsevier. 869–932.

Taylor, S.R. & McLennan, S.M. 1985. *The Continental Crust. Its Composition and Evolution*. Oxford: Blackwell Scientific. 312p.

Thamm, A.G. & Johnson, M.R. 2006. The Cape Supergroup. In *The Geology of South Africa.* M.R. Johnson, C.R. Anhaeusser & R.J. Thomas, Eds. Johannesburg: Geological Society of South Africa /Council for Geoscience. 443–460.

Theron, J. N. & Blignaut, H. J. 1975. A model for the sedimentation of the Dwyka glacials in the southwestern Cape. In *Gondwana Geology*. K. S. W. Campbell, Ed. Australian National University Press. 347–356.

Thomas, R.J., Agenbacht, A.D., Cornell, D.H. & Moore, J.M. 1994. The Kibaran of Southern Africa: Tectonic evolution and metallogeny. Ore Geology Reviews. 9: 131–160.

Trewin, N.H., MacDonald, D.I.M. & Thomas, C.G.C. 2002. Stratigraphy and sedimentology of the Permian of the Falkland Islands: lithostratigraphic and

palaeoenvironmental links with South Africa. Journal of the Geological Society. 159: 5–19.

van Lente, B., 2004. *Chemostratigraphic trends and provenance of the Permian Tanqua and Laingsburg depocentres, southwestern Karoo basin, South Africa.* Unpublished Ph.D. thesis. Stellenbosch: University of Stellenbosch. 269p.

Veevers, J.J., Cole, D.I. & Cowan, E.J. 1994. Southern Africa: Karoo basin and Cape Fold Belt. In *Permian-Triassic Pangean basins and Foldbelts along the Panthalassan margin of Gondwanaland*. J.J. Veevers & C. M. Powell, Eds. Boulder, Colorado: G.S.A. Memoir. 184: 223–279.

Viljoen, J.H.A. 1990. *K-bentonites in the Ecca Group of the southern and central Karoo Basin*. [Abstract] Geocongress '90, Geological Society of South Africa. 576–579.

Viljoen, J.H.A. 1992. Lithostratigraphy of the Collingham Formation (Ecca Group), including the Zoute Kloof, Buffels River and Wilgehout River Members and the Matjiesfontein Chert bed. Lithostratigraphic Series, South African Committee for Stratigraphy, Council for Geoscience. 22: 1–10.

Viljoen, J.H.A. 1998. Distribution of altered volcanic ash beds in the Dwyka and Ecca Groups of the Main Karoo Basin, South Africa. *Journal of Africa Earth Sciences. Gondwana 10: Event Stratigraphy (abstracts).* 204–205.

Visser, J. N. J. 1982. Implications of a diachronous contact between the Dwyka Formation and Ecca Group in the Karoo Basin. *South African Journal Science*. 89: 373–383.

Visser, J.N.J., Hall, K.J. & Loock, J.C. 1986. The application of stone counts in the glacigene Permo-Carboniferous Dwyka Formation, South Africa. *Sedimentary Geology*. 46:197–212.

Visser, J.N.J., Loock, J.C. & Colliston, W.P. 1987. Subaqueous outwash fan and esker sandstones in the Permo-Carboniferous Dwyka Formation of South Africa. *Journal of Sedimentary Research*. 57(3): 467–478.

Visser, J.N.J., von Brunn, V. & Johnson, M.R. 1990. Dwyka Group. In *Catalogue of South African Lithostratigraphic Units*. M.R. Johnson, Ed. Pretoria: South African Committee for Stratigraphy, Council for Geoscience. 2–17.

Visser, J.N.J. 1992. Deposition of the early to Late Permian Whitehill Formation during a sea-level highstand in a juvenile foreland basin. *South Africa Journal of Geology*. 95 (5/6): 181–193.

Visser, J. N. J. 1997. Deglaciation sequences in the Permo-Carboniferous Karoo and Kalahari basins of southern Africa: a tool in the analysis of cyclic glaciomarine basin fills. *Sedimentology.* 44 (3): 507– 521.

Visser, J.N.J. 2003. Lithostratigraphy of the Elandsvlei Formation (Dwyka Group). *Council for Geoscience (South Africa)*. 39: 1–11.

Von Brunn, V.1996. The Dwyka Group in the northern part of Kwazulu Natal, South Africa: sedimentation during late Palaeozoic deglaciation. *Palaeogeography, Palaeoclimatology, Palaeoecology*. 125: 141–163.

von Eynatten, H., Barcelò-Vidal, C. & Pawlowsky-Glahn, V. 2003. Composition and discrimination of sandstones: a statistical evaluation of different analytical methods. *Journal of Sedimentary Research*. 73: 47–57.

von Eynatten, H., Tolosana-Delgado, R. & Karius, V. 2012. Sediment generation in modern glacial settings: grain-size and source-rock control on sediment composition. *Sedimentary Geology.* 280: 80–92.

Vorster, C. 2013. *Laser ablation ICP-MS age determination of detrital zircon populations in the phanerozoic Cape and Lower Karoo Supergroups (South Africa) and correlative in Argentina*. Unpublished Ph.D. thesis, University of Johannesburg. 626p.

Vorster, C., Kramers, J., Beukes, N. & Van Niekerk, H. 2015. Detrital zircon U–Pb ages of the Palaeozoic Natal Group and Msikaba Formation, Kwazulu-Natal, South Africa: provenance areas in context of Gondwana. *Geological Magazine*. 153 (3): 460–486.

Weltje, G. J. & von Eynatten, H. 2004. Quantitative provenance analysis of sediments: review and outlook. *Sedimentary Geology.* 171: 1–11.

Werner, M. 2006. *The stratigraphy, sedimentology and age of the Late Palaeozoic Mesosaurus Inland Sea, SW-Gondwana: new implications from studies on sediments and altered pyroclastic layers of the Dwyka and Ecca Group (lower Karoo Supergroup) in southern Namibia*. Unpublished Ph.D. thesis, University of Würzburg, Germany. 428 p.

Wickens, H. DeV. 1994. *Basin floor fan building turbidites of southwestern Karoo Basin, Permian Ecca Group, South Africa*. Unpublished Ph.D. thesis. University of Port Elizabeth, South Africa. 233p.

Windley, B.F. 1995. *The Evolving Continents*. Chichester, England: John Wiley & Sons Ltd. 526p.

5 Geomechanical properties of the Permian black shales in the southern main Karoo Basin (South Africa): lessons from compositional and petrophysical studies

Abstract

In the southern main Karoo Basin (MKB), Permian black shales, with total organic carbon (TOC) of up to 5.2 wt% in the lower Ecca Group, are primary targets for a potential shale gas exploration in South Africa. This study investigates the influence of shale composition, porosity, pressure (P) and temperatures (T) on the geomechanical properties such as compressive strength and elastic moduli. Results show that the lower Ecca in the MKB has a high proportion, ~ 50–70 vol% of mechanically strong minerals (e.g., quartz, feldspar, pyrite), ~ 30–50 vol% of weak minerals (e.g., clay minerals, organic matter) and ~ 0–50 vol% of intermediate minerals (e.g., carbonates) with highly variable mechanical strength. Constant strain rate deformation experiments (at T ≤ 100 °C; P ≤ 50 MPa), performed perpendicular and parallel to bedding, showed that the Prince Albert Formation is the strongest and most brittle unit in the lower Ecca Group in the southern MKB followed by the Collingham and then the Whitehill Formation. Triaxial compressive strength as well as static Young's moduli are found to increase with increasing hard minerals and decrease with increasing mechanically weak minerals and porosity. On comparison with European and North American shales, the lower Ecca Group shales are geomechanically stronger and more brittle. Dynamic Young's modulus values can be correlated with static Young's modulus (r^2 = 0.9) and demonstrates similar Young's modulus trends. The high TOC content combined with strong mineral composition may allow for fracture propagation without rock breakdown under pressure. Additionally, beef fractures were identified and are evidence for hydrocarbon formation and natural fracturing. Beef fractures are important when predicting artificial fracture propagation if hydrocarbon extraction techniques are pursued. This research provides the foundation for future geomechanical investigations of the petrophysics of these Permian Ecca black shales and their assessment as potential unconventional hydrocarbon reservoirs in the MKB.

KARIN	Karoo Research Initiative	**Py**	Pyrite
CIMERA	DST-NRF Center of Excellence for Integrated Mineral and Energy	**Fsp**	Feldspar
GFZ	Deutsches GeoForschungsZentrum	**Mca**	Mica
RWTH	Rheinisch-Westfälische Technische Hochschule	**QFP**	Quartz + feldspar + pyrite
MKB	Main Karoo Basin	**σ_{TCS}**	Triaxial compressive strength
CFB	Cape Fold Belt	**E**	Young's modulus
BH	Borehole	**YM**	Young's modulus
VR_o	Vitrinite reflectance	**έ**	Strain rate
Φ	Porosity	**ρ**	Density
TOC	Total organic carbon content		
Cly	Clay		
Cb	Carbonate		
Qtz	Quartz		

5.1 Introduction

The South African power sector, and by extension the economy of the southern African region, is highly dependent on burning abundant and locally available Permian coal deposits, which thrusts South Africa into the position of foremost carbon dioxide emitter in Africa and a prominent contributor to the greenhouse gas concentration in the atmosphere (Boden et al., 2011). To reduce this historically large carbon footprint, the country has recently embarked on pursing natural gas as an alternative energy resource (Windham, 2018). Accordingly, this ambition has spurred on a renewed geoscientific interest in the organic matter-rich Early Permian rocks in the southern main Karoo Basin (MKB), which has natural gas resource estimates as high at 390 Tcf and as low as 13 Tcf (Decker & Marot, 2012; Kuuskraa et al., 2013; Cole, 2014; Geel et al., 2015; Mowzer & Adams, 2015). The primary target for shale gas in the MKB is the lower Ecca Group (Karoo Supergroup), namely in the Prince Albert, Whitehill and Collingham formations. While most of the Permian Karoo rocks in the southern MKB are overmature, high TOC contents (up to 14% locally) had been repeatedly demonstrated for the lower Ecca succession. In particular, the large component of solid bitumen in the Whitehill Formation indicates that thermal cracking of oil had occurred, and that gas had been generated (e.g., Geel et al., 2015; Wood et al., 2015), however, the presence of economically viable shale gas in the southern MKB remains uncertain. To access the natural gas potential, the geothermal history and petrophysical characteristics of the Karoo black shales, two boreholes (BH KZF-1 and KWV-1) were recently drilled in the southern MKB by the Karoo Research Initiative (KARIN), which fall under management of the DST-NRF Centre for

Excellence for Integrated Mineral and Energy Resource Analysis (CIMERA). These modern boreholes revealed negligible amounts of desorbed and residual gas volumes due to gas loss via tectonic deformation (BH KZF-1) and thermal degassing (BH KWV-1; de Kock et al., 2017). The southern MKB, however, is still considered a “sweet zone” of possible preserved natural gas with the Whitehill Formation being the most likely shale gas source (Geel et al., 2015). Because in unconventional hydrocarbon reservoirs, gas is present in very small pores and adsorbed by the organic matter (e.g., Chere, 2015; Chukwuma et al., 2018), the composition, texture and porosity of the gas-bearing shales are important not only for resource estimation, but also for successful drilling campaigns. This is because these compositional and petrophysical characteristics of the gas shales affect how the rocks respond to artificially induced stress regimes during drilling and hydrocarbon production. It is therefore imperative to investigate the mechanical behaviour of shales to assess the magnitude and distribution of the rock properties and stresses in any potential shale gas bearing basin, which naturally can have variable hydro-mechanical parameters through time and space (Bjørlykke, 2010).

The geomechanical behaviour of shales in hydrocarbon plays provide information on the strength, stiffness and brittleness of these rocks, which collectively determine fracturing properties, including the amount, dimensions, orientation, interconnectedness of natural fractures and fracture healing rates (e.g., Nygard et al., 2006; Jaeger et al., 2007; Fjaer et al., 2008; Rickman et al., 2008; Holt et al., 2011; Mullen & Enderlin, 2012; Josh et al., 2012). Understanding mechanical properties of rocks is key for hydraulic fracturing to successfully stimulate tight reservoirs rocks, enhance production rates, assess borehole stability and evaluate stable mud weight windows during drilling and hydrofracturing (e.g., Economides & Nolte, 2000; Fjaer et al., 2008; Gholami et al., 2014; Meier et al., 2015).

This study, a first for the southern MKB, investigates how the compositional and petrophysical properties influence the geomechanical behaviour of the Early Permian Ecca Group intersected in BH KZF-1 (Figure 5.1).

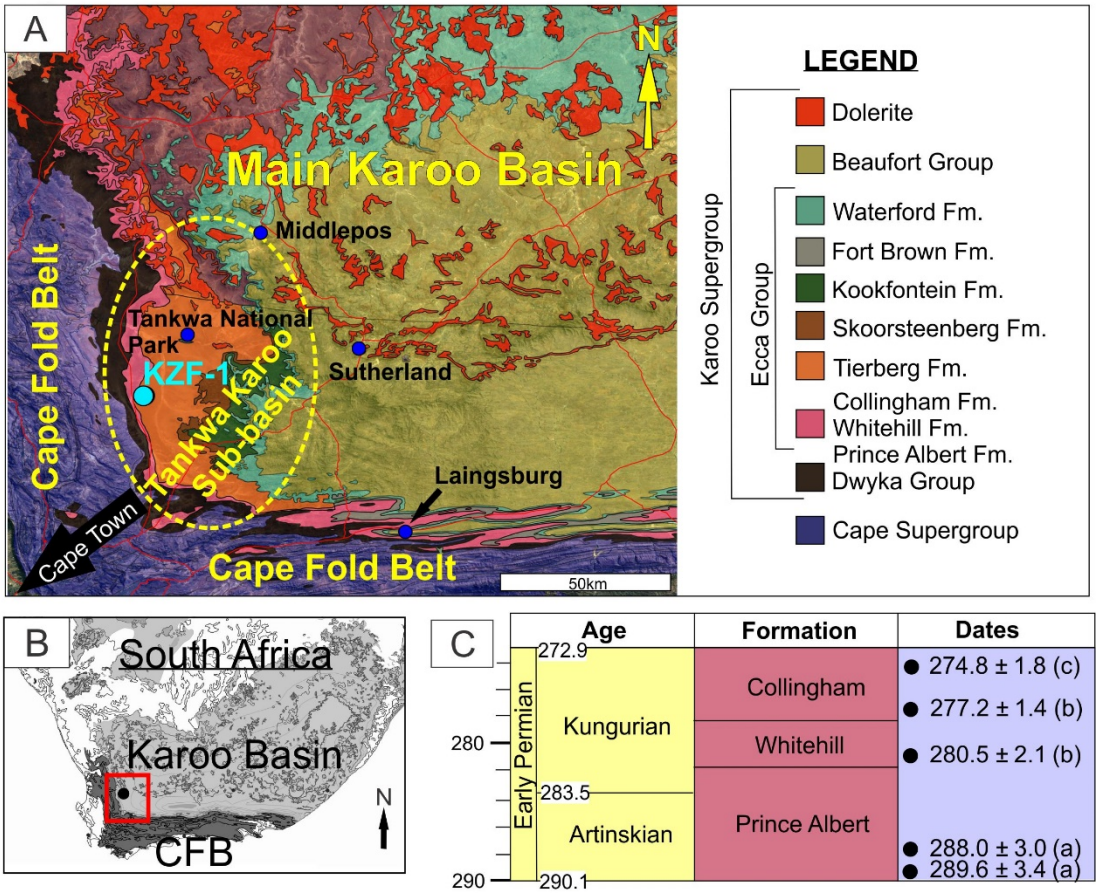

Figure 5.1: A) Location map of borehole KZF-1 in the Tankwa Karoo Sub-basin in the main Karoo Basin of South Africa (32°50' 30.43" S, 19°44' 33.02" E). B) Overview map with insert showing the study area (red rectangle) within southern Africa. C) The chronostratigraphy of the Early Permian Ecca Group (Karoo Supergroup) in the southern main Karoo Basin and Namibia (modified after Rubidge, 2005 and Smithard et al., 2015). Radiometric dates are marked with black circles, shown in million years and taken from a: Bangert et al., 1999; b: Werner, 2006; c: Fildani et al., 2007. Geological time scale based on 2013 ICS Time Chart.

5.2 Geological setting

The MKB was formed as a retroarc foreland basin that was strongly influenced by the tectonic events that lead to the formation of the Cape Fold Belt (CFB), a Permo-Triassic orogen that formed part of the Pan- Gondwanian thrust-fold belt (e.g., Catuneanu et al., 1998; Bordy et al., 2004a, b; Hansma et al., 2015). The samples analysed in this study are from a borehole (BH KZF-1) form the Tankwa Karoo Sub-basin in the western MKB (Figure 5.1). The geology in this region was controlled by mountain-building tectonic forces of the CFB, which surrounds the area from the south and the west (Tankard et al., 2012).

The lower Ecca Group in the Tankwa Karoo Sub-basin comprises the postglacial mudstones of the Prince Albert Formation, black carbonaceous shales (with up to 14 wt% TOC) of the Whitehill Formation and the siliceous mudstones of the Collingham Formation (Figure 5.1C; Cole & McLachlan, 1994). The latter unit contains tuffaceous

beds that grade upwards into fine-grained turbiditic sandstones (e.g., Wickens, 1994; Viljoen, 1994; Turner, 1999; Wickens & Cole, 2017). The depositional period of the lower Ecca Group in the Tankwa Karoo Sub-basin is confined to the Early Permian (Figure 5.1C) and was determined from tuffaceous beds in the Prince Albert and Collingham formations (~ 290–273 Ma), as well as in the fossiliferous Beaufort Group (e.g., Bangert et al., 1999; Fildani et al., 2007; Rubidge et al. 2013; Lanci et al., 2013; Day et al., 2015; Belica et al., 2017). These rocks form part of the Karoo Supergroup, which is a Late Carboniferous to Early Jurassic succession common throughout southern Africa (Johnson et al., 2006). Its youngest unit, the Drakensberg Group, comprises continental flood basalts and dolerite intrusions (both sills and dykes), which formed at the end of the Karoo depositional period ~ 183 Ma ago (e.g., Duncan et al., 2007; Svensen et al., 2012; Moulin et al., 2017)

Following the break-up of Gondwana in post-Karoo times, the southern African region underwent widespread uplift and erosion (e.g., Dingle, 1983; Tinker et al., 2008; Hanson et al., 2009) and at present day only the Ecca Group and lower Beaufort Group remain preserved in the surface rock exposures of the Tankwa Karoo Sub-basin. Assuming that the post-Ecca unit of the Karoo Supergroup extended westwards, the Ecca Group may have been buried by ~ 9000 m of sedimentary rock (Hanson et al., 2009). The deep burial and subsurface palaeo-temperatures that may have ranged from 150 °C to 300 °C, resulted in greenschist facies metamorphism near the CFB (e.g., Rowsell & De Swardt, 1976; Frimmel et al., 2001; Tinker et al., 2008). Vitrinite reflectance values range from 1 in the north to 4.3% VR_o in the south (e.g., Rowsell & De Swardt, 1976; Geel et al., 2015; de Kock et al., 2017; Nolte et al., 2019) and illite crystallinity (KI) values range from > 5 in the north to > 3 in the south and drop to as low as 1 near dolerite intrusions (Rowsell & De Swardt, 1976; Smithard et al., 2015; Adeniyi et al., 2018). Because of the rapid heating of organic matter due to tectonic deformation and contact metamorphic effects from lower Jurassic dolerites, the early gas saturation within the lower Ecca Group likely occurred before the Middle Jurassic. Moreover, taking into consideration the permeability, porosity of these units and their structural deformation linked to the CFB orogeny and then Gondwana break-up, hydrocarbon generation, migration and accumulation likely ended in early post-Karoo times.

5.3 Materials and methods

5.3.1 Mineral composition of the samples

Borehole KZF-1 was drilled in the Tankwa Karoo Sub-basin (western MKB) in the Western Cape Province (32°50'30.43" S, 19°44'33.02" E; Figure 5.1) and intersected 671 m of Karoo rocks. Geophysical data was logged by Weatherford Slimline Services and included *in situ* measurements of the physical rock properties. For this study, the geophysical data from the gamma ray logs and dynamic Young's modulus are used. A total of 33 samples were prepared as standard petrographic thin sections and analysed using a Zeiss Axiocam A1 microscope in the Department of Geosciences at the University of Cape Town (petrology is described in detail in Chapter 2).

Quantitative XRD was carried out on 22 samples from BH KZF-1 and measured in wt% with a Malvern Panalytical AERIS diffractor meter with PIXcel detector and fixed slits with Fe filtred Co- Kα radiation by XRD Analytical and Consulting Laboratory in Pretoria, South Africa. The phases were determined using X'pert Highscore plus software. The results were converted from wt% to vol% by assuming their densities (TOC: 1.3 g/cm^3; quartz: 2.65 g/cm^3; dolomite: 2.71 g/cm^3; pyrite: 5.01 g/cm^3; feldspar: 2.6 g/cm^3; clay: 2.5 g/cm^3; siderite: 3.96 g/cm^3; chlorite: 2.5 g/cm^3; Graf, 1961; Brown & Bailey, 1963, Rybacki et al., 2016).

TOC/Rock Eval analyses were completed on all 33 samples by the Indian Institute of Technology in Bombay, India (Appendix A). Rock-Eval pyrolysis is a technique used to identify the hydrocarbon release of organic rich sedimentary rocks, which helps to analyse the maturity, total organic carbon (TOC) weight percentage and type of the contained organic matter (Nuñez-Betelu & Baceta, 1994).

He pycnometry experiments and vitrinite reflectance measurements were performed on 10 samples (KZF01P to KZF10P) at the Institute of Geology and Geochemistry of Petroleum and Coal at RWTH Aachen University in Germany, during this study. Details of this experimentation was recently documented by Nolte et al. (2019). The porosity measurements and vitrinite reflectance values are summarized in Table 5.1 and are utilized in this study.

The geomechanical properties were measured at the German Research Center for Geoscience (GFZ) in Germany and our results are compared to those from the Alum Shale (Denmark), the Barnett Shale (North America) and the Posidonia Shale (Germany) as reported in Rybacki et al. (2015, 2016) and the Bowland Shale (United Kingdom) as reported in Herrmann et al. (2018). Moreover, we also use the porosity,

permeability and vitrinite reflectance properties of these Early Permian Ecca rocks, which were measured in a collaborative study at RWTH Aachen University, Germany, and reported in Nolte et al. (2019).

Table 5.1: Average quantitative porosity, permeability and vitrinite reflectance values for the Prince Albert, Whitehill and Collingham formations obtained via He pycnometry tests (data published in Nolte et al. (2019)). Abbreviations: VR_o = vitrinite reflectance.

Formation	***Average porosity (%)***	***Average permeability (m^2)***	***VR_o (%)***
Collingham	4.37–4.90	10^{-19}–10^{-20}	4
Whitehill	4.25–6.33	10^{-20} –10^{-22}	4
Prince Albert	4.13	10^{-22}	4

5.3.2 Geomechanics

Triaxial measurements were carried out in the Geomechanics and Rheology Department at the GFZ, Potsdam in Germany. A total of five samples were deformed by triaxial tests. Sample brittleness was calculated using mineralogical composition, porosity and Young's modulus values (Equations 5.2– 5.4). Samples from the lower Ecca Group are compared with samples of the highly overmature Palaeozoic Alum Shale (ALM1) from Denmark, the Bowland Shale (BOS) from the United Kingdom, four Mesozoic Posidonia Shales from Germany and the mature Palaeozoic Barnett Shale (BAR1) from the USA. The four Posidonia Shale samples are: 1) Dotterhausen (DOT1), an immature oil shale; 2) Wickensen (WIC1), an immature shale; 3) Harderode (HAR1), a shale at peak oil maturity; and 4) Haddessen (HAD1,2), an overmature shale. Furthermore, the lower Ecca Group samples are compared to references samples deformed under the same conditions (Tables 5.4 & 5.5). The reference samples represent the main constituents of shale and include granite, novaculite, sandstone, limestone, marble and coal (Rybacki et al., 2015, 2016; Herrmann et al., 2018).

Triaxial deformation experiments were performed in a Paterson-type high pressure, high temperature deformation apparatus (Paterson, 1970) at constant strain rate of 5×10^{-4} s^{-1} at 50 MPa and at 100 °C. Calibration tests on pure AlO_2 specimens have been conducted prior to deformation tests on shales to correct for the system compliance.

Argon gas was used as the confining pressure medium, which allowed for the precise measurements using an internal load cell within the pressure vessel. Samples were jacketed by thin (~ 0.5 mm) copper sleeves to prevent intrusion of the argon gas. The forces that were measured and the axial displacements were converted to axial stress

and strain, assuming constant volume deformation and corrected for the jacket load and system compliance. The estimated error in stress and strain is < 4 %. The estimated uncertainties for the Young's moduli results are about 20 %, due to the low intrinsic stiffness of the apparatus (Rybacki et al., 2015). Stress-strain curves recorded during constant strain rate deformation tests were used to calculate the static Young's modulus. Stress-strain calculations were done measuring the tangent Young's modulus measured at 50 % of the ultimate compressive strength (McCann & Entwisle, 1992; Rybacki et al., 2015).

Dynamic Youngs modulus can be calculated from the full train sonic log of a borehole and can be used to estimate static values if a relationship between the two is established. The static Young's modulus can be calculated from the dynamic Young's modulus with Equation 5.1 if there is a correlation coefficient of 0.9 between the log plot of static and dynamic Youngs modulus (King, 1973; McCann & Entwisle, 1992).

Error! Bookmark not defined.$E_{st} = 1.26\, E_{dy} - 29.5$ (King, 1973) (5.1)

The brittleness of a rock is an empirical rock parameter, which produces values that fall in a range between 1 (brittle) and 0 (ductile). There are many equations that have been developed to calculate brittleness (e.g., Jarvie et al., 2007; Wang & Gale, 2009; Glorioso & Rattia, 2012; Jin et al., 2014; Rybacki et al., 2016). Three brittleness equations are used for in this study:

Error! Bookmark not defined.$Bcompo = \frac{\mathrm{F}_{sb}}{Ftotal}$ (modified from Jin et al., 2014) (5.2)

Bcompo = 1 (brittle)–0 (ductile). Abbreviations: F_{sb} = fraction of strong/brittle minerals (in vol %). $F_{sb} = F_{Qtz + Fsp + Py + Cb}$, F_{total} = total composition.

Error! Bookmark not defined.$Bporocomp = \frac{W_{sb}\, F_{sb}}{W_{sb}\, F_{sb} + W_{Cb}\, F_{Cb} + W_{wd}\, F_{wd} + W_{\Phi}\, \Phi}$ (5.3)

(modified from Rybacki et al., 2016)

Bporocomp = 1 (brittle)–0 (ductile). Abbreviations: F_{sb} = fraction of strong/brittle minerals (in vol %), F_{wd} = fraction of weak/ductile minerals (in vol%), F_{Cb} = fraction of

carbonates (in vol %), Φ = porosity (in vol %), w_{xx} = weighting factor [0-1] for fraction xx.

$F_{sb}= F_{QFP + Cb,}$ $F_{wd}= F_{Cly + Mca + TOC,}$

$W_{sb}= W_{wd} = W_{\Phi}= 1,$ $W_{Cb}= 0.5$

Abbreviations: Qtz= quartz; Fsp = feldspar; Cb = carbonates; Cly = clay; Dol = dolomite; Cal = calcite; Mca = mica; TOC = total organic carbon content; Py = pyrite; QFP = Qtz + Fsp + Py.

Error! Bookmark not defined.$B_E = (0.07 \pm 0.01) \times \left(\frac{E}{E_o}\right)^{0.53 \pm 0.07}$ (Rybacki et al., 2016) (5.4)

E= Young's modulus calculated from stress-strain behaviour, E_0 is a normalization factor in this case E_0= 1 GPa. Equation 5.4 is used to estimate brittleness from Young's modulus for samples with E > 7 GPa.

5.4 Results

5.4.1 Composition

The lithostratigraphy, gamma ray log and TOC of the lower Ecca Group, including the first 20 m of the overlying Tierberg Formation from the upper Ecca Group and 5 m of the underlying Dwyka Group, are illustrated in Figure 5.2. Thrust faulting resulted in duplication of the Whitehill Formation and segments of Prince Albert Formation.

High API values, produced from the gamma ray log, indicate the lower Ecca Group contains an abundance of clay minerals (illite), which is confirmed by XRD data (Figure 5.3). The highest TOC content is detected in the Whitehill Formation (average TOC = 5.17 wt%). Lower gamma ray peaks are associated with TOC-rich calcareous mudstone facies, whereas high gamma ray peaks correspond to carbonate free, clastic mudstone facies (Al Duhalian & Sonneberg, 2015).

The composition of the lower Ecca shales is compared with shale samples outside the MKB from Europe, UK and the USA (Rybacki et al., 2015, 2016; Herrmann et al., 2018). The lower Ecca mudstones (Table 5.2) have a high proportion of strong minerals ~ 50–70 vol%, a moderate proportion of weak minerals (~ 30–50 vol%) and a small proportion of intermediate strength minerals (~ 0–50 vol%). In comparison,

the Alum shale contains up to ~ 60–70 vol% of weak minerals and only 30–40 vol% strong minerals. The Posidonia shale is high in intermediate phase minerals (~ 25–45 vol%) and contains ~ 40–60 vol% weak minerals and ~ 10 – 20 vol% strong minerals. The Barnett shale has ~ 40–50 vol% weak minerals, ~ 30–50 vol% strong minerals phases and ~ 10 vol% intermediate mineral phases. The Bowland shales have a wide range of intermediate mineral phases (7–69 vol %) and hard mineral phases (24–82 vol%) and a narrower range of soft mineral phases (7–35 vol%) (Table 5.2). These comparative compositional data are shown in Figure 5.4, a ternary diagram that differentiates between weak (Clay + TOC + Φ, vol%) components, medium components (Cb, vol%) and strong components (Qtz + Fsp + Py, vol%). Porosity is included as a weak mineral phase, because the compressive strength of a rock may be weakened with an increase in number of pores (Zhang et al., 2018). Only samples with accompanying porosity data were plotted in Figure 5.4.

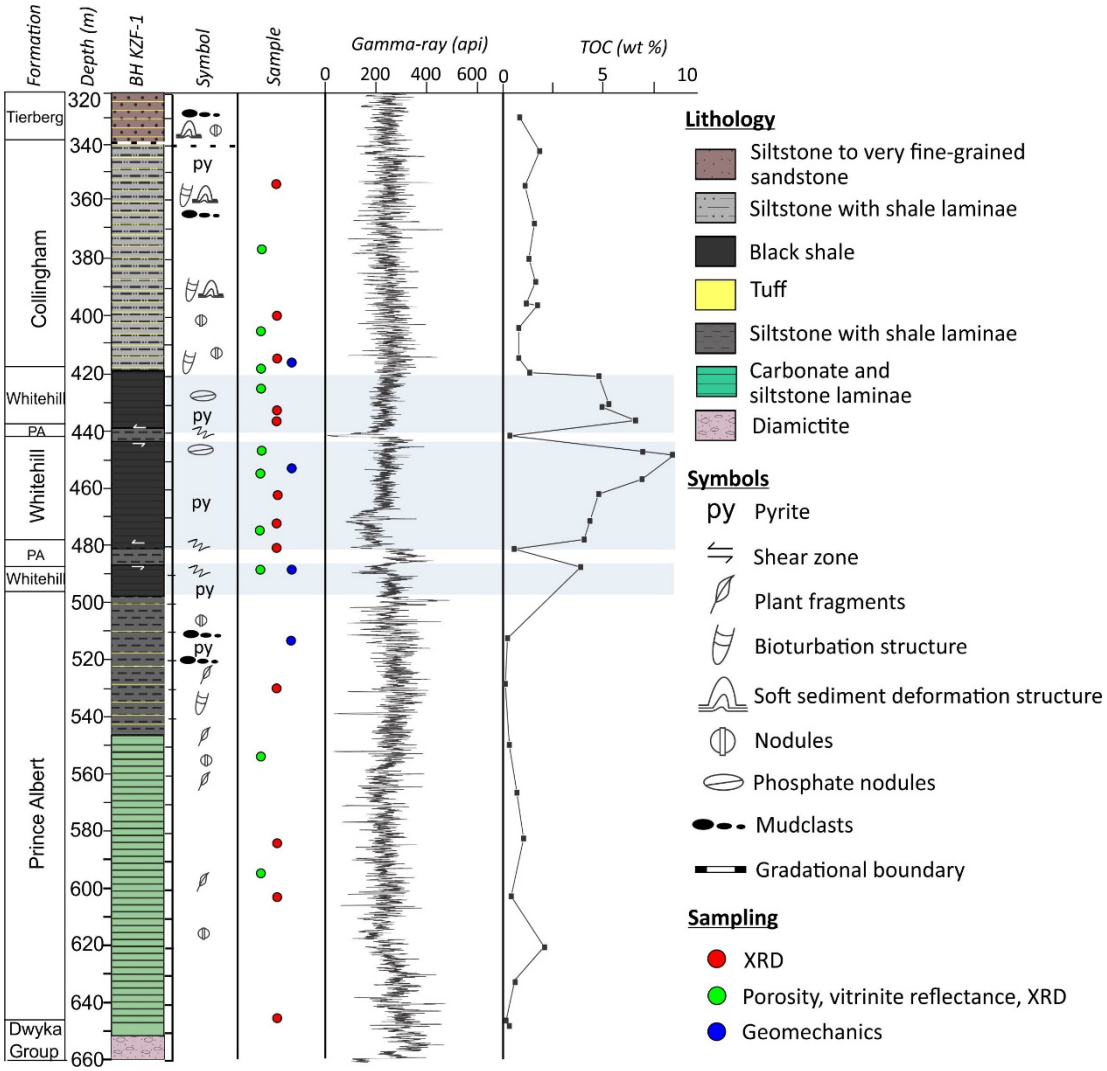

Figure 5.2: Depth profile of BH KZF-1 showing lithostratigraphic units, the main rock types with associated sedimentary features, sampling intervals, gamma-ray (API) and TOC (Total Organic Carbon in wt%) data. Blue shading marks the Whitehill Formation. The position of BH KZF-1 in the MKB is shown in Figure 5.1.

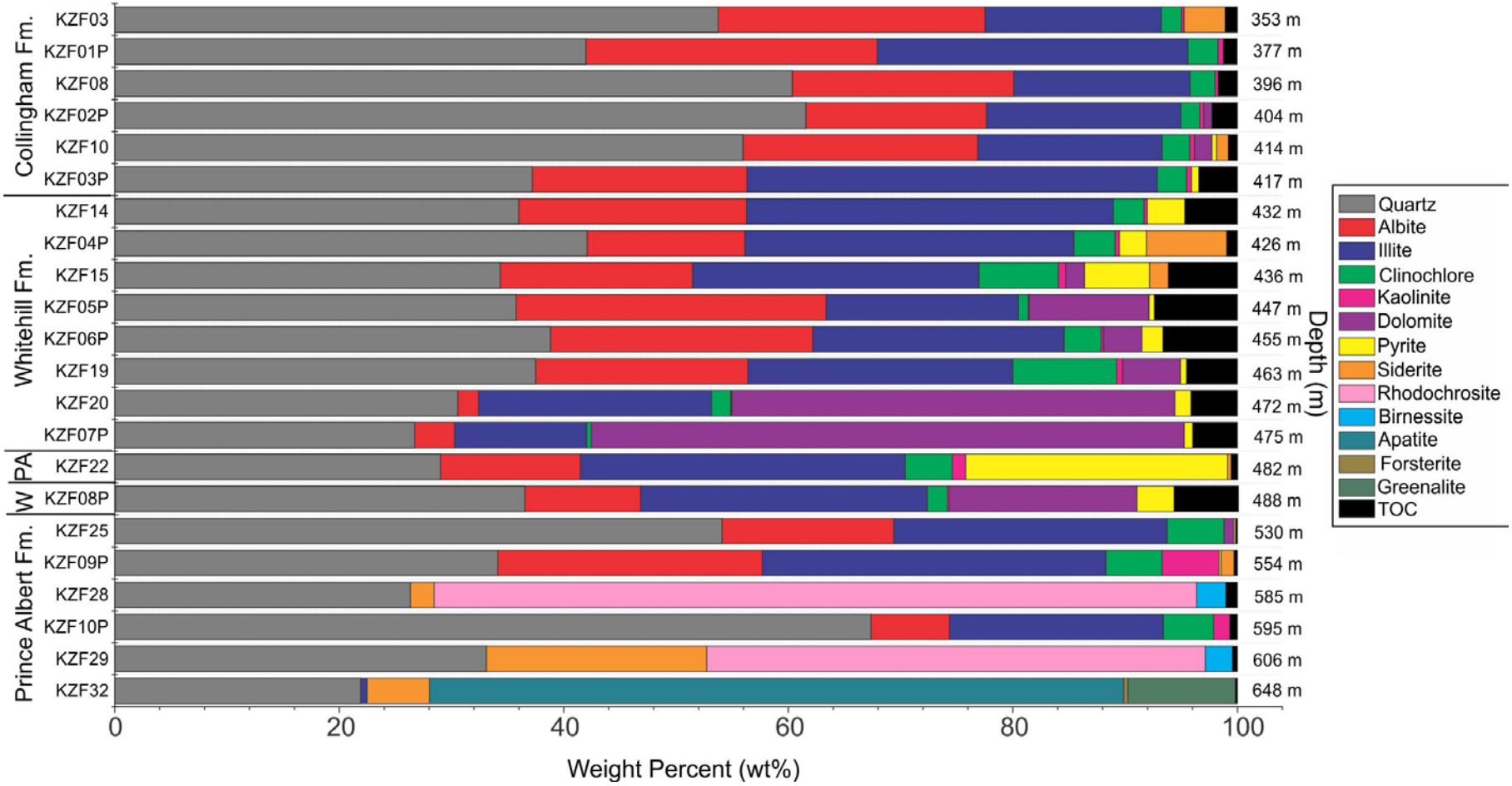

Figure 5.3: Quantitative XRD analyses of the mineralogical composition and TOC content from BH KZF-1 in wt%. PA: Prince Albert Formation; W: Whitehill Formation.

Table 5.2: Compositional data used in the ternary diagram (shown in Figure 5.4). The lower Ecca Group is represented by the Collingham Fm. = Col; Whitehill Fm.= WHI; Prince Albert Fm. = PA from BH KZF-1 from the MKB. Other data points are Alum Shale (ALM 1), Barnett Shale (BAR 1), Posidonia Shales (Dotterhausen Fm. = DOT1; Wickensen Fm. = WIC 1; Harderode Fm.= HAR 1 and Haddessen Fm. = HAD 1) and Bowland shales (BOS). Comparative data obtained from Rybacki et al., (2015); Herrmann et al., (2018). Abbreviations: Qtz: quartz; Fsp: feldspar; Py: pyrite; Cb: carbonate; TOC: total organic carbon.

Sample no.	***Qtz + Fsp+ Py (vol%)***	***Cb (vol %)***	***Clay+ TOC + porosity (vol%)***
(COL) KZF01P	64.9	0,00	35.1
(COL) KZF02P	67.2	0.6	32.2
(COL) KZF03P	51.3	0.00	48.7
(WHI) KZF04P	54.4	4.5	41.1
(WHI) KZF05P	55.8	9.1	35.1
(WHI) KZF06P	55.4	2.9	41.7
(WHI) KZF07P	28.5	47.9	23.6
(PA) KZF08P	43.1	14.5	42.3
(PA) KZF10P	69.9	0.00	30.1
ALM 1	30.9	0.7	68.4
BAR 1	28.4	5.2	66.5
DOT 1	14.5	41.6	43.9
WIC 1	17.00	33.9	49.1
HAR 1	20.8	39.6	39.6
HAD 1	20.8	27.5	51.7
BOS1	24	69	7
BOS6	82	7	11
BOS8	35	58	7
BOS10	59	26	15
BOS11	39	26	35
BOS14	76	7	17

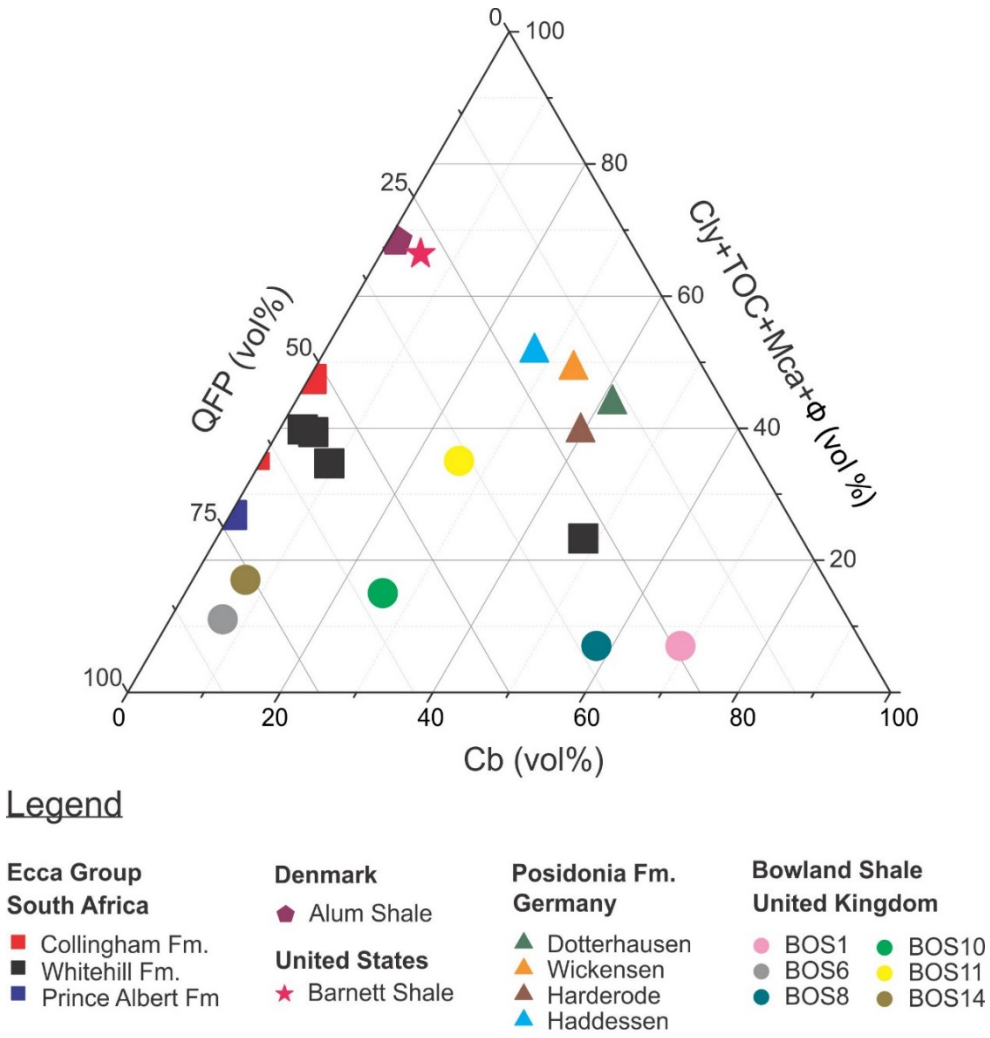

Figure 5.4: Ternary diagram of shale compositions from the lower Ecca Group is shown in relation to Posidonia shale, Bowland shale, Alum shale and the Barnett shale. Weak components are clay and kerogen (TOC), medium components are carbonates (Cb) and strong components are quartz (Qtz), feldspar (Fsp) and pyrite (Py). Comparative data outside the MKB adopted from Rybacki et al. (2015, 2016) and Herrmann et al. (2018). Abbreviations: QFP: quartz + feldspar + pyrite; Cly: clay; TOC: total organic carbon; Mca: mica; Φ: porosity; Cb: carbonate. For details see Table 5.2.

5.4.2 Triaxial deformation experiments

Stress-strain curves were obtained from samples KZF01M, KZF02M, KZF08P-ǁ, KZF08P-45° and KZF03M (Figure 5.5). These samples underwent triaxial deformation conditions of 50 MPa confining pressure, at 100° C and with a strain rate of $\dot{\varepsilon} = 5 \times 10^{-4}\ s^{-1}$. Using the measurements during the triaxial deformation experiments, it was possible to calculate the static Young's modulus (E) and triaxial compressive strength (σ_{TCS}) for the Prince Albert, Whitehill and Collingham formations (Table 5.3). Stress-strain curves show that all the samples have distinct peak stresses. None of the samples display post-peak ductile behaviour, which is typical for brittle deformation. The Young's moduli from the lower Ecca Group were compared

to data reported in Rybacki et al. (2015; 2016) and Herrmann et al. (2018) for shale samples from Europe and the USA, as well as reference samples (Tables 5.4, 5.5; Figure 5.6).

In samples measured perpendicular to bedding, sample KZF03M from the Prince Albert Formation has the highest Young's modulus (E = 58 GPa) and highest maximum compressive strength (σ_{TCS} = 468.7 MPa), therefore this is the strongest sample from the MKB, followed by the Collingham Formation (KZF01M: E = 53 GPa; σ_{TCS} = 402.8 MPa) and then by the Whitehill Formation (KZF02M: E = 43 GPa; σ_{TCS} = 308.1 MPa) (Table 5.4, Figure 5.4). Sample KZF08P was taken near a fracture zone in the Whitehill Formation and was measured parallel and 45° to bedding. Overall KZF08P is the weakest sample (KZF08P-∥: E = 37 GPa; σ_{max} = 315.89 MPa; KZF08P-45°: E = 28 GPa; σ_{max} = 256.7 MPa). The Young's modulus and maximum compressive strength values for the lower Ecca Group are greater than the Posidonia and Alum shales from Germany and Denmark and instead are more like to the Barnett Shale from the USA and some samples from the Bowland shale from the UK (Table 5.5).

Young's modulus is correlated with compressive strength (Figure 5.6 F), therefore both are plotted against mineralogical fractions, density, porosity and vitrinite reflectance values (Figures 5.6; 5.7). The Young's modulus increases with increasing hard fraction minerals, whereas the compressive strength decreases with increasing weak fraction minerals. These trends are specifically noted in samples from the lower Ecca Group. Correlation between increasing compressive strength and density is possible, however, no clear relationship can be determined between compressive strength and vitrinite reflectance and Young's modulus and carbonate minerals. A weak relationship between decreasing compressive strength and increasing porosity is also observed.

Table 5.3: Mechanical data of samples from BH KZF-1 from the MKB obtained at elevated P - T conditions during triaxial deformation experiments. E = Young's modulus, σ_{max} = triaxial compressive strength. T = 100 °C; P = 50 MPa, $\dot{\varepsilon} = 5 \times 10^{-4}\ s^{-1}$.

Formations	***Sample no.***	***Sample Symbol***	***Orientation relative to bedding***	***E [GPa]***	***σTCS [MPa]***
Collingham	KZF01M	COL	⊥	53	402.8
Whitehill	KZF02M	WHI	⊥	43	308.1
Whitehill	KZF08P	WHI 45°	45 °	28	256.7
Whitehill	KZF08P	WHI ∥	∥	37	315.9
Prince Albert	KZF03M	PA	⊥	58	468.7

Table 5.4: Mechanical data of international samples obtained at elevated P - T conditions during triaxial deformation experiments. E = Young's modulus, σ_{max} = triaxial compressive strength. T = 100 °C; P = 50 MPa, $\dot{\varepsilon} = 5 \times 10^{-4}\ s^{-1}$(Rybacki et al., 2015; Herrmann et al., 2018).

International examples	***Symbol symbol***	***Orientation relative to bedding***	***E [GPa]***	***σTCS [MPa]***
Alum (Denmark)	ALM1	⊥	16.7	152
Barnett (USA)	BAR1	⊥	46.4	389
Posidonia (Dotternhausen, Germany)	DOT1	⊥	8	175
Posidonia (Wickensen, Germany)	WIC1	⊥	8	142
Posidonia (Harderode, Germany)	HAR1	⊥	14.1	192
Posidonia (Haddessen, Germany)	HAD1	⊥	11.6	144
Bowland (upper, UK)	BOS 1	⊥	52	429
Bowland (upper, UK)	BOS 6	⊥	28	355
Bowland (lower, UK)	BOS 8	⊥	50	547
Bowland (lower, UK)	BOS 10	⊥	37	375
Bowland (upper, UK)	BOS 11	⊥	6	144
Bowland (upper, UK)	BOS14	⊥	28	356

Table 5.5: Reference samples of granite, novaculite, sandstone, limestone, marble and coal (Rybacki et al., 2015). See Figure 5.6 F for details.

Reference sample name	***Sample symbol***	***Orientation relative to bedding***	***E [GPa]***	***σTCS [MPa]***
Westerly granite	GRA	⊥	64.9	731
Arkansas novaculite	NOV	⊥	58.8	699
Flechtingen sandstone	FST	⊥	33.8	303
Bentheim sandstone	BST	⊥	32.7	210
Solnhofen limestone	LIM	⊥	50.8	321
Carrara marble	MAR	⊥	64	234
Bituminous coal	COA	⊥	7.1	155

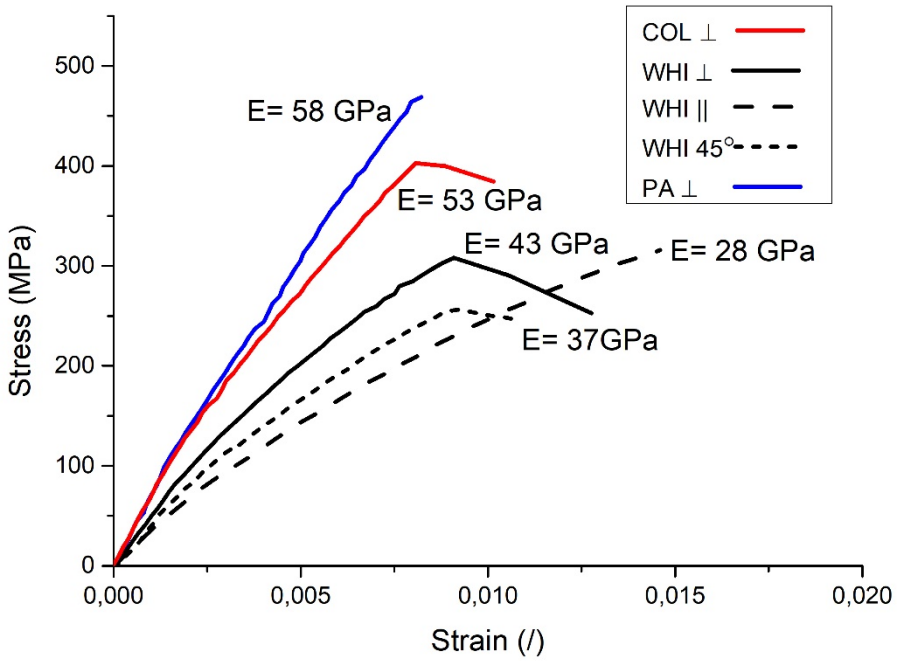

Figure 5.5: Stress-strain curves of deformed samples under triaxial conditions. See Table 5.4 for data.

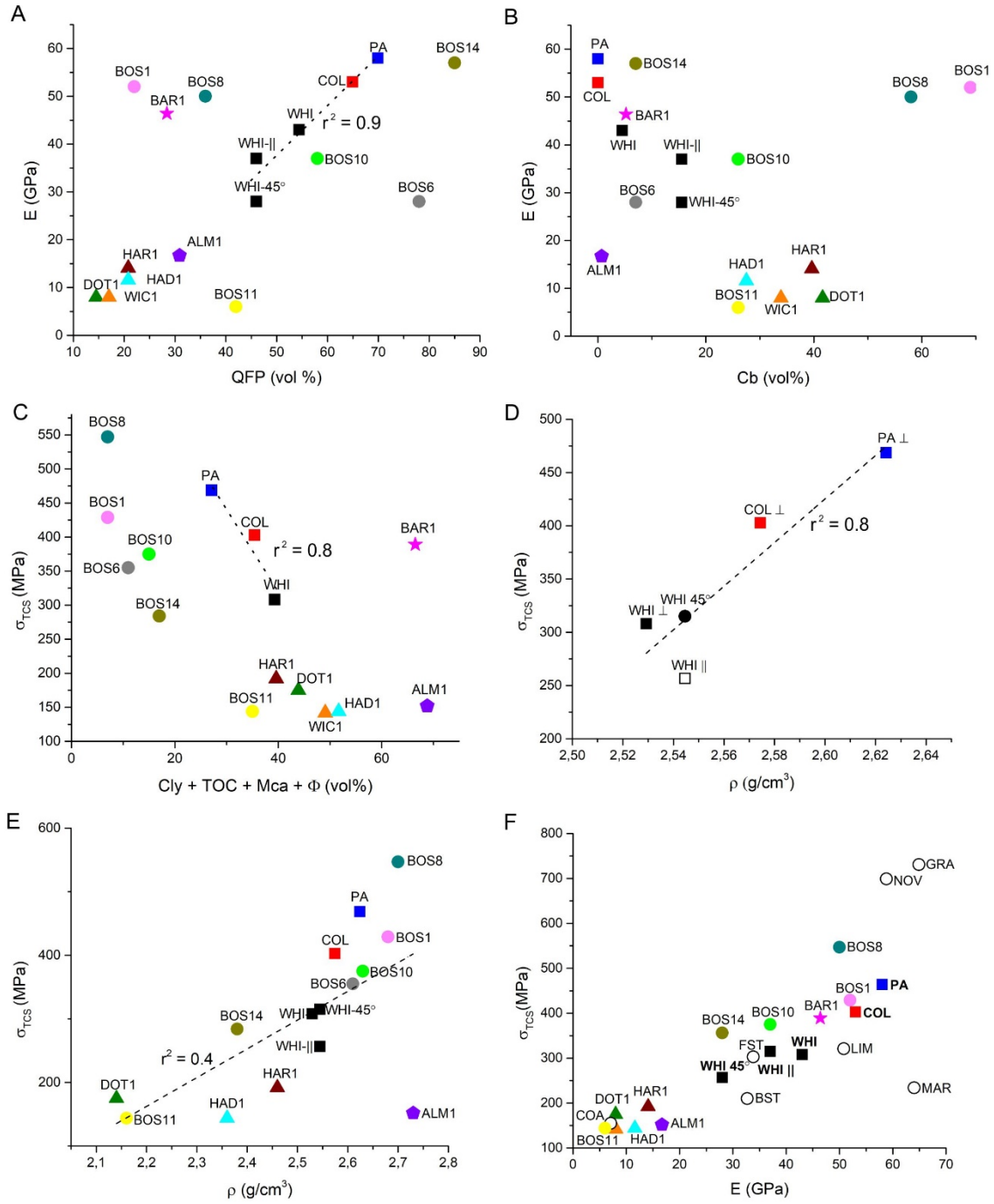

Figure 5.6: Relationships between Young's modulus, triaxial compressive strength, mineral components and density. A) Young's modulus (E) and strong components (QFP). B) Young's modulus (E) and intermediate fraction components (Cb). C)Triaxial compressive strength (σ_{TCS}) and weak components (clay + TOC + Φ). D, E) σ_{TCS} and density (ρ). F) σ_{TCS} and E including reference samples. Linear correlations are denoted by dashed lines (adjusted r^2). Abbreviations: PA = Prince Albert Fm.; COL = Collingham Fm.; WHI = Whitehill Fm.; ALM1 = Alum shale; BAR1 = Barnett shale; DOT1 = Dotterhausen; WIC1 = Wickensen; HAR1 = Harderode; HAD1 = Haddenssen; BOS1,6,8,10,11,14 = Bowland shale; GRA = Westerly granite; NOV = Arkansas novaculite; FST = Flechtingen sandstone; BST = Bentheim sandstone; LIM = Solnhofen limestone; MAR = Carrara marble; COA = Bituminous coal. Comparative data outside the MKB adapted from Rybacki et al., (2015) and Herrmann et al., (2018). See Tables 5.4–5.6 for data.

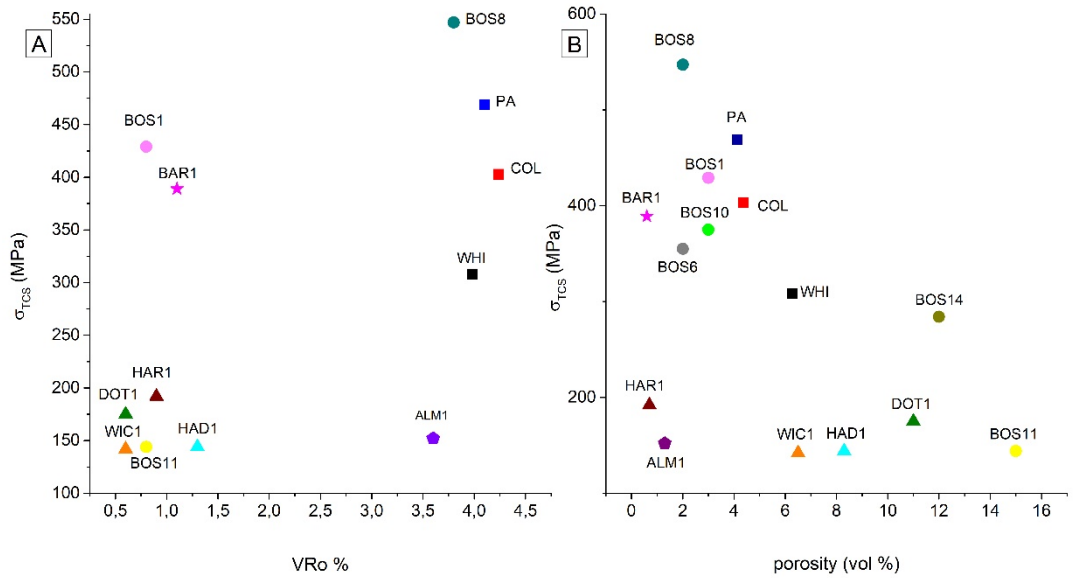

Figure 5.7: The relationship between triaxial compressive strength (σ_{TCS}) and vitrinite reflectance (VR_o) and porosity. A) VR_o vs σ_{TCS}. B) Porosity vs σ_{TCS}. Abbreviations: PA = Prince Albert Fm.; COL = Collingham Fm.; WHI = Whitehill Fm.; ALM1 = Alum shale; BAR1 = Barnett shale; DOT1 = Dotterhausen; WIC1 = Wickensen; HAR1 = Harderode; HAD1 = Haddenssen; BOS1,6,8,10,11,14 = Bowland shale. Comparative data outside the MKB adapted from Rybacki et al., (2015) and Herrmann et al., (2018).

5.4.3 Dynamic Young's modulus

Samples taken for laboratory geomechanical analysis, no matter how carefully sampled in the field, are still subjected to some stress alteration during the drilling process. Therefore, it is important to compare empirical geomechanical data from well logs to assess the *in situ* rock properties (McCann & Entwisle, 1992).

Dynamic elastic moduli are determined from compressional and shear wave velocities from the full wave train sonic log and density is calculated from a gamma ray detector. The dynamic Young's modulus is compared to the static Young's modulus from equivalent sample horizons (Table 5.7; Figure 5.8). *In situ* values of Young's modulus can be estimated from dynamic modulus values, however this is only possible for unfractured rock (McCann & Entwisle, 1992). Therefore, samples KZF08P-45° and KZF08P-Ⅱ, which were sampled near a fracture zone in the Whitehill Formation, should not be used to attempt to correlate with the static Young's modulus. The dynamic Young's modulus is on average 16 GPa lower than the static Young's modulus. Triaxial measurements were performed under 50 MPa of pressure, whereas *in situ* pressures of the lower Ecca Group in BH KZF-1 are between 8 MPa and 17 MPa. The logarithmic plot of static Young's modulus versus dynamic Young's modulus has a correlation coefficient of 0.9 (Figure 5.8). Equation 5.1 is used to calculate the static Young's modulus under *in situ* lithostratigraphic pressures (Table

5.7). Overall, the Whitehill Formation has the lowest dynamic Young's Modulus, which is also evident from the electrical log shown in Figure 5.9.

Table 5.6: The static Young's modulus from samples KZF01M, KZF02M, KZF03M and KZF08P compared with dynamic Young's modulus obtained from geophysical borehole logs from the same depth.

	Samples from the MKB				
	KZF01M (⊥)	**KZF02M (⊥)**	**KZF03M (⊥)**	**KZF08P (45°)**	**KZF08P (∥)**
Sample depth (m)	376.8	426	595	488	
Static Young's modulus (GPa) at 50 MPa	53	43	58	28	37
Dynamic Youngs modulus (GPa)	38	28	40	34	
Static Young's modulus (GPa) at in situ pressure	18.38	5.78	20.9	13.34	

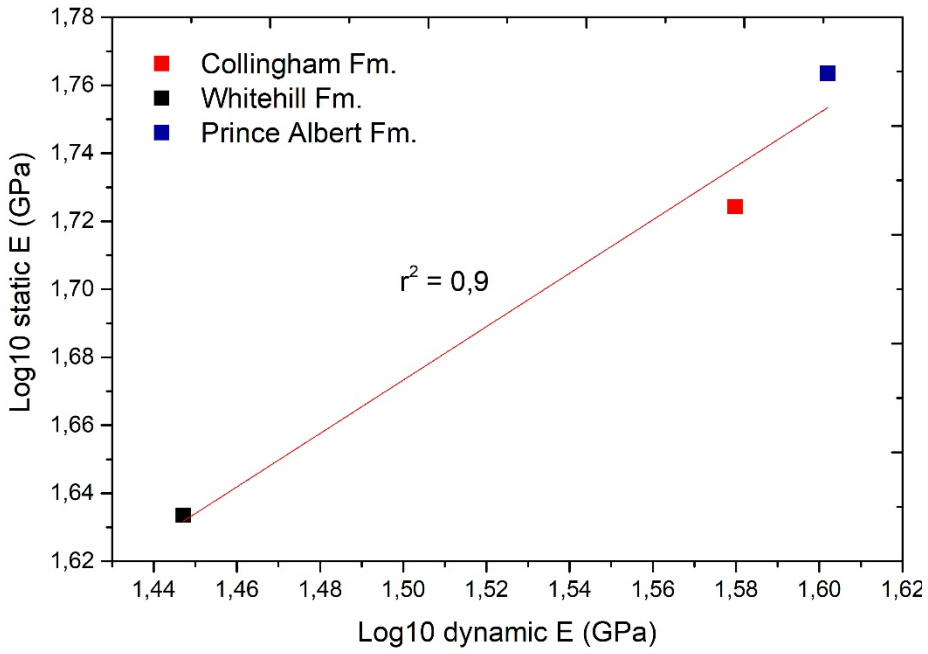

Figure 5.8: Log_{10} plot of static and dynamic values of Young's modulus (E) obtained from samples KZF01M, KZF02M and KZF03M from BH KZF-1. Abbreviations: Young's modulus: E; r^2 = regression analyses

5.4.4 Brittleness index

Brittleness, B, is calculated using Equations 5.2, 5.3 and 5.4. The results are presented in Tables 5.7 and 5.8. The brittleness of a rock is normalized to range

between 0 (ductile) and 1 (brittle). Equation 5.2 (Bcompo) is utilized using mineralogical composition from 22 samples. Bcompo values range between 0.57 and 1.00 in the Prince Albert Formation, between 0.55 and 0.80 in the Whitehill Formation and between 0.54 and 0.81 in the Collingham Formation, respectively. The average Bcompo value is highest (0.81) in the Prince Albert Formation, lowest (0.65) in the Whitehill Formation and intermediate (0.72) in the Collingham Formation.

Equation 5.3 (Bporocomp) uses both mineralogical composition and porosity values, but because porosity values are only available for 7 of the samples, the comparative results are somewhat limited. Bporocomp values are 0.74 in the Prince Albert Formation, 0.36 in the Whitehill Formation and 0.6 in the Collingham Formation. Bporocomp values vary most from Bcompo in dolomite-rich sample KZF07P, which is taken from the Whitehill Formation.

Equation 5.4 (B_E) uses the Young's modulus calculated from triaxial deformation experiments. The B_E values are lower overall compared with Bcompo and Bporocomp (Table 5.9). The B_E value for the Prince Albert Formation is the highest (0.60), followed by the Collingham Formation (0.57) and then by the Whitehill Formation (0.51). Sample KZF08P, measured near to the fracture zone in the Whitehill Formation has the lowest B_E value of 0.44.

Table 5.7: Brittleness index calculated using the mineral composition (Bcompo) of samples from BH KZF-1. Modified from Jin et al. (2014).

Formation	***Sample no.***	***Depth (m)***	***Bcompo (vol%)***
Collingham	KZF03	353	0.79
Collingham	KZF01P	377	0.66
Collingham	KZF08	400	0.78
Collingham	KZF02P	404	0.76
Collingham	KZF10	414	0.81
Collingham	KZF03P	417	0.54
Whitehill	KZF14	426	0.63
Whitehill	KZF04P	432	0.63
Whitehill	KZF15	436	0.55
Whitehill	KZF05P	448	0.69
Whitehill	KZF06P	455	0.62
Whitehill	KZF19	463	0.58
Whitehill	KZF20	472	0.76
Whitehill	KZF07P	475	0.80
Whitehill	KZF08P	482	0.61
Prince Albert	KZF22	488	0.72
Prince Albert	KZF25	530	0.69
Prince Albert	KZF09P	554	0.57
Prince Albert	KZF28	585	1.00
Prince Albert	KZF10P	595	0.73
Prince Albert	KZF29	606	1.00
Prince Albert	KZF32	648	0.99

Table 5.8: Brittleness index calculated using mineral composition (Bcomp), porosity data (Bporocomp) and Young's Modulus (B_E). Adapted from Jin et al., (2014), Rybacki et al., (2016).

Formation	***Sample no.***	***Bcompo***	***Bporocomp***	***B_E (average)***
Collingham	KZF01P	0.66	0.66	-
Collingham	KZF02P	0.76	-	-
Collingham	KZF03P	0.54	0.54	-
Collingham	KZF01M	-	-	0.57
Whitehill	KZF04P	0.63	0.61	
Whitehill	KZF05P	0.69	0.65	-
Whitehill	KZF02M	-	-	0.51
Whitehill	KZF06P	0.62	0.61	-
Whitehill	KZF07P	0.80	0.64	-
Whitehill	KZF08P	0.61	-	0.44
Prince Albert	KZF03M	-	-	0.60
Prince Albert	KZF09P	0.57	-	-
Prince Albert	KZF10P	0.73	0.74	-
Alum	ALM1	0.26	0.31	-
Barnett	BAR1	0.47	0.41	-
Dotterhausen	DOT1	0.61	0.18	0.12
Wickensen	WIC1	0.52	0.20	0.10
Harderode	HAR1	0.58	0.26	0.23
Haddessen	HAD1	0.54	0.19	0.16
Bowland (upper)	BOS 1	-	0.38	0.57
Bowland (upper)	BOS6	-	0.82	0.41
Bowland (lower)	BOS 8	-	0.47	0.56
Bowland (lower)	BOS 10	-	0.68	0.47
Bowland (upper)	BOS 11	-	0.45	0.18
Bowland (upper)	BOS14	-	0.87	0.41

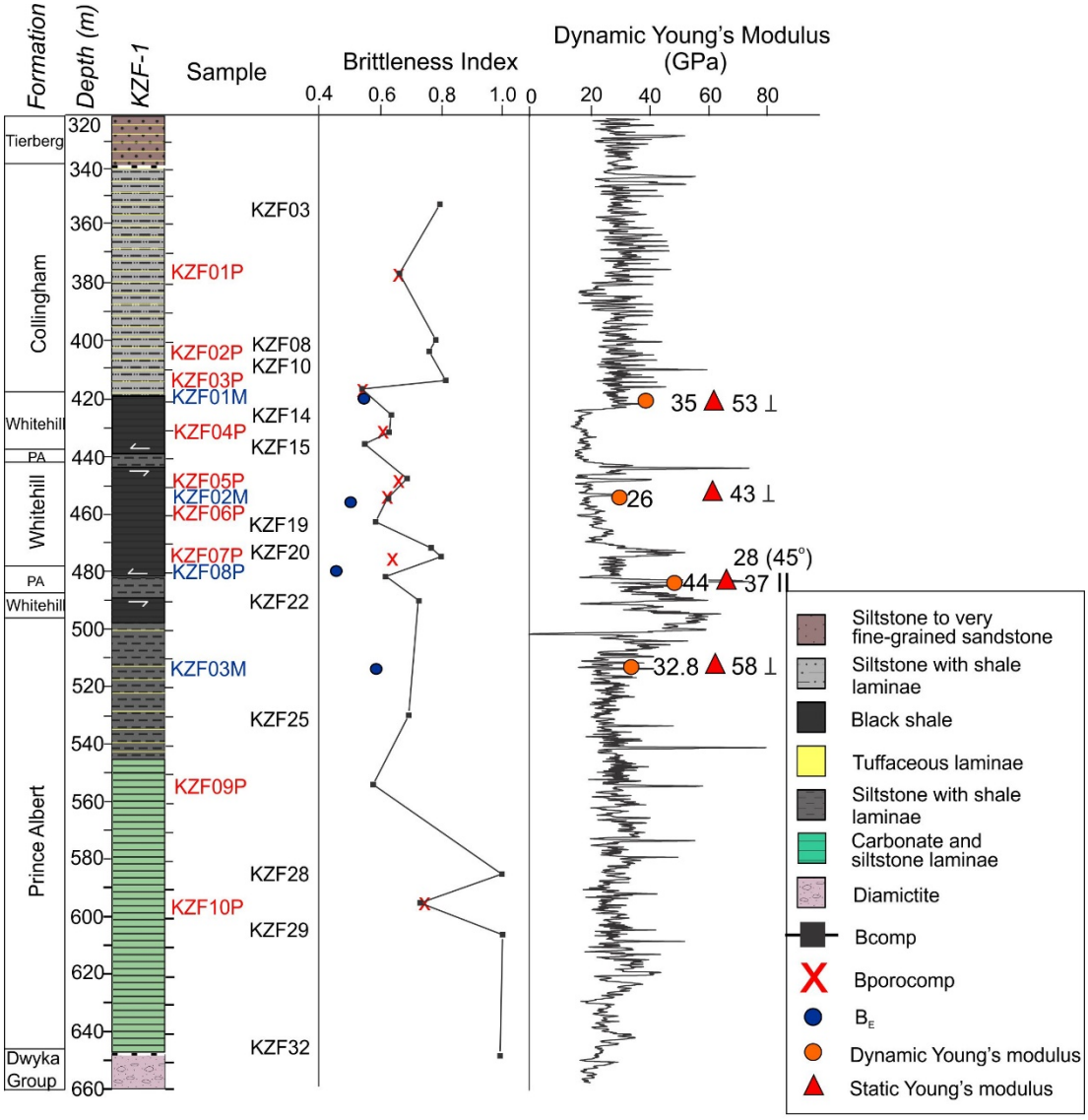

Figure 5.9: Depth profile of BH KZF-1 with brittleness indices and dynamic Young's modulus plotted against static geomechanical measurements.

5.4.5 Natural fractures

The shales of the Whitehill Formation are thinly laminated and have fractures either perpendicular or parallel to bedding (Figure 5.10). Overall, the formation is highly fractured, especially in the regions of thrust faulting. The fractures are filled with crystallized quartz or calcite. Some horizontal fractures are identified as beef fractures, which exhibit a cone-in-cone structures that are around ~ 0.5 mm thick (Figure 5.10 B, C, D). Quartz filled fractures in Figures 5.10 D–H are directly related to thrust faulting.

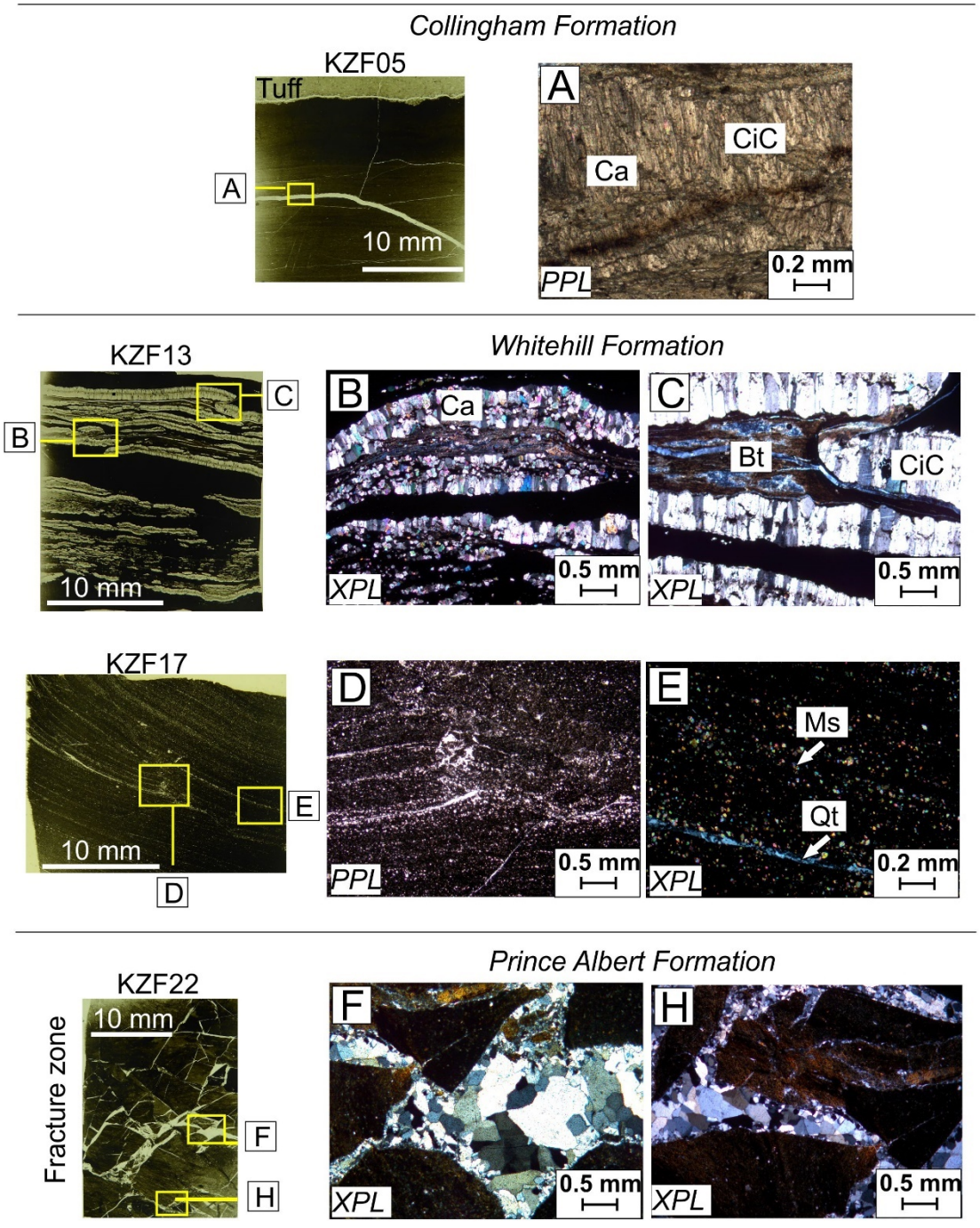

Figure 5.10: Fractures and veining in the lower Ecca Group. A–C) Calcite veins exhibiting cone-in-cone structures. D) Fracture perpendicular to laminae. E) Quartz filled fracture running parallel to lamina. F–H) Brecciated mudstone with quartz fracture infill. Abbreviations: Ca: calcite; Bt: biotite; Qt: quartz; Ms: muscovite; CiC: cone-in-cone.

5.5 Discussion

5.5.1 Effect of sample composition on deformation experiments

Sample petrology and geomechanical properties are intrinsically linked (Ibanez & Kronenberg, 1993; Rickman et al., 2008; Rybacki et al., 2015, 2016). In this study, the composition of organic matter-rich samples from the Prince Albert, Whitehill and Collingham formations, in the western MKB, are compared with international black shales reported in Rybacki et al. (2015, 2016) and Herrmann et al., (2018). Moreover, sample composition is correlated to static Young's modulus and triaxial compressive strengths. Triaxial compressive strength is positively correlated with Young's moduli (Figure 5.6 F) and used to assess correlations with mineralogical composition.

In this analysis, we focus on the hard minerals (QFP) phases, weak mineral phases (Clay + TOC + Φ) and the intermediate mineral phases (Cb). The lower Ecca Group has high proportion of strong mineral factions (QFP = 50–70 vol%). Triaxial deformation experiments show a positive correlation between Young's modulus and hard mineral content (Figure 5.6 A). However, it not only the hard fraction mineral phases which contribute to the strength of the rock. A strong correlation between the increase in compressive strength and sample density for the lower Ecca Group (Figure 5.6 D, E) is also apparent. There is an inverse correlation with increased weak mineral fractions and triaxial compressive strength (Figure 5.6 C). This trend is also detected in samples analysed from the Barnett, Haynesville and Eagle Ford Shales (USA) by Sone & Zoback (2013a). Moreover, thresholds at ~ 30–35 vol% of weak mineral contents and ~ 8–10 vol% of carbonate contents seem to separate strong and weak samples from the lower Ecca Group. A similar threshold of ~ 25–30 vol% of weak mineral phases has been observed by Bourg (2015) and Herrmann et al. (2018) for samples collected from the Bowland Shale. The porosity of the samples from the lower Ecca Group varies from 4.13 to 6.33% and is concentrated in the organic matter that is found between mineral grains (Chapter 2). However, triaxial deformation experiments show a weak correlation with the decrease in Young's modulus and increase in porosity (Figure 5.7 B). Diagenetic carbonates occurring in the lower Ecca Group include ankerite, siderite, rhodochrosite and dolomite (Figure 5.3). No correlation is observed between carbonate minerals and triaxial compressive strength (Figure 5.6 B). However; the samples used in the triaxial measurements are not representative of all the occurring carbonates and more samples should be measured from the lower Ecca Group for more robust correlation.

The Dynamic young's modulus is lower than the static Young's modulus. This is due to the static measurements being calculated at 50 MPa, whereas *in situ* pressures are between 8 and 17 MPa. The logarithmic ratios of static and dynamic Young's modulus are well correlated (0.9). *In situ* static measurements were calculated using Equation 5.1, developed by King, (1983). The recalculated, *in situ*, static values are lower than the dynamic Young's modulus and results from the different stress-strain relationships which occur during laboratory measurements relative to *in situ* conditions (King, 1973; Eissa & Kazi, 1988; McCann & Entwisle, 1992). Both methods for Young's modulus calculation indicate that the Prince Albert Formation is the strongest, followed by the Collingham Formation. The weakest formation of the lower Ecca Group is the Whitehill Formation. This correlated with the fact that the Whitehill Formation has the highest content of weak and ductile mineral phases. The overall strength of the lower Ecca Group rocks will be influenced by the 3D distribution of silt-sized quartz grains within the strata, carbonate nodules and other diagenetic precipitates, trace fossils and soft sediment deformation features.

5.5.2 The effect of thermal maturity on organic matter and porosity

The Karoo Supergroup in the southern MKB, including the Tankwa Karoo Sub-basin, is affected by deformation and low-grade metamorphism as a consequence of the Cape orogeny, which resulted in the CFB (between 292 ± 5 Ma and 245 Ma; Hälbich et al., 1983; Craddock et al., 2008; Milani & de Wit, 2008; Tinker et al., 2008; Hansma et al., 2015; Blewett & Phillips et al., 2019; Blewett et al., 2019). Geothermometry data suggest temperatures reaching ~ 300 °C in the tectonic domains of the CFB, which define lower greenschist facies metamorphic conditions (Frimmel et al., 2001).

In BH KZF-1, there was structural duplication by low angle thrust faults, which resulted in tectonically displaced Whitehill Formation by the Prince Albert Formation with brecciated contacts. Elevated thermal maturity has resulted in over mature organic matter and average vitrinite reflectance (VR_o) of 4 % (Nolte et al., 2019). As a consequence of thrust faulting and brecciation, samples KZF08P-45° and KZF08P-Ⅱ (Whitehill Formation) are the weakest in the triaxial deformation experiments. This implies weakening of the Whitehill Formation as a direct result of tectonic activity. The Whitehill Formation is significantly folded and faulted in outcrop along the southern margin of the MKB (Kingsley, 1981; de Beer et al., 1982; Newton, 1992; Geel et al., 2015). This structural damage implies variability of the strength of the Whitehill Formation depending its proximity to the CFB. There was no significant correlation

observed between triaxial compressive strength and vitrinite reflectance values (Figure 5.7A).

5.5.3 Brittleness indices

The prospectivity of shale gas reservoirs is linked to the brittleness and strength of subsurface rock successions (Holt et al., 2011). Gas shales with weak components (e.g., clay, kerogen), but high brittleness may develop and preserve natural fractures. Brittle rocks may also facilitate hydraulic fracturing due to high anisotropy of the *in situ* stress field and low fracture closure rates. However, brittle rocks with high Young's modulus and fracture toughness may have a higher breakdown pressure than ductile rocks, which would imply poor ability of the rock to develop a complex fracture network in response to artificial fracture stimulation (i.e., poor fracability). Quartz is considered to represent a brittle mineral phase, whereas clay is commonly characterized to deform in a more ductile manner. Therefore, quartz-rich rocks may deform in a more brittle manner than clay-rich rocks. Low porosity corresponds to high internal friction angles and therefore high brittleness (Rybacki et al., 2016). Consequently, brittle shales with strong components (e.g., quartz, feldspar) and porous ductile shales may be less over-pressured allowing for fracture propagation (Rybacki et al., 2016).

Without universal method for brittleness calculations (Yang et al., 2013), brittleness indices are either based on the composition of the rocks (e.g., Jarvie et al., 2007; Wang & Gale, 2009; Glorioso & Rattia, 2012; Rybacki et al. 2016) or on their deformational behaviour and elastic properties (e.g., Smoltczyk & Gartung, 1979; Andreev, 1995; Rickman et al., 2008). Regardless, a combination of techniques is required when interpreting brittleness due to multiple variables that influence the outcome. In this study, three equations were used to calculate the brittleness index of the lower Ecca Group samples (Equations 5.2, 5.3 and 5.4), which resulted in different brittleness values. Equation 5.2 (Bcomp, Jin et al., 2014) was used for 22 samples with quantitative XRD data and plotted as a depth profile in Figure 5.9. Equation 5.2 produced the highest BI values overall. Equation 5.3 (Bporocomp, Rybacki et al., 2016) was only used for the seven samples that have porosity data. These values were slightly lower than those obtained from Equation 5.2 as it includes porosity as a weak material faction. The greatest difference between Bporocomp and Bcompo is observed in sample KZF07P. This is likely due to the high dolomite content in the sample. Carbonates are included as a strong mineral faction in Equation 5.2 and weak to intermediate mineral faction in Equation 5.3. Carbonates do not behave like QFP hard mineral factions when plotted against Young's modulus (Figures 5.6 A, B) and

more detailed work is required on the carbonate components in the lower Ecca Group before brittleness values can be determined for dolomite-rich samples. Equations 5.4 (B_E, Rybacki et al., 2016) produced the lowest brittleness index and was the only equation to include deformation properties. A brittleness threshold of B_E ~ 0.4 +/- 1 separates brittle from ductile with B_E < 0.4 = ductile and B_E > 0.4 = brittle (Herrmann et al., 2018). All the samples measured from the lower Ecca Group using B_E are > 0.4, therefore regarded as brittle. When considering the results from all three equations, it is determined that the Prince Albert Formation rocks is the most brittle unit in the lower Ecca Group, followed closely by the Collingham Formation and then the Whitehill Formation. Overall, the lower Ecca Group is more brittle than the European, UK and USA shales used for comparative purposes in this paper, with an exception of a few samples from the Bowland Shale from the UK.

5.5.4 The implication of beef fractures

Horizontal beef fractures, containing cone-in-cone structures, are identified in the lower Ecca Group (Figure 5.10). Beef fractures are common in compressional tectonic settings (Ramsay, 1980). They are taken as evidence for natural hydraulic fracturing and become filled by successive phases of crystallization either continuously or by a crack-seal mechanism (Ramsay, 1980; Means & Li, 2001; Rodrigues et al., 2009). The formation of beef fractures is associated with organic matter and hydrocarbon generation (Rodrigues et al., 2009; Zanella et al., 2014). With an increase in the maturity of the rocks, there is increase of fluid pressure within source rocks. This combined with horizontal compressive stress, results in the development of horizontal fractures (Zanella et al., 2014.). Therefore, development of beef veins may be synchronous with a compressive period occurring in the basin. Based on a study by Al Duhalian & Sonneberg, (2015), attributes of rock formations associated with beef fractures are: 1) organic richness; 2) overpressuring; 3) thermal maturity; 4) presence of calcareous material (e.g. dolomite); 5) mechanical anisotropy. These five characteristics can all present in the lower Ecca Group, thereby suggesting that the beef fractures may have formed as a response to hydrocarbon generation, likely before ~ 183 Ma. Beef fractures will be expected to be helpful in the prediction and facilitation of artificial fracture propagation if the lower Ecca Group would be hydraulically fractured.

5.6 Conclusion

In unconventional shale gas reservoirs, geomechanical properties are important for predicting fracture initiation and propagation, which are key characteristics of gas

shales, and show much variability due to variable compositional and petrophysical proxies. The propagation of hydraulic fractures is dependent on a combination of the *in situ* stress field, the pore pressure, fracturing fluid pressure and the mechanical properties (e.g., composition, anisotropy) of the rock (Warpinski & Smith, 1990).

The elastic properties of the lower Ecca Group shales are strongly related to their material composition. Deformation experiments carried out on samples from the lower Ecca Group suggest brittle deformation and high Young's modulus. The latter correlates well with the high brittleness index values of this rock succession. The Prince Albert and Collingham formations are strongest and most brittle due to the high proportion of hard and intermediate mineral fractions. The Whitehill Formation is the weakest and least brittle but is stronger still than the comparative international shale samples from the Posidonia, Bowland, Alum and Barnett Shale formations. The brittleness of the Whitehill Formation promises easy hydraulic fracturing. However, the irregular spatial distributions of fracture zones and carbonate horizons in this unit may complicate matters. The dolomite in the Whitehill Formation may drastically change the brittleness and the strength of the rock at least locally.

The high maturity (with VR_o values of ~ 4 %) of the samples has resulted in grain boundary recrystallization, cement and nodule precipitation. Hard mineral phases such as diagenetic quartz and intermediate phases such as dolomite, ankerite, siderite increase the density of the rock, which correlates to an increase in triaxial compressive strength. The degree of maturity and corresponding diagenetic effect on the rocks, therefore, influences the brittleness of the lower Ecca Group. Minerals that precipitate as cement between primary grains can then cause a significant increase in stiffness and seismic velocity (Bjørlykke, 2010). High maturity is also associated with the formation of beef fractures and is an indication of hydrocarbon development in tectonically active regions and are useful for facilitation of hydraulic fracturing if gas extraction techniques are pursued.

The results from this study provide information on the lower Ecca Group found at shallower depths (8–17 MPa) and pressures up to 50 MPa. However, the same rock units in the lower Ecca Group can be found up to ~ 6 km depths in certain parts of the southern MKB, therefore for further regional assessment of the geomechanical characteristics of this Permian succession is required. Measurements will have to be performed at pressures and temperatures that closely replicate those depth variable, dynamic subsurface conditions.

Within the western MKB, the Tankwa Karoo Sub-basin may not be eligible for further exploration due to the high maturity of the rocks and negligible gas detected during the drilling of BH KZF-1 (de Kock et al., 2017). In the likelihood of future exploration, the strength, stiffness and brittleness of these rocks will have to be thoroughly investigated before going ahead with extraction. The data from this study should be built upon to create a robust understanding of the fracability of the lower Ecca Group across the southern MKB.

Suggestions for future studies are measurements of the Young's modulus calculated under increasing temperatures and pressures and creep measurements. Fracture toughness of shales with different microstructures and layering orientations should be processed with computational modelling framework to simulate fracture propagation. Additional studies using uniaxial compressive tests and the Brazillian disc method can be used to calculate properties such as fracture toughness.

5.7 References

Al Duhalian, M. A. & Sonneberg, S. A. 2015. Analyzing beef fractures: genesis and relationship with organic-rich shale facies. *Unconventional Resources Technology Conference.* 20–22 July 2015. San Antonio, Texas.

Adeniyi, E. O., Ossa O. F., Kramers, J. D., de Kock, M. O., Belyanin, G. & Beukes, N. J. Cause and timing of the thermal over-maturation of hydrocarbon source rocks of the Ecca Group (Main Karoo Basin, South Africa). *Marine and Petroleum Geology*. 91: 480–500.

Andreev, G.E. 1995. *Brittle failure of rock materials*. Rotterdam: Balkema. 456p.

Bangert, B., Stollhofen, H., Lorenz, V. & Armstrong, R. 1999. The geochronology and significance of ash-fallout tuffs in the glaciogenic Carboniferous-Permian Dwyka Group of Namibia and South Africa. *Journal of African Earth Sciences*. 29 (1): 33–49.

Belica, M.E., Tohver, E., Poyatos-Moré, M., Flint, S., Parra-Avila, L.A., Lanci, L., Denyszyn, S., Pisarevsky, S.A. 2017. Refining the chronostratigraphy of the Karoo Basin, South Africa: magnetostratigraphic constraints support an Early Permian age for the Ecca Group. *Geophysical Journal International*. 211(3): 1354–1374.

Bjørlykke, K., 2010. *Petroleum geoscience: from sedimentary environments to rock physics*. Berlin: Springer. 508p.

Blewett, S.C.J. & Phillips, D. 2016. An overview of Cape Fold Belt geochronology: Implications for sediment provenance and the timing of orogenesis. In *Origin and evolution of the Cape Mountains and Karoo Basin: Geo-biohistory in a terrain with*

shale gas resources and need for conservation. B. Linol & M. de Wit, Eds. Part of the series Regional Geology Reviews. 8643: 45–55.

Blewett, S.C.J., Phillips, D. & Matchan. E.L. 2019. Provenance of Cape Supergroup sediments and timing of Cape Fold Belt orogenesis: Constraints from high-precision $^{40}Ar/^{39}Ar$ dating of muscovite. *Gondwana Research*. 70: 201–221.

Boden, T.A., Marland G. & R.J. Andres. 2011. *Global, Regional, and National Fossil-Fuel CO_2 Emissions*. Carbon Dioxide Information Analysis Center, Oak Ridge National Laboratory. U.S. Department of Energy, Oak Ridge, Tennessee., U.S.A.

Bordy, E. M., Hancox, P.J & Rubidge, B. S. 2004a. Basin development during the deposition of the Elliot Formation (Late Triassic - Early Jurassic), Karoo Supergroup, South Africa. *South African Journal of Geology*. 107: 395–410.

Bordy, E. M., Hancox, P. J. & Rubidge, B. S. 2004b. Fluvial style variations in the Late Triassic - Early Jurassic Elliot Formation, main Karoo Basin, South Africa. *Journal of African Earth Sciences*. 38: 383–400.

Bourg, I.C. 2015. Sealing shales versus brittle shales: a sharp threshold in the material properties and energy technology uses of fine-grained sedimentary rocks. *Environmental Science & Technology Letters*. 2(10): 255–259.

Brown, B. E. & Bailey, S. W. 1963. Chlorite polytypism: II. Crystal structure of a one-layer Cr-chlorite, Note: variety called kammererite. *American Mineralogist*. 48: 42–61.

Catuneanu, O., Hancox, P.J. & Rubidge, B.S. 1998. Reciprocal flexural behaviour and contrasting stratigraphies: a new basin development model for the Karoo retroarc foreland system, South Africa. *Basin Research*. 10: 417–439.

Catuneanu, O., Wopfner, H., Eriksson, P.G., Cairncross, B., Rubidge, B.S. & Smith R.M.H. 2005. Main Karoo Basin's of south-central Africa. *Journal of African Earth Sciences*. 43: 211–253.

Chere, N. 2015. *Sedimentological and geochemical investigations on borehole cores of the lower Ecca Group black shales, for their gas potential: Karoo basin, South Africa*. Unpublished M.Sc. dissertation. Nelson Mandela Metropolitan University, Port Elizabeth. 268p.

Chukwuma, K., Bordy, E.M. & Coetzer A. 2018. Evolution of porosity and pore geometry in the Permian Whitehill Formation of South Africa – A FE-SEM image analysis study. *Marine and Petroleum Geology.* 91: 262–278.

Cole, D.I. & McLachlan I.R. 1994. *Oil shale potential and depositional environment of the Whitehill Formation in the main Karoo Basin. SOEKOR, now PASA, Petroleum Agency of South Africa, Cape Town*. Unpublished Report No. 1994–0213.

Cole, D.I. 2014. Geology of Karoo shale gas and how this can influence economic gas recovery. *Presentation, Gas – The Game Changer for Southern Africa?* Glen Hove, Johannesburg: Fossil Fuel Foundation, Abstracts, 11–12.

Craddock, J.P., Alex, W., McKiernan, A.W. & de Wit, M.J. 2008. Calcite twin analysis in syntectonic calcite, Cape Fold Belt, South Africa: Implications for fold and cleavage formation within a shallow thrust front. *Journal of Structural Geology*. 29:1100–1113.

Day, M.O., Ramezani, J., Bowring, S.A., Sadler, P.M., Erwin, D.H., Abdala F. & Rubdige, B.S. 2015. When and how did the terrestrial mid-Permian mass extinction occur? Evidence from the tetrapod record of the Karoo Basin, South Africa. *Proceedings of the Royal Society B, Biological Sciences*. 282 (1811).

De Beer, J.H., Van Zijl, J.S.V. & Gough, D.I. 1982. The Southern Cape Conductive Belt (South Africa): Its composition, origin and tectonic significance. *Tectonophysics.* 83: 205–225.

de Kock, M.O., Beukes, N.J., Adeniyi, E.O., Cole, D., Götz, A.E., Geel., C. & Ossa, F-G. 2017. Deflating the shale gas potential of South Africa's Main Karoo basin. South African Journal of Science. 113 (9/10).

de Wit, M.J. & I.G.D. Ransome, 1992. Regional inversion tectonics along the southern margin of Gondwana. In *Inversion tectonics of the Cape Fold Belt, Karoo and Cretaceous Basins of Southern Africa*. M.J. de Wit & I.G.D. Ransome, Eds. Netherlands: Balkema, Rotterdam. 15–20.

Decker, J. & Marot, J. 2012. Investigation of hydraulic fracturing in the Karoo of South Africa. *Annexure A, Resource Assessment, Petroleum Agency SA*. Available: http://www.dmr.gov.za/publications/viewdownload/182/854.html [2018, November 20].

Dingle, R.V., Siesser, W.G. & Newton, A.R. 1983. *Mesozoic and Tertiary Geology of Southern Africa. A Global Approach to Geology.* Rotterdam: Balkema. 375p.

Duncan, R.A., Hooper, P., Rehacek, J., Marsh, J. & Duncan, A.R. 1997. The timing and duration of the Karoo igneous event, southern Gondwana. *Journal of Geophysical Research: Solid Earth*. 102(B8):18127–38.

Economides, M.J. & Nolte, K.G. 2000. *Reservoir stimulation (3rd Ed).* New York: Wiley Ltd. 856p.

Eissa, E. A. & Kazi, A. 1988. Relation between static and dynamic Young's moduli of rocks. *International Journal of Rock Mechanics, Mining Science and Geomechanical Abstracts*. 25:479-482.

Fildani, A., Drinkwater, N.J., Weislogel, A., McHargue, T., Hodgson, D.M. & Flint, S.S. 2007. Age controls on the Tanqua and Laingsburg deep-water systems: new insights on the evolution and sedimentary fill of the Karoo basin, South Africa. Journal of Sedimentary Research. 77: 901–908.

Fjaer, E., Holt, R.M., Horsrud, P., Raaen, A.M. & Risnes, R. 2008. *Petroleum related rock mechanics, 2nd ed*. Amsterdam: Elsevier. 514p.

Frimmel, H.E., Fölling, P.G. & Diamond, R. 2001. Metamorphism of the Permo-Triassic Cape Fold Belt and its basement, South Africa. *Mineralogy and Petrology*. 73 (4): 325–346.

Geel, C., de Wit, M.J., Booth, P, Schulz, H-M. & Horsfield, B. 2015. Palaeo-environment, diagenesis and characteristics of Permian black shales in the lower Karoo Supergroup flanking the Cape Fold Belt near Jansenville, Eastern Cape, South Africa: Implications for the shale gas potential of the Karoo Basin. South African Journal of Geology. *South African Journal of Geology*. 118 (3): 248–274.

Gholami, R., Moradzadeh, A., Rasouli, V. & Hanachi, J.2014. Practical application of failure criterial in determining safe mud weight windows in drilling operations. *Journal of Rock Mechanics and Geotechnical Engineering*. 6: 13–15.

Glorioso, J.C. & Rattia, A. 2012. Unconventional reservoirs: Basic petrophysical concepts for shale gas. *SPE/EAGE European Unconventional Resources Conference and Exhibition.* 20–22 March 2012. Vienna, Austria: Society of Petroleum Engineers.

Graf, D. L. 1961. Crystallographic tables for the rhombohedral carbonates. *American Mineralogist*. 46: 1283–1316.

Hälbich, H. 1983. A tectogenesis of the Cape Fold Belt CFB. *Special publication - Geological Society of South Africa.* 12: 165–175.

Hansma, J., Tohver, E., Jourdan, F., Schrank, C. & Adams, D. 2015. The timing of the Cape Orogeny: New $^{40}Ar/^{39}Ar$ age constraints on deformation and cooling of the Cape Fold Belt, South Africa. *Gondwana Research.* 32: 122–137.

Hanson, E.K., Moore, J.M., Bordy, E.M., Marsh, J.S., Howarth G. & Robey, J. 2009. Cretaceous Erosion in Central South Africa: Evidence from Upper-Crustal Xenoliths in Kimberlite Diatremes. *South African Journal of Geology.* 112: 125-140.

Herrmann, J., Rybacki, E., Sone, H. & Dresen., G. 2018. Deformation Experiments on Bowland and Posidonia Shale- Part: Strength and Young's Modulus at Ambient and In Situ p_c – T conditions. *Rock Mechanics and Rock Engineering*. 12: 3645–3666.

Holt, R.M., Fjaer, E., Nes, O.M. & Alassi, H.T. 2011. A shaly look at brittleness. *45th U.S. Rock Mechanics / Geomechanics Symposium.* 26–29 June 2011. San Francisco, California: American Rock Mechanics Association.

Ibanez, W.D. & Kronenberg, A.K. 1993. Experimental deformation of shale: mechanical properties and microstructural indicators of mechanisms. *International Journal of Rock Mechanics and Mining Sciences & Geomechanics Abstracts*. 30(7): 723–734.

Jaeger, J.C., Cook, N.G.W. & Zimmerman, R.W. 2007*. Fundamentals of rock mechanics, 4th ed*. Oxford: Blackwell. 475p.

Jarvie, D.M., Hill, R.J., Ruble, T.E. & Pollastro, R.M. 2007. Unconventional shale-gas systems: the Mississippian Barnett shale of north-central Texas as one model for thermogenic shale-gas assessment. *AAPG Bulletin*. 91:475–499.

Jin, X., Shah, S.N., Roegiers, J.C. & Zhang, B. 2014. Fracability evaluation in shale reservoirs – an integrated petrophysics and geomechanics approach. *SPE Hydraulic Fracturing Technology Conference*. 4–6 February 2014. The Woodlands, Texas, USA: Society of Petroleum Engineers.

Johnson, M.R., Van Vuuren, C.J., Visser, J.N.J., Cole, D.I., Wickens, H. deV., Christie, A.D.M., Roberts, D.L. & Brandl, G. 2006. Sedimentary rocks of the Karoo Supergroup. In *The Geology of South Africa.* M.R. Johnson, C.R., Anhaeusser & R.J. Thomas, Eds. Johannesburg: Geological Society of South Africa/Council for Geoscience. 461–499.

Josh, M., Esteban, L., Delle Piane, C., Sarout, J., Dewhurst, D.N. & Clennell, M.B. 2012. Laboratory characterisation of shale properties. *Journal of Petroleum Science and Engineering*. 88–89: 107–124.

King, M.S. 1973. Static and dynamic elastic properties of rocks from the Canadian Shield. *International Journal of Rock Mechanics, Mining Science and Geomechanical Abstracts.* 20: 237–241.

Kingsley, C.S. 1981. A composite submarine fan-delta-fluvial model for the Ecca and lower Beaufort Groups of Permian age in the Eastern Cape Province, South Africa. *Transactions of the Geological Society of South Africa*. 84: 27–40.

Kuuskraa, V., Stevens, S., Van Leeuwen, T., Moodhe, K., 2011. World shale gas resources: An initial assessment. Prepared for: United States Energy Information Administration. *World Shale Gas Resources: An Intital Assessment of 14 Regions Outside the United States*. Available: http://www.eia.doe.gov/analysis/studies/worldshalegas [2015, July 13].

Lanci, L., Tohver, E., Wilson, A. & Flint, S. 2013. Upper Permian magnetic stratigraphy of the lower Beaufort Group, Karoo Basin. *Earth and Planetary Science Letters*. 375(0): 123–134.

McCann, D.M. & Entwisle, D.C. 1992. Determination of Young's modulus of the rock mass from geophysical well logs. In *Geological Applications of Wireline Logs II.* A. Hurst, C.M. Griffith & P.F. Worthington, Eds. Geological Society Special Publication. 65: 317–325.

Means, W.D. & Li, T. 2001. A laboratory simulation of fibrous veins: some first observations. *Journal of Structural Geology*. 23: 857– 863.

Meier, T., Rybacki, E., Backers, T. & Dresen, G. 2015. Influence of bedding angle on borehole stability: a laboratory investigation of transverse isotropic oil shale. *Rock Mechanics and Rock Engineering*. 48:1535–1546.

Milani, E.J. & de Wit, M.J. 2008. Correlations between the classic Paraná and Cape Karoo sequences of South America and southern Africa and their basin infills flanking the Gondwanides: du Toit revisited. In *West Gondwana: Pre-Cenozoic Correlations across the South Atlantic Region*. R.J. Pankurst, R.A.J. Trouw, B.B. Brito Neves & M.J. de Wit, Eds. Geological Society of London, Special Publications. 294: 319–342.

Moulin, M., Fluteau, F., Courtillot, V., Marsh, J., Delpech, G., Quidelleur, X. & Gérard, M. 2017. Eruptive history of the Karoo lava flows and their impact on early Jurassic environmental change. *Journal of Geophysical Research: Solid Earth*. 122(2):738–72.

Mowzer, Z. & Adams, S. 2015. *Shale gas prospectivity analysis of the southern main Karoo Basin. Petroleum Agency South Africa contribution to the strategic environmental assessment*. Agency report FG 2015. Cape Town: Petroleum Agency of South Africa.

Mullen, M. & Enderlin, M. 2012. Fracability index – More than just calculating rock properties. *SPEPap*.159755,10.

Newton, A.R. 1992. Thrusting on the northern margin of the Cape Fold Belt, near Laingsburg. In *Inversion Tectonics of the Cape Fold Belt, Karoo and Cetaceous Basins of Southern Africa*. M.J. de Wit & l.D.G. Ransome, Eds. Rotterdam, The Netherlands: Balkema. 193–196.

Nolte, S., Geel, C., Amann-Hildenbrand, A., Krooss, M.B. & Littke, R. 2019. Petrophysical and geochemical characterization of potential unconventional gas shale reservoirs in the southern Karoo Basin, South Africa. *International Journal of Coal Geology*. 212: 103249.

Nuñez-Betelu, L. & Baceta, J.L. 1994. Basics and application of Rock-Eval/TOC pyrolysis: an example from the uppermost Paleocene/lowermost Eocene in the Basque Basin, western Pyrenees. *Munibe (Ciencias Naturales - Natur Zientziak)*. 46: 43–62.

Nygard, R., Gutierrez, M., Bratli, R.K. & Hoeg, K. 2006. Brittle-ductile transition, shear failure and leakage in shales and mudrocks. *Marine Petroleum Geology*. 23: 201–212.

Paterson, M.S. 1970. A High-Pressure, High-Temperature Apparatus for Rock Deformation. *International Journal of Rock Mechanics and Mining Sciences and Geomechanics Abstracts*. 7: 517–526.

Ramsay, J.G. 1980. The crack-seal mechanism of rock deformation. *Nature*. 284: 135–139.

Rickman, R., Mullen, M., Grieser, B. & Kundert, D. 2008. A practical use of shale petrophysics for stimulation design optimization: All shale plays are not clones of the Barnett shale. *SPE Pap*. 115258, 11.

Rodrigues, N., Cobbold, P.R., Loseth, H. & Ruffet, G. 2009. Widespread bedding-parallel veins of fibrous calcite (“beef”) in a mature source rock (Vaca Muerta Fm, Neuquén Basin, Argentina): evidence for overpressure and horizontal compression. *Journal of the Geological Society of London*. 166: 695–709.

Rowsell, D.M. & De Swart, A.M.J.1976. Diagenesis in Cape and Karroo sediments, South Africa, and its bearing on their hydrocarbon potential. *Transactions of the Geology Society of South Africa*. 79: 81–145.

Rubidge, B.S. 2005. Re-uniting lost continents -Fossil reptiles from the ancient Karoo and their wanderlust. *South African Journal Geology*. 108: 135–172.

Rubidge, B.S., Erwin, D.H., Ramezani, J., Bowring, S.A. & de Klerk, W.J. 2013. High-precision temporal calibration of late Permian vertebrate biostratigraphy: U-Pb constraints from the Karoo Supergroup. *Journal of South African Geology*. 41: 363–366.

Rybacki, E., Reinicke, A., Meier, T., Makasi, M. & Dresen, G. 2015. What controls the mechanical properties of shale rocks ? – Part I : Strength and Young's modulus. *Journal of Petroleum Science and Engineering*. 135: 702–722.

Rybacki, E., Meier, T. & Dresen, G. 2016. What controls the mechanical properties of shale rocks?- Part II: Brittleness. *Journal of Petroleum Science and Engineering*. 144: 39–58.

Smithard, T., Bordy, E.M. & Reid, D.L. 2015. The effect of dolerite intrusions on the hydrocarbon potential of the lower Permian Whitehill Formation (Karoo Supergroup) in South Africa and southern Namibia: A preliminary study. *South African Journal of Geology*. 118(4): 489–510.

Smoltczyk, U. & Gartung, E. 1979. Geotechnical properties of a soft Keuper sandstone. *Proceedings of the 4th ISRM Congress*. Montreux. 639–644.

Sone, H. & Zoback, M.D. 2013. Mechanical properties of shale-gas reservoir rocks—part 1: static and dynamic elastic properties and anisotropy. *Geophysics*. 78(5): D381–D392.

Svensen, H., Corfu, F., Polteau, S., Hammer, Ø. & Planke, S. 2012. Rapid magma emplacement in the Karoo large igneous province. *Earth Planetary Science Letters*. 325: 1–9.

Tankard, A., Welsink, H., Aukes, P., Newton, R., Stattker, E. 2012. Geodynamic interpretation of the Cape and Karoo basins, South Africa. In: *Phanerozoic Passive Margins, Cratonic Basins and Global Tectonics Maps*. D.G. Roberts, Ed. USA & UK: Elsevier. 869p.

Tinker, J., de Wit, M. & Brown, R. 2008. Mesosoic exhumation of the southern Cape, South Africa, quantified using apatite fission track thermochronology. *Tectonophyiscs*. 455: 77–93.

Turner, B.R. 1999. Tectonostratigraphical development of the upper Karoo foreland basin: orogenic unloading versus thermally-induced Gondwana rifting. *Journal of African Earth Sciences*. 28: 215–238.

Viljoen, J.H.A. 1994. Sedimentology of the Collingham Formation, Karoo Supergroup. *South African Journal of Geology*. 97: 167–183.

Wang, F.P. & Gale, J.F.W. 2009. Screening criteria for shale-gas systems. *Gulf Coast Association of Geological Societies Transactions*. 59:779–793.

Warpinski, N. & Smith., M. 1990. Rock Mechanics and Fracture Geometry. *Recent Advances in Hydraulic Fracturing*. 12: 57–80.

Werner, M. 2006. *The stratigraphy, sedimentology and age of the Late Palaeozoic Mesosaurus Inland Sea, SW-Gondwana: new implications from studies on sediments and altered pyroclastic layers of the Dwyka and Ecca Group (lower Karoo Supergroup) in southern Namibia.* Unpublished Ph.D. thesis, University of Würzburg, Germany. 428 p.

Wickens, H. DeV. 1994. *Basin floor fan building turbidites of southwestern Karoo Basin, Permian Ecca Group, South Africa.* Unpublished Ph.D. Thesis. University of Port Elizabeth. 223p.

Wickens, H..de V. & Cole, D.I. 2017. Lithostratigraphy of the Kookfontein Formation (Ecca Group, Karoo Supergroup), South Africa. *South African Journal of Geology*. 120 (3): 447-458.

Windham, J. 2018*. South Africa urgently seeking gas as energy transition stalls.* Available: http://www.petroleum-economist.com/articles/politics economics/africa/2018/south-africa-urgently-seeking-gas-as-energy-transition-stalls [2019, June 01].

Wood., J.M., Sanei., H., Curtis., M.E. & Clarkson., C.R. 2015. Solid bitumen as a determinant of reservoir quality in an unconventional tight gas siltstone play. *International Journal of Coal Geology*. 150–151: 287–295.

Yang, Y., Sone, H., Hows, A. & Zoback, M.D. 2013. Comparison of brittleness indices in organic-rich shale formations. *47th U.S. Rock Mechanics/Geomechanics Symposium*. 23–26 June 2013. San Francisco, California: American Rock Mechanics Association.

Zanella, A., Cobbold, P.R. & Rojas, L. 2014. Beef veins and thrust detachments in Early Cretaceous source rocks, foothills of Magallanes-Austral Basin, southern Chile

and Argentina: structural evidence for fluid overpressure during hydrocarbon maturation. *Marine Petroleum Geology*. 55: 250–261.

Zhang, C., Tu, S. & Bai, Q. 2018. Evaluation of Pore Size and Distribution Impacts on Uniaxial Compressive Strength of Lithophysical Rock. *Arabian Journal for Science and Engineering*. 43: 1235–1246.

6 Synthesis and conclusion

The oldest post-glacial rocks of the main Karoo Basin (MKB) are the Prince Albert, Whitehill and Collingham formations, which are referred to here as the lower Ecca Group. They mainly constitute organic-matter-rich mudstone and shale as well as subordinate tuffs (Cole & Basson, 1991; Viljoen, 1992; Cole, 2005; Johnson, 2009). Economic interest in the shale gas potential of these rocks reinvigorated the geological investigation of the southern MKB, and resulted, among others, in drilling of two boreholes in vastly different regions of the basin. Situated ~ 830 km apart they are in the Tankwa Karoo Sub-basin (BH KZF-1; western MKB) and the eastern MKB (BH KWV-1). In summary, BH KZF-1 is discussed as part of the western MKB, because during the time of the deposition of the lower Ecca Group the sub-basins (Tankwa Karoo and Laingsburg) of the MKB had not been fully developed.

The source rock potential of the lower Ecca Group depends on characteristics such as total organic carbon (TOC) content, thermal maturity, porosity and permeability, which are governed by both syn- and post-depositional processes. Episodic changes to the sedimentation processes during the Early Permian resulted in fluctuations of OM preservation, bottom water oxygenation, and major and trace element accumulation during the deposition of the lower Ecca Group. This study aims to address two major themes: 1) the palaeo-environment and provenance settings that prevailed during the deposition of the lower Ecca Group; 2) the effect of diagenesis and metamorphism on petrophysical and geomechanical properties of the lower Ecca Group.

6.1 Comparison between the lower Ecca Group in western and eastern MKB

The Prince Albert Formation shows the greatest mineralogical and thickness variation between the western and eastern MKB. The Prince Albert Formation in BH KZF-1, in the western MKB, is 158.55 m thick and is divided into two units: a lower, calcareous mudstone part and an upper, more heterolithic unit in which mudstones are intercalated with siltstones and ash-fall tuffs layers. Changes from the lower to the upper part include increasing illite content that ranges from 4.91 wt% to 27.96 wt%, albite from 1.75 wt% to 17.11 wt%, clinochlore from 1.12 wt% to 4.75 wt% and kaolinite from 0.36 wt% to 2.09 wt%. Greenalite, rhodochrosite (in Mn-carbonate nodules), apatite and birnessite (in Mn-nodules) only occur in BH KZF-1. Assuming these are primary precipitates in the Prince Albert Formation, their occurrence suggests the presence of hydrothermal processes and an influx of saline water into

the western MKB. In BH KWV-1, in the eastern MKB, the Prince Albert Formation is only 30 m thick and thus ~ 130 m thinner than in western MKB and with lower overall carbonate content. Here, the Prince Albert Formation has the highest quantity of illite (37.83 wt%) and clinochlore (9.41 wt%) in the lower Ecca Group in both BH KWV-1 and BH KZF-1.

Following the final deglaciation event in the Early Permian, the western MKB was initially anoxic, with increasing temperature, pH and salinity (Rb/K $4*10^{-3}$ to > Rb/K $6*10^{-3}$). The bottom sediments of the Prince Albert Formation became increasing oxygenated as cold water near glacial peripheries sank. These oxygenated traction currents allowed for the persistence of biological activity indicated by possible bioturbation structures. The water in the basin was highly alkaline with low sedimentation rates, which allowed for the extensive precipitation of rhodochrosite and birnessite. If the birnessite nodules were formed syn-depositionally, it would indicate that the water depth of the lower Prince Albert Formation was up to 6500 m deep. However, post-depositional features are also observed, and water depth estimates must be made with extreme caution. In the eastern MKB, the basin became oxygenated soon after the final deglaciation event and was possibly also subjected to marine incursion shown by phosphorites and Rb/K values. The low carbonate content and absence of Mn nodules may cautiously suggest that the eastern MKB was shallower and less alkaline with lower pCO_2.

The Whitehill Formation is 19.5 m thick in the western MKB and 13 m thick in the eastern MKB. The Whitehill Formation has high quartz (BH KZF-1 = 35.36 wt%; BH KWV-1 = 42.86) and illite content (BH KZF-1 = 23.19 wt%; KWV-1 = 24.83 wt%) in both boreholes. Phosphate nodules, observed in both boreholes, suggests that marine conditions may have occurred at least intermittently. Based on Rb/K values (>$6*10^{-3}$), the Whitehill Formation in the western MKB may have been deposited under fully marine conditions at least for some part of overall Whitehill depositional episode, whereas in the eastern MKB the conditions fluctuated between marine and brackish water (Rb/K = $4*10^{-3}$ to > Rb/K $6*10^{-3}$). In both boreholes, the transition from the Prince Albert Formation to the Whitehill Formation shows fluctuations between dysoxic and oxic conditions during deposition. Periods of anoxia may have been seasonal to allow for the preservation of OM and enrichment of V, but not frequently enough to preserve significant quantities of S, Ni, Co, Cu and Mo typical of anoxic black shales. Pyrrhotite (altered pyrite) content (8.20 wt%) in BH KWV-1 is higher than pyrite content in BH KZF-1 (2.22 wt%). This implies that sulfate reduction and anoxic settings were more prevalent in the eastern MKB than in the western MKB, however organic matter

perseveration was still high in both regions (average TOC = 5 wt%). Like the Prince Albert Formation, the major difference between the Whitehill Formation in the boreholes is the lack of carbonate minerals in BH KWV-1. In BH KZF-1 dolomite is usually concentrated in the lower half of the Whitehill Formation. It is possible that the dolomite was formed by methanogenesis in a shallow sea with increased levels of pCO_2 by organic organisms in the water column, which could have contribute to the precipitation of carbonates (Tourtelot, 1979; Curtis, 1978; Surdam et al., 1989). Another possibility is that the carbonate was formed as calcite mud-mounds that altered to dolomite during mesogenesis (Saller, 1984; 1986). Last but not least, it also may be that the dolomite formed due to post-depositional diagenetic processes.

With the melting of the Gondwana-wide ice-sheets, there was an increase in chemical weathering in the source regions. This is demonstrated by high Chemical Index of Alteration (CIA) in both boreholes and the high carbonate content detected in the Prince Albert and Whitehill formations in the western MKB. A higher percentage of carbonate minerals detected in the Prince Albert and Whitehill formations in the western and southern central MKB (e.g., BH SFT2 fully investigated by Geel 2014) implies that carbonates may have been introduced from the southern Kango Group (Saldania Belt). Additional source regions for this western half of the MKB were dominated by the Cape Supergroup, Cape Granite Suite and the Dwyka Group. At the same time, in the eastern MKB, source regions were predominantly made up of rocks of the Dwyka Group, Namaqua-Natal Belt, Natal Group, Mozambique and Maud Belts.

The Collingham Formation in both boreholes is intercalated with organic-matter-rich mudstone, siltstones and tuffaceous laminae. The Collingham Formation has the highest quartz (BH KZF-1= 51.80 wt%; BH KWV-1= 43.53 wt%) and albite (BH KZF-1= 20.93 wt%; BH KWV-1= 18.86 wt%) content of all three formations in both boreholes. Other common features of the Collingham Formation are bioturbation structures, microbial filaments, framboidal pyrite and intraclasts. The major difference between the boreholes is that the tuffs in BH KZF-1 are diagenetically altered to ankerite, ferroan-dolomite, albite and calcite. Similar alteration is not detected in BH KWV-1. In BH KZF-1, the Collingham strata were not as over-pressured as in BH KWV-1, and thus likely allowed for fluid migration and diagenetic reactions to proceed. Rb/K values in the Collingham Formation in BH KZF-1 ($>6*10^{-3}$) indicate that deposition may have occurred under fully marine conditions in the western MKB. In contrast to this, in the eastern MKB, deposition may have initially been under marine conditions, but became increasingly brackish over time. During the depositional

history of the Collingham Formation, the sedimentation processes occurred under episodically fluctuating dysoxic, suboxic and oxic conditions as hyperpycnal density flows waxed and waned in both regions of the MKB. The Collingham Formation had the lowest CIA of the lower Ecca Group, indicating decreased weathering in the source areas due to cooling temperatures and reduced transportation distances. The sediments that comprise the Collingham Formation likely originated from nearby regions to the south (CFB), dominated by the Cape Supergroup and the Cape Granite Suite.

6.2 Shale gas prospectivity of the lower Ecca Group

The average TOC content is high in the Whitehill Formation (4.87–5.17 wt%) and moderate for the Prince Albert Formation (0.81 wt%) and Collingham Formation (0.83–1.44 wt%). It was determined that intraparticle porosity in OM is the most common type of porosity preserved in the lower Ecca Group with total porosity being the highest in the Whitehill Formation (4.25–6.33 %; Nolte et al., 2019). As a result, the permeability is limited to the connectivity of the OM within the rock. In BH KZF-1, some interparticle porosity may be preserved in very thin siltstone laminae, whereas as no intergranular porosity is detected in BH KWV-1 due to dissolution and recrystallization of grain boundaries. Interparticle porosity is greatly reduced in the lower Ecca Group by the precipitation of diagenetic minerals. Illite is the dominant clay mineral formed during mesogenesis by smectite-illite conversion. Other common diagenetic minerals include chlorite, calcite, siderite, ankerite and ferroan-dolomite. During early diagenesis, the precipitation of illite between mineral grains was accompanied by syntaxial quartz overgrowths. Later, increased compaction from burial diagenesis resulted in dissolution of minerals, mineral replacement and precipitation of quartz and carbonate cements.

The western MKB, as with the entire southern MKB, was highly influenced by Cape Orogeny. This is evident by thrust faulting, diagenetic mineral formation, high vitrinite reflectance (~ 4 % VR_o; Nolte et al., 2017), high Tmax values (418.44 °C–571.80 °C) and low HI (2.41–15.56 mg HC/g TOC) values. In addition to the tectonic (structural) impact from the Cape Orogeny, the eastern MKB was greatly influenced by the contact metamorphism due to the emplacement of dolerite intrusions in the Early Jurassic. In BH KWV-1, there are 18 dolerite intrusions, one of which intruded into the top 13 cm of the Whitehill Formation. The lower Ecca Group in some sections can be described as a spotted hornfels and contains metamorphic minerals such as cordierite, garnet (pyralspite), staurolite, biotite and chalcedony nodules. These

minerals form under intermediate to high metamorphic conditions at temperatures between 500 and 600 °C (Winkler, 1980). The bitumen reflectance (BR_o) values were high for BH KWV-1 (4.7–5.6 %), but surprisingly, the Tmax values were lower (409–334.14 °C) and HI values were higher (2.57–167 HC/g TOC) than those for BH KZF-1.

Most of the OM in the lower Ecca Group has been identified as solid bitumen. The presence of solid bitumen indicates that thermal cracking of kerogen has taken place and the remaining preserved organic matter was converted to thermogenic gas (Tissot & Welte, 1984; Ungerer, 1990; Hunt, 1996). Hydrothermal events can either enhance the gas potential or destroy it. For kerogen to produce oil or gas (catagenesis), the temperature must reach range from 50–150 °C, under pressure of 300 and 1500 bars (Tissot & Welte, 1984) and span over 1–100 million years. Methane is thermodynamically stable even at 500–600 °C or more and can exist at great depths (6–8 km) within the crust (Bjørlykke, 2010). Therefore, it is highly probable that gas had been produced and stored in the lower Ecca Group, however, only trace amounts of methane was detected from the Whitehill Formation in the boreholes drilled for this study (de Kock et al., 2017).

The elastic properties of the lower Ecca Group shales are strongly related to their material composition. Deformation experiments carried out on samples from the lower Ecca Group suggest brittle deformation and high Young's modulus. The latter correlates well with the high brittleness index values of this rock succession. The Prince Albert and Collingham formations are strongest and most brittle due to the high proportion of hard and intermediate mineral fractions. The Whitehill Formation is the weakest and least brittle but is still stronger than the comparative international shale samples from the Posidonia, Bowland, Alum and Barnett Shale formations (Rybacki et al., 2015;2016 & Herrmann et al., 2018). The brittleness of the Whitehill Formation promises easy hydraulic fracturing. However, fracture zones and carbonate horizons may complicate matters. For example, the dolomite in the Whitehill Formation may drastically change the brittleness and the strength of the rock. The diagenetic precipitation of hard mineral phases such as quartz and intermediate phases such as dolomite, ankerite, siderite increases the density of the rock, which correlates to an increase in overall triaxial compressive strength. The degree of maturity and corresponding diagenetic effect on the rocks, therefore, influences the brittleness of the lower Ecca Group. Minerals that precipitate as cement between primary grains can then cause a significant increase in stiffness and seismic velocity (Bjørlykke, 2010). High maturity is also associated with the formation of beef fractures and is an

indication of hydrocarbon development in tectonically active regions (Rodrigues et al., 2009; Zanella et al., 2014) and are useful for facilitation of hydraulic fracturing if gas extraction techniques are pursued.

The low quantities of gas detected during drilling implies that gas has escaped from the intersected formations, a likely consequence of tectonic thrust-faulting across the southern margin of the MKB and thermal degassing in dolerite-rich regions, like the area around BH KWV-1. For this study, the TOC content of the Whitehill Formation remains high in samples near intruded dolerite sill, even where the rock has been altered to hornfels. While gas most likely formed in the MKB, the preservation of this gas still needs to be determined. The Whitehill Formation is the most likely formation to produce exploitable gas, because of its high TOC and the nano-pores preserved in the OM. However, the western MKB (e.g., the Tankwa Karoo Sub-basin) may not be eligible for further exploration due to the high maturity of the rocks and negligible gas detected during drilling (de Kock et al., 2017). The thermal impact of irregular spaced dolerite intrusions in the eastern MKB make reservoir estimates difficult to predict. While the intrusion of dolerite would have facilitated the early conversion of kerogen to oil and gas, these intrusions may could have caused degassing in regions with high dolerite densities. It has been repeatedly shown in this study and others too that the hydrocarbon potential for the MKB will only truly be determined once regional “sweet spots” are identified, most probably in areas of low dolerite concentrations and VR_o values below 3.5 % (e.g., Cole, 2014; Geel et al., 2015; Smithard et al., 2015; de Kock et al., 2017).

6.3 Recommendation for future studies

Going forward the geochemical investigation of the birnessite nodules would be useful to understand their syn- or post-depositional genesis. Furthermore, the compilation of geochemical data of the Ecca Group could facilitate an integrated, and more robust basin-wide palaeo-environmental reconstruction. Trace elements and light rare earth elements (e.g., La, Ce, Nb, Yb, Eu, Sm, Gd) could also provide more accurate provenance discrimination for the lower Ecca Group across the MKB.

The comprehensive investigation of dolomite formation in the lower Whitehill Formation is required to better understand the palaeo-environmental conditions during deposition, especially via the trace element, ^{18}O and ^{13}C isotopes studies of these rocks. Because porous dolomite could greatly improve the physical properties of a hydrocarbon reservoir, investigating the porosity patterns in these Whitehill dolomite is also important. Furthermore, research should be conducted on the illite-

smectite conversion and TOC/Rock Eval measurements near the dolerite intrusions to determine the extent at which dolerite intrusions affected the progression eogenesis and the hydrocarbon potential of proximal mudstones.

When investigating the geomechanical properties of the lower Ecca Group, it is suggested that Young's modulus is calculated under increasing temperatures and pressures and creep measurements. Fracture toughness of shales with different microstructures and layering orientations should be processed with computational modelling framework to simulate fracture propagation. Additional studies using uniaxial compressive tests and the Brazillian disc method can be used to calculate properties such as fracture toughness.

6.4 References

Bjørlykke, J. & Jahren, J. 2012. Open or closed geochemical systems during diagenesis in sedimentary basins: Constraints on mass transfer during diagenesis and the prediction of porosity in sandstone and carbonate reservoirs. *AAPG Bulletin*. 96 (12): 2193–2214.

Cole, D.I. & Basson, W.A. 1991. Whitehill Formation. In *Catalogue of South African Lithostratigraphic Units*. M.R. Johnson, Ed. South African Committee for Stratigraphy, Pretoria. 3: 51–52.

Cole, D.I. 2005. Prince Albert Formation. *Geological Survey of South Africa: Catalogue of South Africa Lithostratigraphic Units*. 8: 33–36.

Cole, D.I. 2014*.* Geology of Karoo shale gas and how this can influence economic gas recovery. *Presentation, Gas – The Game Changer for Southern Africa?* Glen Hove, Johannesburg: Fossil Fuel Foundation, Abstracts, 11–12.

Curtis, C. D. 1978. Possible links between sandstone diagenesis and depth-related geochemical reactions occurring in enclosing mudstones. *Journal of the Geological Society.* 135: 107–117.

de Kock, M.O., Beukes, N.J., Adeniyi, E.O., Cole, D., Götz, A.E., Geel, C. et al. 2017. Deflating the shale gas potential of South Africa's Main Karoo basin. *South African Journal of Science*.113(9-10).

Geel, C. 2014. *Shale gas characteristics of Permian black shales in the Ecca Group, Near Jansenville, Eastern Cape, South Africa*. Unpublished M.Sc. dissertation. Nelson Mandela Metropolitan University. 163p.

Geel, C., de Wit, M., Booth, P., Schulz, H-M. & Horsfield, B. 2015. Palaeo-environment, diagenesis and characteristics of Permian black shales in the lower Karoo Supergroup flanking the Cape Fold Belt near Jansenville, Eastern Cape, South Africa: Implications for the shale gas potential of the Karoo Basin. *South African Journal of Geology*.118(3): 249–274.

Herrmann, J., Rybacki, E., Sone, H. & Dresen., G. 2018. Deformation Experiments on Bowland and Posidonia Shale- Part: Strength and Young's Modulus at Ambient and In Situ p_c – T conditions. *Rock Mechanics and Rock Engineering*. 12: 3645–3666.

Hunt, J. M. 1996. *Petroleum Geochemistry and Geology (2nd Edition)*. New York: W.H. Freeman. 743p.

Johnson, M.R. 2009. Ecca Group. Karoo Supergroup. *Catalogue of South African Lithostratigraphic Units. SACS*. 10: 5–7.

Nolte, S., Geel, C., Amann-Hildenbrand, A., Krooss, M.B. & Littke, R. 2019. Petrophysical and geochemical characterization of potential unconventional gas shale reservoirs in the southern Karoo Basin, South Africa. *International Journal of Coal Geology*. 212: 103249.

Rodrigues, N., Cobbold, P.R., Loseth, H. & Ruffet, G. 2009. Widespread bedding-parallel veins of fibrous calcite ("beef") in a mature source rock (Vaca Muerta Fm, Neuquén Basin, Argentina): evidence for overpressure and horizontal compression. *Journal of the Geological Society of London*. 166: 695–709.

Rybacki, E., Reinicke, A., Meier, T., Makasi, M. & Dresen, G. 2015. What controls the mechanical properties of shale rocks ? – Part I : Strength and Young's modulus. *Journal of Petroleum Science and Engineering*. 135: 702–722.

Rybacki, E., Meier, T. & Dresen, G. 2016. What controls the mechanical properties of shale rocks?- Part II: Brittleness. *Journal of Petroleum Science and Engineering*. 144: 39-58.

Saller, A.H. 1984. *Diagenesis of Cenozoic Limestones on Enewetak Atoll.* Unpublished Ph.D. thesis. Louisiana State University, Baton Rouge, Louisiana. 363 pp.

Saller, A.H. 1986. Radiaxial calcite in lower Miocene strata, subsurface Enewetak atoll. *Journal of Sedimentary Petrology*. 56: 743–762.

Smithard, T., Bordy, E.M. & Reid, D.L. 2015. The effect of dolerite intrusions on the hydrocarbon potential of the lower Permian Whitehill Formation (Karoo Supergroup)

in South Africa and southern Namibia: A preliminary study. *South African Journal of Geology*. 118(4): 489–510.

Surdam, R.C., Crossey, L.J., Hagen, E.S. & Heasler, H.P. 1989. Organic-inorganic interactions and sandstone diagenesis. *American Association of Petroleum Geologists Bulletin*. 73:1–23.

Tissot, B. P. & Welte, D. H. 1984. *Petroleum Formation and Occurrence*. New York: Springer. 540p.

Tourtelot, H.A. 1979. Black Shale- Its Deposition and Diagenesis 1. *Clays and Clay Minerals*. 27(5): 313–321.

Ungerer, P. 1990. State of the art research in kinetic modeling of oil formation and expulsion. *Organic Geochemistry*. 16**:** 1–25.

Viljoen, J.H.A. 1992. Lithostratigraphy of the Collingham Formation (Ecca Group), including the Zoute Kloof, Buffels River and Wilgehout River Members and the Matjiesfontein Chert bed. *Lithostratigraphic Series, South African Committee for Stratigraphy, Council for Geoscience*. 22: 1–10

Winkler, H.C.R., Zhang, Qi, Zhou, Yunsheng, Translated by, 1980. *Origin of metamorphic rock*. Science Press, Beijing.

Zanella, A., Cobbold, P.R. & Rojas, L. 2014. Beef veins and thrust detachments in Early Cretaceous source rocks, foothills of Magallanes-Austral Basin, southern Chile and Argentina: structural evidence for fluid overpressure during hydrocarbon maturation. *Marine Petroleum Geology*. 55: 250–261.

7 Appendices

Appendix A - Geochemistry: pages 283–294

Appendix B - 1D Models: pages 295–297

Appendix C - Gamma ray logs: pages 297–306

Appendix D - BH KZF-1 stratigraphic log:

https://doi.org/10.6084/m9.figshare.13108112.v1

Appendix E - BH KWV-1 stratigraphic log:

https://doi.org/10.6084/m9.figshare.13108118.v1

Appendix A1- Quantitative XRD

Appendix A1a: Normalized XRD data from BH KZF-1.

Formation	Sample	Depth (m)	Quartz (wt	Albite	Illite/Musocvite	Clinochlore (wt	Dolomite	Pyrite	Kaolinite (wt %)	Siderite
Collingham	KZF03	353	53.75	23.78	5.45	1.81	0.00	0.00	0.23	3.64
Collingham	KZF01P	377	41.98	25.95	27.67	2.69	0.00	0.00	0.47	0.00
Collingham	KZF08	400	60.36	19.73	15.69	2.24	0.00	0.00	0.29	0.00
Collingham	KZF02P	404	61.56	16.09	17.32	1.68	0.70	0.00	0.00	0.03
Collingham	KZF10	414	55.97	20.92	16.42	2.47	1.55	0.42	0.42	1.05
Collingham	KZF03P	417	37.20	19.13	36.53	2.62	0.00	0.65	0.44	0.00
Whitehill	KZF04P	426	42.08	14.06	29.31	3.67	0.00	2.42	0.38	7.14
Whitehill	KZF14	432	35.98	20.29	32.67	2.74	0.00	3.35	0.30	0.00
Whitehill	KZF15	436	34.33	17.13	25.52	7.08	1.69	5.79	0.63	1.67
Whitehill	KZF05P	448	35.75	27.61	17.14	0.87	10.67	0.47	0.09	0.00
Whitehill	KZF06P	455	38.82	23.36	22.39	3.31	3.42	1.88	0.21	0.00
Whitehill	KZF19	463	37.50	18.90	23.59	9.25	5.16	0.54	0.54	0.00
Whitehill	KZF20	472	30.56	1.84	20.76	1.71	39.48	1.44	0.09	0.00
Whitehill	KZF07P	475	26.72	3.55	11.78	0.40	52.82	0.76	0.00	0.00
Prince Albert	KZF22	482	29.01	12.45	28.93	4.20	0.00	23.32	1.21	0.32
Whitehill	KZF08P	488	36.46	10.29	25.55	1.78	16.74	3.31	0.16	0.00
Prince Albert	KZF25	530	54.10	15.31	24.34	5.05	0.00	0.89	0.00	0.16
Prince Albert	KZF09P	554	34.11	23.57	30.62	5.01	0.00	0.20	5.06	1.15
Prince Albert	KZF28	585	26.34	0.00	0.00	0.00	0.00	0.00	0.00	0.00
Prince Albert	KZF10P	595	67.36	7.00	19.04	4.47	0.00	0.00	1.46	0.00
Prince Albert	KZF29	606	33.11	0.00	0.00	0.00	0.00	0.00	0.00	0.00
Prince Albert	KZF32	648	21.91	0.00	0.58	0.00	0.00	0.00	0.00	0.00

Appendix A1b: Normalized XRD data from BH KZF-1.

Formation	Sample	Depth	Rhodochrosite	Calcite	Birnessite (wt	Apatite	Foresterite (wt	Greenalite	TOC (wt
Collingham	KZF03	353	0.00	0.00	0.00	0.00	0.00	0.00	1.10
Collingham	KZF01P	377	0.00	0.00	0.00	0.00	0.00	0.00	1.21
Collingham	KZF08	400	0.00	0.00	0.00	0.00	0.00	0.00	1.70
Collingham	KZF02P	404	0.00	0.00	0.00	0.00	0.00	0.00	2.26
Collingham	KZF10	414	0.00	0.00	0.00	0.00	0.00	0.00	0.80
Collingham	KZF03P	417	0.00	0.00	0.00	0.00	0.00	0.00	3.44
Whitehill	KZF04P	426	0.00	0.00	0.00	0.00	0.00	0.00	0.96
Whitehill	KZF14	432	0.00	0.00	0.00	0.00	0.00	0.00	4.68
Whitehill	KZF15	436	0.00	0.00	0.00	0.00	0.00	0.00	6.16
Whitehill	KZF05P	448	0.00	0.00	0.00	0.00	0.00	0.00	7.40
Whitehill	KZF06P	455	0.00	0.00	0.00	0.00	0.00	0.00	6.63
Whitehill	KZF19	463	0.00	0.00	0.00	0.00	0.00	0.00	4.53
Whitehill	KZF20	472	0.00	0.00	0.00	0.00	0.00	0.00	4.13
Whitehill	KZF07P	475	0.00	0.00	0.00	0.00	0.00	0.00	3.97
Prince Albert	KZF22	482	0.00	0.00	0.00	0.00	0.00	0.00	0.58
Whitehill	KZF08P	488	0.00	0.00	0.00	0.00	0.00	0.00	5.71
Prince Albert	KZF25	530	0.00	0.00	0.00	0.00	0.00	0.00	0.15
Prince Albert	KZF09P	554	0.00	0.00	0.00	0.00	0.00	0.00	0.30
Prince Albert	KZF28	585	67.92	2.11	2.59	0.00	0.00	0.00	1.04
Prince Albert	KZF10P	595	0.00	0.00	0.00	0.00	0.00	0.00	0.67
Prince Albert	KZF29	606	44.42	19.61	2.42	0.00	0.00	0.00	0.44
Prince Albert	KZF32	648	0.00	5.54	0.00	61.84	0.38	9.57	0.18

Appendix A1c: Normalized XRD data from BH KWV-1.

Formation	sample #	Depth	Quartz	Calcite	Albite (wt%)	Muscovite/Illite	Clinochlore	Cordierite	Pyrrhotite
Collingham	KVW01	2189	39.68	0.00	19.87	35.18	3.36	0.00	0.00
Collingham	KVW02	2205	0.00	43.05	23.00	25.42	5.84	0.00	0.00
Collingham	KVW03	2220	56.35	0.00	24.92	13.26	1.98	0.01	0.00
Collingham	KVW04	2227	61.19	0.00	24.63	11.05	1.57	0.00	0.00
Collingham	KVW05	2248	45.56	0.00	12.07	28.55	0.65	11.81	0.00
Collingham	KVW06	2257	45.55	0.00	12.06	28.55	0.65	11.80	0.00
Collingham	KVW07	2270	56.38	0.00	15.50	25.17	1.67	0.01	0.00
Whitehill	KVW08-A	2276	32.86	0.00	24.92	23.09	0.63	0.00	11.43
Whitehill	KVW08-B	2276	42.85	0.00	17.63	28.44	0.87	0.03	5.15
Whitehill	KVW09	2297	49.24	0.00	13.83	23.53	0.74	0.00	10.31
Whitehill	KVW10	2302	54.06	0.00	5.26	25.61	0.29	0.00	6.86
Whitehill	KVW11	2303	46.31	0.00	2.04	31.98	0.49	0.00	11.63
Whitehill	KVW12	2305	5.67	58.82	0.00	0.00	0.00	0.00	2.34
Whitehill	KVW13	2307	38.55	0.00	1.88	41.20	0.32	0.00	9.72
Prince Albert	KVW14	2317	45.75	0.00	0.00	14.36	7.74	0.00	0.00
Prince Albert	KVW15	2323	48.18	0.00	1.77	36.58	11.43	0.00	0.00
Prince Albert	KVW16	2329	47.16	0.00	1.03	36.42	14.12	0.00	0.00
Prince Albert	KVW17	2335	30.35	0.00	0.00	63.97	4.33	0.00	0.00

Appendix A1d: Normalized XRD data from BH KWV-1.

Formation	sample #	Depth	Pyrite (wt%)	Kaolinite (wt%)	Siderite (wt %)	Talc (wt%)	Diopside	Anorthite	TOC (wt%)
Collingham	KVW01	2189	0.00	0.44	0.00	0.00	0.00	0.00	1.47
Collingham	KVW02	2205	0.31	0.63	0.25	0.00	0.00	0.00	1.51
Collingham	KVW03	2220	0.00	0.23	2.20	0.00	0.00	0.00	1.06
Collingham	KVW04	2227	0.00	0.19	0.00	0.00	0.00	0.00	1.38
Collingham	KVW05	2248	0.00	1.33	0.00	0.00	0.00	0.00	0.02
Collingham	KVW06	2257	0.00	1.33	0.00	0.00	0.00	0.00	0.02
Collingham	KVW07	2270	0.00	0.86	0.13	0.00	0.00	0.00	0.30
Whitehill	KVW08A	2276	0.00	0.59	0.00	0.00	0.00	0.00	6.50
Whitehill	KVW08B	2276	0.00	0.31	0.18	0.00	0.00	0.00	4.55
Whitehill	KVW09	2297	0.00	0.42	0.00	0.00	0.00	0.00	1.94
Whitehill	KVW10	2302	0.00	2.76	0.00	0.00	0.00	0.00	5.16
Whitehill	KVW11	2303	0.00	3.12	0.10	0.00	0.00	0.00	4.34
Whitehill	KVW12	2305	5.69	0.00	0.00	6.68	16.45	0.00	4.34
Whitehill	KVW13	2307	0.00	2.76	0.00	0.00	0.00	0.00	5.57
Prince Albert	KVW14	2317	0.00	0.85	0.54	0.00	0.00	30.51	0.25
Prince Albert	KVW15	2323	0.00	1.76	0.00	0.00	0.00	0.00	0.29
Prince Albert	KVW16	2329	0.00	1.02	0.00	0.00	0.00	0.00	0.26
Prince Albert	KVW17	2335	0.00	1.34	0.00	0.00	0.00	0.00	0.01

Appendix A2- TOC/Rock Eval

Appendix A2: TOC/Rock Eval data from BH KZF-1 and BH KWV-1. Abbreviations: PA= Prince Albert Formation; WH: Whitehill Formation.

Formation	Sample	S1 -	S2 -	Tmax(°C)	S3 -	TOC	HI	OI
Collingham	KZF01	0.01	0.05	608	0.20	0.86	6	23
Collingham	KZF02	0.02	0.06	604	0.26	1.84	3	14
Collingham	KZF03	0.03	0.05	608	0.30	1.12	4	27
Collingham	KZF04	0.02	0.05	607	0.16	1.58	3	10
Collingham	KZF05	0.05	0.99	354	0.90	1.31	76	69
Collingham	KZF06	0.02	0.05	607	0.21	1.64	3	13
Collingham	KZF07	0.01	0.05	602	0.30	1.18	4	25
Collingham	KZF08	0.02	0.05	606	0.17	1.73	3	10
Collingham	KZF09	0.01	0.05	607	0.20	0.81	6	25
Collingham	KZF10	0.02	0.06	600	0.21	0.81	7	26
Collingham	KZF11	0.03	0.05	358	0.25	1.35	4	19
Whitehill	KZF12	0.02	0.04	334	0.26	4.76	1	5
Whitehill	KZF13	0.02	0.06	608	0.30	5.24	1	6
Whitehill	KZF14	0.04	0.19	443	0.16	4.91	4	3
Whitehill	KZF15	0.02	0.05	336	0.22	6.56	1	3
PA- WH	KZF16	0.02	0.02	338	0.10	0.37	5	27
Whitehill	KZF17	0.05	0.07	608	0.28	8.45	1	3
Whitehill	KZF18	0.06	0.06	309	0.23	6.88	1	3
Whitehill	KZF19	0.02	0.05	607	0.18	4.74	1	4
Whitehill	KZF20	0.04	0.18	609	0.34	4.31	4	8
Whitehill	KZF21	0.02	0.06	310	0.20	4.03	1	5
PA-WH	KZF22	0.02	0.05	346	0.10	0.58	9	17
PA	KZF23	0.03	0.10	341	0.37	3.86	3	10
PA	KZF24	0.03	0.08	494	0.30	0.26	31	115
PA	KZF25	0.01	0.04	325	0.12	0.15	27	80
PA	KZF26	0.02	0.02	473	1.61	0.35	6	460
PA	KZF27	0.02	0.04	328	0.15	0.72	6	21
PA	KZF28	0.02	0.13	436	5.77	1.05	12	550
PA	KZF29	0.01	0.02	442	1.48	0.44	5	336
PA	KZF30	0.02	0.07	605	0.20	2.08	3	10
PA	KZF31	0.03	0.08	338	0.10	0.63	13	16
PA	KZF32	0.01	0.06	449	0.49	0.18	33	272
PA-Dwyka	KZF33	0.02	0.06	487	0.11	0.35	17	31
Collingham	KWV01	0.02	0.07	607	0.14	1.49	5	9
Collingham	KWV02	0.02	0.10	609	0.16	1.53	7	10
Collingham	KWV03	0.02	0.08	448	0.23	1.07	7	21
Collingham	KWV04	0.02	0.07	353	0.16	1.40	5	11
Collingham	KWV05	0.01	0.07	336	0.10	0.02	350	500
Collingham	KWV06	0.01	0.06	331	0.07	0.03	200	233
Collingham	KWV07	0.03	0.10	331	0.12	0.30	33	40
Whitehill	KWV08A	0.02	0.08	334	0.18	6.95	1	3
Whitehill	KWV08B	0.01	0.05	354	0.09	4.77	1	2
Whitehill	KWV09	0.01	0.06	447	0.09	1.98	3	5
Whitehill	KWV10	0.06	0.17	338	0.12	5.44	3	2
Whitehill	KWV11	0.07	0.16	351	0.09	4.54	4	2
Whitehill	KWV12	0.09	0.12	303	0.56	4.54	3	12
Whitehill	KWV13	0.16	0.19	303	0.15	5.90	3	3
PA	KWV14	0.02	0.06	417	0.10	0.25	24	40
PA	KWV15	0.02	0.06	418	0.10	0.29	21	34
PA	KWV16	0.02	0.06	461	0.07	0.26	23	27
PA	KWV17	0.02	0.06	343	0.08	0.01	600	800

Appendix A3- XRF Data

Appendix A3a: XRF major element data for BH KZF-1 in wt%. Abbreviations: PA= Prince Albert Formation; WH: Whitehill Formation.

Formation	Sample	SiO2	TiO2	Al2O3	Fe2O3	MnO	MgO	CaO	Na2O	K2O	P2O5	SO3	Cr2O3	NiO
Collingham	70.36	0.49	12.85	5.15	0.13	1.02	0.62	2.16	2.73	0.13	0.09	b.d.	0.01	70.36
Collingham	59.09	0.66	17.11	6.64	0.12	1.35	0.45	2.15	3.99	0.15	0.12	0.01	0.01	59.09
Collingham	66.53	0.47	12.76	6.35	0.30	0.95	0.94	2.91	2.25	0.16	0.13	b.d.	0.01	66.53
Collingham	68.91	0.50	14.26	3.73	0.03	0.83	0.32	2.84	2.86	0.12	0.05	b.d.	0.01	68.91
Collingham	38.41	0.32	21.19	3.67	0.22	1.34	11.93	0.74	5.36	0.09	0.31	b.d.	0.01	38.41
Collingham	63.04	0.62	16.24	4.43	0.08	1.08	0.96	2.67	3.36	0.15	0.08	b.d.	0.01	63.04
Collingham	48.43	0.46	26.84	4.55	0.08	1.60	0.82	0.84	6.81	0.28	0.31	b.d.	0.01	48.43
Collingham	68.41	0.55	14.11	4.19	0.05	0.98	0.58	2.47	2.89	0.13	0.15	b.d.	0.01	68.41
Collingham	67.85	0.52	13.90	4.88	0.10	0.88	0.44	2.16	3.34	0.13	0.10	b.d.	0.01	67.85
Collingham	68.04	0.42	15.09	3.48	0.04	0.96	0.75	2.42	3.39	0.11	0.08	b.d.	0.01	68.04
Collingham	73.90	0.50	11.52	2.30	0.06	0.54	0.93	3.05	1.86	0.15	0.28	b.d.	0.01	73.90
Whitehill	59.08	0.47	14.37	6.51	0.18	0.90	0.88	3.48	2.81	0.13	0.52	b.d.	0.01	59.08
Whitehill	55.87	0.59	15.46	6.62	0.08	2.29	0.70	2.07	3.39	0.21	0.30	0.01	0.01	55.87
Whitehill	57.68	0.66	17.53	4.94	0.02	1.50	0.42	2.19	3.96	0.19	0.19	0.01	0.01	57.68
Whitehill	51.35	0.57	14.55	8.79	0.06	2.76	0.90	1.72	3.02	0.27	0.50	0.01	0.01	51.35
PA-WH	62.25	0.36	20.47	2.55	0.01	1.14	0.22	1.48	4.09	0.14	0.07	b.d.	0.01	62.25
Whitehill	61.04	0.49	12.93	3.06	0.06	1.43	1.97	2.25	2.37	0.18	1.03	0.01	0.01	61.04
Whitehill	61.35	0.53	13.90	4.15	0.05	1.43	1.25	2.52	2.40	0.14	0.80	b.d.	0.01	61.35
Whitehill	55.60	0.56	15.86	6.55	0.08	2.56	1.99	2.07	2.65	0.16	1.17	0.01	0.01	55.60
Whitehill	42.14	0.48	12.79	4.03	0.18	5.12	9.31	0.96	2.90	0.15	2.01	0.01	0.01	42.14
Whitehill	45.42	0.58	18.14	12.00	0.15	1.38	1.27	1.68	3.75	0.23	0.19	0.01	0.02	45.42
PA-WH	43.71	0.40	15.91	18.57	0.03	1.10	0.19	1.14	3.17	0.13	0.19	b.d.	0.01	43.71
Prince Albert	36.23	0.39	14.86	9.37	0.88	4.01	7.92	1.26	3.14	0.36	5.76	b.d.	0.01	36.23
Prince Albert	38.99	0.49	21.23	11.96	0.13	2.59	7.24	1.20	2.99	4.77	0.16	b.d.	0.01	38.99
Prince Albert	62.78	0.48	18.36	4.85	0.06	1.10	0.75	1.70	3.09	0.47	0.04	b.d.	0.01	62.78
Prince Albert	42.00	0.31	8.36	28.21	3.23	1.86	0.90	0.52	0.36	0.28	0.11	b.d.	0.01	42.00
Prince Albert	65.62	0.68	18.46	3.44	0.06	0.69	0.23	2.18	2.93	0.11	0.01	b.d.	0.01	65.62
Prince Albert	25.97	0.11	3.93	36.93	8.26	0.88	1.41	0.27	0.06	0.40	0.18	b.d.	0.01	25.97
Prince Albert	32.54	0.14	4.27	24.94	7.19	0.91	8.75	0.18	0.05	0.83	0.11	b.d.	0.00	32.54
Prince Albert	62.29	0.74	17.91	6.09	0.18	0.89	0.20	1.03	3.39	0.08	0.01	0.01	0.01	62.29

Prince Albert	65.09	0.65	16.30	6.57	0.14	0.88	0.19	0.83	3.21	0.08	0.00	b.d.	0.01	65.09
Prince Albert	21.52	0.33	5.81	10.78	2.06	1.38	29.36	0.19	0.50	18.94	0.59	b.d.	0.01	21.52
Prince	63.90	0.55	17.11	5.57	0.16	1.43	0.75	0.92	4.15	0.23	0.07	0.01	0.01	63.90

Appendix A3b: XRF trace element data for BH KZF-1 in ppm. Abbreviations: PA= Prince Albert Formation; WH: Whitehill Formation.

Formation	Sample	Zn	Cu	Ni	Mo	Nb	Zr	Y	Sr	Rb	U	Th	Pb	Co	Mn	Cr	V	F	S	Cl	Sc	Ba
Collingham	KZF-1	57	20	<5	<5	14	152	29	126	125	<5	13	24	9	1110	35	92	488	337	107	11	744
Collingham	KZF-2	81	32	16	<5	16	200	39	153	178	<5	18	38	19	1104	47	139	669	1412	115	16	1092
Collingham	KZF-3	59	23	8	<5	12	146	23	141	103	<5	15	31	12	2502	32	78	504	468	108	11	703
Collingham	KZF-4	61	25	10	<5	12	169	29	124	122	<5	14	20	5	200	56	97	377	404	103	13	782
Collingham	KZF-5	342	<5	7	7	13	226	22	352	182	<5	26	56	<5	2095	2	33	647	519	118	19	937
Collingham	KZF-6	89	41	6	<5	15	187	31	189	151	<5	16	28	<5	727	42	130	500	354	114	16	1019
Collingham	KZF-7	82	7	9	10	23	450	30	306	236	<5	43	81	25	653	3	53	799	1993	111	11	1122
Collingham	KZF-8	84	40	8	<5	12	138	30	198	125	<5	13	30	10	379	40	112	393	454	103	14	967
Collingham	KZF-9	52	44	10	<5	10	131	24	133	145	<5	12	24	12	828	49	99	476	1306	109	12	1013
Collingham	KZF-10	43	26	<5	<5	11	149	29	160	142	<5	15	30	<5	353	29	71	432	389	112	13	997
Collingham	KZF-11	45	19	<5	<5	17	148	36	165	78	<5	13	13	<5	493	31	54	362	833	107	10	616
Whitehill	KZF-12	107	40	10	<5	12	151	40	127	126	<5	15	23	6	1555	41	99	580	4991	125	15	960
Whitehill	KZF-13	103	32	20	<5	14	146	32	157	166	<5	16	25	9	727	66	127	766	2253	127	19	759
Whitehill	KZF-14	112	36	25	<5	16	141	35	153	195	<5	19	27	11	145	66	110	729	5936	120	16	840
Whitehill	KZF-15	116	48	25	5	13	128	29	202	155	<5	16	42	15	549	69	125	956	9411	126	19	658
PA-WH	KZF-16	67	13	<5	5	15	240	47	189	178	<5	29	24	<5	90	20	52	735	3553	102	13	1174
Whitehill	KZF-17	93	23	18	<5	12	131	35	147	127	<5	14	17	6	523	59	116	582	2140	127	19	582
Whitehill	KZF-18	87	32	24	<5	12	131	34	119	129	<5	14	23	11	363	66	110	661	3536	126	16	551
Whitehill	KZF-19	83	21	11	<5	14	150	31	120	131	<5	17	17	14	661	58	117	754	1618	117	19	620
Whitehill	KZF-20	79	24	16	<5	11	101	22	271	147	<5	11	25	12	1796	55	109	674	3984	152	21	642
Whitehill	KZF-21	127	52	16	7	17	261	42	166	194	<5	19	37	11	1211	39	91	1179	23495	109	18	939
PA-WH	KZF-22	29	43	8	<5	12	114	26	125	157	<5	21	40	13	220	32	59	1262	35603	126	9	898
PA	KZF-23	97	15	9	45	13	121	28	346	159	<5	18	20	9	8361	41	80	1245	19070	139	16	880
PA	KZF-24	59	24	6	<5	24	185	141	406	163	29	60	329	9	1095	15	83	2876	319	206	21	763
PA	KZF-25	33	22	<5	<5	23	234	58	203	181	<5	22	46	<5	551	24	72	644	285	109	15	922
PA	KZF-26	124	25	<5	<5	5	108	25	64	23	<5	10	28	32	31165	13	51	1411	335	195	9	290
PA	KZF-27	77	36	<5	<5	18	209	36	200	165	<5	15	21	<5	469	40	108	338	300	114	19	978
PA	KZF-28	45	21	<5	<5	<5	49	46	49	7	<5	5	15	35	90811	10	34	2432	397	142	3	284
PA	KZF-29	59	24	<5	<5	<5	60	37	127	5	<5	<5	14	18	76070	11	33	1989	341	186	12	145
PA	KZF-30	94	64	18	<5	19	238	53	134	153	<5	17	23	11	1566	72	109	361	374	119	21	966
PA	KZF-31	65	39	12	<5	15	220	43	115	137	<5	14	14	8	1103	42	84	322	298	126	17	790
PA	KZF-32	75	27	7	<5	12	71	85	610	25	<5	11	11	6	19085	46	49	7854	911	249	25	145
PA-Dwyka	KZF-33	58	36	8	<5	10	114	22	135	191	<5	16	18	<5	1363	68	100	591	295	106	15	806

Appendix A3c: XRF major element data for BH KWV-1 in wt%.

Formation	Sample	SiO2	TiO2	Al2O3	Fe2O3	MnO	MgO	CaO	Na2O	K2O	P2O5	SO3	Cr2O3	NiO
Collingham	KWV-1	59.79	0.68	19.11	5.15	0.06	1.39	0.66	2.30	4.34	0.18	0.06	b.d.	0.01
Collingham	KWV-2	61.22	0.66	16.97	5.65	0.08	1.32	0.50	2.24	3.95	0.17	0.13	b.d.	0.01
Collingham	KWV-3	68.37	0.46	12.87	5.60	0.21	0.86	0.89	2.98	2.25	0.18	0.23	b.d.	0.01
Collingham	KWV-4	71.10	0.48	13.50	3.04	0.03	0.72	0.40	3.02	2.59	0.12	0.03	b.d.	0.01
Collingham	KWV-5	62.29	0.57	20.27	4.92	0.16	1.31	1.07	1.63	4.58	0.13	0.02	0.01	0.02
Collingham	KWV-6	62.44	0.61	20.17	4.32	0.09	1.22	0.90	1.66	4.36	0.14	0.01	0.01	0.01
Collingham	KWV-7	64.25	0.43	17.42	5.17	0.12	1.12	1.33	1.10	3.47	0.07	0.04	0.01	0.01
Whitehill	KWV8A	51.00	0.99	14.90	11.56	0.18	6.84	10.69	2.31	0.57	0.18	0.07	0.05	0.02
Whitehill	KWV8B	51.38	0.49	13.37	10.39	0.06	1.29	1.54	1.72	2.54	0.16	0.10	0.01	0.01
Whitehill	KWV-9	54.65	0.59	15.51	7.77	0.05	1.91	2.71	0.93	2.48	0.25	0.17	0.01	0.01
Whitehill	KWV-10	51.60	0.62	16.90	13.60	0.08	1.21	1.48	2.47	3.28	0.20	0.05	0.01	0.01
Whitehill	KWV-11	55.71	0.60	16.42	7.60	0.07	1.19	0.83	1.78	3.77	0.18	0.05	0.01	0.01
Whitehill	KWV-12	51.57	0.64	17.35	11.16	0.04	2.17	1.69	0.81	3.13	0.42	0.23	0.01	0.01
Whitehill	KWV-13	24.90	0.02	0.42	8.47	0.40	7.56	30.14	-0.02	0.02	0.20	7.50	b.d.	0.01
Prince Albert	KWV-14	48.69	0.70	18.06	9.86	0.34	1.88	1.27	0.20	4.85	0.42	0.22	0.01	0.01
Prince Albert	KWV-15	56.30	0.69	19.50	8.96	0.56	1.28	5.28	0.76	1.87	0.12	0.22	0.01	0.01
Prince Albert	KWV-16	57.46	0.78	19.93	9.05	0.15	1.20	0.96	0.32	4.22	0.15	0.01	0.01	0.01
Prince Albert	KWV-17	59.55	0.63	18.78	9.58	0.14	1.10	0.69	0.31	3.85	0.09	0.01	b.d.	0.01

Appendix A3d: XRF trace element data for BH KWV-1 in ppm. Abbreviation: PA= Prince Albert Formation.

Formation	Sample	Zn	Cu	Ni	Mo	Nb	Zr	Y	Sr	Rb	U	Th	Pb	Co	Mn	Cr	V	F	S	Cl	Sc	Ba
Collingham	KWV-1	73	27	5	<5	23	268	39	180	196	<5	23	25	8	497	35	124	647	353	117	16	1091
Collingham	KWV-2	90	32	11	<5	16	195	38	152	175	<5	16	35	14	681	45	136	616	1278	112	16	1056
Collingham	KWV-3	54	25	12	<5	11	142	24	138	101	<5	14	15	14	1741	35	76	468	706	109	10	729
Collingham	KWV-4	70	24	6	<5	13	175	31	129	114	<5	14	17	<5	218	47	99	337	409	112	13	801
Collingham	KWV-5	116	23	7	<5	26	276	41	419	209	3	19	38	4	1290	54	88	725	280	105	17	1107
Collingham	KWV-6	91	37	<5	<5	21	197	32	421	204	7	23	27	2	717	38	80	655	285	113	12	1049
Collingham	KWV-7	88	24	9	<5	18	185	33	391	192	1	15	27	3	992	69	99	530	438	129	18	1049
Whitehill	KWV8A	84	76	68	<5	5	108	32	207	14	<5	<5	6	48	1502	339	251	554	526	218	41	233
Whitehill	KWV8B	74	127	44	29	16	173	66	254	134	10	20	65	22	653	71	204	896	16434	125	27	890
Whitehill	KWV-9	65	80	33	16	16	146	54	221	164	<5	18	35	13	635	65	140	585	8426	118	20	1380
Whitehill	KWV-10	263	69	26	10	14	166	44	263	129	5	19	84	15	552	64	107	960	14990	113	20	559
Whitehill	KWV-11	101	58	31	8	14	157	40	278	138	5	20	37	15	406	82	121	836	10319	125	21	983
Whitehill	KWV-12	103	69	32	10	16	148	35	253	174	5	22	55	19	343	72	134	963	13981	122	22	776
Whitehill	KWV-13	75	9	5	<5	1	32	14	449	1	<5	<5	11	-3	4096	17	30	933	17167	142	25	<5
PA	KWV-14	70	30	29	6	16	129	21	113	251	<5	16	26	16	3048	80	124	814	11865	123	18	1395
PA	KWV-15	109	53	14	<5	19	177	37	532	147	6	18	113	21	4766	67	190	644	782	121	25	561
PA	KWV-16	100	64	11	<5	16	209	35	142	211	<5	20	23	17	1330	60	180	520	297	116	22	747
PA	KWV-17	130	43	11	<5	18	200	36	112	185	<5	20	29	10	1226	40	111	510	328	136	20	847

Appendix A3e: XRF major element data for BH SFT1 in wt%.

Formation	Sample	SiO2	TiO2	Al2O3	Fe2O3	MnO	MgO	CaO	Na2O	K2O	P2O5	S (Eltra)
Collingham	G011485	64.70	0.52	12.30	4.88	0.20	1.09	3.83	2.13	1.88	0.16	0.03
Collingham	G011486	76.10	0.13	13.50	1.02	0.02	0.74	0.50	0.24	3.68	0.03	0.06
Collingham	G011487	81.10	0.09	9.50	0.86	0.03	0.46	0.60	0.19	2.54	0.04	0.08
Collingham	G011489	74.00	0.38	11.70	2.12	0.08	0.61	1.39	1.52	2.46	0.09	0.02
Whitehill	G011491	76.20	0.31	11.90	1.48	0.03	0.47	0.63	2.25	2.24	0.07	0.31
Whitehill	G011497	65.70	0.22	11.90	4.36	0.06	1.16	1.66	0.95	2.51	0.12	0.56
Whitehill	G011499	54.70	0.53	14.50	7.83	0.02	1.23	0.50	2.40	2.45	0.25	4.01
Whitehill	G011505	52.40	0.59	15.00	7.04	0.03	1.34	1.33	1.31	3.08	0.33	3.79
Whitehill	G011509	38.60	0.44	13.20	9.77	0.15	1.15	7.66	0.02	3.01	0.12	8.87
Whitehill	G011510	46.80	0.57	19.90	5.44	0.08	3.57	3.10	0.17	3.02	0.24	2.93
Prince Albert	G011518	53.30	0.61	15.70	7.97	0.05	2.15	1.08	0.06	3.23	0.37	3.90
Prince Albert	G011522	16.50	0.11	2.80	5.06	1.10	12.72	23.85	0.06	0.42	0.34	3.11
Prince Albert	G011528	62.70	0.49	18.30	6.63	0.15	1.12	0.58	0.50	2.82	0.41	0.02
Prince Albert	G011531	65.00	0.46	14.50	9.84	0.22	1.38	0.18	0.17	1.79	0.04	0.02

Appendix A3f: XRF trace element data for BH SFT2 in ppm.

Formation	Sample	Ba	Cr	Ga	Nb	Ni	Rb	Sr	V	Y	Zn	Zr
Collingham	G011485	338	19	15	12	14	94	337	55	22	88	155
Collingham	G011486	705	<10	18	14	<10	150	202	<10	24	25	166
Collingham	G011487	536	<10	11	<10	<10	113	157	<10	19	23	100
Collingham	G011489	625	26	15	16	<10	127	392	44	24	57	158
Whitehill	G011491	680	<10	16	12	11	106	172	42	27	72	152
Whitehill	G011497	599	<10	18	11	17	125	221	37	35	76	150
Whitehill	G011499	541	43	21	12	35	133	164	95	33	150	138
Whitehill	G011505	629	11	18	12	<10	141	536	44	33	87	252
Whitehill	G011509	817	36	26	18	27	157	196	74	35	171	319
Whitehill	G011510	817	36	26	18	27	157	196	74	35	171	319
Prince Albert	G011518	593	57	23	13	29	175	169	108	29	135	144
Prince Albert	G011522	192	<10	<10	<10	<10	32	1098	43	23	14	75
Prince Albert	G011528	767	32	25	14	<10	171	198	81	44	54	226
Prince Albert	G011531	518	21	21	10	19	125	189	64	22	87	172

Appendix A4- Trace element enrichment

Appendix A4: Enrichment of trace elements in BH KZF-1 and BH KWV-1. Abbreviations: PA= Prince Albert Formation; WH: Whitehill Formation

Formation	***Samples***	***EF Mn***	***EF Ba***	***EF Co***	***EF Cr***	***EF Cu***	***EF Mo***	***EF Ni***	***EF V***	***EF Zn***
Collingham	KZF-1	27.6	15.0	6.2	5.1	5.9	--	--	9.3	7.9
Collingham	KZF-2	14.0	16.5	9.9	5.1	7.0	--	2.3	10.5	8.4
Collingham	KZF-3	3.4	14.2	8.1	4.7	6.7	--	1.5	7.9	8.1
Collingham	KZF-4	115.9	14.2	3.4	7.4	6.7	--	1.8	8.8	7.5
Collingham	KZF-5	10.2	11.4	--	0.1	--	45.7	0.9	2.0	28.6
Collingham	KZF-6	6.7	16.2	--	4.8	9.4	--	0.9	10.4	9.7
Collingham	KZF-7	229.5	10.8	8.3	0.2	0.9	49.6	0.8	2.5	5.4
Collingham	KZF-8	6.6	17.7	6.0	5.3	10.5	--	1.4	10.2	10.5
Collingham	KZF-9	1291.0	18.8	7.5	6.6	11.8	--	1.7	9.2	6.6
Collingham	KZF-10	996.1	17.1	--	3.6	6.5	--	--	6.1	5.1
Collingham	KZF-11	26.9	13.8	--	5.0	6.2	--	--	6.0	6.8
Whitehill	KZF-12	15.2	17.3	3.7	5.3	10.5	--	1.8	8.9	13.2
Whitehill	KZF-13	244.0	12.7	5.1	7.9	7.8	--	3.2	10.6	11.8
Whitehill	KZF-14	15.4	12.4	5.5	7.1	7.8	--	3.5	8.1	11.3
Whitehill	KZF-15	7.5	11.7	8.9	8.9	12.2	42.6	4.2	11.1	14.1
PA-WH	KZF-16	0.9	14.8	--	1.9	2.4	32.8	--	3.3	5.8
Whitehill	KZF-17	8.0	11.6	4.2	8.4	6.5	--	3.5	11.6	12.6
Whitehill	KZF-18	5.2	10.2	6.7	8.8	8.6	--	4.2	10.2	11.0
Whitehill	KZF-19	8.2	10.1	7.8	6.9	5.1	--	1.6	9.5	9.3
Whitehill	KZF-20	27.7	13.0	8.2	8.0	7.1	--	3.0	11.0	10.9
Whitehill	KZF-21	13.2	13.4	5.2	4.0	10.7	50.6	2.2	6.5	12.4
PA- WH	KZF-22	2.7	14.6	7.1	3.8	10.0	--	1.3	4.8	3.3
Prince Albert	KZF-23	111.2	15.3	5.2	5.1	3.8	388.7	1.4	7.0	11.5
Prince Albert	KZF-24	10.2	9.3	3.9	1.4	4.3	--	0.7	5.1	4.9
Prince Albert	KZF-25	5.9	13.0	--	2.4	4.4	--	--	5.1	3.2
Prince Albert	KZF-26	737.0	9.0	34.3	3.0	11.1	--	--	7.9	26.2
Prince Albert	KZF-27	5.0	13.7	--	4.0	7.3	--	--	7.6	7.3
Prince Albert	KZF-28	4562.8	18.7	78.6	4.7	19.6	--	--	11.1	20.4
Prince Albert	KZF-29	3516.7	8.7	37.7	4.8	20.6	--	--	9.8	24.2
Prince Albert	KZF-30	17.3	13.9	5.5	7.5	13.3	--	2.5	7.9	9.2
Prince Albert	KZF-31	13.4	12.5	4.2	4.8	9.0	--	1.8	6.6	7.1
Prince Albert	KZF-32	649.2	6.4	8.7	14.7	17.3	--	3.0	11.0	22.7
PA/Dwyka	KZF-33	15.7	12.2	--	7.4	7.9	--	1.2	7.5	6.0
Collingham	KWV-1	11.5	14.8	3.8	3.4	5.3	--	0.6	8.4	6.7
Collingham	KWV-2	12.9	16.1	7.4	5.0	7.1	--	1.6	10.3	9.4
Collingham	KWV-3	38.4	14.6	9.3	5.0	7.1	--	2.4	7.7	7.4
Collingham	KWV-4	2.9	15.3	--	6.5	6.6	--	1.0	9.5	9.2
Collingham	KWV-05	20.4	14.1	1.6	5.0	4.2	--	0.9	5.6	10.1
Collingham	KWV-06	7.1	13.4	1.1	3.5	6.9	--	--	5.1	8.0
Collingham	KWV-07	7.4	15.6	1.6	7.4	5.2	--	1.2	7.4	8.9
Whitehill dolerite contact	KWV-08A	12.2	17.2	14.2	9.8	35.4	279.0	8.1	19.7	9.8
Whitehill dolerite contact	KWV-08B	4.5	23.0	7.5	7.8	19.3	132.1	5.3	11.7	7.5
Whitehill	KWV-09	5.8	8.5	8.0	7.1	15.3	73.7	3.8	8.2	27.5
Whitehill	KWV-10	18.7	15.5	8.1	9.4	13.3	62.6	4.6	9.5	10.9
Whitehill	KWV-11	8.3	11.6	9.9	7.8	14.8	72.1	4.5	10.0	10.5
Whitehill	KWV-13	6.0	20.0	8.0	8.2	6.3	40.4	4.0	8.9	6.8
Whitehill	KWV-14	0.9	7.4	9.7	6.4	10.1	--	1.8	12.6	9.9
Prince Albert	KWV-15	5.2	9.7	7.7	5.6	11.9	--	1.3	11.7	8.8
Prince Albert	KWV-16	3.8	11.6	4.5	4.0	8.6	--	1.4	7.6	12.2
Prince Albert	KWV-17	4.9	6.7	0.8	0.6	26.1	--	0.7	7.3	8.1

Appendix B- 1D models

Model Parameters

1D models were generated for BH KZF-1 and BH KWV-1 using PetroMod at RWTH Aachen University, to show the effect of basin burial and temperature variation in a basin over time (Figures 7.1; 7.2). The parameters required to create a 1D model are: 1) formation thickness; 2) estimated eroded thickness of overlying strata; 3) dates for burial; 4) subsidence and uplift events; 5) TOC and HI values; 6) dolerite intrusions; 7) lower Ecca Group porosity and 8) vitrinite reflectance. The 1D models were created based on the following information:

During the deposition of the Karoo Supergroup (~ 307.8 Ma to max. 183 Ma), tectonic events related to the formation of the Cape Fold Belt (CFB) occurred between 292 ± 5 Ma and 245 Ma, with the main phase of CFB deformation occurring ~ 258 Ma (Hälbich, 1983; de Wit & Ransome, 1992; Isbell et al., 2008; Linol et al., 2015; Hansma et al., 2015; Blewett & Phillips et al., 2016; Blewett et al., 2019). The initiation of the pan-Gondwanan mobile belt and the tectonic activity associated with loading and flexural subsidence started before the deposition of the Dwyka Group (Isbell et al., 2008). Later basin subsidence, during early Karoo sedimentation, in the Western Cape Province occurred ~ 292 ± 5 to 245 Ma and in the Eastern Cape Province from ~ 275 Ma to 208 Ma. (Cloetingh et al., 1989; 1992). The break-up of Gondwana began ~ 136 Ma (Martin & Hartnady, 1986; Eagles, 2007) and resulted in the intrusion of dolerite and outpouring of continental flood basalts, which occurred ~ 183 Ma (Hälbich, 1983; de Wit & Ransome, 1992). Erosion of the continent started after final dolerite intrusion. Periods of uplift and increased erosion occurred ~ 136 to 120 Ma; 130 to 115 Ma; 93 to 67 Ma and 86 to 78 Ma (Dingle et al., 1983; Tinker et al., 2008; Hanson et al., 2009).

For BH KZF-1 we infer that the Dwyka Group is ~ 342 m thick (e.g. Roswell & De Swart, 1976; Visser, 1997). The Prince Albert, Whitehill and Collingham Formations are ~ 318 m thick. In the location of BH KZF-1, where the Tierberg Formation is partially removed by erosion. The total thickness of the Tierberg Formation is 550 m thick in the Tankwa Karoo sub-basin. The overlying Skoorsteenberg Formation is ~ 400 m thick and overlying Waterford (Koedeosberg Formation) is 200 m thick (Wickens & Cole, 2017a, b). The Ecca Group in total is ~ 1468 m thick (Roswell and De Swart, 1976; Wickens 1984; Catuneanu et al., 2005; Alao, 2012; Belica et al., 2017). The Beaufort Group has also been completely removed from this area. However, if we assume a similar overlying thickness from the MKB, the total thickness

could be up to 7000 m. Assuming a widespread initial extend of the continental flood basalts (900 m), brings the total removed thickness to a maximum of 8961 m. Additionally, the thrust faulting, vitrinite reflectance, porosity data and formation ages were included in the model.

BH KWV-1 is 2353 m deep. The Prince Albert, Whitehill and Collingham Formations are 134 m thick. The overlying Ripon Formation is 1286 m thick and the Fort Brown Formation is 481 m thick. BH KWV-1 is capped by the Koonap Formation of the Beaufort Group and is 212 m thick. The thickness of the remaining Beaufort Group strata that were removed by erosion was probably ~ 3600 m. The thickness of removed Stormberg Group strata was probably ~ 1380 m and the thickness of Drakensburg Group Basalts around ~ 1370 m. This brings the total thickness of formations removed by erosion to ~ 6350 m (Visser, 1994; Smith et al., 1993; Johnson et al., 2006; Catuneanu et al., 2005). BH KWV-1 has 18 dolerite intrusions from 0.03 m to 149 m in thickness and a total thickness of 408.09 m. Crystallization heat of dolerite intrusion is 1185 MJ/m^3. Intrusion temperature is 1300 °C, solidus temperature is 700 °C, magma density is 3000 kg/m^3 with magma heat capacity of 0.36 kcal/kg/K (Neumann et al., 2011).

Results and interpretation

According to a 1D model for BH KZF-1 (Figure 7.1), the Prince Albert Formation could have reached a temperature of 277 °C, ~ 181 Ma ago. The 1D model for BH KWV-1 (Figure 7.2), suggests that the lower Ecca Group could have reached a temperature of 1120.35 °C ~ 180 Ma ago

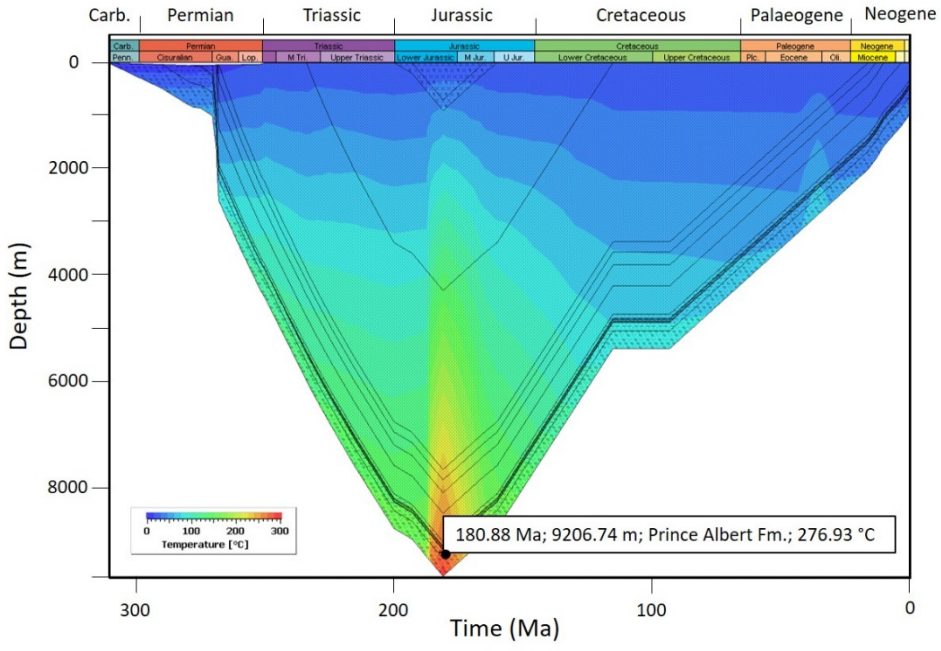

Figure 1: 1D models indicating that the lower Ecca Group in the Tankwa Karoo sub-basin reached a maximum temperature of 276.93 °C ca. 180.88 Ma ago.

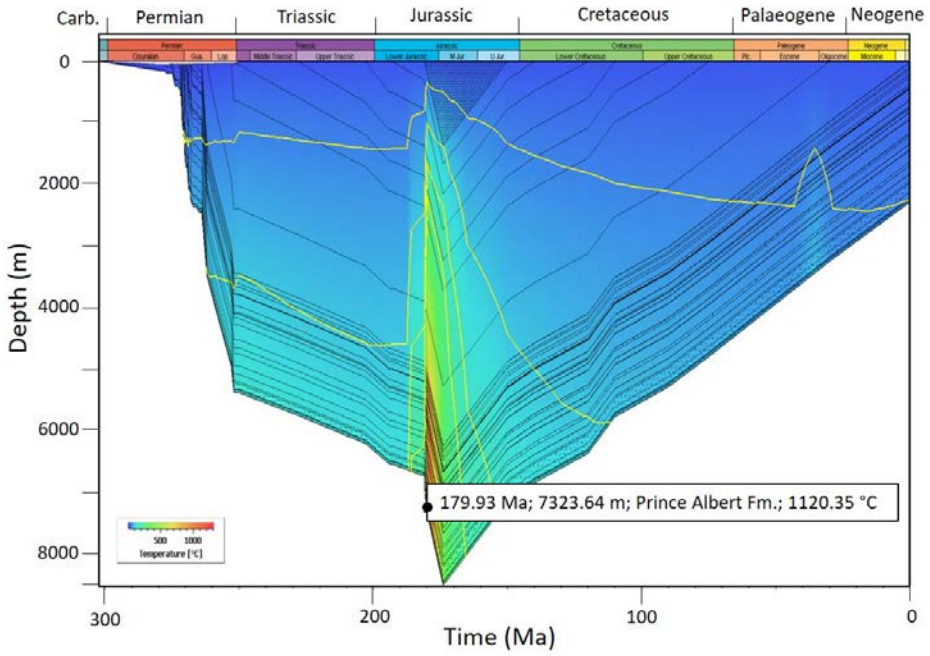

Figure 2: 1D models indicating that the lower Ecca Group in the eastern main Karoo Basin reached a maximum temperature of 1120.35 °C ca. 179.93 Ma ago.

Appendix C- Gamma-ray logs

Methods

Gamma-ray (GR) well-logs were obtained for BH KZF-1 and BH KWV-1 by Weatherford Exploration Services. The GR logs are smoothed to 50 window points using the adjacent average smoothing method. Statistical analyses with GR logs, measure the natural radioactivity of rocks and are useful in determining rock lithology and depositional environments (Selley, 1976; 1978). However, interpretation must be done with care (Rider, 1990). Natural gamma radiation is detected in K, U and Th. K-feldspars, micas and illitic clays are rich in K, while Th is often detected in sand- and silt- sized heavy minerals that are concentrated in clays or phosphates and U is hosted by heavy minerals, but can be enriched in anoxic, organic-rich sediments (Myers & Wignall, 1987; Anderson et al., 1989). Quartz does not have radioactive elements and should have low log values. Therefore, it has been assumed that high log values are associated with fine-grained minerals and low values with coarser-grained minerals. Using this logic, GR log profiles can be used to distinguish between depositional facies. However, interpretation becomes complicated in sedimentary rocks that have a mixture of quartz and clay minerals. In this case the gamma radiation omitted will remain high (Rider, 1990). Therefore, the GR reading is rather a function of mineralogy than a function of grain size (Myers & Bristow, 1989).

Results and interpretation

GR logs, U (ppm), Th (ppm), K (wt%) data and Th/K ratios are tabulated in Table 7.1 and are compared in Figures 7.3 and 7.4. U values are low in both boreholes and therefore are excluded from the depth profiles.

In BH KZF-1, U content is below 5 ppm. In BH KWV-1, U was detected in small amounts in the lower Collingham Formation (1–7 ppm) and the Whitehill Formation (5–10 ppm). The Prince Albert Formation had the highest U content ranging from 5–77 ppm, with the highest U content (77 ppm) detected in the lowermost sample (Table 1). Overall, the GR signatures for the lower Ecca Group have high API values, which are indicative of high clay-mineral contents.

In BH KZF-1, the GR signature (Figure 7.3) has the highest peaks in the lower 25 m of the Prince Albert Formation, which correlates with high apatite, birnessite and rhodochrosite content detected by XRD (see Chapter 2). The GR log in the Whitehill Formation is interrupted by thrust faulting.

The Th content is higher in BH KZF-1 than in BH KWV-1. In BH KZF-1 the Th signals show the greatest fluctuation within the Whitehill and Collingham Formations. Whereas, K content fluctuates greatly in the Prince Albert and Collingham Formations and is more consistent in the Whitehill Formation. Th/K ratios can be correlated with the decrease in quartz/feldspar ratio and therefore an increase in grain size. The increasing Th/K ratio detected in the Prince Albert Formation indicates that the grain size increases towards the top of the formation. In the Whitehill Formation, the Th/K ratio fluctuates significantly, due to the thrust faulting, and accurate trends are difficult to determine due to hydrothermal-mineral enrichment.

In BH KWV-1, the GR log (Figure 7.4) the GR readings are difficult to evaluate in the Whitehill Formation, due to the dolerite intrusion. Overall Th content in BH KWV-1 does not exhibit high variation, except for in sample KWV17 at the bottom of the Prince Albert Formation, which displays a high Th peak, as well as being high in U (77 ppm). Th/K ratios decrease where GR trends increase, which corresponds to the coarsening-upward grain-size trend for the Prince Albert Formation, the fining-upward grain-size trend for the Whitehill Formation, and the grain-size fluctuations observed in the Collingham Formation.

The GR log from the bottom 10 m of the Prince Albert Formation in both BH KZF-1 and BH KWV-1, shows an initial increase in API values. This represents an increase in coarser-grained minerals being introduced to the basin after initial glacial melt. Th is correlated with clay minerals, feldspars, micas, phosphates (fluorapatite), heavy minerals and apatite (Ruffell et al., 2006). The high apatite content in the lower Prince Albert Formation is partly responsible for the high GR peaks and is indicative of the phosphogenesis of erosional organic matter-rich sediments being introduced into the basin (Trappe, 2001; Schulz et al., 2018).

The GR log for the Whitehill Formation in BH KZF-1 is difficult to interpret due to thrust faulting and in BH KWV-1, the Whitehill Formation GR log is disturbed by a dolerite intrusion.

Although the Collingham Formation has a high overall quartz content (45–52 wt%), the API values also remain high. This is a response to the increased amount of tuffaceous material (K-bentonite) in the Collingham Formation. An increase in Th/K ratios is correlated with tuffaceous material, which is rich in zircons.

API values from GR logs and Th/K ratios from BH KZF-1, show greater fluctuations in the Prince Albert and Collingham Formations than in BH KWV-1, due to both the proximity to orogenic loading, as well as to the source of the tuffaceous material

(Patagonia, South America; Hälbich, 1983; Tankard et al., 2012 ; Navarrete et al., 2019).

Table 1: U, Th, K and Th/K ratios for BH KZF-1 and BH KWV-1.

BH KZF-1	U	Th	K	Th/K	BH KWV-1	U	Th	K	Th/K
KZF-1	<5	12,8	2,3	5,6	KWV-1	<5	22,7	3,6	6,3
KZF-2	<5	17,5	3,3	5,3	KWV-2	<5	15,9	3,3	4,9
KZF-3	<5	14,7	1,9	7,9	KWV-3	<5	13,5	1,9	7,2
KZF-4	<5	14,4	2,4	6,1	KWV-4	<5	13,7	2,1	6,4
KZF-5	<5	25,9	4,4	5,8	KWV-05	2,7	18,9	3,8	5
KZF-6	<5	16,1	2,8	5,8	KWV-06	7,4	23,1	3,6	6,4
KZF-7	<5	43,2	5,7	7,6	KWV-07	1,1	14,5	2,9	5
KZF-8	<5	13,5	2,4	5,6	KWV-08A	10,5	20,4	2,1	9,7
KZF-9	<5	12,1	2,8	4,4	KWV-08B	<5	18,3	2,1	8,9
KZF-10	<5	15,4	2,8	5,5	KWV-09	5	19,1	2,7	7
KZF-11	<5	12,7	1,5	8,2	KWV-10	4,8	20,4	3,1	6,5
KZF-12	<5	14,6	2,3	6,3	KWV-11	5,2	21,5	2,6	8,3
KZF-13	<5	15,8	2,8	5,6	KWV-13	<5	15,9	4	4
KZF-14	<5	18,8	3,3	5,7	KWV-14	5,6	18	1,6	11,6
KZF-15	<5	16,4	2,5	6,5	KWV-15	<5	19,6	3,5	5,6
KZF-16	<5	28,6	3,4	8,4	KWV-16	<5	20,4	3,2	6,4
KZF-17	<5	14,2	2	7,2	KWV-17	77	40,6	5,8	7
KZF-18	<5	14,4	2	7,3					
KZF-19	<5	17,1	2,2	7,8					
KZF-20	<5	11,4	2,4	4,7					
KZF-21	<5	18,5	3,1	5,9					
KZF-22	<5	21,1	2,6	8					
KZF-23	<5	18,1	2,6	6,9					
KZF-24	28,9	60,1	2,5	24,2					
KZF-25	<5	22	2,6	8,6					
KZF-26	<5	10,1	0,3	33,8					
KZF-27	<5	14,6	2,4	6					
KZF-28	<5	4,9	0	106					
KZF29	<5	0	0	--					
KZF-30	<5	17	2,8	6					
KZF-31	<5	13,9	2,7	5,2					
KZF-32	<5	10,6	0,4	25,4					
KZF-33	<5	16,1	3,4	4,7					

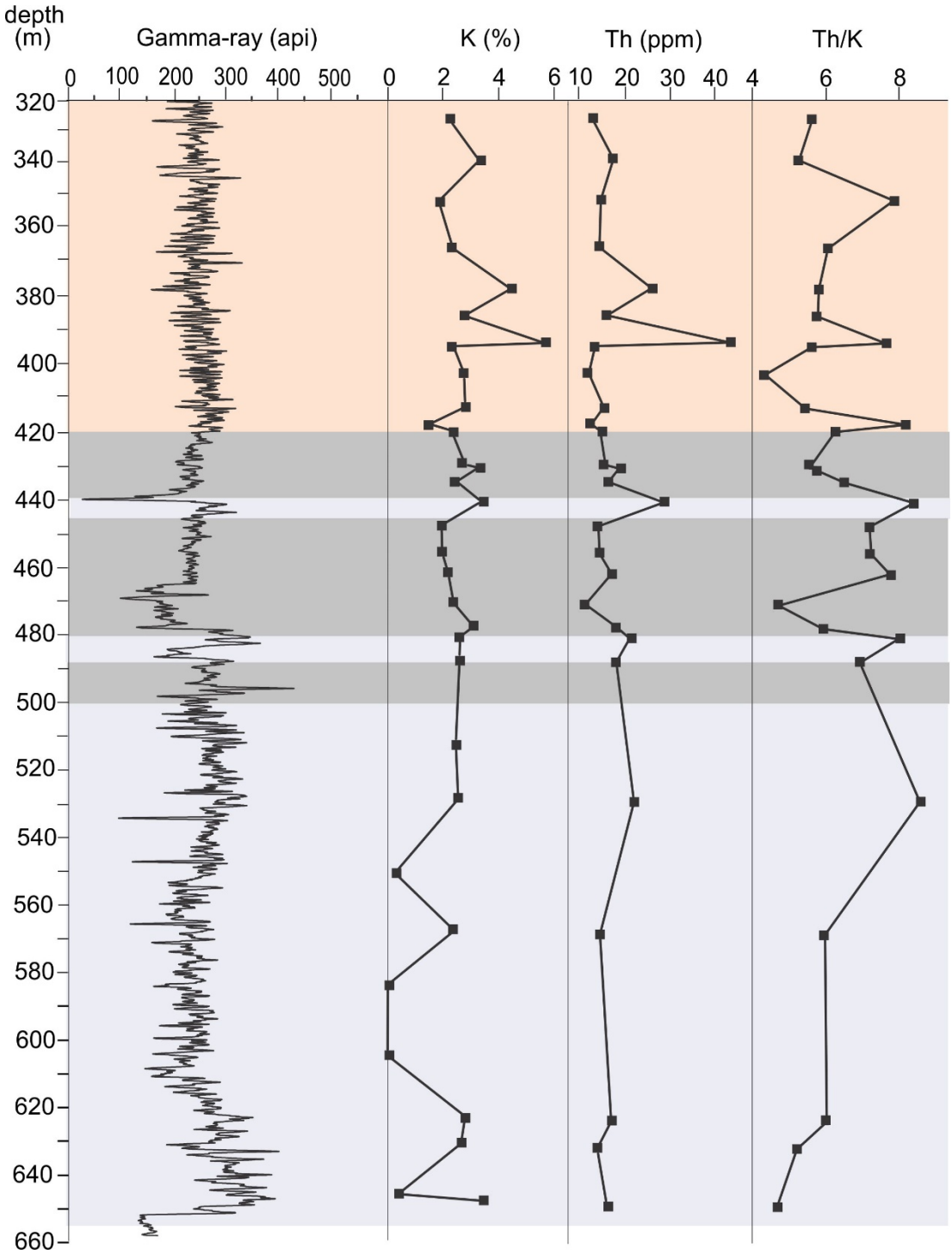

Figure 3: Depth profile for BH KZF-1 showing gamma-ray log, Th and K trends and Th/K ratios.

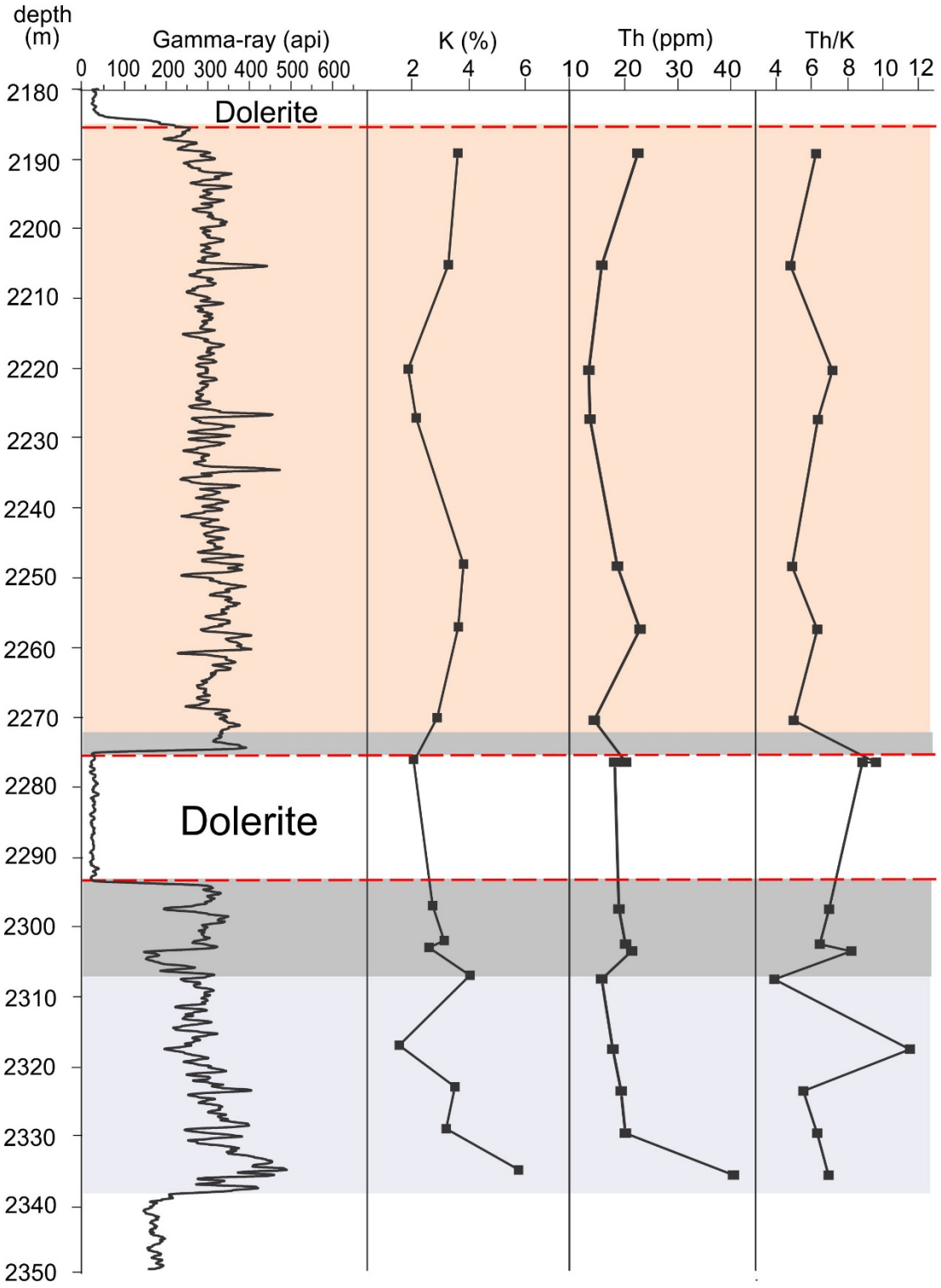

Figure 4: Depth profile for BH KWV-1 showing gamma-ray log, Th and K trends and Th/K ratios

References

Alao, A.O. 2012. *Basinfill of the Permian Tanqua Depocenter, SW Karoo Basin, South Africa*. M.Sc. Thesis. Stellenbosch University, South Africa. 168p.

Anderson, R.F., LeHuray, A.P., Fleisher, M.Q. & Murray, J.W. 1989. Uranium deposition in the Saanich Inlet sediments, Vancouver Island. *Geochimica et Cosmochimica Acta*. 53: 2205–2213.

Belica, M.E., Tohver, E., Poyatos-Moré, M., Flint, S., Parra-Avila, L.A., Lanci, L., Denyszyn, S. & Pisarevsky, S.A. 2017. Refining the chronostratigraphy of the Karoo Basin, South Africa: magnetostratigraphic constraints support an Early Permian age for the Ecca Group. *Geophysical Journal International*. 211(3): 1354–1374.

Blewett, S.C.J. & Phillips, D. 2016. An overview of Cape Fold Belt geochronology: Implications for sediment provenance and the timing of orogenesis. In *Origin and evolution of the Cape Mountains and Karoo Basin: Geo-biohistory in a terrain with shale gas resources and need for conservation.* B. Linol & M. de Wit (Eds). Part of the series Regional Geology Reviews. 8643: 45-55.

Blewett, S.C.J., Phillips, D. & Matchan. E.L. 2019. Provenance of Cape Supergroup sediments and timing of Cape Fold Belt orogenesis: Constraints from high-precision $^{40}Ar/^{39}Ar$ dating of muscovite. *Gondwana Research*. 70: 201–221.

Catuneanu, O., Wopfner, H., Eriksson, P.G., Cairncross, B., Rubidge, B.S., Smith R.M.H. & Hancox P.J. 2005. The Karoo basins of south-central Africa. *Journal of African Earth Sciences*. 43: 211–253.

Cloetingh, S., Kooi, H. & Groenewoud, W. 1989. Intraplate stress and sedimentary basin evolution. In *Origin and evolution of sedimentary basins and their energy and mineral resources*. R.A. Price, Ed. American Geophysical Union, Geophysical Monograph. 48: 1–16.

Cloetingh, S., Lankreijer., A.,de Wit., M.J., & Matrinez, I. 1992. Subsidence history analysis and forward modelling of the Cape and Karoo Supergroups. In *Inversion tectonics of the Cape Fold Belt, Karoo and Cretaceous basins of Southern Africa*. M.J. de Wit & I.D.G. Ransome, Eds. Rotterdam: Balkema. 239–248.

de Wit, M.J. & I.G.D. Ransome, 1992. Regional inversion tectonics along the southern margin of Gondwana. In *Inversion Tectonics of the Cape Fold Belt, Karoo and Cretaceous Basins of Southern Africa*. M.J. de Wit & I.G.D. Ransome, Eds. Netherlands: Balkema. 15–20.

Dingle, R.V., Siesser, W.G. & Newton, A.R. 1983. *Mesozoic and Tertiary Geology of Southern Africa. A Global Approach to Geology.* Rotterdam: Balkema. 375p.

Eagles, G. 2007. New angles on South Atlantic opening. *Geophysical Journal International*. 166: 353–361.

Hälbich, H. 1983. A tectogenesis of the Cape Fold Belt CFB. *Special publication - Geological Society of South Africa*. 12: 165–175.

Hansma, J., E. Tohver, C. Schrank, F. Jourdan, and D. Adams. 2015. The Timing of the Cape Orogeny: New $^{40}Ar/^{39}Ar$ age constraints on deformation and cooling of the Cape Fold Belt, South Africa. *Gondwana Research.* 32: 122–137.

Hanson, E.K., Moore, J.M., Bordy, E.M., Marsh, J.S., Howarth, G. & Robey, J.V.A. Cretaceous erosion in central South Africa: evidence from the upper-crustal xenoliths in Kimberlite diatremes. *South African Journal of Geology*. 112 (2): 125–140.

Isbell, J.L., Cole, D.I. & Catuneanu, I. 2008. Carboniferous-Permian glaciation in the main Karoo Basin, South Africa: Stratigraphy, depositional controls, and glacial dynamics. In *Resolving the Late Paleozoic ice age in time and space*. C.R. Fielding, T.D. Frank. & J.L. Isbell, Eds. Geological Society of America Special Paper. 441:71–82.

Johnson, M.R., Van Vuuren, C.J., Visser, J.N.J., Cole, D.I., Wickens, H. deV., Christie, A.D.M., Roberts, D.L. & Brandl, G. 2006. Sedimentary rocks of the Karoo Supergroup. In *The Geology of South Africa*. M.R. Johnson, C.R., Anhaeusser & R.J. Thomas, Eds. Johannesburg: Geological Society of South Africa/Council for Geoscience. 461–499.

Linol, B., de Wit, M.J., Milani, E. J., Guillocheau, F. & Scherer, C. 2015. New regional correlations between the Congo, Parana´ and Cape-Karoo Basins of Southwest Gondwana In *Geology and Resource Potential of the Congo Basin, Regional Geology Reviews*. M.J. de Wit, F. Guillocheau & M.C.J. de Wit, Eds. Germany: Springer-Verlag. 245–268

Martin, A.K. & Hartnady, C.J.H. 1986. Plate tectonic development of the southwest Indian Ocean—a revised reconstruction of east Antarctica and Africa. *Journal of Geophysical Research*. 91: 4767–4786.

Myers, K.J. & Wignall, P.B. 1987. Understanding Jurassic organic-rich mudrocks – new concepts using gamma-ray spectrometry and palaeoecology: examples from the Kimmeridge Clay of Dorset and Jet Rock of Yorkshire. In *Marine Clastic Sedimentology: Concepts and Case Studies*. J.K. Leggett & G.G. Zuffa, Eds. London: Graham & Trotman. 172–189.

Myers K. J. & Bristow C. S. 1989. Detailed sedimentology and gamma-ray log characteristics of a Namurian deltaic succession II: Gamma-ray logging. *Geological Society, London, Special Publications*. 41: 81–88.

Navarrete, C., Gianna, G., Encinas, A., Márquez, M., Kamerbeek., Y., Valle, M. & Folguera, A. 2019. Triassic to Middle Jurassic geodynamic evolution of southwestern Gondwana: From a large flat-slab to mantle plume suction in a rollback subduction setting. *Earth-Science Reviews*. 194: 12–159.

Neumann, E-R., Svensen, H., Galerne, C.Y. & Planke, S. 2011. Multistage evolution of dolerites in the Karoo Large Igneous Province, Central South Africa. *Journal of Petrology*. 52: 959–984.

Rider, M.H. 1990. Gamma-ray log shape used as a facies indicator: critical analysis of an oversimplified methodology. *Geological Society, London, Special Publications*. 48: 27–37.

Ruffell, A., Mckinley, J.M., Lloyd C.D. & Graham, C. 2006. Th/K and Th/U ratios from spectral gamma-ray surveys improve the mapped definition of subsurface structures. *Journal of Environmental and Engineering Geophysics*. 11: 53–61.

Roswell, D.M. & De Swart, A.M.J.1976. Diagenesis in Cape and Karroo sediments, South Africa, and its bearing on their hydrocarbon potential. *Transactions of the Geology Society of South Africa*. 79: 81–145.

Schulz, H-M., Linol, B, de Wit, M., Schuck, B., Schaepan, I & Wirth, R. 2018. Early diagenetic signals archived in black shales of the Dwyka and lower Ecca Groups of the southern Karoo Basin (South Africa): Keys to the deglaciation history of Gondwana during the Early Permian, and its effect on potential gas storage. *South African Journal of Geology*.121 (1): 69–94.

Selley, R. C. 1976. Subsurface environmental analysis of North Sea sediments. *Bulletin of the AAPG*. 60: 184–195.

Selley, R.C. 1978. Concepts and methods of subsurface facies analysis. USA: AAPG continuing education course note series No. 9. 82p.

Smith, R.M.H, Eriksson, P.G. & Botha, W.J. 1993. A review of the stratigraphy and sedimentary environments of the Karoo-aged basins of Southern Africa. *Journal of African Earth Sciences*. 16: 143–169.

Tankard, A., Welsink, H., Aukes, P., Newton, R. & Stattker, E. 2012. Geodynamic interpretation of the Cape and Karoo basins, South Africa. In *Phanerozoic Passive Margins, Cratonic Basins and Global Tectonics Maps*. D.G. Roberts, Ed. USA & UK: Elsevier. 869–932.

Tinker, J., de Wit, M. & Brown, R. 2008. Mesosoic exhumation of the southern Cape, South Africa, quantified using apatite fission track thermochronology. *Tectonophyiscs*. 455: 77–93.

Trappe, J. 2001. A nomenclature system for granular phosphate rocks according to depositional texture. Sedimentary Geology. 145: 135–150.

Visser, J.N.J. 1994. A Permian argillaceous syn- to post-glacial foreland sequence in the Karoo Basin, South Africa. In *Earth's Gacial Record: International Geological Correlation Project 260*. M. Deynoux, J.M.G. Miller, E.W. Domack, N. Eyles, I.J. Fairchild & G.M. Young, Eds. Cambridge: Cambridge University Press. 193–203.

Visser, J. N. J. 1997. Deglaciation sequences in the Permo-Carboniferous Karoo and Kalahari basins of southern Africa: a tool in the analysis of cyclic glaciomarine basin fills. *Sedimentology*. 44 (3): 507–521.

Wickens, H. DeV. 1994. *Basin floor fan building turbidites of southwestern Karoo Basin, Permian Ecca Group, South Africa*. Ph.D Thesis. University of Port Elizabeth. 223p.

Wickens, H. de V. & Cole, D.I. 2017a. Lithostratigraphy of the Kookfontein Formation (Ecca Group, Karoo Supergroup), South Africa. *South African Journal of Geology*. 120 (3): 447–458.

Wickens, H. de V. & Cole, D.I. 2017b. Lithostratigraphy of the Skoorsteenberg Formation (Ecca Group, Karoo Supergroup), South Africa. *South African Journal of Geology*. 120 (3): 433–446.